The State of Stress as Inferred from Deviated Boreholes: Constraints on the Tectonics of Offshore Central California and Cook Inlet, Alaska

Thesis by

Blair J. Zajac, Jr.

In Partial Fulfillment of the Requirements

for the Degree of

Doctor of Philosophy

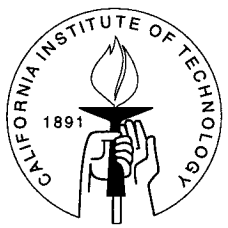

Caltech

Pasadena, California

1998

(Submitted May 13, 1997)

Portions published as Zajac, B. J., and J. M. Stock, *J. Geophys. Res., 102*(B5), 10,083–10,100, 1997 and

Acknowledgements

If I was to acknowledge everyone who contributed to the completion of this work, it would take as long as it took to write the thesis. Up front, I want to apologize to anyone omitted here; the time is to blame, the memories pass. To all those who contributed, my most profound appreciation.

First and foremost, I want to acknowledge two people whose love, support, and belief in me made this dream possible, my Mom and Dad, Barbara and Blair Zajac. I am eternally grateful to them. And to my brother Bard, thanks for patiently listening to my complaining and for your love and support.

To Ashley, my life partner, without whose loving support I would have never completed this task, my everlasting gratitude. She prodded me on when I needed it, adding her unique touch of finesse to keep the project moving. She has opened my heart to a world of love, passion, and commitment I never knew. I bless every day that I am with her.

Thanks to Joann Stock, my advisor, who through patience, professionalism, and academic expertise, guided me through this journey, allowing me to develop my own scientific interests, to pursue them, and integrate them in this body of work. I thank Rob Clayton, who always kept me on course when things got rough. I acknowledge the charming Tom Ahrens, who irked me by constantly asking more from me than I wanted to deliver.

My profound gratitude goes to my fellow collaborator, Julie Shemeta, who worked with me on the initial development of this work. I greatly appreciate Melita Wilde and Martha Kuykendall's work. They digitized my paper well logs saved my back from a tedious job.

My thanks go to Mitch Edwards and Pericles Rellas for their diligent support and phone calls, and to Karin Bellomy for her patience. To my fellow cohorts at Caltech who made my stay bearable, Hong Kie Thio, David Wald, and Bruce Worden, my thanks. And to all of those who persuaded me to stay and not give up, Petr Pich and Don Banfield, my thanks. To those who did not have a direct connection with my thesis, such as Richard Fagen, Cheryl Contopulos, Jean Grinols, and Jim Bys, I express my thanks for their generosities. My thanks goes to Ann Freemen, the den mother of the Seismo Lab, whose care and concern brought warmth to a busy place. My final thanks goes to Landmark Education Corporation, where I learned that anything is possible when one is committed.

Abstract

This thesis introduces a new method of constraining the vector directions of the three principal stresses and their relative magnitudes, by using borehole breakouts in non-vertical drill holes. Unlike older stress state measurements from breakouts, this work does not presume that one of the principal stresses is vertical. This method has important uses in complicated three-dimensional structures, such as in the Los Angeles basin, and in oil drilling applications.

Chapter 1 discusses why knowledge of the three-dimensional stress tensor is relevant to today's science and examines the applications of the stress state determination technique discussed herein. The history of previous work is also described.

In Chapter 2 I discuss the techniques of determining the stress tensor from borehole breakouts, examining the physics of borehole breakouts, the theory of the inversion technique used, and data processing issues. The theory and data processing issues are not discussed separately in this work, since data processing issues often prompted new theoretical techniques. I first examine the physics of borehole breakouts and how the orientation of breakouts on the borehole wall relates to the local stress field. A new borehole breakout selection scheme which takes into account highly non-vertical boreholes is then presented along with a discussion of the real world problems of data gathering, identification, and processing. Having selected a borehole breakout data set using the criteria, I invert for the best fitting stress state using a new technique combining genetic algorithms and non-differential function optimizers. Finally, I present a way in which 95% confidence limits can be placed on the resulting stress tensor.

With all of the technical and theoretical pieces in place, I now examine several different data sets. Chapter 3 examines a borehole breakout data set publish by *Qian and Pedersen* [1991] from the Siljan Deep Drilling Project in Sweden and demonstrates that even for simple borehole breakout data sets, the stress state inversions assuming a vertical principal stress direction may fall outside of the 95% confidence limits of an inversion allowing non-vertical principal stress directions. My technique of displaying the borehole breakout data makes the data quality more obvious as compared to the way *Qian and Pedersen* [1991] plotted the data.

Chapter 4 examines a borehole breakout data set from the offshore Santa Maria Basin, California. This analysis presents vertical borehole breakout data that represent a maximum horizontal principal stress direction of N7°E, roughly consistent with other earthquake focal mechanism, GPS, and borehole breakout studies in the area. However, the stress state inversion of breakouts identified in the vertical and a limited number of nearly horizontal boreholes suggests a stress state very different

from any other stress state results. This could imply that the three dimensional stress in the Santa Maria Basin is very complicated. However, given the limited amount of borehole breakouts identified in nearly horizontal wells, the stress state results from this data set are inconclusive.

Chapter 5 examines the largest data set used in this study, from a series of oil wells in Cook Inlet, Alaska. These are borehole caliper arm data from 21 different wells reaching a maximum deviation of 54° and 3,223 m true vertical depth. Stress state inversions of 31 different subsets of the borehole breakout data were performed. Inversion of breakouts identified in the top two of three marker beds analyzed in wells drilled from the Baker platform identified nearly degenerate thrust faulting stress states with the maximum principal stress axis, S_1, oriented horizontally WNW–ESE, perpendicular to the NNE-trending anticlinal structures. The stress state from the deepest marker is also a nearly degenerate thrust faulting stress state with S_1 oriented NNW–SSE, aligned with the regional direction of relative plate motion between the North American and Pacific plates. In between the shallow and deep stress state is an apparent normal faulting stress state with S_2 oriented subhorizontally ENE–WSW. This clockwise rotation of the stress tensor as a function of depth suggests that the stress field changes with depth, from a shallow stress state responsible for the local NNE-trending structures to a deeper one from the North American and Pacific plates' collision zone. The observed normal faulting stress state between the two thrust faulting stress states is anomalous and may represent some sort of transition from the shallow to the deep stress state. Stress state profiles in 500 m true vertical depth (TVD) intervals show consistently oriented thrust faulting stress regimes with NNW–SSE trending S_1 azimuths. The thrust faulting S_3 principal stress direction is consistently within 30° of vertical, suggesting that while the assumption of a purely vertical principal stress direction is not valid, the stress tensor does not significantly rotate away from the surface conditions that require a purely vertical stress tensor. The nearly degenerate thrust faulting stress states determined from the Granite Point and the 10.8 km distant Baker platform breakouts are nearly identical, implying that the technique of using deviated borehole breakouts to invert for the regional stress is valid. The orientations of the maximum horizontal stress determined from the Cook Inlet borehole breakouts are consistent with other stress indicators in south-central Alaska and consistent with the direction of relative plate motion between the North American Plate and the Pacific plate. The S_1 axis for the Cook Inlet field trends due south plunging 3°. The 95% confidence limits allow the S_1 azimuth to vary from N156°E to N195°E and the plunge to vary from 10° to -4°. This stress state does not appear representative of the stress field for each subset of breakouts. The Granite Point S_1 axis trends N19°W plunging 3°; the 95% confidence limits allow the azimuth to vary from N42°W to N7°E and the plunge to vary from 1° to 6°. The Baker platform S_1 axis trends N170°E plunging 8°; the 95% confidence limits on S_1 allow its azimuth to vary from N139°E to N191°E and its plunge to vary from 1° to 15°. Finally, the Dillon platform S_1 axis trends N69°W plunging 2°; the 95% confidence limits constrain the S_1 azimuth from N268°E to N324°E

and the plunge from 8° to -4°. The more westerly orientation of S_1 at the Dillon platform may be related to the local NNE-trending anticlinal structures in the Cook Inlet Basin.

Chapter 6 concludes and summarized the results and conclusions from the thesis.

The first appendix contains in minute detail some of the mathematics describing the boreholes, breakouts, and coordinate system rotations used to perform this work. The second appendix contains the individual discussion and plots of the raw dipmeter data from all of the Cook Inlet, Alaska wells.

Contents

List of Figures

List of Tables

Chapter 1 Introduction

1.1 Objective and Motivation

An understanding of the state of stress in the earth is important for many different fields including plate tectonics, oil production, seismic hazards, and mining. Improvements in the knowledge of regional states of stress provide baseline stress measurements for understanding future earthquakes and comparing the state of stress before and after earthquakes. The stress state is also important in understanding seismic and aseismic faulting, and the rheology of crustal and upper mantle materials. Assessments of seismic hazards, mine stability, and underground waste containment [*Stock et al.*, 1985] all require stress measurements. Finally, the state of stress plays an important role in many different aspects of oil production including proper well path design to most effectively produce oil and avoid borehole failure [*Addis et al.*, 1993; *Peška and Zoback*, 1995], using proper mud weight to avoid borehole failure [*Addis et al.*, 1993], and the prediction of the direction of hydraulic fractures.

Currently many different data are available for determining the stress in the earth including fault slip data [*Angelier*, 1984; *Michael*, 1984], focal mechanisms [*Michael*, 1987], stress induced borehole breakouts [*Zajac and Stock*, 1997; this thesis, 1997), and *in-situ* hydraulic fractures [e.g., *Haimson and Fairhurst*, 1970; *Stock et al.*, 1985]. This thesis introduces a new method of constraining the vector directions of the three principal stresses and their relative magnitudes, by using borehole breakouts identified in many, differently oriented, nonvertical boreholes. Borehole breakouts are two zones on opposites sides of an otherwise cylindrical borehole, where fracture and spalling have enlarged it in cross section from a circular to roughly an elliptical shape (Figure 1.1) [*Mastin*, 1984].

I begin by reviewing some of the previous work in understanding borehole breakout formation and in utilizing borehole breakouts to constrain the regional stress state. The first studies of the shape of the borehole wall, using four-arm dipmeters, showed that borehole breakouts are a common feature in boreholes and showed a consistent orientation over large geographic areas [*Bell and Gough*, 1979]. *Bell and Gough* [1979] examined a highly consistent data set of NW–SE oriented borehole breakout observations from Alberta, western Canada observed over a 3 x 10^5 km^2 region. *Bell and Gough* [1979] assumed that one of the principal stress directions was vertical and that the breakouts will form centered at the azimuth of greatest compressive stress at the borehole wall. The Kirsch equations that describe the stress concentration around a circular hole in a stressed medium show that the location of the greatest compressive stress on the borehole wall occurs 90° away from the orientation of the far-field horizontal maximum principal stress direction. The orientation of borehole breakouts

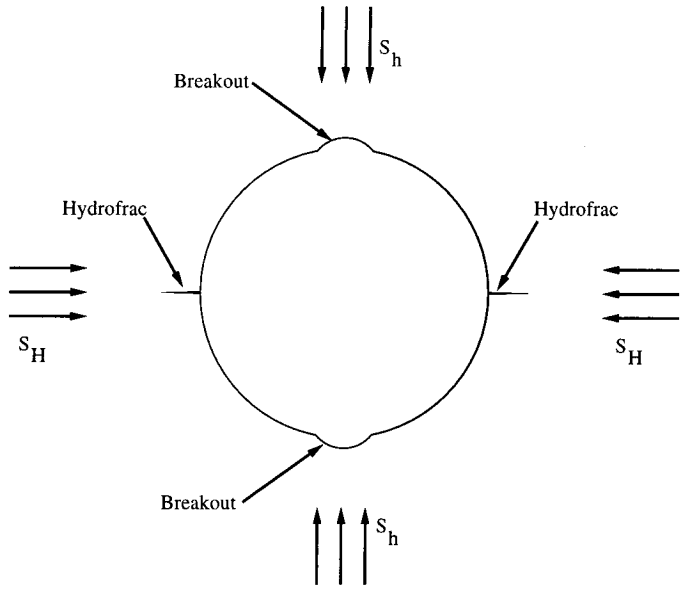

Figure 1.1: Cross section of a borehole showing the predicted orientation of the minimum and maximum principal stress directions and the locations of borehole breakouts and hydrofractures in the borehole assuming that the borehole axis is parallel to one of the principal stress directions. Borehole breakout shapes are highly irregular and may not appear as the breakouts shown in this figure.

thus constrains the directions of the minimum horizontal principal stress, S_h, and the maximum horizontal stress, S_H. *Bell and Gough* [1979] concluded that the NW–SE oriented breakouts are due to a NE–SW directed maximum horizontal principal stress, which is normal to the Rocky Mountain fold axes, suggesting that the stress state responsible for the thrust faulting in the mountains is still present. Following *Bell and Gough*'s [1979] work, highly localized studies using breakouts, such as the stress profile as a function of depth near the San Andreas fault zone [*Shamir and Zoback*, 1992], and regional to global studies [*Zoback et al.*, 1989], have been performed. Stress orientation results from borehole breakouts have been shown to be consistent with other indicators of stress direction, such as hydraulic fractures, earthquake focal mechanisms, and overcoring measurements, on both local and regional scales [e.g., *Bell and Gough*, 1979, 1983; *Zoback and Zoback*, 1980; *Gough and Bell*, 1981; *Plumb and Hickman*, 1985; *Stock et al.*, 1985; *Zoback et al.*, 1989; *Zoback and Healy*, 1992; *Zoback*, 1992].

In addition to the stress state studies using borehole breakouts, the last two decades have seen much research into the formation of borehole breakouts. *Gough and Bell* [1982] applied brittle shear fracture theory to the borehole wall and predicted pairs of conjugate shear fractures that are tangential to the borehole wall and oriented $\pi/4 - \phi/2$ to the maximum horizontal principal stress direction, where ϕ is the angle of internal friction of the rock. The shear fractures intersect and create sharp, pointed, "dog eared" breakouts. Since *Gough and Bell*'s [1982] study, borehole

televiewers have been used to generate accurate images of the borehole wall. The borehole televiewer is a well-logging tool that contains a spinning transducer that radiates acoustic pulses and receives and measures the timing and the amount of energy of the return pulse that is reflected from the borehole wall [*Zemanek et al.*, 1970]. Using the reflected energy, the televiewer can generate both accurate cross sections and a map of the reflectance of the borehole wall. Observations of borehole breakouts using borehole televiewer logs have shown that breakouts do not have the shape predicted by *Gough and Bell* [1982] [*Zoback et al.*, 1985]. Borehole breakouts are observed to be anywhere from broad, shallow, and flat-bottomed to deep with pointed ends. Televiewer logs also show that both deep and shallow breakouts have the same angular extent around the borehole wall [*Zoback et al.*, 1985].

Both *Mastin* [1984] and *Zoback et al.* [1985] extended *Gough and Bell*'s [1982] work and developed a model in which material would be removed from the borehole wall at locations where the elastic stresses exceeded the strength of the rock as defined by the Mohr-Coulomb shear failure criterion. This model also predicts breakout formation at the azimuth of the minimum horizontal principal stress direction. To model breakout development, *Mastin* [1984] and *Zoback et al.* [1985] started with a circular hole and removed those sections of the wall where the stress exceeded the rock strength. Taking this shape of borehole, further sections of borehole wall were removed that were unable to support the shear stresses. Repeated iterations of this process did not generate a stable breakout shape. *Zoback et al.* [1985] concluded that application of the Mohr-Coulomb shear fracture model to the borehole wall was insufficient and that the formation of breakouts is a more complex process.

A model presented by *Zheng et al.* [1989] assumed that failure of the borehole wall occurred due to extensile splitting very close to the borehole at the location of maximum compressive stress on the borehole wall, where the fractures are oriented parallel to the maximum compressive stress direction. Such splitting has been experimentally observed [*Mastin*, 1984]. The numerical model presented by *Zheng et al.* [1989] predicts breakouts that deepen but do not widen as they form and eventually stabilize into a fairly pointed shape. Many observations of breakout shape do not show the breakout shape predicted by this model.

Finally, a model invoking a rigid-plastic pressure sensitive material with dilatancy is used by *Vardoulakis et al.* [1988] to examine the different failure modes of boreholes.

Experimental studies have shown that the formation of breakouts is not a simple process. For example, *Mastin* [1984] compressed eight sandstone blocks containing cylindrical holes and observed five successive stages of breakout formation. According to *Mastin* [1984], the stages are:

1. Formation of extensional fractures within a few hundredths of a borehole radius from the hole wall, located at 90° around the borehole from the direction of applied load. These fractures are parallel to both the borehole wall and the applied stress direction. They initiate from intragranular fractures which extend between contact points in individual grains.

2. Buckling of the thin rock slab between the fracture and the wellbore. This causes the fractures to propagate toward, and intersect, the borehole wall, forming small thrusted wedges that are sheared into the wellbore. The breaking off of these wedges exposes a spalled area bounded by the location of the former extensional fracture, and/or by a small scarp on one side of the spalled area where the wedge broke off.

3. Disaggregation of rock inside the breakout, and/or formation of more extensional fractures parallel to the initial one, father away from the wellbore. Extensional fractures link together at their ends to form two shear surfaces that converge in the direction away from the borehole wall.

4. Expulsion of the material between these surfaces by shearing into the borehole. The resulting breakout is v-shaped to cuspate in cross section, and approximately as wide as the initial spalled area in step 2.

5. Development of a zone of inelastic yielding around the breakout, composed of fractured and disaggregated grain particles. The arch-like shape of the breakout tip prevents expulsion of this material, thereby inhibiting further growth. In some cases, fractures extend from the side of this zone toward the borehole wall.

Regardless of the exact model of breakout formation, it is generally held that the location of the breakouts on the borehole wall corresponds to the location of the maximum compressive stress concentration. Commonly, breakout data are used to constrain directions of stress but not their relative magnitudes. If hydrofracture and the mechanical properties of core samples are available, the magnitudes of the principal stresses can be estimated [*Vernik and Zoback*, 1992; *Peška and Zoback*, 1995]. However, in principle, the presence of breakouts can also yield information on stress magnitudes, both because the presence of a breakout indicates that the hoop stress exceeds the yield strength of the rock and because, when the borehole is not aligned with a principal stress axis, the breakout orientation depends on the relative magnitudes of all three principal stresses, as well as on the orientations of the stresses. Thus additional information about the stress tensor can be obtained from the directions of breakouts in deviated (nonvertical) drill holes; one can estimate the directions of all three principal stresses and provide some constraint on their relative magnitudes. Such a technique provides a more complete knowledge of the stress tensor and works even if none of the principal stresses is vertical.

The smallest data set applicable to this technique would most likely consist of a few, closely spaced, variably oriented wells logged with oriented caliper arm data. Offshore oil platforms provide good sources of such data, since the wells are drilled in many directions and at nonvertical deviations to fully develop the oil fields. Depending upon the number of wells and the horizontal extent of the caliper data, this technique determines a regional stress state localized over a spatial extent of kilometers to tens of kilometers.

Other authors have presented different techniques using deviated boreholes to determine the local

stress state. *Qian and Pedersen* [1991] applied a nonlinear inversion technique to a set of borehole breakout data. *Aadnoy* [1990a, b] examined fractures in deviated boreholes. *Peška and Zoback* [1995] developed a technique using leak-off tests, microfracture measurements, pore pressure measurements, breakout, and tensile fractures with theoretical borehole failure calculations to determine the stress directions and magnitudes from a single, deviated well. Neither the technique of *Peška and Zoback* [1995] nor the technique presented in this paper assumes a vertical principal stress direction. Multiple applications of the *Peška and Zoback* [1995] technique over a region would yield a more regional stress tensor.

The theoretical basis of this technique has been recognized for nearly a decade, but it has only been applied in a few areas, perhaps because of the lack of strongly deviated drill holes in most regions. It is based on the elastic equations for stress surrounding an arbitrarily oriented cylindrical hole in a medium with known far-field stresses. Equations for the stress field surrounding a circular hole in an elastic plate subjected to plane strain are given by *Kirsch* [1898] and various other authors [e.g., *Hubbert and Willis*, 1957; *Timoshenko and Goodier*, 1970; *Jaeger and Cook*, 1979]. The equations for the stress components at the wall of a cylindrical hole in a polyaxial stress field are given by *Hiramatsu and Oka* [1962], *Youngdahl and Sternberg* [1966], *Fairhurst* [1968], *Daneshy* [1973], *Richardson* [1983], *Mastin* [1988], and *Qian and Pedersen* [1991].

If a drill hole is parallel to one of the principal stress directions, the rock strength and the relative magnitudes of the remaining two stresses affect the presence or absence of breakouts but not their azimuth in the borehole reference frame. The magnitudes of the principal stresses must be inferred by another technique rather than just by observations of breakout orientation.

The final azimuthal extent, or width, of the breakout after breakout formation is thought by some authors to be controlled by the relative magnitudes of the principal stresses, so that if one of the principal horizontal stresses is known, and the rock strength is known or estimated, the magnitude of the other principal horizontal stress can be estimated [*Moos and Zoback*, 1990; *Vernik and Zoback*, 1992]. However, other authors have argued that this may not be the case, because the angle subtended by the breakout may vary with the stress history [*Zheng et al.*, 1989]. The angle subtended by a breakout may also depend on the mode of failure during breakout formation, which is still debated, as mentioned above.

However, in a nonvertical hole, or a hole oriented obliquely to the three principal stress directions, one does not necessarily need independent measurements of one principal stress to infer the relative magnitudes of another principal stress, because the magnitudes of the principal stresses, as well as their directions, influence the position of the maximum compressive stress at the borehole wall [*Richardson*, 1983] and hence the position at which breakouts would form. This fact was further elaborated by *Mastin* [1988], who showed stereographic projections [*Hobbs et al.*, 1976] indicating the direction of breakouts expected in variably oriented drill holes for different stress orientations

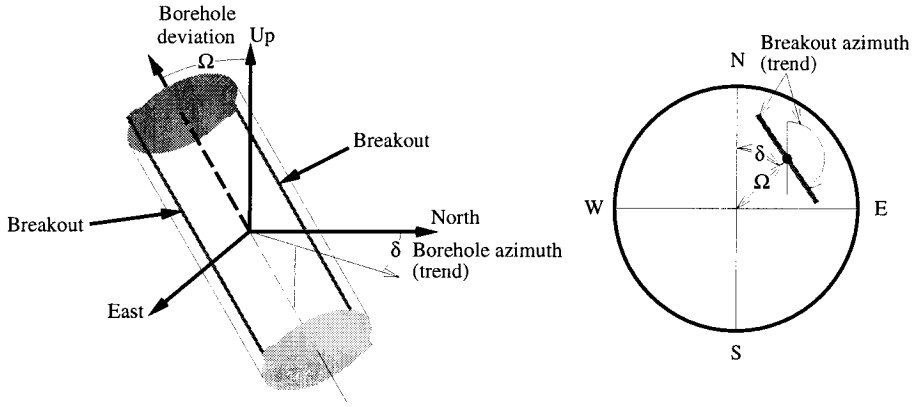

Figure 1.2: Relationship between an arbitrarily oriented borehole containing a breakout and how this borehole and its breakout orientation would be plotted on a lower hemisphere stereograph of borehole azimuth and deviation. The breakouts on either side of the borehole are assumed to be on opposite sides of the borehole and hence there exists a single plane which contains the borehole axis and the locus of breakouts. The intersection of this plane with the horizontal plane defines a line which plots as the orientation of the breakout in the lower hemisphere stereographic projection plot.

and principal stress magnitudes. Thus, if several drill holes of different deviations are present in a given area, and if these drill holes are subject to the same stress tensor, the orientations of the breakouts in these holes may provide strong constraints on the orientations and magnitudes of the principal stresses at that location [*Zajac and Stock*, 1992, 1997].

To plot the breakout data from arbitrarily oriented boreholes and the calculated breakout positions for theoretical far-field stress states, lower hemisphere stereographic projections of the borehole azimuth and deviation (e.g., Figures 1.2 and 1.3) are used.

This dependence of breakout position on the far-field tectonic stress is illustrated in Figure 1.4, where I show patterns of breakout orientations that would be predicted for arbitrarily oriented drill holes subjected to characteristic stress fields. These are similar to the quadrant plots of *Mastin* [1988] and illustrate the degree to which an inversion or forward modeling of borehole breakout observations would constrain the stress regime for a given distribution of borehole orientations. The characteristic stress fields are defined by the orientations of the principal stresses S_1, S_2, and S_3 and the stress ratio

$$\phi = \frac{S_2 - S_3}{S_1 - S_3}, \tag{1.1}$$

where S_1 is the maximum compressive stress, S_2 is the intermediate stress, and S_3 is the minimum compressive stress.

Note that, given enough variation in borehole orientations, the stress state can be reasonably constrained, since the patterns vary continuously from an entirely radial distribution of breakout azimuths (for degenerate thrust faulting, $S_H = S_h > S_v$) to an entirely circumferential distribution

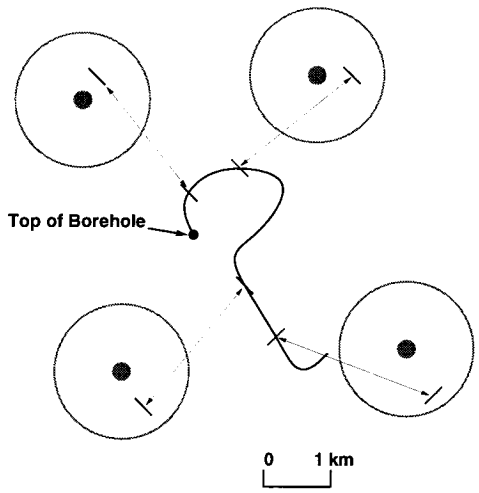

Figure 1.3: Map view of a hypothetical borehole and four observed breakouts and how the breakouts are displayed on lower hemisphere stereographic projection plots.

of breakout azimuths (for degenerate normal faulting, $S_v > S_H = S_h$). Here a "degenerate case" is defined when two of the principal stresses are equal in magnitude. The nodal points represent borehole orientations where circumferential stress on the borehole wall is uniform, and there is no preferred direction of breakouts; at these orientations the maximum stress at the borehole wall is relatively low and less likely to exceed rock strength, so that breakouts may be absent altogether. Note that the nodal point for degenerate thrust faulting is in the center of the projection corresponding to a vertical drill hole; as the ratio of S_H to S_h increases, two nodal points appear and move radially away from the center along the S_H direction. The nodal points reach horizontal borehole orientations for the degenerate case when $S_h = S_v$ (combined thrust and strike-slip faulting): as S_h continues to decrease, the nodal points split again and move along the circumference of the plot. For the degenerate case of $S_H = S_v > S_h$ (combined strike-slip and normal faulting) the two nodal points again correspond to horizontal borehole orientations, aligned along the direction of S_h; as the stress ratios progress through the normal faulting stress regime, the nodal points again approach the center of the plot.

Although in theory these patterns will vary continuously as a function of the stress regime, our ability to resolve them depends on the distribution and quality of the data, particularly on the available borehole orientations. Since few drill holes approach the horizontal, data near the nodal points for some patterns may be hard to obtain. If the boreholes within a study region are all within 30° of vertical, then our ability to resolve the stress ratios will depend on the stress regime; stress ratios in normal faulting or thrust faulting stress regimes will be better resolved than those in strike-slip faulting stress regimes [*Mastin*, 1988]. However, in recent industry drilling programs it is common for boreholes to be deviated more than 30°. Our ability to resolve the stress state will

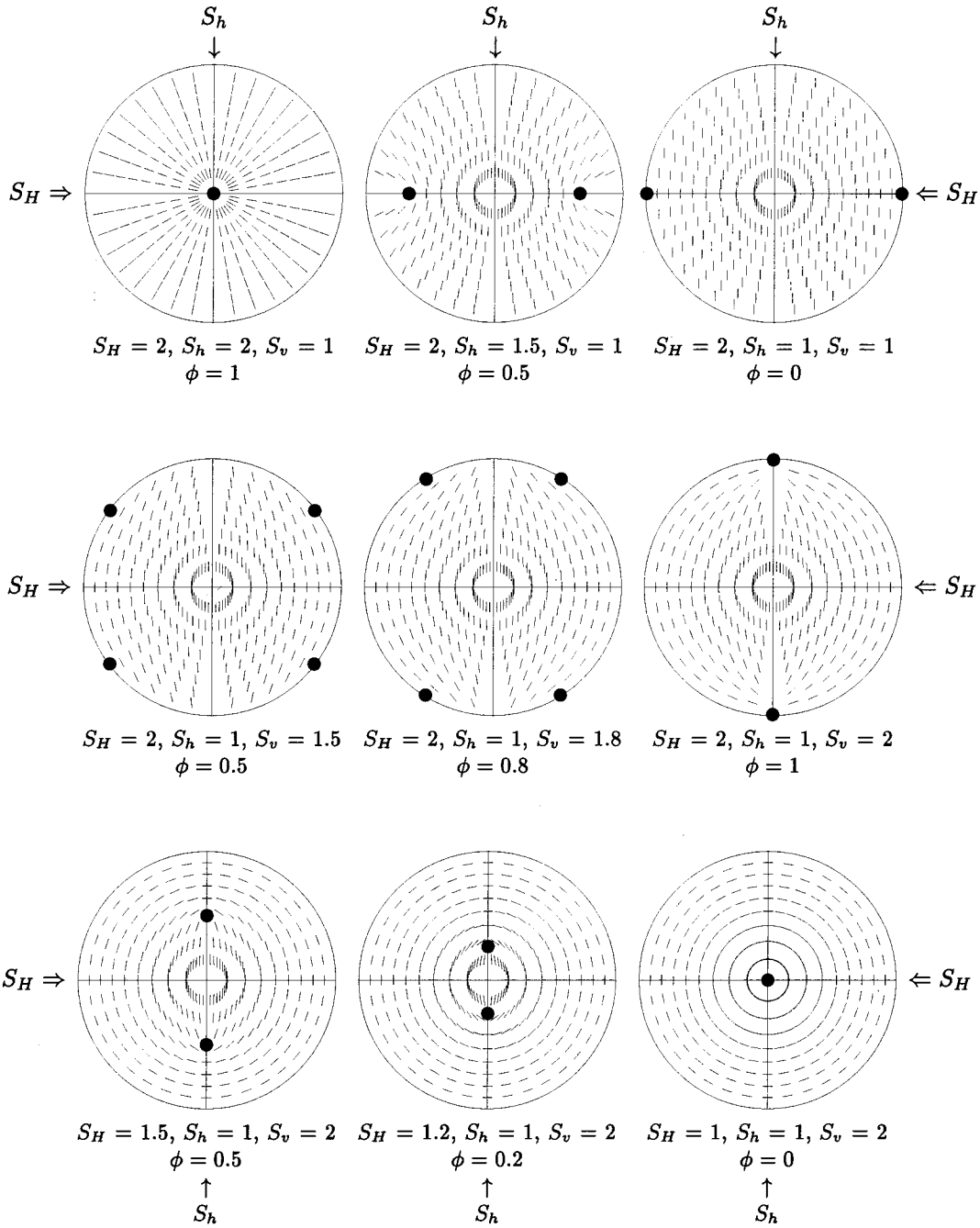

Figure 1.4: Relationship of breakout orientations to stress directions and magnitudes in arbitrarily oriented drill holes [*Mastin*, 1988]. Lower hemisphere stereographic projections show the breakout orientations, projected onto the horizontal plane, for a variety of drill hole orientations and stress regimes. Solid circles are "nodal" points at which the stress anisotropy is zero, corresponding to borehole orientations with no preferred breakout direction. The low maximum compressive stress at the borehole wall at these positions indicates that breakouts might be absent. If breakouts are present near the nodal points, however, they will change orientation rapidly as borehole orientations vary. In these figures, Poisson's ratio was taken to be 0.25, and the orientation of the maximum horizontal principal stress is always east-west for nondegenerate stress regimes.

also depend on the consistency of the data, since I assume that all data plotted or inverted together correspond to the same stress tensor, including both the orientations of the principal axes and the stress ratio, ϕ.

1.2 Overview of Thesis

In Chapter 2 I discuss the techniques of determining the stress tensor from borehole breakouts, examining the physics of borehole breakouts, the theory of the inversion technique used, and data processing issues. The theory and data processing issues are not discussed separately in this work, since data processing issues often prompted new theoretical techniques. I first examine the physics of borehole breakouts and how the orientation of breakouts on the borehole wall relates to the local stress field. A new borehole breakout selection scheme which takes into account highly non-vertical boreholes is then presented along with a discussion of the real world problems of data gathering, identification, and processing. Having selected a borehole breakout data set using the criteria, I invert for the best fitting stress state using a new technique combining genetic algorithms and non-differential function optimizers. Finally, I present a way in which 95% confidence limits can be placed on the resulting stress tensor.

With all of the technical and theoretical pieces in place, several different data sets are examined in the remaining chapters of the thesis. Chapter 3 examines a small borehole breakout data set publish by *Qian and Pedersen* [1991] from the Siljan Deep Drilling Project in Sweden. Chapter 4 examines a borehole breakout data set from the offshore Santa Maria Basin, California. The final and largest data set from a series of oil wells in Cook Inlet, Alaska is examined in Chapter 5. Finally, Chapter 6 concludes and summarized the results and conclusions from the thesis.

Portions of Chapters 1, 2, 3, and 4 have been previously published as "Using borehole breakouts to constrain the complete stress tensor: Results from the Sijan Deep Drilling Project and offshore Santa Maria Basin, California," in *J. Geophys. Res., 102*(B5), 10,083–10,100, 1997 by myself and Joann M. Stock. Note that the title of this paper contains a misspelling of the word "Siljan." This paper introduces the stress state inversion technique and analyzes the Siljan Deep Drilling Project and Santa Maria Basin breakout data sets. Many improvements have been made to the research published in this paper and are included in this thesis. The most significant change is the introduction of a new inversion misfit scheme that more accurately reflects the physics of borehole breakout formation and improves the quality of the stress state inversion results. The Siljan and Santa Maria Basin data have been reinverted using the new misfit scheme and the results are presented in this thesis.

The two appendices contains in minute detail some of the mathematics describing the boreholes, breakouts, and coordinate system rotations used to perform this work and the individual discussion

and plots of the raw dipmeter data from all of the Cook Inlet, Alaska wells.

Chapter 2 Borehole Breakout Data: Gathering, Processing and Inverting

This chapter introduces the different tools used to gather, process, analyze, and invert borehole breakout data. I start by discussing two reference coordinate systems, the geographic and borehole coordinate systems used throughout the work. This provides a mathematical basis for all of the physical measurements that take place in the borehole. I then examine the different types of physical measurements made of the borehole orientation in space and measurements made of the physical properties of the borehole wall. The relevant derived quantities needed to perform a stress state inversion from the many different types of borehole measurements and the statistical tools used to describe the consistency of the data are then discussed. I then examine a new set of borehole breakout selection and identification criteria that was generated specifically for data from deviated boreholes.

After identifying the breakouts, I describe the stress state inversion technique. I begin by looking into binning of the borehole breakouts, which may be a technique useful for some noisy data sets. An Euler angle approach to the parameterization of the stress state is then introduced. I then examine the equations which give the breakout orientation on a borehole wall given a far-field stress state and the borehole orientation. A misfit between the observed and the predicted breakout orientations for a given stress state can be calculated. The misfit is then used in a genetic algorithm (GA) and Powell optimizer search for the optimum stress state. Finally, I derive the confidence limits on the optimum stress state.

2.1 Mathematical and Physical Description of Boreholes and Data Processing

2.1.1 Defining the Borehole and Geographic Coordinate Systems

This work employs two reference frames: the geographic reference frame and the borehole reference frame (Figure 2.1). The geographic reference frame is an orthonormal reference frame with its **X** axis horizontal and pointing due east. The **Y** axis is also horizontal and points due north. The **Z** axis is perpendicular to both the **X** and **Y** axis and points up. This geographic reference frame will often be referred to as the **XYZ** reference frame.

The borehole reference frame stays aligned with the borehole axis as the borehole orientation

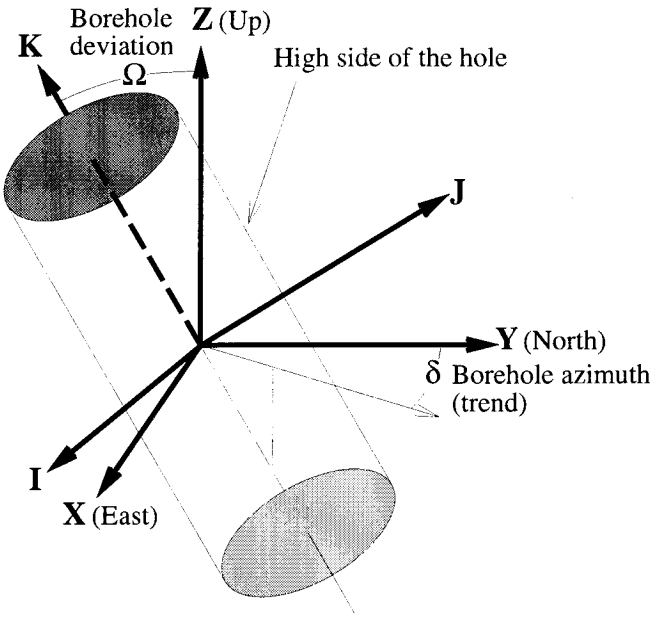

Figure 2.1: View of the two coordinate systems associated with the borehole. The **X**, **Y**, and **Z** axes are aligned with the geographic coordinate system. The **IJK** coordinate system rotates as the borehole orientation changes.

changes with depth. Thus, the orientation of this reference frame changes with respect to the geographic (**XYZ**) reference frame along the borehole. The axes are named **I**, **J**, and **K** and are oriented as follows. The **K** axis is parallel to and points upwards along the borehole axis, the **J** axis is perpendicular to the **K** axis and in the same plane as the **K** and **Z** axes, while **I** is perpendicular to both the **J** and **K** axes and lies in the horizontal plane. The positive direction of **I** is set such that the **IJK** coordinate system is right-handed. With this definition the **J** axis always points to the high side of the hole. If the borehole is vertical, then this coordinate system coincides with the geographic coordinate system. The borehole reference frame will be referred to as the **IJK** reference frame for short.

A sequence of two rotations is used to rotate a coordinate system that is initially aligned with the **XYZ** coordinate system into alignment with the **IJK** coordinate system. The first rotation about the **Z** axis rotates the geographic coordinate system clockwise by the angle δ until **X** coincides with **I**. The resulting coordinate system will be referred to as the $\xi\eta\zeta$ axes. The second step rotates the $\xi\eta\zeta$ axes about the ξ axis by a counterclockwise angle Ω, producing the **IJK** coordinate system. The two angles, δ and Ω, in geological terms, are the borehole azimuth and deviation, respectively (Figure 2.1).

The definition of angular measurements requires a special note for the two reference frames. I use the term "azimuth" to refer to a direction measured east from north in the geographic coordinate

system. I do not use the term "azimuth" in the borehole coordinate system, since north is not a special direction in that coordinate system. Rather, all angles are measured counterclockwise from the **I** axis when one looks down the **K** axis. I use the word "azimuth" to refer to angles measured only in the geographic coordinate system and the word "angle" to refer to angles measured in the borehole coordinate system. When the two coordinate systems coincide, then the "azimuth" is calculated by subtracting the "angle" from 90°:

$$\text{azimuth} = 90° - \text{angle}. \tag{2.1}$$

The mathematical derivations of the rotation matrices and the transformation of vectors, angles, and stress tensors between the borehole and geographic coordinate have been included as an appendix (sections A.1-A.4).

2.1.2 Data Collection from Well Logs & Well Log Measurements

In this section I describe the process of converting unprocessed dipmeter data into a list of borehole breakouts which can be analyzed for a stress state. The first step is calculation of a borehole elongation direction from the many different types of dipmeter data that exist. Once completed, selection criteria are applied to the borehole elongation data to select borehole breakouts.

After a well is drilled it is logged with a variety of tools. The tools of interest in this thesis are those used to measure the borehole orientation and the shape of the borehole wall. Both sets of measurements are done with the four- or six-arm dipmeter. This is a tool with either four or six spring-loaded pads that press against the borehole wall. The four-arm dipmeter has its pads 90° away from its neighbors and the six-arm dipmeter has them 60° apart from each other. The sensors attached to the pads rub against the rock and measure various physical properties of the rock, such as its resistivity. In addition, the extension of each pair of arms is measured. The dipmeter also measures the borehole deviation away from vertical and its trend.

Since many of the borehole measurement tools use the Earth's magnetic field to orient themselves, it is worth examining how the magnetic declination can affect some of the measurements and how it can be corrected for. The magnetic declination is the angle between geographic north and the map projection of the magnetic field lines. This angle is positive when the field lines lie east of geographic north. The Earth's magnetic field is used by some of the tools to measure the map view (**XYZ**) azimuth of the borehole or the azimuth of the tools' pad number one. So the magnetic declination must be added to these values before any further calculations are undertaken. This could either be undertaken while logging the well or during the post-processing analysis. The dipmeter tool could also measure angles in the plane perpendicular to the borehole axis. Hopefully, none of these measurements are made with respect to the magnetic field lines since the magnetic field's inclination

would also have to be taken into account.

The different borehole measurements can be grouped into two different sets. One set of measurements are taken in the geographic reference frame and the other are taken in a borehole reference frame. Measurements typically taken in the borehole coordinate system are various diameters of the hole as measured in a plane perpendicular to the borehole axis by the four- or six-arm dipmeter, and the angular distance between the highest point of the borehole wall and one of the caliper arms. Measurements taken in the geographic reference frame include the azimuth of the borehole and its deviation away from vertical.

Between all of these different measurements, three final quantities are desired as a function of depth. These are the trend or azimuth of the borehole, the borehole deviation away from vertical, and the borehole elongation angle. With these three values as a function of depth, the complete stress tensor can be constrained given sufficient variation in borehole orientations.

2.1.3 Calculation of Elongation IJK Angles

Calculation of the elongation direction for a four-arm dipmeter is straightforward. I assume that the dipmeter is centered in the borehole, so the elongation direction is parallel to the direction of the longer caliper arm (See Section 2.1.6 for a discussion of the basis for this assumption). I also make the assumption that the breakout is symmetric about 180°, so that all elongation orientations lie between 0° and 180° without any loss of generality.

The six-arm dipmeter is similar to the four-arm dipmeter except that it has two extra arms and all of the arms are separated by 60° intervals. Calculation of the borehole elongation direction from a six-arm dipmeter is more complicated, since it is not as obvious that any one set of caliper arms will be aligned with the breakout. In addition, the extra two pads on the borehole wall may change the threshold of detection of breakouts, because the increased friction on the borehole wall requires less ellipticity to counteract tool torque (see Section 2.1.6). I am not aware of any study in which the breakout directions calculated from a six-arm dipmeter have been compared to those found either from a borehole televiewer tool or from a four-arm dipmeter.

Here I describe two methods of calculating the elongation direction from six-arm dipmeter data. The first method uses the orientation of the longest caliper arm as the elongation direction. However, the longest caliper arm may not track the breakout, so the second method, which I use on our data, fits an ellipse to the caliper arm data and takes the orientation of the semimajor axis as the elongation direction.

I briefly describe the second method here. The six-arm dipmeter measures three independent diameters that are separated by 60°. These three values define three vectors, which originate at the origin of a suitable coordinate system and are separated by 60° intervals. I assume that the three vectors constrain an ellipse centered at the origin of the coordinate system. I parameterize

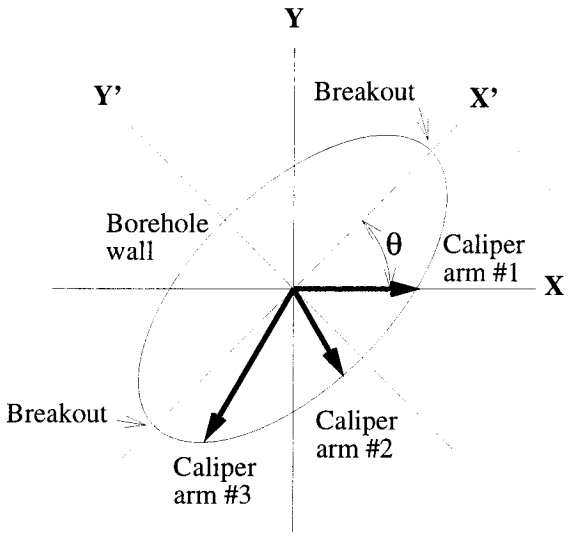

Figure 2.2: Geometry of the caliper arms in the six-arm dipmeter looking down onto the tool and ellipse used to find the breakout orientation.

the orientation of this ellipse, using θ, the angle between the semimajor axis of the ellipse, and the direction of caliper arm 1 (Figure 2.2). To determine θ, I write three equations describing the ellipse, inserting the vector positions of the endpoints of the caliper arms. The three equations are then written in matrix form. As in many linear algebra problems, for a solution to exist the determinant of the matrix must be zero. Here the matrix will have zero determinant when the angle of rotation of the ellipse is found. Once this angle of rotation is found, the lengths of the semimajor and semiminor axes are easily calculated. Using this information with the rotation angle allows calculation of the elongation direction with respect to the azimuth of pad 1.

One potential problem with this method is that the three caliper arm vectors might define a hyperbola instead of an ellipse. This problem occurred with some of the data from Point Pedernales, and I choose to not select any breakouts where this happens.

The mathematical details of this technique are as follows:

I start off by defining two coordinate systems that share the same origin. The first, unprimed, coordinate system (**XY**) is oriented such that its **X** axis is aligned with caliper arm number 1. Since the caliper arms are numbered clockwise, caliper arm number 2 is 60° away from the **X** axis and in the lower right quadrant. The third caliper arm is 120° away from the first caliper arm and lies in the lower left quadrant. The second, primed, reference frame (**X'Y'**) is defined to be the coordinate system in which the equation for the ellipse can be written as

$$a_1(x')^2 + a_2(y')^2 + a_3 = 0, \tag{2.2}$$

that is, the **X'** and **Y'** axes coincide with the semi-major and semi-minor axes of the ellipse. The

coordinates of a point in the two coordinate systems are related by the transformation

$$\begin{aligned} x' &= x\cos\theta + y\sin\theta \\ y' &= -x\sin\theta + y\cos\theta \end{aligned}$$

where theta is the counterclockwise angle measured from the **X** to the **X'** axis in the **XY** coordinate system. The equation for the ellipse in unprimed coordinates is

$$a_1(x\cos\theta + y\sin\theta)^2 + a_2(-x\sin\theta + y\cos\theta)^2 + a_3 = 0. \tag{2.3}$$

Now one must define the vectors representing the three caliper arms, and enter them into (2.3). If the lengths of the caliper arms are c_1, c_2, and c_3, respectively, then

$$\begin{aligned} \mathbf{x}_1 &= (c_1, 0)^T \\ \mathbf{x}_2 &= (c_2\cos 60, -c_2\sin 60)^T \\ \mathbf{x}_3 &= (-c_3\cos 60, -c_3\sin 60)^T. \end{aligned}$$

Three independent equations are obtained when the caliper arm vectors are substituted into (2.3)

$$\begin{aligned} a_1(c_1\cos\theta)^2 + a_2(-c_1\sin\theta)^2 + a_3 &= 0 \\ a_1(c_2\cos 60\cos\theta - c_2\sin 60\sin\theta)^2 + a_2(-c_2\cos 60\sin\theta - c_2\sin 60\cos\theta)^2 + a_3 &= 0 \\ a_1(-c_3\cos 60\cos\theta - c_3\sin 60\sin\theta)^2 + a_2(c_3\cos 60\sin\theta - c_3\sin 60\cos\theta)^2 + a_3 &= 0 \end{aligned}$$

The equations can be expressed in matrix form

$$\begin{pmatrix} (c_1\cos\theta)^2 & (-c_1\sin\theta)^2 & 1 \\ (c_2\cos 60\cos\theta - c_2\sin 60\sin\theta)^2 & (-c_2\cos 60\sin\theta - c_2\sin 60\cos\theta)^2 & 1 \\ (-c_2\cos 60\cos\theta - c_3\sin 60\sin\theta)^2 & (c_3\cos 60\sin\theta - c_3\sin 60\cos\theta)^2 & 1 \end{pmatrix} \begin{pmatrix} a_1 \\ a_2 \\ a_3 \end{pmatrix} = \begin{pmatrix} 0 \\ 0 \\ 0 \end{pmatrix}$$

$$\begin{pmatrix} c_1^2\cos^2\theta & c_1^2\sin^2\theta & 1 \\ c_2^2\cos^2(60+\theta) & c_2^2\sin^2(60+\theta) & 1 \\ c_3^2\cos^2(60-\theta) & c_3^2\sin^2(60-\theta) & 1 \end{pmatrix} \begin{pmatrix} a_1 \\ a_2 \\ a_3 \end{pmatrix} = \begin{pmatrix} 0 \\ 0 \\ 0 \end{pmatrix}$$

$$\mathbf{M}\ \mathbf{a} = 0. \tag{2.4}$$

For (2.4) to be satisfied the determinant of **M** must be 0. This condition constrains θ, so the **X'Y'** coordinate system has now been defined. To numerically find θ, the Newton-Raphson method for finding roots of functions can be applied to the determinant. The angle θ is not unique, since an

extra rotation of 90° will just switch a_1 and a_2.

The semi-major and semi-minor axis lengths and the ellipticity are determined by the constants a_1, a_2, and a_3. I now use the equation of the ellipse with the caliper arm locations as expressed in the **X'Y'** coordinate system:

$$\begin{aligned}
\mathbf{x'}_1 &= (c_1 \cos\theta, -c_1 \sin\theta)^T \\
\mathbf{x'}_2 &= (c_2 \cos[60+\theta], -c_2 \sin[60+\theta])^T \\
\mathbf{x'}_3 &= (-c_3 \cos[60-\theta], -c_3 \sin[60-\theta])^T.
\end{aligned}$$

I again write three equations:

$$\begin{aligned}
a_1(x')^2 + a_2(y')^2 + a_3 &= 0 \\
a_1(c_1\cos\theta)^2 + a_2(-c_1\sin\theta)^2 + a_3 &= 0 \\
a_1(c_2\cos 60\cos\theta - c_2\sin 60\sin\theta)^2 + a_2(-c_2\cos 60\sin\theta - c_2\sin 60\cos\theta)^2 + a_3 &= 0
\end{aligned}$$

Written in matrix form the equations become

$$\begin{pmatrix} (x')^2 & (y')^2 & 1 \\ (c_1\cos\theta)^2 & (-c_1\sin\theta)^2 & 1 \\ (c_2\cos 60\cos\theta - c_2\sin 60\sin\theta)^2 & (-c_2\cos 60\sin\theta - c_2\sin 60\cos\theta)^2 & 1 \end{pmatrix} \begin{pmatrix} a_1 \\ a_2 \\ a_3 \end{pmatrix} = \begin{pmatrix} 0 \\ 0 \\ 0 \end{pmatrix}$$

$$\begin{pmatrix} (x')^2 & (y')^2 & 1 \\ c_1^2\cos^2\theta & c_1^2\sin^2\theta & 1 \\ c_2^2\cos^2(60+\theta) & c_2^2\sin^2(60+\theta) & 1 \end{pmatrix} \begin{pmatrix} a_1 \\ a_2 \\ a_3 \end{pmatrix} = \begin{pmatrix} 0 \\ 0 \\ 0 \end{pmatrix}$$

$$\mathbf{N}\ \mathbf{a} = 0. \tag{2.5}$$

The determinant of **N** must be zero for (2.5) to be satisfied. This results in the following equation, defining the lengths of the semi-major and semi-minor axes:

$$[c_1^2\sin^2\theta - c_2^2\sin^2(60+\theta)](x')^2 + [-c_1^2\cos^2\theta + c_2^2\cos^2(60+\theta)](y')^2 + [c_1^2c_2^2\sin 60\sin(60+2\theta)] = 0. \tag{2.6}$$

Equation (2.6) can be rewritten in standard elliptical form:

$$\frac{c_2^2\sin^2(60+\theta) - c_1^2\sin^2\theta}{c_1^2c_2^2\sin 60\sin(60+2\theta)}(x')^2 + \frac{c_1^2\cos^2\theta - c_2^2\cos^2(60+\theta)}{c_1^2c_2^2\sin 60\sin(60+2\theta)}(y')^2 = 1 \tag{2.7}$$

$$\left(\frac{x'}{l_1}\right)^2 + \left(\frac{y'}{l_2}\right)^2 = 1$$

So the semi-major and semi-minor axes lengths are known, along with the angle θ. The breakout

direction is therefore either θ degrees away from caliper arm number one if $l_1 > l_2$ or $\theta + 90$ degrees away if $l_1 < l_2$.

Equation (2.7) fails if $60 + 2\theta = n\pi$. In this case, caliper arm number 3 can be used instead of caliper arm number 2 in equation (2.5):

$$\begin{pmatrix} (x')^2 & (y')^2 & 1 \\ c_1^2\cos^2\theta & c_1^2\sin^2\theta & 1 \\ c_3^2\cos^2(60-\theta) & c_3^2\sin^2(60-\theta) & 1 \end{pmatrix} \begin{pmatrix} a_1 \\ a_2 \\ a_3 \end{pmatrix} = \begin{pmatrix} 0 \\ 0 \\ 0 \end{pmatrix}$$

Calculating the determinant of the above matrix and setting it to 0, I find:

$$[c_1^2\sin^2\theta - c_3^2\sin^2(60-\theta)](x')^2 + [-c_1^2\cos^2\theta + c_3^2\cos^2(60-\theta)](y')^2 + [c_1^2c_3^2\sin 60\sin(60-2\theta)] = 0. \quad (2.8)$$

This results in the following equation for the ellipse:

$$\frac{c_3^2\sin^2(60-\theta) - c_1^2\sin^2\theta}{c_1^2c_3^2\sin 60\sin(60-2\theta)}(x')^2 + \frac{c_1^2\cos^2\theta - c_3^2\cos^2(60-\theta)}{c_1^2c_3^2\sin 60\sin(60-2\theta)}(y')^2 = 1.$$

2.1.4 Calculation of Borehole and Elongation XYZ Azimuths

In some cases it may be necessary to calculate the borehole and elongation **XYZ** azimuths. The borehole azimuth may need to be calculated if for some reason the well log does not list the borehole azimuth. The only method that does not involve using angles measured with respect to the Earth's magnetic field in the borehole coordinate system is to subtract the **XYZ** relative bearing from the **XYZ** pad number one azimuth. This orientation then points at the high side of the hole, which is in the same direction as the **XYZ** borehole azimuth.

While most of the work in this thesis uses just the borehole elongation or breakout angle in the borehole coordinate system, notably for the stress state inversion calculation, the elongation direction as projected to the horizontal is used, for illustration purposes, such as in the lower hemisphere stereographic projection plots.

There are three different methods for calculating the **XYZ** breakout azimuth. They all rely on the knowledge of the borehole azimuth. The different methods are:

1. Take the **IJK** relative bearing to find the **IJK** angle of pad number one. Find the breakout orientation with respect to pad number one using the caliper arm length logs and get the **IJK** angle of the breakout. Convert this **IJK** angle into a **XYZ** azimuth using the equations derived in Section A.4.1.

2. Take the **XYZ** azimuth of pad number one, convert it into an angle in the borehole

frame (Section A.4.2), find the breakout angle using the caliper distances and move this angle into the geographic reference frame.

3. Use the **XYZ** relative bearing to find the **XYZ** azimuth of pad number one. Then go through the same steps as in 2) above.

With these different methods, it should be possible to calculate the breakout azimuth using any kind of well log.

2.1.5 Statistics of Angular Data

Various statistics of borehole breakout data are calculated throughout this work. For example, the mean and standard deviation of the **IJK** breakout angle over a particular depth range is used throughout the borehole breakout selection scheme. The statistical techniques appropriate for linear data are not always appropriate for circular or angular data. For example, consider two rays aligned 1° and 359° away from the **X** axis. Intuitively, we expect the average ray to lie directly on the **X** axis with a standard deviation somewhere around 1°. Calculating the mean using a linear approach, however, would yield an average orientation of the ray to be 180°. One solution to this problem is to translate all of the measurements by 90°, perform the mean calculation, and then translate the result back by -90°. This would give us the correct mean of 0°. However, there are more complicated data sets for which there is no unique translation of the coordinate system that will give a satisfactory answer.

A more general solution to the problem follows the one described by *Mardia* [1972] with minor differences, which will be outlined below. A complete derivation of the results from *Mardia* [1972] will not be presented here, just the major results. First I present the results from circular, two-dimensional, data.

Let the angles $\theta_1, \ldots, \theta_n$ represent n measurements. Let each measurement have an associated weight w_i. The weight w_i can represent any associated weight of the measurement, such as the number of measurements at the particular angle or the error associated in the measurement of that angle. The mean direction $\overline{\theta}$ of $\theta_1, \ldots, \theta_n$ is defined as the angle that the weighted sum of the vectors makes with the **X** axis. This vector sum is represented by $(\overline{C}, \overline{S})$, where

$$\overline{C} = \frac{\sum w_i \cos\theta_i}{\sum w_i}, \tag{2.9}$$

$$\overline{S} = \frac{\sum w_i \sin\theta_i}{\sum w_i}. \tag{2.10}$$

Define $\overline{R}$ as

$$\overline{R} = \sqrt{\overline{C}^2 + \overline{S}^2}.$$

The mean angle $\overline{\theta}$ satisfies the equations

$$\begin{aligned} \overline{C} &= \overline{R}\cos\overline{\theta} \\ \overline{S} &= \overline{R}\sin\overline{\theta} \end{aligned}$$

and can be calculated using the arctan function. It can be shown that this definition of $\overline{\theta}$ has some useful properties. First of all, if the angles $\theta_1, \ldots, \theta_n$ are uniformly rotated by an angle α, then $\overline{\theta}$ will experience the same amount of rotation. Secondly,

$$\sum w_i \sin(\theta_i - \overline{\theta}) = 0. \tag{2.11}$$

This is equivalent to the expression

$$\sum w_i(x_i - \overline{x}) = 0$$

for the linear case.

Mardia [1972] introduces a term called the dispersion, D, which measures the amount of dispersion between a list of angles and a given angle, α. The dispersion is defined as

$$D = \frac{\sum w_i[1 - \cos(\theta_i - \alpha)]}{\sum w_i}. \tag{2.12}$$

The dispersion D is minimized when $\alpha = \overline{\theta}$. This can be shown by setting the derivative of equation (2.12) to 0.

$$\sum w_i \sin(\theta_i - \alpha) = 0. \tag{2.13}$$

This is equivalent to equation (2.11) when α is equal to $\overline{\theta}$.

I define a new value, the circular variance, as

$$S_0 = 1 - \overline{R}.$$

Since the range of $\overline{R}$ is from 0 to 1, the circular variance also ranges from 0 to 1. If the angular measurements cluster then $\overline{R}$ will be near 1 and S_0 will be near 0. One would like to relate the circular variance to a linear standard deviation. *Mardia* [1972] derives an appropriate transformation of the circular variance from the range $(0, 1)$ to a linear standard deviation on the range $(0, \infty)$ as

$$s_o = \sqrt{-2\ln(1 - S_0)}\sqrt{n/(n-1)}.$$

Mardia [1972] does not include the $\sqrt{n/(n-1)}$ term in the calculation of s_0. I do so to represent the fact that one degree of freedom is lost from the data when the mean is calculated. This term

is intuitive if one thinks of making one measurement and attempting to calculate the mean and standard deviation. The mean of a sample of one is just the measurement itself. However, one would have no idea of the quality of the measurement, so it would be assigned a standard deviation of ∞. The term $\sqrt{n/(n-1)}$ gives ∞ if there is only one measurement.

All of the discussion above applies to directed angular data. I also have undirected data, such as borehole breakout direction data, which I assume has a 180° symmetry. There might be other data types that have a 90° symmetry. For this reason I discuss the statistics of data with $2\pi/l$ symmetry. The appropriate transformation of this data is to increase the angular range from $(0, 2\pi/l)$ to $(0, 2\pi)$ using

$$\theta' = l\theta.$$

One can then find the mean direction, $\overline{\theta}'$, and the circular variance, S_0', of the transformed data. It can be shown that the mean, circular variance, and standard deviation of the original data are related to the mean and the circular variance of the transformed data by the following equations [*Mardia*, 1972]

$$\begin{aligned} \overline{\theta} &= \overline{\theta}'/l, \\ S_0 &= 1 - (1 - S_0')^{\frac{1}{l^2}}, \\ s_0 &= \sqrt{-2\ln(1 - S_0)}\sqrt{n/(n-1)}/l. \end{aligned}$$

2.1.6 Identification of Breakouts

Here we discuss criteria for identification of breakouts, and calculation of breakout azimuths, given either oriented four- or six-arm caliper data. Oriented four- or six-arm caliper data are measured on a variety of different well-logging tools, such as low-angle dipmeters, high-angle dipmeters, formation microscanners/microimagers, and stratigraphic high-resolution dipmeter tools (SHDTs).

Plumb and Hickman [1985] examined the validity of using four-arm dipmeters to identify borehole breakouts. They logged a well in Auburn, New York, twice with a four-arm dipmeter and once with a borehole televiewer. The borehole televiewer is an acoustic logging tool that provides high-resolution information about borehole elongation and the distribution of natural fractures in wells [*Zemanek et al.*, 1970]. The acoustic transit time can be used to construct detailed borehole cross sections. By comparing the orientation of breakouts from the four-arm dipmeter with borehole cross sections constructed from the televiewer data they found that the four-arm dipmeters generally had their long axes aligned with the breakouts. This is a critical observation, since borehole televiewer logs are not commonly run in most drill holes, and many wells logged with four-arm dipmeters lack the

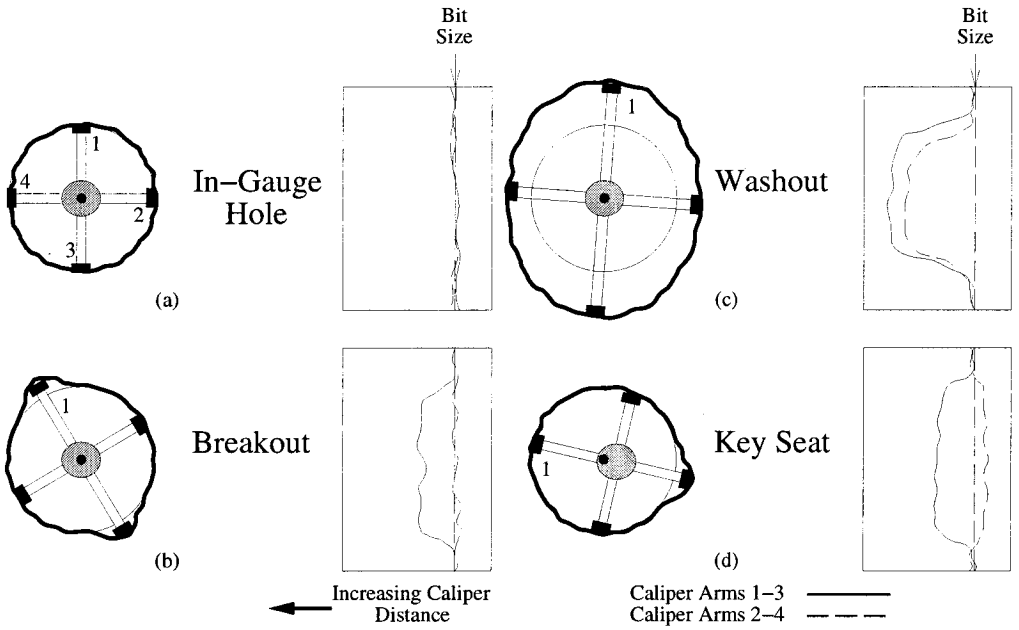

Figure 2.3: Examples of four-arm dipmeter caliper logs and common interpretations of borehole geometry. Caliper arms 1-3 and caliper arms 2-4 indicate the borehole diameter as measured between opposing dipmeter arms. (a) An in-gauge hole. (b) The geometry resulting from stress-induced borehole breakouts. (c) A minor "washout" with superimposed elongation. (d) A key seat where the dipmeter is not centered in the borehole resulting in one caliper reading being less than the bit size. Increasing caliper arm distances are to the left. Figure after *Plumb and Hickman* [1985].

more detailed televiewer observations.

Plumb and Hickman [1985] defined five criteria they used to identify zones of breakouts from four-arm dipmeter logs:

1. The tool rotation stops in the zone of elongation.
2. The caliper arm difference is greater than 0.6 cm.
3. The smaller of the caliper readings is close to bit size, or if the smaller caliper reading is greater than bit size, it should exhibit less variation than the larger caliper.
4. The length of the breakout zone is greater than 30 cm.
5. The direction of elongation should not consistently coincide with the azimuth of the high side of the borehole when the hole deviates from vertical.

These criteria attempt to eliminate some commonly observed complications in borehole shape (Figure 2.3). The first two criteria relate to rotation of the dipmeter due to cable torque as the tool is winched up the hole. The first criterion requires the dipmeter to track the breakout, and the second deals with the observation that a 0.6 cm borehole elongation was sufficient to stop tool rotation for *Plumb and Hickman*'s [1985] winch and cable setup. The third criterion eliminates positions where the dipmeter is not centered in the borehole or where the borehole has been washed-out. The fourth criterion addresses the fact that breakouts shorter than the length of the caliper pads cannot be

measured (the dipmeter used by *Plumb and Hickman* [1985] had a pad length of 30 cm). The last criterion addresses cable and tool drag on the borehole wall when the hole is not vertical. The cable, or other tools previously used in the hole, can scrape the wall and create a channel on the low side of the hole ("tool marks" or "key seats") yielding a roughly elliptical borehole shape that could be interpreted as a breakout if only four-arm caliper data were available.

From our experience with examining deviated boreholes we have slightly modified *Plumb and Hickman*'s [1985] breakout selection criteria. The new criteria used are as follows:

1. The tool rotation stops in the zone of elongation. Dipmeter logs record either pad 1 azimuth or the relative bearing of pad 1, or both. The pad 1 azimuth is the **XYZ** azimuth of the number 1 dipmeter pad. The relative bearing is the **IJK** angle between the high side of the hole and pad number 1. Both of these measure the orientation of the tool in the hole. Our selection criterion for nondigital data sets is that the maximum variation of either measurement should be less than 10°. When digital data are available, the standard deviation of either data type must be less than 1.25°. We use *Mardia*'s [1972] work in the statistics of angular data to calculate the average borehole elongation direction and its standard deviation for a particular section of hole.

2. The largest and smallest caliper arms should be at least 5% different from each other.

3. The smallest caliper arm should be larger than or equal to the bit size and smaller than 1.1 times the bit size.

4. The standard deviation of each caliper arm over a breakout interval should be less than 2.54 cm (1 inch).

5. The length of the breakout zone should be at least 3 m.

6. The maximum difference between the bit size and the largest caliper arm should be 7.62 cm (3 inches).

Criterion 1 of *Plumb and Hickman* [1985] was tightened to be more quantitative regarding the variation in the quality of the breakout direction. Criterion 2 was changed to demand a 5% difference between the caliper arms instead of a 0.6 cm difference. This criterion is more flexible for boreholes of different radii. Criterion 3 was slightly changed to state that the smallest caliper arm is always as large as the bit size and no larger than 1.1 times the bit size. The minimum breakout length of criterion 4 was increased to 3 m to find longer, more consistent breakout intervals. Criterion 5 of Plumb and Hickman discards breakouts that fit all other selection criteria but are parallel to the high and low sides of the hole. We keep such data initially, since the theoretical breakout patterns for most stress regimes (Figure 1.4) show that in certain borehole orientations the breakouts are expected to be aligned with the high and low side of the hole. After initial data analysis, if we determine that some of these elongation directions are probably due to key seats, we remove them manually from the data set. We also note that *Qian and Pedersen* [1991] performed an inversion of a set of breakouts measured with four-arm dipmeter data containing radial breakouts (Figure 3.2).

Finally, we add one more criterion, which discards breakouts with very large spalled regions, since other processes, such as wholesale failure along fault zones, might account for large spalled regions.

2.1.7 Propagation of Errors

As with any study, the propagation of errors through the data analysis should be studied. Here, the errors involved in measuring the borehole diameters will first be considered, followed by consideration of the angular measurements, which prove to be more important.

There are two main sources of error to consider. The first is systematic errors associated with the logging equipment. This is sometimes compensated for at the well site by taking extra measurements that are used while logging the well. Examples of this are calibration measurements for the caliper arms and declination measurements to correctly orient the tool in the hole. The other source of errors is in the digitization of paper well logs if digital data are not available. Digitization errors can result in apparent misalignment between different measurements, such as caliper one and caliper two showing the start of a washout at different depths. Also, the magnitude of the washout could be digitized poorly showing that the washout is not as large as it actually is.

The error of measuring the borehole diameter with a four-arm caliper does not weigh too heavily in calculating the borehole breakout direction. Since the breakout direction is assumed parallel to the more extended caliper arms, only a comparison between caliper arm 1 and caliper arm 2 must be made. If caliper arms 1 and 2 are equal within the errors of the measurements the breakout direction would be unconstrained, but the data would not be used since it does not meet Plumb and Hickman's criteria (specifically 2 and 4).

The case of a six-arm caliper is harder, since the breakout direction depends strongly on the caliper arm lengths. However, much of our data is from four-arm calipers, in this study, so this is not too important.

The most important source of errors is from angular measurements, particularly in calculating the breakout azimuth map view (**XYZ**). These errors are magnified when the borehole is highly deviated, which is an important point considering that the objective of this work is to analyze very deviated boreholes.

Consider a breakout direction angle measured by the pad number one azimuth in the borehole (**IJK**) reference frame where the borehole is deviated by 80°. The borehole angle lies in a circle perpendicular to the borehole axis. This circle becomes an ellipse with a large ellipticity when projected to the horizontal. This means that unless the **IJK** angle points in the high or low side of the hole, it will be rotated such that the breakout orientation (Figure 1.2) appears more azimuthal than radial. This has important consequences for a thrust faulting regime, where the breakout pattern is expected to be radial (Figure 1.4).

This can be easily visualized in a plot of the **XYZ** breakout azimuth, for a variety of **IJK**

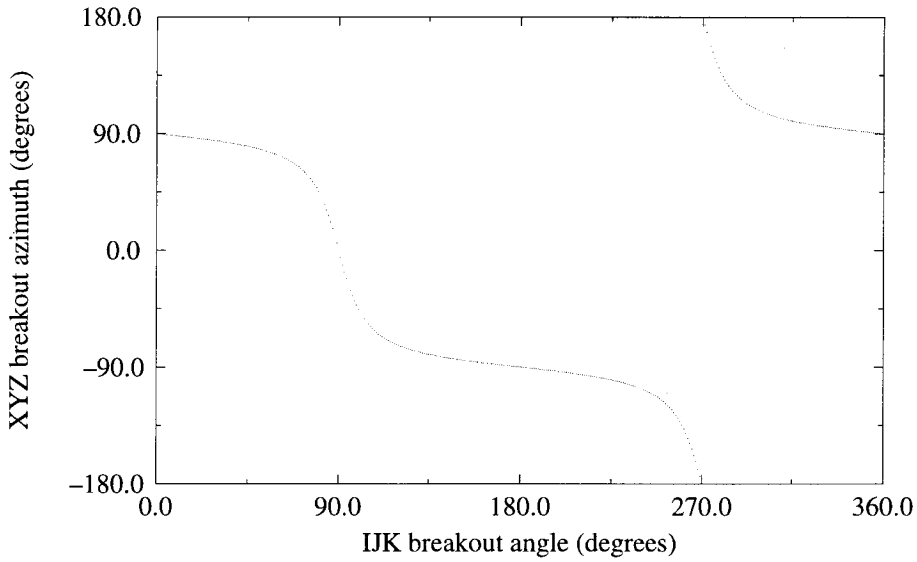

Figure 2.4: Plot of the **XYZ** breakout azimuth against the **IJK** breakout angle for a 80° deviated, north plunging well. Note that any errors in the **IJK** angle are magnified when the angle lies near 90° and 270°, angles which correspond to a breakout at the high and low side of the hole.

breakout angles, for a 80° deviated borehole plunging due north (Figure 2.4). An **IJK** breakout angle of 90° represents the high side of the hole and an angle of 270° points at the low side of the hole. Notice that any error in the angular measurement itself, or in the digitization, is magnified here. For example, if the breakout was on the high side of the hole (90°), but digitization error put the angle at 85°, then the **XYZ** angle is 27°, roughly 5 times greater than the error in the borehole coordinate system.

In light of this, then field measurements showing consistent non-azimuthally trending breakout orientations should be evaluated carefully.

2.2 Inverting the Breakout Data

In this section I describe the steps taken after a dipmeter data set is gathered to determine the stress state that best describes the data. Briefly, the steps are:

1. Calculate the **IJK** elongation angle for all wells at 0.125 m depth spacing.
2. Use the breakout selection criteria listed above to identify breakouts.
3. Optionally bin the breakouts into bins of **XYZ** borehole azimuth and borehole deviation.

I calculate a weighted average breakout direction and a weighted standard deviation of the breakout angles [*Mardia*, 1972]. The individual breakouts are weighted linearly with their length and inversely with the standard deviation of the breakout angle over the breakout's length.

4. Use a genetic algorithm (GA) to identify the region of the stress state solution space that

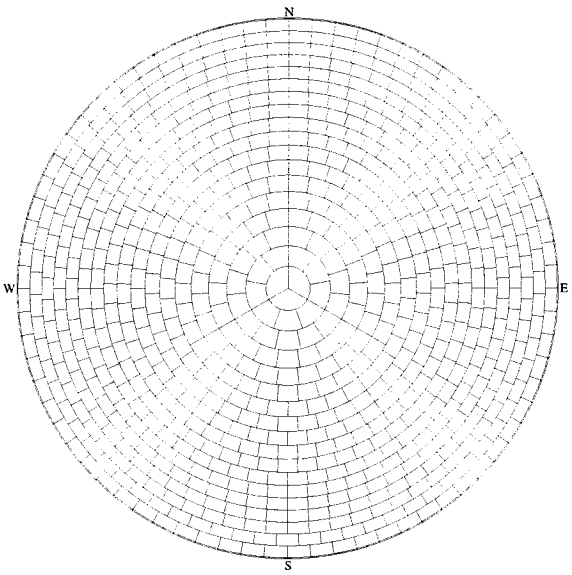

Figure 2.5: A lower hemisphere stereographic projection showing the grid used to bin the borehole breakout data. Each bin has an area equivalent to a 5° x 5° bin at the center of the projections.

most likely contains the minimum weighted one-norm misfit between a stress state and the, possibly binned, breakout data.

5. Run a N-dimensional optimizer with the results from the GA to find the minimum misfit.
6. Calculate error bounds on the best fitting stress state.

2.2.1 Binning of Breakout Data

Much of the borehole breakout data I have examined is very scattered both in the orientation of breakouts and in the orientations of the boreholes in a particular field of study (i.e., Figure 4.2). The data might also show a large group of breakouts at one borehole orientation and a few scattered breakouts in others. I would like the few scattered breakouts to have a comparable weight for the optimization as the group of more numerous breakouts since the variation of borehole orientations is equally as important to our optimization as the quantity of breakouts.

For these reasons, I may bin the borehole breakout data into equal-area stereographic area bins. These bins are equivalent in size to a 5° x 5° bin located at the center of a stereographic projection (Figure 2.5).

To arrive at an **IJK** borehole breakout orientation for each bin, I use the statistics of angular data as described in Section 2.1.5, weighting the mean breakout direction linearly with the breakouts' length and inversely by the square of the standard deviation of the breakout orientation:

$$w_j = \frac{l_j}{\sigma_j^2}.$$

Here, w_j is the weighting factor appearing in equations (2.9), (2.9), and (2.12), a_j is the **IJK** angle of the j-th breakout, l_j is its length and σ_j is the standard deviation of the **IJK** breakout angle. Calculation of the mean breakout angle in this manner favors longer breakouts with smaller variations in the breakout angle. To calculate the mean and standard deviation of nonangular measurements associated with each breakout, I use the following equations [*Bevington*, 1969]:

$$\begin{aligned} \overline{x} &= \frac{\sum w_j x_j}{\sum w_j}, \\ \sigma_x^2 &= \frac{N \sum [w_j (x_j - \overline{x})^2]}{(N-1) \sum w_j}. \end{aligned}$$

2.2.2 Euler Angle Description of a Stress State

A stress tensor can be described in a number of ways. I would like a parameterization of the stress tensor that separates the magnitudes of the principal stresses from the orientation of the principal stress directions.

I choose to parameterize the stress state with four parameters: three Euler angles and the stress state ratio ϕ (equation 1.1). The three Euler angles describe three successive rotations about various coordinate axes and are a natural representation often used to completely describe the orientation of a set of axes attached to a body in space [*Goldstein*, 1950]. I use this formalism to describe the orientation of the eigenvectors of a stress tensor.

Since the stress tensor is completely described by six parameters and three of the parameters describe the stress state orientation, the two parameters I am not constraining describe the magnitudes of the principal stresses. I can parameterize the magnitudes of the principal stress directions as

$$S_1 = a(b+1) \tag{2.14}$$

$$S_2 = a(b+\phi) \tag{2.15}$$

$$S_3 = a(b) \tag{2.16}$$

where ϕ is the ratio previously defined (equation 1.1) and a and b are unknown constants. Examination of equations (2.18) through (2.24) shows that the location of the axis of greatest compressive stress, $\sigma_{t\mathrm{max}}$, is unaffected by the constant multiplicative factor a in equations (2.14)–(2.16). The remaining parameter, b, does effect the position of $\sigma_{t\mathrm{max}}$ and $\sigma_{t\mathrm{min}}$. However, I choose to ignore b in the parameterization of the stress state by setting it equal to 1.

To describe the arbitrary orientation of a body with Euler angles, the angles must be allowed

to vary from 0 to 2π. However, since a rotation of a stress tensor by π leaves the stress tensor invariant, the Euler angles can be limited to $[0, \pi]$. The largest problem with this parameterization is when the amount of the second rotation is 0. In this case, the first and third rotations rotate the coordinate system about the same axis leading to multiple parameterizations that describe the same eigenvector orientations.

2.2.3 Theoretical Breakout Directions in Arbitrary Stress Fields

Here we discuss how the theoretical breakout direction is calculated, given an arbitrary borehole orientation and far-field stress state. First, the far-field tectonic stress is transformed or rotated into the coordinate system associated with the borehole, as the stress tensor

$$\mathbf{S}_{IJK} = \begin{pmatrix} S_{ii} & S_{ij} & S_{ki} \\ S_{ij} & S_{jj} & S_{jk} \\ S_{ki} & S_{jk} & S_{kk} \end{pmatrix} \tag{2.17}$$

with compressional stress positive.

Hiramatsu and Oka [1962] and *Fairhurst* [1968] derived the relationship between far-field stresses and stresses on the wall of a cylindrical hole, assuming that the medium is isotropic, homogeneous, and linearly elastic with constant fluid pressure in the borehole. The stresses on the borehole wall in the borehole coordinate system are given by

$$\sigma_{kk} = S_{kk} - 2\nu(S_{ii} - S_{jj})\cos 2\alpha - 4\nu S_{ij}\sin 2\alpha \tag{2.18}$$

$$\sigma_{\alpha\alpha} = S_{ii} + S_{jj} - 2(S_{ii} - S_{jj})\cos 2\alpha - 4S_{ij}\sin 2\alpha - \Delta P \tag{2.19}$$

$$\tau_{k\alpha} = 2(S_{jk}\cos\alpha - S_{ki}\sin\alpha) \tag{2.20}$$

$$\sigma_{rr} = \Delta P \tag{2.21}$$

where ΔP is the difference between the borehole fluid pressure and the in situ pore pressure, ν is Poisson's ratio of the rock and is taken to be 0.25. Throughout this work ΔP is taken to be 0. The angle α is measured from the **I** axis toward the **J** axis. The **K** axis in the $\alpha r\mathbf{K}$ coordinate system is the same **K** axis in the **IJK** coordinate system (Figure 2.6). Note that the form of equations (2.18)-(2.21) is different from that of equations appearing in *Mastin* [1988] (equations A1 and A2), *Qian and Pedersen* [1991] (equation 5), and *Peška and Zoback* [1995] (equation A9). *Mastin* [1988] and *Qian and Pedersen* [1991] contain errors in the definition of σ_{kk} and $\sigma_{\alpha\alpha}$. *Peška and Zoback*'s [1995] α increases in a clockwise sense while the α appearing in equations (2.18)-(2.21) increases in a counterclockwise sense.

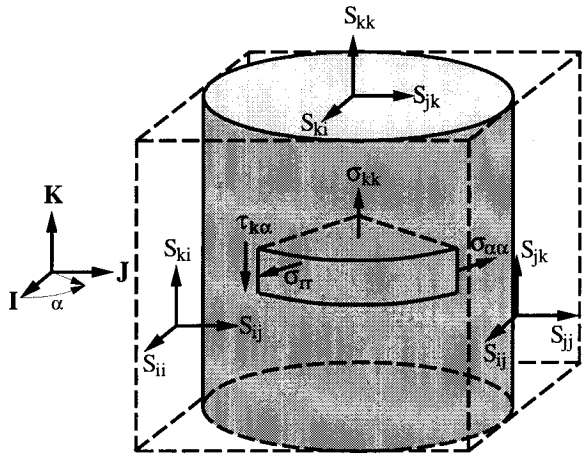

Figure 2.6: View of the borehole and the components of the stress tensor in the borehole coordinate system. The angle α is used in finding the cylindrical components of the stress tensor on the borehole wall. After *Mastin* [1988].

The principal stresses at any given point on the borehole wall are

$$\sigma_{t\max} = \frac{1}{2}\left(\sigma_{kk} + \sigma_{\alpha\alpha} + \sqrt{(\sigma_{kk} - \sigma_{\alpha\alpha})^2 + 4\tau_{k\alpha}^2}\right) \tag{2.22}$$

$$\sigma_{t\min} = \frac{1}{2}\left(\sigma_{kk} + \sigma_{\alpha\alpha} - \sqrt{(\sigma_{kk} - \sigma_{\alpha\alpha})^2 + 4\tau_{k\alpha}^2}\right) \tag{2.23}$$

$$\sigma_{rr} = \Delta P \tag{2.24}$$

where $\sigma_{t\max}$ and $\sigma_{t\min}$ are the maximum and minimum principal stresses in the plane tangential to the borehole wall. The location of the maximum and minimum values of the tangential principal stresses define the location of borehole breakouts and tensile fractures if the rock strength is exceeded; borehole breakouts occur where $\sigma_{t\max}$ is a maximum and tensile fractures occur where $\sigma_{t\min}$ is minimized [*Peška and Zoback*, 1995]. The easiest way to obtain the angles where $\sigma_{t\max}$ is maximized and $\sigma_{t\min}$ is minimized, given the square root term in the definition of $\sigma_{t\max}$ and $\sigma_{t\min}$, is to use Brent's computational method which does not rely upon first derivative information of the function being optimized [*Brent*, 1973; *Press et al.*, 1992].

2.2.4 Selection and Calculation of a Misfit Measure

Optimization of a model from data requires a misfit measure that describes how well a particular model fits the observed data. A class of misfit measures is based on the p norm [*Parker and McNutt*, 1980]:

$$\mu^{(p)} = \left(\sum_{j=1}^{n} \left|\frac{\theta_j - o_j}{\sigma_j}\right|^p\right)^{1/p} \tag{2.25}$$

where θ_j is a theoretical value for an observation o_j and σ_j is the measure of error in the observation. Different values of p lead to different weightings of outlying data. For example, the uniform norm, $\mu^{(\infty)}$, minimizes the largest difference between an observed and modeled value. The familiar χ^2 misfit measure is recognized as $(\mu^{(2)})^2$. In the same manner that the $p = \infty$ norm is strongly influenced by extreme and outlier data, *Parker and McNutt* [1980] raise the same criticism about the χ^2 measure. *Parker and McNutt* [1980] suggest a one-norm misfit measure ($p = 1$)

$$M^{(1)} = \sum_{j=1}^{n} \frac{|\theta_j - o_j|}{\sigma_j} \tag{2.26}$$

and derive the statistics, i.e. the mean, variance, and confidence tables, associated with the one-norm measure. *Gephart and Forsyth* [1984] use the one-norm misfit to determine the stress state from earthquake focal mechanism data.

In addition to testing to determine which order of p to use in the misfit measure, two different misfit calculations are introduced here. The first misfit calculation sums the angular difference between the predicted and observed breakout location on the borehole wall

$$m_\alpha = \sum_{j=1}^{n} l_j \frac{\left|\alpha_j^o - \alpha_j^m(S)\right|}{\sigma_j} \tag{2.27}$$

where l_j is the length of the j-th breakout, α_j^o is the breakout **IJK** angle, $\alpha_j^m(S)$ is the **IJK** angle of the predicted location of the breakout on the borehole wall for a given stress state S, and σ_j is the standard deviation of the **IJK** breakout angle for a single breakout or the standard deviation of the **IJK** breakout angles from binned breakouts.

The second misfit measure sums the difference between $\sigma_t\mathrm{max}$ (equation 2.22) at the angle of the breakout and $\sigma_t\mathrm{max}$ at the predicted location of the breakout on the borehole wall. A first attempt at creating a misfit measure using a stress difference is

$$\sum_{j=1}^{n} l_j \frac{\sigma_t\mathrm{max}(\alpha_j^m(S)) - \sigma_t\mathrm{max}(\alpha_j^o)}{S_d[\max_{\alpha=\alpha_j^o-\sigma_j}^{\alpha=\alpha_j^o+\sigma_j} |\sigma_t\mathrm{max}(\alpha) - \sigma_t\mathrm{max}(\alpha_j^o)|]}. \tag{2.28}$$

The two factors in the denominator of the stress misfit measure need some explanation. The term S_d is the maximum value of the difference between the maximum and minimum values of $\sigma_t\mathrm{max}$ on the borehole wall for a particular borehole orientation, and is maximized when the borehole is oriented parallel to the S_2 axis. If the principal stresses S_1, S_2, and S_3 are aligned with S_{ii}, S_{jj}, and S_{kk} respectively, then from equations (2.18)-(2.22)

$$\begin{aligned} S_d &= \sigma_t\mathrm{max}(\frac{\pi}{2}) - \sigma_t\mathrm{max}(0) \\ &= 2(1+\nu)(S_1 - S_3) + \end{aligned}$$

$$\frac{1}{2}|(2\nu-3)S_1+S_2-(2\nu-1)S_3|-$$
$$\frac{1}{2}|-(2\nu-1)S_1+S_2+(2\nu-3)S_3| \tag{2.29}$$

The S_d term is introduced so that the stress misfit for different breakouts are weighted evenly, even if the stress model for the breakout data imposes different stress states at different borehole breakout locations; otherwise, a misfit measure without the S_d term would weight deeper breakouts more than shallow breakouts if a depth dependent stress model is used.

The second term in the denominator,

$$\max_{\alpha=\alpha_j^o-\sigma_j}^{\alpha=\alpha_j^o+\sigma_j}|\sigma_{t\max}(\alpha)-\sigma_{t\max}(\alpha_j^o)| \tag{2.30}$$

tries to serve as a measure of the standard deviation of $\sigma_{t\max}$ in the same sense that σ_j measures the standard deviation of α_j^o. This term calculates the maximum change in $\sigma_{t\max}$ as α varies between $\alpha_j^o-\sigma_j$ and $\alpha=\alpha_j^o+\sigma_j$. Two problems with this term prevent its use in calculating m_σ. First, there are borehole orientations where $\sigma_{t\max}$ does not change with α, leading to a denominator equal to or close to 0. Secondly, calculating the term is computationally infeasible since $\sigma_{t\max}$ is itself a function of the stress state. For these reasons, the **IJK** breakout angle is used to weigh the stress misfit and m_σ is defined as

$$m_\sigma=\sum_{j=1}^{n} l_j\frac{\sigma_{t\max}(\alpha_j^m(S))-\sigma_{t\max}(\alpha_j^o)}{S_d\sigma_j}. \tag{2.31}$$

The stress misfit measure, m_σ, has some properties that make it a better misfit measure than the angular misfit measure, m_α. First, breakouts occur at orientations where the rock strength is exceeded by the stresses at the borehole wall, and hence, stresses are the natural measure of misfit between model and observation. Secondly, the angular difference between predicted and observed breakout orientations do not accurately represent the misfit between observation and data. For certain borehole orientations where $\sigma_{t\max}$ around the borehole is constant, breakouts, if they occur, may occur at almost any orientation (Figure 1.4). The angular misfit measure for these breakouts will artificially inflate the misfit measure. These breakouts will not contribute significantly to the stress misfit measure because at these borehole orientations $\sigma_{t\max}$ is constant or nearly constant.

Stress inversion results from a one-norm angular inversion (equation 2.27), a one-norm stress difference inversion (equation 2.31), and a χ^2 stress difference inversion with

$$m_\sigma^{(2)}=\sum_{j=1}^{n}\frac{l_j}{S_d}\left(\frac{\sigma_{t\max}(\alpha_j^m(S))-\sigma_{t\max}(\alpha_j^o)}{\sigma_j}\right)^2 \tag{2.32}$$

are now compared (Figures 2.7-2.10). The data used to perform the comparisons are from Cook Inlet,

Table 2.1: Comparison of stress state inversion results using three different misfit measures.

Misfit measure	S_1 Azi	S_1 Dev	S_2 Azi	S_2 Dev	S_3 Azi	S_3 Dev	ϕ
One-norm angular difference	165.6	40.1	62.2	78.9	323.4	52.1	$0.274^{0.957}_{0.100}$
One-norm stress difference	179.6	87.3	89.2	81.5	287.1	8.9	$0.924^{0.988}_{0.875}$
Two-norm stress difference	2.8	89.7	92.9	83.0	270.5	7.0	$0.880^{0.978}_{0.841}$

The data used to perform the comparisons are from Cook Inlet, Alaska, and are composed of 142 nonradial borehole breakouts identified from all of the wells except Gp51 and Smgs6 (see Chapter 5).

Alaska, and are composed of 142 nonradial borehole breakouts identified from all of the wells except Gp51 and Smgs6 (see Chapter 5). Nonradial breakouts are those breakouts where the **IJK** breakout angle is at least 15° away from the high-side of the hole. The two stress difference inversions, the first using a one-norm misfit measure and the second using a χ^2 misfit measure, show very similar results (Table 2.1, Figures 2.9 and 2.10). Except for the one-norm ϕ value of 0.924, the principal stress directions and the ϕ values from both misfit measure solutions occur in the other solution's 95% confidence region. Given the similarity of the two solutions for a complicated breakout data set, only the one-norm misfit measure is used in all subsequent inversions.

The one-norm stress difference misfit measure and the one-norm angular difference misfit inversions have substantially different stress state and ϕ value results (Table 2.1, Figures 2.9 and 2.10). The angular inversion identified an oblique normal faulting stress state with $\phi = 0.274^{0.957}_{0.100}$. The stress state is oriented such that breakouts observed in the more highly deviated, southward plunging boreholes are satisfactorily fit. The stress difference inversion results found an almost degenerate thrust faulting stress state with $\phi = 0.924^{0.988}_{0.875}$. Unlike the angular difference inversion results, the stress difference inversion results have much smaller confidence limits, particularly on the ϕ value. The smaller 95% confidence regions are probably due to less accumulated misfit when highly variably oriented borehole breakouts are included in the misfit calculations. In these cases the stress difference misfit can stay small if it places a nodal point near variably oriented breakout data, while the angular difference misfit always accumulates a larger misfit for variably oriented data.

A similar comparison of inversion results from the angular difference misfit measure, m_α, and the stress difference misfit measure, m_σ, are performed on the *Qian and Pedersen* [1991] (Chapter 3) and the Cook Inlet, Alaska (Chapter 5) data sets. Unlike the borehole breakout data used in the above comparison, these two data sets are much smaller, more internally consistent, and occupy less of the borehole orientation space. In these cases the angular and stress difference inversion results were very similar. The principal difference between the sets of inversion results are the smaller 95% confidence regions identified in the stress difference inversion.

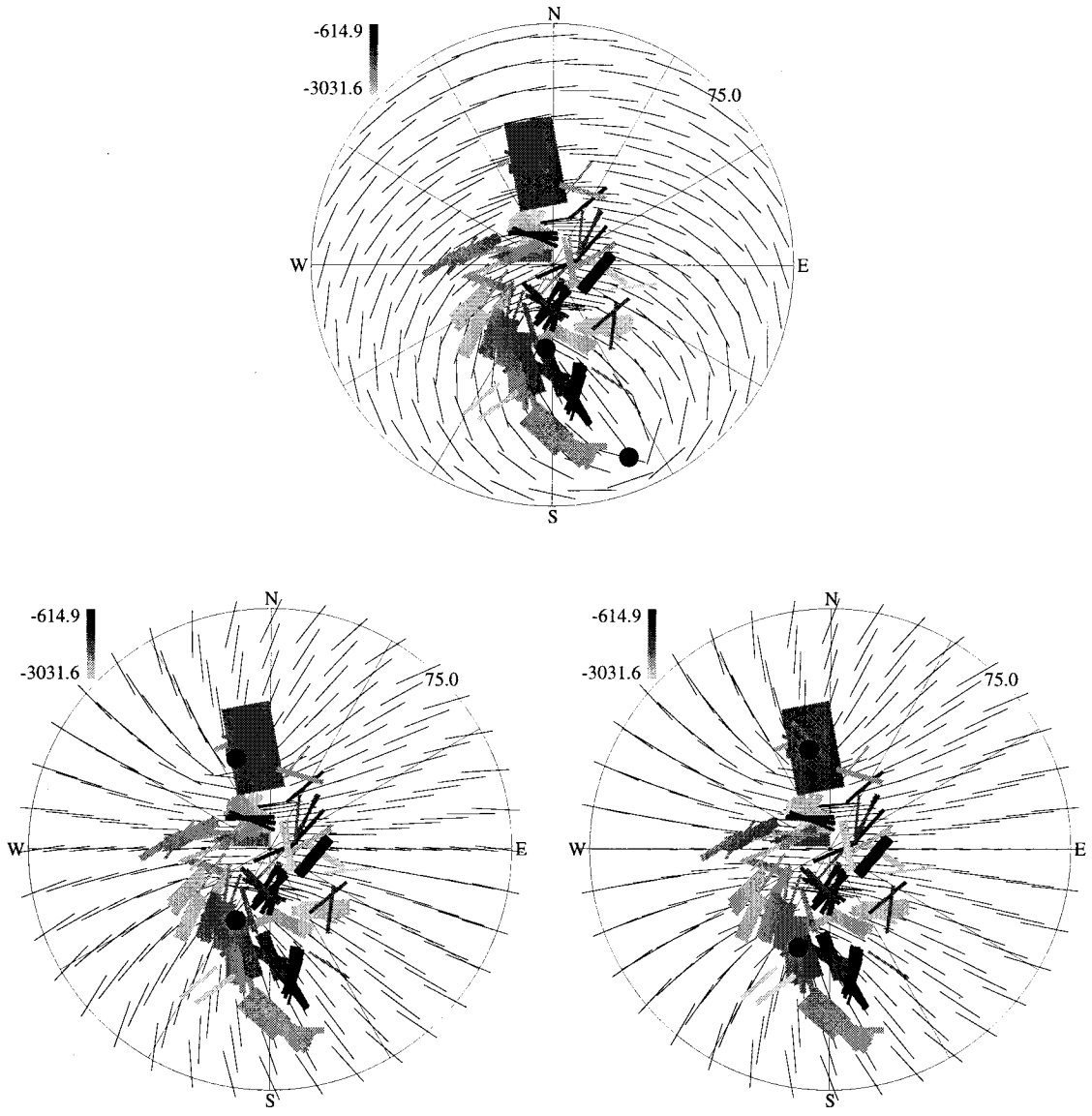

Figure 2.7: Comparison of stress state inversion results using three different misfit measures. (top) Results using a one-norm angular difference measure. (bottom left) Results using a one-norm stress difference measure. (bottom right) Results using a χ^2 stress difference measure. Lower hemisphere stereographic projection of 142 nonradial identified breakouts from all available wells, excluding the breakouts from wells Gp51 and Smgs6, in Cook Inlet, Alaska (see Chapter 5) plotted on top of the theoretical breakout pattern of a best fitting stress state. Nonradial breakouts are those breakouts where the **IJK** breakout angle is at least 15° away from the high-side of the hole. The graduated scale shows the depth of the selected breakouts in meters. Solid circles are "nodal" points at which the stress anisotropy is zero, corresponding to borehole orientations with no preferred breakout direction. Width of the breakout azimuth line is proportional to the breakout length divided by the standard deviation of the **IJK** breakout angle over the length of the breakout.

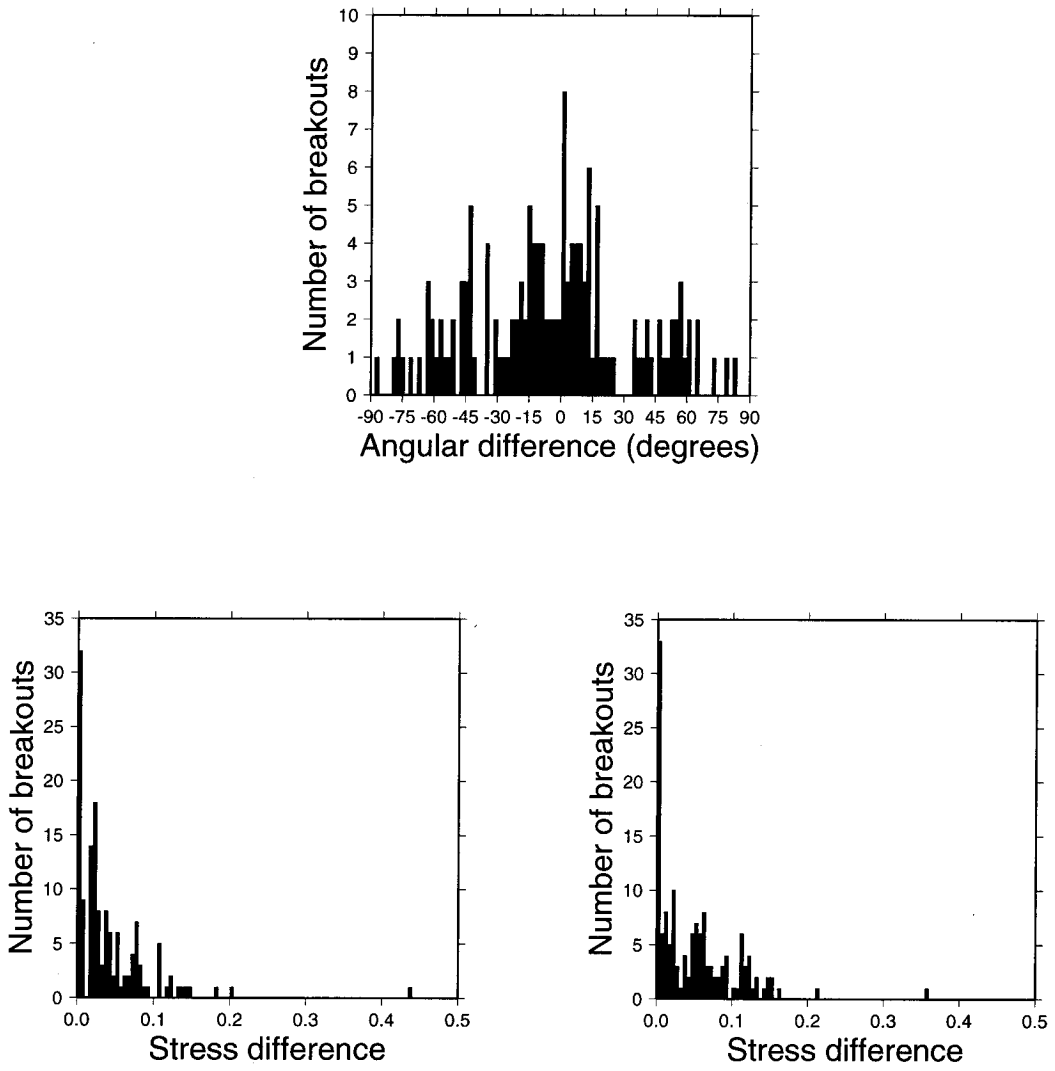

Figure 2.8: Histograms of residuals between the borehole breakout data plotted in Figure 2.7 and the best fitting stress state for a particular misfit measure. (top) Histogram of the residual angular difference $\alpha_j^o - \alpha_j^m(S)$ in 2° bins using the one-norm angular misfit measure inversion results. (bottom left) Histogram of the residual stress difference $(\sigma_t\max(\alpha_j^m(S)) - \sigma_t\max(\alpha_j^o))/S_d$ between the theoretical $\sigma_t\max$ at the predicted location of the breakout and $\sigma_t\max$ at the breakout using the one-norm stress difference measure. (bottom right) Histogram of the residual stress difference $(\sigma_t\max(\alpha_j^m(S)) - \sigma_t\max(\alpha_j^o))/S_d$ between the theoretical $\sigma_t\max$ at the predicted location of the breakout and $\sigma_t\max$ at the breakout using the χ^2 stress difference measure.

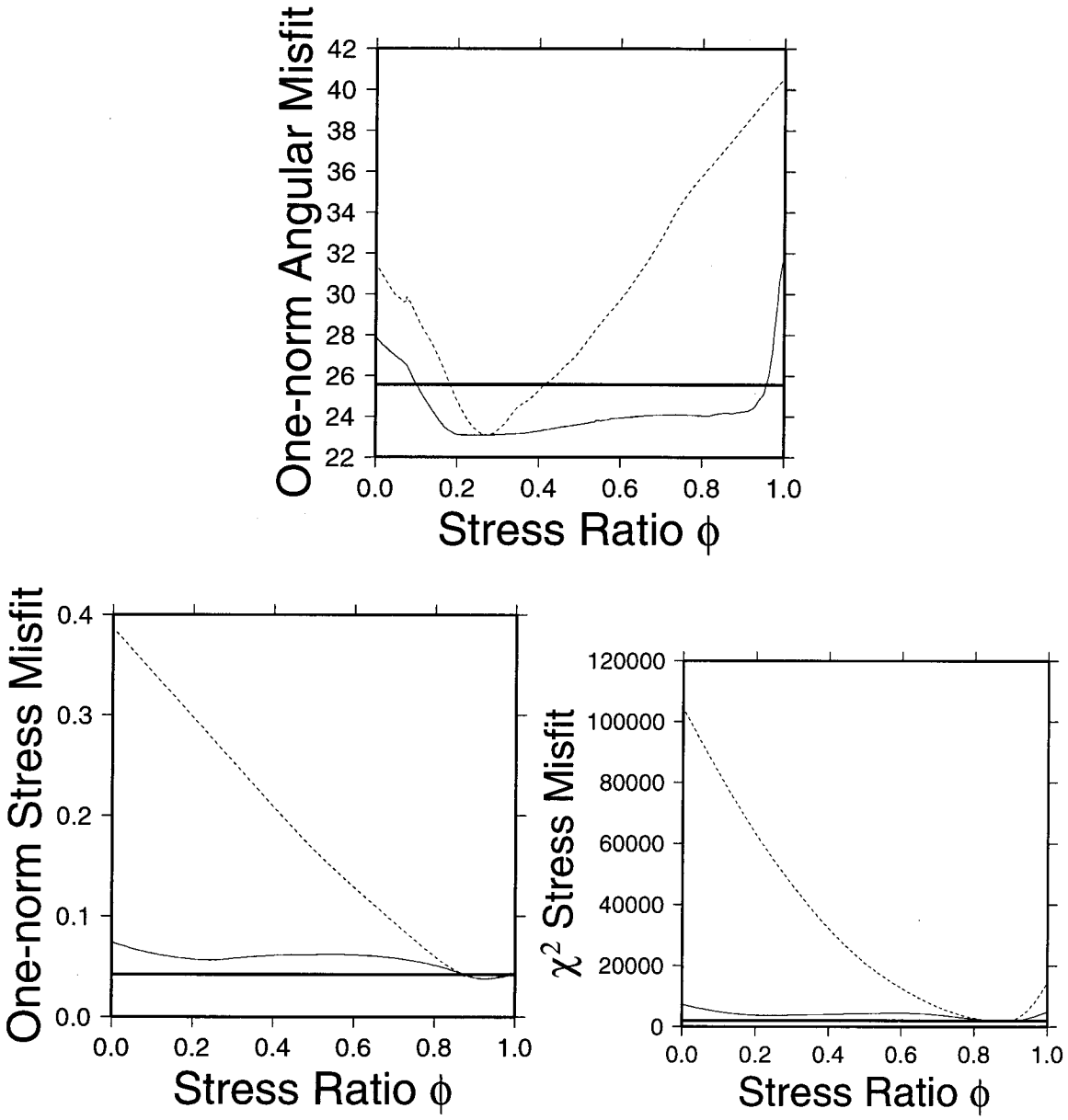

Figure 2.9: Various weighted misfit measures plotted as a function of ϕ for the borehole breakout data shown in Figure 2.7, where the thick solid line is the 95% confidence limit for the inversion, the thin solid line is the minimized misfit where for each value of ϕ the directions of the principal stress axes are allowed to vary so that the minimum misfit is obtained, and the dotted line is the misfit using the principal stress directions from the respective best fitting model. The 95% confidence value is plotted at the constant, solid line. (top) One-norm angular difference misfits. (bottom left) One-norm stress difference misfits. (bottom right) χ^2 stress difference misfits.

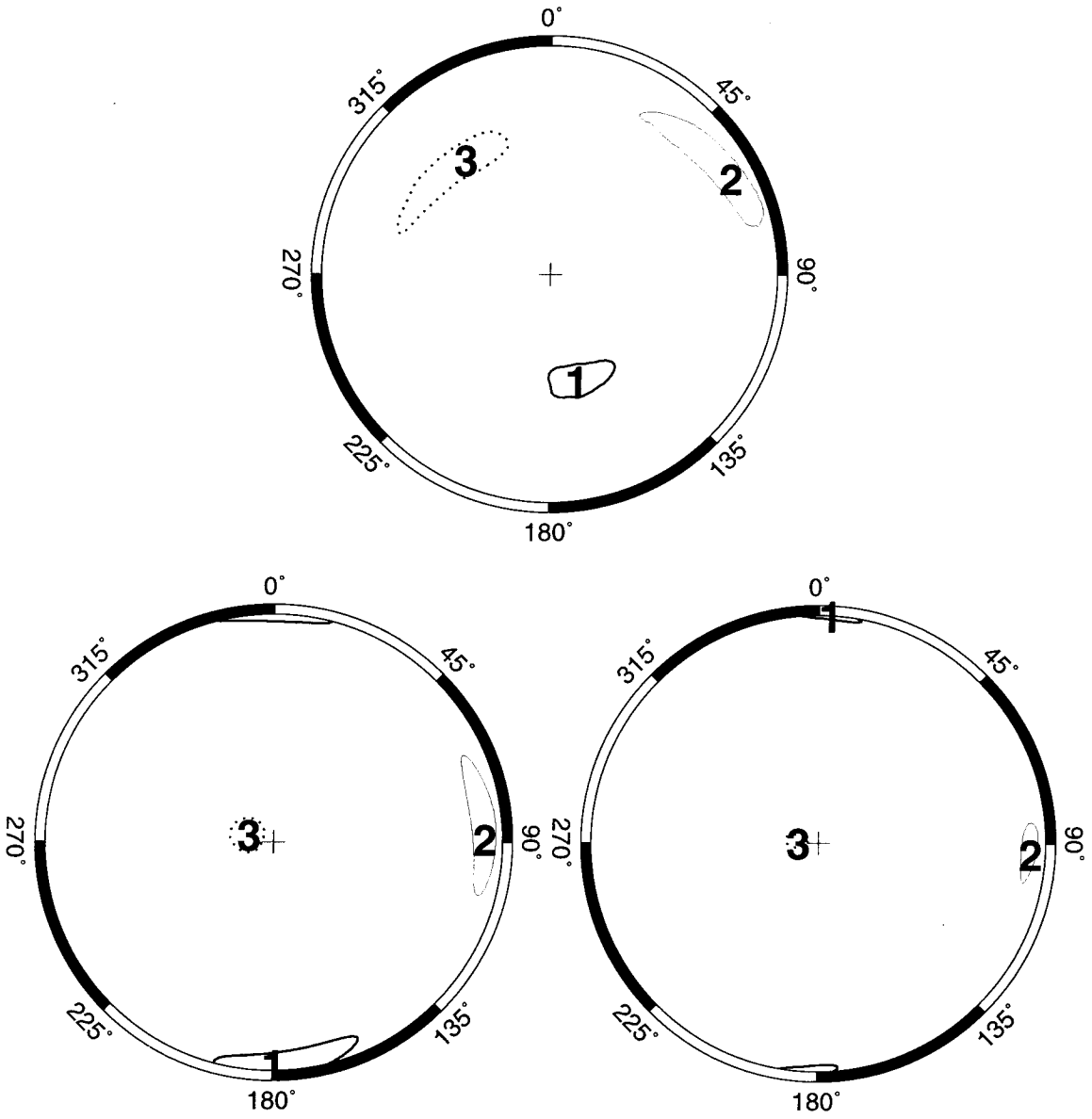

Figure 2.10: Comparison of stress state inversion results using three different misfit measures. (top) Results using a one-norm angular difference measure. (bottom left) Results using a one-norm stress difference measure. (bottom right) Results using a χ^2 stress difference measure. Lower hemisphere stereographic projection plot where the digits 1, 2, and 3 show the best fitting orientation of the S_1, S_2, and S_3 principal stress axes for the borehole breakout data plotted in Figure 2.7. The 95% confidence limits of the S_1, S_2, and S_3 orientations are plotted as thick solid lines, thin solid lines, and dotted lines, respectively.

2.2.5 Fitting the Breakout Data

Since the determination of the best fitting stress state for a set of borehole breakout data is inherently nonlinear, forward modeling is used instead of an inversion technique. Inversions have been used by others [e.g., *Qian and Pedersen*, 1991]. A two-step forward modeling approach is used here. First, a genetic algorithm or GA [*Holland*, 1975; *Davis*, 1987; *Goldberg*, 1989] is applied to the problem to find an approximate best fitting stress state, using the stress state parameterization described above, consisting of the variables $(\phi, \delta, \Omega, \psi)$. Here the borehole azimuth, δ, and the borehole deviation, Ω, are the first two Euler angles, and ψ is the third Euler angle. A N-dimensional optimizer is then initialized with the GAs results to find the best fitting stress state.

Genetic algorithms are an attractive approach to solving hard, nonlinear problems in which the forward calculation is straightforward but more traditional techniques might fail. Some of the advantages of GAs are that they efficiently search the model space, do not require a good starting model, and do not get trapped in local minima (unlike gradient search methods).

GAs operate on a population of models (Figure 2.11). The models are often binary coded, just as floating point numbers are encoded in a computer. An individual binary-encoded model is termed a chromosome. The first generation of chromosomes is randomly generated. Each chromosome has associated with it an "objective value," which is a problem-specific measure of how well the chromosome solves the problem. From the objective value is calculated a "fitness value"; the higher the fitness, the better the chromosome. In this work, each chromosome represents a distinct regional stress state, and the objective value is the weighted one-norm misfit between the observed and theoretical **IJK** breakout angles. Since smaller one-norm misfits correspond to higher levels of fitness, we use the following equation to relate the two:

$$f_i = \frac{\bar{o} + \sigma_o - o_i}{\sigma_o}, \tag{2.33}$$

where $\bar{o}$ is the population's mean objective value, σ_o is the standard deviation of the objective values, o_i is the ith chromosome's objective value, and f_i is the ith fitness value [*Holland*, 1975].

After the fitness values have been calculated, chromosomes are randomly selected to "mate" to create the next generation of chromosomes. Chromosomes with higher fitness values on average mate more often. Mating between two chromosomes is performed by randomly exchanging part of the binary patterns of both parent chromosomes. This operation is known as "crossover." Crossover is performed only roughly 60% of the time between two chromosomes. In the other 40% of matings the two chromosomes are carried directly into the next generation without crossover.

The final operation of the GA is mutation, whereby a small fraction of the bits of a chromosome are flipped. This process introduces variability into the population and allows broader searching of the solution space. The next generation of chromosomes has now been created, and the cycle begins

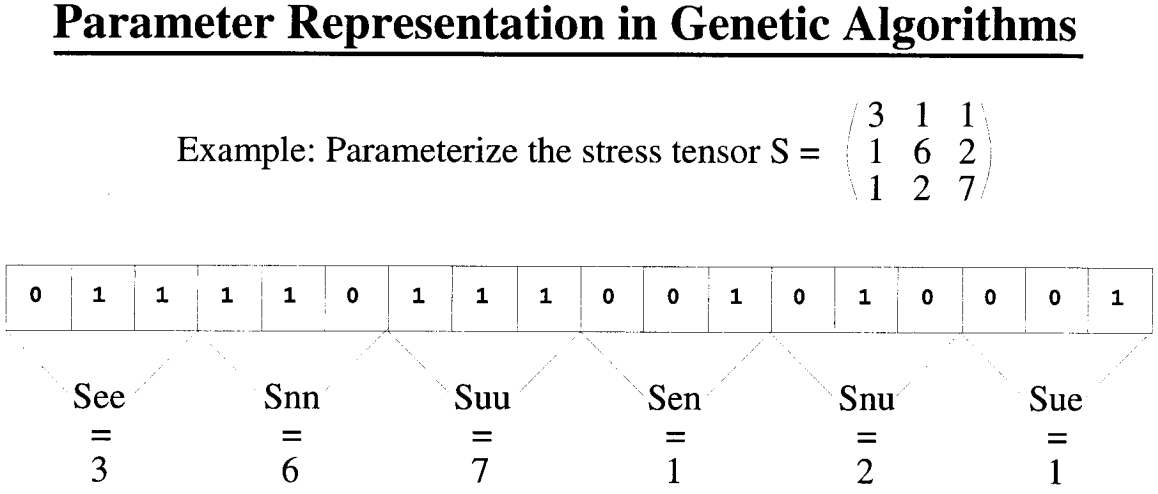

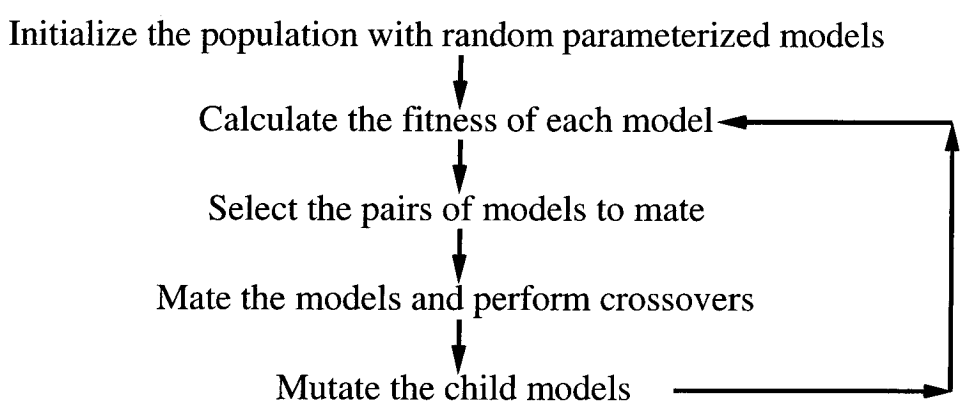

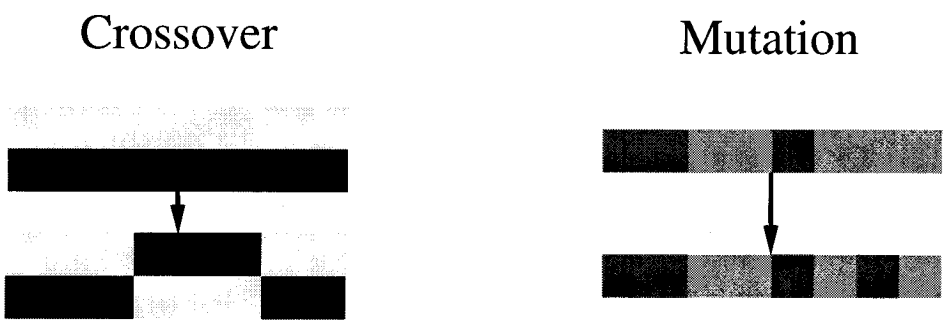

Figure 2.11: (top) Example parameterization of a stress tensor into a binary encoded chromosome. (middle) Flow diagram of a genetic algorithm. (bottom) Example of the crossover and mutation operators on chromosomes.

anew with the calculation of the population's objective values.

The GAs used in this research are run with populations of several hundred chromosomes for several hundred generations. Since GAs do not guarantee that they find the optimal solution to a problem, the particular stress state corresponding to the minimum misfit observed for all of the GA runs completed is taken as the starting point for a general N-dimensional optimizer routine. The Powell optimizer is used as described and coded by *Brent* [1973]. This particular optimizer does not require the use of derivatives of the function it is trying to optimize, a feature that makes it attractive for the borehole breakout problem.

Experience with various breakout data sets has shown that starting the Powell optimizer with a purely random stress state does not lead to a global minimum of the one-norm misfit, even for theoretically generated breakout data. The GA thus supplies an important first step in efficiently searching the space of stress states for good starting stress states for the Powell optimizer. In practice, each data set is run through GA with different random numbers several times to make sure that an acceptable global one-norm misfit minimum is found. Even though the Powell optimizer is used after the GA, the misfit is not a smooth function of the stress state, since different GA and Powell runs find different local minima. A localized GA search could be used to identify a better fitting stress state than the one the Powell search generated, but such a search is not performed because it would probably not improve the results significantly.

2.2.6 Confidence Limits

A genetic algorithm and Powell optimization search identifies the best fitting stress state model for a set of borehole breakout data. The next step calculates the region of stress state space that with a 95% chance contains the true stress state parameter values. The confidence limits on the best fitting stress state are determined using a modification of *Gephart and Forsyth*'s [1984] technique for defining confidence limits on stress state determinations from focal mechanisms. Confidence limits for both one-norm ($p = 1$) and two-norm ($p = 2$) misfit measures are calculated.

The first step in calculating the 95% confidence region for a best fitting model is to assume that by performing this one experiment (an experiment in the sense that oil wells were drilled and borehole breakout orientations were measured), something is known about the ensemble of misfits of the best fitting models that would result if the experiment were performed infinitely many times. The statistics of the misfit measures gathered by performing the experiment many times over can be calculated from the misfit measure itself. Relating the experimentally determined misfit measure gathered in the one performed experiment to the statistics of the distribution of misfit measures leads to the calculation of the misfit measure, $M^{(p)}(P)$, such that a certain percentage, P, of all misfit measures have misfits less than $M^{(p)}(P)$. If it is known that 95% of all of the misfit measures from these experiments have misfit measures $m^{(p)} < M^{(p)}(0.95)$, then the 95% confidence limit has

been identified.

It should be stated that the distributions of $m^{(p)}$ values calculated in searching for the best fitting model for the single experiment are not being considered. In the single experiment the best fitting model has a misfit $m^{(p)}$ at one end of a distribution of misfits corresponding to slightly different stress states. Instead, consider that when the best model for the experiment has been identified, all of the other possible stress states for the data in this experiment are ignored. Here the distribution of best fitting models, or misfits, that would be found if all of the boreholes were redrilled and breakout orientations remeasured are considered.

The statistics of the one-norm misfit ($p = 1$) are considered first, followed by a similar analysis for the two-norm misfit ($p = 2$). The results of *Parker and McNutt* [1980], who calculated the statistics of the one-norm misfit, are used here. Express the one-norm misfit as

$$m^{(1)} = \sum_{j=1}^{n} |x_j| / \sigma_j \tag{2.34}$$

where x_j are independent normal random variables with zero mean and standard deviations σ_j. The expected value of $m^{(1)}$ is

$$\overline{m^{(1)}} = \sqrt{\frac{2}{\pi}} n \approx 0.79788n. \tag{2.35}$$

Parker and McNutt [1980] also wrote a program, which, given a probability P and n, calculates the misfit $M^{(1)}(P, n)$ such that the probability is P that $m^{(1)} \leq M^{(1)}(P, n)$. In other words, this program finds $M^{(1)}(P, n)$ such that the integral from $-\infty$ to M of the one-norm distribution is P for a one-norm distribution of the order of n. $M^{(1)}(P, n)$ is used later to calculate the 95% confidence limit.

To find the 95% confidence limit, begin by defining $\sum_{min}^{(1)}$ to be the misfit measure of the best fitting model. Assume that this particular one-norm misfit corresponds to the mean misfit of a one-norm distribution. Of course, the mean misfit and the minimized misfit will differ, so the assumption is made that the errors, σ_j, were incorrectly estimated. To correct this estimation a new constant factor, f, is introduced which multiplies all of the standard deviations, σ_j, such that a new misfit sum is equal to the expected misfit. Since the best fitting model has already been identified, k degrees of freedom have been lost, where k is the number of variables in the problem. Therefore, the expected one-norm mean for $n - k$ observations is used. Mathematically, this becomes

$$\begin{aligned} \sum_{min}^{(1)} &= \sum_{j=1}^{n} \frac{|\theta_j - o_j|}{\sigma_j} \\ (2/\pi)^{1/2}(n-k) &= \sum_{j=1}^{n} \frac{|\theta_j - o_j|}{f\sigma_j} \qquad \text{from (2.35)} \end{aligned}$$

$$= \frac{\sum_{min}^{(1)}}{f}$$

$$f = \frac{\sum_{min}^{(1)}}{(2/\pi)^{1/2}(n-k)}$$

Finally, to find the $P\%$ confidence misfit value, $\sum_P^{(1)}$, the following expression is used

$$\frac{\sum_P^{(1)}}{f} = M^{(1)}(P, n-k) \tag{2.36}$$

where $M^{(1)}(P, n-k)$ is the function given by *Parker and McNutt* [1980]. The number of parameters identified in the genetic algorithm and Powell search, k, must still be subtracted from n to use $M^{(1)}$. Solving for $\sum_P^{(1)}$

$$\sum_P^{(1)} = \frac{M(P, n-k)}{(2/\pi)^{1/2}(n-k)} \sum_{min}^{(1)}. \tag{2.37}$$

Gephart and Forsyth [1984] find a similar expression in their equation (7), except they assumed that for large n one can replace the one-norm inverse cumulative function $M^{(1)}(P, n)$ with values from standard tables of Gaussian statistics. Since a code was obtained that calculates $M^{(1)}(P, n)$, there was no reason to make this assumption.

The logic that led to equation (2.37) can be used to calculate the 95% misfit value for a two-norm ($p = 2$) misfit measure. Instead of using $\mu^{(2)}$ which involves the square root of the sum of misfits (equation 2.25), the $(\mu^{(2)})^2 = \chi^2$ misfit measure will be used. Define $m^{(2)}$ as

$$m^{(2)} = \sum_{j=1}^{n} \left(\frac{x_j}{\sigma_j} \right)^2 \tag{2.38}$$

where x_j are independent normal random variables with zero mean and standard deviations σ_j. The expected value of $m^{(2)}$ is

$$\overline{m^{(2)}} = n. \tag{2.39}$$

Define $\sum_{min}^{(2)}$ as the minimum two-norm misfit measure determined from the genetic algorithm and Powell optimization search

$$\sum_{min}^{(2)} = \sum_{j=1}^{n} \left(\frac{\theta_j - o_j}{\sigma_j} \right)^2 \tag{2.40}$$

The same logic that led to equation (2.37) results in the following mathematical steps

$$n - k = \sum_{j=1}^{n} \left(\frac{\theta_j - o_j}{g\sigma_j} \right)^2 \qquad \text{from (2.39)}$$

$$= \frac{\sum_{min}^{(2)}}{g^2}$$

$$
\begin{aligned}
g^2 &= \frac{\sum_{min}^{(2)}}{n-k} \\
\frac{\sum_{P}^{(2)}}{g^2} &= M^{(2)}(P, n-k) \\
\sum_{P}^{(2)} &= \frac{M^{(2)}(P, n-k)}{n-k} \sum_{min}^{(2)}
\end{aligned}
$$

Here, $M^{(2)}(P, n-k)$ is the inverse probability distribution function for the χ^2 distribution and $\sum_P^{(2)}$ is the misfit measure that contains P percent of the misfit measures for an experiment with n observations and k modeled parameters.

2.2.7 Confidence Limits on Individual Stress State Parameters

Unlike other inversion methods the forward modeling approach does not by default give confidence limits on individual parameters of the model. The confidence limits on the stress state ratio ϕ are calculated by finding the values of ϕ for which the misfit measure is equal to the 95% confidence misfit value. In searching for these ϕ values, the principal stress directions are allowed to rotate to minimize the misfit for a particular ϕ value. The confidence limits on the Euler angles are not calculated since the successive nature of the Euler angle rotations to the principal stress directions removes any simple meaning between the Euler angle confidence limits and the principal stress direction confidence limits.

To calculate the 95% confidence limits on the principal stress directions, the stress state ratio ϕ is fixed and the borehole azimuth δ is iterated from 0° to 360° and the borehole deviation Ω is iterated from 0° to 90° in 1° increments. This iteration rotates the **J** axis across the lower hemisphere of a stereographic plot. For each orientation of **J** within the lower hemisphere, the misfit measure is minimized as a function of the third Euler angle, ψ. Since there are three confidence limits to calculate, S_{jj} is set to 2 to identify the S_1 confidence limits, S_{jj} is set to $\phi + 1$ to identify the S_2 confidence limits, and S_{jj} is set to 1 to identify the S_3 confidence limits. In each of the three cases, S_{ii} and S_{kk} are set to the other two principal stress values. The particular choice of the assignment of S_{ii} and S_{kk} to the remaining two principal stress values is irrelevant once the misfit measure has been minimized as a function of the third Euler angle, ψ. Contour plots of the 95% confidence limits on the principal stress directions show smaller 95% contour regions that are sometimes rotated away from their minimized locations when the stress state ratio ϕ is varied away from the minimum misfit.

Chapter 3 Analysis of the Siljan Deep Drilling Project Breakout Data

The intention of this chapter is to compare the *Qian and Pedersen* [1991] nonlinear borehole breakout inversion technique and the genetic algorithm and Powell optimizer inversion technique developed above by reanalyzing the borehole breakout data presented by *Qian and Pedersen* [1991] from the Siljan Deep Drilling Project in Sweden. The regional tectonic implications of this reanalysis will not be examined here. The borehole breakout data are taken from Table 3 of *Qian and Pedersen* [1991] and are plotted in Figure 3.1. This table lists the average borehole azimuth, deviation, and breakout orientation for each 100 m depth range. Also listed is the variance of the breakout direction in degrees over that 100 m interval. No conclusions regarding the relationship between breakout length and the in-situ stress state can be gathered here because *Qian and Pedersen* [1991] did not publish information on breakout length. Figure 3.2 plots a histogram of the angular difference between the location of the high side of the borehole and the breakout angle as measured in the plane perpendicular to the borehole axis for all of the data. The breakouts are clustered around the high side of the hole and could possibly be due to tool drag. However, the breakout azimuth is constant, regardless of the borehole azimuth, suggesting that it is unlikely that the breakouts are caused only by tool drag.

Qian and Pedersen [1991] applied a nonlinear inversion technique to their data, assuming a vertical principal stress direction with Poisson's ratio, ν, equal to 0.25. They found the stress state to be a strike-slip regime ($S_H > S_v > S_h$) with the maximum horizontal stress located $108.4^{\circ}{}^{108.7^{\circ}}_{108.0^{\circ}}$ east of north. The ratio of stresses was $S_H/S_v = 1.2^{\infty}_{1.05}$ and $S_h/S_v = 0.6^{0.98}_{0.0}$, which corresponds to a stress ratio ϕ varying from 0 to 0.952 with an optimal value of 2/3. The error bounds listed here are nonlinear error bounds calculated by varying the stress parameters until a large enough misfit was observed.

Qian and Pedersen's [1991] data are plotted in Figure 3.1 with the theoretical breakout pattern expected for the stress state resulting from their inversion. A Poisson's ratio of 0.25 was used in this calculation. The data show almost constant breakout azimuths regardless of the borehole orientation. Because of the relatively restricted range of borehole azimuths present in this data set, a large number of nondegenerate normal and strike-slip faulting stress regimes could fit these observations with nearly constant breakout orientations up to the maximum deviation of 45° (Figure 1.4). Clearly, the data are not well distributed in order to constrain the complete stress tensor. *Qian and Pedersen*'s [1991] high uncertainty in the S_h/S_v ratio reflects exactly this problem with the data distribution.

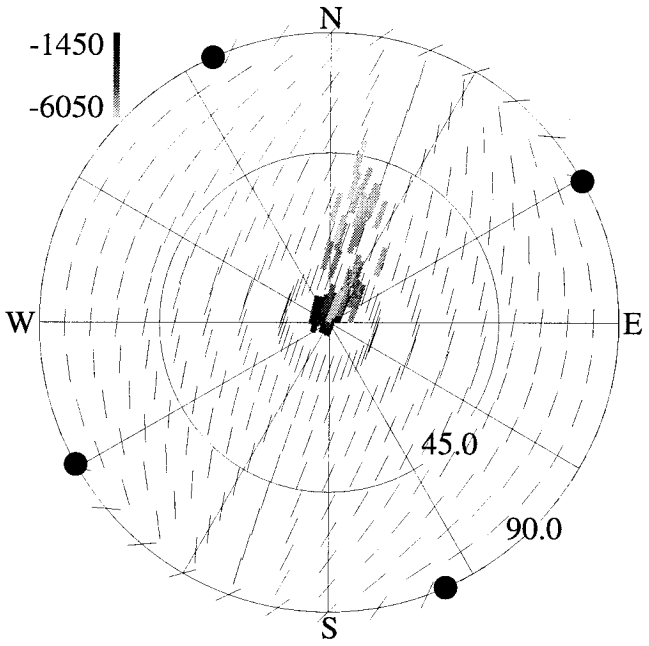

Figure 3.1: Compiled and processed data from the Siljan Deep Drilling Project in Sweden from *Qian and Pedersen* [1991] plotted on top of the theoretical breakout pattern for their best fitting stress state of $S_H/S_v = 1.2$ and $S_h/S_v = 0.6$, where S_H lies 108.4° east of north. Solid circles are "nodal" points at which the stress anisotropy is zero, corresponding to borehole orientations with no preferred breakout direction. The nodal points for this stress state lie at a deviation of 90°. A Poisson's ratio of 0.25 was used to calculate the breakout pattern. The vertical depth scale is in meters.

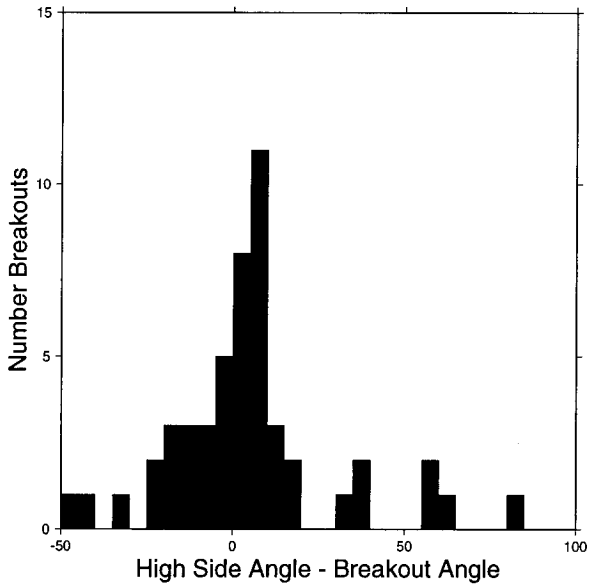

Figure 3.2: Histogram of the angular difference measured in the plane perpendicular to the borehole axis between the breakout orientation and the high and low sides of the borehole for the *Qian and Pedersen* [1991] data.

Table 3.1: Characteristics of the stress state that minimized the weighted one-norm angular difference misfit of the *Qian and Pedersen* [1991] borehole breakout data.

	S_1	S_2	S_3
Azimuth	N106.8°E	N16.7°E	N251.7°E
Plunge	3.5°	2.5°	85.7°
Value	2	1.40	1

Optimized $\phi, 0.40^{1.00}_{0.00}$; minimum weighted one-norm angular difference misfit, 1.71°; 95% confidence level for weighted one-norm angular difference misfit, 2.03°.

Table 3.2: Characteristics of the stress state that minimized the weighted one-norm stress difference misfit of the *Qian and Pedersen* [1991] borehole breakout data.

	S_1	S_2	S_3
Azimuth	N108.5°E	N198.9°E	N7.3°E
Plunge	2.2°	10.7°	79.1°
Value	2	1.88	1

Optimized $\phi, 0.88^{0.95}_{0.76}$; minimum weighted one-norm stress difference misfit, 0.000471; 95% confidence level for weighted one-norm stress difference misfit, 0.000600.

This will be a common problem in strike-slip stress regimes if highly deviated holes are not available. The only way to remedy this is to either find or drill boreholes that are nearly horizontal.

The stress inversion results presented by *Qian and Pedersen* [1991] are now compared to the stress inversion results generated by the genetic algorithm and Powell optimizer stress inversion technique using both the one-norm angular difference misfit measure, m_α (equation 2.27), and the one-norm stress difference misfit measure, m_σ (equation 2.31). The *Qian and Pedersen* [1991] borehole breakout data is used unmodified; the breakout selection criteria introduced above (Section 2.1.6) were not used since the original caliper curves were not available and the data were not gridded since the data are highly consistent.

The stress inversion results using the m_α and m_σ misfit measures are very similar (Figures 3.3-3.5). Both inversions identified a thrust faulting stress state. The principal stress directions identified using the two different misfit measures are almost identical as shown in Figure 3.4 which plots orientations of the principal stress directions and their 95% confidence regions on a lower hemisphere stereographic projection plot keeping ϕ constant. The angular difference inversion found a stress state (Table 3.1) in which S_1 is oriented N106.8°E plunging 3.5°, S_2 is also almost horizontal, oriented N16.7°E, plunging 2.5°, and S_3 is almost vertical, plunging 85.7° at an azimuth of N251.7°E. The stress difference inversion found a stress state (Table 3.2) with S_1 oriented at an azimuth of 108.5°E plunging 2.2°, S_2 oriented at an azimuth of 198.9°E plunging 10.7°, and S_3 oriented almost vertical at an azimuth of 7.3°E plunging 79.1°. The angular difference measure identified much larger 95%

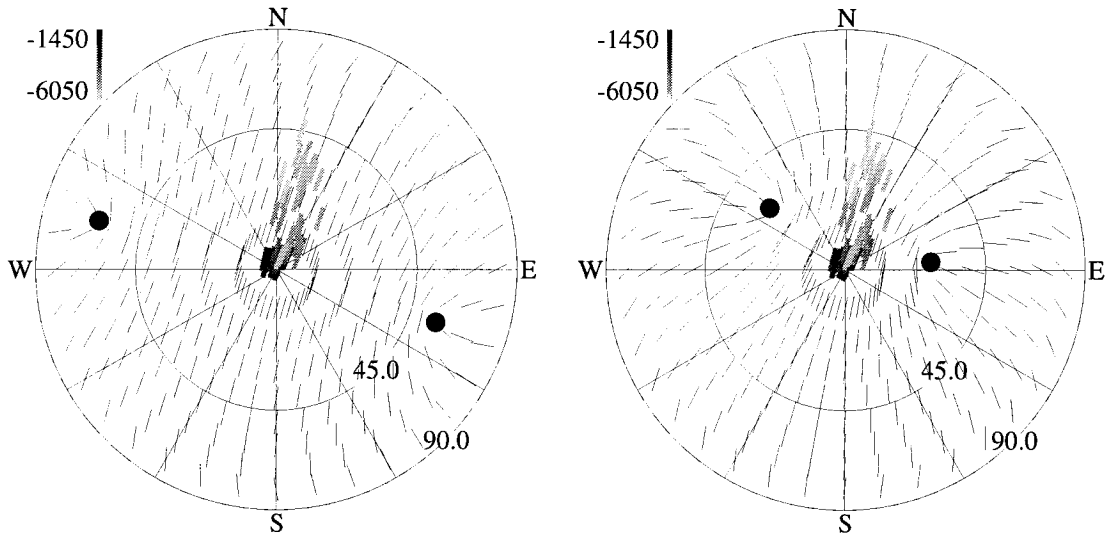

Figure 3.3: Compiled and processed *Qian and Pedersen* [1991] borehole breakout data plotted on top of the theoretical breakout pattern for a best fitting stress state generated using the genetic algorithm and Powell optimizer inversion technique. Solid circles are "nodal" points at which the stress anisotropy is zero, corresponding to borehole orientations with no preferred breakout direction. A Poisson's ratio of 0.25 was used to calculate the breakout pattern. The vertical depth scale is in meters. (left) Theoretical breakout pattern from the one-norm angular difference misfit measure inversion. (right) Theoretical breakout pattern from the one-norm stress difference misfit measure inversion.

confidence regions for the principal stress directions. The principal stress directions found by the stress difference misfit measure inversion lie within the 95% confidence region of those found by the angular misfit measure inversion. The two best fitting stress state ratios, ϕ, are substantially different (Figure 3.5); the angular difference misfit measure found $\phi = 0.40^{1.00}_{0.00}$, while the stress difference misfit measure found $\phi = 0.88^{0.95}_{0.76}$. However, given that the 95% confidence limits for the angular difference ϕ value span the range from 0 to 1, the two inverted stress states may be considered identical.

The largest difference between the two inversions is that the 95% confidence regions for the stress difference misfit measure are much smaller than those for the angular difference misfit measure (Figure 3.4). This may be due to the fact that the stress difference inversion was able to almost perfectly fit the data ($m_\sigma = 0.000471$) and thus any small changes to the optimum stress will very quickly result in a larger misfit value. This can be seen by comparing the minimum misfit identified to the average misfit of all stress states. The stress difference misfit for the best fitting stress state ($m_\sigma = 0.000471$) is 141 times smaller than the average stress difference misfit ($\overline{m_\sigma} = 0.0666$). On the other hand, the smallest angular difference misfit $m_\alpha = 1.71$ is a roughly one-tenth the size of the average angular difference misfit $\overline{m_\alpha} = 17.75$. So the stress difference inversion has many fewer stress states with associated misfit values near the minimum misfit than does the angular difference

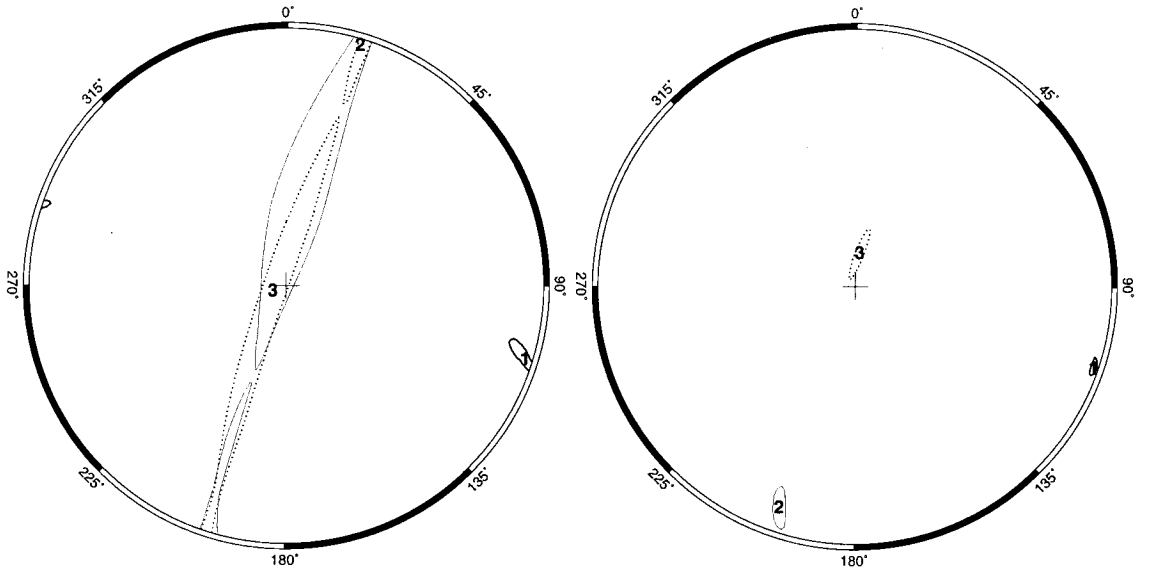

Figure 3.4: Results from the reanalysis of the *Qian and Pedersen* [1991] borehole breakout data. Lower hemisphere stereographic projection plot where the digits 1, 2, and 3 show the optimized orientation of the S_1, S_2, and S_3 principal stress axes, respectively. The 95% weighted one-norm misfit confidence limits of the S_1, S_2, and S_3 orientations are plotted as thick solid lines, thin solid lines, and dotted lines, respectively. (left) Inversion using the one-norm angular difference misfit measure. The stress state ratio ϕ is held constant at 0.40. Note that the direction of S_1 is very well constrained, but S_2 and S_3 can lie virtually anywhere within a vertical plane striking N16.7°E. (right) Inversion using the one-norm stress difference misfit measure. ϕ is held constant at 0.88. The best fitting principal stress directions are within the 95% confidence limits identified in left figure.

inversion. Examination of the stress difference confidence regions for 96% and above confidence limits show that the S_2 and S_3 contours extend in a NNE–SSW direction, following the trend of the S_2 and S_3 angular difference confidence limits.

Aside from the principal stress directions, the stress state implications of these two inversions are quite different. The angular difference inversion implies that only the direction of S_1 is constrained and that the orientations of S_2 and S_3 are unconstrained about an arbitrary rotation about the S_1 axis. Figure 3.5 demonstrates that the stress ratio ϕ is unconstrained, since there exists a stress state that can be rotated in such a way to fit the borehole breakout data within the 95% confidence limits for any ϕ. The stress difference inversion identifies the same stress state within the angular difference inversion's 95% confidence limits, but does not allow an arbitrary rotation of the S_2 and S_3 axes about the S_1 direction and it also tightly constrains ϕ. Given that the stress difference inversion is more physically realistic (Section 2.2.4), and given the unconstrained nature of the angular difference inversion, the stress difference inversion will be used as the representative stress state for the genetic algorithm and Powell inversion technique and will be used as a comparison against *Qian and Pedersen*'s [1991] best fitting stress state.

The orientations of S_H determined by *Qian and Pedersen* [1991] and determined here differ by

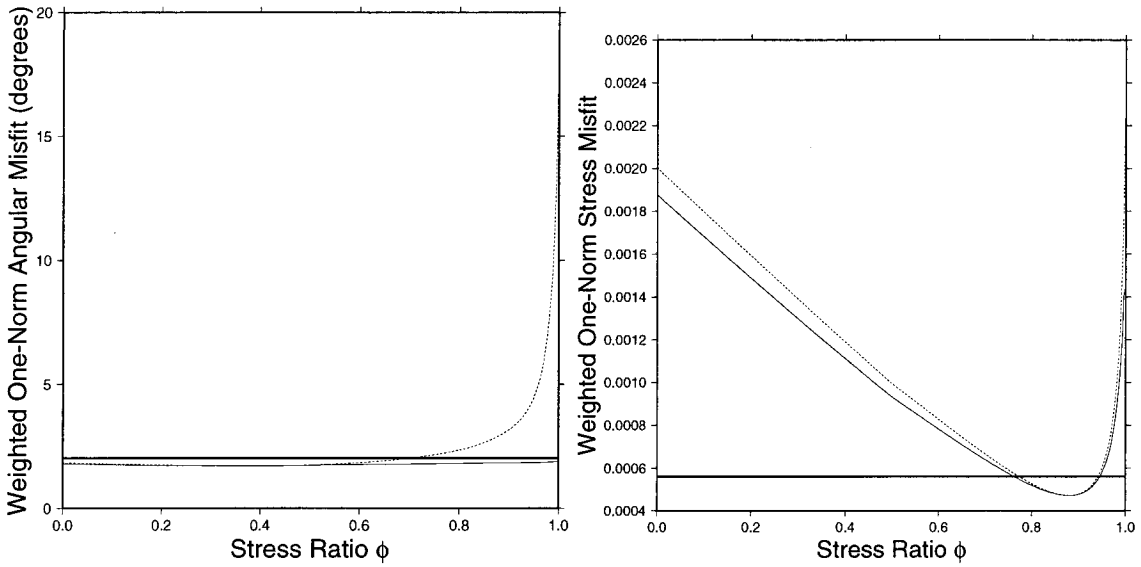

Figure 3.5: Results from the reanalysis of the *Qian and Pedersen* [1991] borehole breakout data. Plot of the weighted one-norm misfit as a function of ϕ, where the thick solid line is the 95% confidence limit, the thin solid line is the minimized misfit where for each value of ϕ the directions of the principal stress axes are allowed to vary so that the minimum misfit is obtained, and the dotted line is the misfit using the principal stress directions from the best fitting model. (left) Inversion using the one-norm angular difference misfit measure. (right) Inversion using the one-norm stress difference misfit measure.

only 0.1°. However, the remaining components of the stress state differ considerably. *Qian and Pedersen* [1991] found a strike-slip stress state with $\phi = 2/3$. The genetic algorithm and Powell optimizer search found a thrust faulting stress state with $\phi = 0.88$. *Qian and Pedersen* [1991] concluded that their data clearly showed a strike-slip stress regime. Even using the less constrained stress state implications of the angular difference inversion, which allows for either strike-slip or thrust faulting stress state solutions, it appears that *Qian and Pedersen*'s [1991] conclusion is too strong, given their breakout data and the analysis presented here.

Qian and Pedersen [1991] concluded that it was not feasible to relax the assumption of a vertical principal stress direction given their analysis of inversions of theoretical breakout data. However, there are several reasons why stress states with nonvertical principal stresses should be considered. First, the extra degree of freedom gives a clearer sense of how poorly or well the available data constrain the stress state. Second, it allows a much better fit of the data. The weighted stress difference misfit of the data using *Qian and Pedersen*'s [1991] best fitting stress state is 0.00214, which is outside the 95% confidence limit of 0.000600. The *Qian and Pedersen* [1991] solution is even outside of the 95% confidence limits of the angular difference inversion; the *Qian and Pedersen* [1991] misfit of 2.15° is larger than the 2.03° 95% confidence limit. Finally, there might be some breakout data sets in which the assumption of a vertical principal stress direction is invalid, leading

to an improper understanding of a region's stress state. The cost of this extra degree of freedom is slight in comparison with the potential gain in understanding of stress states.

In conclusion, while the stress difference misfit inversion uses a more physically realistic misfit approach to fitting borehole breakout data, the angular difference inversion can produce very similar stress state inversion results. The largest difference between the two misfit measure inversion techniques, when applied to the *Qian and Pedersen* [1991] data, is the implication regarding the best fitting stress state resulting from the smaller 95% confidence limits in the stress difference inversion. Also, relaxing the constraint of having a vertical principal stress may allow a much better determination of the stress state and introduce stress state solutions that fit the data much better.

Chapter 4 Analysis of the Point Pedernales Data

The borehole breakout inversion technique is applied to wells drilled by the Unocal Company from an offshore platform in the Point Pedernales oil field to determine the state of stress in the offshore Santa Maria Basin, California (Figure 4.1). The offshore Santa Maria Basin is an elongated, structural basin parallel to the California coast northwest of Point Arguello [*McCulloch*, 1987]. It lies between two NNW-trending structural boundaries: a zone of east-dipping normal faults, including the Santa Lucia Bank fault, on the west side, and the Hosgri fault on the east side. However, it appears to be stratigraphically continuous with the onshore Santa Maria Basin, east of the Hosgri fault, and to have experienced a similar Miocene deformational history [*Sorlien*, 1994].

The basal Tertiary section in the offshore Santa Maria Basin comprises volcanic rocks of probable early Miocene age which rest on basement and have been displaced by normal faults [*McCulloch*, 1987]. This volcanism and a subsequent phase of subsidence 18–16 Ma, documented by use of backstripping techniques in several wells in the region, have been attributed to the capture of the Monterey microplate by the Pacific plate [*Sorlien*, 1994] and the beginning of clockwise rotation of the western Transverse Ranges [*McCrory et al.*, 1995]. This development was followed by slow thermal subsidence from ~16 to ~7 Ma [*McCrory et al.*, 1995]. Since 6 Ma the tectonics of this offshore region has been locally complicated because of an overall transpressional regime, which produced NE–SW directed shortening between 5 and 3 Ma and much slower deformation in Quaternary time [e.g., *Clark et al.*, 1991; *Crouch et al.*, 1984].

Unocal provided five paper logs of four wells from the Point Pedernales field. All four wells were drilled from the same platform and all of the dipmeter data lies within a 4.3 km radius of the platform. Table 4.1 lists the type of tool used to log each hole and some of the properties of the wells, including the logged depth interval, the depth interval of processed dipmeter data, and the maximum deviation of the well over the processed interval.

The raw dipmeter data was run through a series of steps to analyze it for the ambient tectonic stress. The steps were as follows:

1. Digitize the paper logs and resample them to 0.125 m intervals.

2. Apply caliper calibration corrections to the caliper arm data for those wells in which the well log shows a caliper correction.

3. Compare the dipmeter's borehole azimuth data with the data from an independent directional survey of the hole (single-shot deviation surveys or gyroscopic logs). If the two data sets differ by roughly the magnetic declination (15°E for this location), then apply the declination correction

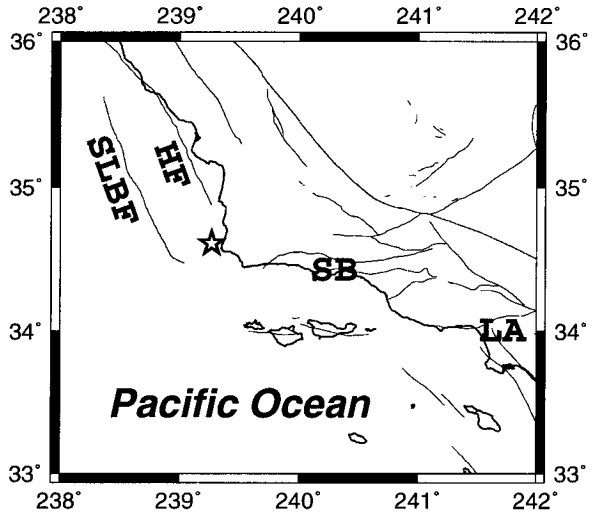

Figure 4.1: Location (star) of the Point Pedernales field in the offshore borderland along with some of the major Quaternary faults in the southern California region. LA, downtown Los Angeles; SB, Santa Barbara; SLBF, Santa Lucia Bank Fault; and HF, Hosgri Fault.

Table 4.1: Digitized well logs from the Unocal Company of wells drilled offshore from Point Pedernales, California, in the Santa Maria Basin.

Well Name	Log Type	Logged Depth Interval, m	Processed True Vertical Depth Interval, m	Maximum Deviation
A-1	Gearhart four electrode dipmeter survey	710–1788 logged 715–1784 processed	605–1672	7.0°
A-7	Gearhart six electrode dipmeter survey	732–2226 logged 733–2197 processed	686–1802	45.1°
A-13 Log1	Schlumberger SHDT monitor log	1729–2284 logged 1730–2288 processed	969–1088	80.5°
A-13 Log2	Schlumberger dipmeter monitor log	2300–2606 logged 2301–2497 processed	1092–1138	79.7°
A-16	Schlumberger formation microscanner log	2643–4267 logged 2646–4201 processed	1008–1254	89.6°

Two separate paper logs were received for well A-13. "Logged depth" is measured along the well bore but is greater than the true vertical depth where the borehole is deviated.

to the dipmeter's borehole azimuth and pad 1 azimuth (the **XYZ** azimuth of the number 1 dipmeter pad) data. The declination correction was applied to A-1 and A-7. The data from A-13 and A-16 agreed with their directional surveys to within 5° and hence were not further corrected.

4. Calculate the borehole elongation direction, using the four- and six-arm technique described above (Section 2.1.3). These data are plotted at every meter in Figure 4.2 as lower hemisphere stereographic projections of the borehole elongation. Also shown are enlargements of certain regions of the plot to better show the borehole elongation directions.

5. Select breakouts from the borehole elongation data, using the breakout selection criteria described above (Section 2.1.6). As an example the calibrated caliper and declination-corrected digitized dipmeter data and derived quantities are plotted as a function of log depth with the selected breakouts from well A-1 in Figure 4.3. 41 borehole breakouts were identified in the Point Pedernales caliper arm data. Two N–S oriented, short borehole breakouts from A-1 were manually removed from the list of breakouts since they were perpendicular to the average E–W trend of A-1 borehole breakouts. The remaining 39 breakouts total 232 m in length and are plotted in Figure 4.5. No breakouts due to key seats were manually removed from the list of computer selected breakouts. Note that no breakouts were found in the data from well A-7 because of the odd character of the data from the caliper arms, which routinely showed caliper arm diameters quite a bit larger and smaller than the bit size and caused the data to fail at matching criterion 3 described earlier. Since well A-7 was the only well logged with a six-arm dipmeter, the particular technique used to calculate six-arm borehole elongation angles becomes moot.

Figure 4.4 shows a histogram of the angular differences between the location of the high and low sides of the borehole and the breakout angle measured in the plane perpendicular to the borehole axis for all of the selected breakouts. There is roughly a 20° spread of breakout angles about the high side of the hole. These data show the same clustering of breakout angles near the high and low sides of the hole as *Qian and Pedersen*'s [1991] data (Figure 3.2).

6. Invert the selected breakout data for the best fitting stress state, using the combined GA and Powell optimization technique described above with both the angular difference misfit measure, m_α (equation 2.27), and the stress difference misfit measure, m_σ (equation 2.31). The results of the inversions are shown in Tables 4.2 and 4.3.

Analogous to the inversion results from the reanalysis of the *Qian and Pedersen* [1991] data, the angular difference and stress difference results of the Point Pedernales inversion are very similar and the stress difference inversion has much smaller 95% confidence limits. The 95% confidence limits on the principal stress directions determined by the stress difference inversion are smaller than the digits used to plot the orientations of the principal stresses in Figure 4.6. While the two inversions found very similar stress states and locations of nodal points (compare Tables 4.2 and Table 4.3) the inversion results differ enough from each other that neither the principal stress directions nor the

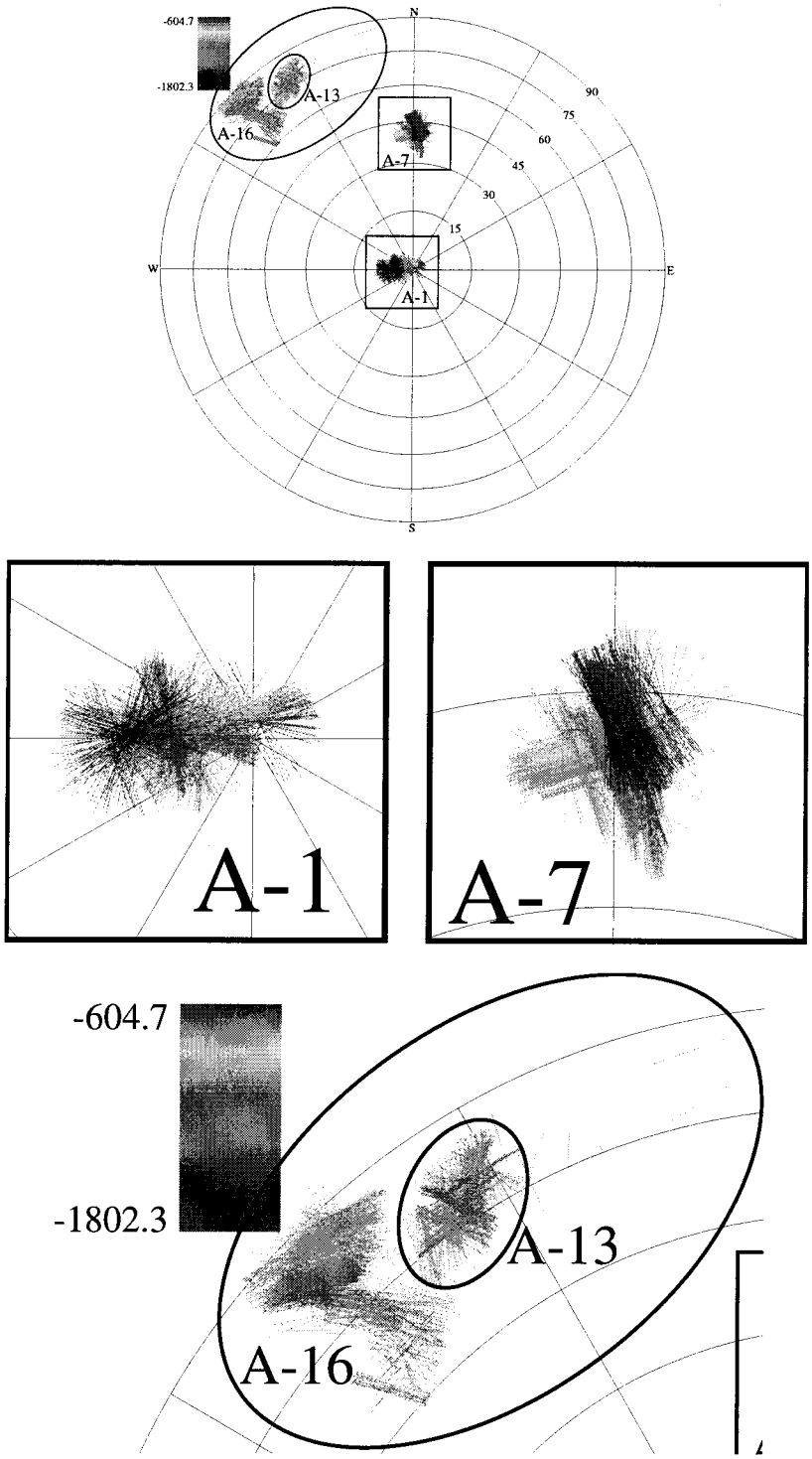

Figure 4.2: Lower hemisphere stereographic projection plots of the azimuth of borehole elongation at 1 m log depth intervals from the four wells drilled in the Point Pedernales field. (top) Lower hemisphere with all the well data plotted. (bottom) Enlargements of the top figure. The graduated depth scale shows the true vertical depth in meters.

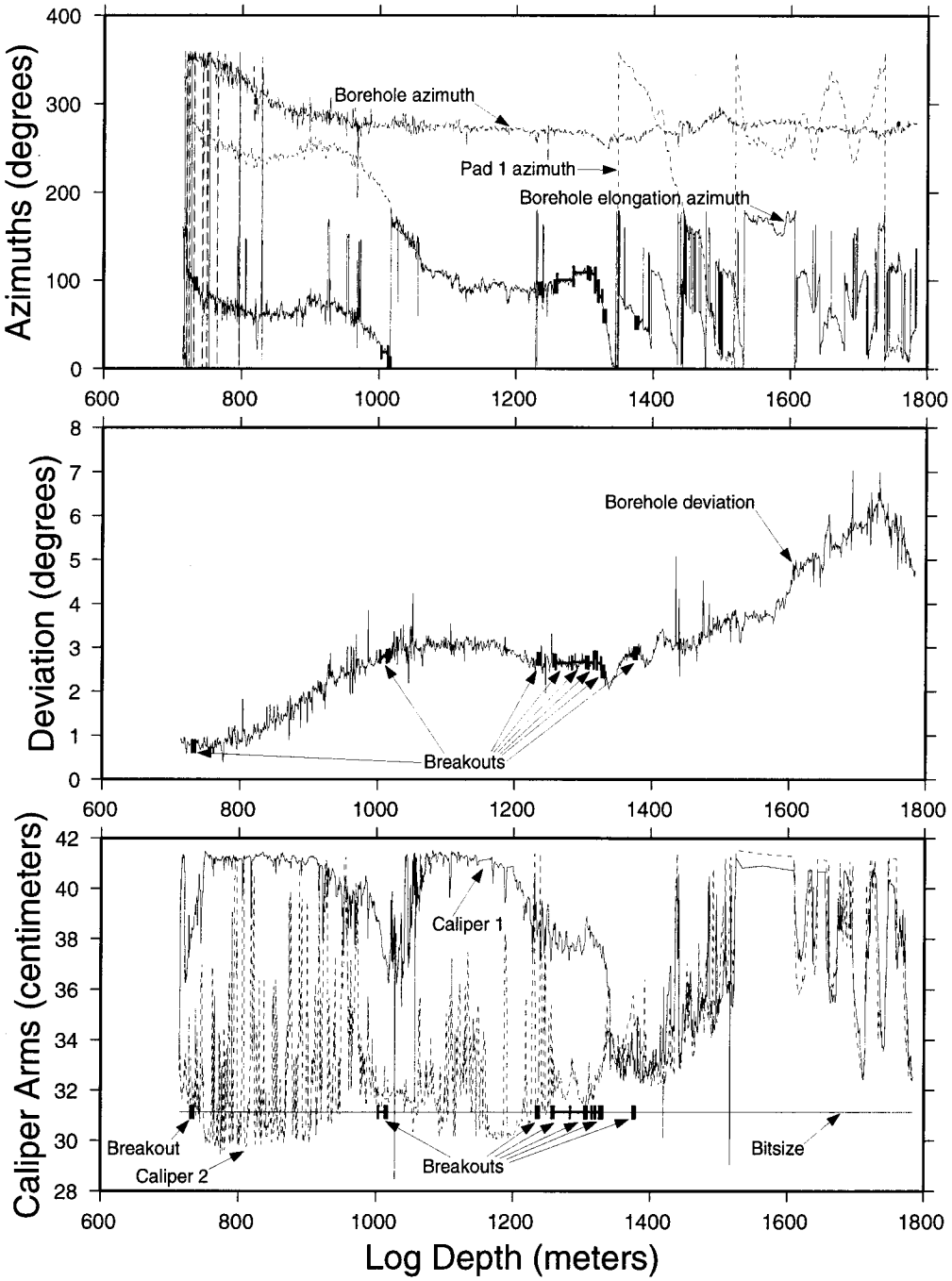

Figure 4.3: Plots of the caliper-calibrated and declination-corrected digitized dipmeter data and derived quantities as a function of log depth from well A-1. (top) Borehole elongation direction (solid line), pad 1 azimuth (long dashed line), and borehole azimuth (short dashed line). (middle) Borehole deviation. (bottom) Bit size (straight solid line), caliper arm 1 (solid line), and caliper arm 2 (dashed line). Selected breakout regions are plotted as horizontal bars showing the depth extent of the breakouts.

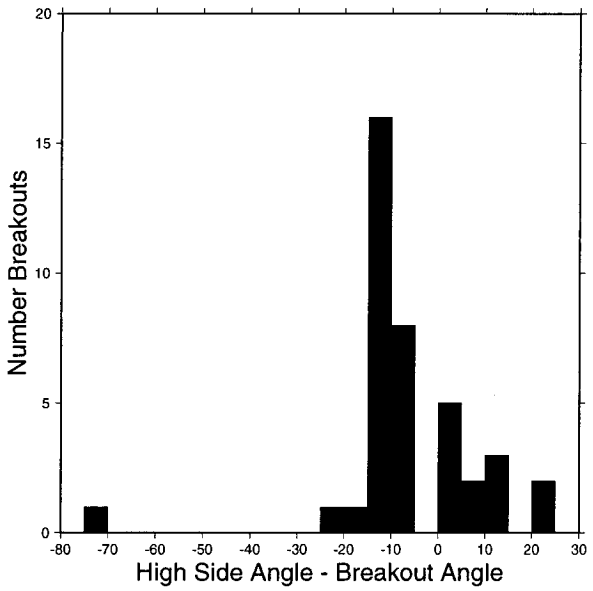

Figure 4.4: Histogram of the angular difference measured in the plane perpendicular to the borehole axis between the breakout orientation and the high and low sides of the borehole for the Point Pedernales data.

Table 4.2: Characteristics of the stress state that minimized the weighted one-norm angular difference misfit of the Point Pedernales borehole breakout data.

	S_1	S_2	S_3
Azimuth	N150.0°E	N56.7°E	N317.9°E
Plunge	31.3°	5.4°	58.2°
Value	2	$1.82^{2}_{1.31}$	1

Optimized $\phi, 0.82^{1.00}_{0.31}$; minimum weighted one-norm angular difference misfit, 5.76°; 95% confidence level for weighted one-norm angular difference misfit, 7.00°.

ϕ values fall inside of the other inversion's 95% confidence region. The similarity of the inversion results between the *Qian and Pedersen* [1991] and Point Pedernales inversion also extends to the ratio of the angular difference misfit value to the stress difference misfit value: For the *Qian and Pedersen* [1991] data this ratio was 3630 and the Point Pedernales data it was 3291.

After inverting the Point Pedernales data the theoretical breakout pattern is compared with the selected borehole breakouts (Figure 4.5). Both inversions placed their nodal points of the theoretical breakout pattern near the two sets of borehole breakout data. One nodal point lies between the A-13 and A-16 clusters of breakouts, which have a distinctly different trend. The other nodal point is placed almost on top of the borehole breakouts observed in the vertical A-1 borehole in such an orientation to minimize the misfit between the theoretical breakout pattern and A-1's borehole breakouts. Finally, it should be noted even with the relative shallowness of the breakout data,

Table 4.3: Characteristics of the stress state that minimized the weighted one-norm stress difference misfit of the Point Pedernales borehole breakout data.

	S_1	S_2	S_3
Azimuth	N143.4°E	N51.7°E	N317.9°E
Plunge	34.0°	2.6°	55.9°
Value	2	$1.79^{1.82}_{1.77}$	1

Optimized $\phi, 0.79^{0.82}_{0.77}$; minimum weighted one-norm stress difference misfit, 0.0017; 95% confidence level for weighted one-norm stress difference misfit, 0.0021.

the deepest breakout being 1.2 km deep, the stress state has no vertical principal stress direction since the nodal points are not symmetric about the origin of the plot, unlike the simple stress state examples shown in Figure 1.4. The minimum stress, S_3, is the closest principal stress direction to vertical, being 31.8° away from vertical.

Because the locations of the two nodal points are reasonably well constrained by the data, and the ϕ ratio is directly related to the distance between the two nodal points (Figure 1.4), the ϕ ratio is reasonably well constrained at the 95% confidence level (Figure 4.7). Compare this to the *Qian and Pedersen* [1991] inversion results, where the nodal points were not constrained by the borehole breakout data and, hence, the ϕ ratio was unconstrained for the angular difference misfit.

To see if the second nodal point's location was only determined by the small scale variation in A-1's borehole azimuth, borehole deviation, and breakout angle data, an inversion was performed of a gridded Point Pedernales data set containing only 6 breakouts, one of which represented the near-vertical A-1 breakouts. The inversion results were almost identical to the results of the nongridded inversion, suggesting that the nongridded inversion did fit the larger borehole breakout pattern while at the same time minimizing the misfit between the theoretical breakout pattern and A-1's breakouts.

The small 95% confidence limits on the principal stress directions obtained from the stress difference inversion (Figure 4.6) are probably due to the limited number of borehole breakouts identified at different borehole orientations. Since the inversion was able to place the two nodal points on top of both subsets of borehole breakouts, and the stress difference misfit for each identified breakout is small near the nodal points (Section 2.2.4), the accumulated misfit for the Point Pedernales inversion is very small. A slight change in the stress state will move the nodal points further away from the breakouts and cause the misfit to quickly grow much larger than the 95% confidence misfit, hence leading to the artificially small 95% confidence limits on the principal stress directions. For this reason and since the principal stress directions and ϕ values for the angular difference and stress difference inversions are almost identical, the stress difference inversion results will not be used in the analysis of the Point Pedernales stress regime.

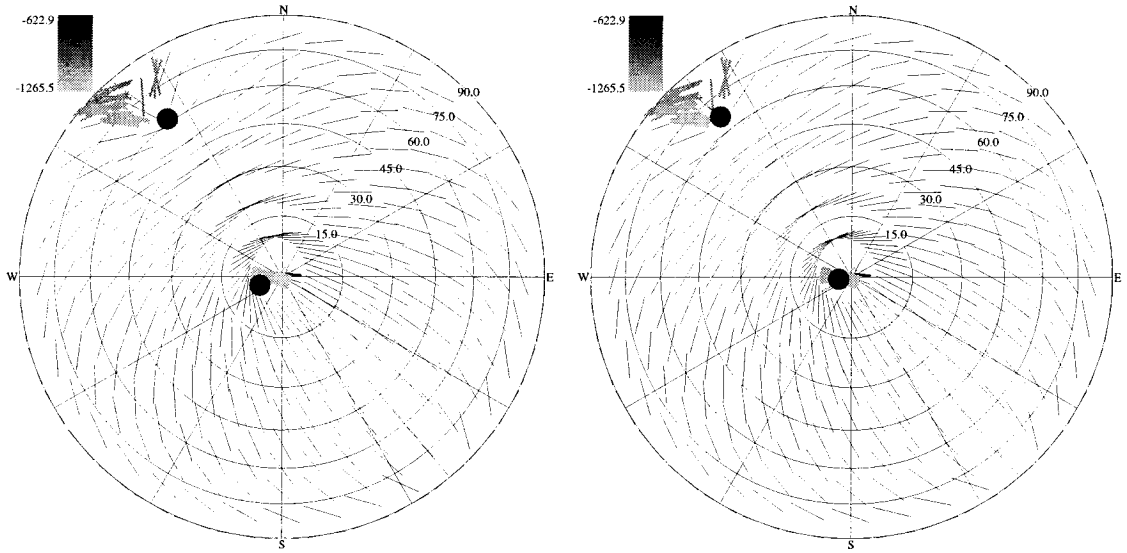

Figure 4.5: Compiled and processed Point Pedernales borehole breakout data plotted on top of the theoretical breakout pattern for a best fitting stress state generated using the genetic algorithm and Powell optimizer inversion technique. Solid circles are "nodal" points at which the stress anisotropy is zero, corresponding to borehole orientations with no preferred breakout direction. A Poisson's ratio of 0.25 was used to calculate the breakout pattern. The vertical depth scale is in meters. (left) Theoretical breakout pattern from the one-norm angular difference misfit measure inversion. (right) Theoretical breakout pattern from the one-norm stress difference misfit measure inversion.

The best fit orientation of the greatest principal stress direction, S_1, is N150.0°E plunging 31.3° for the angular difference inversion. The 95% confidence levels on this S_1 direction would permit it to lie in the azimuth range from N37.0°W to N25.1°E (Figure 4.6). If the borehole breakouts identified in the nearly horizontal wells (A-13 and A-16) are not naturally occurring breakouts but caused by some other mechanism, such as tool drag, then a simple estimate of S_H can be made if the stress state is assumed to have a vertical principal stress direction. In this case, only the near vertical A-1 breakouts remain. Using the weighted binning technique (Section 2.2.1), the average A-1 borehole breakout azimuth is N97.1°E. This corresponds to an S_H orientation of N7.1°E. This orientation of S_H falls within the angular difference 95% confidence limits (Figure 4.7).

Other studies have estimated the state of stress in the Santa Maria Basin and the western Transverse Ranges using geologic, earthquake, borehole breakout, and fracture data (Table 4.4). *Feigl et al.* [1993] used GPS receivers to calculate strain rates and orientations in small triangular portions of Central and Southern California. If the assumption is made that the principal strain axes are colinear with the principal stress axes, then the maximum horizontal principal stress direction in offshore Santa Maria Basin encompassed by the three GPS stations BLAN (Navy Dept 12 Naval District), LOSP (Mt. Lospe, Vandenberg AFB), and VNDN (VLBI STA 7223 RM 1 1983 DET 1 GSS) is oriented N24°E. The results presented by *Huang* [1995] were obtained by performing a

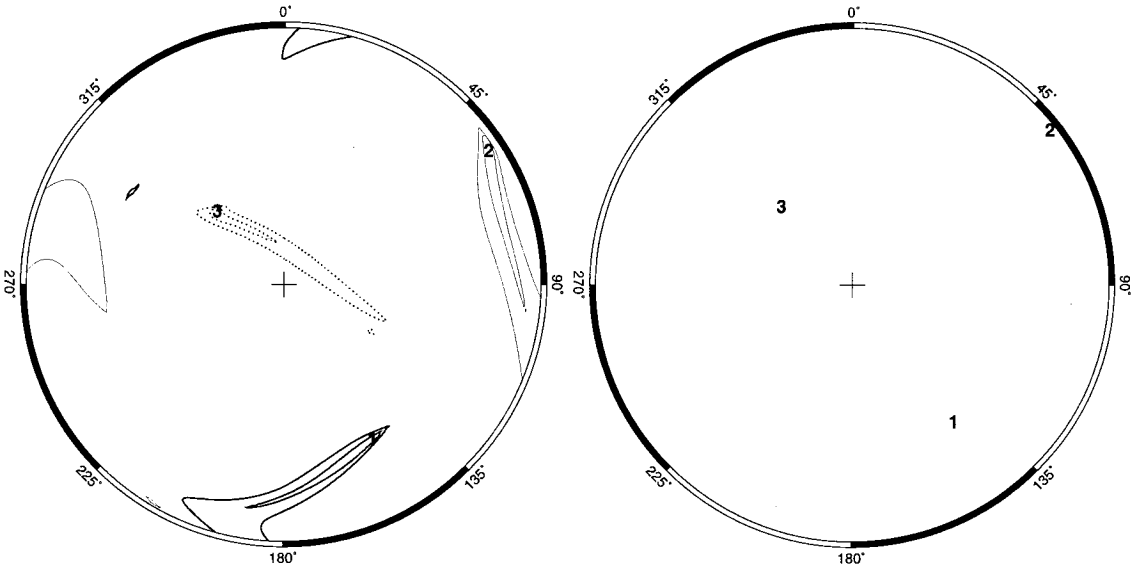

Figure 4.6: Results from the analysis of the Point Pedernales borehole breakout data. Lower hemisphere stereographic projection plot where the digits 1, 2, and 3 show the optimized orientation of the S_1, S_2, and S_3 principal stress axes, respectively. The 95% weighted one-norm misfit confidence limits of the S_1, S_2, and S_3 orientations are plotted as thick solid lines, thin solid lines, and dotted lines, respectively. (left) Inversion using the one-norm angular difference misfit measure. The stress state ratio ϕ is held constant at 0.82. Inner contours are the 75% confidence limits. (right) Inversion using the one-norm stress difference misfit measure. ϕ is held constant at 0.79. The 95% confidence limits are smaller than the size of the 1, 2, and 3 digits.

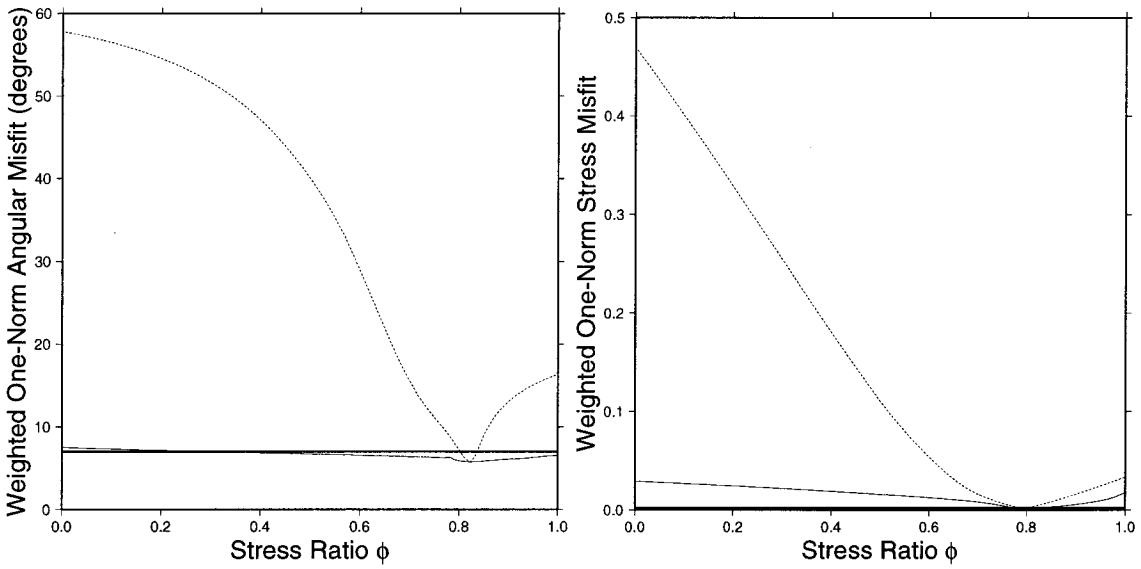

Figure 4.7: Results from the analysis of the Point Pedernales borehole breakout data. Plot of the weighted one-norm misfit as a function of ϕ, where the thick solid line is the 95% confidence limit, the thin solid line is the minimized misfit where for each value of ϕ the directions of the principal stress axes are allowed to vary so that the minimum misfit is obtained, and the dotted line is the misfit using the principal stress directions from the best fitting model. (left) Inversion using the one-norm angular difference misfit measure. (right) Inversion using the one-norm stress difference misfit measure.

stress state inversion of $3.0 \leq M \leq 6.0$ earthquakes that occurred in the western Transverse Ranges, the Santa Barbara Channel, and the Santa Maria Basin Region from 1981 to 1991. *Huang* [1995] reports S_1 oriented N12°E inclined 1° away from the horizontal. The stress state results presented by *Mount and Suppe* [1992] are calculated using the average breakout azimuth observed in the O8, O9, and O10 wells in the Santa Maria Basin presented in their paper. Assuming that the breakout orientation is perpendicular to the S_H azimuth, then S_H is oriented N63°E. *Varga and Hickman* [1992] studied naturally tensile occurring fractures observed in drill cores obtained from well A-1 in the Point Pedernales field and observed an average fracture azimuth of N32°E, suggesting that the maximum horizontal stress was oriented in the same direction when the fractures were created. The difference in the fracture azimuth and the S_H azimuth determined from the borehole breakouts in the same hole differ, suggesting a change in the stress state since the time when the fractures formed [*Clark et al.*, 1991].

While the stress state results for the Santa Maria Basin and western Transverse Ranges show a large amount of variation (Figure 4.8), the stress inversion results using the breakouts identified in both the vertical and horizontal boreholes is completely different than the other stress state results. This suggests that either the stress state in the Point Pedernales is field very different than that of surrounding regions, or that the borehole breakout data are suspect. Since the S_H azimuth

Table 4.4: Stress state results from studies performed in the Santa Maria basin and the western Transverse Ranges.

Study	Measurement Type	S_1 or S_H	Azimuth	Inclination
This study	Borehole breakouts	S_1	N150.0°E	31.3°
This study	Borehole breakouts	S_H	N7.1°E	0°
Huang [1995]	Earthquake focal mechanisms	S_1	N12°E	1°
Mount and Suppe [1992]	Borehole breakouts	S_H	N63°E	0°
Varga and Hickman [1992]	Fractures in boreholes	S_H	N32°E	0°

A Global Positioning System (GPS) survey of the offshore Point Pedernales area by *Feigl et al.* [1993] determined a principle strain shortening azimuth of N24°E.

calculated using the vertical A-1 borehole is fairly consistent with the other stress state studies, it appears that the stress state results using the complete breakout data set are controlled by the poor borehole orientation coverage and the fact that the inversion process places the breakout nodal points near the data. For this reason, the general three-dimensional stress results are inconclusive, and require better data coverage to gain an understanding of the complete stress state in the offshore Santa Maria Basin using this technique. More complete coverage of the borehole orientation space represented by the plot in Figure 4.5 would also allow a better estimation of the overall variability of the measurements and show whether the inferred positions of the nodal points are likely to be correct on a more regional scale.

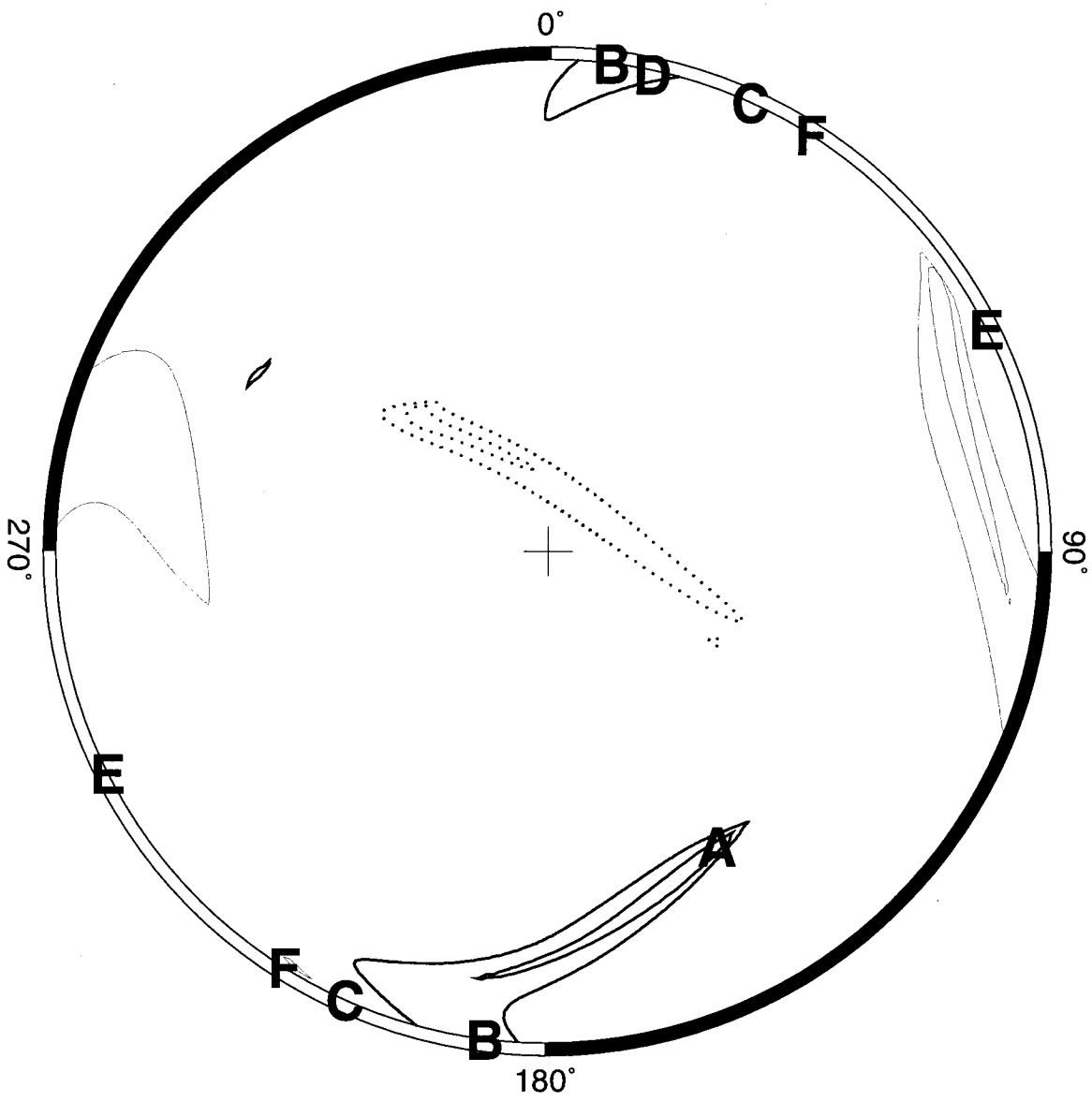

Figure 4.8: Lower hemisphere stereographic projection plot of S_1 or S_H orientations from studies performed in the Santa Maria basin and the western Transverse Ranges. The contours are the same 75% and 95% angular difference confidence limits plotted in Figure 4.6. The letters A–F refer to the stress state results generated by: (A) all the Point Pedernales breakouts identified in this study; (B) Point Pedernales breakouts identified in the vertical A-1 well; (C) *Feigl et al.* [1993]; (D) *Huang* [1995]; (E) *Mount and Suppe* [1992]; (F) *Varga and Hickman* [1992].

Chapter 5 The Stress State and Its Depth Dependence in Cook Inlet, Alaska

5.1 Abstract

The stress state and its depth dependence in Cook Inlet, Alaska were determined using breakouts identified in deviated boreholes drilled from offshore oil platforms in Cook Inlet. Twenty-one separate boreholes, reaching deviations of 54° and 3,223 m true vertical depth, were examined from five offshore oil platforms that produce oil from narrow NNE-trending anticlines: Granite Point, Anna, and Bruce platforms in the Granite Point field; and Baker and Dillon platforms in the Middle Ground Shoals field. The breakouts were calculated from analog and digital dipmeter and formation microscanner (FMS) data.

A total of 279 usable breakouts totaling 1,860.8 m in length were identified; of these, 142 breakouts totaling 880.5 m in length had their breakout orientations at least 15° away from the low and high side of the borehole (i.e., nonradial). Stress state inversions of 31 different subsets of the borehole breakout data were performed. Inversion of breakouts identified in the top and middle marker beds of three marker beds analyzed in wells drilled from the Baker platform identified nearly degenerate thrust faulting stress states with the maximum principal stress axis, S_1, oriented horizontally WNW–ESE, perpendicular to the NNE-trending anticlinal structures. The stress state from the deepest marker is also a nearly degenerate thrust faulting stress state with S_1 oriented NNW–SSE, aligned with the regional direction of relative plate motion between the North American and Pacific plates. In between the shallow and deep stress state is an observed normal faulting stress state with S_2 oriented subhorizontally ENE–WSW. This clockwise rotation of the stress tensor as a function of depth suggests that the stress field changes from a shallow stress state responsible for the local NNE-trending structures and a deeper one from the North American and Pacific plates collision zone. The observed normal faulting stress state between the two thrust faulting stress states is anomalous and may represent some sort of transition from the shallow to the deep stress state. Stress state profiles in 500 m true vertical depth (TVD) intervals show consistently oriented thrust faulting NNW–SSE trending S_1 azimuths. The thrust faulting S_3 principal stress direction is consistently within 30° of vertical, suggesting that the stress tensor does not significantly rotate away from the surface conditions that require a purely vertical stress tensor. However, the $\sim$ 30° deviation of the S_3 axes implies that the assumption of a purely vertical principal stress direction is not valid. The

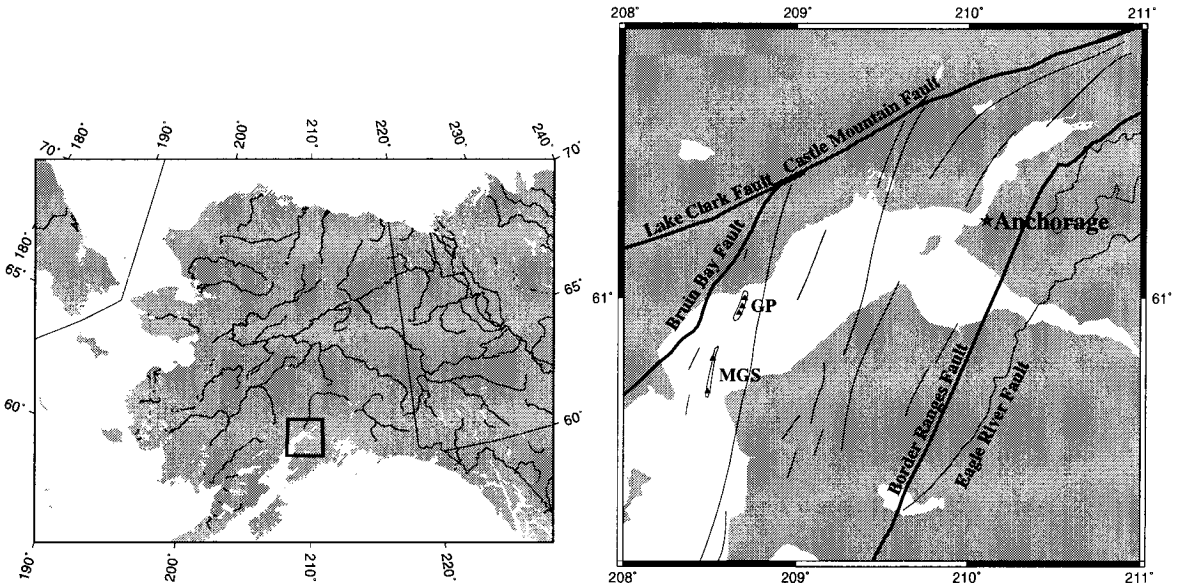

Figure 5.1: (left) Stereographic projection map of Alaska. The boxed area in this plot is shown in the right plot. (right) Mercator projection of Cook Inlet, Alaska plotting major structural faults (thick lines), minor faults (thin lines), the oil fields examined in this study (thin ellipses), and the offshore oil platforms where deviated boreholes were drilled from (triangles). The northern oil field is Granite Point ("GP") and the southern oil field is Middle Ground Shoals ("MGS"). From north to south, the platforms are Granite Point Bruce, Granite Point Anna, Granite Point Granite Point, Middle Ground Shoals Baker, and Middle Ground Shoals Dillon.

nearly degenerate thrust faulting stress states inverted from the Granite Point and the 10.8 km distant Baker platform breakouts are nearly identical, implying that the technique of using deviated borehole breakouts to invert for the regional stress is valid. The orientations of the maximum horizontal stress determined from the Cook Inlet borehole breakouts are consistent with other stress indicators in south-central Alaska and consistent with the direction of relative plate motion between the North American Plate and the Pacific plate. The S_1 axis for the Cook Inlet field trends N179.6°E plunging 2.7°, but does not appear representative of the stress field for each subset of breakouts. The Granite Point S_1 axis trends N19.4°W plunging 3.4°, the Baker platform S_1 axis trends N10.2°W plunging -7.7°, and the Dillon platform S_1 axis trends N69.4°W plunging 1.7°. The more westerly Dillon platform S_1 orientation of the may be related to the local NNE-trending anticlinal structures in the Cook Inlet Basin.

5.2 Introduction

The stress state inversion technique developed in previous chapters determines the orientation and relative magnitudes of the principal stress orientations from a set of borehole breakouts identified in deviated boreholes. Previous applications of this technique used borehole breakout data sets with limited depth and borehole deviation and borehole azimuth coverage. Here, the technique is applied

to a large breakout data set covering a 38 km region obtained from 21 wells drilled into the Middle Ground Shoals and Granite Point oil fields in Cook Inlet, Alaska, where borehole breakouts were identified between 2,800 and 3,900 m true vertical depth. The large quantity of data allows stress state inversions of smaller subdivisions of the data and an examination of stress state changes as a function of depth. The principal stress directions and the stress state ratio ϕ may change as a function of depth for many reasons: 1) the stress ratio ϕ can change as the overburden pressure increases with depth (Chapter 1.1), 2) the stress state may change as the borehole enters into different areas of the local geologic structure, and 3) different geologic formations have different material properties.

This chapter begins by discussing the geology and stratigraphy of the Cook Inlet Basin, then examines the data processing and analysis issues that emerged and were resolved in this study. The data from each borehole are individually examined and analyzed. Finally, data are then inverted and the results are discussed.

5.3 Geology and Stratigraphy of the Cook Inlet Basin

Cook Inlet is a very large estuary in south central Alaska with Anchorage lying at its northeastern end. It lies within the Cook Inlet Basin, which is a 320 km long, 96.5 km wide NNE–SSW striking forearc basin in the Pacific and North American plate subduction margin (Figures 5.1 and 5.2). The tectonic framework of southern Alaska and the Cook Inlet Basin is dominated by the convergence between the subducting Pacific Plate and the overriding North American plate. The region is tectonically complex, given that it lies between the purely convergent margin along the Aleutian trench to the west and the transform plate boundary to the east expressed by the Fairweather and Queen Charlotte faults.

The Cook Inlet Basin is about the same size as the San Joaquin Basin and shares many of the same structural settings [*Boss et al.*, 1976]. It is bounded on the north and west by the Bruin Bay and Castle Mountain faults and the Alaska-Aleutian Range (Figure 5.1). On the south and east it is bounded by the Border Ranges fault and by the Kenai Mountains. The Border Ranges fault is a 2,100 km long suture that can be traced from Baranof Island in the Alaskan panhandle to Kodiak Island. It separates a forearc basin sequence (on the Peninsular terrane) on the northern side of the fault from rocks inferred to have been deposited in a subduction accretionary complex (Chugach terrane) (Figure 5.2) and shares many analogies with California's Coast Range fault system [*Boss et al.*, 1976; *Little and Naeser*, 1989; *Plafker et al.*, 1994]. Both terranes are exotic to Alaska and the Chugach terrane is the more newly accreted terrane [*Schmoll et al.*, 1984]. In the Cook Inlet area, the Border Ranges fault separates the Chugach terrane on the south from pre-Late Cretaceous sequence and correlative rocks of the Alaska-Aleutian Range batholith [*Magoon*, 1994]. The Border Ranges

fault has history of Early Jurassic through Late Cretaceous subduction. In places it is offset and modified by younger, strike-slip, and normal faults [*Little and Naeser*, 1989; *Plafker et al.*, 1994]. Recent seismicity may be associated with the Border Ranges fault, however, uncertainties in the epicentral locations cannot definitely relate earthquakes with the Border Ranges fault [*Ratchkovsky et al.*, 1997].

The Castle Mountain fault is the northern boundary to the Cook Inlet Basin. The fault displays Holocene oblique-slip offsets and has been historically active. In 1984, a buried 10 km segment of the Castle Mountain fault broke to generate the m_b 5.6 Sutton earthquake, which involved right-lateral slip [*Page et al.*, 1991]. The Castle Mountain fault is one of at least three fault systems that absorb the relative plate motion between the subducting Pacific Plate and the deforming North American plate.

The western boundary of the Cook Inlet Basin is the Bruin Bay fault, a major northeast-trending fault that has been mapped from near Mt. Spurr to Becharof Lake for 530 km and may extend an additional 140 km to the southwest [*Miller and Richter*, 1994]. It, along with the Lake Clark fault, is a probable southwestern extension of the Castle Mountain fault [*Detterman et al.*, 1976]. The Bruin Bay fault is a high-angle reverse fault and displays evidence of up to 3 km of stratigraphic throw [*Nokleberg et al.*, 1994]. There is no evidence of Holocene displacement on either the Bruin Bay or the Lake Clark faults. This fault zone is at least of Middle Jurassic age, but some of its small high-angle faults in the northwest have Miocene movement. No significant lateral displacement is associated with this fault [*Boss et al.*, 1976].

In the Cook Inlet area, most of the oil and gas is produced from rocks in the Kenai Group, which range in age from the Upper Oligocene through Upper Pliocene and unconformably overlie source rocks of Mesozoic age [*Magoon*, 1994; *Wahrhaftig et al.*, 1994]. The Kenai Group is composed from older to younger of the Hemlock Conglomerate, the Tyonek Formation, the Beluga Formation, and the Sterling Formation. The Oligocene Hemlock Conglomerate, which contains 80% of the oil in Cook Inlet, consists of conglomerate and conglomeratic sandstone containing quartz and chert, and pebbles of metamorphic, volcanic, and plutonic rocks [*Magoon*, 1994; *Wahrhaftig et al.*, 1994]. It also contains a few thin coal seams [*Boss et al.*, 1976]. The Tyonek Formation, consisting of as much as 2,330 m of sandstone, conglomeratic sandstones, shale, conglomeratic shales, and coal beds deposited in a braided-stream environment, is of Lower Oligocene through middle Miocene age. The Tyonek Formation contains the bulk of the coal resources in Cook Inlet. The Beluga Formation is of Upper and Middle Miocene age, and it, along with the Sterling Formation, are the major producers of methane gas in Cook Inlet. The whole formation is of continental origin, with a large variation of lithologies. This formation consists of floodplain shales with minor interbedded coal seams and thin channel sandstones [*Boss et al.*, 1976]. The Sterling Formation is of latest Miocene and Pliocene age and consists of massive sandstone, conglomeratic sandstone, and interbedded claystone, and some

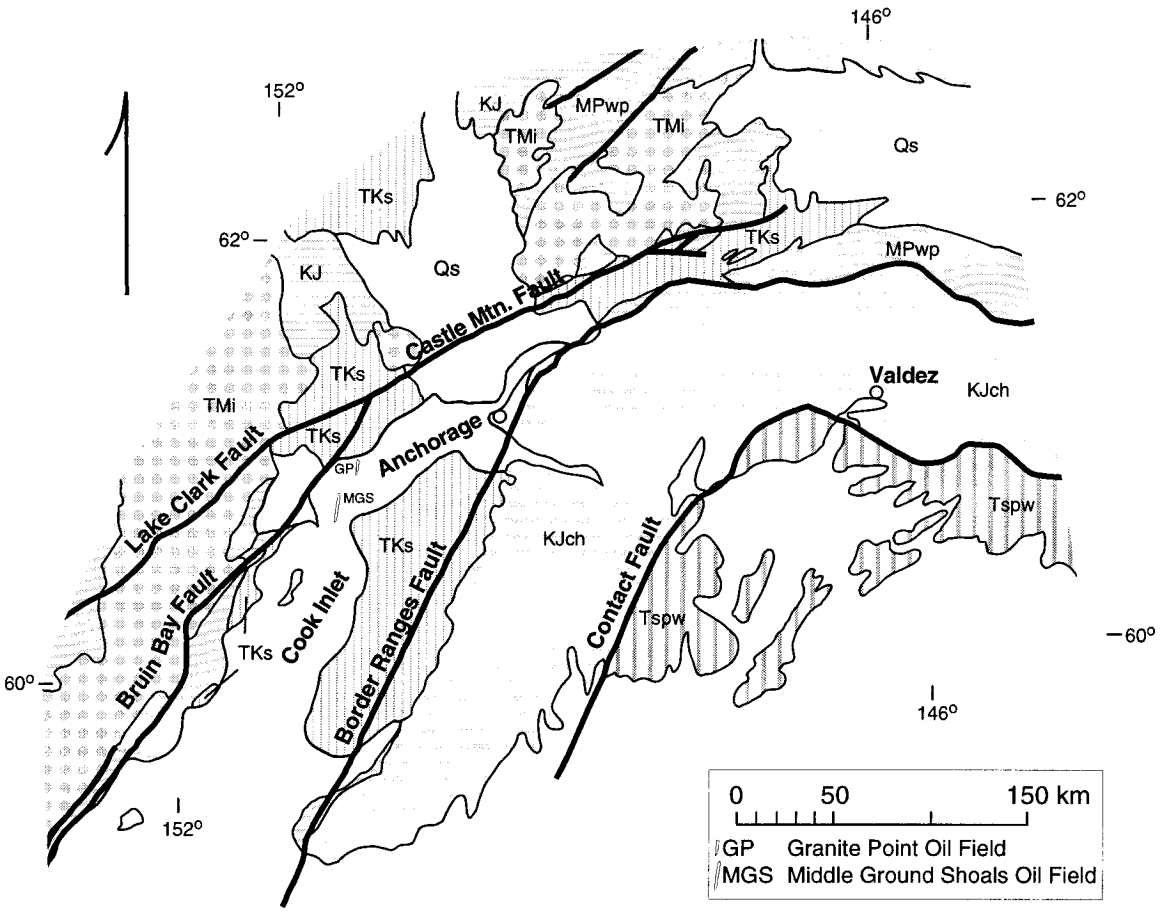

Qs	Quaternary Sediments and Volcanic Rocks
TKs	Cretaceous and Tertiary Sedimentary Rocks including Cook Inlet forearc deposits
Tspw	Tertiary Sedimentary Rocks of the Prince William Terrane
KJch	Cretaceous and Jurassic Sedimentary Rocks of the Chugach Terrane
KJ	Cretaceous and Jurassic Sedimentary and Metasedimentary Rocks
TMi	Mesozoic and Tertiary Igneous Rocks primarily intrusives
MPwp	Mesozoic and Paleozoic Rocks of the Peninsular and Wrangellia Terranes

Figure 5.2: Geologic and terrane map of Cook Inlet, Alaska modified from *Bunds et al.* [1997]. The Granite Point and Middle Ground Shoals oil fields are shown as small, empty ellipses.

thin coal and tuff beds. It reaches a maximum thickness of 3,350 m [*Wahrhaftig et al.*, 1994] and contains most of the gas reservoirs in the Cook Inlet Basin [*Magoon*, 1994].

The typical Cook Inlet oil fields lie in narrow, NNE-SSW trending anticlines whose major growth occurred very late in the Tertiary–late Pliocene and/or early Pleistocene time [*Boss et al.*, 1976]. The anticlines are overlain by Pleistocene to recent undeformed (flat-lying) sediments, suggesting that they are no longer active. The Middle Ground Shoal oil field lies in the center of the Cook Inlet basin, roughly 97 km by air southwest of Anchorage, Alaska, beneath an average of 30 m of water. The oil-producing section of this field is a narrow anticline which is up to 15.3 km long and 1.2 km wide, striking N10°E. The east flank dips from 30° to 50° east. The southern end plunges gently to the south-southwest at about 5°. The western flank of the anticline dips between 60° and 70° and may contain some east-dipping reverse faults, one of which may transect the northern end of the structure. The Middle Ground Shoal field produces oil from a gross interval of roughly 850 m in the lower Tyonek Formation between 1,550 and 2,960 m depth [*Boss et al.*, 1976].

The Granite Point oil field lies approximately 18 km NNE of the Middle Ground Shoal oil field and 64 km southwest of Anchorage. Like the Middle Ground Shoals field, the oil producing interval is a 8.3 km long and 1.7 km wide north-northeast trending slightly asymmetrical anticline, where the east flank dips 27°E and the west flank dips 58°W [*Laughbaum et al.*, 1970].

5.4 Data Description and Processing

5.4.1 Offshore Oil Platforms and Summary of Raw Data

The Unocal Company provided dipmeter data from five different offshore oil platforms located in two oil fields: platforms Granite Point, Anna, and Bruce in the Granite Point field; and platforms Baker and Dillon in the Middle Ground Shoals field (Figure 5.1). The five oil platforms are fairly close to each other; using the Baker platform as a reference, Dillon is 10.8 km away at S15.4°W, Anna is 23.2 km away at N45.2°E, Bruce is 26.1 km away at N43.7°E, and Granite Point is 20.6 km away at N45.9°E.

Throughout this chapter specific wells and well log data sets are referred to by abbreviations: wells drilled in the Granite Point field are abbreviated "Gp" (e.g, Gp11-13rd); wells drilled in the Middle Ground Shoals field from the Baker platform are abbreviated "Mgs" (e.g., Mgs8rd); and the wells drilled in the Middle Ground Shoals field from the Dillon platform are abbreviated "Smgs," S for south (e.g., Smgs15). All wells drilled in the Granite Point field from either the Granite Point, Anna, or Bruce platforms are referred to as "Gp." A name followed by the characters "rd" refer to a re-drilled well (e.g., Gp13rd). See Table 5.1 for a summary of the wells analyzed and some of their properties.

Figures 5.3, 5.4, and 5.5 show paths of the wells in map view from the Granite Point platforms,

Table 5.1: Well log data that were analyzed for breakouts.

Well name	Tool type	Start length, m	End length, m	Start TVD, m	End TVD, m	Max devi, °	Meters of breakouts, m	Digital data	Breakout selection
Gp11-13rd	U	2397	3520	2374	3473	19	81	Yes	Computer
Gp13rd	U	2436	3137	2281	2971	28	29	Yes	Computer
Gp20rd	U	2127	3180	2079	2945	45	62	Yes	Computer
Gp32rd	U	3098	3267	2619	2774	56	106	Yes	Computer
Gp37	U	3259	3322	3015	3074	31	9	Yes	Computer
Gp42	U	3147	3561	2558	2951	48	13	Yes	Computer
Gp50	U	2486	3063	2440	2988	21	66	Yes	Computer
Gp51	U	2984	3524	2867	3343	38	68	Yes	Computer
Mgs8rd	L	610	2804	588	2753	29	221	No	Eye
Mgs12	H	2225	3048	1915	2710	45	121	No	Eye
Mgs13	L	610	3258	600	3158	23	97	No	Eye
Mgs14	L	2743	3170	2352	2738	46	42	No	Eye
Mgs15	H	1067	2835	1066	2704	38	124	No	Eye
Mgs16	L	1219	2926	1206	2890	12	256	No	Eye
Mgs28	U	629	1089	605	847	71	0	Yes	Eye
Mgs29	U	1795	2746	1779	2530	54	245	Yes	Eye
Mgs30	U	611	2158	610	2004	60	40	Yes	Eye
Smgs5	L	969	3109	927	2816	39	288	No	Computer
Smgs6	L	834	3204	834	3200	5	361	No	Computer
Smgs8	L	2625	3212	2404	2965	32	5	No	Computer
Smgs15	H	3226	3932	2511	3043	51	57	No	Computer

"Tool type" shows type" shows if the well was logged with a low-angle (L), high-angle (H), or unknown (U) type of dipmeter. "Start length" and "End length" refer to the distance along the borehole axis where dipmeter data was examined. The "Start TVD" and "End TVD" columns list the true vertical depth (TVD) range covered by the dipmeter data. Not all of the wells have dipmeter data throughout the whole depth range listed above, notably the Granite Point wells, where small individual sections of data were obtained. The maximum deviation from vertical as measured in the hole by the directional survey is listed, even though breakouts may not have been identified at these high deviations. The number of meters of breakouts selected in each well is listed under "Meters of breakouts." The column "Digital data" lists if digital dipmeter data was received instead of paper well logs. "Breakout selection" notes if the breakouts were identified by computer or by eye. If breakouts were identified by computer on a non-digital well log, this means that the well log was digitized for processing.

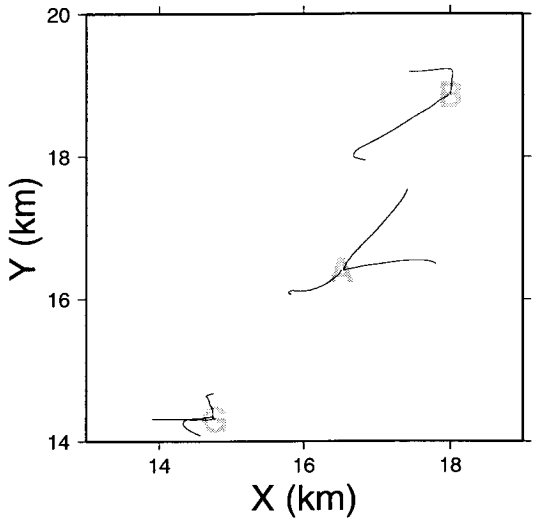

Figure 5.3: Map view of the paths of the wells from the Granite Point (G), Anna (A), and Bruce (B) platforms. Distances are in meters away from top of the Middle Ground Shoals number 8 redrill borehole.

the Baker platform, and the Dillon platform, respectively. All of the platforms show good spatial distributions of boreholes drilled into different regions of the anticlines and a good coverage of the borehole azimuth, borehole deviation space.

5.4.2 Well Log Processing

The Baker and Dillon platform dipmeter data are all paper logs except for Mgs28, Mgs29, and Mgs30, which are digital. The Granite Point dipmeter data are also digital. Given the large amount of paper and digital data from different well-logging tools (Table 5.1), a few different processing techniques were used to integrate the data together into a consistent whole.

All wells were logged with Schlumberger dipmeters. The bit size information was not included in some of the digital dipmeter logs. In these cases, the bit size was estimated by examining the caliper arm data and comparing it to one of the common bit sizes that best matched the caliper arm data (21.91 cm (8.625 inches), 31.12 cm (12.25 inches), or 44.45 cm (17.5 inches)). This technique worked for most of the digital data except for Mgs30 and Gp37. Mgs30 has widely varying caliper arm data, ranging from 22.9 cm (9 inches) to the maximum caliper arm diameter of 49.5 cm (19.5 inches). Mgs30's bit size was 44.45 cm (17.5 inches) in the upper portion of the hole and decreased to 31.12 cm (12.25 inches) in the remaining part of the hole (Unocal, *personal communication*). Neither of these bit sizes agree with the caliper arm data (Figure B.63).

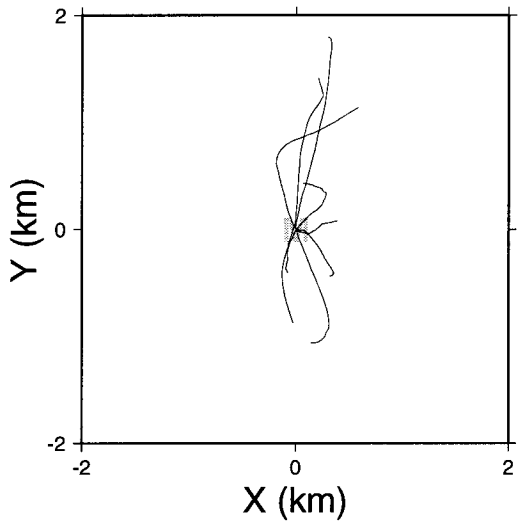

Figure 5.4: Map view of the paths of the wells from the Baker platform (M) in the Middle Ground Shoals field. Distances are in meters away from the top of the Middle Ground Shoals number 8 redrill borehole.

Some of the paper well logs were digitized for computerized borehole breakout selection and other paper logs were examined by eye for breakouts. All of the paper Baker platform wells were examined by eye and all of the Dillon platform wells were digitized. Sections of the Dillon paper logs were digitized by a company which specializes in digitizing paper logs and the remaining sections were digitized at Caltech. One complication of the paper well logs is a nonlinear caliper arm scale, in which the spatial location of a data point on the paper log is not a linear function of the caliper arm diameter. This nonlinear caliper arm scale needs to be taken into account when the caliper arm data are digitized. In examining the digitized caliper arm data obtained from the digitizing company, it appears that the nonlinearity was not properly corrected. Because of the errors inherent in digitizing paper well logs, I only applied a simple linear offset to the caliper arm data if the digitized data were much different than the caliper arm data plotted on paper.

A major complication in the uncorrected dipmeter data is the issue of magnetic declination. It is unclear whether various dipmeter azimuthal measurements, such as the borehole and pad 1 azimuths, were measured with respect to magnetic or geographic north. Fortunately, gyroscopic directional survey logs which measure the borehole azimuth and deviation as a function of well depth with respect to geographic north were obtained from Unocal. The directional survey information was used in place of the dipmeter azimuthal measurements. In some cases the difference is on the order of several degrees, but in other cases the azimuthal correction amounts to roughly 30°.

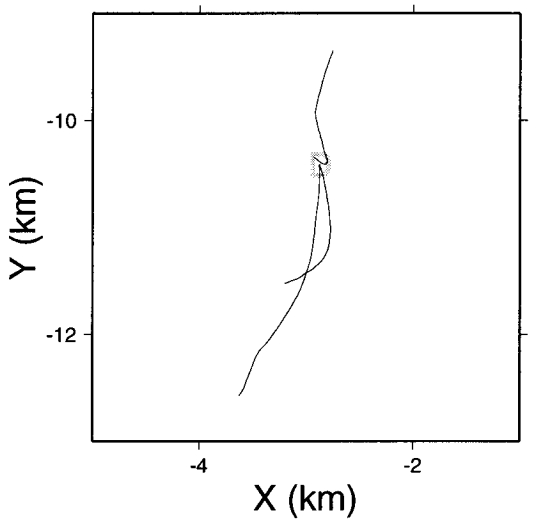

Figure 5.5: Map view of the paths of the wells from the Dillon (D) platform in the Middle Ground Shoals field. Distances are in meters away from the top of the Middle Ground Shoals number 8 redrill borehole.

Replacing dipmeter azimuth measurements with directional survey data has some advantages and disadvantages. The primary advantage is the consistency in the processing technique and using a known quantity for the borehole azimuth and deviation data. There are two potentially serious problems. One problem occurs when the log depths measured by the two tools are offset from each other. Tools stuck in the hole and cable stretch could lead to a depth difference between the two data sets. However, borehole azimuth and deviation curves do not vary quickly over a 100 m interval so this issue, while important, will not be addressed in this thesis. The second problem lies with the differences between low- and high-angle dipmeters. Low-angle dipmeters are typically used in holes with deviations less than 36°. They measure the pad 1 azimuth and the relative bearing, but they do not measure the borehole azimuth, since at low deviations, the borehole azimuth can fluctuate widely. High-angle dipmeters are used in holes with deviations higher than 36° and measure the relative bearing and the borehole azimuth. High-angle dipmeters do not measure pad 1 azimuths, since at high borehole deviations, the map projection of the line drawn from the center of the dipmeter to the end of pad 1 approaches a constant azimuth, regardless of the orientation of pad 1. If pad 1 azimuths were measured, then pad 1 azimuths lying 90° away from the borehole azimuth would preferentially be measured. Given the different orientation information measured by the low- and high-angle tools, different techniques are required for integrating the data into a collective whole. These differences could lead to systematic inconsistencies between data from high- and low-angle

tools.

It was only possible to positively determine if a low- or high-angle dipmeter was used to log the borehole in cases when paper well logs were received. In over half of the boreholes (Table 5.1) digital dipmeter was received and it was presumed that a low-angle dipmeter was used to log the borehole if digital pad 1 azimuth data were one of the measurements obtained from the well log. If borehole azimuth data were received instead, then the dipmeter was presumed to be a high-angle dipmeter. Regardless of the style of dipmeter used to log a borehole, the data processing calculations properly transformed the raw dipmeter data into a set of borehole azimuth, borehole deviation, and **IJK** elongation angle as a function of depth along the borehole axis.

The directional survey data were also used to calculate the location of the borehole through the earth as a function of well depth. These positional data, consisting of the east, north, and vertical distance in meters away from the drilling platform, were then merged with the breakout data to obtain the horizontal and vertical location of the breakouts. While the same problem of merging the dipmeter data with directional survey data can lead to a mismatch between the real and calculated location of the breakout, these errors are not considered here since the inversion technique does not depend upon the breakout location. These errors are considered when the breakout location is compared to the location of known geological structures.

Several other processing steps were done while processing the dipmeter and directional survey data. These steps included converting from English to metric units and calibrating the caliper arm data if the well log showed a calibration measurement.

5.4.3 Borehole Breakout Selection

A modified version of the borehole selection criteria described in section 2.1.6 was used to identify more borehole breakouts than would be normally identified. Instead of limiting the standard deviation of the **IJK** breakout angle in a breakout to 1.25°, breakouts with **IJK** breakout angle standard deviations of 2.5° were allowed. The minimum ellipticity of the breakout was also lowered from 1.05 to 1.03. On the other hand, the maximum allowed caliper arm standard deviation was lowered from 2.54 cm (1 inch) to 1.27 cm (0.5 inch).

5.4.4 Selection of Borehole Breakout Data Subsets

To study depth dependent and material dependent aspects of the stress state, the complete set of Cook Inlet borehole breakout data was subdivided into various subsets and separately inverted for the stress state. A list of the number of breakouts and the length of breakouts for a particular subset of breakouts is shown in Table 5.2.

Material property differences between adjacent beds or formations can rotate the stress tensor

[*Bruno and Winterstein*, 1992]. To study this effect in the Cook Inlet data set, marker files that Unocal supplied were used to subdivide the breakouts into different. The marker files list the well log depth of horizons of markers, horizons of oil pools, and the well log depth of faults which the well may cross. The oil-producing interval was separated into seven pools designated "A" through "G" by the State of Alaska Oil and Gas Committee. After identifying breakouts in all of the Cook Inlet wells, those markers that contained a large number of breakouts at different borehole orientations were selected and breakouts in those markers were independently analyzed. To get larger spatial and borehole orientation coverage of the breakouts from a set of markers, the marker files were examined to see if the breakouts from two or more markers could be combined. Only the G3 and G4 markers from the Baker platform were always adjacent to each other in the marker files and were never separated by a fault or any other markers. In the Granite Point oil field the T45XSS marker was chosen since this particular Granite Point marker had the most identified breakouts: 13 identified breakouts totaling 67.7 m in length. The Dillon platform wells had 7 breakouts totaling 36.6 m in length in the TE1 marker. Enough breakouts were identified in the Baker platform wells such that several different markers could be independently analyzed. The chosen markers were B40SS with 25 breakouts totaling 180.7 m in length, D with 15 breakouts totaling 120.5 m in length, and the combined markers G3 and G4, which have 12 breakouts totaling 96.6 m in length.

While the marker data has proven to be very useful, no description of the material and elastic properties of the markers were ever received from Unocal to make this analysis complete. The information would have been helpful since one of the many factors that can cause the rotation of the stress tensor across the contact between two beds or formations is the contrast between the elastic properties [*Bruno and Winterstein*, 1992].

In addition to analyzing the breakouts occurring in particular markers, identified breakouts were also separated into several different subsets and analyzed. The first division separated those breakouts with their **IJK** breakout angle more than 15° from either the high or low side of the hole from the remaining breakouts. The latter group includes those breakouts that could be caused by tool drag. The former group of breakouts are termed nonradial, since the orientation of a breakouts aligned with the high and low sides of the borehole, when plotted on a lower hemisphere stereographic projection, trend radially toward the center of the plot (Figure 1.2). The second separation grouped breakouts into 500 m true vertical depth intervals to study the depth dependent effects on the stress state.

5.4.5 Individual Discussion of Wells

Each of the 21 well logs and their identified breakouts were individually analyzed. The analysis included understanding inconsistently oriented breakouts, simple stress state analyses for those wells with a large number of breakouts, and evaluation of other problems that needed to be fixed with

Table 5.2: Statistics of various selected subsets of breakouts.

Field or Platform	Selection	Number of breakouts	Total length of breakouts, m
All	All	279	1860.8
All	Nonradial	142	880.5
All	Nonradial between 500–1000 m TVD	6	25.8
All	Nonradial between 1000–1500 m TVD	19	136.0
All	Nonradial between 1500–2000 m TVD	29	160.9
All	Nonradial between 2000–2500 m TVD	48	321.0
All	Nonradial between 2500–3000 m TVD	38	228.6
Gp	All	61	365.4
Gp	Nonradial	34	183.5
Gp	Nonradial between 2000–2500 m TVD	10	59.9
Gp	Nonradial between 2500–3000 m TVD	23	120.3
Baker	All	152	1146.4
Baker	Nonradial	72	509.1
Baker	Marker B40SS	25	180.7
Baker	Nonradial marker B40SS	10	64.0
Baker	Marker D	15	120.5
Baker	Nonradial marker D	7	43.5
Baker	Markers G3 and G4	12	96.6
Baker	Nonradial markers G3 and G4	8	67.1
Baker	Nonradial between 500–1000 m TVD	3	12.2
Baker	Nonradial between 1000–1500 m TVD	16	124.7
Baker	Nonradial between 1500–2000 m TVD	17	102.3
Baker	Nonradial between 2000–2500 m TVD	28	199.8
Baker	Nonradial between 2500–3000 m TVD	8	70.1
Dillon	All	64	349.0
Dillon	All excluding Smgs8	63	344.5
Dillon	Nonradial	36	187.9
Dillon	Nonradial excluding Smgs8	35	183.4
Dillon	Marker TE1	7	36.6
Dillon	Nonradial marker TE1	3	16.6
Dillon	Nonradial between 1500–2000 m TVD	12	58.6
Dillon	Nonradial between 2000–2500 m TVD	10	61.3
Dillon	Nonradial between 2500–3000 m TVD	7	38.2

Gp refers to those breakouts identified in the Granite Point field from any of the three oil platforms. The sets of breakouts do not include breakouts from Granite Point 51 or South Middle Ground Shoals 6 since the breakouts from these wells had no consistent breakout orientations and an in-depth analysis of the dipmeter logs did not lead to an interpretation of the breakout data with more consistent orientations. Stress state inversions were done on all of these selected breakout subsets except those containing fewer than 5 breakouts.

the data. This analysis is included in Appendix B. The major conclusion of this work is that the breakouts identified in Gp51 and Smgs6 are highly inconsistently oriented and a detailed analysis of these breakouts was unable to determine which of these breakouts could be used in a stress inversion. As such, the breakouts from these two wells are not used in any of the following stress inversions.

5.4.6 Inversion of Borehole Breakouts

The inversion process described in Chapter 2 was used to invert various groups of borehole breakouts for the best fitting stress tensor. The breakouts from Granite Point 51 and South Middle Ground Shoals 6 were not included in any of the inversions since the breakouts from these wells had no consistent breakout orientations and an in-depth analysis of the dipmeter logs did not lead to an interpretation of the breakout data with more consistent orientations. Removing the breakout data from these two wells reduced the minimum weighted one-norm misfits of the inversion results by 3° to 5°. The inversion results also show much better constrained principal stress directions.

A total of 279 breakouts summing to 1,861 m in length were available for various inversions. Figures 5.6–5.67 show the stress inversion results for 31 different subsets of borehole breakouts (Table 5.2). Each subset was inverted using the angular difference and stress difference misfit measure. The subsets are: all breakouts (Figures 5.6 and 5.7), all nonradial breakouts (Figures 5.8 and 5.9), all nonradial breakouts between 500 and 1,000 m TVD (Figures 5.10 and 5.11), all nonradial breakouts between 1,000 and 1,500 m TVD (Figures 5.12 and 5.13), all nonradial breakouts between 1,500 and 2,000 m TVD (Figures 5.14 and 5.15), all nonradial breakouts between 2,000 and 2,500 m TVD (Figures 5.16 and 5.17), all nonradial breakouts between 2,500 and 3,000 m TVD (Figures 5.18 and 5.19), all Granite Point breakouts (Figures 5.20 and 5.21), all nonradial Granite Point breakouts (Figures 5.22 and 5.23), nonradial breakouts between 2,000 and 3,000 m TVD in the Granite Point field (Figures 5.24 and 5.25), and nonradial breakouts between 2,500 and 3,000 m TVD in the Granite Point field (Figures 5.26 and 5.27). Inversions of sets of breakouts in wells drilled from the Baker platform in the Middle Ground Shoals field are: all breakouts (Figures 5.28 and 5.29), all nonradial breakouts (Figures 5.30 and 5.31), all breakouts and all nonradial breakouts occurring in the B40SS marker (Figures 5.32–5.35), all breakouts and all nonradial breakouts occurring in the D marker (Figures 5.36–5.39), all breakout and all nonradial breakouts occurring in the G3 and G4 markers (Figures 5.40–5.43), nonradial breakouts between 1,000 and 1,500 m TVD, (Figures 5.44 and 5.45), nonradial breakouts between 1,500 and 2,000 m TVD (Figures 5.46 and 5.47), nonradial breakouts between 2,000 and 2,500 m TVD (Figures 5.48 and 5.49), and nonradial breakouts between 2,500 and 3,000 m TVD (Figures 5.50 and 5.51). Breakouts in wells drilled from the Dillon platform in the Middle Ground Shoals field were analyzed in the following groups: all breakouts (Figures 5.52 and 5.53), all nonradial breakouts (Figures 5.54 and 5.55), all breakouts excluding those from Smgs8 (Figures 5.56 and 5.57), all nonradial breakouts excluding those from Smgs8 (Figures 5.58 and 5.59),

all breakouts and all nonradial breakouts occurring in the TE1 marker (Figures 5.60 and 5.61), nonradial breakouts between 1,500 and 2,000 m TVD (Figures 5.62 and 5.63), nonradial breakouts between 2,000 and 2,500 m TVD (Figures 5.64 and 5.65), and nonradial breakouts between 2,500 and 3,000 m TVD (Figures 5.66 and 5.67). Subsets of data containing less than five breakouts were not inverted since the inversion process needs five breakouts to constrain the three stress tensor Euler angles and the stress state ϕ value.

Each figure shows a large amount of information for each individual inversion. The upper left panel shows the number of breakouts and the total length of breakouts used in the inversion, the optimized value of ϕ, the 95% confidence limits on ϕ, and the minimum and 95% weighted one-norm misfit values for this data set. Also shown are the azimuth, deviation, and stress state magnitudes for the S_1, S_2, and S_3 principal stresses. The upper right plot is a lower hemisphere stereographic projection plot of breakouts used for the inversion. Each breakout plots as a single line with constant length. The width of the line is proportional to the length of the breakout and inversely proportional to the **IJK** breakout angle variance over the breakout length. Breakouts from shallow depths plot at dark shades of gray and breakouts from greater depths plot at lighter shades of gray. Lines beneath the breakouts are the predicted orientations of breakouts for the best fitting stress state from the inversion. The lower left panel plots the 95% confidence limits on the orientation of the principal stress directions. The lower right panel plots three separate weighted one-norm misfit curves as a function of ϕ. The thick solid line is the 95% confidence limit for this inversion, the thin solid line is the minimized misfit where for each value of ϕ the directions of the principal stress axes are allowed to vary so that the minimum misfit is obtained, and the dotted line is the misfit using the principal stress directions from the best fitting model. The misfit curve where the principal stress axes are allowed to vary should always be lower than the dotted curve, which plots the weighted one-norm misfit as a function of ϕ keeping the orientation of the stress tensor fixed.

As in the confidence limit analyses of the *Qian and Pedersen* [1991] and Point Pedernales data, 95% confidence limits on the stress state ϕ value were calculated by iterating ϕ from 0 to 1 and searching for the Euler angles that minimized the one-norm misfit for each ϕ value. The ϕ value could then be found for which the one-norm misfit exceeded the 95% confidence misfit. Using this method to place confidence limits on ϕ, only 14 out of the 31 Cook Inlet angular misfit inversions had the minimum and maximum 95% ϕ values differ by less than 0.5. In contrast, none of the stress misfit inversions had a maximum and minimum ϕ value differing by more than 0.17. The poor stress tensor constraints using the angular misfit inversion demonstrates that in many cases stress tensors with different ϕ values can be rotated to fit the data within the 95% confidence limits.

The 95% confidence limits for the individual principal stress directions (S_1, S_2, and S_3) do not overlap in 24 out of the 31 angular misfit inversions and 26 out of 31 stress misfit inversions. In six out of twelve inversions with overlapping principal stress direction confidence limits, the inversions

produced irregularly shaped principal stress direction 95% confidence regions (Figures 5.17, 5.23, 5.27, 5.45, 5.49, and 5.51). These occurred in only the angular misfit inversions, in cases with multiple local one-norm misfit minima below the 95% confidence limit, corresponding to substantially different ϕ values. This behavior has not been observed in any stress misfit inversions. The remaining six inversions with overlapping confidence regions for S_1 and S_2 occur when the ϕ value is near 1 and the best fitting stress state is free to have its S_1 and S_2 orientations rotate about the S_3 axis (Figures 5.12, 5.32, 5.33, 5.36, 5.42, and 5.44).

The 31 borehole breakout data subsets were inverted using both the stress and angular misfit measure. Eleven of the 31 data subsets had significantly different stress and angular misfit inversion results. Of these eleven data sets, five had 19 or fewer breakouts and these breakouts did not display a consistent breakout pattern over the lower hemisphere stereographic projection plots (Figures 5.12 and 5.13, 5.34 and 5.35, 5.36 and 5.37, 5.40 and 5.41, 5.42 and 5.43). Given the small number of breakouts, the stress and angular misfit inversions were able to fit the breakout data using significantly different stress states. Two other data sets contained 29 or more breakouts, and in these cases, there were enough breakouts, but the breakout orientations were very heterogeneous (Figures 5.8 and 5.9, 5.14 and 5.15). Finally, four other data sets had very consistent orientations, but the two different stress misfit measures identified substantially different stress states (Figures 5.52 and 5.53, 5.54 and 5.55, 5.56 and 5.57, 5.58 and 5.59).

The remaining 20 borehole breakout data sets yielded stress and angular misfit inversions that were visually similar, although not equivalent if one were to compare them using both inversions 95% confidence regions. While the stress state determined from the stress misfit measure has been determined to be the stress state best representing the stress state responsible the identified breakouts, the angular difference stress state results will also be used to gauge the goodness of fit of a particular data set.

Stress misfit inversion results using all Cook Inlet breakouts excluding breakouts from wells Gp51 and Smgs6.

Number of breakouts	279
Total length of breakouts	1860.8 m
Optimized ϕ with 95% confidence limits	0.984 $^{1.000}_{0.959}$
Minimum weighted one-norm stress misfit	0.0256
95% confidence level for weighted one-norm stress misfit	0.0276

	Azimuth	Deviation	Value
S_1	N5.1°E	88.1°	2
S_2	N95.2°E	85.4°	1.984
S_3	N253.2°E	5.0°	1

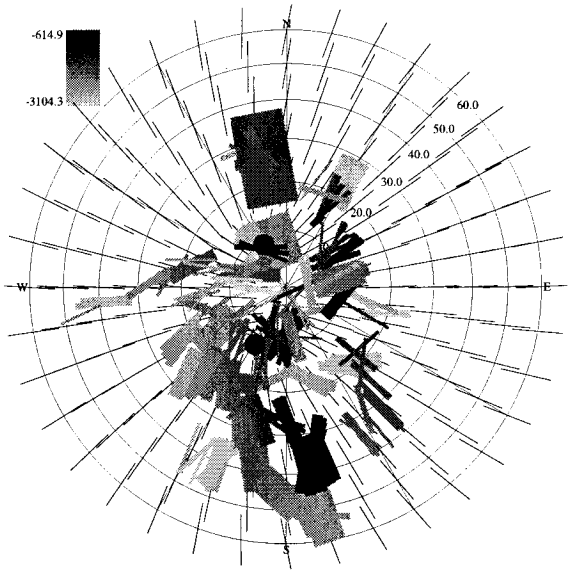

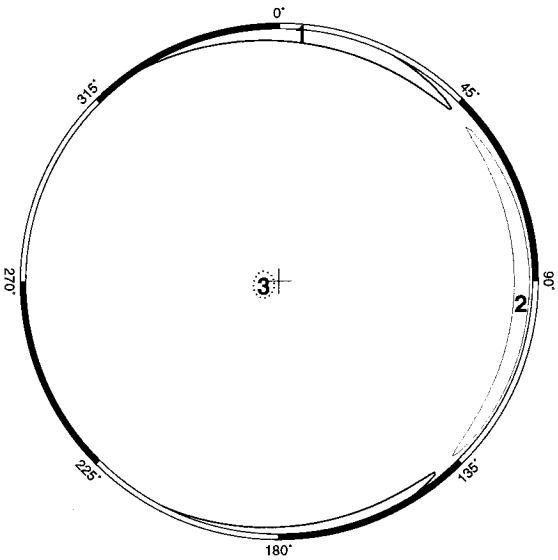

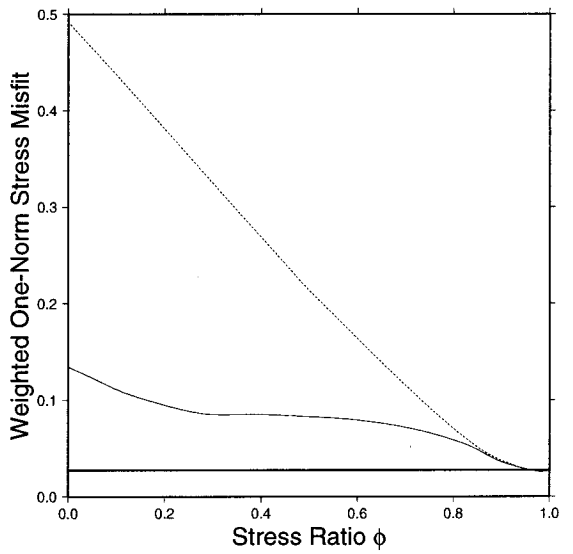

Figure 5.6: Stress inversion results in Cook Inlet, Alaska using all identified breakouts from all available wells excluding the breakouts from wells Gp51 and Smgs6. (upper left) Statistics of the breakouts in this data set in the results of the inversion. (upper right) Lower hemisphere stereographic projection of the breakouts plotted on top of the theoretical breakout pattern of the best fitting stress state. The graduated scale shows the depth of the selected breakouts in meters. Solid circles are "nodal" points at which the stress anisotropy is zero corresponding to borehole orientations with no preferred breakout direction. (lower left) Lower hemisphere stereographic projection in which the digits 1, 2, and 3 show the optimized orientation of the S_1, S_2, and S_3 principal stress axes, respectively. The 95% weighted one-norm misfit confidence limits of the S_1, S_2, and S_3 orientations are plotted as thick solid lines, thin solid lines, and dotted lines, respectively. The stress state ϕ ratio was held constant at 0.984. (lower right) The weighted one-norm misfit for the breakouts as a function of ϕ, where the thick solid line is the 95% confidence limit for this inversion, the thin solid line is the minimized misfit where for each value of ϕ the directions of the principal stress axes are allowed to vary so that the minimum misfit is obtained, and the dotted line is the misfit using the principal stress directions from the best fitting model.

Angular misfit inversion results using all Cook Inlet breakouts excluding breakouts from wells Gp51 and Smgs6.

Number of breakouts	279
Total length of breakouts	1860.8 m
Optimized ϕ with 95% confidence limits	$0.994^{1.000}_{0.981}$
Minimum weighted one-norm stress misfit	22.41°
95% confidence level for weighted one-norm stress misfit	24.11°

	Azimuth	Deviation	Value
S_1	N197.2°E	88.7°	2
S_2	N107.2°E	86.7°	1.994
S_3	N307.9°E	3.6°	1

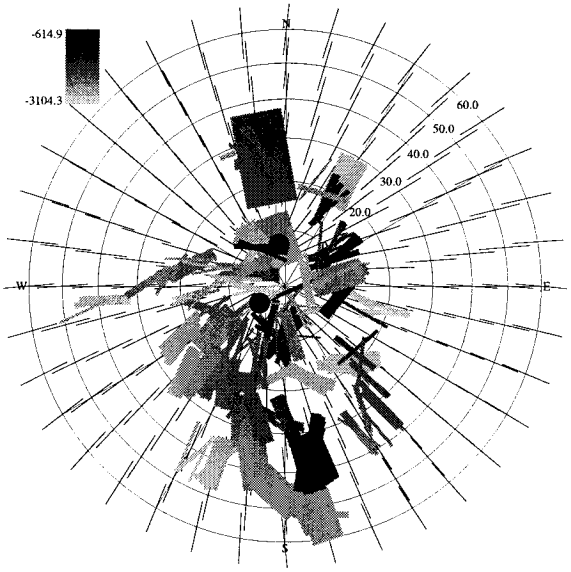

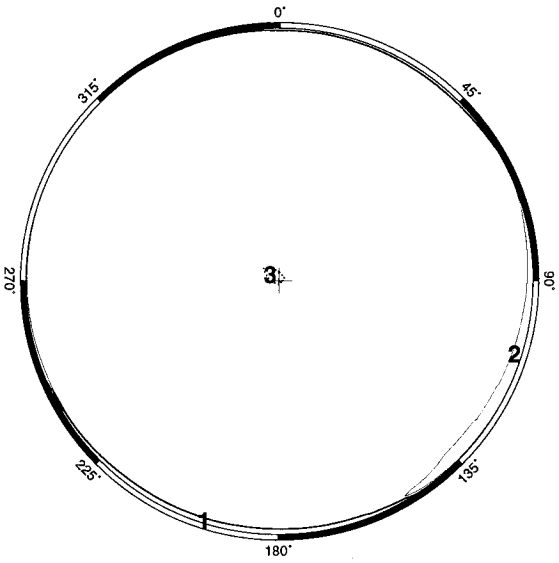

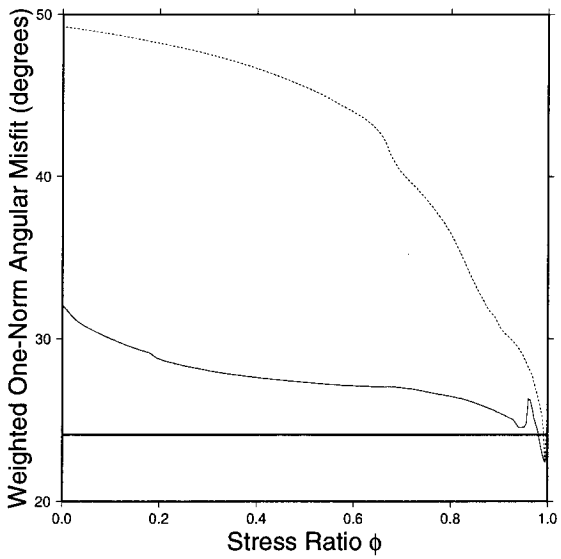

Figure 5.7: Stress inversion results in Cook Inlet, Alaska using all identified breakouts from all available wells excluding the breakouts from wells Gp51 and Smgs6. Plotting conventions are the same as Figure 5.6.

Stress misfit inversion results using all Cook Inlet nonradial breakouts excluding breakouts from wells Gp51 and Smgs6.

Number of breakouts	142
Total length of breakouts	880.5 m
Optimized ϕ with 95% confidence limits	0.924 $^{0.988}_{0.875}$
Minimum weighted one-norm stress misfit	0.0379
95% confidence level for weighted one-norm stress misfit	0.0420

	Azimuth	Deviation	Value
S_1	N179.6°E	87.3°	2
S_2	N89.2°E	81.5°	1.924
S_3	N287.1°E	8.9°	1

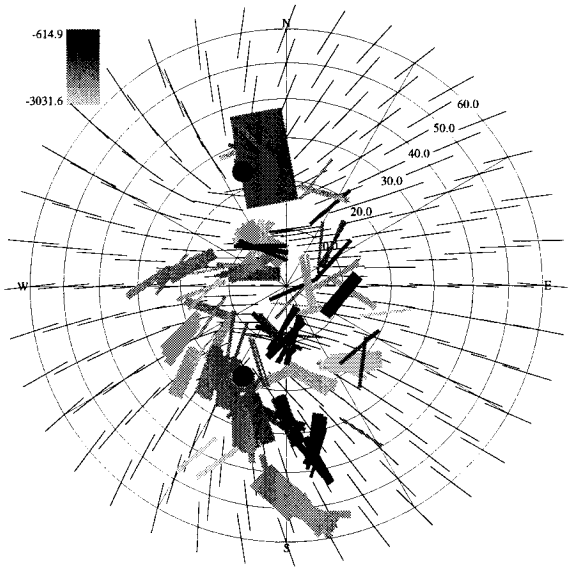

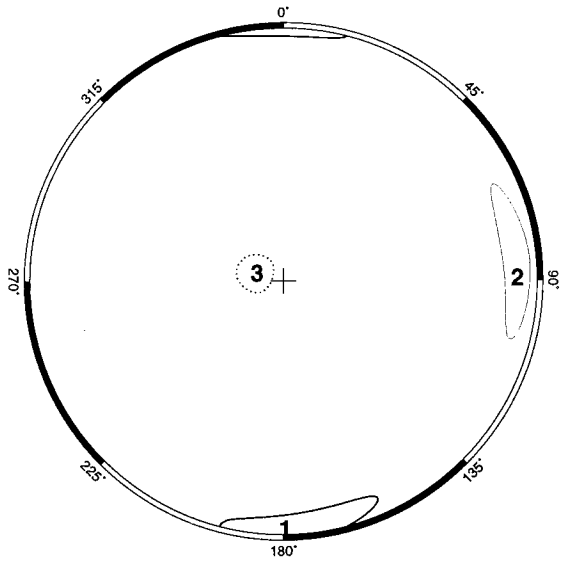

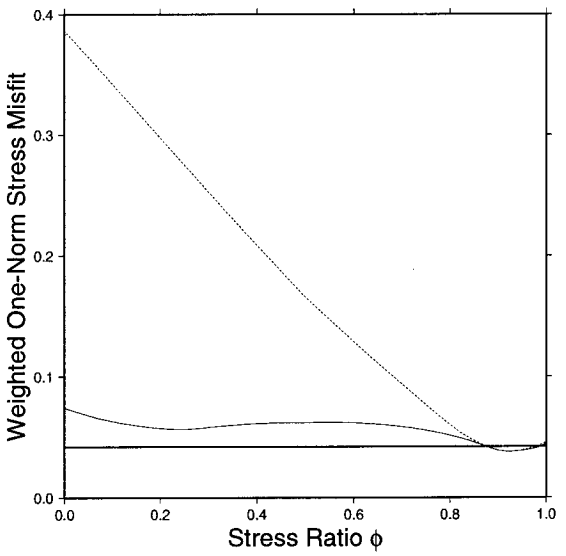

Figure 5.8: Stress inversion results in Cook Inlet, Alaska using all nonradial identified breakouts from all available wells excluding the breakouts from wells Gp51 and Smgs6. Nonradial breakouts are those breakouts where the **IJK** breakout angle is at least 15° away from the high-side of the hole. Plotting conventions are the same as Figure 5.6.

Angular misfit inversion results using all Cook Inlet nonradial breakouts excluding breakouts from wells Gp51 and Smgs6.

Number of breakouts	142
Total length of breakouts	880.5 m
Optimized ϕ with 95% confidence limits	$0.274^{0.957}_{0.100}$
Minimum weighted one-norm stress misfit	23.08°
95% confidence level for weighted one-norm stress misfit	25.55°

	Azimuth	Deviation	Value
S_1	N165.6°E	40.1°	2
S_2	N62.2°E	78.9°	1.274
S_3	N323.4°E	52.1°	1

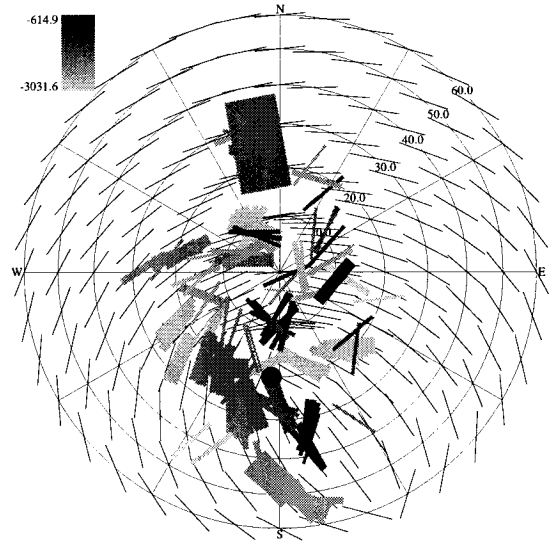

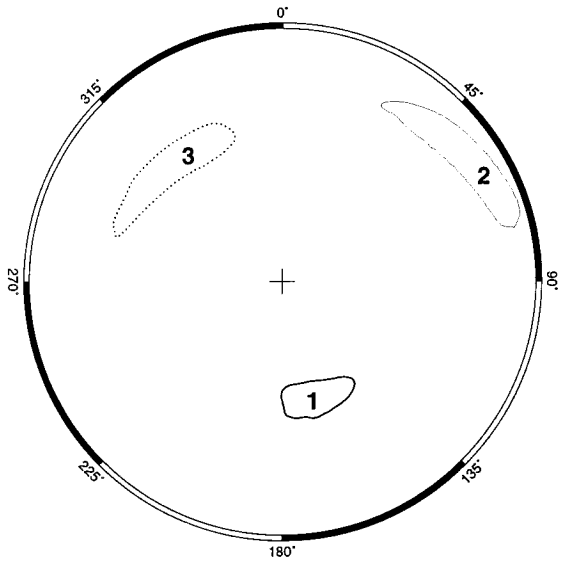

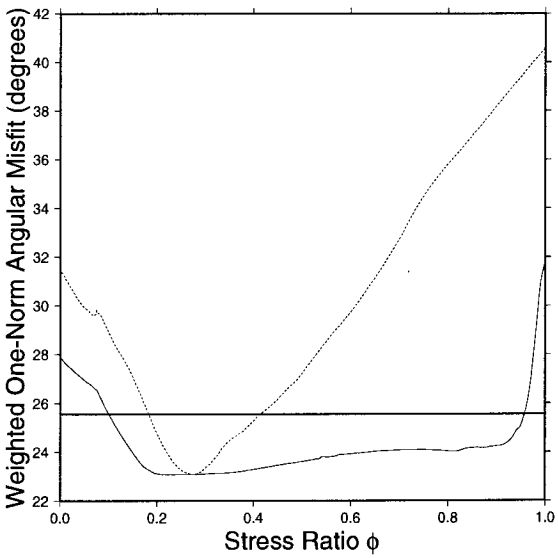

Figure 5.9: Stress inversion results in Cook Inlet, Alaska using all nonradial identified breakouts from all available wells excluding the breakouts from wells Gp51 and Smgs6. Nonradial breakouts are those breakouts where the **IJK** breakout angle is at least 15° away from the high-side of the hole. Plotting conventions are the same as Figure 5.6.

Stress misfit inversion results using all Cook Inlet nonradial breakouts between 500–1,000 m TVD excluding breakouts from wells Gp51 and Smgs6.

Number of breakouts	6
Total length of breakouts	25.8 m
Optimized ϕ with 95% confidence limits	$0.241^{0.256}_{0.222}$
Minimum weighted one-norm stress misfit	$2.34\text{x}10^{-4}$
95% confidence level for weighted one-norm stress misfit	$4.64\text{x}10^{-4}$

	Azimuth	Deviation	Value
S_1	N178.5°E	14.2°	2
S_2	N76.6°E	87.0°	1.241
S_3	N345.9°E	76.1°	1

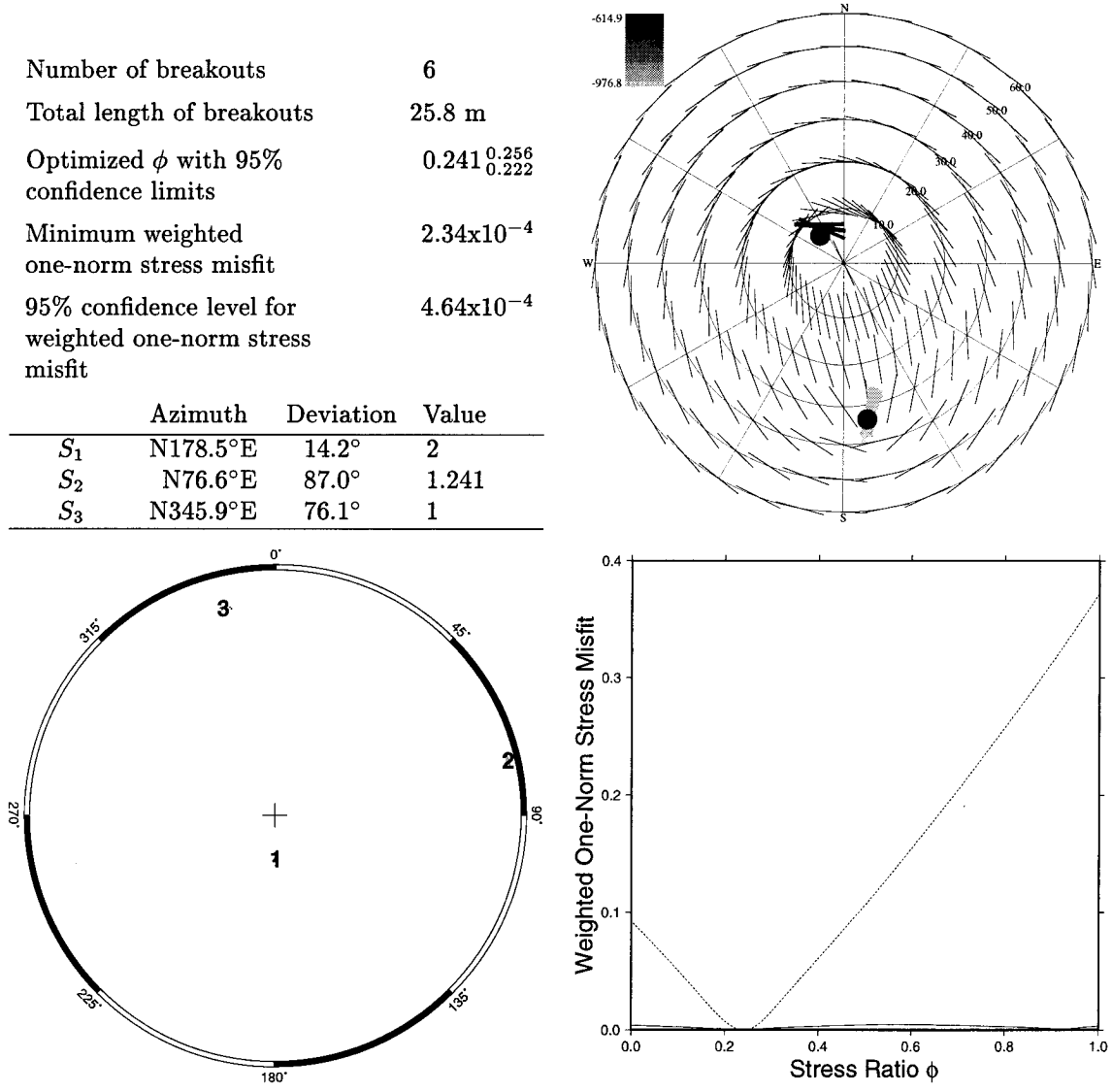

Figure 5.10: Stress inversion results in Cook Inlet, Alaska using all nonradial identified breakouts between 500 and 1,000 m TVD from available wells excluding the breakouts from Gp51 and Smgs6. Nonradial breakouts are those breakouts where the **IJK** breakout angle is at least 15° away from the high-side of the hole. Plotting conventions are the same as Figure 5.6.

Angular misfit inversion results using all Cook Inlet nonradial breakouts between 500–1,000 m TVD excluding breakouts from wells Gp51 and Smgs6.

Number of breakouts	6
Total length of breakouts	25.8 m
Optimized ϕ with 95% confidence limits	$0.243^{0.910}_{0.000}$
Minimum weighted one-norm stress misfit	2.55°
95% confidence level for weighted one-norm stress misfit	5.05°

	Azimuth	Deviation	Value
S_1	N179.8°E	15.0°	2
S_2	N77.3°E	87.7°	1.243
S_3	N346.4°E	75.4°	1

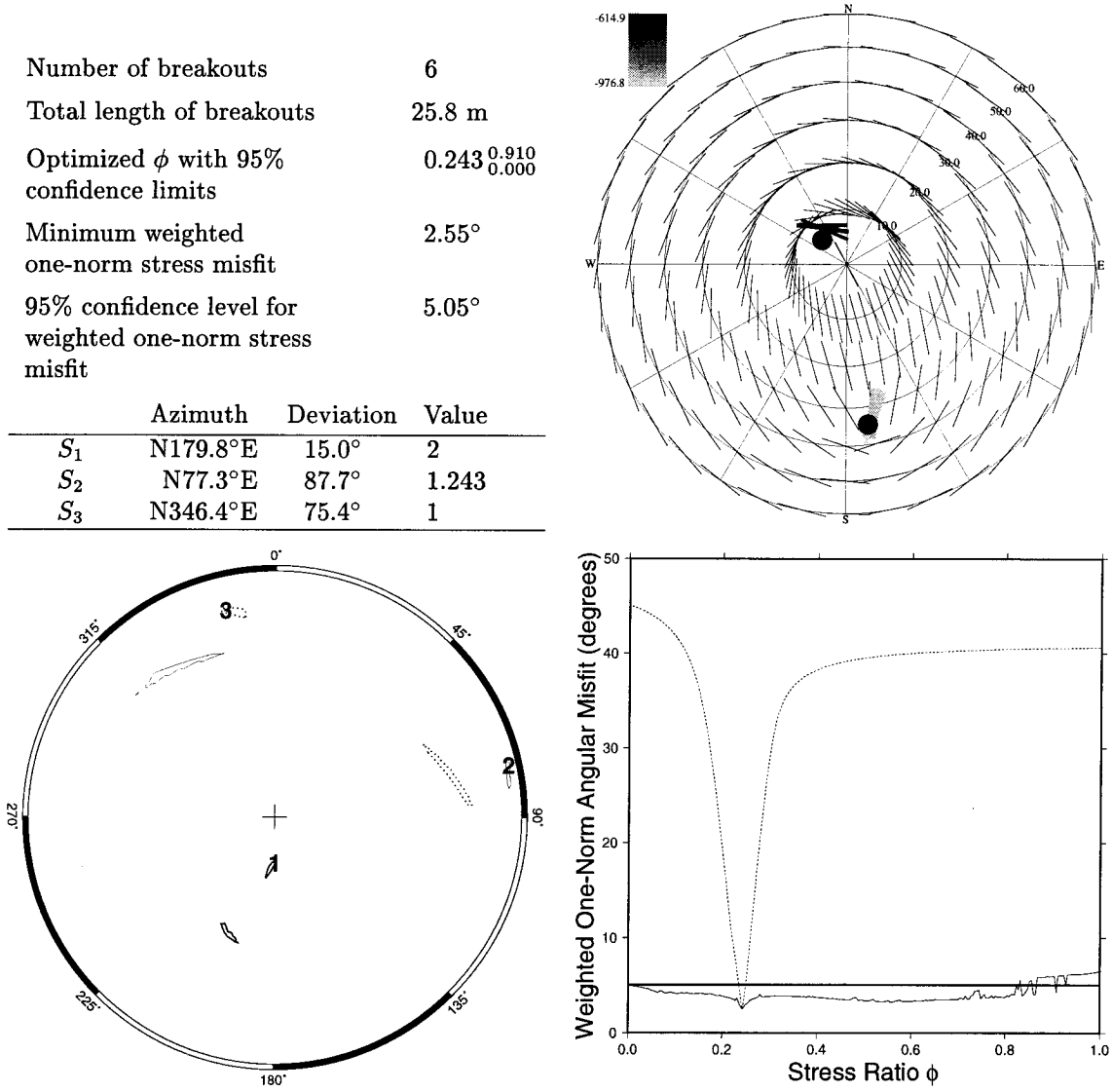

Figure 5.11: Stress inversion results in Cook Inlet, Alaska using all nonradial identified breakouts between 500 and 1,000 m TVD from available wells excluding the breakouts from Gp51 and Smgs6. Nonradial breakouts are those breakouts where the **IJK** breakout angle is at least 15° away from the high-side of the hole. Plotting conventions are the same as Figure 5.6.

Stress misfit inversion results using all Cook Inlet nonradial breakouts between 1,000–1,500 m TVD excluding breakouts from wells Gp51 and Smgs6.

Number of breakouts	19
Total length of breakouts	136.0 m
Optimized ϕ with 95% confidence limits	$0.998^{1.000}_{0.975}$
Minimum weighted one-norm stress misfit	$5.89\text{x}10^{-3}$
95% confidence level for weighted one-norm stress misfit	$7.86\text{x}10^{-3}$

	Azimuth	Deviation	Value
S_1	N59.0°E	81.7°	2
S_2	N327.8°E	82.1°	1.998
S_3	N194.8°E	11.6°	1

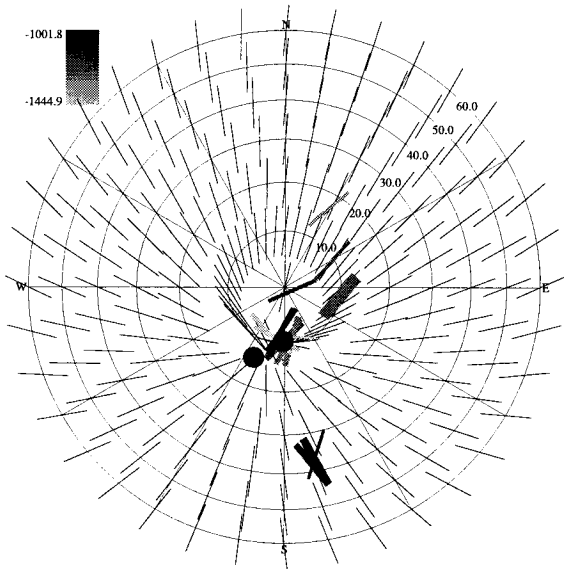

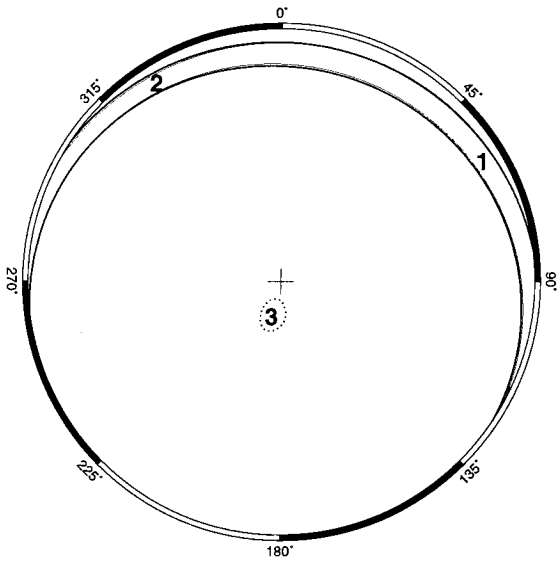

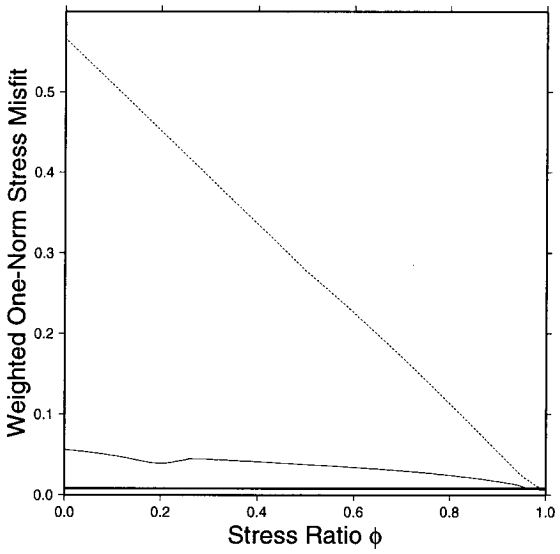

Figure 5.12: Stress inversion results in Cook Inlet, Alaska using all nonradial identified breakouts between 1,000 and 1,500 m TVD from available wells excluding the breakouts from Gp51 and Smgs6. Nonradial breakouts are those breakouts where the **IJK** breakout angle is at least 15° away from the high-side of the hole. Plotting conventions are the same as Figure 5.6.

Angular misfit inversion results using all Cook Inlet nonradial breakouts between 1,000–1,500 m TVD excluding breakouts from wells Gp51 and Smgs6.

Number of breakouts	19
Total length of breakouts	136.0 m
Optimized ϕ with 95% confidence limits	$0.484^{1.000}_{0.000}$
Minimum weighted one-norm stress misfit	17.00°
95% confidence level for weighted one-norm stress misfit	22.68°

	Azimuth	Deviation	Value
S_1	N111.5°E	43.7°	2
S_2	N332.1°E	54.0°	1.484
S_3	N225.6°E	68.7°	1

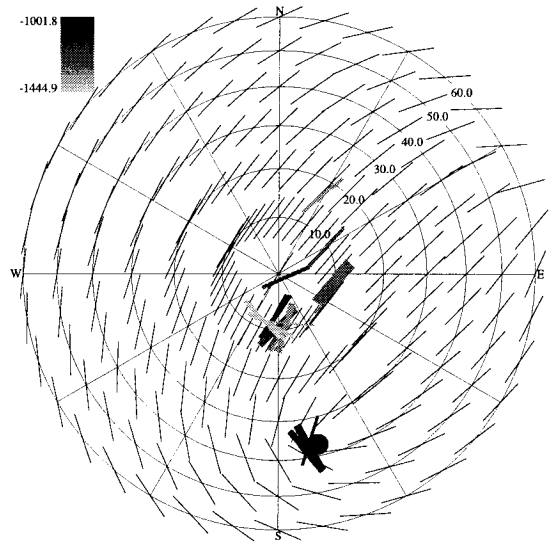

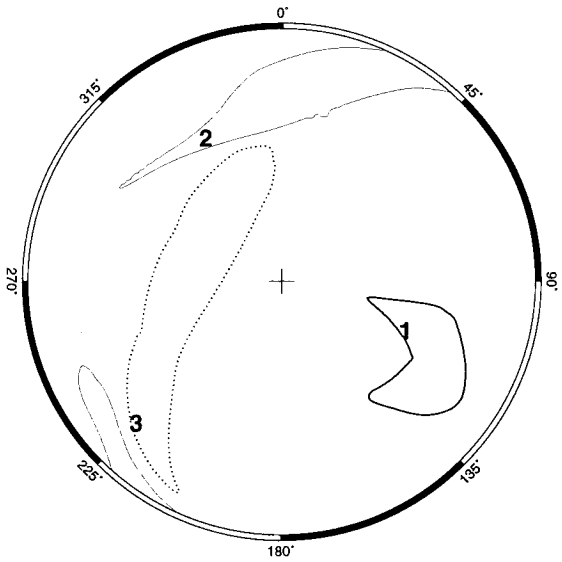

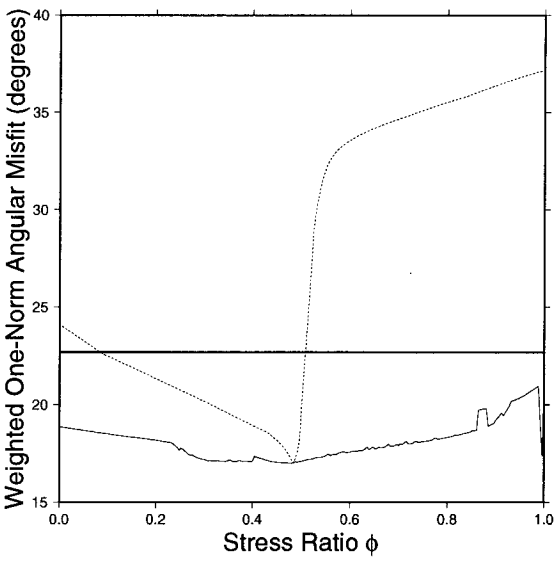

Figure 5.13: Stress inversion results in Cook Inlet, Alaska using all nonradial identified breakouts between 1,000 and 1,500 m TVD from available wells excluding the breakouts from Gp51 and Smgs6. Nonradial breakouts are those breakouts where the **IJK** breakout angle is at least 15° away from the high-side of the hole. Plotting conventions are the same as Figure 5.6.

Stress misfit inversion results using all Cook Inlet nonradial breakouts between 1,500–2,000 m TVD excluding breakouts from wells Gp51 and Smgs6.

Number of breakouts	29
Total length of breakouts	160.9 m
Optimized ϕ with 95% confidence limits	0.886 $^{0.925}_{0.847}$
Minimum weighted one-norm stress misfit	0.0116
95% confidence level for weighted one-norm stress misfit	0.0146

	Azimuth	Deviation	Value
S_1	N181.6°E	88.8°	2
S_2	N91.5°E	84.6°	1.886
S_3	N284.5°E	5.5°	1

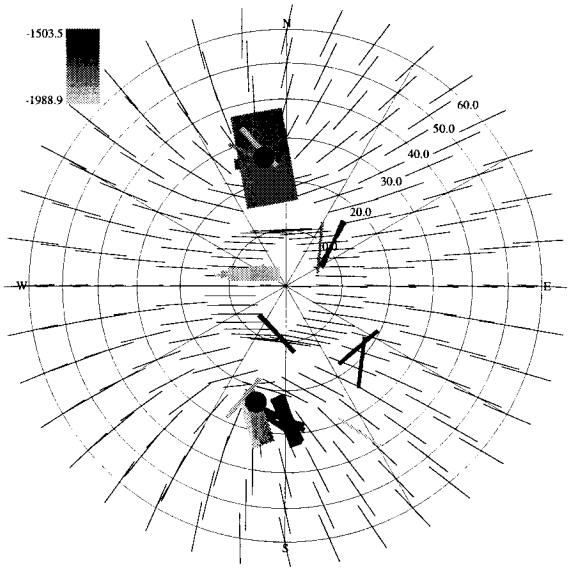

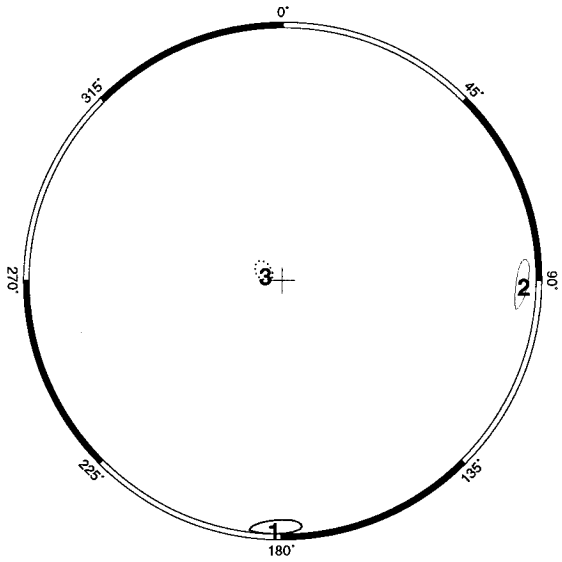

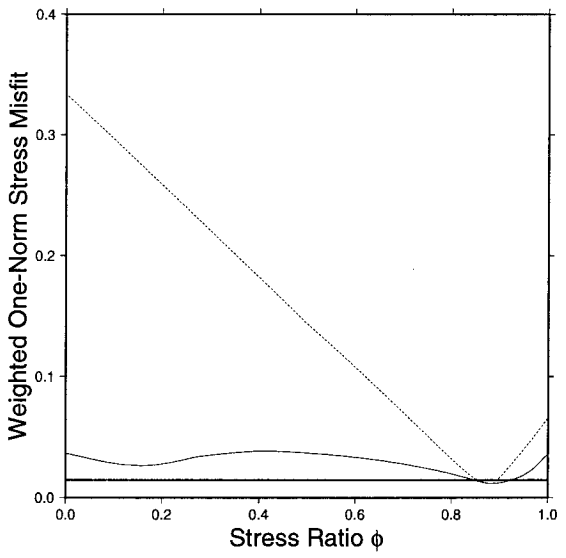

Figure 5.14: Stress inversion results in Cook Inlet, Alaska using all nonradial identified breakouts between 1,500 and 2,000 m TVD from available wells excluding the breakouts from Gp51 and Smgs6. Nonradial breakouts are those breakouts where the **IJK** breakout angle is at least 15° away from the high-side of the hole. Plotting conventions are the same as Figure 5.6.

Angular misfit inversion results using all Cook Inlet nonradial breakouts between 1,500–2,000 m TVD excluding breakouts from wells Gp51 and Smgs6.

Number of breakouts	29
Total length of breakouts	160.9 m
Optimized ϕ with 95% confidence limits	$0.743^{0.958}_{0.016}$
Minimum weighted one-norm stress misfit	11.00°
95% confidence level for weighted one-norm stress misfit	13.82°

	Azimuth	Deviation	Value
S_1	N164.2°E	55.2°	2
S_2	N67.6°E	80.6°	1.743
S_3	N324.6°E	36.4°	1

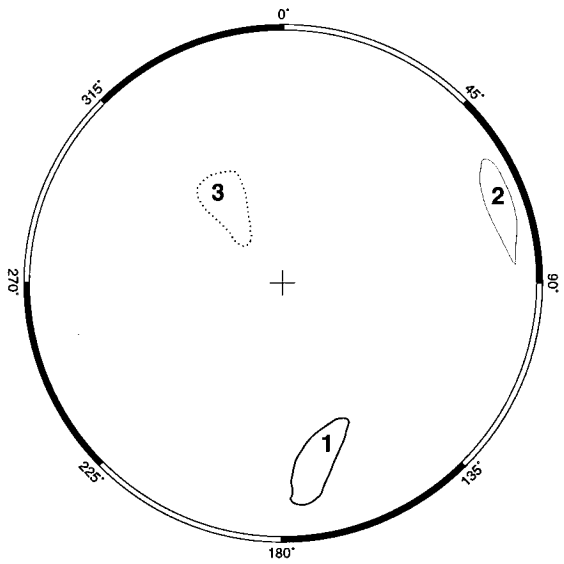

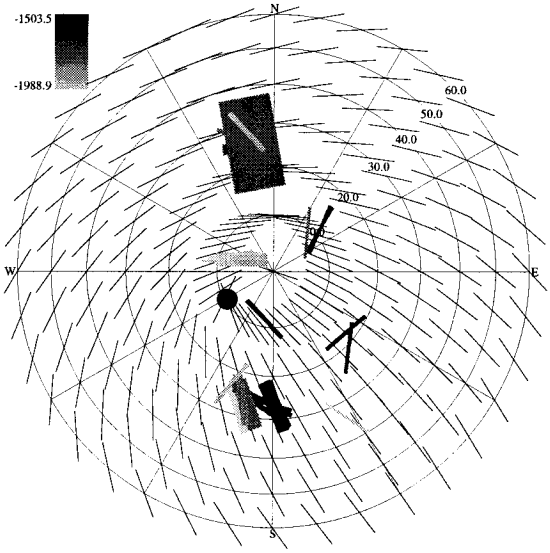

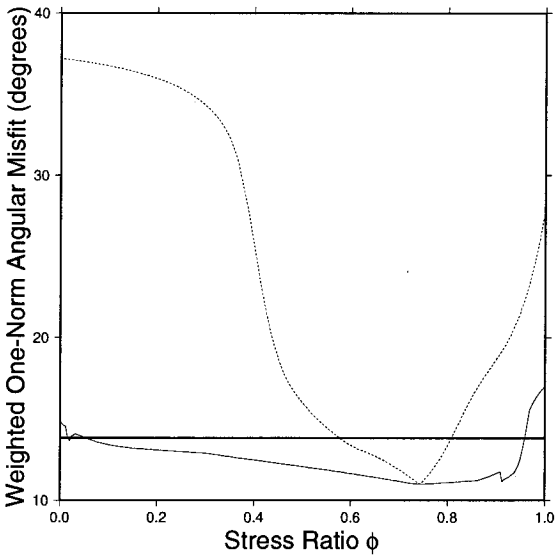

Figure 5.15: Stress inversion results in Cook Inlet, Alaska using all nonradial identified breakouts between 1,500 and 2,000 m TVD from available wells excluding the breakouts from Gp51 and Smgs6. Nonradial breakouts are those breakouts where the **IJK** breakout angle is at least 15° away from the high-side of the hole. Plotting conventions are the same as Figure 5.6.

Stress misfit inversion results using all Cook Inlet nonradial breakouts between 2,000–2,500 m TVD excluding breakouts from wells Gp51 and Smgs6.

Number of breakouts	48
Total length of breakouts	321.0 m
Optimized ϕ with 95% confidence limits	$0.236\ ^{0.981}_{0.187}$
Minimum weighted one-norm stress misfit	0.0221
95% confidence level for weighted one-norm stress misfit	0.0263

	Azimuth	Deviation	Value
S_1	N182.2°E	34.7°	2
S_2	N72.3°E	76.7°	1.236
S_3	N334.0°E	58.6°	1

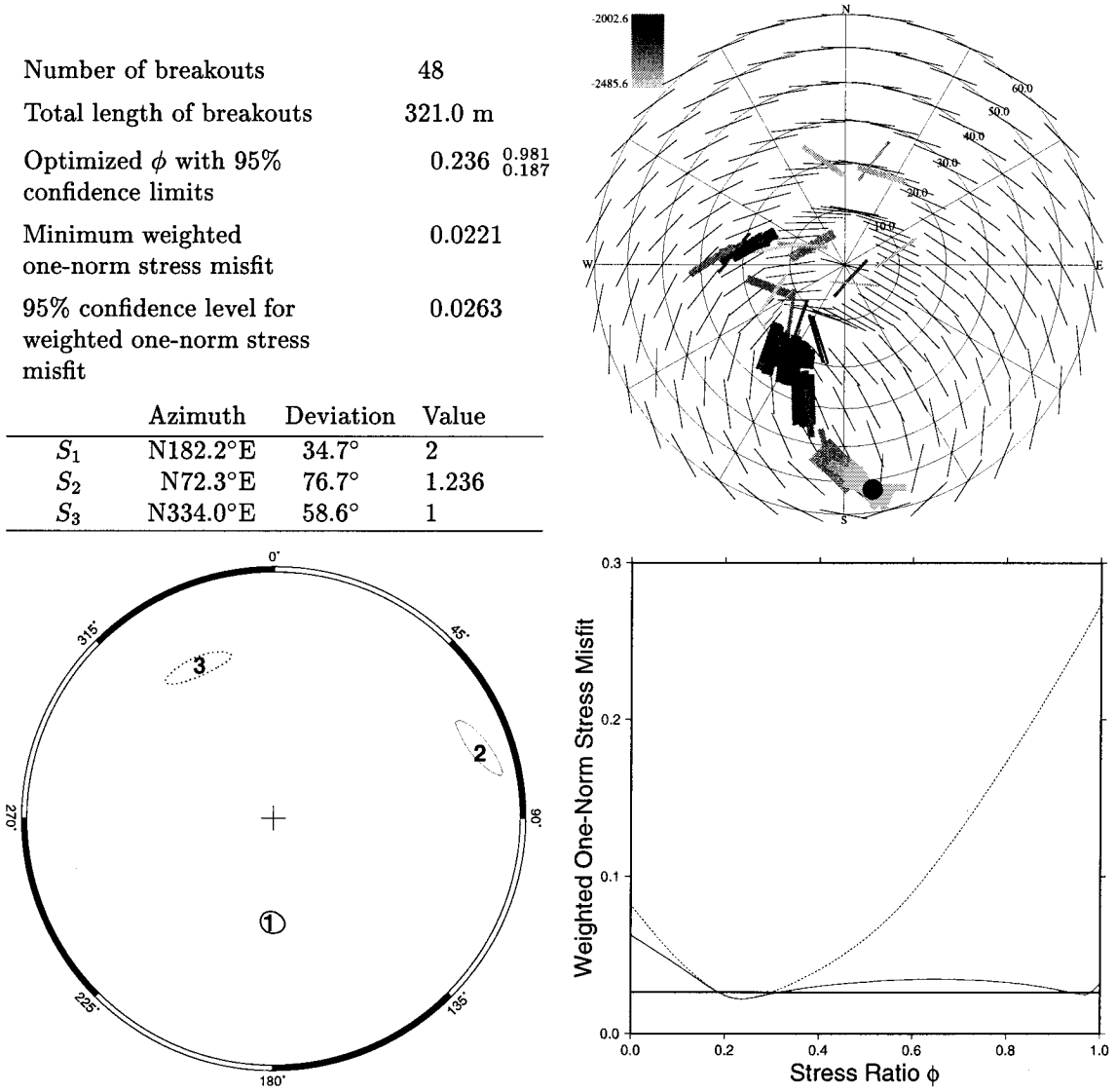

Figure 5.16: Stress inversion results in Cook Inlet, Alaska using all nonradial identified breakouts between 2,000 and 2,500 m TVD from available wells excluding the breakouts from Gp51 and Smgs6. Nonradial breakouts are those breakouts where the **IJK** breakout angle is at least 15° away from the high-side of the hole. Plotting conventions are the same as Figure 5.6.

Angular misfit inversion results using all Cook Inlet nonradial breakouts between 2,000–2,500 m TVD excluding breakouts from wells Gp51 and Smgs6.

Number of breakouts	48
Total length of breakouts	321.0 m
Optimized ϕ with 95% confidence limits	$0.236^{0.988}_{0.000}$
Minimum weighted one-norm stress misfit	17.84°
95% confidence level for weighted one-norm stress misfit	21.27°

	Azimuth	Deviation	Value
S_1	N172.7°E	32.4°	2
S_2	N78.4°E	87.3°	1.236
S_3	N346.6°E	57.8°	1

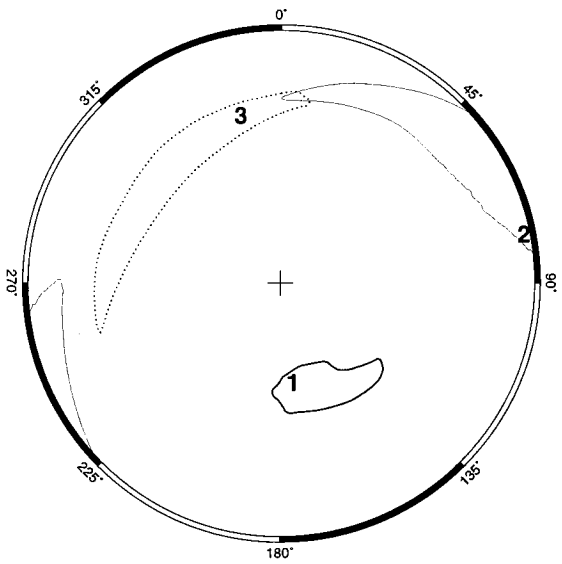

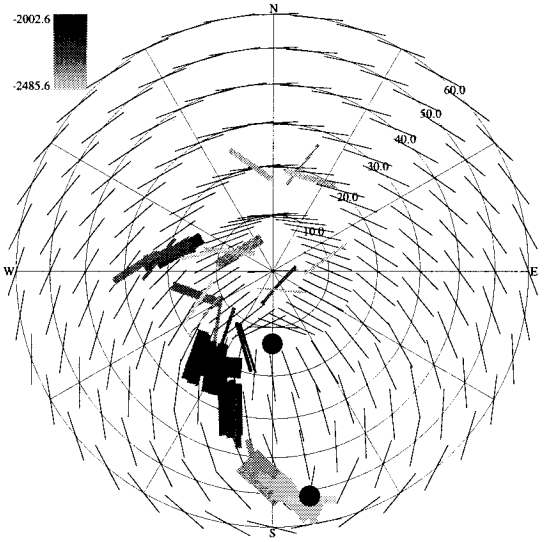

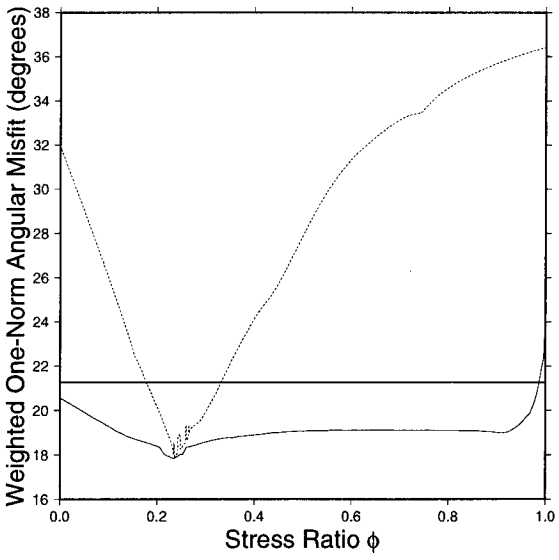

Figure 5.17: Stress inversion results in Cook Inlet, Alaska using all nonradial identified breakouts between 1,500 and 2,000 m TVD from available wells excluding the breakouts from Gp51 and Smgs6. Nonradial breakouts are those breakouts where the **IJK** breakout angle is at least 15° away from the high-side of the hole. Plotting conventions are the same as Figure 5.6.

Stress misfit inversion results using all Cook Inlet nonradial breakouts between 2,500–3,000 m TVD excluding breakouts from wells Gp51 and Smgs6.

Number of breakouts	38
Total length of breakouts	228.6 m
Optimized ϕ with 95% confidence limits	$0.972\ ^{0.997}_{0.953}$
Minimum weighted one-norm stress misfit	0.0177
95% confidence level for weighted one-norm stress misfit	0.0216

	Azimuth	Deviation	Value
S_1	N349.4°E	86.4°	2
S_2	N79.6°E	87.0°	1.972
S_3	N208.7°E	4.7°	1

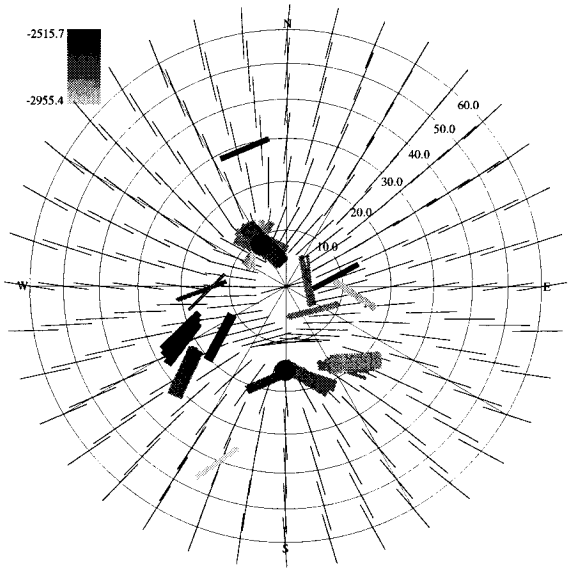

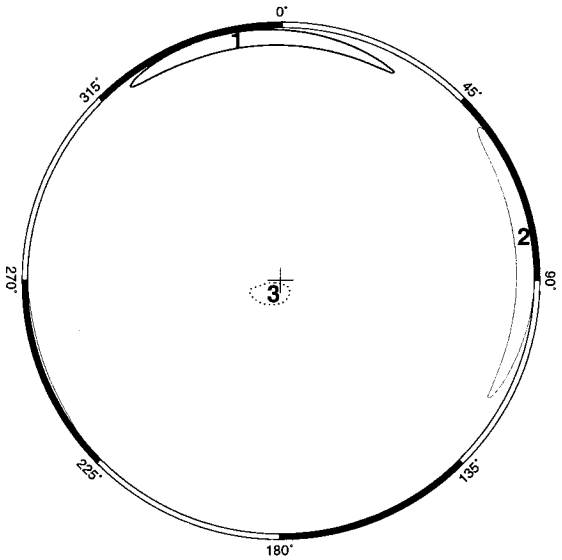

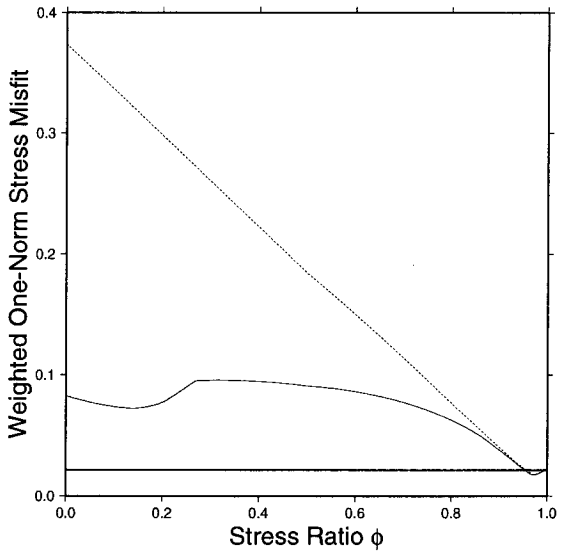

Figure 5.18: Stress inversion results in Cook Inlet, Alaska using all nonradial identified breakouts between 2,500 and 3,000 m TVD from available wells excluding the breakouts from Gp51 and Smgs6. Nonradial breakouts are those breakouts where the **IJK** breakout angle is at least 15° away from the high-side of the hole. Plotting conventions are the same as Figure 5.6.

Angular misfit inversion results using all Cook Inlet nonradial breakouts between 2,500–3,000 m TVD excluding breakouts from wells Gp51 and Smgs6.

Number of breakouts	38
Total length of breakouts	228.6 m
Optimized ϕ with 95% confidence limits	$0.965^{1.000}_{0.023}$
Minimum weighted one-norm stress misfit	24.75°
95% confidence level for weighted one-norm stress misfit	30.18°

	Azimuth	Deviation	Value
S_1	N347.0°E	84.5°	2
S_2	N77.1°E	88.3°	1.965
S_3	N184.1°E	5.7°	1

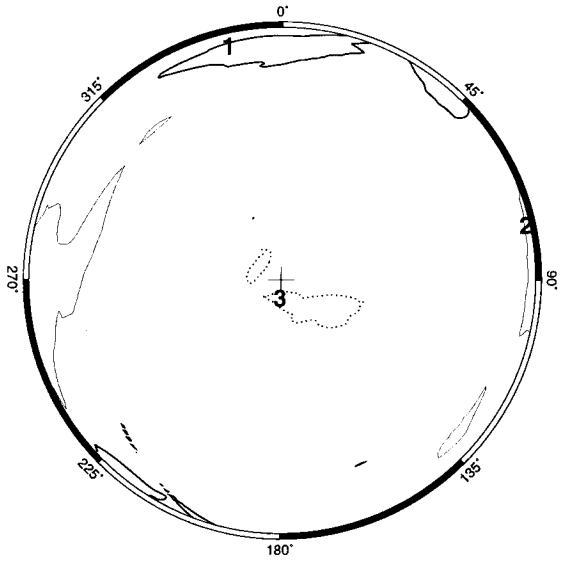

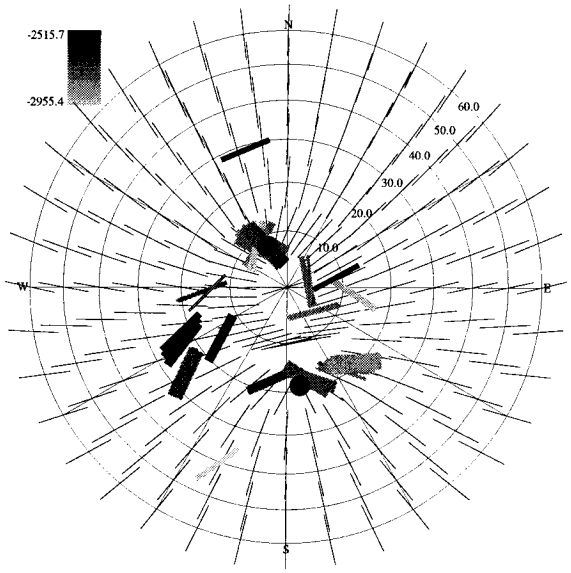

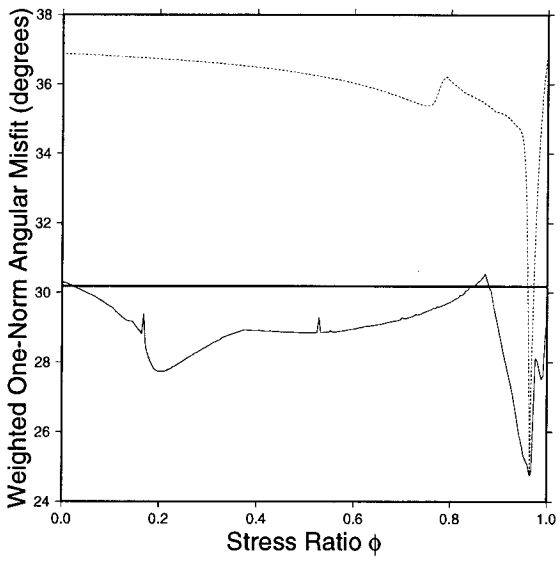

Figure 5.19: Stress inversion results in Cook Inlet, Alaska using all nonradial identified breakouts between 2,500 and 3,000 m TVD from available wells excluding the breakouts from Gp51 and Smgs6. Nonradial breakouts are those breakouts where the **IJK** breakout angle is at least 15° away from the high-side of the hole. Plotting conventions are the same as Figure 5.6.

Stress misfit inversion results using all Granite Point breakouts excluding breakouts from well Gp51.

Number of breakouts	61
Total length of breakouts	365.4 m
Optimized ϕ with 95% confidence limits	$0.976\ ^{0.996}_{0.959}$
Minimum weighted one-norm stress misfit	0.0104
95% confidence level for weighted one-norm stress misfit	0.0121

	Azimuth	Deviation	Value
S_1	N340.6°E	86.6°	2
S_2	N70.6°E	89.6°	1.976
S_3	N166.7°E	3.4°	1

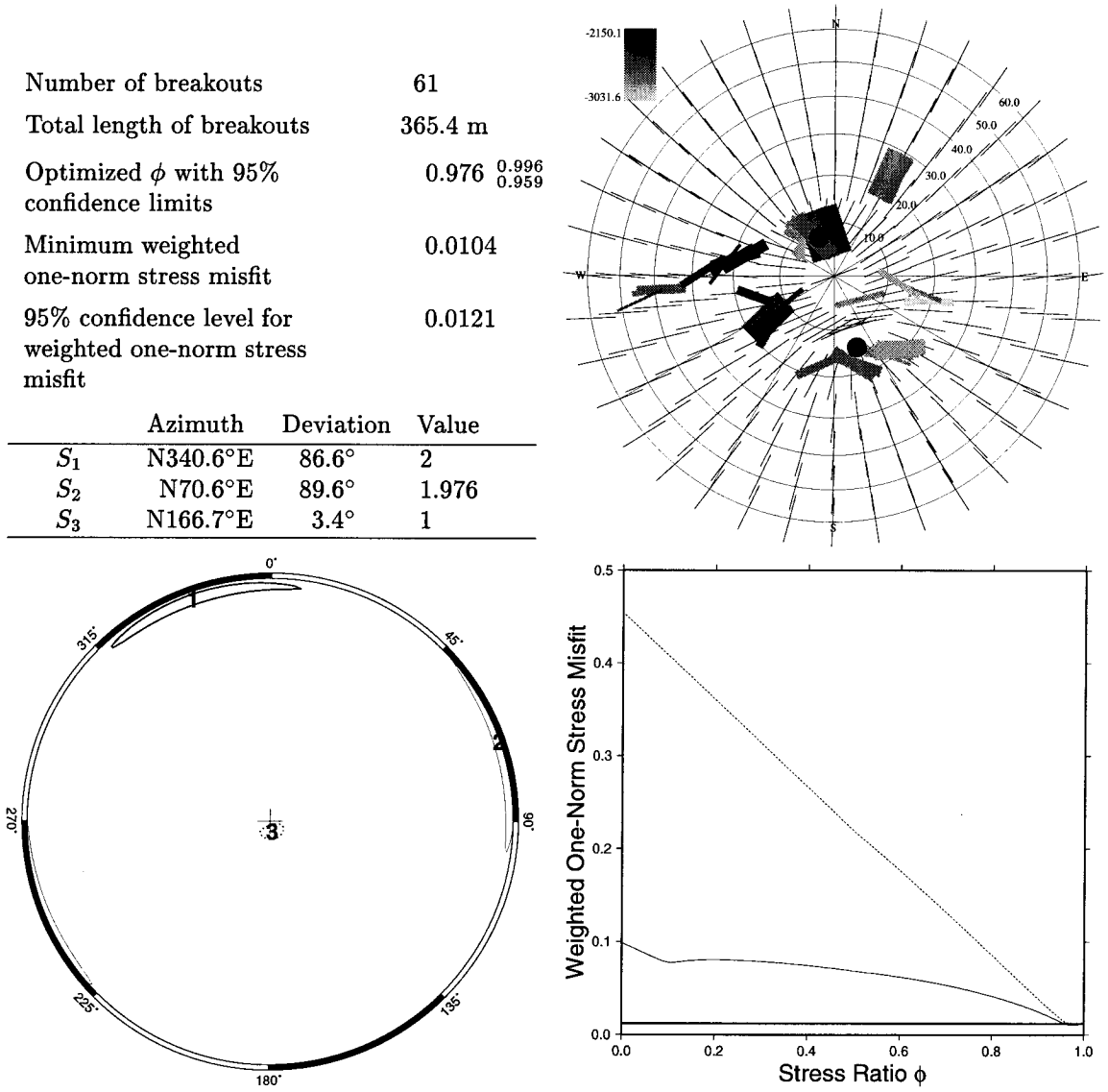

Figure 5.20: Stress inversion results in Cook Inlet, Alaska using all identified breakouts from all of the wells drilled into the Granite Point oil field excluding the breakouts from well Gp51. Plotting conventions are the same as Figure 5.6.

Angular misfit inversion results using all Granite Point breakouts excluding breakouts from well Gp51.

Number of breakouts	61
Total length of breakouts	365.4 m
Optimized ϕ with 95% confidence limits	$0.971^{0.982}_{0.899}$
Minimum weighted one-norm stress misfit	15.35°
95% confidence level for weighted one-norm stress misfit	17.93°

	Azimuth	Deviation	Value
S_1	N349.7°E	84.4°	2
S_2	N259.7°E	90.0°	1.971
S_3	N169.2°E	5.6°	1

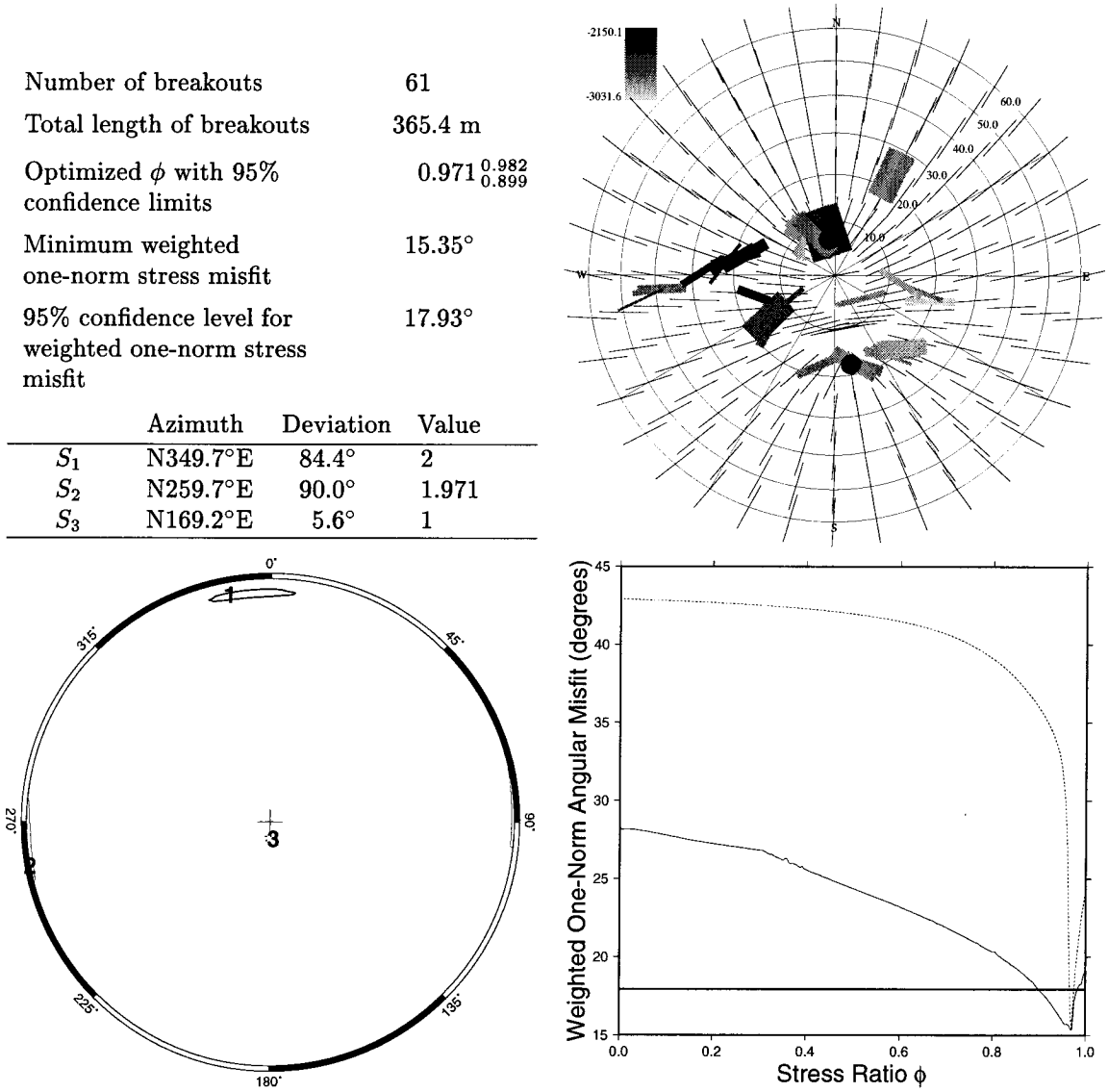

Figure 5.21: Stress inversion results in Cook Inlet, Alaska using all identified breakouts from all of the wells drilled into the Granite Point oil field excluding the breakouts from well Gp51. Plotting conventions are the same as Figure 5.6.

Stress misfit inversion results using all Granite Point nonradial breakouts excluding breakouts from well Gp51.

Number of breakouts	34
Total length of breakouts	183.5 m
Optimized ϕ with 95% confidence limits	$0.967\ ^{0.988}_{0.949}$
Minimum weighted one-norm stress misfit	0.0155
95% confidence level for weighted one-norm stress misfit	0.0191

	Azimuth	Deviation	Value
S_1	N341.2°E	85.5°	2
S_2	N71.3°E	88.2°	1.967
S_3	N183.5°E	4.8°	1

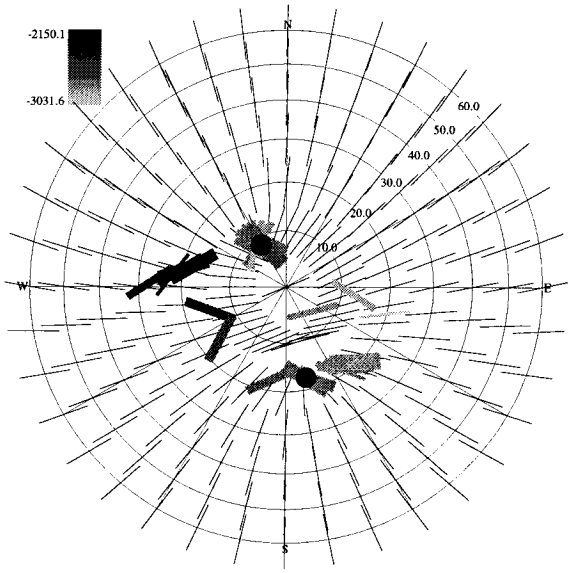

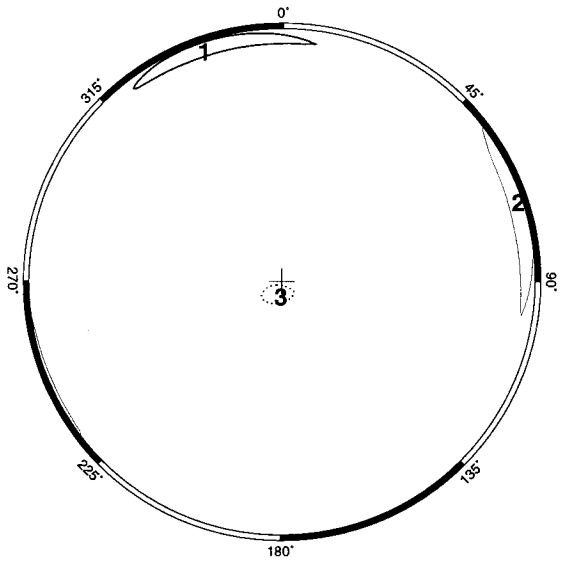

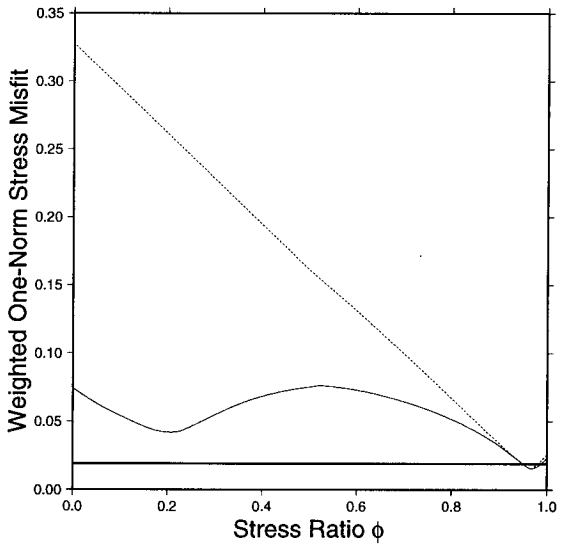

Figure 5.22: Stress inversion results in Cook Inlet, Alaska using all identified nonradial breakouts from all of the wells drilled into the Granite Point oil field excluding the breakouts from well Gp51. Nonradial breakouts are those breakouts where the **IJK** breakout angle is at least 15° away from the high-side of the hole. Plotting conventions are the same as Figure 5.6.

Angular misfit inversion results using all Granite Point nonradial breakouts excluding breakouts from well Gp51.

Number of breakouts	34
Total length of breakouts	183.5 m
Optimized ϕ with 95% confidence limits	$0.962^{1.000}_{0.000}$
Minimum weighted one-norm stress misfit	22.84°
95% confidence level for weighted one-norm stress misfit	28.18°

	Azimuth	Deviation	Value
S_1	N352.8°E	83.8°	2
S_2	N83.1°E	87.9°	1.962
S_3	N192.0°E	6.6°	1

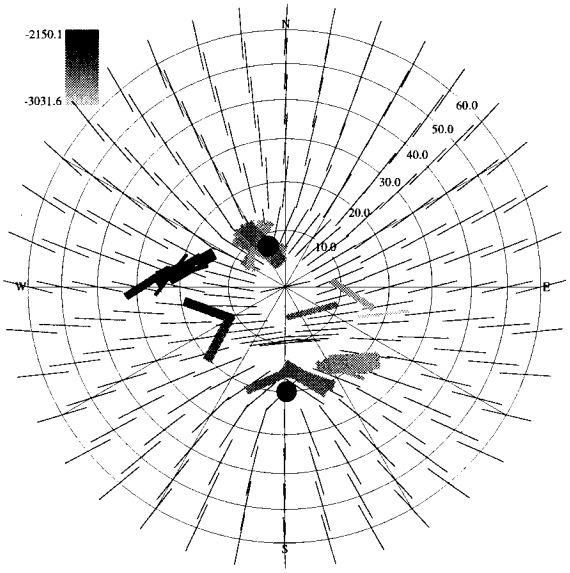

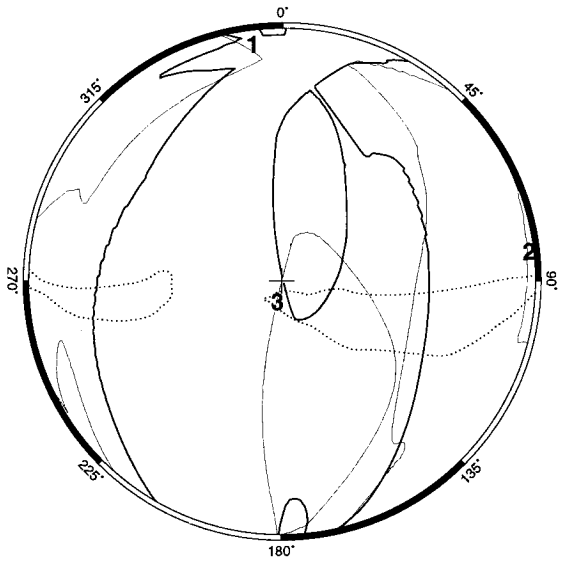

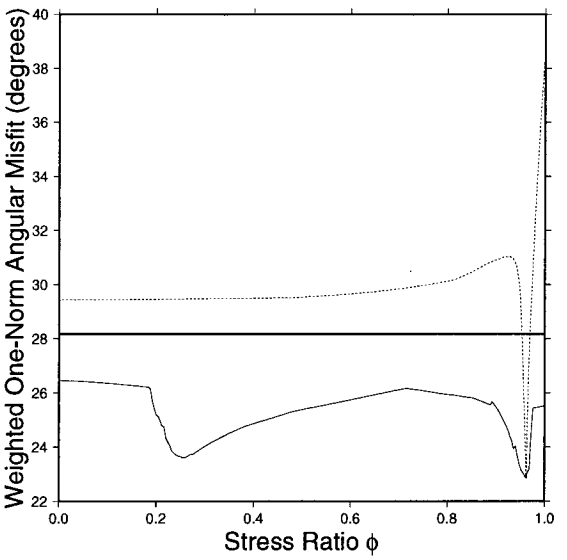

Figure 5.23: Stress inversion results in Cook Inlet, Alaska using all identified nonradial breakouts from all of the wells drilled into the Granite Point oil field excluding the breakouts from well Gp51. Nonradial breakouts are those breakouts where the **IJK** breakout angle is at least 15° away from the high-side of the hole. Plotting conventions are the same as Figure 5.6.

Stress misfit inversion results using all Granite Point nonradial breakouts between 2,000–2,500 m TVD excluding breakouts from well Gp51.

Number of breakouts	10
Total length of breakouts	59.9 m
Optimized ϕ with 95% confidence limits	$0.999^{1.000}_{0.990}$
Minimum weighted one-norm stress misfit	$1.46\text{x}10^{-4}$
95% confidence level for weighted one-norm stress misfit	$2.26\text{x}10^{-4}$

	Azimuth	Deviation	Value
S_1	N141.1°E	73.0°	2
S_2	N45.4°E	71.9°	1.999
S_3	N271.6°E	25.2°	1

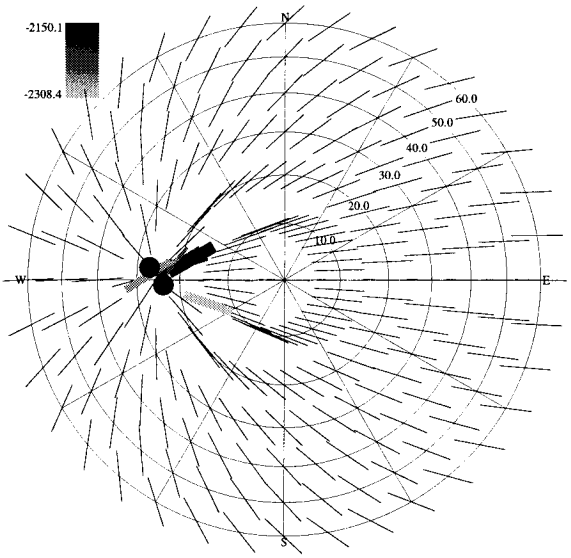

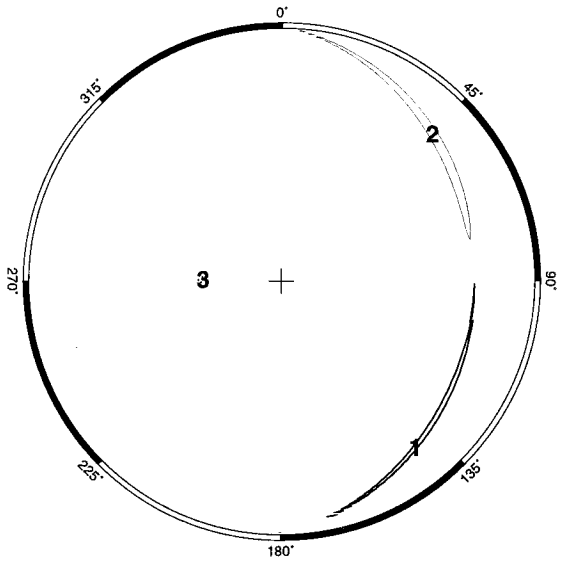

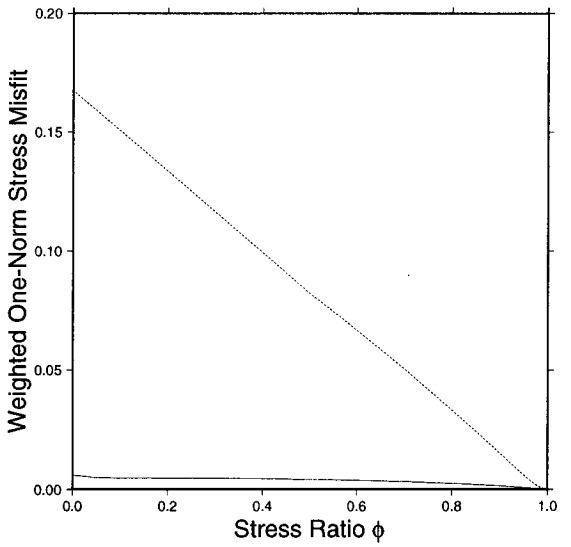

Figure 5.24: Stress inversion results in Cook Inlet, Alaska using all nonradial identified breakouts between 2,000 and 2,500 m TVD from all of the wells drilled into the Granite Point oil field excluding the breakouts from well Gp51. Nonradial breakouts are those breakouts where the **IJK** breakout angle is at least 15° away from the high-side of the hole. Plotting conventions are the same as Figure 5.6.

Angular misfit inversion results using all Granite Point nonradial breakouts between 2,500–3,000 m TVD excluding breakouts from well Gp51.

Number of breakouts	10
Total length of breakouts	59.9 m
Optimized ϕ with 95% confidence limits	$0.977^{1.000}_{0.867}$
Minimum weighted one-norm stress misfit	4.42°
95% confidence level for weighted one-norm stress misfit	6.81°

	Azimuth	Deviation	Value
S_1	N154.0°E	76.6°	2
S_2	N60.3°E	74.9°	1.977
S_3	N283.8°E	20.4°	1

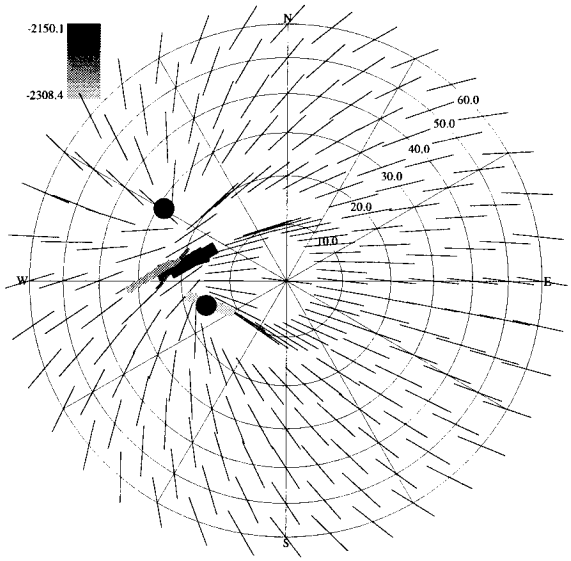

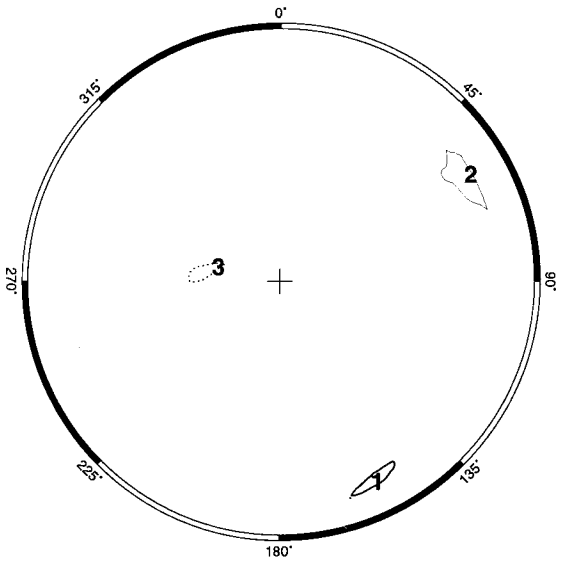

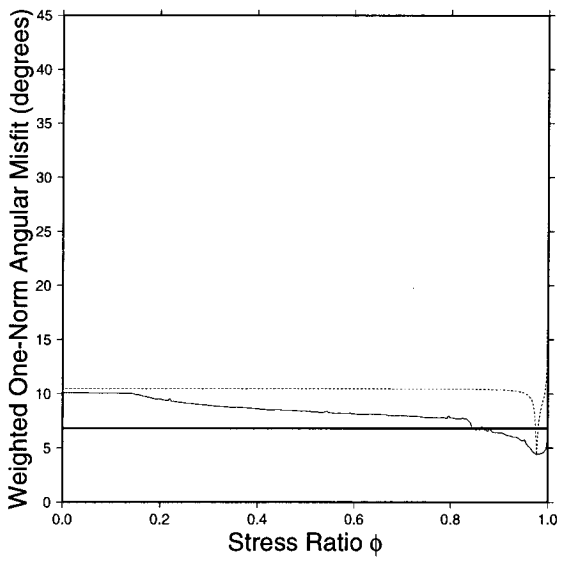

Figure 5.25: Stress inversion results in Cook Inlet, Alaska using all nonradial identified breakouts between 2,000 and 2,500 m TVD from all of the wells drilled into the Granite Point oil field excluding the breakouts from well Gp51. Nonradial breakouts are those breakouts where the **IJK** breakout angle is at least 15° away from the high-side of the hole. Plotting conventions are the same as Figure 5.6.

Stress misfit inversion results using all Granite Point nonradial breakouts between 2,500–3,000 m TVD excluding breakouts from well Gp51.

Number of breakouts	23
Total length of breakouts	120.3 m
Optimized ϕ with 95% confidence limits	$0.964^{0.974}_{0.946}$
Minimum weighted one-norm stress misfit	$5.53\text{x}10^{-3}$
95% confidence level for weighted one-norm stress misfit	$7.17\text{x}10^{-3}$

	Azimuth	Deviation	Value
S_1	N343.0°E	84.8°	2
S_2	N73.2°E	88.4°	1.964
S_3	N180.3°E	5.5°	1

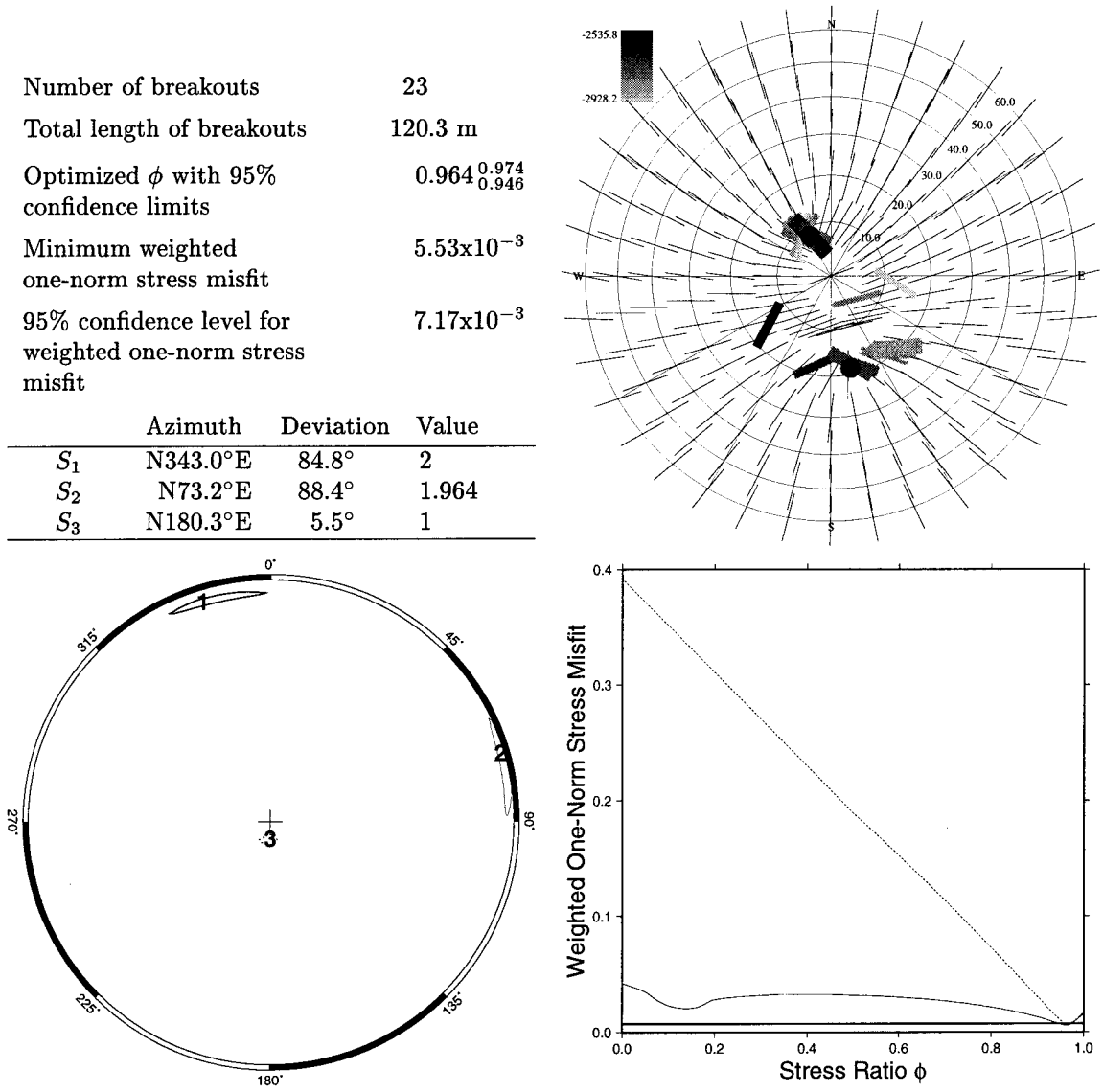

Figure 5.26: Stress inversion results in Cook Inlet, Alaska using all nonradial identified breakouts between 2,500 and 3,000 m TVD from all of the wells drilled into the Granite Point oil field excluding the breakouts from well Gp51. Nonradial breakouts are those breakouts where the **IJK** breakout angle is at least 15° away from the high-side of the hole. Plotting conventions are the same as Figure 5.6.

Angular misfit inversion results using all Granite Point nonradial breakouts between 2,500–3,000 m TVD excluding breakouts from well Gp51.

Number of breakouts	23
Total length of breakouts	120.3 m
Optimized ϕ with 95% confidence limits	$0.961\,^{1.000}_{0.000}$
Minimum weighted one-norm stress misfit	17.53°
95% confidence level for weighted one-norm stress misfit	22.71°

	Azimuth	Deviation	Value
S_1	N352.1°E	83.5°	2
S_2	N82.3°E	88.0°	1.961
S_3	N189.3°E	6.8°	1

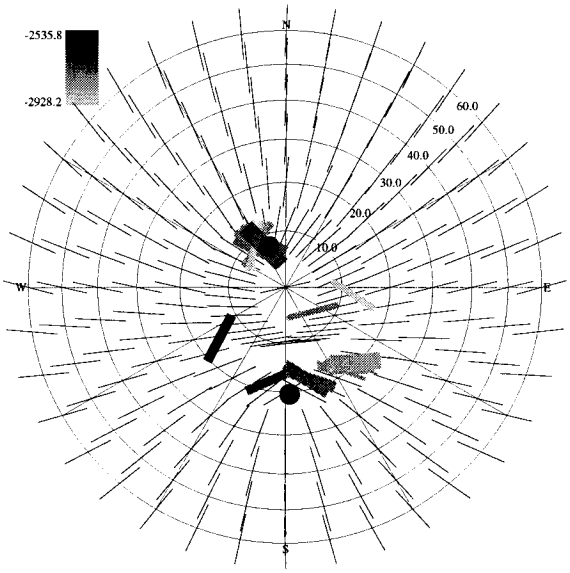

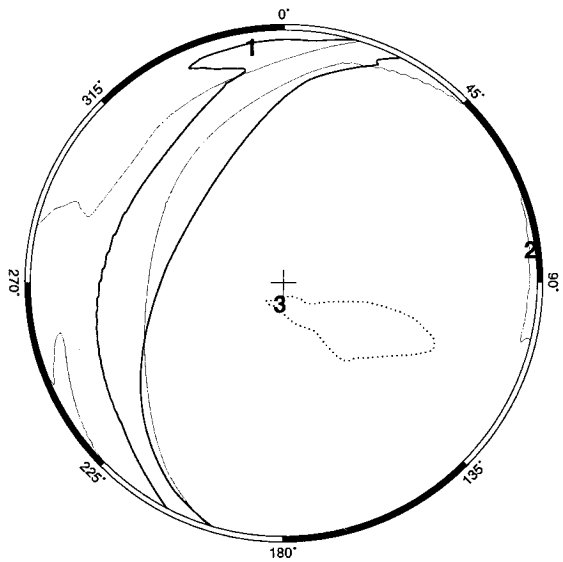

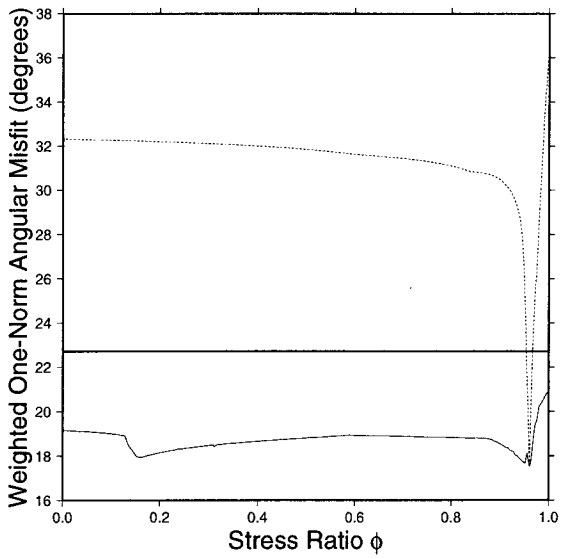

Figure 5.27: Stress inversion results in Cook Inlet, Alaska using all nonradial identified breakouts between 2,500 and 3,000 m TVD from all of the wells drilled into the Granite Point oil field excluding the breakouts from well Gp51. Nonradial breakouts are those breakouts where the **IJK** breakout angle is at least 15° away from the high-side of the hole. Plotting conventions are the same as Figure 5.6.

Stress misfit inversion results using all Baker platform breakouts.

Number of breakouts	154
Total length of breakouts	1146.4 m
Optimized ϕ with 95% confidence limits	0.944 $^{0.989}_{0.898}$
Minimum weighted one-norm stress misfit	0.0319
95% confidence level for weighted one-norm stress misfit	0.0352

	Azimuth	Deviation	Value
S_1	N169.8°E	82.3°	2
S_2	N79.1°E	84.6°	1.944
S_3	N314.0°E	9.4°	1

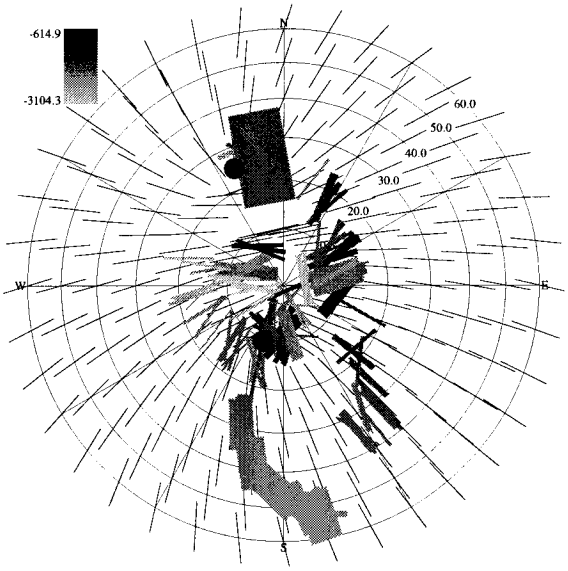

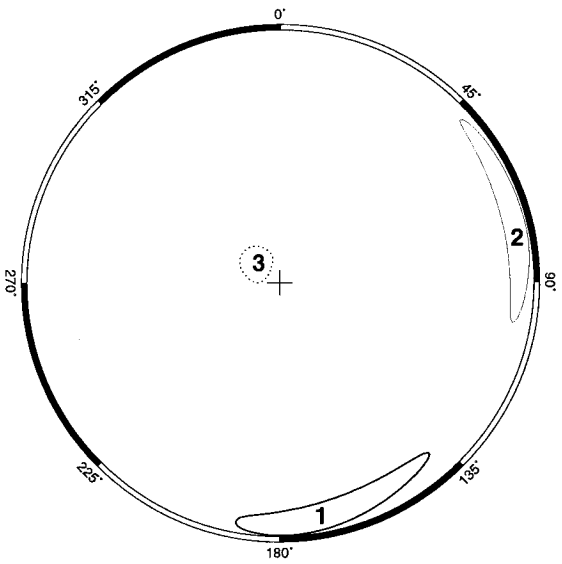

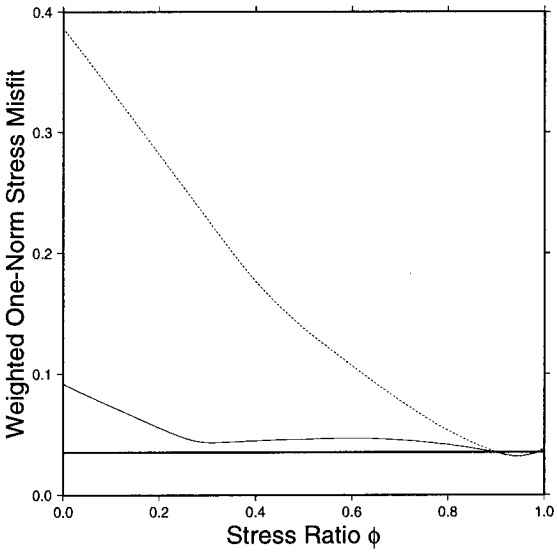

Figure 5.28: Stress inversion results in Cook Inlet, Alaska using all identified breakouts from wells drilled from the Baker platform in the Middle Ground Shoals oil field. Plotting conventions are the same as Figure 5.6.

Angular misfit inversion results using all Baker platform breakouts.

Number of breakouts	154
Total length of breakouts	1146.4 m
Optimized ϕ with 95% confidence limits	$0.940^{0.967}_{0.192}$
Minimum weighted one-norm stress misfit	20.24°
95% confidence level for weighted one-norm stress misfit	22.32°

	Azimuth	Deviation	Value
S_1	N180.6°E	79.8°	2
S_2	N89.6°E	84.4°	1.940
S_3	N331.3°E	11.7°	1

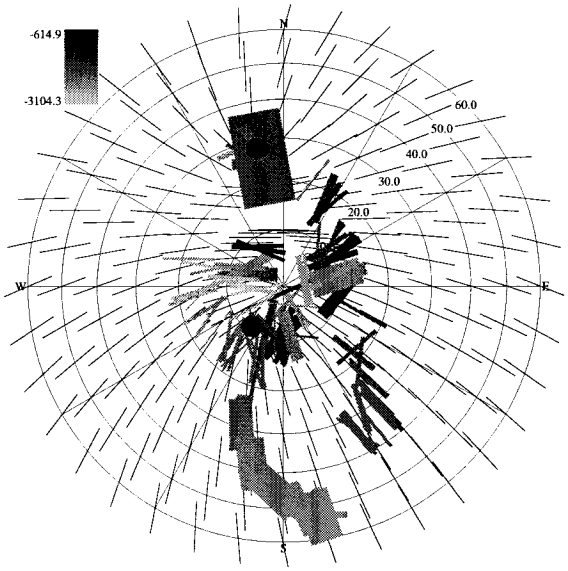

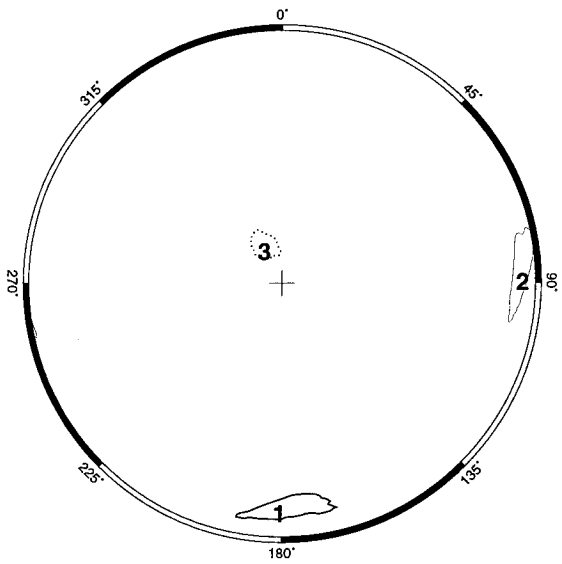

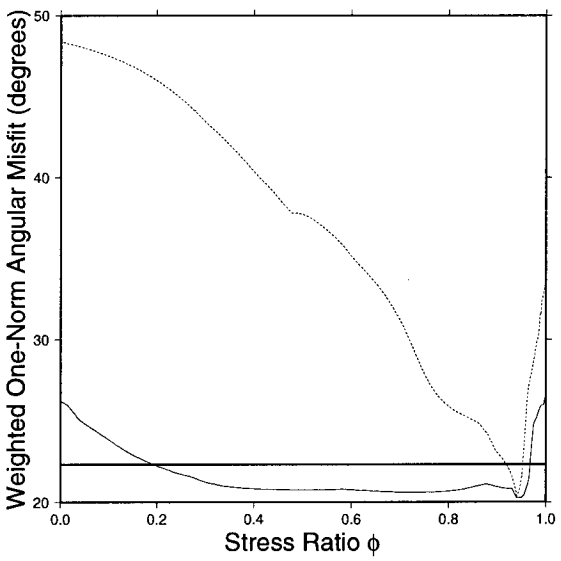

Figure 5.29: Stress inversion results in Cook Inlet, Alaska using all identified breakouts from wells drilled from the Baker platform in the Middle Ground Shoals oil field. Plotting conventions are the same as Figure 5.6.

Stress misfit inversion results using all Baker platform nonradial breakouts.

Number of breakouts	72
Total length of breakouts	509.1 m
Optimized ϕ with 95% confidence limits	$0.302\ ^{0.384}_{0.219}$
Minimum weighted one-norm stress misfit	0.0351
95% confidence level for weighted one-norm stress misfit	0.0405

	Azimuth	Deviation	Value
S_1	N170.8°E	27.9°	2
S_2	N262.6°E	89.0°	1.302
S_3	N353.2°E	62.1°	1

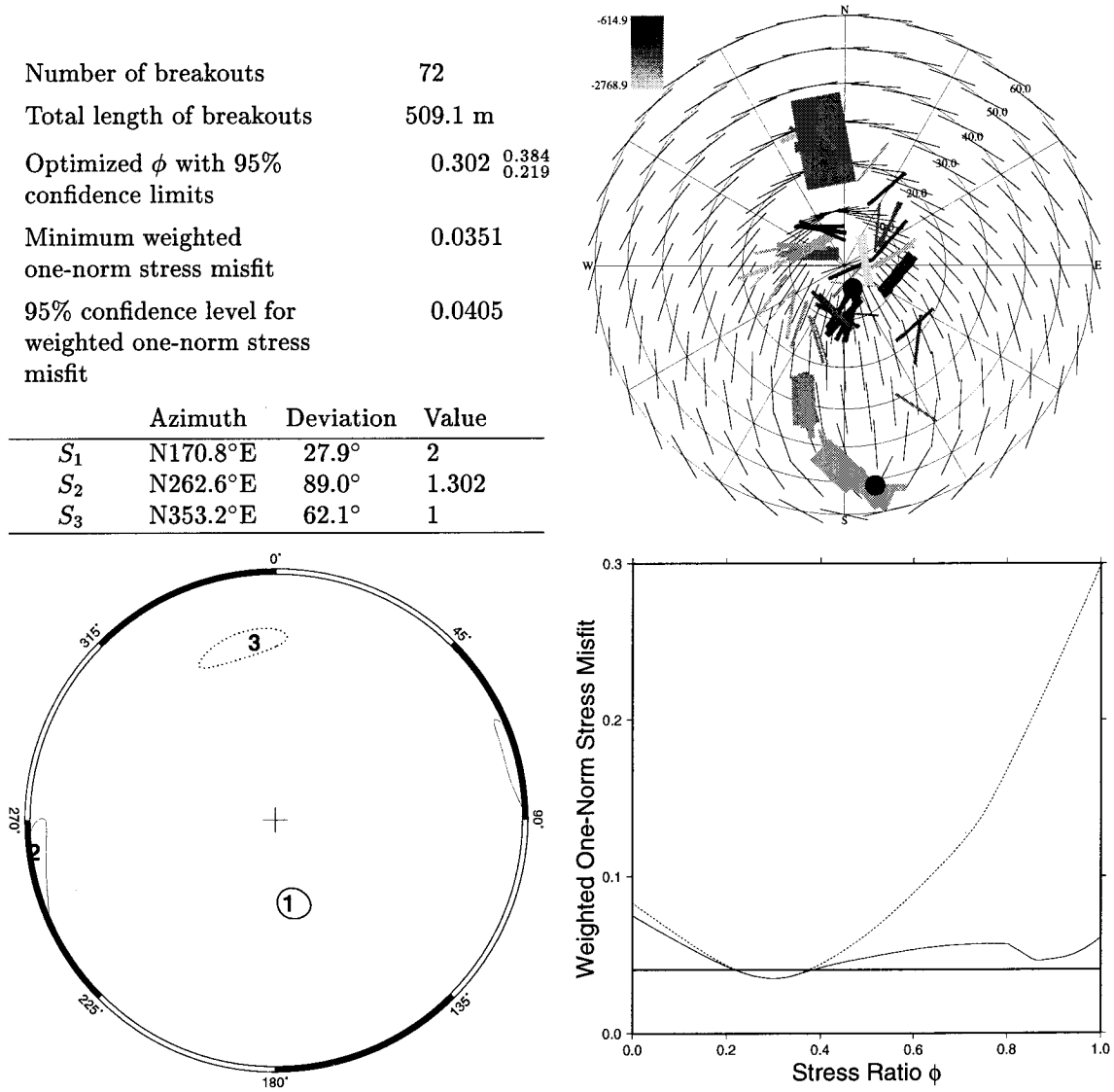

Figure 5.30: Stress inversion results in Cook Inlet, Alaska using all nonradial identified breakouts from wells drilled from the Baker platform in the Middle Ground Shoals oil field. Nonradial breakouts are those breakouts where the **IJK** breakout angle is at least 15° away from the high-side of the hole. Plotting conventions are the same as Figure 5.6.

Angular misfit inversion results using all Baker platform nonradial breakouts.

Number of breakouts	72
Total length of breakouts	509.1 m
Optimized ϕ with 95% confidence limits	$0.260^{0.946}_{0.000}$
Minimum weighted one-norm stress misfit	20.15°
95% confidence level for weighted one-norm stress misfit	23.25°

	Azimuth	Deviation	Value
S_1	N169.4°E	30.5°	2
S_2	N261.4°E	88.8°	1.260
S_3	N352.1°E	59.5°	1

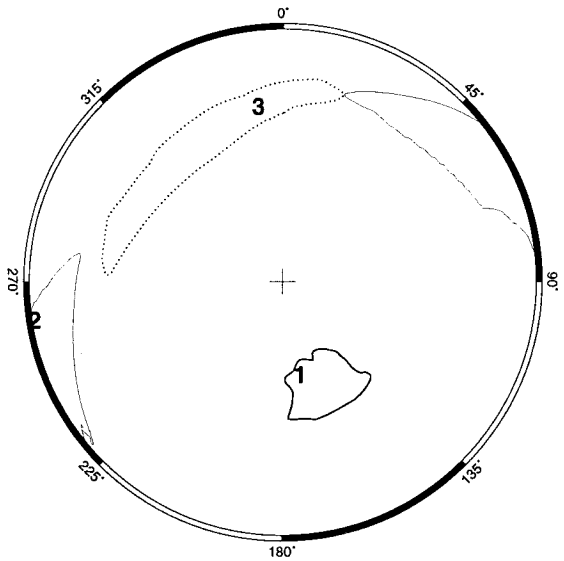

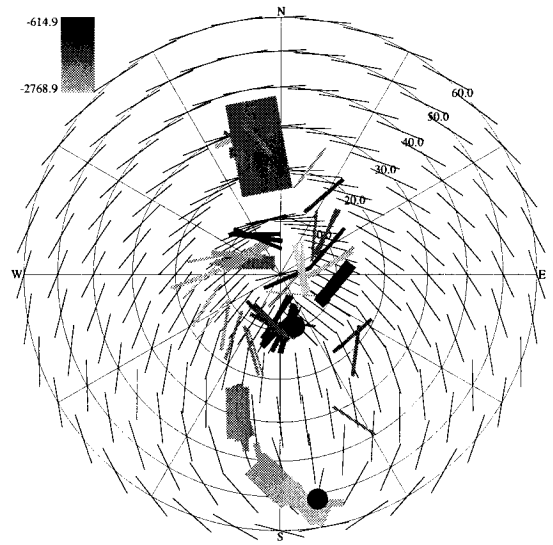

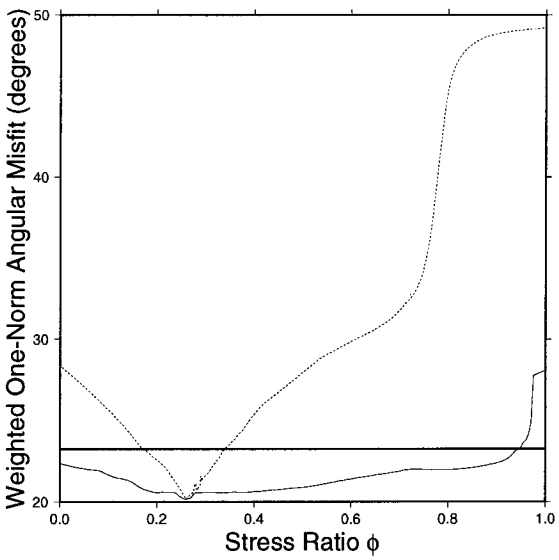

Figure 5.31: Stress inversion results in Cook Inlet, Alaska using all nonradial identified breakouts from wells drilled from the Baker platform in the Middle Ground Shoals oil field. Nonradial breakouts are those breakouts where the **IJK** breakout angle is at least 15° away from the high-side of the hole. Plotting conventions are the same as Figure 5.6.

Stress misfit inversion results using all Baker platform breakouts in the B40SS formation.

Number of breakouts	25
Total length of breakouts	180.7 m
Optimized ϕ with 95% confidence limits	$0.993^{1.000}_{0.979}$
Minimum weighted one-norm stress misfit	$6.25\text{x}10^{-3}$
95% confidence level for weighted one-norm stress misfit	$8.00\text{x}10^{-3}$

	Azimuth	Deviation	Value
S_1	N27.1°E	88.0°	2
S_2	N297.0°E	88.2°	1.993
S_3	N165.0°E	2.7°	1

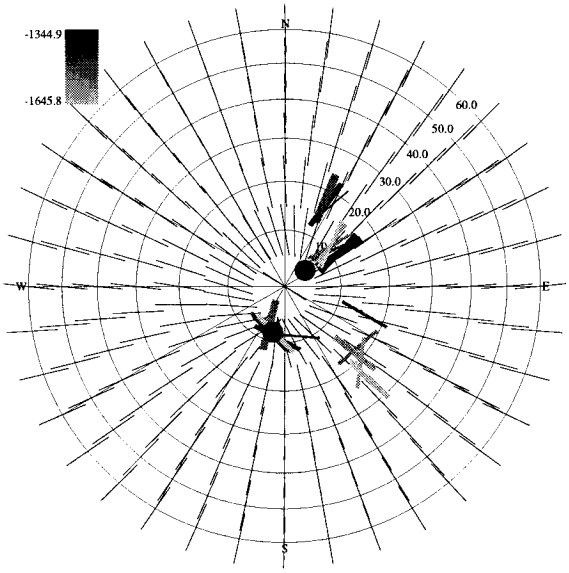

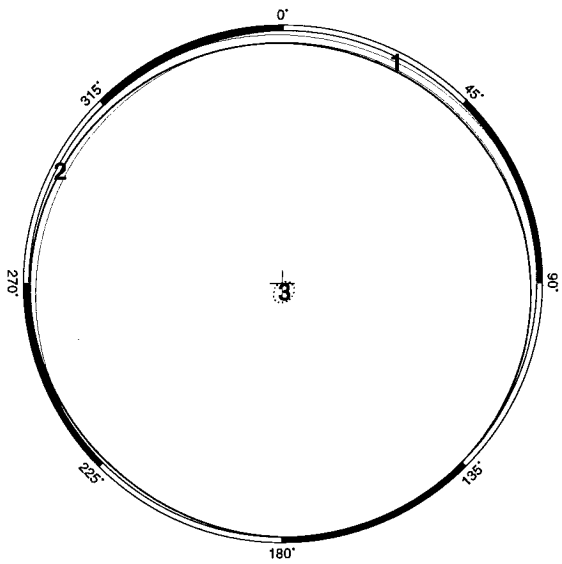

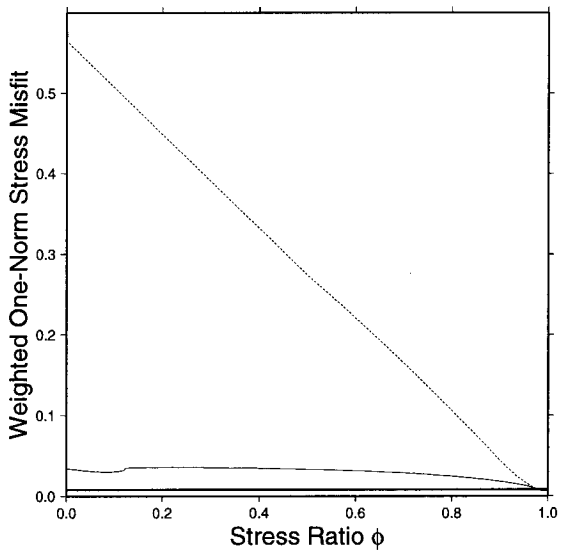

Figure 5.32: Stress inversion results in Cook Inlet, Alaska using all identified breakouts occurring in the B40SS formation from wells drilled into the Middle Ground Shoals oil field from the Baker platform. Plotting conventions are the same as Figure 5.6.

Angular misfit inversion results using all Baker platform breakouts in the B40SS formation.

Number of breakouts	25
Total length of breakouts	180.7 m
Optimized ϕ with 95% confidence limits	$0.993^{1.000}_{0.505}$
Minimum weighted one-norm stress misfit	15.54°
95% confidence level for weighted one-norm stress misfit	18.63°

	Azimuth	Deviation	Value
S_1	N99.6°E	82.8°	2
S_2	N8.7°E	83.0°	1.993
S_3	N234.9°E	10.1°	1

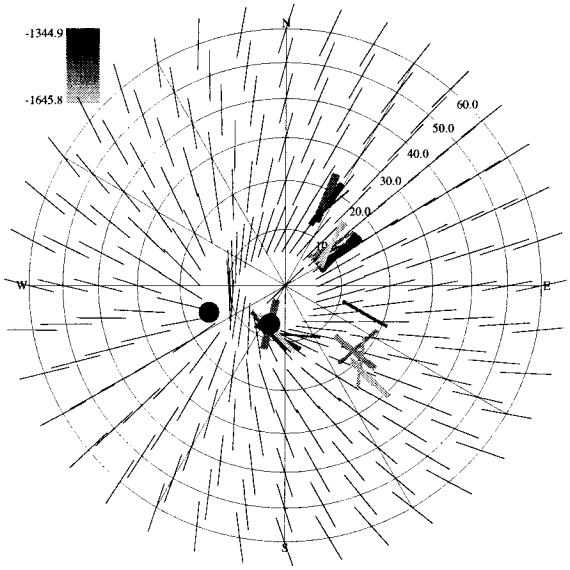

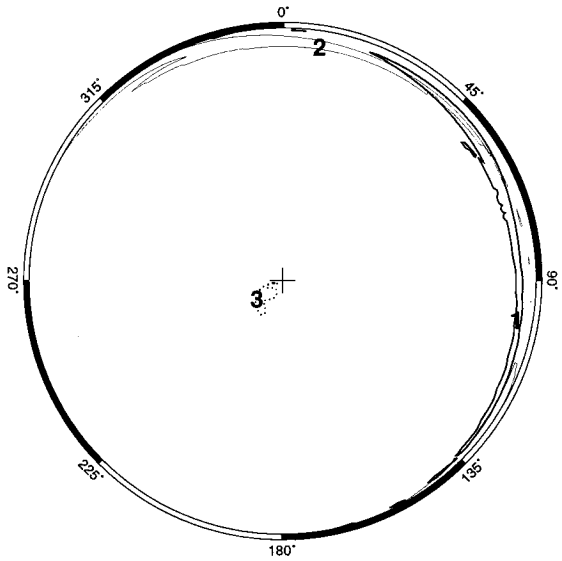

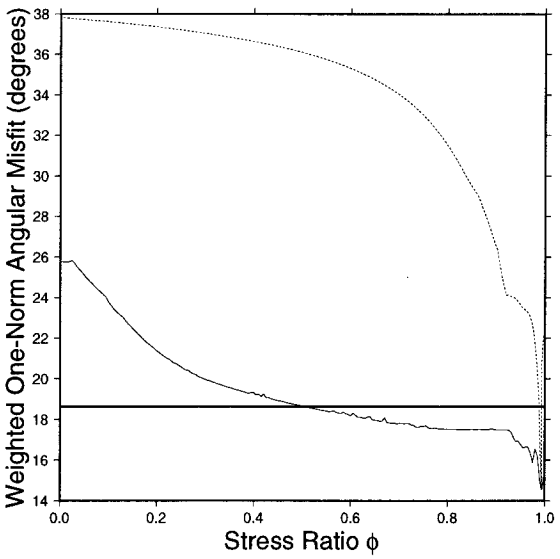

Figure 5.33: Stress inversion results in Cook Inlet, Alaska using all identified breakouts occurring in the B40SS formation from wells drilled into the Middle Ground Shoals oil field from the Baker platform. Plotting conventions are the same as Figure 5.6.

Stress misfit inversion results using all Baker platform nonradial breakouts in the B40SS formation.

Number of breakouts	10
Total length of breakouts	64.0 m
Optimized ϕ with 95% confidence limits	$0.988^{1.000}_{0.975}$
Minimum weighted one-norm stress misfit	$5.27\text{x}10^{-3}$
95% confidence level for weighted one-norm stress misfit	$8.13\text{x}10^{-3}$

	Azimuth	Deviation	Value
S_1	N287.9°E	80.4°	2
S_2	N19.4°E	81.0°	1.988
S_3	N152.0°E	13.2°	1

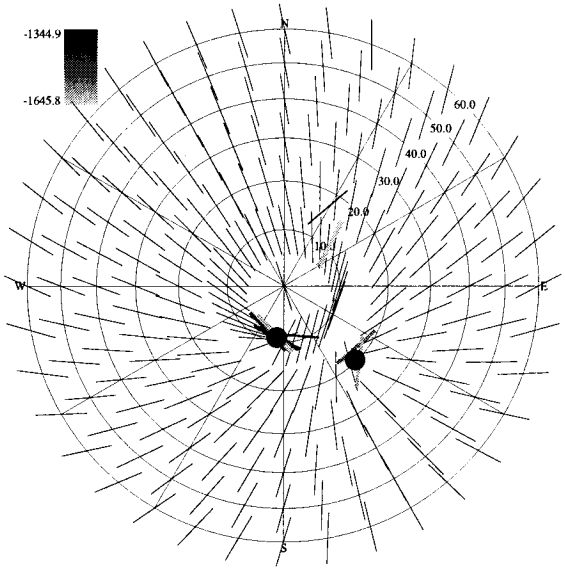

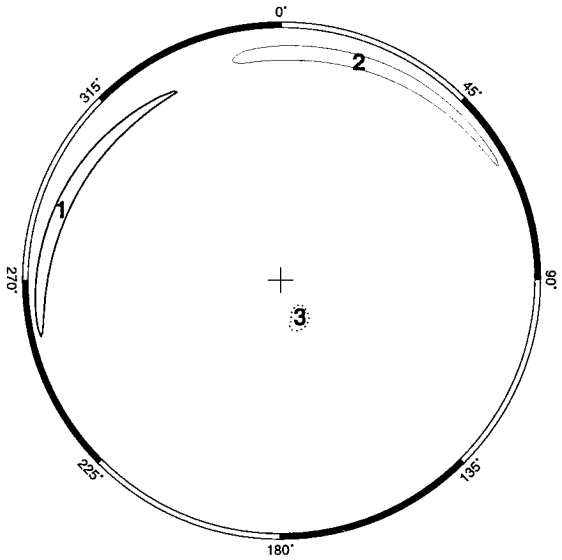

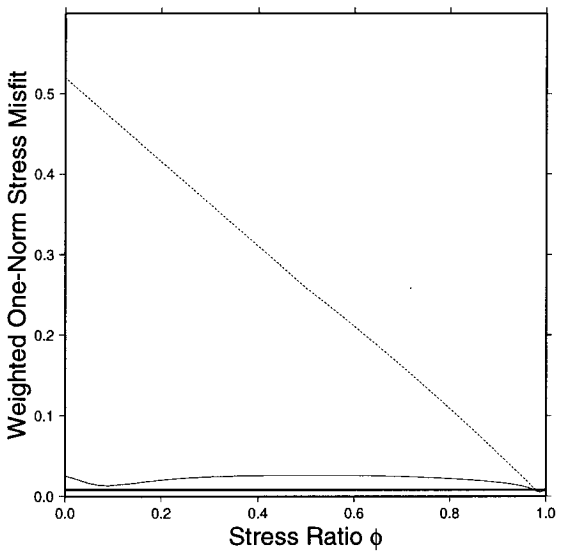

Figure 5.34: Stress inversion results in Cook Inlet, Alaska using all nonradial identified breakouts occurring in the B40SS formation from wells drilled into the Middle Ground Shoals oil field from the Baker platform. Nonradial breakouts are those breakouts where the **IJK** breakout angle is at least 15° away from the high-side of the hole. Plotting conventions are the same as Figure 5.6.

Angular misfit inversion results using all Baker platform nonradial breakouts in the B40SS formation.

Number of breakouts	10
Total length of breakouts	64.0 m
Optimized ϕ with 95% confidence limits	$0.073^{0.938}_{0.037}$
Minimum weighted one-norm stress misfit	8.89°
95% confidence level for weighted one-norm stress misfit	13.71°

	Azimuth	Deviation	Value
S_1	N68.9°E	5.8°	2
S_2	N298.5°E	86.2°	1.073
S_3	N208.2°E	85.6°	1

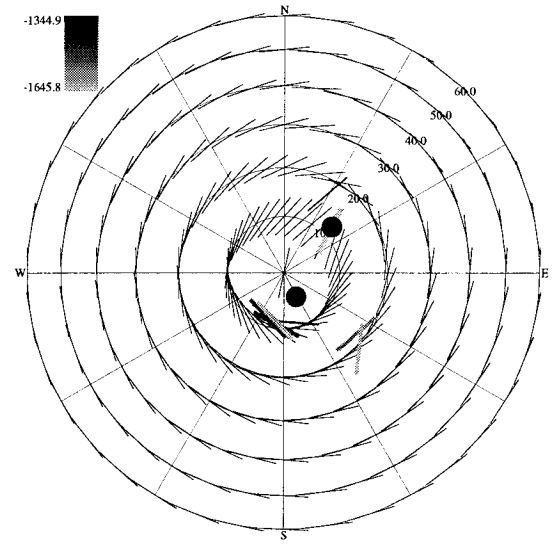

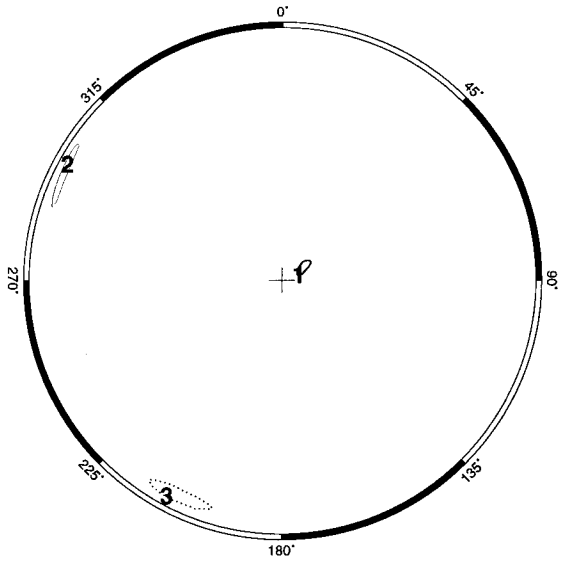

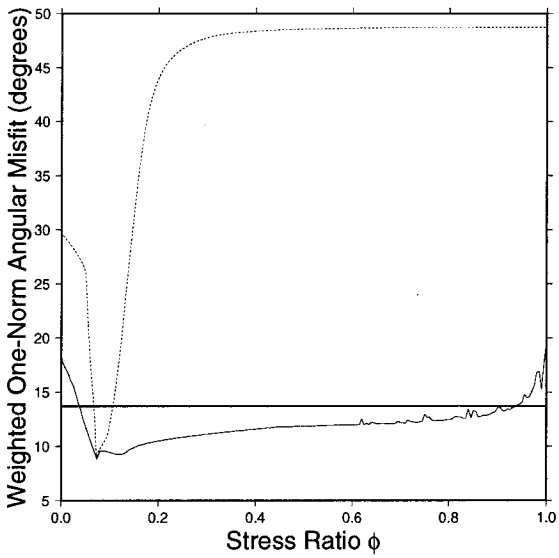

Figure 5.35: Stress inversion results in Cook Inlet, Alaska using all nonradial identified breakouts occurring in the B40SS formation from wells drilled into the Middle Ground Shoals oil field from the Baker platform. Nonradial breakouts are those breakouts where the **IJK** breakout angle is at least 15° away from the high-side of the hole. Plotting conventions are the same as Figure 5.6.

Stress misfit inversion results using all Baker platform breakouts in the D formation.

Number of breakouts	15
Total length of breakouts	120.5 m
Optimized ϕ with 95% confidence limits	$0.988^{1.000}_{0.915}$
Minimum weighted one-norm stress misfit	$2.90\text{x}10^{-3}$
95% confidence level for weighted one-norm stress misfit	$4.04\text{x}10^{-3}$

	Azimuth	Deviation	Value
S_1	N79.7°E	84.5°	2
S_2	N349.4°E	87.0°	1.988
S_3	N230.6°E	6.2°	1

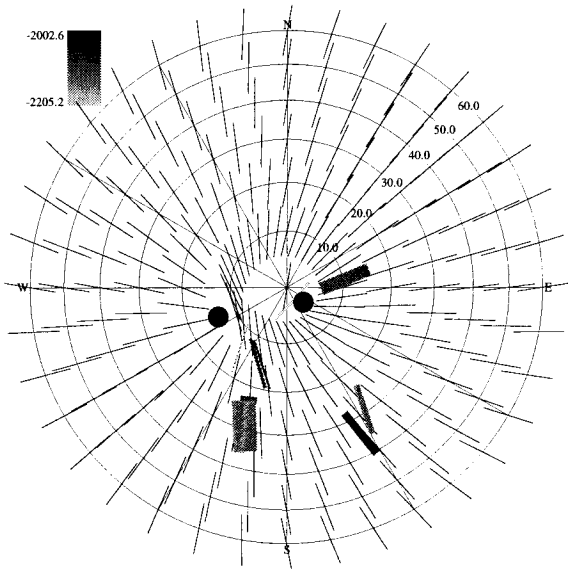

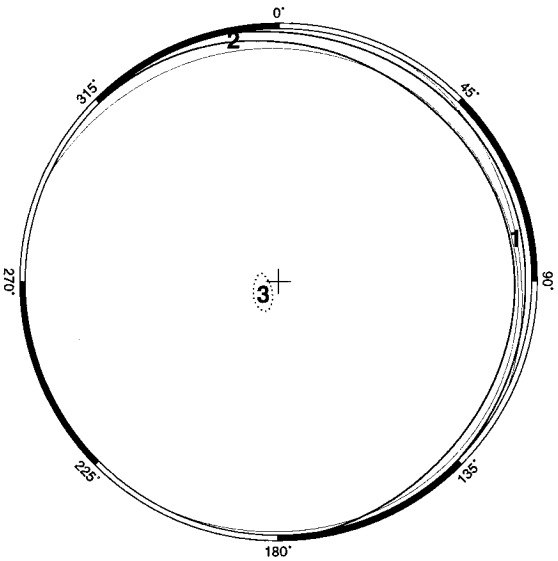

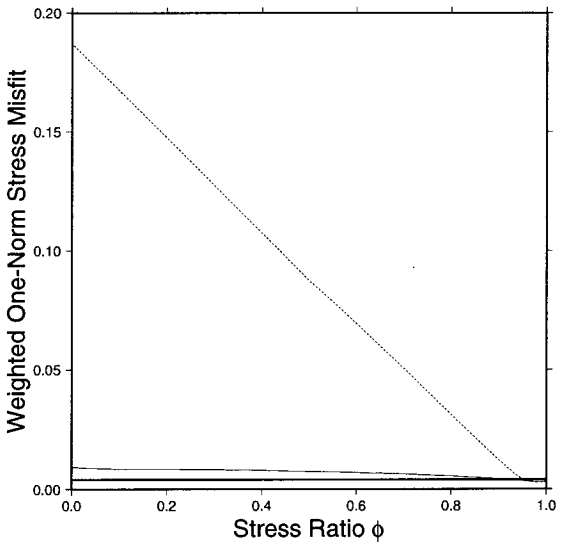

Figure 5.36: Stress inversion results in Cook Inlet, Alaska using all identified breakouts occurring in the D formation from wells drilled into the Middle Ground Shoals oil field from the Baker platform. Plotting conventions are the same as Figure 5.6.

Angular misfit inversion results using all Baker platform breakouts in the D formation.

Number of breakouts	15
Total length of breakouts	120.5 m
Optimized ϕ with 95% confidence limits	$0.102^{1.000}_{0.010}$
Minimum weighted one-norm stress misfit	5.41°
95% confidence level for weighted one-norm stress misfit	7.53°

	Azimuth	Deviation	Value
S_1	N139.6°E	37.7°	2
S_2	N36.0°E	79.7°	1.102
S_3	N298.5°E	54.2°	1

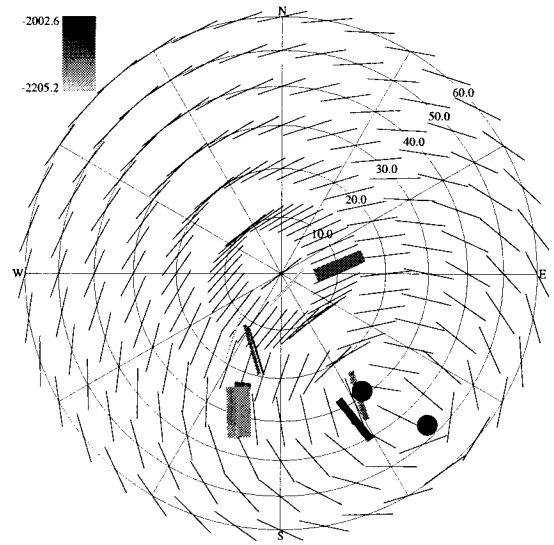

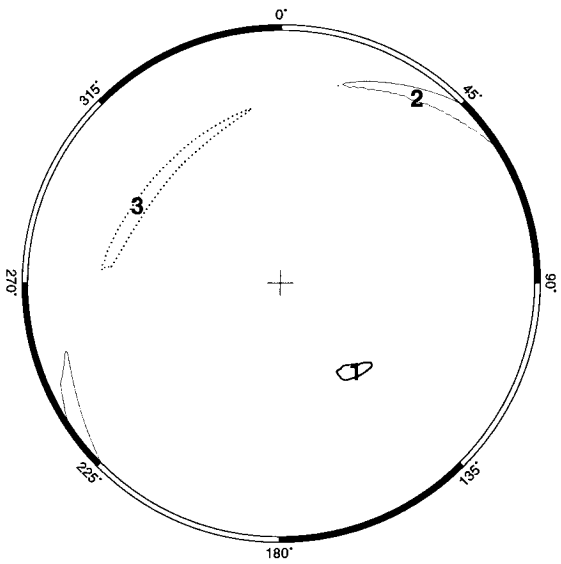

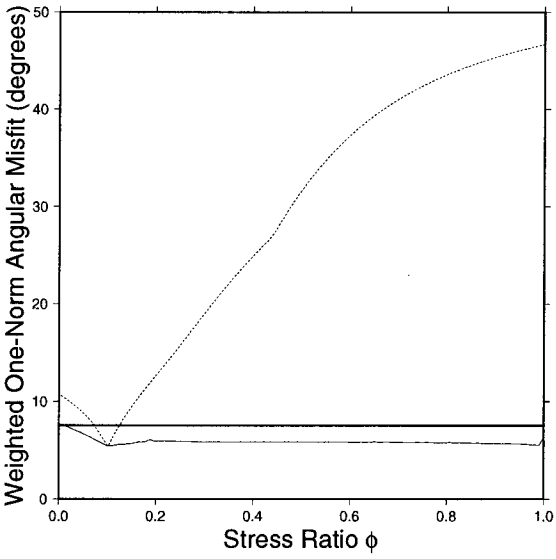

Figure 5.37: Stress inversion results in Cook Inlet, Alaska using all identified breakouts occurring in the D formation from wells drilled into the Middle Ground Shoals oil field from the Baker platform. Plotting conventions are the same as Figure 5.6.

Stress misfit inversion results using all Baker platform nonradial breakouts in the D formation.

Number of breakouts	7
Total length of breakouts	43.5 m
Optimized ϕ with 95% confidence limits	$0.996^{0.998}_{0.990}$
Minimum weighted one-norm stress misfit	$5.51\text{x}10^{-5}$
95% confidence level for weighted one-norm stress misfit	$9.84\text{x}10^{-5}$

	Azimuth	Deviation	Value
S_1	N105.6°E	84.9°	2
S_2	N14.3°E	76.1°	1.996
S_3	N215.3°E	14.9°	1

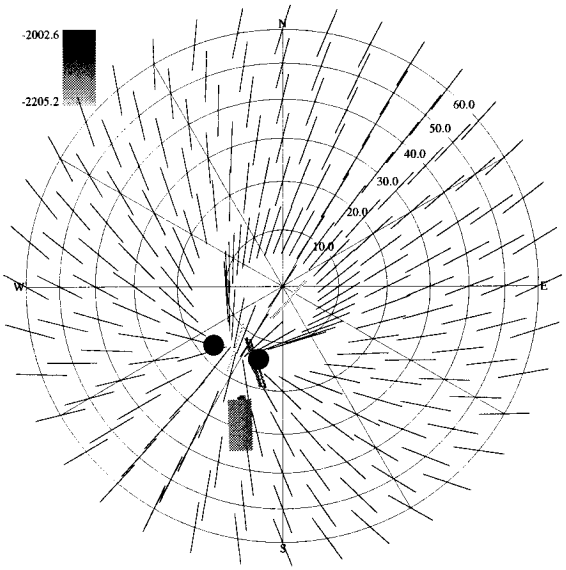

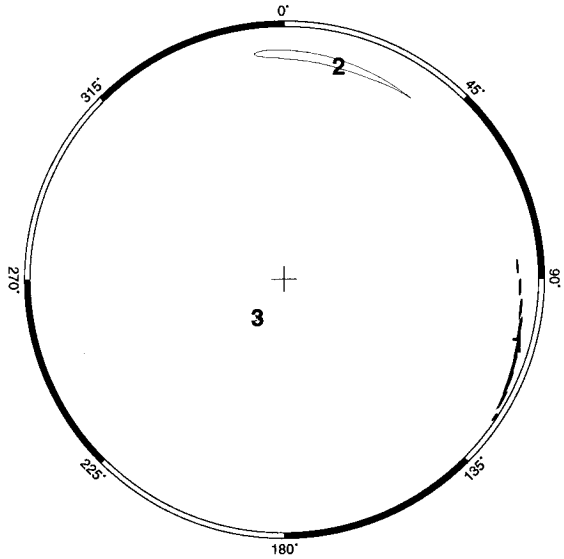

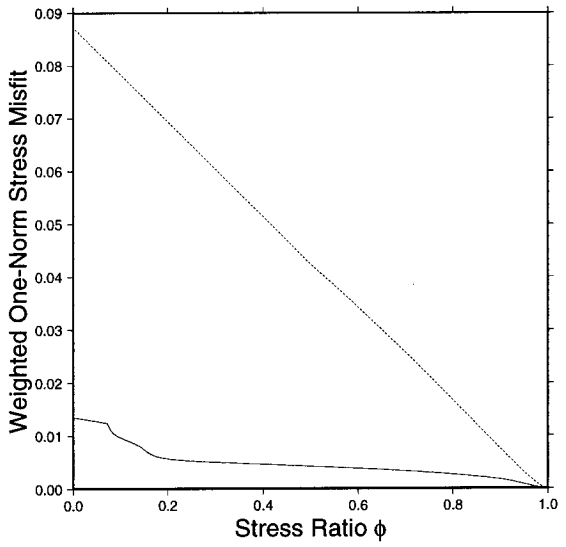

Figure 5.38: Stress inversion results in Cook Inlet, Alaska using all nonradial identified breakouts occurring in the D formation from wells drilled into the Middle Ground Shoals oil field from the Baker platform. Nonradial breakouts are those breakouts where the **IJK** breakout angle is at least 15° away from the high-side of the hole. Plotting conventions are the same as Figure 5.6.

Angular misfit inversion results using all Baker platform nonradial breakouts in the D formation.

Number of breakouts	7
Total length of breakouts	43.5 m
Optimized ϕ with 95% confidence limits	$0.995^{0.998}_{0.971}$
Minimum weighted one-norm stress misfit	1.27°
95% confidence level for weighted one-norm stress misfit	2.27°

	Azimuth	Deviation	Value
S_1	N96.5°E	82.8°	2
S_2	N5.0°E	78.1°	1.995
S_3	N217.0°E	13.9°	1

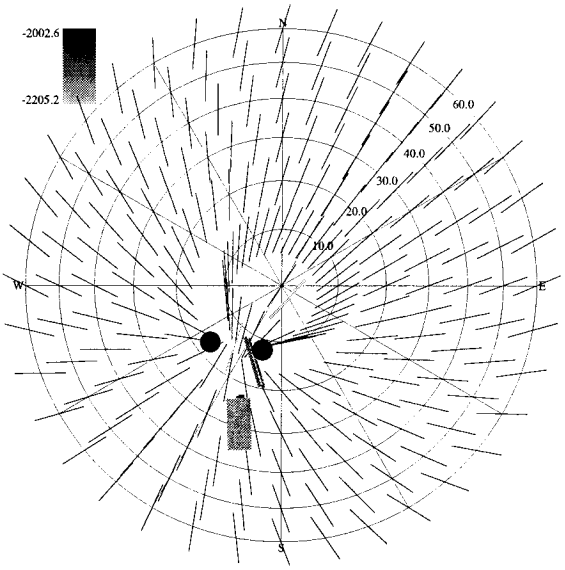

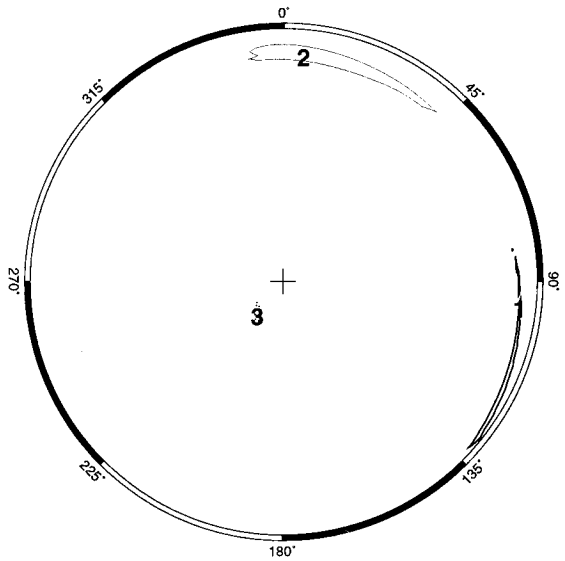

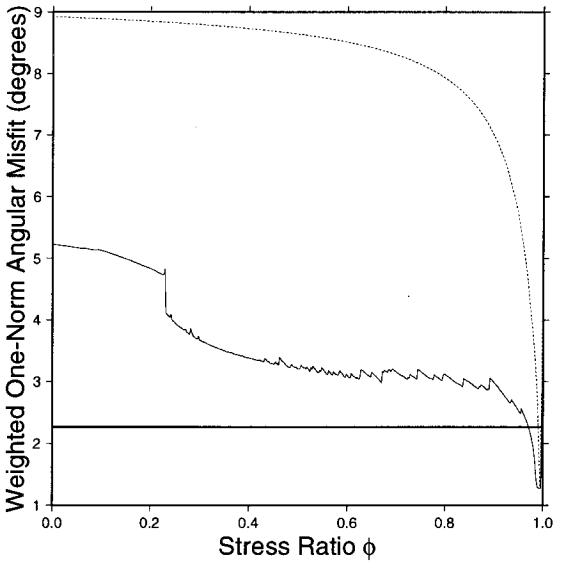

Figure 5.39: Stress inversion results in Cook Inlet, Alaska using all nonradial identified breakouts occurring in the D formation from wells drilled into the Middle Ground Shoals oil field from the Baker platform. Nonradial breakouts are those breakouts where the **IJK** breakout angle is at least 15° away from the high-side of the hole. Plotting conventions are the same as Figure 5.6.

Stress misfit inversion results using all Baker platform breakouts in the G3 and G4 formations.

Number of breakouts	12
Total length of breakouts	96.6 m
Optimized ϕ with 95% confidence limits	0.977 $^{1.000}_{0.951}$
Minimum weighted one-norm stress misfit	0.0106
95% confidence level for weighted one-norm stress misfit	0.0155

	Azimuth	Deviation	Value
S_1	N160.9°E	79.5°	2
S_2	N251.5°E	86.7°	1.977
S_3	N358.8°E	11.1°	1

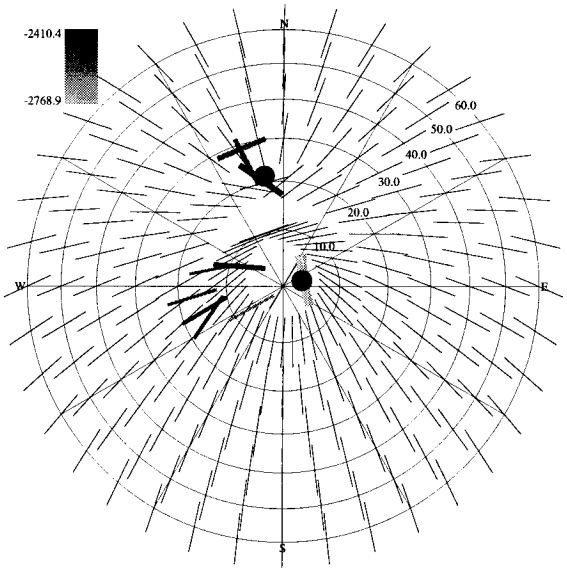

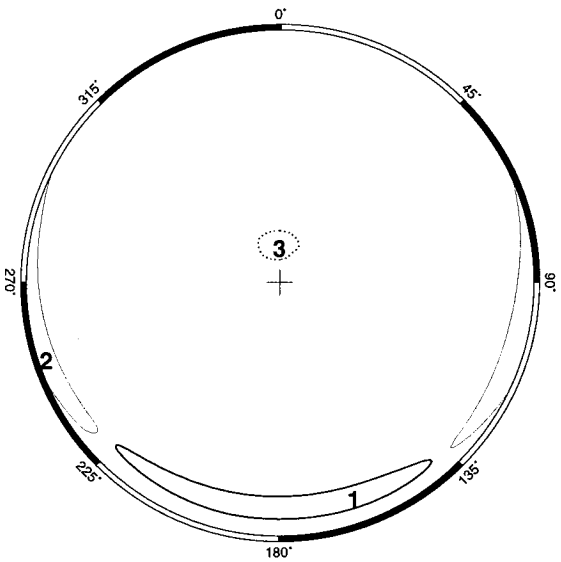

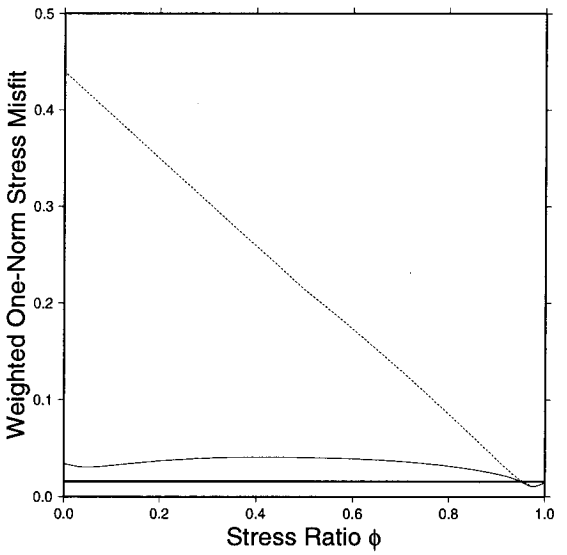

Figure 5.40: Stress inversion results in Cook Inlet, Alaska using all identified breakouts occurring in the G3 and G4 formations from wells drilled into the Middle Ground Shoals oil field from the Baker platform. Plotting conventions are the same as Figure 5.6.

Angular misfit inversion results using all Baker platform breakouts in the G3 and G4 formations.

Number of breakouts	12
Total length of breakouts	96.6 m
Optimized ϕ with 95% confidence limits	$0.803^{1.000}_{0.042}$
Minimum weighted one-norm stress misfit	13.74°
95% confidence level for weighted one-norm stress misfit	20.14°

	Azimuth	Deviation	Value
S_1	N245.0°E	61.9°	2
S_2	N153.0°E	86.3°	1.803
S_3	N56.2°E	28.4°	1

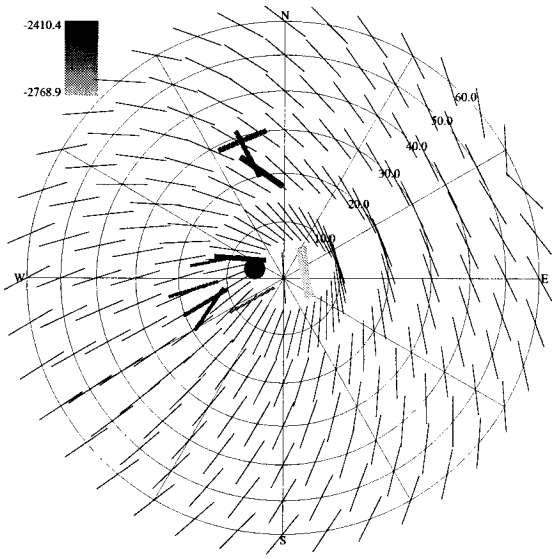

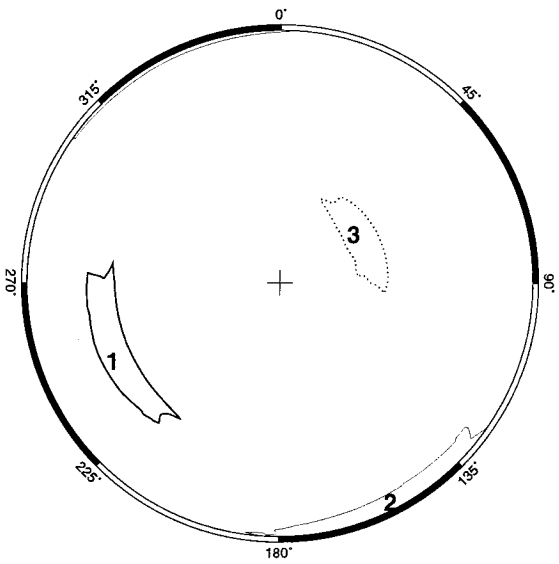

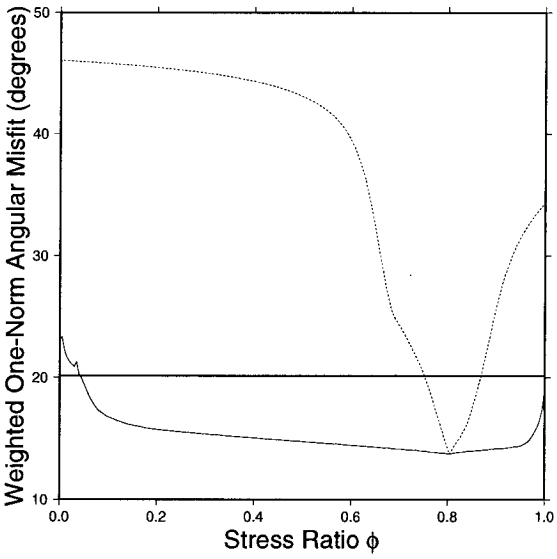

Figure 5.41: Stress inversion results in Cook Inlet, Alaska using all identified breakouts occurring in the G3 and G4 formations from wells drilled into the Middle Ground Shoals oil field from the Baker platform. Plotting conventions are the same as Figure 5.6.

Stress misfit inversion results using all Baker platform nonradial breakouts in the G3 and G4 formations.

Number of breakouts	8
Total length of breakouts	67.1 m
Optimized ϕ with 95% confidence limits	0.972 $^{1.000}_{0.897}$
Minimum weighted one-norm stress misfit	0.0112
95% confidence level for weighted one-norm stress misfit	0.0187

	Azimuth	Deviation	Value
S_1	N165.6°E	75.6°	2
S_2	N256.2°E	87.8°	1.972
S_3	N354.5°E	14.6°	1

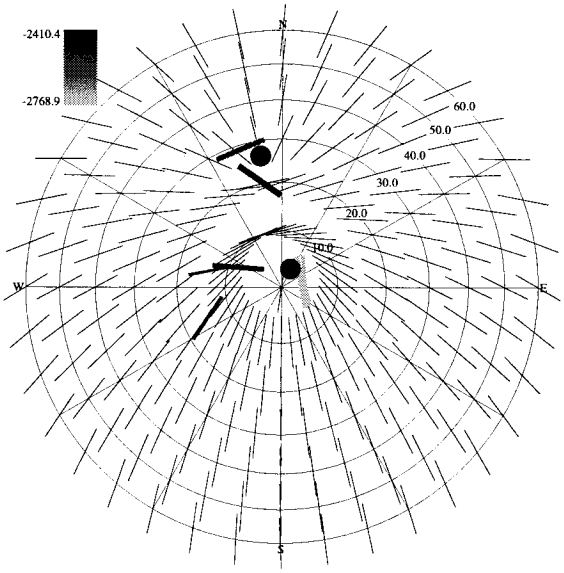

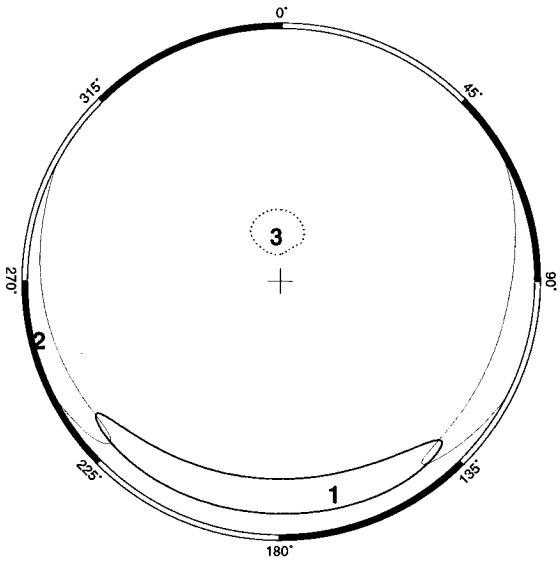

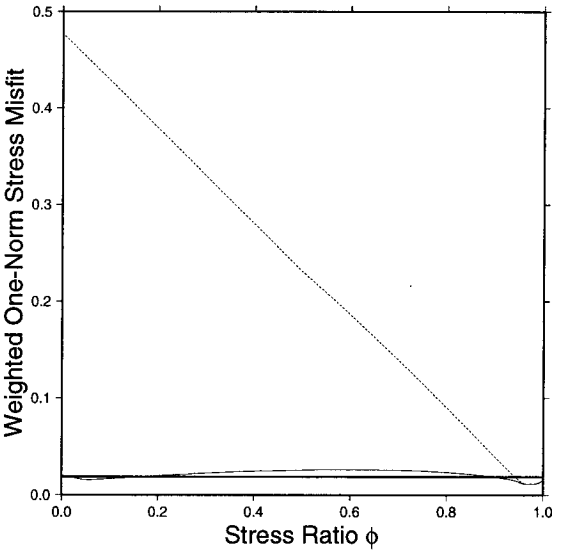

Figure 5.42: Stress inversion results in Cook Inlet, Alaska using all nonradial identified breakouts occurring in the G3 and G4 formations from wells drilled into the Middle Ground Shoals oil field from the Baker platform. Nonradial breakouts are those breakouts where the **IJK** breakout angle is at least 15° away from the high-side of the hole. Plotting conventions are the same as Figure 5.6.

Angular misfit inversion results using all Baker platform nonradial breakouts in the G3 and G4 formations.

Number of breakouts	8
Total length of breakouts	67.1 m
Optimized ϕ with 95% confidence limits	$0.044^{0.981}_{0.000}$
Minimum weighted one-norm stress misfit	10.81°
95% confidence level for weighted one-norm stress misfit	18.09°

	Azimuth	Deviation	Value
S_1	N250.0°E	11.4°	2
S_2	N139.3°E	85.7°	1.044
S_3	N48.5°E	79.4°	1

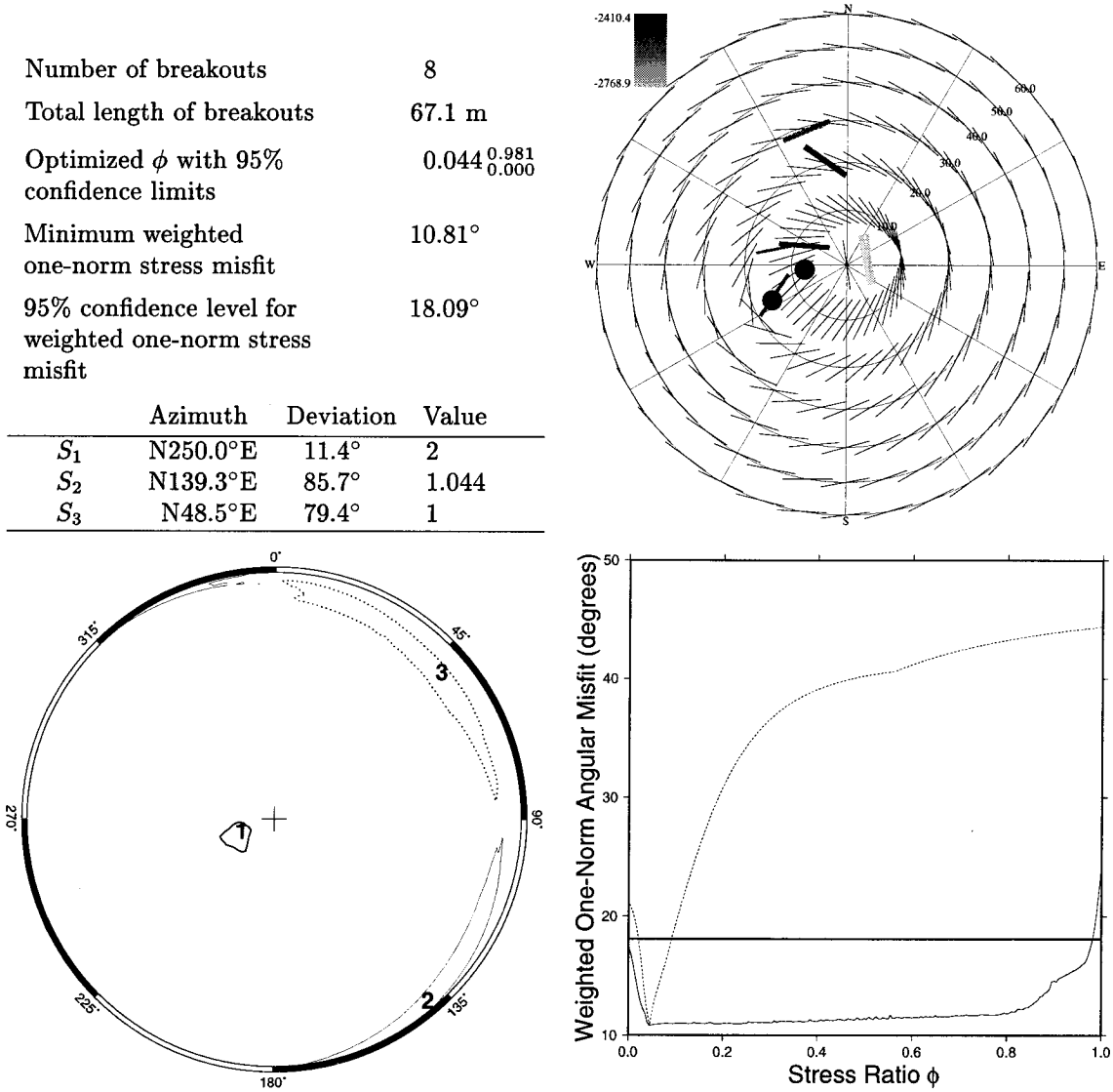

Figure 5.43: Stress inversion results in Cook Inlet, Alaska using all nonradial identified breakouts occurring in the G3 and G4 formations from wells drilled into the Middle Ground Shoals oil field from the Baker platform. Nonradial breakouts are those breakouts where the **IJK** breakout angle is at least 15° away from the high-side of the hole. Plotting conventions are the same as Figure 5.6.

Stress misfit inversion results using all Baker platform nonradial breakouts between 1,000–1,500 m TVD.

Number of breakouts	16
Total length of breakouts	124.7 m
Optimized ϕ with 95% confidence limits	$0.999^{1.000}_{0.992}$
Minimum weighted one-norm stress misfit	$3.21\text{x}10^{-3}$
95% confidence level for weighted one-norm stress misfit	$4.42\text{x}10^{-3}$

	Azimuth	Deviation	Value
S_1	N310.5°E	85.1°	2
S_2	N41.1°E	83.6°	1.999
S_3	N183.1°E	8.1°	1

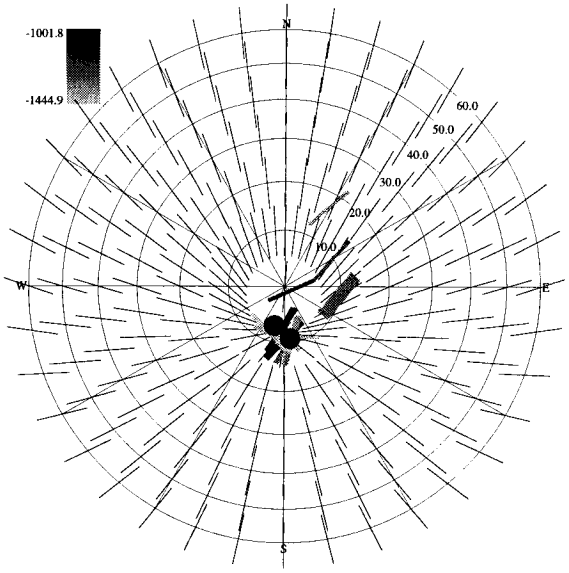

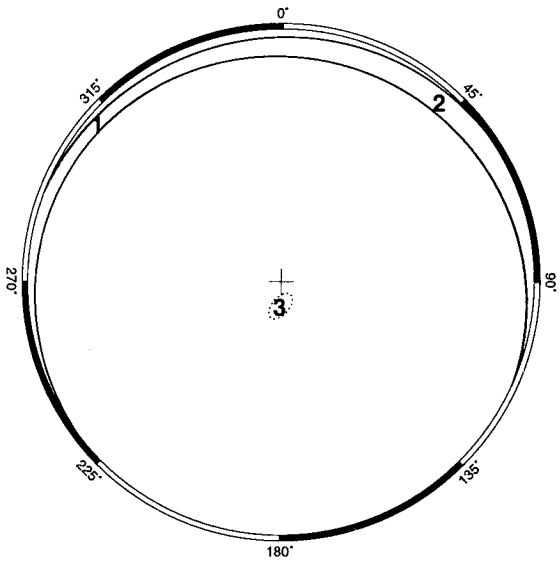

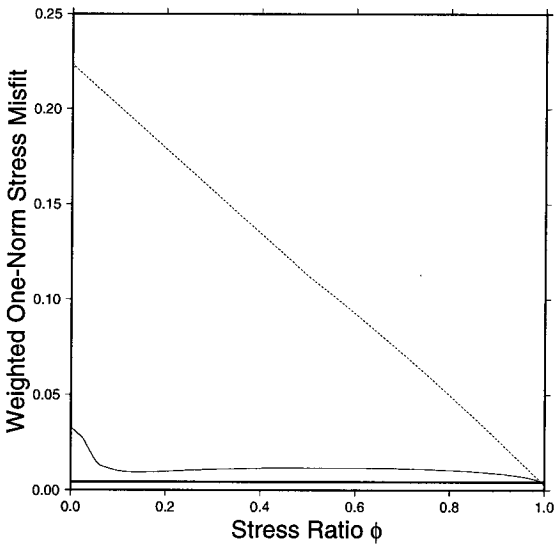

Figure 5.44: Stress inversion results in Cook Inlet, Alaska using all nonradial identified breakouts between 1,000 and 1,500 m TVD from wells drilled from the Baker platform in the Middle Ground Shoals oil field. Nonradial breakouts are those breakouts where the **IJK** breakout angle is at least 15° away from the high-side of the hole. Plotting conventions are the same as Figure 5.6.

Angular misfit inversion results using all Baker platform nonradial breakouts between 1,000–1,500 m TVD.

Number of breakouts	16
Total length of breakouts	124.7 m
Optimized ϕ with 95% confidence limits	$0.990^{1.000}_{0.000}$
Minimum weighted one-norm stress misfit	18.32°
95% confidence level for weighted one-norm stress misfit	25.21°

	Azimuth	Deviation	Value
S_1	N346.5°E	74.4°	2
S_2	N77.4°E	86.8°	1.990
S_3	N178.8°E	15.9°	1

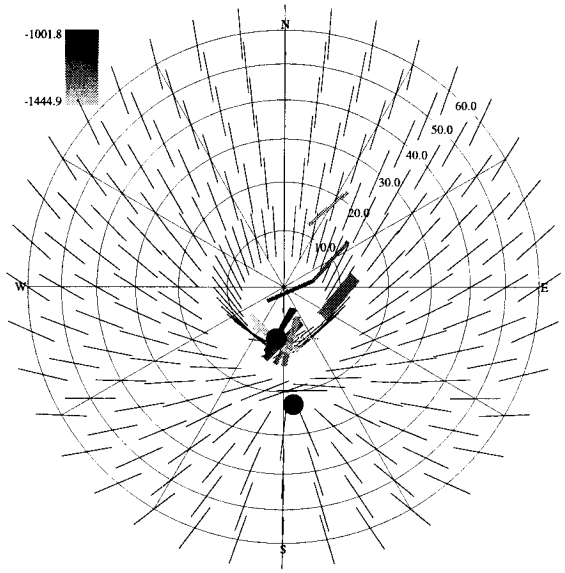

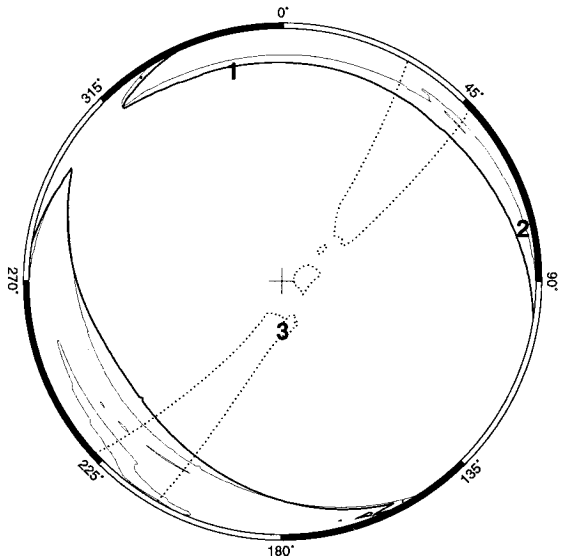

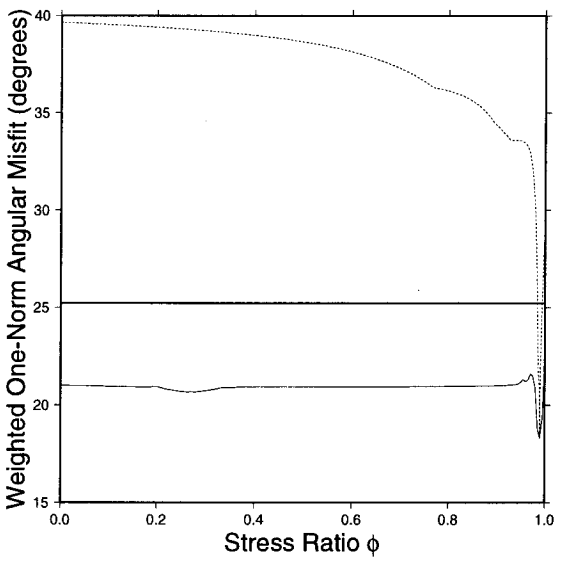

Figure 5.45: Stress inversion results in Cook Inlet, Alaska using all nonradial identified breakouts between 1,000 and 1,500 m TVD from wells drilled from the Baker platform in the Middle Ground Shoals oil field. Nonradial breakouts are those breakouts where the **IJK** breakout angle is at least 15° away from the high-side of the hole. Plotting conventions are the same as Figure 5.6.

Stress misfit inversion results using all Baker platform nonradial breakouts between 1,500–2,000 m TVD.

Number of breakouts	17
Total length of breakouts	102.3 m
Optimized ϕ with 95% confidence limits	$0.943\ ^{0.979}_{0.872}$
Minimum weighted one-norm stress misfit	0.0112
95% confidence level for weighted one-norm stress misfit	0.0152

	Azimuth	Deviation	Value
S_1	N175.3°E	81.3°	2
S_2	N85.0°E	87.7°	1.943
S_3	N340.4°E	9.0°	1

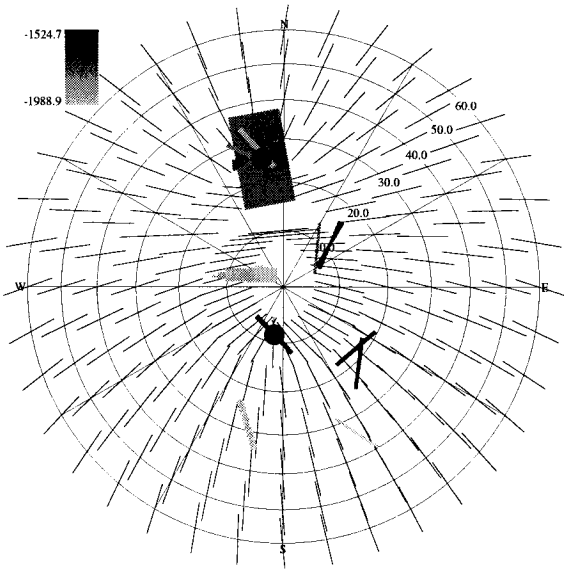

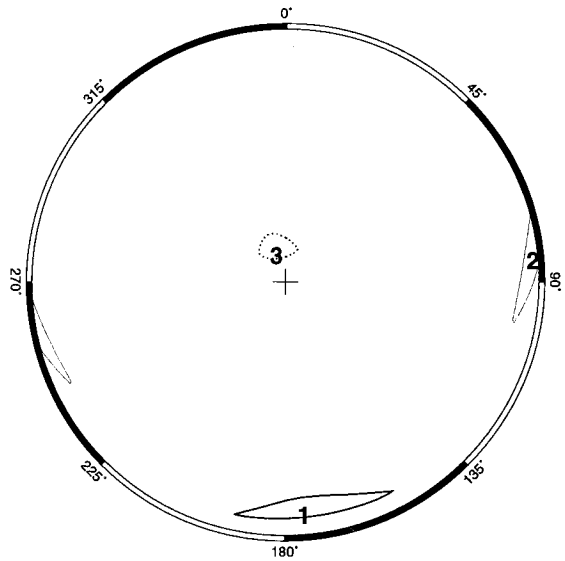

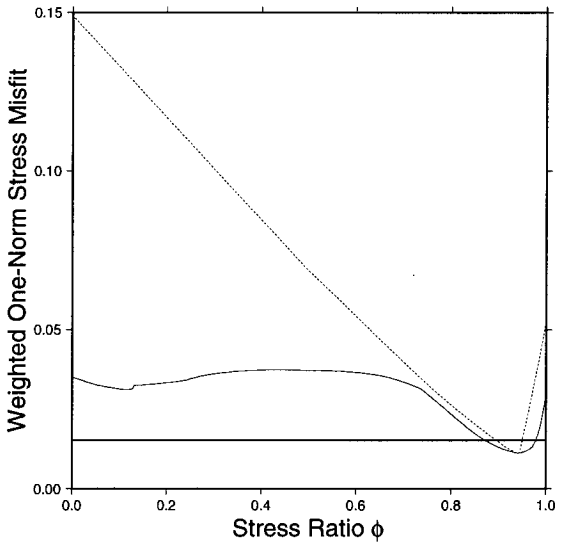

Figure 5.46: Stress inversion results in Cook Inlet, Alaska using all nonradial identified breakouts between 1,500 and 2,000 m TVD from wells drilled from the Baker platform in the Middle Ground Shoals oil field. Nonradial breakouts are those breakouts where the **IJK** breakout angle is at least 15° away from the high-side of the hole. Plotting conventions are the same as Figure 5.6.

Angular misfit inversion results using all Baker platform nonradial breakouts between 1,500–2,000 m TVD.

Number of breakouts	17
Total length of breakouts	102.3 m
Optimized ϕ with 95% confidence limits	$0.935^{0.968}_{0.290}$
Minimum weighted one-norm stress misfit	8.98°
95% confidence level for weighted one-norm stress misfit	12.22°

	Azimuth	Deviation	Value
S_1	N179.4°E	80.1°	2
S_2	N88.5°E	84.9°	1.935
S_3	N331.5°E	11.2°	1

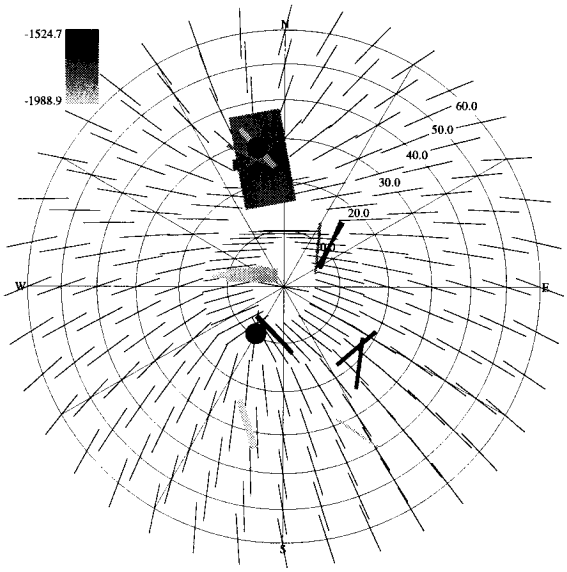

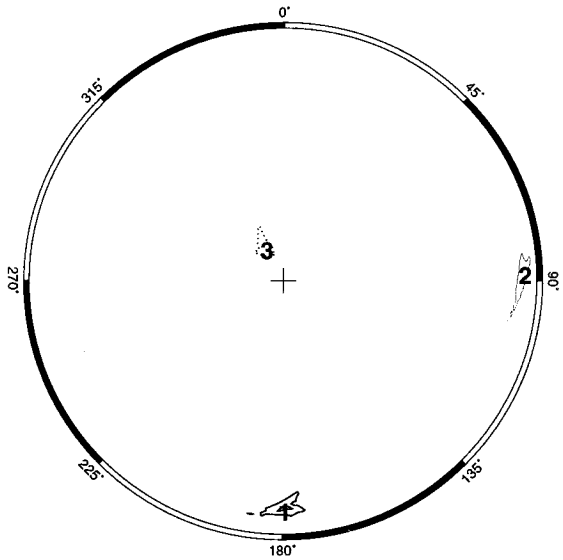

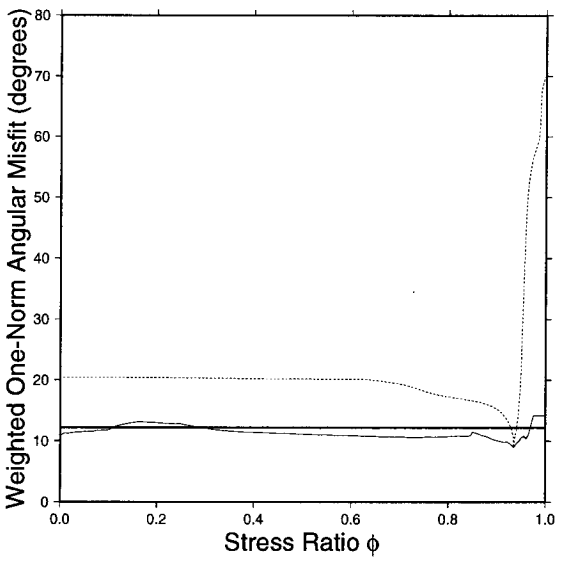

Figure 5.47: Stress inversion results in Cook Inlet, Alaska using all nonradial identified breakouts between 1,500 and 2,000 m TVD from wells drilled from the Baker platform in the Middle Ground Shoals oil field. Nonradial breakouts are those breakouts where the **IJK** breakout angle is at least 15° away from the high-side of the hole. Plotting conventions are the same as Figure 5.6.

Stress misfit inversion results using all Baker platform nonradial breakouts between 2,000–2,500 m TVD.

Number of breakouts	28
Total length of breakouts	199.8 m
Optimized ϕ with 95% confidence limits	$0.310\ ^{0.381}_{0.228}$
Minimum weighted one-norm stress misfit	0.0160
95% confidence level for weighted one-norm stress misfit	0.0202

	Azimuth	Deviation	Value
S_1	N171.6°E	27.8°	2
S_2	N80.8°E	89.5°	1.310
S_3	N350.5°E	62.2°	1

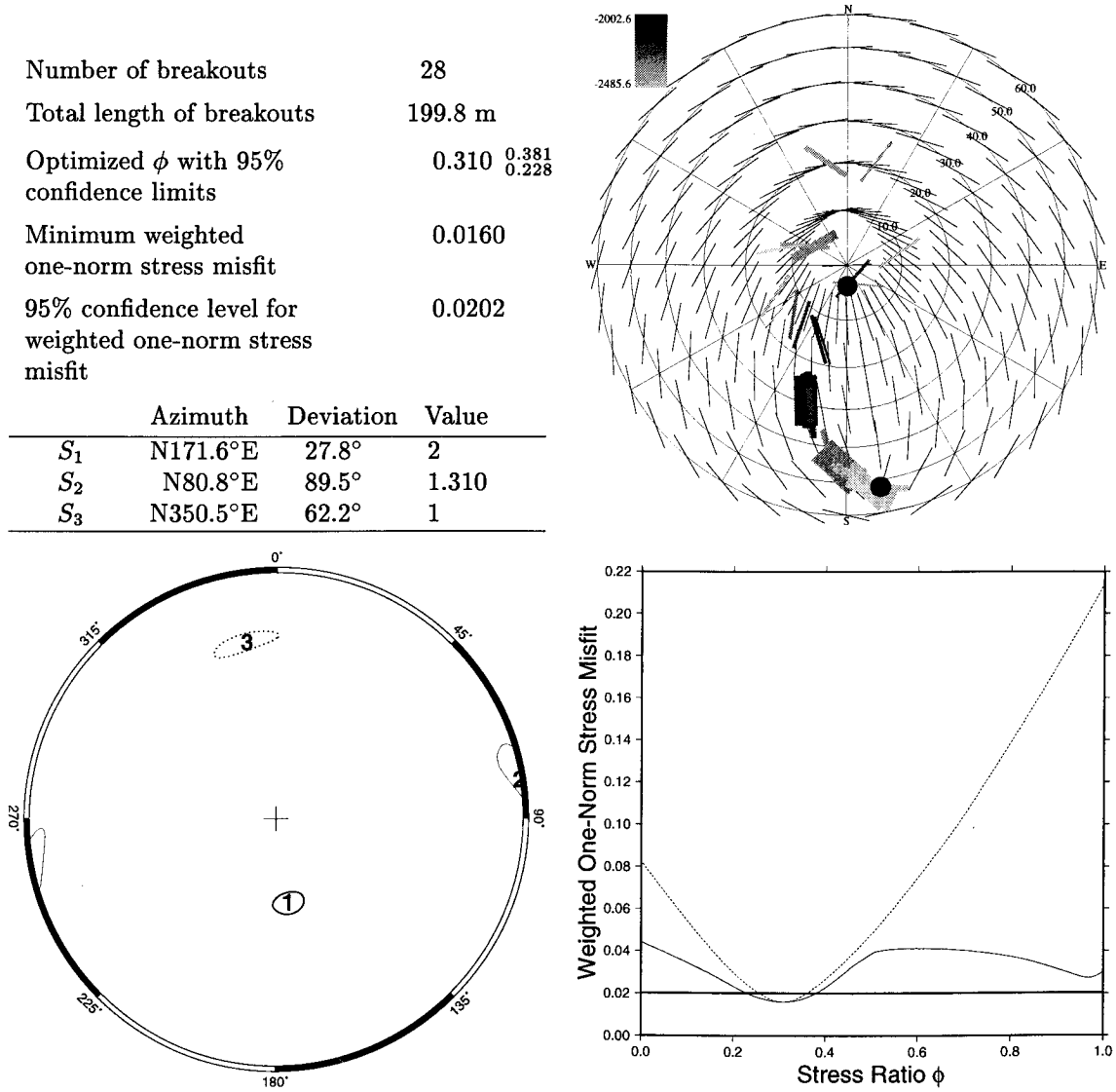

Figure 5.48: Stress inversion results in Cook Inlet, Alaska using all nonradial identified breakouts between 2,000 and 2,500 m TVD from wells drilled from the Baker platform in the Middle Ground Shoals oil field. Nonradial breakouts are those breakouts where the **IJK** breakout angle is at least 15° away from the high-side of the hole. Plotting conventions are the same as Figure 5.6.

Angular misfit inversion results using all Baker platform nonradial breakouts between 2,000–2,500 m TVD.

Number of breakouts	28
Total length of breakouts	199.8 m
Optimized ϕ with 95% confidence limits	$0.268^{0.949}_{0.000}$
Minimum weighted one-norm stress misfit	12.38°
95% confidence level for weighted one-norm stress misfit	15.63°

	Azimuth	Deviation	Value
S_1	N168.1°E	30.0°	2
S_2	N262.3°E	87.6°	1.268
S_3	N353.7°E	60.1°	1

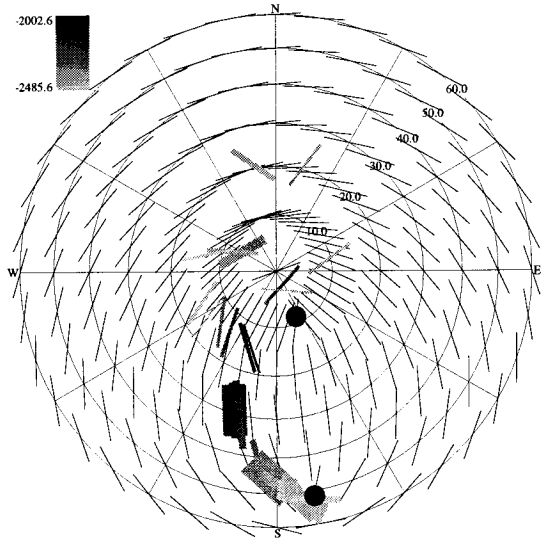

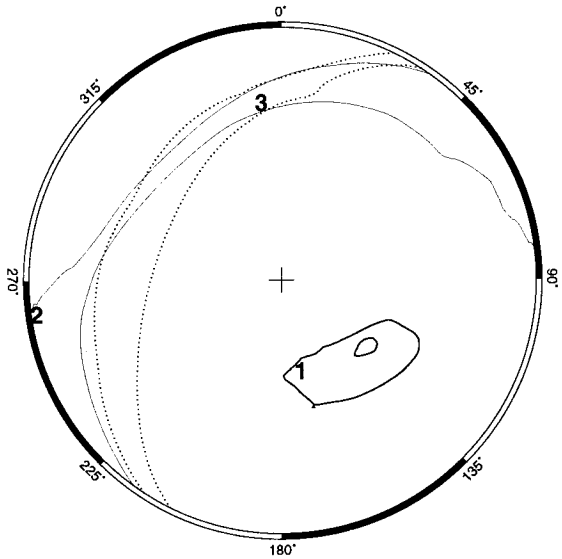

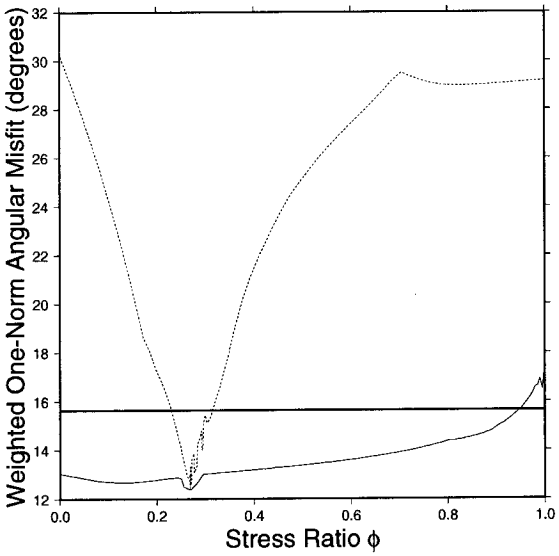

Figure 5.49: Stress inversion results in Cook Inlet, Alaska using all nonradial identified breakouts between 2,000 and 2,500 m TVD from wells drilled from the Baker platform in the Middle Ground Shoals oil field. Nonradial breakouts are those breakouts where the **IJK** breakout angle is at least 15° away from the high-side of the hole. Plotting conventions are the same as Figure 5.6.

Stress misfit inversion results using all Baker platform nonradial breakouts between 2,500–3,000 m TVD.

Number of breakouts	8
Total length of breakouts	70.1 m
Optimized ϕ with 95% confidence limits	$0.957^{0.977}_{0.917}$
Minimum weighted one-norm stress misfit	0.0079
95% confidence level for weighted one-norm stress misfit	0.0132

	Azimuth	Deviation	Value
S_1	N154.5°E	76.0°	2
S_2	N245.5°E	85.9°	1.957
S_3	N351.6°E	14.6°	1

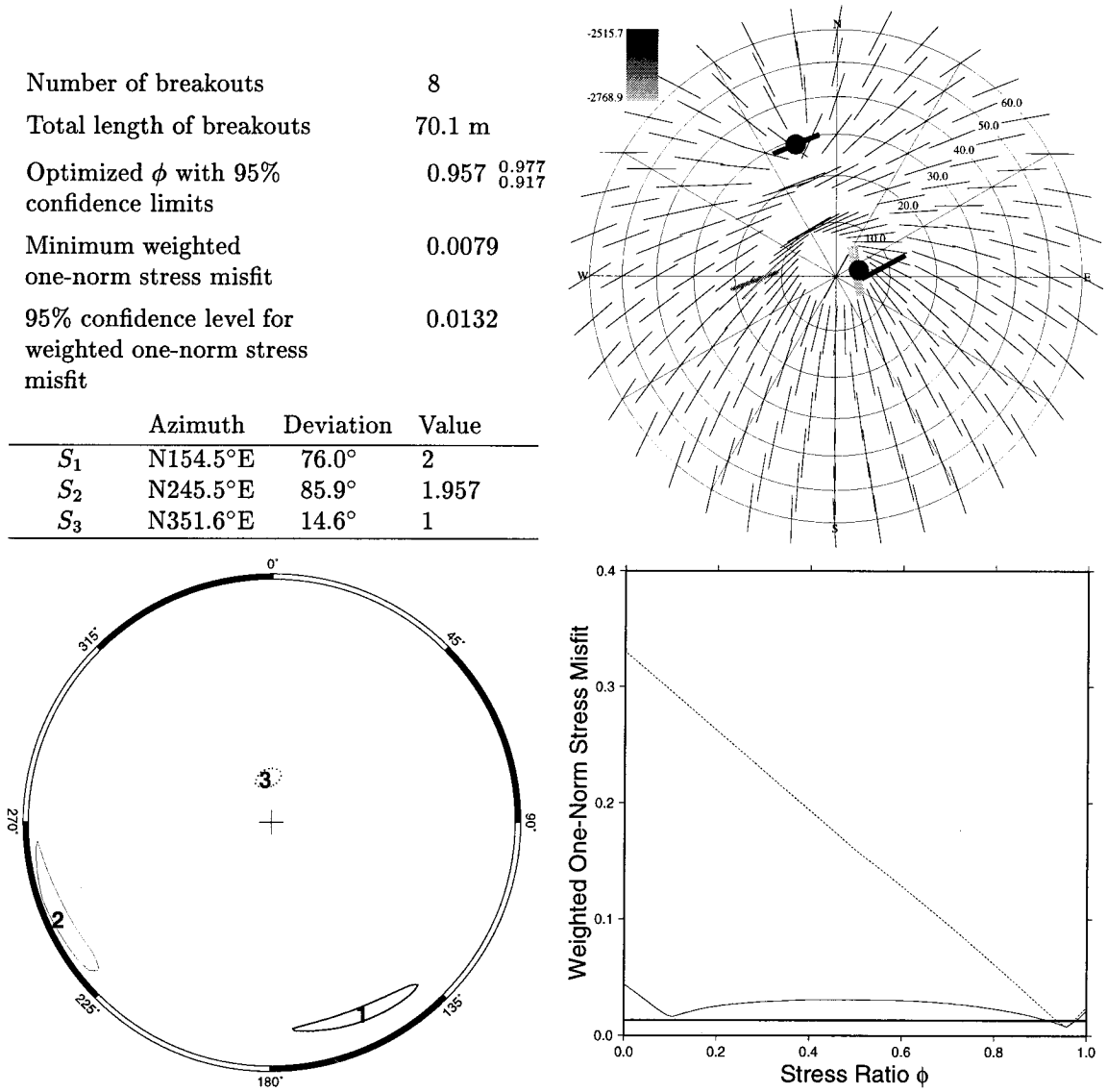

Figure 5.50: Stress inversion results in Cook Inlet, Alaska using all nonradial identified breakouts between 2,500 and 3,000 m TVD from wells drilled from the Baker platform in the Middle Ground Shoals oil field. Nonradial breakouts are those breakouts where the **IJK** breakout angle is at least 15° away from the high-side of the hole. Plotting conventions are the same as Figure 5.6.

Angular misfit inversion results using all Baker platform nonradial breakouts between 2,500–3,000 m TVD.

Number of breakouts	8
Total length of breakouts	70.1 m
Optimized ϕ with 95% confidence limits	$0.960^{1.000}_{0.000}$
Minimum weighted one-norm stress misfit	18.08°
95% confidence level for weighted one-norm stress misfit	30.25°

	Azimuth	Deviation	Value
S_1	N154.2°E	75.4°	2
S_2	N245.3°E	85.8°	1.960
S_3	N351.1°E	15.2°	1

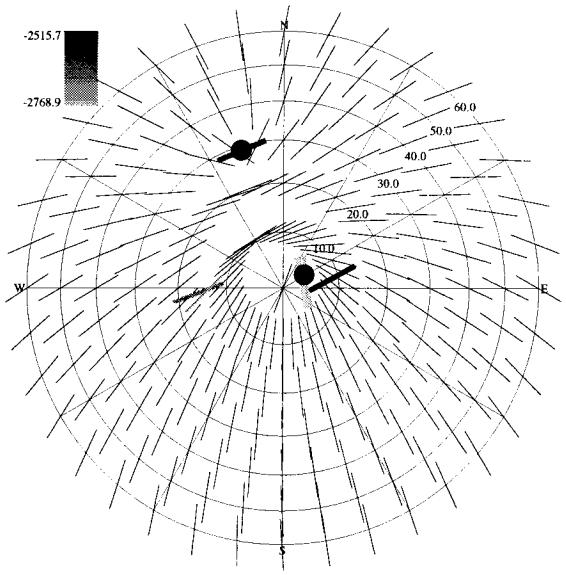

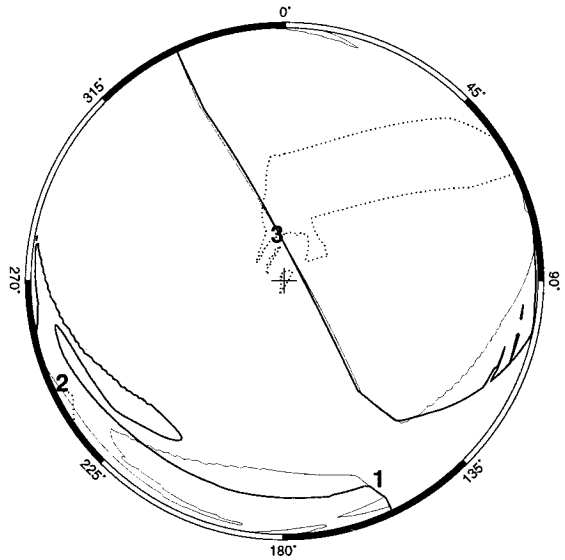

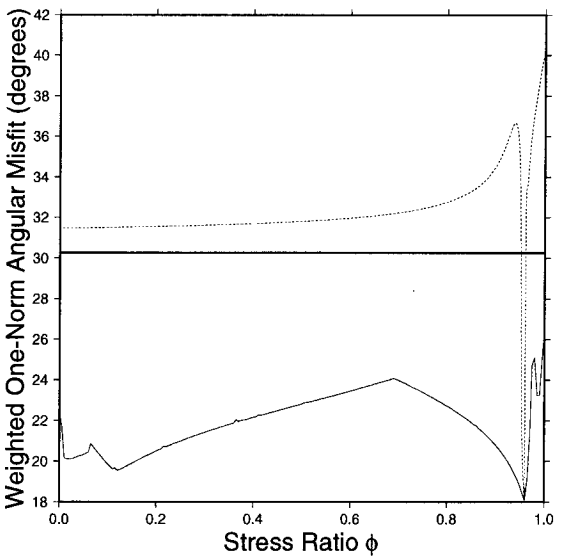

Figure 5.51: Stress inversion results in Cook Inlet, Alaska using all nonradial identified breakouts between 2,500 and 3,000 m TVD from wells drilled from the Baker platform in the Middle Ground Shoals oil field. Nonradial breakouts are those breakouts where the **IJK** breakout angle is at least 15° away from the high-side of the hole. Plotting conventions are the same as Figure 5.6.

Stress misfit inversion results using all Dillon platform breakouts excluding breakouts from well Smgs6.

Number of breakouts	64
Total length of breakouts	349.0 m
Optimized ϕ with 95% confidence limits	$0.966\ ^{0.995}_{0.956}$
Minimum weighted one-norm stress misfit	0.0123
95% confidence level for weighted one-norm stress misfit	0.0143

	Azimuth	Deviation	Value
S_1	N287.7°E	89.7°	2
S_2	N17.8°E	71.3°	1.966
S_3	N196.7°E	18.7°	1

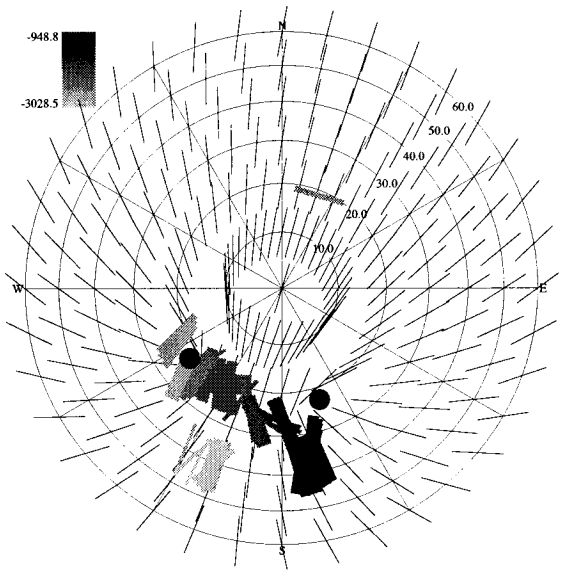

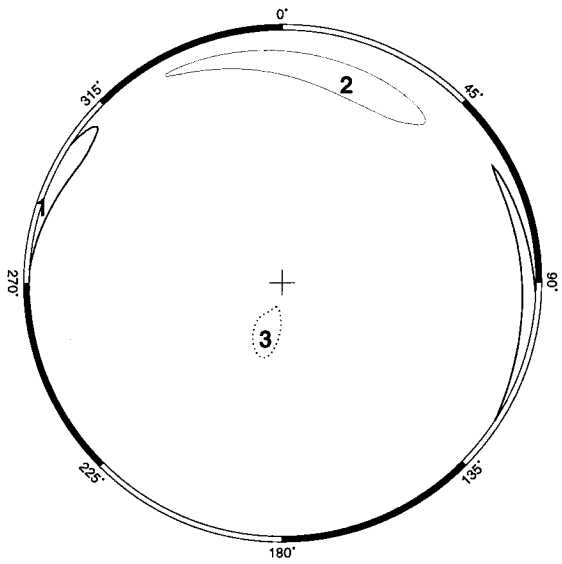

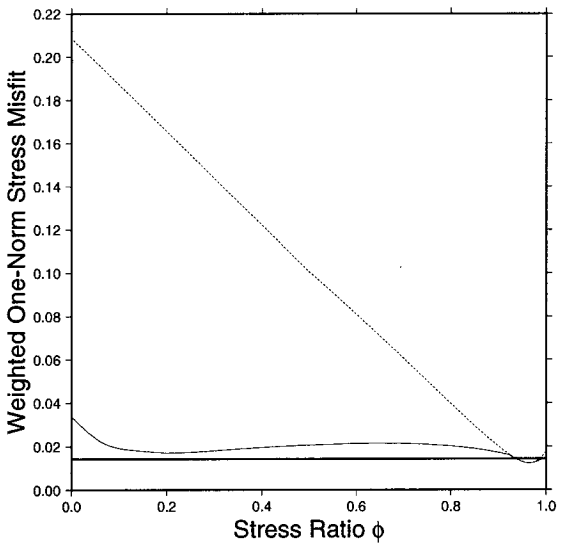

Figure 5.52: Stress inversion results in Cook Inlet, Alaska using all identified breakouts from wells drilled from the Dillon platform in the Middle Ground Shoals oil field excluding the breakouts from well Smgs6. Plotting conventions are the same as Figure 5.6.

Angular misfit inversion results using all Dillon platform breakouts excluding breakouts from well Smgs6.

Number of breakouts	64
Total length of breakouts	349.0 m
Optimized ϕ with 95% confidence limits	$0.581^{1.000}_{0.177}$
Minimum weighted one-norm stress misfit	14.42°
95% confidence level for weighted one-norm stress misfit	16.78°

	Azimuth	Deviation	Value
S_1	N186.8°E	57.0°	2
S_2	N91.2°E	81.5°	1.581
S_3	N348.6°E	34.4°	1

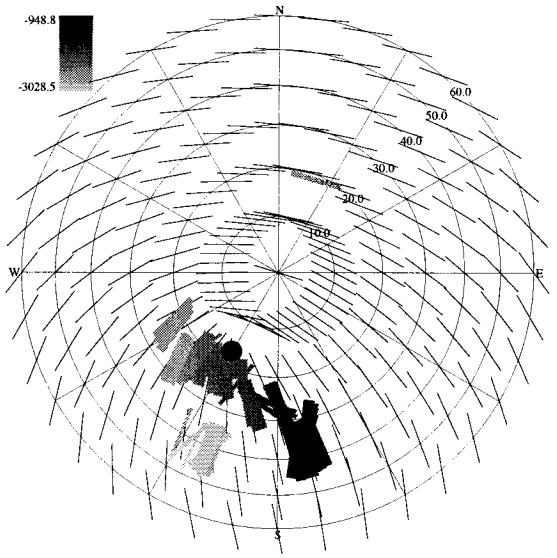

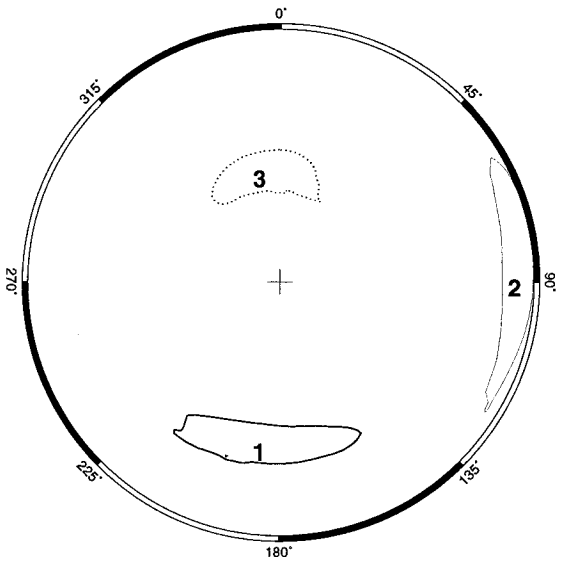

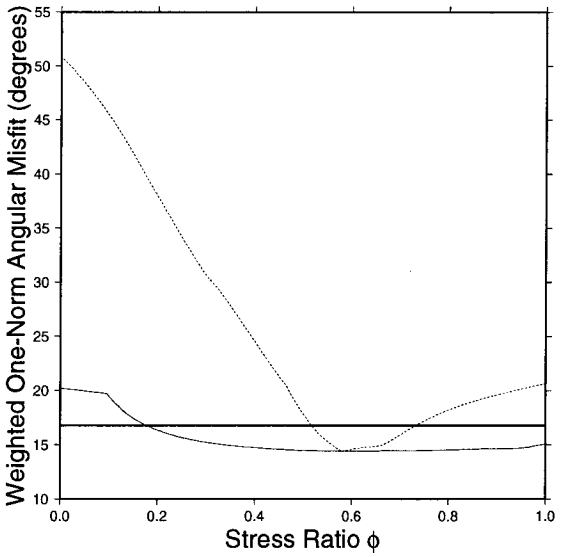

Figure 5.53: Stress inversion results in Cook Inlet, Alaska using all identified breakouts from wells drilled from the Dillon platform in the Middle Ground Shoals oil field excluding the breakouts from well Smgs6. Plotting conventions are the same as Figure 5.6.

Stress misfit inversion results using all Dillon platform nonradial breakouts excluding breakouts from well Smgs6.

Number of breakouts	36
Total length of breakouts	187.9 m
Optimized ϕ with 95% confidence limits	$0.104\ ^{0.198}_{0.046}$
Minimum weighted one-norm stress misfit	0.0152
95% confidence level for weighted one-norm stress misfit	0.0174

	Azimuth	Deviation	Value
S_1	N191.9°E	28.7°	2
S_2	N68.7°E	73.3°	1.104
S_3	N331.5°E	67.4°	1

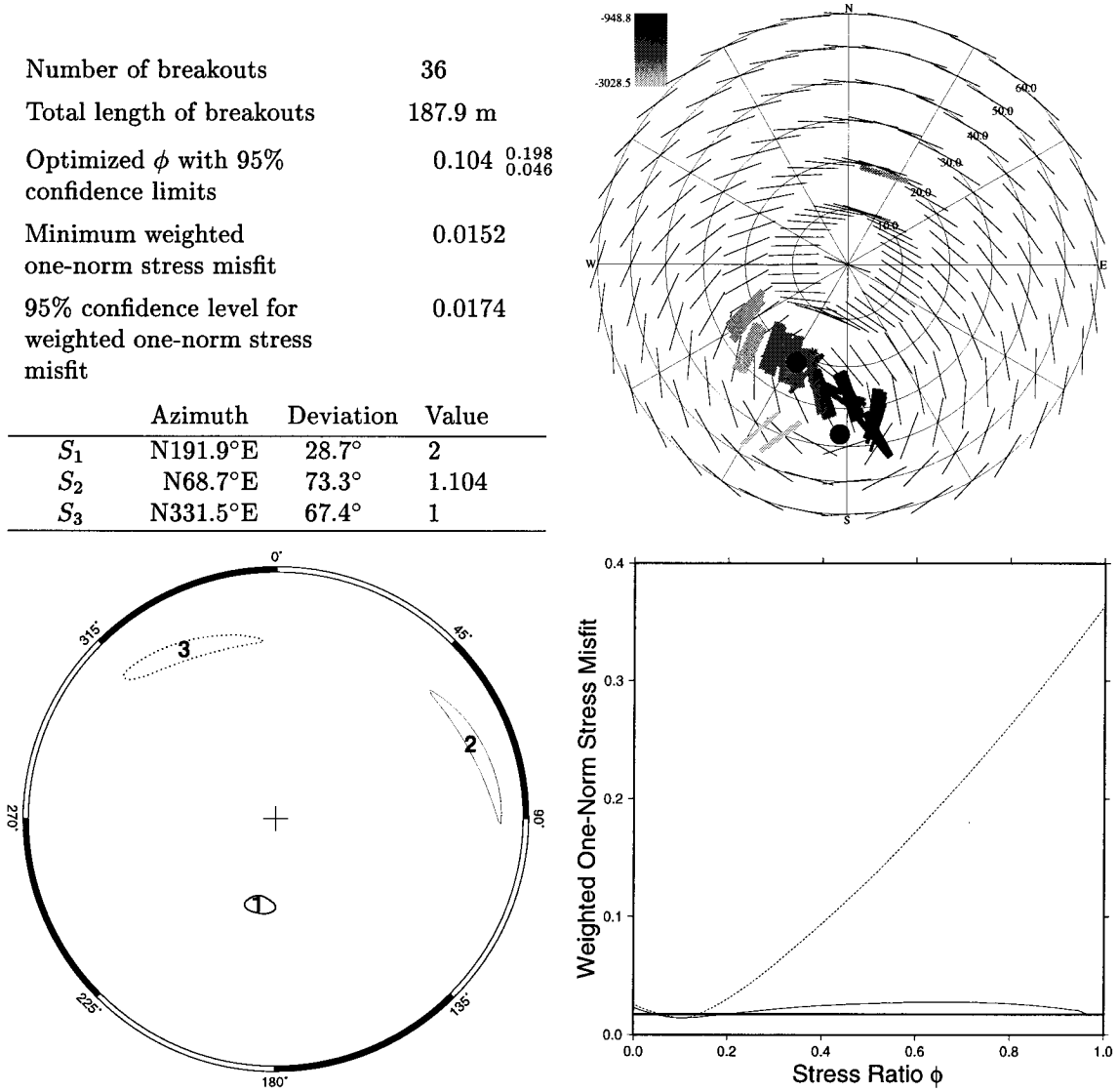

Figure 5.54: Stress inversion results in Cook Inlet, Alaska using all nonradial identified breakouts from wells drilled from the Dillon platform in the Middle Ground Shoals oil field excluding the breakouts from well Smgs6. Nonradial breakouts are those breakouts where the **IJK** breakout angle is at least 15° away from the high-side of the hole. Plotting conventions are the same as Figure 5.6.

Angular misfit inversion results using all Dillon platform nonradial breakouts excluding breakouts from well Smgs6.

Number of breakouts	36
Total length of breakouts	187.9 m
Optimized ϕ with 95% confidence limits	$0.668^{1.000}_{0.029}$
Minimum weighted one-norm stress misfit	17.21°
95% confidence level for weighted one-norm stress misfit	21.11°

	Azimuth	Deviation	Value
S_1	N180.0°E	58.0°	2
S_2	N84.0°E	80.4°	1.668
S_3	N339.4°E	33.7°	1

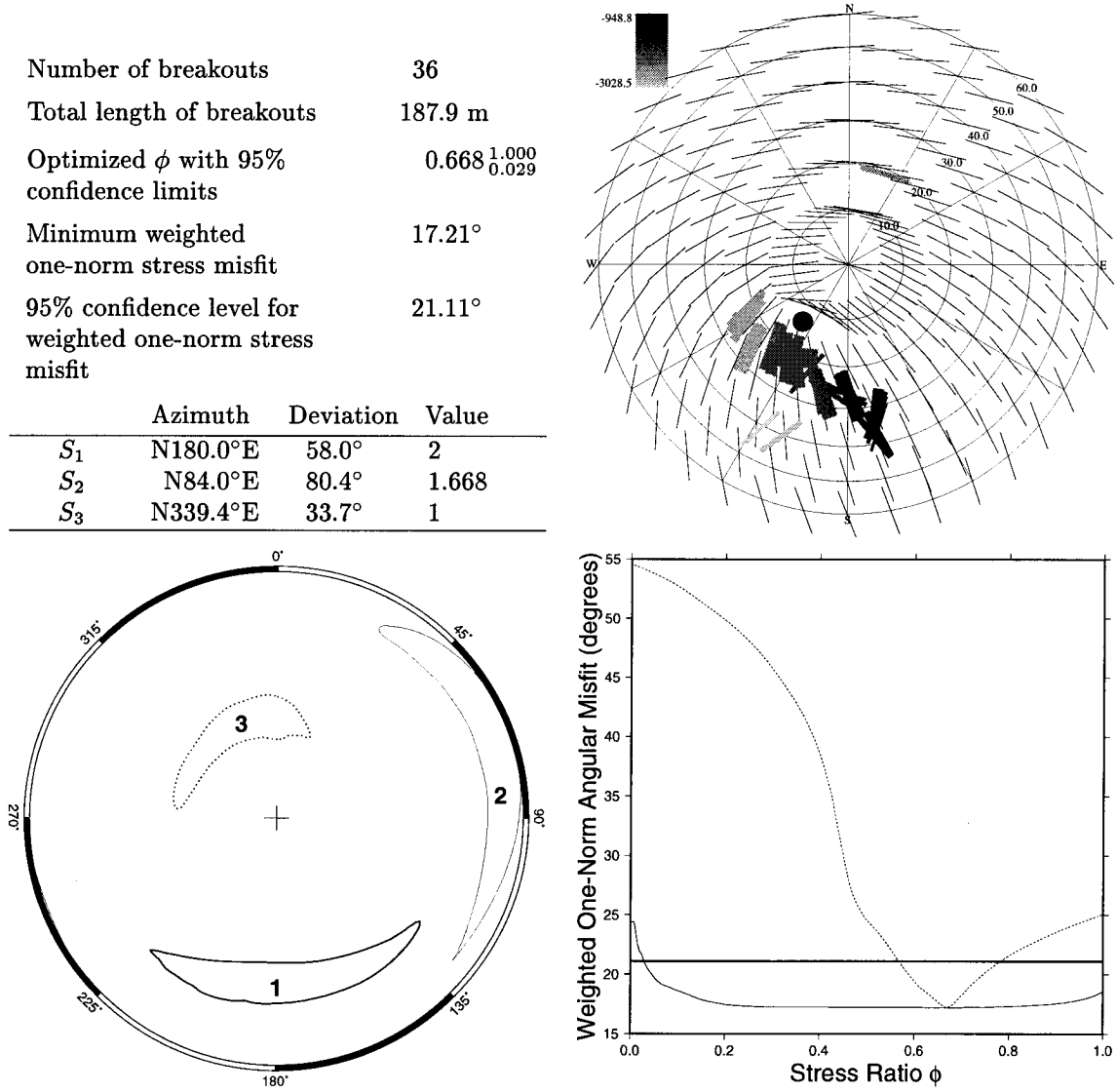

Figure 5.55: Stress inversion results in Cook Inlet, Alaska using all nonradial identified breakouts from wells drilled from the Dillon platform in the Middle Ground Shoals oil field excluding the breakouts from well Smgs6. Nonradial breakouts are those breakouts where the **IJK** breakout angle is at least 15° away from the high-side of the hole. Plotting conventions are the same as Figure 5.6.

Stress misfit inversion results using all Dillon platform breakouts excluding breakouts from wells Smgs6 and Smgs8.

Number of breakouts	63
Total length of breakouts	344.5 m
Optimized ϕ with 95% confidence limits	$0.964\ ^{0.983}_{0.939}$
Minimum weighted one-norm stress misfit	0.0087
95% confidence level for weighted one-norm stress misfit	0.0102

	Azimuth	Deviation	Value
S_1	N290.6°E	88.3°	2
S_2	N21.3°E	69.3°	1.964
S_3	N196.0°E	20.8°	1

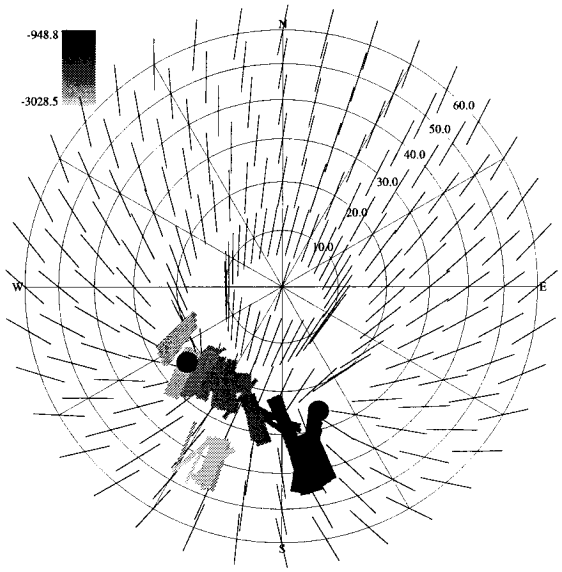

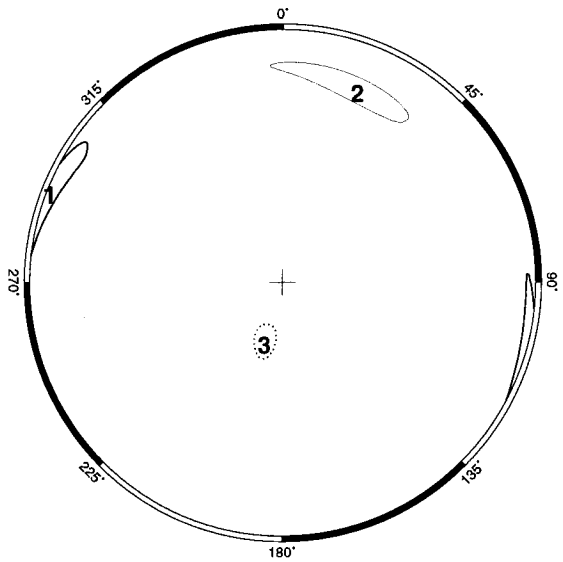

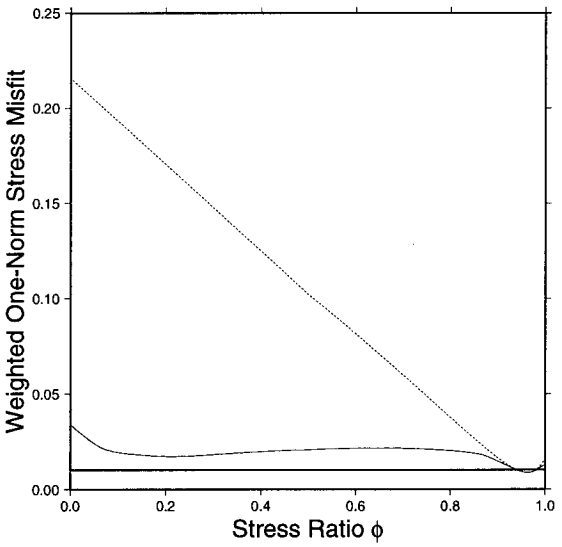

Figure 5.56: Stress inversion results in Cook Inlet, Alaska using all identified breakouts from wells drilled from the Dillon platform in the Middle Ground Shoals oil field excluding the breakouts from wells Smgs6 and Smgs8. Plotting conventions are the same as Figure 5.6.

Angular misfit inversion results using all Dillon platform breakouts excluding breakouts from wells Smgs6 and Smgs8.

Number of breakouts	63
Total length of breakouts	344.5 m
Optimized ϕ with 95% confidence limits	$0.580^{1.000}_{0.175}$
Minimum weighted one-norm stress misfit	14.42°
95% confidence level for weighted one-norm stress misfit	16.78°

	Azimuth	Deviation	Value
S_1	N186.8°E	56.9°	2
S_2	N91.2°E	81.5°	1.580
S_3	N348.7°E	34.4°	1

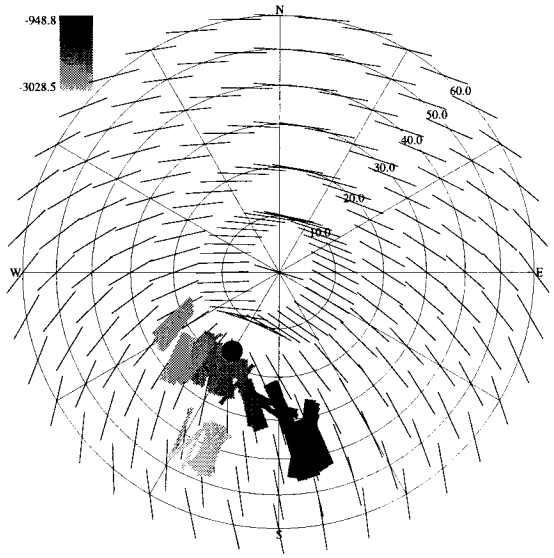

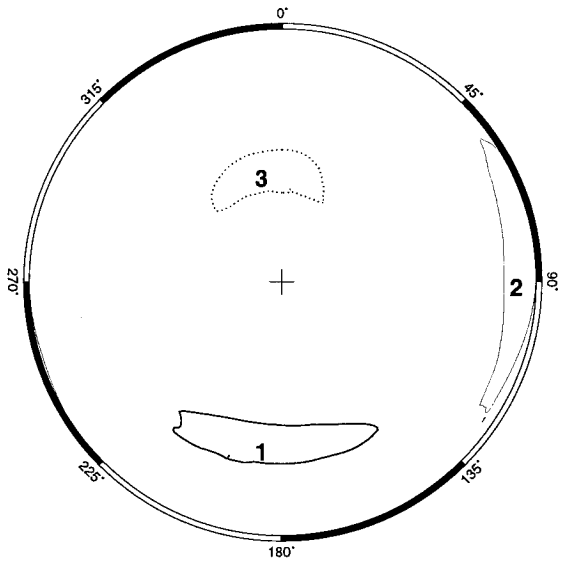

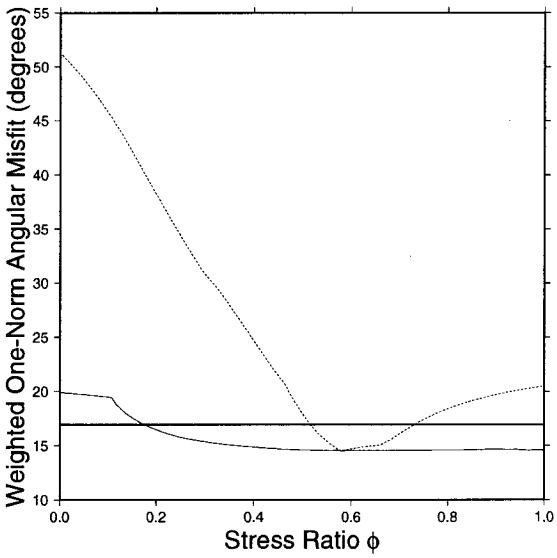

Figure 5.57: Stress inversion results in Cook Inlet, Alaska using all identified breakouts from wells drilled from the Dillon platform in the Middle Ground Shoals oil field excluding the breakouts from wells Smgs6 and Smgs8. Plotting conventions are the same as Figure 5.6.

Stress misfit inversion results using all Dillon platform nonradial breakouts excluding breakouts from wells Smgs6 and Smgs8.

Number of breakouts	35
Total length of breakouts	183.4 m
Optimized ϕ with 95% confidence limits	$0.976\ ^{0.997}_{0.954}$
Minimum weighted one-norm stress misfit	0.0104
95% confidence level for weighted one-norm stress misfit	0.0128

	Azimuth	Deviation	Value
S_1	N116.6°E	89.8°	2
S_2	N26.5°E	68.7°	1.976
S_3	N207.2°E	21.3°	1

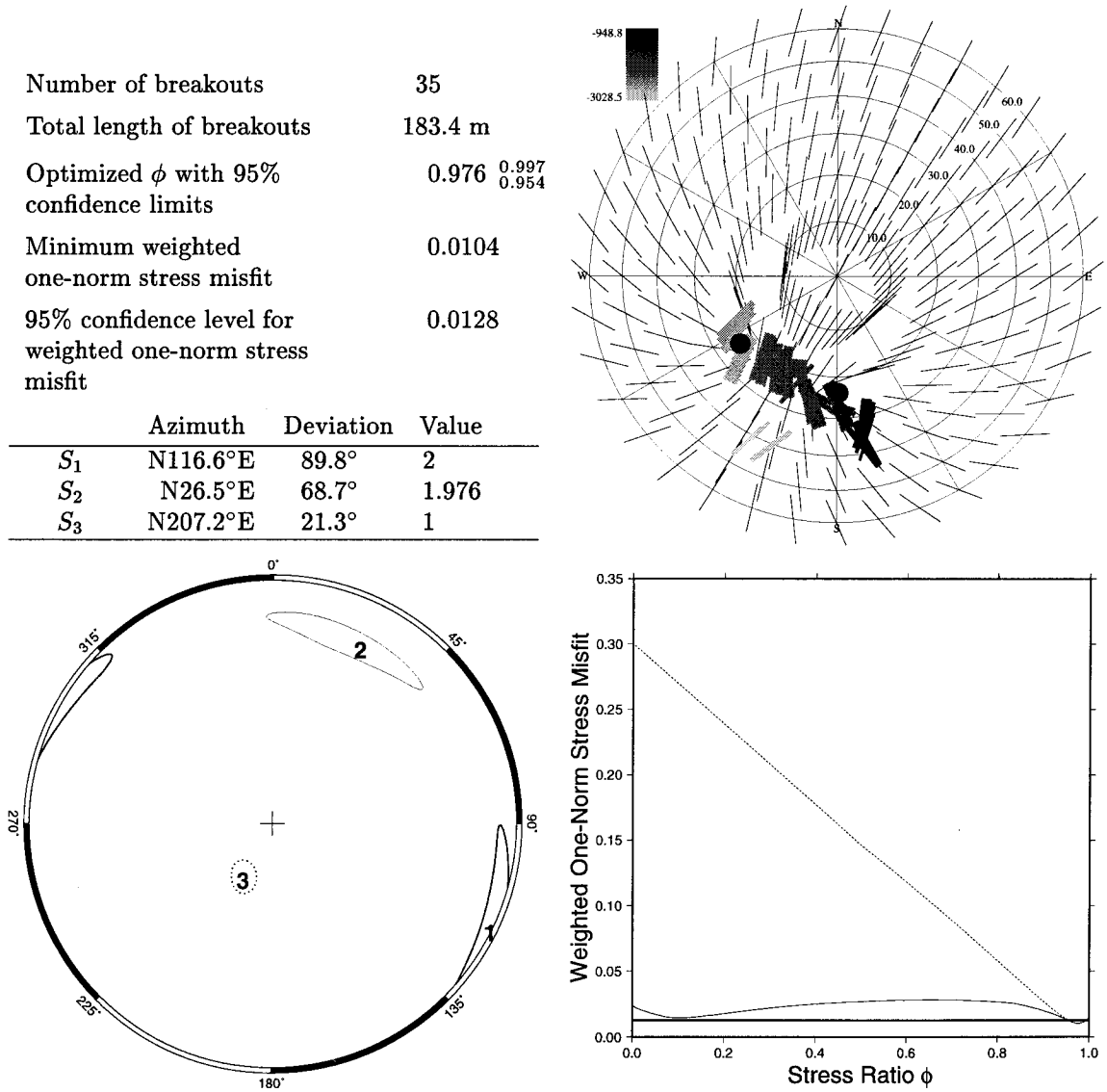

Figure 5.58: Stress inversion results in Cook Inlet, Alaska using all nonradial identified breakouts from wells drilled from the Dillon platform in the Middle Ground Shoals oil field excluding the breakouts from wells Smgs6 and Smgs8. Nonradial breakouts are those breakouts where the **IJK** breakout angle is at least 15° away from the high-side of the hole. Plotting conventions are the same as Figure 5.6.

Angular misfit inversion results using all Dillon platform nonradial breakouts excluding breakouts from wells Smgs6 and Smgs8.

Number of breakouts	35
Total length of breakouts	183.4 m
Optimized ϕ with 95% confidence limits	$0.824^{1.000}_{0.031}$
Minimum weighted one-norm stress misfit	17.37°
95% confidence level for weighted one-norm stress misfit	21.36°

	Azimuth	Deviation	Value
S_1	N170.7°E	68.0°	2
S_2	N77.3°E	81.6°	1.824
S_3	N327.7°E	23.7°	1

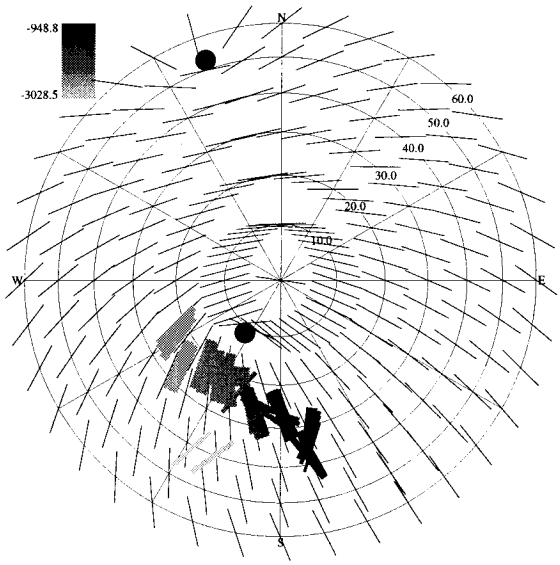

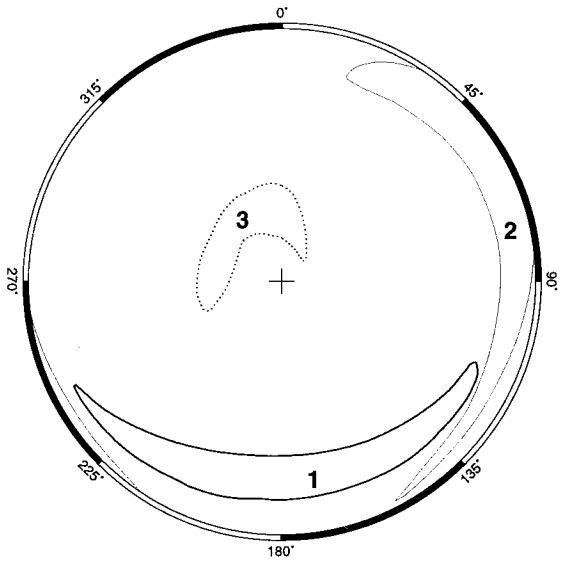

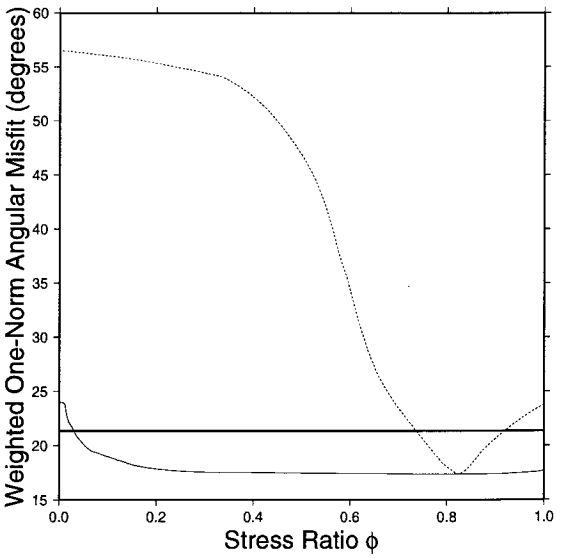

Figure 5.59: Stress inversion results in Cook Inlet, Alaska using all nonradial identified breakouts from wells drilled from the Dillon platform in the Middle Ground Shoals oil field excluding the breakouts from wells Smgs6 and Smgs8. Nonradial breakouts are those breakouts where the **IJK** breakout angle is at least 15° away from the high-side of the hole. Plotting conventions are the same as Figure 5.6.

Stress misfit inversion results using all Dillon platform breakouts in the TE1 formation excluding breakouts from well Smgs6.

Number of breakouts	7
Total length of breakouts	36.6 m
Optimized ϕ with 95% confidence limits	$0.970^{0.976}_{0.941}$
Minimum weighted one-norm stress misfit	$4.19\text{x}10^{-6}$
95% confidence level for weighted one-norm stress misfit	$7.48\text{x}10^{-6}$

	Azimuth	Deviation	Value
S_1	N310.3°E	83.2°	2
S_2	N44.0°E	62.2°	1.970
S_3	N207.7°E	28.8°	1

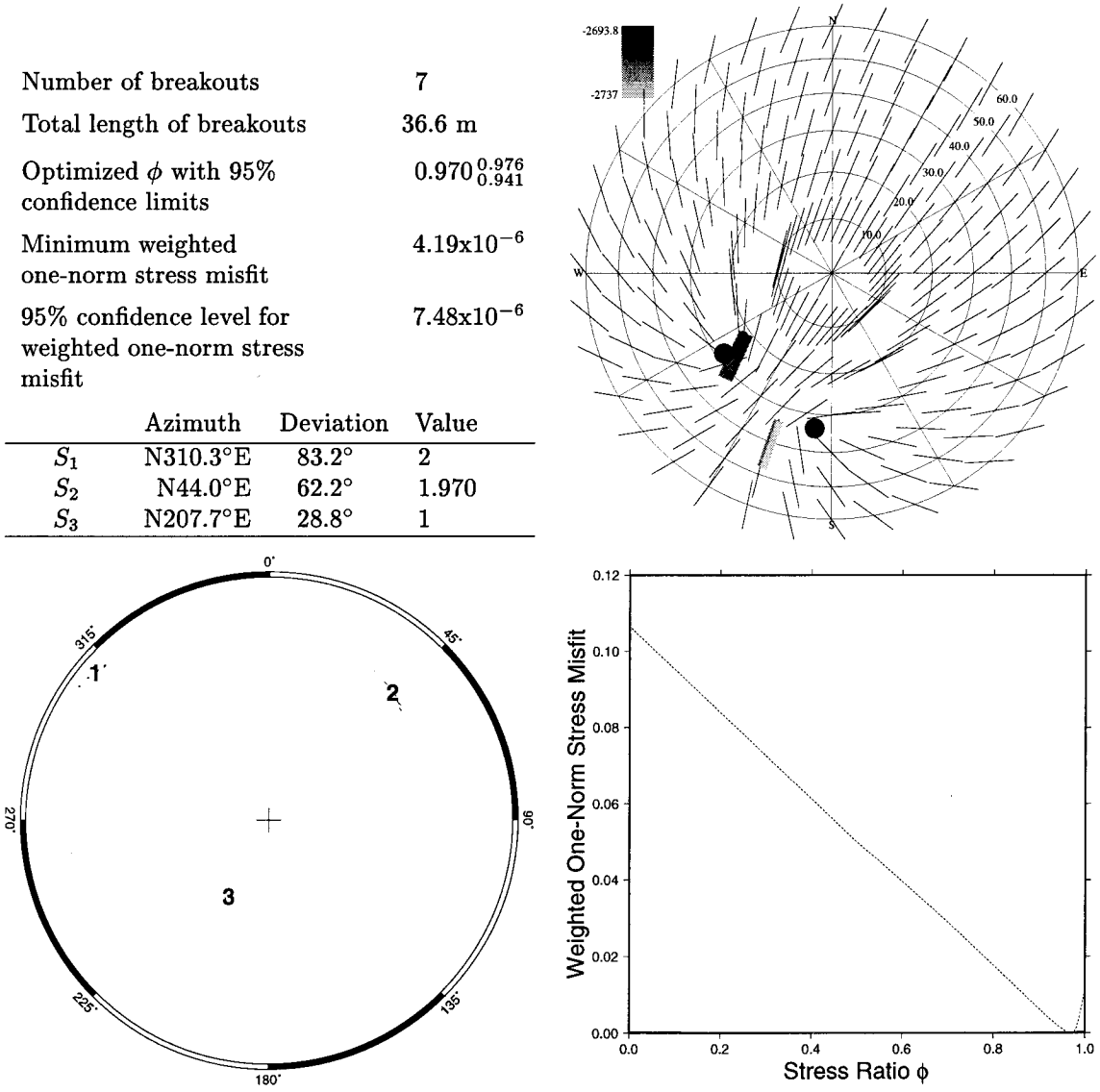

Figure 5.60: Stress inversion results in Cook Inlet, Alaska using all identified breakouts occurring in the TE1 formation from wells drilled from the Dillon platform in the Middle Ground Shoals oil field excluding the breakouts from well Smgs6. Plotting conventions are the same as Figure 5.6.

Angular misfit inversion results using all Dillon platform breakouts in the TE1 formation excluding breakouts from well Smgs6.

Number of breakouts	7
Total length of breakouts	36.6 m
Optimized ϕ with 95% confidence limits	$0.952^{0.959}_{0.941}$
Minimum weighted one-norm stress misfit	0.23°
95% confidence level for weighted one-norm stress misfit	0.41°

	Azimuth	Deviation	Value
S_1	N108.9°E	89.9°	2
S_2	N18.8°E	67.5°	1.952
S_3	N199.0°E	22.5°	1

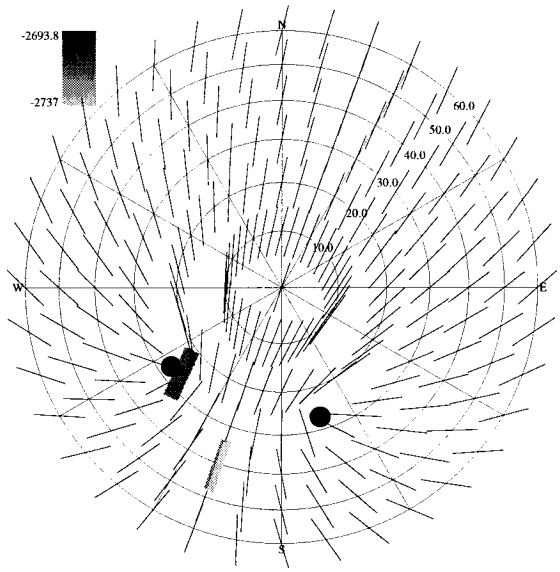

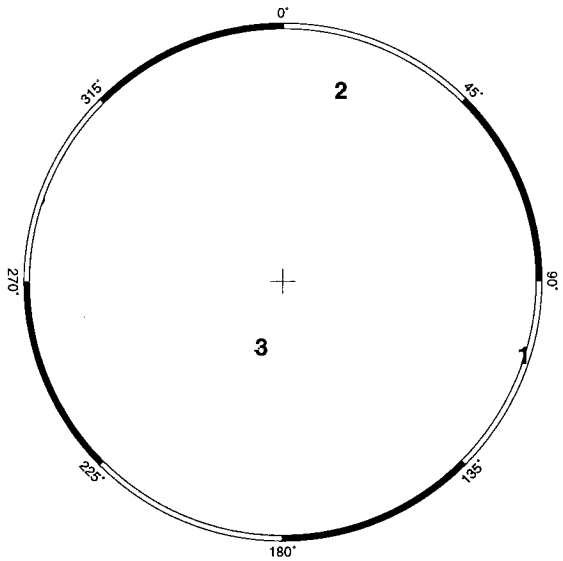

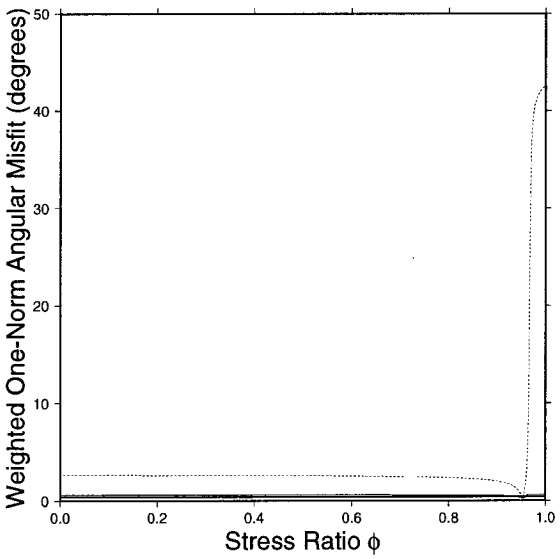

Figure 5.61: Stress inversion results in Cook Inlet, Alaska using all identified breakouts occurring in the TE1 formation from wells drilled from the Dillon platform in the Middle Ground Shoals oil field excluding the breakouts from well Smgs6. Plotting conventions are the same as Figure 5.6.

Stress misfit inversion results using all Dillon platform nonradial breakouts between 1,500–2,000 m TVD excluding breakouts from well Smgs6.

Number of breakouts	12
Total length of breakouts	58.6 m
Optimized ϕ with 95% confidence limits	$0.018^{0.021}_{0.015}$
Minimum weighted one-norm stress misfit	$2.07\text{x}10^{-4}$
95% confidence level for weighted one-norm stress misfit	$3.03\text{x}10^{-4}$

	Azimuth	Deviation	Value
S_1	N183.9°E	26.3°	2
S_2	N24.9°E	65.3°	1.018
S_3	N291.1°E	81.7°	1

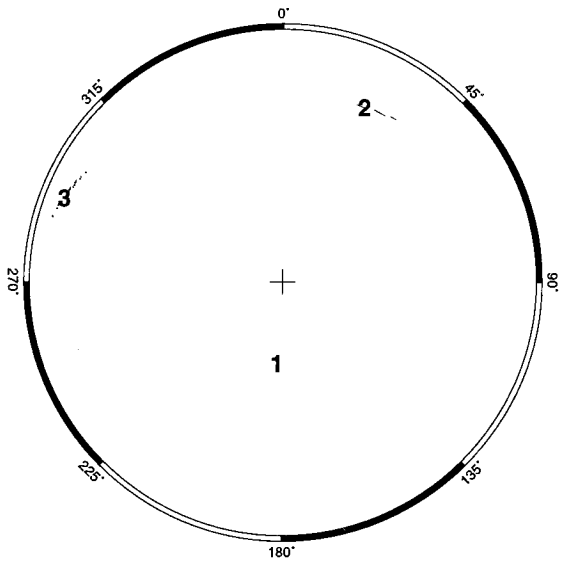

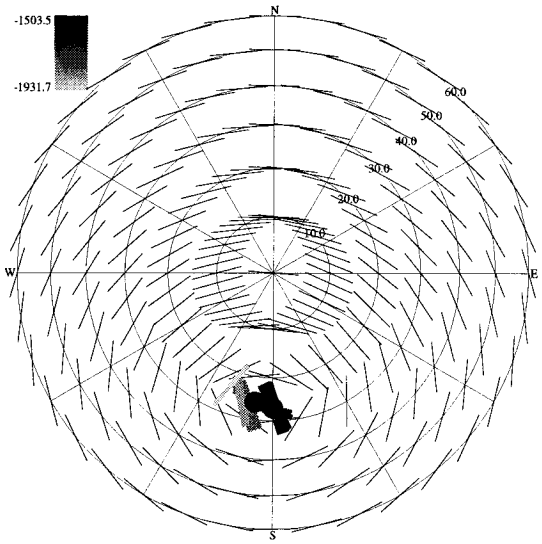

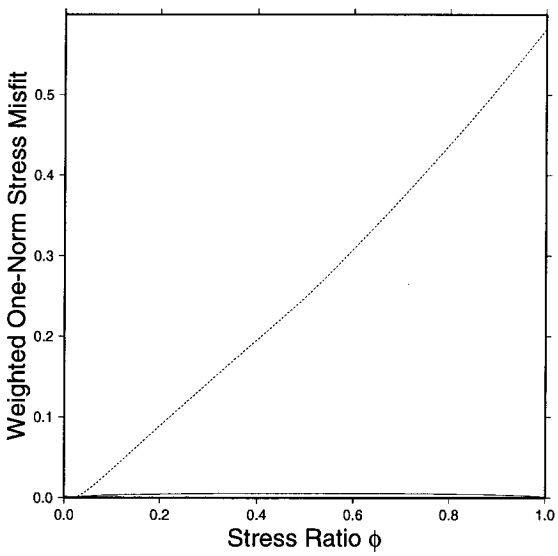

Figure 5.62: Stress inversion results in Cook Inlet, Alaska using all nonradial identified breakouts between 1,500 and 2,000 m TVD from wells drilled from the Dillon platform in the Middle Ground Shoals oil field excluding the breakouts from well Smgs6. Nonradial breakouts are those breakouts where the **IJK** breakout angle is at least 15° away from the high-side of the hole. Plotting conventions are the same as Figure 5.6.

Angular misfit inversion results using all Dillon platform nonradial breakouts between 1,500–2,000 m TVD excluding breakouts from well Smgs6.

Number of breakouts	12
Total length of breakouts	58.6 m
Optimized ϕ with 95% confidence limits	$0.021^{0.504}_{0.013}$
Minimum weighted one-norm stress misfit	6.38°
95% confidence level for weighted one-norm stress misfit	9.34°

	Azimuth	Deviation	Value
S_1	N183.0°E	26.1°	2
S_2	N51.7°E	72.0°	1.021
S_3	N315.5°E	71.7°	1

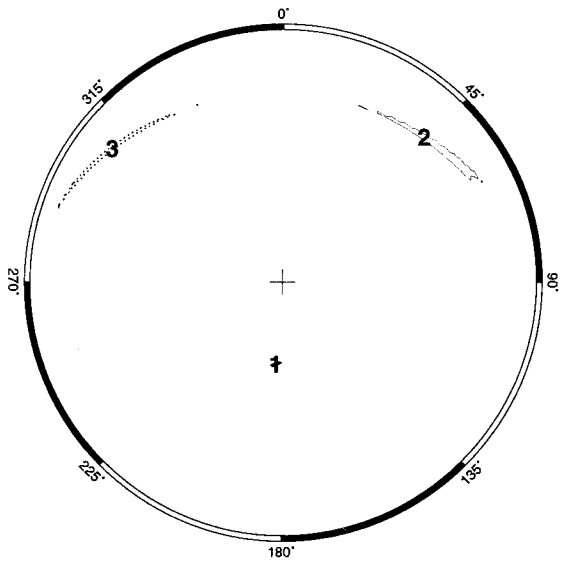

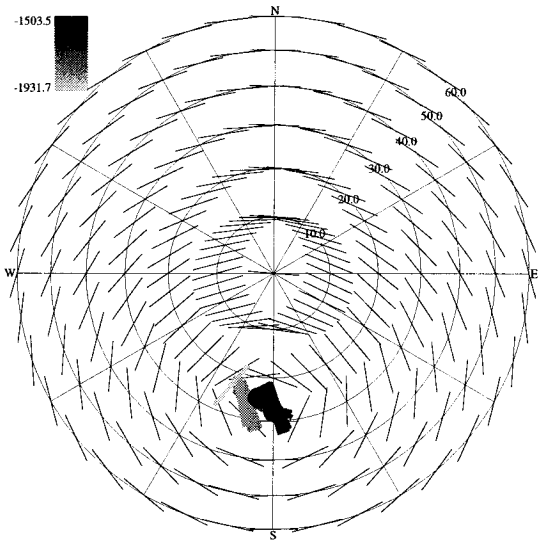

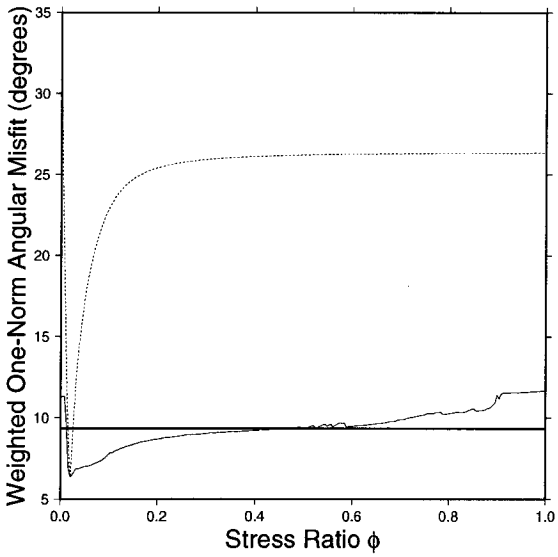

Figure 5.63: Stress inversion results in Cook Inlet, Alaska using all nonradial identified breakouts between 1,500 and 2,000 m TVD from wells drilled from the Dillon platform in the Middle Ground Shoals oil field excluding the breakouts from well Smgs6. Nonradial breakouts are those breakouts where the **IJK** breakout angle is at least 15° away from the high-side of the hole. Plotting conventions are the same as Figure 5.6.

Stress misfit inversion results using all Dillon platform nonradial breakouts between 2,000–2,500 m TVD excluding breakouts from well Smgs6.

Number of breakouts	10
Total length of breakouts	61.3 m
Optimized ϕ with 95% confidence limits	$0.092^{0.177}_{0.032}$
Minimum weighted one-norm stress misfit	$8.12\text{x}10^{-4}$
95% confidence level for weighted one-norm stress misfit	$1.25\text{x}10^{-3}$

	Azimuth	Deviation	Value
S_1	N190.5°E	26.0°	2
S_2	N52.3°E	70.0°	1.092
S_3	N316.3°E	74.1°	1

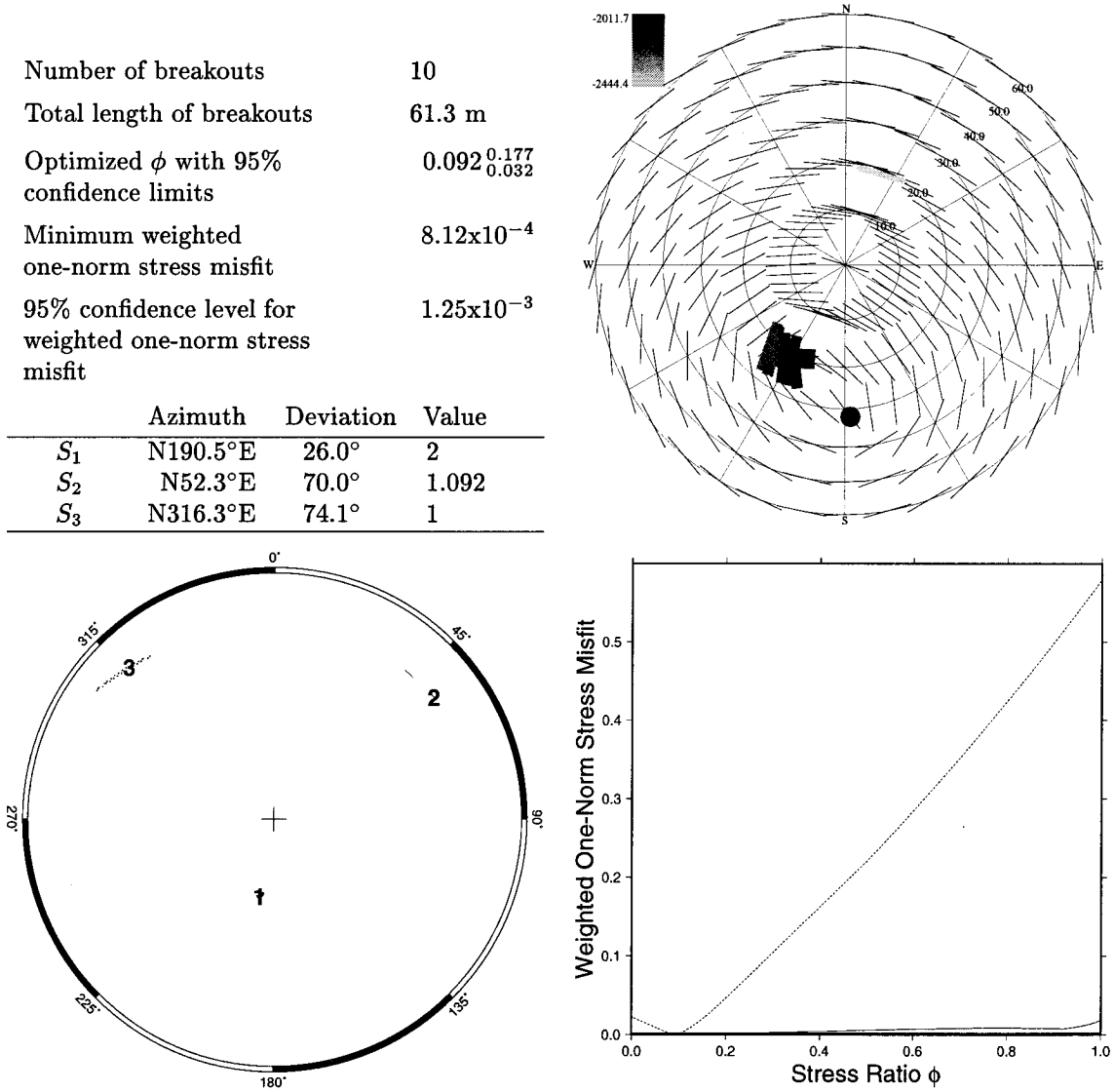

Figure 5.64: Stress inversion results in Cook Inlet, Alaska using all nonradial identified breakouts between 2,000 and 2,500 m TVD from wells drilled from the Dillon platform in the Middle Ground Shoals oil field excluding the breakouts from well Smgs6. Nonradial breakouts are those breakouts where the **IJK** breakout angle is at least 15° away from the high-side of the hole. Plotting conventions are the same as Figure 5.6.

Angular misfit inversion results using all Dillon platform nonradial breakouts between 2,000–2,500 m TVD excluding breakouts from well Smgs6.

Number of breakouts	10
Total length of breakouts	61.3 m
Optimized ϕ with 95% confidence limits	$0.118^{0.467}_{0.000}$
Minimum weighted one-norm stress misfit	10.99°
95% confidence level for weighted one-norm stress misfit	16.94°

	Azimuth	Deviation	Value
S_1	N186.6°E	27.0°	2
S_2	N50.3°E	69.8°	1.118
S_3	N313.8°E	72.9°	1

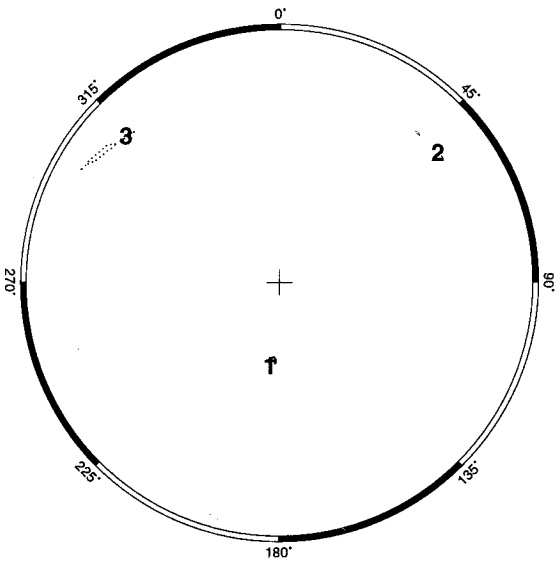

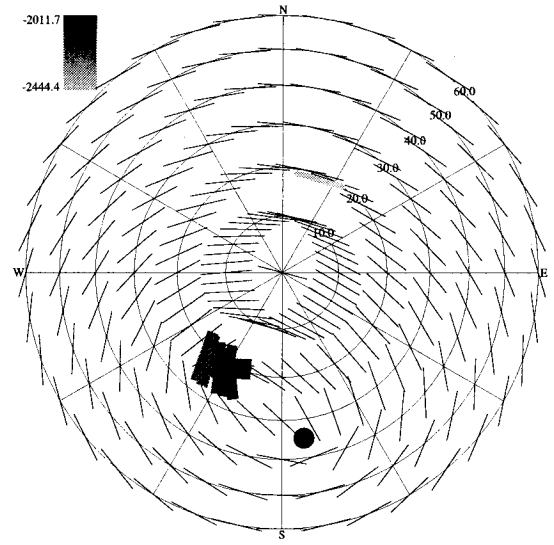

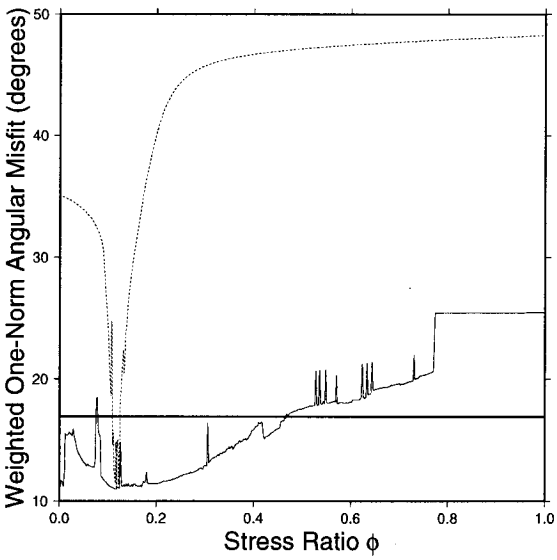

Figure 5.65: Stress inversion results in Cook Inlet, Alaska using all nonradial identified breakouts between 2,000 and 2,500 m TVD from wells drilled from the Dillon platform in the Middle Ground Shoals oil field excluding the breakouts from well Smgs6. Nonradial breakouts are those breakouts where the **IJK** breakout angle is at least 15° away from the high-side of the hole. Plotting conventions are the same as Figure 5.6.

Stress misfit inversion results using all Dillon platform nonradial breakouts between 2,500–3,000 m TVD excluding breakouts from well Smgs6.

Number of breakouts	7
Total length of breakouts	38.2 m
Optimized ϕ with 95% confidence limits	$0.161^{0.177}_{0.145}$
Minimum weighted one-norm stress misfit	$6.39\text{x}10^{-5}$
95% confidence level for weighted one-norm stress misfit	$1.14\text{x}10^{-4}$

	Azimuth	Deviation	Value
S_1	N226.1°E	29.5°	2
S_2	N117.7°E	79.8°	1.161
S_3	N22.3°E	62.6°	1

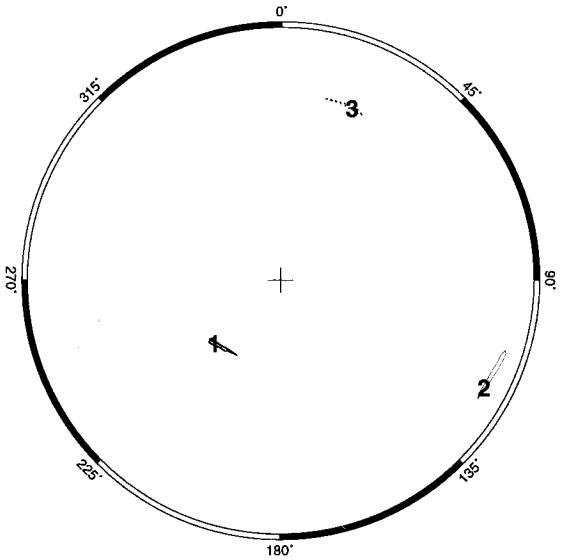

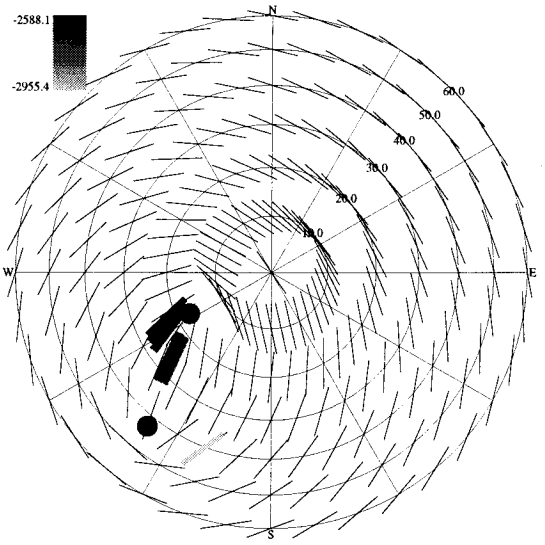

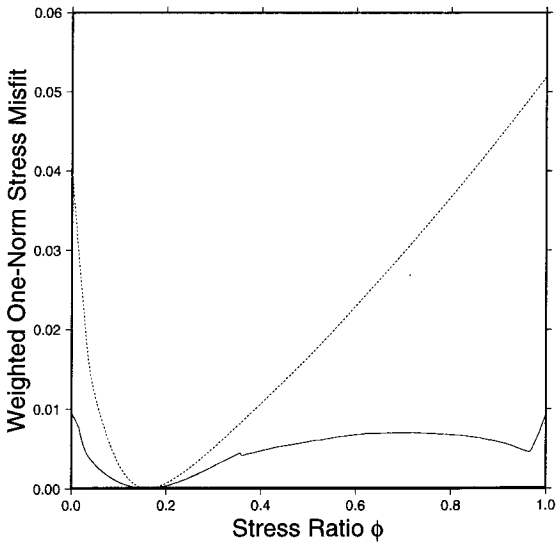

Figure 5.66: Stress inversion results in Cook Inlet, Alaska using all nonradial identified breakouts between 2,500 and 3,000 m TVD from wells drilled from the Dillon platform in the Middle Ground Shoals oil field excluding the breakouts from well Smgs6. Nonradial breakouts are those breakouts where the **IJK** breakout angle is at least 15° away from the high-side of the hole. Plotting conventions are the same as Figure 5.6.

Angular misfit inversion results using all Dillon platform nonradial breakouts between 2,500–3,000 m TVD excluding breakouts from well Smgs6.

Number of breakouts	7
Total length of breakouts	38.2 m
Optimized ϕ with 95% confidence limits	$0.168^{0.190}_{0.147}$
Minimum weighted one-norm stress misfit	0.67°
95% confidence level for weighted one-norm stress misfit	1.20°

	Azimuth	Deviation	Value
S_1	N226.3°E	29.5°	2
S_2	N118.9°E	80.4°	1.168
S_3	N23.8°E	62.4°	1

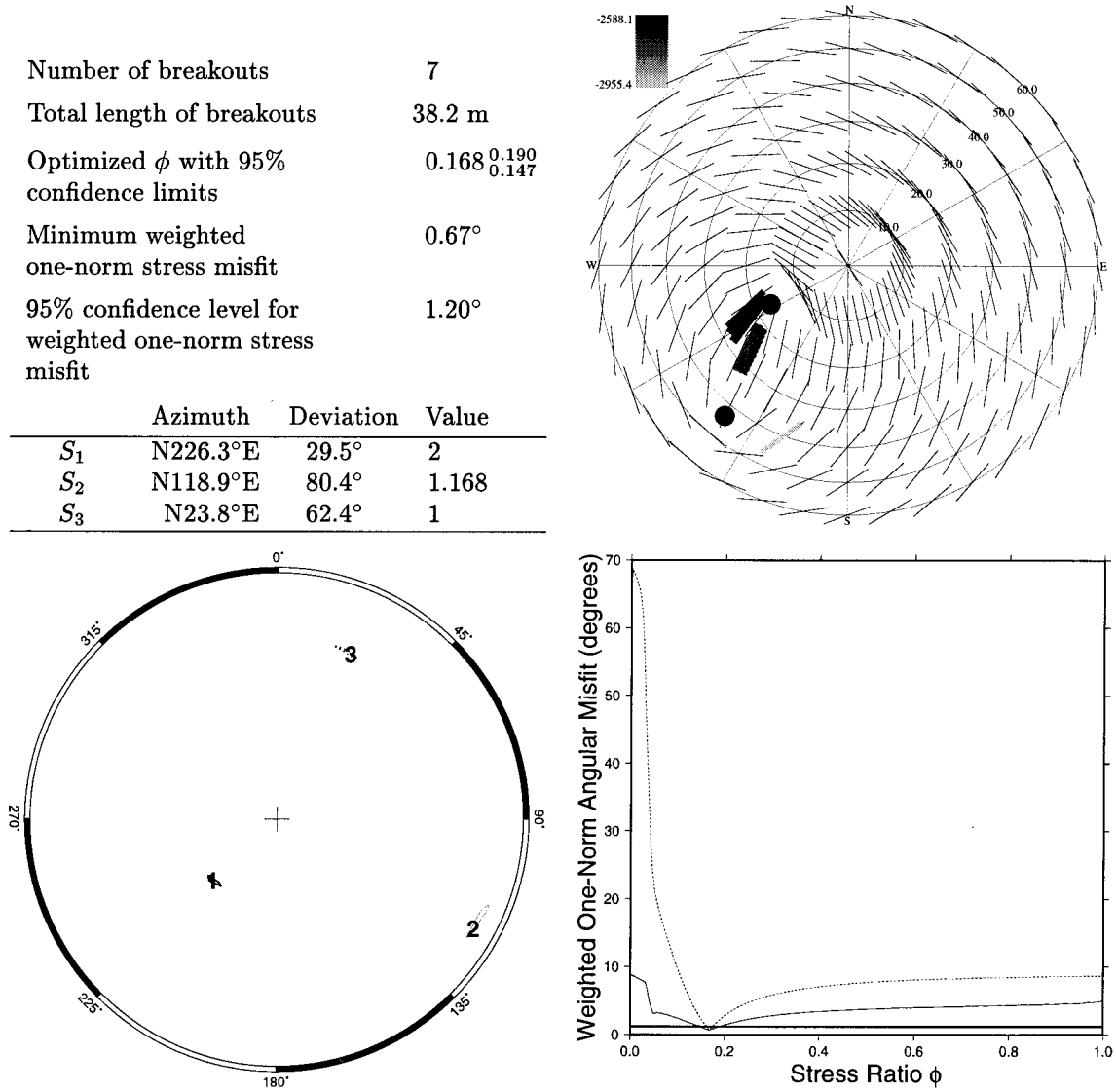

Figure 5.67: Stress inversion results in Cook Inlet, Alaska using all nonradial identified breakouts between 2,500 and 3,000 m TVD from wells drilled from the Dillon platform in the Middle Ground Shoals oil field excluding the breakouts from well Smgs6. Nonradial breakouts are those breakouts where the **IJK** breakout angle is at least 15° away from the high-side of the hole. Plotting conventions are the same as Figure 5.6.

5.5 Stress State Analyses

5.5.1 Granite Point Oil Field Inversion

Eight separate inversions of subsets of the Granite Point breakouts excluding the breakouts from Gp51 were performed. These subsets were: all of the breakouts (Figures 5.20 and 5.21), nonradial breakouts (Figures 5.22 and 5.23), nonradial breakouts between 2,000 and 2,500 m TVD (Figures 5.24 and 5.25), and nonradial breakouts between 2,500 and 3,000 m TVD (Figures 5.26 and 5.27). All of the stress and angular misfit inversion results have the maximum principal stress direction oriented subhorizontally NNW–SSE in a thrust faulting stress state with a large ϕ value. S_1 consistently plunges slightly to the NNW, except for the inversions of the nonradial breakouts between 2,000 and 2,500 m TVD, where S_1 plunges 18.1° to the SSE. The S_2 and S_3 principal stresses are also fairly consistently oriented between the different inversion results. S_3 is consistently oriented near the vertical and S_2 is oriented ENE–WSW. The stress state ϕ values from the various misfits range from 0.964 to 0.999. These data suggest that a thrust-faulting stress state with S_1 oriented in a NNE–SSW sense is responsible for these breakout orientations.

The Granite Point T45XSS marker was initially identified as the marker containing the most identified Granite Point breakouts. All but one of the T45XSS breakouts were identified in Gp51. Since the breakouts from Gp51 were not included in the inversion of the Granite Point data due to inconsistent breakout orientations (Section B.8), no inversions of breakouts occurring in Granite Point marker horizons were performed. An examination of other potential markers for study did not yield any markers containing a large number of breakouts.

The irregular 95% confidence limits in the angular misfit inversion of the nonradial breakouts and nonradial breakouts between 2,500 and 3,000 m TVD are due to two separate distinct misfit minima below the 95% misfit confidence limit (Figures 5.23 and 5.27). Since both minima are less than the 95% confidence limit, the inversion results are extremely poor. The stress misfit inversions also identified similar local minima (Figures 5.22 and 5.26), but in the case of the stress misfit local minima, only one fell within the 95% confidence misfit limit for each inversion.

A comparison of stress misfit inversion results for two depth ranges, 2,000–2,500 m and 2,500–3,000 m TVD, is shown in Figure 5.68. The two stress states are visually distinct from each other. However, both S_1 azimuths are in sector defined by NNW–SSE and NW–SE directed azimuths, and the S_3 axes are nearly vertically oriented. *Michael and Julian* [1994] developed a method to calculate the rotation axis and angle of rotation needed to align one set of principal stress axes with another. A rotation of 36.6° around an axis trending N203.9°E and plunging 39.5° brings the shallower stress state in alignment with the deeper one. The upper 2,000 to 2,500 m TVD depth range identified a nearly degenerate ($\phi = 0.999$) thrust faulting stress state with S_1 striking N38.9°W; the 95% confidence limits on S_1 allow its azimuth to vary from N89.3°W to N10.5°W. The deeper breakouts

identified from 2,500 to 3,000 m TVD were best fit by a less degenerate ($\phi = 0.964$) thrust faulting stress state with the S_1 azimuth more northerly oriented at N17.0°W; the 95% confidence limits on S_1 allow its azimuth to vary from N26.1°W to N0.6°W.

The best fitting stress state theoretical breakout pattern for all of the Granite Point breakouts and the breakout pattern for the nonradial breakouts visually agree (Figures 5.20–5.23). All four inversions placed breakout nodal points at orientations plunging to the north and to the south of the breakout data to fit the more variably oriented breakouts. The stress misfit inversion of the complete Granite Point data set (Figure 5.20), including the radial breakouts, is taken as the inversion that best represents the Granite Point stress state. This thrust faulting stress state has S_1 oriented N19.4°W plunging 3.4°; the 95% confidence limits allow the azimuth to vary from N42.4°W to N7.4°E and the plunge to vary from 1.4° to 6.2°. The optimized ϕ is $0.976^{0.996}_{0.959}$.

5.5.2 Baker Platform Inversion

Twenty-four separate inversions were done of various subsets of breakouts identified from wells drilled from the Baker platform. Eight inversions were performed of nonradial breakouts separated into 500 m TVD zones from 1,000 to 3,000 m (Figures 5.44–5.51). Figure 5.69 plots a vertical profile of the stress misfit nonradial breakout inversion results. The stress misfit S_1 azimuth over the 2,000 m TVD depth interval is oriented in a NNW–SSE to NW–SE sector: N49.5°W (1,000–1,500 m TVD), N175.3°E (1,500–2,000 m TVD), N171.6°E (2,000–2,500 m TVD), and N154.5°E (2,500–3,000 m TVD). The S_1 azimuth in the shallowest interval is essentially unconstrained: 95% confidence limits allow S_1 to vary from N120.7°W to N114.2°E due to a degenerate stress field ($\phi \leq 1$). The S_1 azimuth in the three deeper depth intervals is much better constrained: N152.2°E–N192.2°E (1,500–2,000 m TVD), N160.0°E–N182.6°E (2,000–2,500 m TVD), and N137.7°E–N173.8°E. Over the same depth interval the plunge of the maximum principal stress direction rotated from plunging north 4.9° (1,000–1,500 m TVD), to plunging south 8.7° (1,500–2,000 m TVD), south 62.2° (2,000–2,500 m TVD), and lastly south 14.0° (2,500–3,000 m TVD).

The largest change in stress state as a function of depth is the switch from an almost degenerate thrust faulting stress state in the 1,000 to 2,000 m TVD depth range to a normal faulting stress state in the 2,000 to 2,500 m TVD depth range and a return to the nearly degenerate thrust faulting from 2,500 to 3,000 m TVD (Figure 5.69). In the same normal stress state region is a change from a NNW–SSE directed S_H and S_1 orientation to a ENE–WSW directed S_H and S_2 orientation. Along the same depth interval, the stress state ϕ ratio moves from 0.999 to 0.943 to 0.310 to 0.957. For each depth interval the stress state results from the angular misfit inversion are almost identical to the stress misfit inversion results, suggesting that the normal faulting stress state observed in the 2,500 to 3,000 m TVD is not an artifact of the inversion. The data from 2,000 to 2,500 m TVD also contained the largest number of identified breakouts, the second longest total length of breakouts,

2,000–2,500 m TVD
Figure 5.24

$n = 10$
$l = 59.9$ m
$\phi = 0.999^{1.000}_{0.990}$

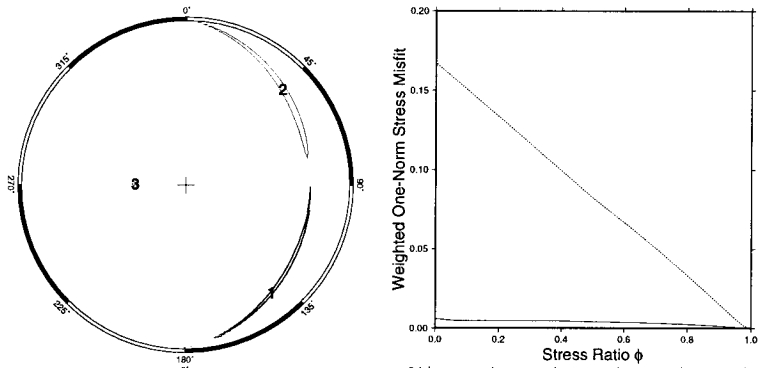

2,500–3,000 m TVD
Figure 5.26

$n = 23$
$l = 120.3$ m
$\phi = 0.964^{0.974}_{0.946}$

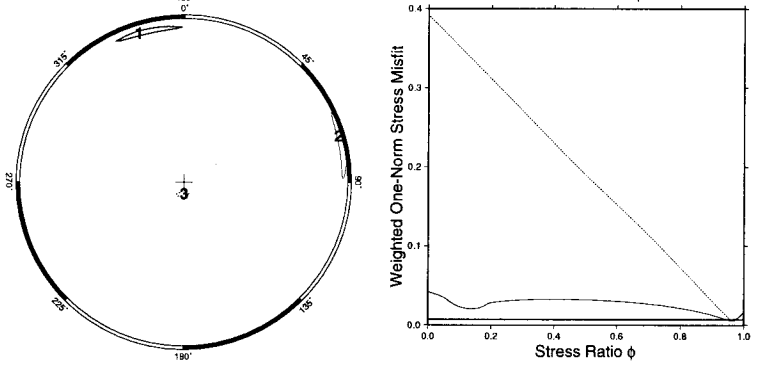

Figure 5.68: Depth variation of the nonradial Granite Point stress misfit stress inversion results. (left) The figure number refers to the figure containing all of the plots and information regarding this inversion. n is the number of breakouts and l is the total length of the n breakouts in the inversion. (middle) Lower hemisphere stereographic projection plot where the digits 1, 2, and 3 show the optimized orientation of the S_1, S_2, and S_3 principal stress axes, respectively. The 95% weighted one-norm misfit confidence limits of the S_1, S_2, and S_3 orientations are plotted as thick solid lines, thin solid lines, and dotted lines, respectively. The stress state ϕ ratio was held constant at the minimum of the misfit versus ϕ curve on the right. (right) The weighted one-norm misfit for the breakouts as a function of ϕ, where the thick solid line is the minimized misfit when ϕ is held constant and the principal stress directions are unconstrained, and the dotted line is the misfit using the principal stress directions from the best fitting model. A rotation of 36.6° around an axis trending N203.9°E and plunging 39.5° is required to bring the shallower stress state in alignment with the deeper one.

1,000–1,500 m TVD
Figure 5.44

$n = 16$
$l = 124.7$ m
$\phi = 0.999^{1.000}_{0.992}$

1,500–2,000 m TVD
Figure 5.46

$n = 17$
$l = 102.3$ m
$\phi = 0.943^{0.979}_{0.872}$

2,000–2,500 m TVD
Figure 5.48

$n = 28$
$l = 119.8$ m
$\phi = 0.310^{0.381}_{0.228}$

2,500–3,000 m TVD
Figure 5.50

$n = 8$
$l = 70.1$ m
$\phi = 0.957^{0.977}_{0.917}$

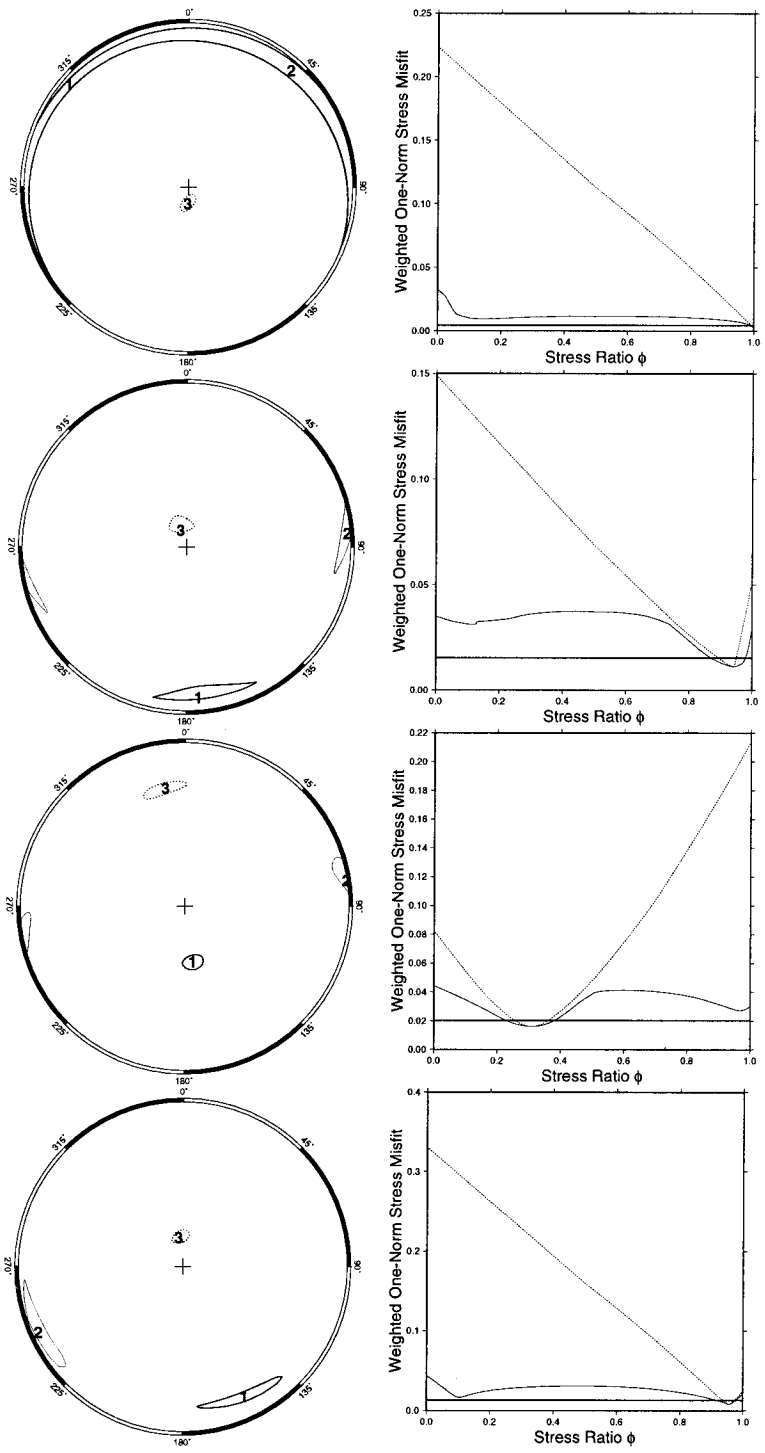

Figure 5.69: Depth variation of the nonradial Baker Platform stress misfit stress inversion results. The S_1 and S_2 95% confidence contours in the 1,000–1,500 m TVD depth range are almost identical and plot on top of each other. Plotting conventions are the same as in Figure 5.68.

and had a better data distribution, so the normal faulting stress state is probably not a sampling problem. No similar changes in stress state occur as a function of depth in either the Granite Point or Dillon platform breakouts.

The breakouts occurring in the selected B40SS, D, G3, and G4 markers come from the same set of breakouts used in the inversions of breakouts separated into 500 m intervals. The B40SS marker spans the TVD range 1,345 to 1,646 m, D spans 2,003 to 2,205 m and G3 combined with G4 spans 2,410 to 2,769 m TVD. As a group, the stress state results from inversions of breakouts and nonradial breakouts occurring in the B40SS (Figures 5.32–5.35), D (Figures 5.36–5.39), and G3 combined with G4 (Figures 5.40–5.43) markers are highly inconsistent. Stress states determined using the stress difference and angular difference inversions were markedly different in four out of the six marker horizon data sets inverted (compare Figure 5.34 with 5.35, 5.36 with 5.37, 5.40 with 5.41, and 5.42 with 5.43). The angular misfit inversion yielded significantly different stress state results when radial breakouts were included in the inversion (compare Figure 5.33 with 5.35, 5.37 with 5.39, and 5.41 with 5.43). However, stress states determined from the stress misfit inversion of complete sets of borehole breakouts were highly consistent with the stress states determined from the nonradial breakouts (compare Figure 5.32 with 5.34, 5.36 with 5.38, and 5.40 with 5.42). If only the stress misfit inversion results are considered, then overall, the data indicate nearly degenerate thrust faulting stress states where S_3 is within 14.9° of vertical and S_1 is unconstrained to rotate about the S_3 axes or oriented clockwise of E–W and counterclockwise of N–S.

Figure 5.70 compares the stress state results from the nonradial subset of breakouts identified in each marker. The nonradial breakouts from the B40SS and the D markers are best fit by almost identical nearly degenerate thrust faulting stress states; only a -15.6° rotation around an axis trending N178.3°E and plunging 7.7° is required to bring these two stress states into coincidence. The -15.6° of rotation is the among the smallest amounts of rotation needed to align two stress tensors that has been observed in any of these data subsets. The similarity of the inversion results from these two distinct sets of breakouts suggests that the stress state is real. The B40SS S_1 azimuth (N287.9°E) and the D S_1 azimuth (N105.6°E) are within 2.3° of each other. The breakouts from the G3 and G4 markers appear to have been generated from a nearly degenerate thrust faulting stress state where S_1 trends N160.9°E. The consistent ESE–NNW S_1 azimuth of the B40SS and the D markers is almost perpendicular to the N10°E striking trend of the Middle Ground Shoal anticline, suggesting that these breakouts may be related to the growth of the anticline and not the regional tectonic stresses, which may control the G3 and G4 breakouts. This change in stress states occurs between the 2205 m TVD of the deepest D breakout and the 2410 m TVD of the shallow G3 breakout.

The breakouts in the D marker and in the G3 and G4 markers overlap to some extent the breakouts in the 2,000–2,500 m TVD depth interval where a normal faulting stress state was identified. However, none of the inversions of breakouts in these particular markers identified a similar normal

B40SS marker
1,345–1,646 m TVD
Figure 5.34

$n = 10$
$l = 64.0$ m
$\phi = 0.988^{1.000}_{0.975}$

D marker
2,003–2,205 m TVD
Figure 5.38

$n = 7$
$l = 43.5$ m
$\phi = 0.996^{0.998}_{0.990}$

Between D and G3
2,168–2,516 m TVD

$n = 20$
$l = 133.2$ m
$\phi = 0.305^{0.365}_{0.172}$

G3 and G4 markers
2,410–2,769 m TVD
Figure 5.42

$n = 8$
$l = 67.1$ m
$\phi = 0.972^{1.000}_{0.897}$

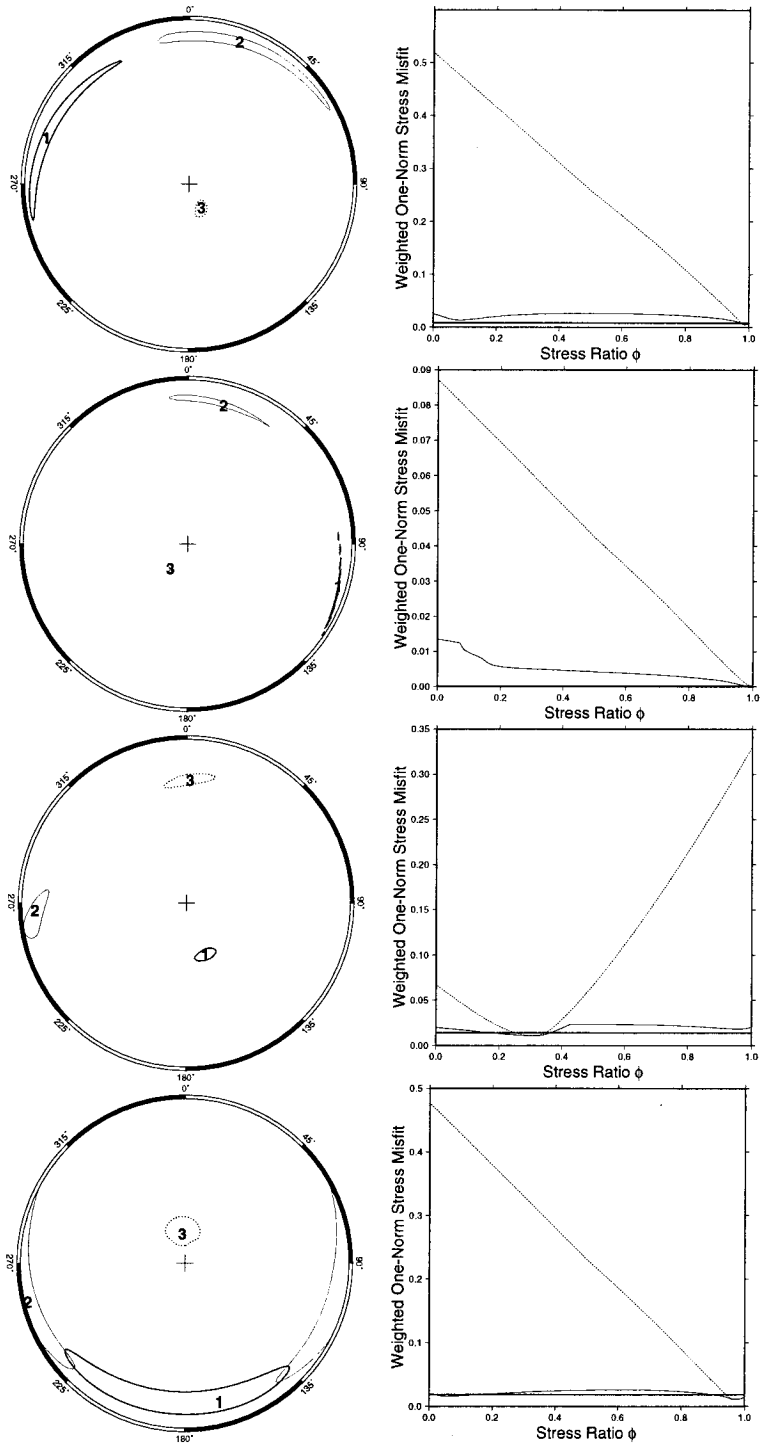

Figure 5.70: Comparison of nonradial Baker Platform stress misfit stress inversion results from breakouts occurring in different markers and between the D and G3 markers. The true vertical depth range shown for each marker shows the maximum vertical extent of the breakouts from each marker. Breakouts not in the marker but within the depth range are not included. A rotation of -15.6° around an axis trending N178.3°E and plunging 7.7° is required to bring the stress state determined by the B40SS breakouts into alignment with the stress state from the breakouts identified in the D marker. Plotting conventions are the same as in Figure 5.68.

faulting stress state. A stress misfit inversion of the nonradial breakouts between 2,002 and 2,769 m TVD excluding those breakouts above and inside the D marker and below and inside the G3 marker was performed. The stress state determined from this set of breakouts was also a normal faulting stress state very similar to the 2,000–2,500 m TVD breakout inversion. This suggests that as a function of depth the shallowest stress state is related to the local structure of the anticline, then an anomalous normal faulting stress state is observed at the next deeper level, and at the deepest level, the regional stress state is measured.

Inversion of all of the Baker breakouts and the nonradial Baker breakouts yielded substantially different stress tensors (Figures 5.28–5.31). Both the stress misfit and the angular misfit inversions yielded similar stress state results for each data set. The stress misfit inversion of the complete Baker platform breakouts identified a nearly degenerate ($\phi = 0.944$) thrust faulting stress state with S_1 plunging 7.7° southward at an azimuth of N169.8°E. The stress state generated by the stress misfit inversion of the nonradial borehole breakouts identified a normal faulting stress state with ϕ near 0.3. It appears that the nonradial breakout inversion was controlled by the same nonradial breakouts that generated the normal faulting stress state in the 2,000 to 2,500 m TVD depth range. Because the normal faulting stress state was shown to arise in a particular depth range, the stress state results using the complete set of Baker platform breakouts is considered as the stress state indicative of the volume sampled by the Baker wells (Figure 5.28). This stress state has S_1 plunging 7.7° southward at an azimuth of N169.8°E with S_3 nearly vertical. The 95% confidence limits on S_1 allow its azimuth to vary from N138.6°E to N190.6°E and its plunge to vary from 0.7° to 14.8°.

5.5.3 Dillon Platform Inversion

Except for a single breakout identified in the northeastward plunging Smgs8 well, all breakouts from the Dillon platform were identified in south- to west-plunging sections of borehole (Figure 5.52). The breakouts in the southwest-plunging boreholes are very consistently oriented in a general N–S to NE–SW direction.

Sixteen separate inversions were performed on subsets of the Dillon platform breakouts. The first set of inversions are of seven breakouts identified in the TE1 marker (Figures 5.60 and 5.61). Three of these seven breakouts are nonradial. Three breakouts cannot constrain a stress tensor and hence no inversion of the nonradial TE1 breakouts was performed. The inversion of all seven breakouts yielded an extremely small weighted stress misfit of 4.19×10^{-6} and a small weighted angular misfit of 0.23° for these data. The small misfits were obtained since the seven breakouts in TE1 are located in two localized regions on the borehole azimuth and deviation space (Figure 5.60), which limits the inversion to effectively inverting for two breakouts. The inversions placed a breakout nodal point on top of the breakouts identified in the more westerly plunging drillhole. The resolved stress state from the stress misfit inversion is nearly degenerate thrust faulting ($\phi = 0.970$) with the S_1 azimuth

at N310.3°E. The angular misfit inversion stress results agree closely with the stress misfit inversion results. This orientation of the maximum horizontal principal stress is midway between the NNW–SSE S_H stress direction and an orientation perpendicular to the N10°E strike of the Middle Ground Shoals oil field.

Three 500 m true vertical depth intervals contained a large number of identified nonradial breakouts: between 1,500 and 2,000 m TVD there were 12 breakouts totaling 58.6 m in length (Figures 5.62 and 5.63), between 2,000 and 2,500 m TVD there were 10 breakouts totaling 61.3 m in length (Figures 5.64 and 5.65), and between 2,500 and 3,000 m TVD there were 7 breakouts totaling 38.2 m in length (Figures 5.64 and 5.65). The three stress misfit inversions from 1,500 to 3000 m TVD exhibit extremely small principal stress direction 95% confidence regions (Figure 5.71). Given that the breakout pattern nodal points were preferentially placed near the moderately deviated breakouts and that the breakouts occupied a very limited amount of borehole azimuth and deviation space, the inversions yielded nearly degenerate normal faulting stress states with S_1 deviating nearly 30° away from vertical. Given the extremely limited coverage of borehole azimuth and deviation covered by the breakouts separated into 500 m intervals, these inversion results will not be considered as representative of the stress state in the depth intervals. While the number of breakouts in these intervals is equal to or larger than the number of breakouts performed in the 500 m TVD depth intervals from the Baker platform, the Baker platform breakouts cover a much larger range in borehole azimuth and deviation space, and hence the Baker platform results are considered to be more reliable, and were included in the conclusions about the Baker stress state. Finally, because the breakouts from the Dillon platform are in boreholes deviating roughly 30° away from the vertical, these breakouts will not be considered as indicators of the maximum horizontal principal stress direction, S_H.

In contrast to the TE1 and 500 m TVD depth interval breakout subsets, the nonradial and the radial combined with the nonradial breakout subsets have a large number of breakouts and a large variation in borehole azimuth and borehole deviation. The stress and angular misfit inversion results for all Dillon breakouts and all nonradial Dillon breakouts are not consistent (Figures 5.52–5.55). The substantial differences between these inversions stems from the single nonradial Smgs8 breakout. Only one breakout was identified in Smgs8, in a noisy section of the four-arm dipmeter caliper curves; this suggests that inversions should be performed of the data without this breakout (Figure B.78). Figures 5.56–5.58 show the stress and angular misfit inversions of the same complete and nonradial data sets excluding the Smgs8 breakout. The stress misfit inversion results generated from the complete set of breakouts excluding Smgs8 and the nonradial breakouts excluding Smgs8 are very consistent (Figures 5.56 and 5.58), requiring only a 6.3° rotation around an axis trending N6.8°E plunging 71.7° to align the principal stress directions. The stress state generated from the complete set of breakouts excluding Smgs8 is only slightly different than the stress state including Smgs8 (Figures 5.52 and 5.56): a 3.9° rotation of the principal stress axes around a horizontal axis

1,500–2,000 m TVD
Figure 5.62

$n = 12$
$l = 58.6$ m
$\phi = 0.018^{0.021}_{0.015}$

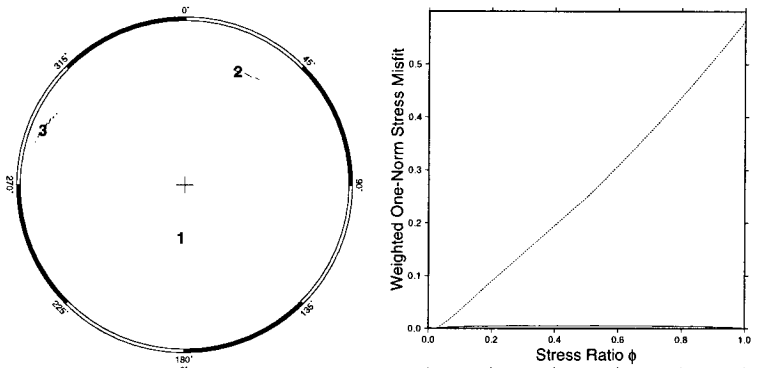

2,000–2,500 m TVD
Figure 5.64

$n = 10$
$l = 61.3$ m
$\phi = 0.092^{0.177}_{0.032}$

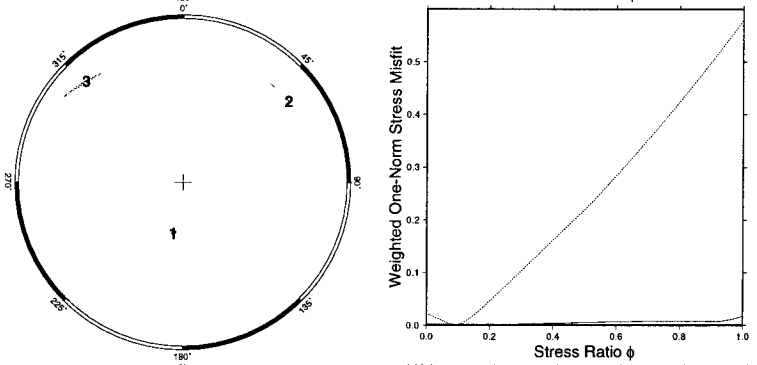

2,500–3,000 m TVD
Figure 5.66

$n = 7$
$l = 38.2$ m
$\phi = 0.161^{0.177}_{0.145}$

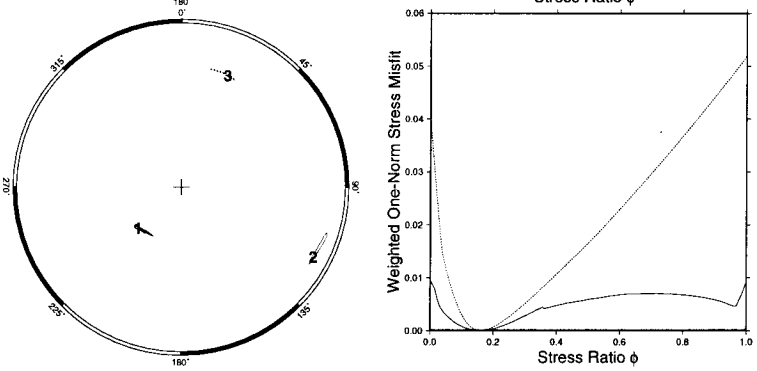

Figure 5.71: Comparison of the nonradial Dillon Platform stress misfit stress inversion results. Plotting conventions are the same as in Figure 5.68.

trending N96.8°E would bring the two sets of principal stress axes into alignment. When the Smgs8 breakout was removed from the nonradial breakout stress misfit version the best fitting stress state ratio ϕ changed from 0.104 to 0.976, consistent with the other inverted stress state ratios.

Given the questionable Smgs8 breakout and the consistency of stress states when the inversions do not include this breakout, the stress misfit inversion results from the complete data set excluding Smgs8 will be considered representative of the stress state as a whole (Figure 5.56). This best-fitting stress state has S_1 oriented N69.4°W plunging 1.7°. The 95% confidence limits constrain the S_1 azimuth from N92.4°W to N35.6°W and the plunge from -4.3° to 8.2°. The stress state ϕ ratio is $0.964^{0.983}_{0.939}$. This stress state has S_1 oriented almost perpendicular to the N20°E trending section of the South Middle Ground Shoals oil field.

5.5.4 Cook Inlet Inversion

Fourteen separate inversions were made of all of the Cook Inlet breakouts excluding the breakouts in wells Gp51 and Smgs6. The first ten stress and angular misfit inversions were of the breakouts separated into 500 m TVD depth intervals (Figures 5.10–5.19). Figure 5.72 compares the stress states determined by these inversions. Six nonradial breakouts between 500 and 1,000 m TVD were identified (Figure 5.10), three from an almost vertical section of Mgs30 and the other three from a southward plunging section of Smgs5. The breakouts from each well were identified in almost identically oriented sections of borehole, and hence, the inversion effectively inverted for 2 breakouts. The inversion placed the breakout nodal points at the orientation of both breakout data sets and identified a normal faulting stress state with the maximum horizontal principal stress oriented N76.6°E. If only the vertical Mgs30 breakout were used for the inversion and if one of the principal stress directions were vertical, then a N–S oriented S_H would be inferred, instead of a ENE–WSW oriented S_H inferred from the inversion. For this reason, the stress state results from this depth interval will be disregarded.

The remaining stress states from the four deeper depth intervals are similar to those obtained by inversions of subsets of the Cook Inlet data. In particular, the inversion of breakouts between 2,000 and 2,500 m TVD obtained the same normal faulting stress state that was obtained in the Baker platform 2,000 to 2,500 m TVD interval (Figures 5.69 and 5.72). The other three inversions produced thrust faulting stress states with S_1 either unconstrained in its azimuth, such as between 1,000 and 1,500 m TVD, or oriented N–S. The largest distinction between the stress state derived from the complete Cook Inlet data sets and the subsets of data from each platform or oil field is a N–S oriented S_1 instead of a more NNE–SSE or WNW–ESE orientation. Unlike the Baker platform inversions the inversions of the complete set of Cook Inlet data did not identify any WNW–ESE orientations of S_1 either.

Taken together, all of the Cook Inlet data excluding those from Gp51 and Smgs6 consists of

279 separate breakouts totaling 1,860.8 m in length. The nonradial subset of this data consists of 142 breakouts totaling 880.5 m in length. The stress misfit inversions of these two data sets yielded almost identical stress states: 8.1° of rotation about an axis trending N231.7°E plunging 42.3° brings the two principal stress axes into alignment. The identified stress state from the complete data set has S_1 oriented N5.1°E plunging 1.9°. The stress state ϕ value is $0.984^{1.000}_{0.959}$. The largest difference between the two inversions are the principal stress direction 95% confidence regions. The inversion of nonradial data produced much smaller confidence regions. This is most likely due to the number of breakouts involved in the inversion and the noisy orientations of breakouts. As more breakouts are involved in the inversion, the inversion is unable to exactly match all subsets of the data and it performs an average over the whole data set. It does this by using a more degenerate thrust faulting stress state in the case of the complete data set (with $\phi = 0.984$) as compared to the nonradial data set with ($\phi = 0.924$).

Because the stress misfit inversion results for the nonradial Cook Inlet data set exhibit much smaller principal stress direction 95% confidence limits than the inversion using the complete data set, and because both stress state results are very similar, the nonradial stress state results are chosen as representative of the Cook Inlet field (Figure 5.8). This stress state is almost degenerate thrust faulting, where the S_1 orientation is N179.6°E plunging 2.7°. The 95% confidence limits allow the S_1 azimuth to vary from N156.4°E to N194.5°E and the plunge to vary from 10.1° to -3.6°. The stress state ratio ϕ is $0.924^{0.988}_{0.875}$. As in the case of the 500 m depth groupings of borehole breakouts, the inversion of the complete set of Cook Inlet breakouts yielded in more N–S S_1 orientations than the NNW–SSE or even WNW–ESE orientations observed in subsets of the data.

5.6 Results and Conclusions

5.6.1 Overview of Results

Borehole breakouts from 21 borehole dipmeter logs from Cook Inlet, Alaska were inverted to determine the local stress state. Breakouts reached deviations of 54° and 3,223 m true vertical depth (TVD). The dipmeter data sampled a 38 km long, narrow NNE-trending region of Cook Inlet where oil is produced from NNE-trending anticlines. Breakout selection criteria identified a total of 279 breakouts summing to 2,289 m in length. Data in two boreholes, Granite Point 51 and South Middle Ground Shoals 6, were removed from the data sets prior to inversion due to inconsistent borehole breakout orientations. Thirty-one different inversions were performed on subsets of the cumulative borehole breakout data set. Subsets of the breakout data included breakouts grouped into 500 m TVD depth intervals, and breakouts grouped according to the marker bed in which they occurred. More sets would have been chosen, but a data set had to have at least five breakouts for a successful inversion.

500–1,000 m TVD
Figure 5.10

$n = 6$
$l = 25.8$ m
$\phi = 0.241^{0.256}_{0.222}$

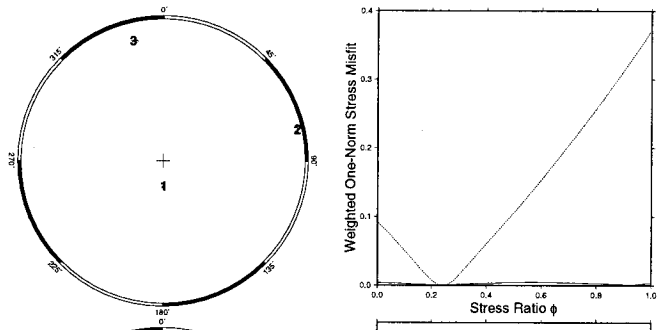

1,000–1,500 m TVD
Figure 5.12

$n = 19$
$l = 136.0$ m
$\phi = 0.998^{1.000}_{0.975}$

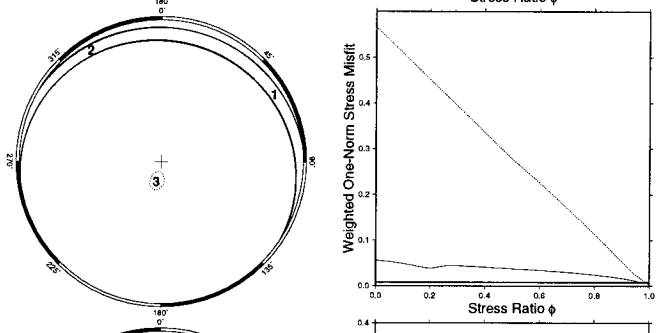

1,500–2,000 m TVD
Figure 5.14

$n = 29$
$l = 160.9$ m
$\phi = 0.886^{0.925}_{0.847}$

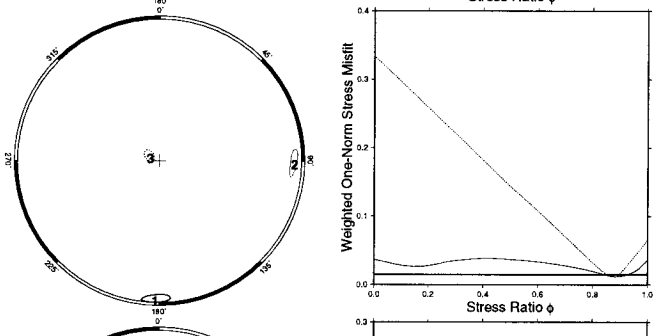

2,000–2,500 m TVD
Figure 5.16

$n = 48$
$l = 321.0$ m
$\phi = 0.236^{0.981}_{0.187}$

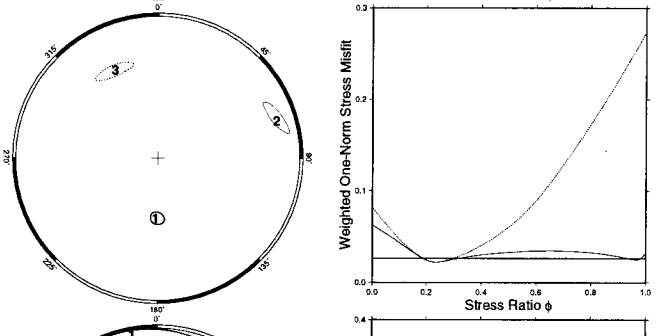

2,500–3,000 m TVD
Figure 5.18

$n = 38$
$l = 228.6$ m
$\phi = 0.972^{0.997}_{0.953}$

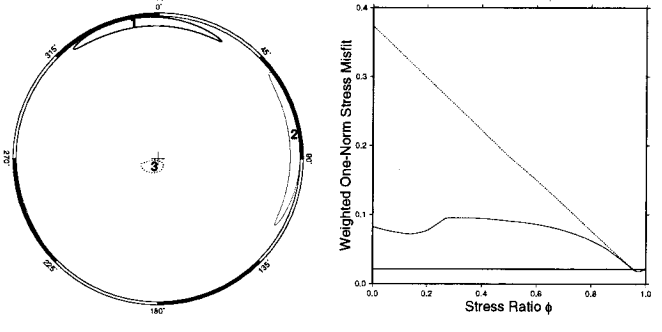

Figure 5.72: Comparison of the nonradial Cook Inlet stress misfit stress inversion results in 500 m increments from 500 to 3,000 m TVD. Plotting conventions are the same as in Figure 5.68.

The genetic algorithm and Powell optimizer technique were used to find the best fitting stress state for each of the thirty-one breakout data sets. The angular misfit measure and the more physically realistic stress misfit measure were used to invert each data subset. Confidence limits were then placed on the results by using statistics of one-norm misfit data to calculate the 95% confidence limits on both the principal stress directions and on the stress state ϕ ratio. In many, but not all cases, both inversions yielded similar stress inversion results for a given breakout data subset. In cases where the two stress inversion results differed, both stress states were examined, but the stress misfit inversion results were always used as the definitive stress state for the breakout data set.

To remove the effect of possible misidentification of tool-drag-induced elongations as "breakouts," radial breakouts were removed from the data sets when at least five nonradial breakouts remained for an inversion. In many, but not all cases, the stress inversion results for the breakout data set without the radial breakouts agreed with the inversion results which included the radial breakouts. In those cases where the results differed, the data set was analyzed further. In the cases when the two inversions were both acceptable, the results exhibiting the smaller 95% confidence limits were declared as being representative of the area covered by the breakouts.

Breakouts were grouped into 500 m TVD depth intervals to study possible variations in the stress state. It is expected that the stress tensor near the earth's surface should have two purely horizontal principal stresses since the earth's free surface requires a purely vertical principal stress direction. The stress away from the free surface is not constrained and rotations of the stress tensor can be expected. Inversions of four different subsets of nonradial breakouts, corresponding to 500 m TVD depth intervals, were performed. These subsets included the Granite Point oil field breakouts, the Baker platform breakouts, the Dillon platform breakouts, and all of the breakouts. The Dillon platform breakouts when separated into 500 m subsets occupied an extremely small portion of the borehole azimuth and borehole deviation space. Because the data were so limited, the inversions results were not considered as representative of the stress state within the 500 m depth intervals and no conclusions could be made regarding these results. The Granite Point breakouts spanned the 2,000–3,000 m TVD depth range. Both the shallow and deep data sets yielded a nearly degenerate thrust faulting stress state. The S_1 azimuth rotated clockwise from N38.9°W (with the 95% confidence limits allowing the azimuth to vary from N89.3°W to N10.5°W) in the shallow section to N17.0°W (with the 95% confidence limits allowing the azimuth to vary from N26.1°W to N0.6°W) in the deeper section. The borehole breakouts identified from the Baker platform were separated into four 500 m depth intervals from 1,000 to 3,000 m TVD. In this data set the S_1 azimuth did not appreciably change as a function of depth. In the shallowest depth range 1,000–1,500 m TVD, the S_1 azimuth was unconstrained. In the deeper three intervals the S_1 azimuth was consistently NNW–SSE aligned. The 2,000 to 2,500 m TVD breakouts yielded a normal faulting stress state with

the S_H azimuth rotated 90° away from the S_H azimuths observed in the other depth intervals. The normal faulting stress state inferred from Baker platform nonradial breakouts in the 2,000 to 2,500 m TVD interval may bear some similarity to the nonradial Granite Point breakout results from the same depth interval. Both the Granite Point and the Baker platform 2,000–2,500 m TVD inverted stress states had the most vertically oriented principal stress direction deviated substantially away from the vertical: $25.2°^{27.1°}_{23.7°}$ for the Granite Point S_3 axis and $27.8°^{32.1°}_{24.4°}$ for the Baker platform S_1 axis. This may indicate of a stress state change from 2,000 to 2,500 m TVD, but given that these are the only two depth intervals available, the quantity of data does not allow a definitive answer to this question.

The inversion results of the complete set of nonradial Cook Inlet borehole breakouts separated into 500 m intervals yielded stress states with N–S directed S_1 azimuths. The stress inversion results from the complete set of breakouts is very similar to the results generated using the Baker platform breakouts. The largest distinction between the stress state derived from the complete Cook Inlet data sets and the subsets of data from each platform or oil field is a N–S oriented S_1 instead of a more NNE–SSE or WNW–ESE orientation. Unlike the Baker platform inversions the inversions of the complete set of Cook Inlet data did not identify any WNW–ESE orientations of S_1. In all of the inverted thrust faulting stress states the S_3 axes were within 30° of vertical.

Borehole breakouts observed in preselected marker horizons were also separated into subsets and inverted. Only the three markers chosen for study in the Baker platform wells contained enough identified breakouts to perform inversions. As a function of increasing depth, the shallowest two inversions of the nonradial breakouts identified in the B40SS and the D markers covering the 1,345 to 2,205 m TVD depth range yielded nearly degenerate thrust faulting stress states with the S_1 azimuth oriented WNW–ESE. The two stress state inversion results from these two different sets of breakouts were nearly identical, supporting the idea that these WNW–ESE directed maximum principal stresses are real. The deepest breakouts from the G3 and G4 markers spanning the 2,410 to 2,769 m TVD depth range yielded a nearly degenerate thrust faulting stress state with the S_1 azimuth oriented NNW–SSE. Between the two shallower WNW–ESE directed S_1 azimuths and the deeper NNW–SSE directed S_1 azimuth is an apparent normal faulting stress state with S_1 nearly vertical, leaving S_2 as the maximum horizontal principal stress direction trending ENE–WSW. The stress states inverted from breakouts in the two shallow marker horizons may represent the maximum compressive stress direction acting perpendicular to the trend of the oil-producing anticline and the stress state in the deeper marker horizons may represent the more NNW–SSE oriented S_H azimuth from the Pacific and North American plate interaction. The normal faulting stress state observed in the intervening marker horizons is anomalous and may represent some sort of transition from the shallow to the deep stress state.

The stress states determined for spatially separate groups of breakouts, such as the Baker and

Granite Point
Figure 5.20

$n = 61$
$l = 365.4$ m
$\phi = 0.976^{0.996}_{0.959}$

Baker platform
Figure 5.28

$n = 154$
$l = 1146.4$ m
$\phi = 0.944^{0.989}_{0.898}$

Dillon platform
Figure 5.56

$n = 63$
$l = 344.5$ m
$\phi = 0.964^{0.983}_{0.939}$

Cook Inlet
Figure 5.8

$n = 142$
$l = 880.5$ m
$\phi = 0.924^{0.988}_{0.875}$

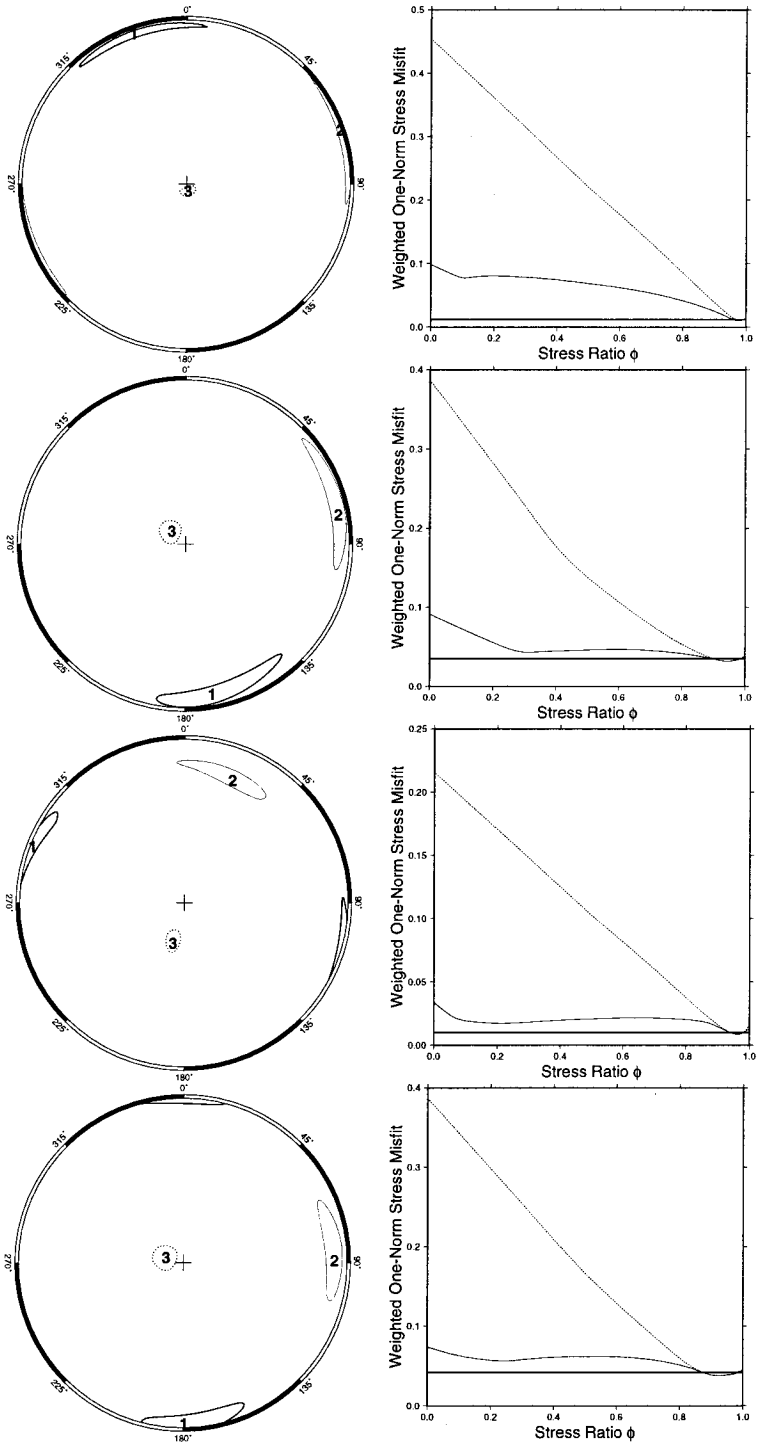

Figure 5.73: Comparison of chosen best fitting stress misfit stress states from each platform or oil field. No stress state inversion included breakouts from Gp51 and Smgs6. (top) Granite Point using radial and nonradial borehole breakouts. (second from top) Baker platform using the nonradial and radial borehole breakouts. (third from top) Dillon platform using the nonradial and radial borehole breakouts excluding the Smgs8 breakout. (bottom) Stress state results using nonradial borehole breakouts from all Cook Inlet wells. Plotting conventions are the same as in Figure 5.68.

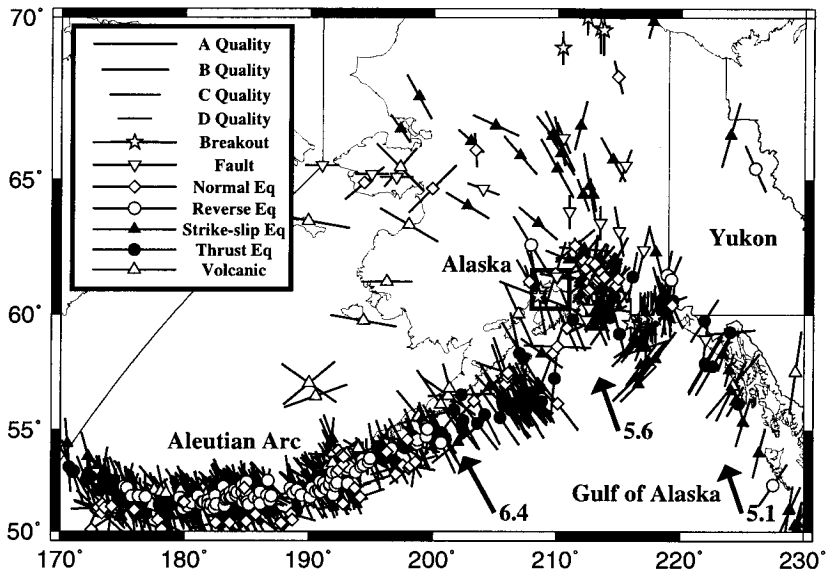

Figure 5.74: Mercator projection plot of the maximum principal stress direction projected to the horizontal across Alaska obtained from different stress measurements, including borehole breakouts, volcanic indicators, and earthquake focal mechanisms. Stress orientations are from this thesis, *Estabrook and Jacob* [1991], and *Jolly et al.* [1994]. Vectors are velocities of the Pacific Plate relative to North America in centimeters per year [*DeMets et al.*, 1990]. Quality of data ranking system from *Zoback and Zoback* [1991]. The boxed area is the area shown in Figure 5.1.

Dillon platform breakouts which are located 10.8 km apart (Figure 5.73), are very similar to one another. This suggests an overall consistency to the stress field in the region and indicates that stress state conclusions from the two platforms are valid.

5.6.2 Regional Stress State

Cook Inlet, Alaska, lies within the NNE–SSW trending forearc basin of the Pacific and North American plate subduction margin (Figures 5.1 and 5.2). The stress field from this collision dominates the stress field across south-central Alaska as determined from many volcanic, earthquake focal mechanism, fault plane solution, and borehole breakout stress indicators [*Estabrook and Jacob*, 1991]. The general stress pattern in south-central Alaska is fan shaped and theoretical models that have the Pacific plate rigidly indenting a plastically deforming North American plate accurately match the regional stress trajectories [*Estabrook and Jacob*, 1991] (Figure 5.74). The global plate motions from *DeMets et al.* [1990] imply that at the mouth of the Cook Inlet Basin the relative plate motion is 5.8 cm/yr directed at N18.6°W. In the Cook Inlet region, multiple stress state indicators suggest a NNW–SSE oriented maximum principal stress direction aligned with the relative plate motions (Figure 5.75). Table 5.3 summarizes some of the specific stress state studies performed in the region. The Cook Inlet breakouts as a whole and subsets of this data set identified an overall NNW–SSE

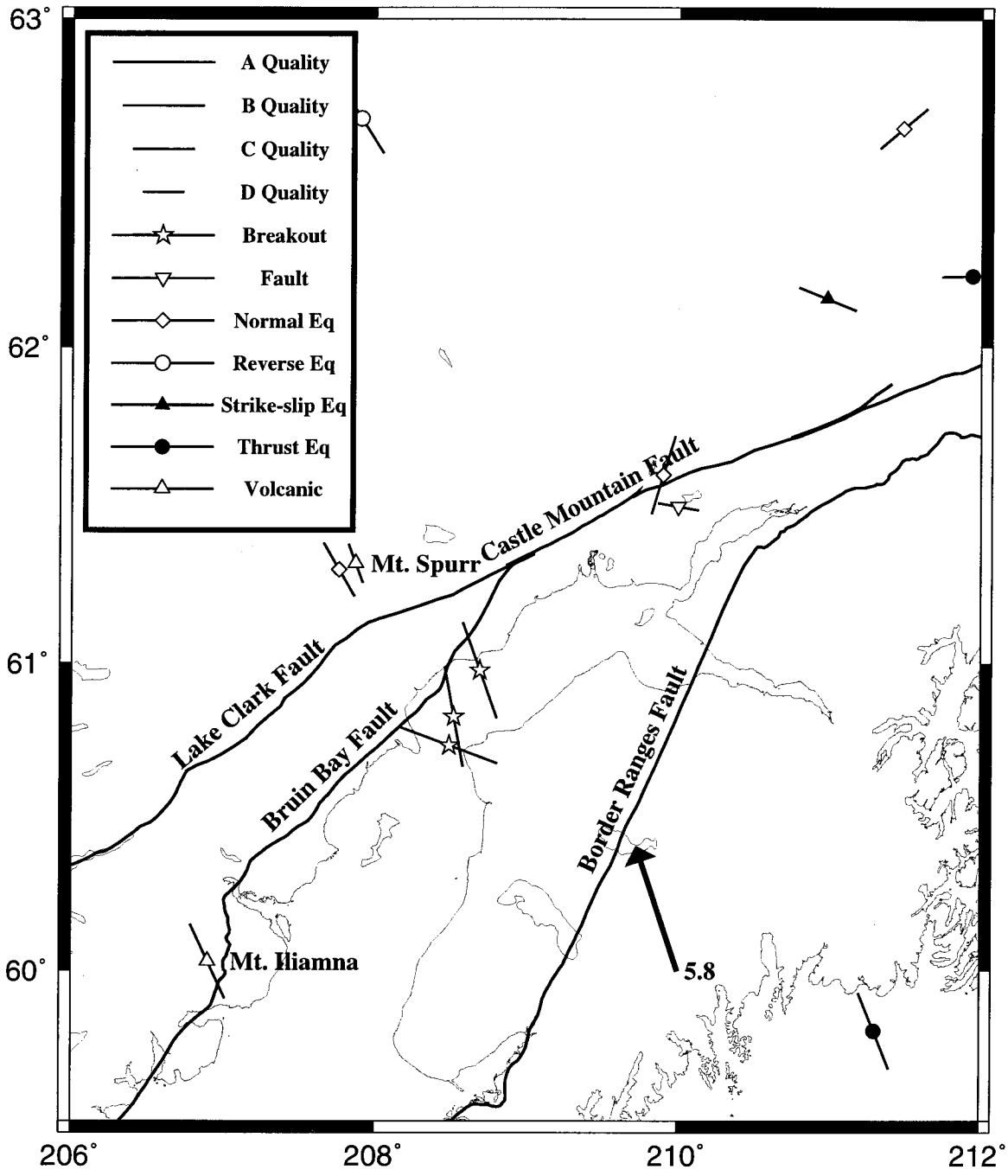

Figure 5.75: Mercator projection plot of the maximum principal stress direction projected to the horizontal around Cook Inlet, Alaska obtained from different stress measurements, including borehole breakouts, volcanic indicators, and earthquake focal mechanisms. Stress orientations are from this thesis, *Estabrook and Jacob* [1991] and *Jolly et al.* [1994]. This figure does not include earthquake focal mechanism stress state inversions where the focal mechanisms cover a large geographic area. Vector is velocity of the Pacific Plate relative to North America in centimeters per year [*DeMets et al.*, 1990]. Quality of data ranking system from *Zoback and Zoback* [1991].

Table 5.3: Stress state results from studies performed in south-central Alaska.

Study	Measurement Type	S_1 or S_H	Azimuth	Plunge
Granite Point breakouts	Breakouts (this study)	S_1	$N19.4^{\circ}{}^{42.4^{\circ}}_{-7.4^{\circ}}W$	$3.4^{\circ}{}^{6.2^{\circ}}_{1.4^{\circ}}$
Baker platform breakouts	Breakouts (this study)	S_1	$N10.2^{\circ}{}^{41.4^{\circ}}_{-10.6^{\circ}}W$	$-7.7^{\circ}{}^{-14.8^{\circ}}_{-0.7^{\circ}}$
Dillon platform breakouts	Breakouts (this study)	S_1	$N69.4^{\circ}{}^{92.4^{\circ}}_{35.6^{\circ}}W$	$1.7^{\circ}{}^{8.2^{\circ}}_{-4.3^{\circ}}$
Cook Inlet breakouts	Breakouts (this study)	S_1	$N0.4^{\circ}{}^{23.6^{\circ}}_{-14.5^{\circ}}W$	$-2.7^{\circ}{}^{3.6^{\circ}}_{-10.1^{\circ}}$
Caldentey and Lana [1990]	Earthquake focal mechanisms	S_1	N26.8 ± 6°W	-0.2°
Lu et al. [1997]	Earthquake focal mechanisms	S_1	N184°E	43°
Jolly et al. [1994]	Earthquake focal mechanisms	S_1	N30°W	30°
Nakamura et al. [1980]	Volcano dikes: Mt. Iliamna	S_H	N25 ± 10°W	0°
Nakamura et al. [1980]	Volcano dikes: Mt. Spurr	S_H	N20 ± 20°W	0°

Table of various stress state studies performed in south-central Alaska. Global plate motions from *DeMets et al.* [1990] imply that at the mouth of the Cook Inlet Basin the relative plate motion is 5.8 cm/yr directed at N18.6°W.

trending horizontal S_1 axis in a nearly degenerate thrust faulting stress state. The exception to this is the Dillon platform breakouts which yielded a NNW–SSE orientation of S_1, which may be related to the local NNE-trending anticlinal structures in the Cook Inlet Basin. *Nakamura et al.* [1980] compiled a preliminary stress map of Alaska using volcanoes and faults to calculate the direction of maximum horizontal stress. Two of *Nakamura et al.*'s [1980] stress indicators were surficial dike features from Mount Iliamna and Mount Spurr, both of which are within $\sim$ 100 km of Cook Inlet, Alaska. The maximum horizontal stress directions calculated were N25 ± 10°W and N20 ± 20°W from Mount Iliamna and Mount Spurr, respectively. To the east of Cook Inlet, *Caldentey and Lana* [1990] studied focal mechanisms from 19 large earthquakes ($m_b \sim$ 5.1–6.2 and $M_s \sim$ 5.4–8.2 from 0 to 40 km depths) in the eastern Gulf of Alaska and found a stress tensor with the S_1 axis oriented N26.8 ± 6°W plunging -0.2°. They found a ϕ value of 0.84 ± 0.05. This stress state does not lie within any of the 95% confidence limits for the individual oil platform stress states nor the Cook Inlet stress state as a whole. However, the *Caldentey and Lana* [1990] and Cook Inlet borehole breakout S_1 azimuths and plunges are visually consistent with each other. The stress state ratio ϕ obtained by *Caldentey and Lana* [1990] is smaller than the ratio yielded by the breakouts. *Lu et al.* [1997] identified the boundaries between regions with different stress states in Alaska using small ($M_L \sim 3$) and large ($M_s \sim 5$) earthquakes. They divided the Alaskan subduction zone into different regions and determined the stress state in each region separately. While the earthquakes ranged in depth from 0 to 140 km and studied the state of stress much deeper than the 3.2 km deep stress measurements done in this study, they identified a stress state with the maximum principal stress direction oriented N184°E plunging 43° in a zone 40–50 km deep underneath Cook Inlet. The ϕ value for their inversion was 0.6. While outside the 95% confidence limits found in this study,

the borehole breakout and earthquake focal mechanism stress states have the same orientation of the maximum principal stress direction. The S_1 axis must rotate from subhorizontal at the 3 km depth level to plunging southward 43° in 40 km depth range as determined by *Lu et al.* [1997]. *Jolly et al.* [1994] performed an earthquake focal mechanism study of events at -3.2 to 30 KM depth in the vicinity of Mount Spurr and found a maximum principal stress direction of N330°E plunging 30° with $\phi = 0.2$. This result has an S_1 azimuth close to the results found here, but the plunge of the maximum principal stress direction, S_1, and the stress state ratio ϕ are very different.

The stress state inversion results using the Powell and genetic algorithm optimizer are very consistent with other stress state indicators in the region. The borehole breakout data also suggest that the minimum principal stress axis remains within 30° of vertical in a thrust faulting stress state. A significant departure away from the NNW–SSE directed S_1 azimuth was observed in small subsets of breakouts identified in specific markers, suggesting that there are small-scale heterogeneities in the stress field over the volume spanned by the data set. Some of the heterogeneity may reflect a stress field similar to that which formed the anticlines.

Chapter 6 Conclusions

This thesis developed a new technique for constraining the complete stress tensor using borehole breakouts identified in nonvertical, i.e. deviated, boreholes. An entire process from digitizing to processing to inverting the borehole data was created. The analysis of borehole caliper arm data for the stress tensor begins by digitizing the caliper arm data and calculating the orientation of maximum elongation. Using a version of *Plumb and Hickman*'s [1985] borehole breakout selection criteria designed for deviated caliper arm data, a selection of borehole breakouts from a given well log can be generated. If the borehole breakout orientations are highly variable, then the technique of averaging the orientations over small borehole azimuth and borehole deviations sections can be used.

A particular strategy was chosen for inverting the borehole breakout data. Because the equations describing the maximum and minimum principal stresses around the borehole wall are nonlinear in the borehole azimuth, in the borehole deviation, and in the farfield stress tensor, a purely forward modeling approach was taken to invert the data. A genetic algorithm technique was chosen, whereby a population of random stress state models are generated and tested to see how well each model fits the borehole breakout data. Those models that fit the data better than other models are allowed to "mate" and create children models that constitute the next generation of models. The better fitting models are randomly paired off and mated in such a way that characteristics of each model are swapped between the two models. This allows for the characteristics of particular models that cause better fits to the data to migrate into different members of the populations of model. After the mating between models, small random changes are made to the children models so that they better explore the model space. Finally, the cycle begins anew and each child model is evaluated to see how well the child fits the data. The genetic algorithm is run for a set number of generations or until the statistics of the misfits for all of the models meet some criteria. The genetic algorithm technique offers several advantages over other inversion techniques. The first is that only a forward model that takes the model parameters and calculates a misfit between the model and data is needed. The genetic algorithm has been shown to effectively search and escape local minima in the model space. However, the genetic algorithm also has several disadvantages. The genetic algorithm does not guarantee that the global minimum has been found in the model space. For this reason, an optimizer that does not depend upon the derivatives of the misfit function is used to take the best fitting model from the genetic algorithm and use that as a starting point for locating the global minimum. The second disadvantage to the genetic algorithm is that it does not produce 95% confidence regions

on the model parameters. To solve this, the model space is searched around the best fitting model and the 95% confidence limits on the model are placed when the misfit between the model and the data reach a specified level. In this study, the misfit function between the data and a model was chosen to be a one-norm misfit and the 95% confidence limits were calculated using the statistics of the one-norm misfit. Two different misfit functions were presented in this thesis. The first, less physically realistic, summed the angular differences between the predicted and measured breakout orientation on the borehole wall. The second, more realistic, misfit measure summed the stress differences between the stress at the measured breakout location and the stress at the predicted breakout location for a particular stress state. The second technique works better at nodal points, where the breakout orientation is expected to vary wildly because the stress concentration around the borehole wall does not vary with azimuth.

The genetic algorithm and the search for the 95% confidence limits was successfully used on three different data sets to invert three sets of borehole breakout data. The first set of data was gathered by *Qian and Pedersen* [1991] and consisted of borehole breakouts identified in the Siljan Deep Drilling Project in Sweden. *Qian and Pedersen* [1991] chose to fit the breakout data using the assumption that one of the principal stress directions in the stress state was vertical. This assumption was tested by the technique developed here. While both the *Qian and Pedersen* [1991] and the genetic algorithm techniques yielded very similar stress states in their inversions, the 95% confidence limits on the principal stress directions identified using the genetic algorithm technique suggested that the stress state was not well constrained. *Qian and Pedersen* [1991] stated that the best fitting stress state was clearly strike-slip faulting with S_H oriented N108.4°E. The results presented in this thesis show that a range of stress states from thrust faulting to strike-slip faulting could easily fit the data. Also, the best fitting stress state did not have a vertical principal stress direction and the data were much better fit using this stress state. Finally, the best fitting stress state determined by *Qian and Pedersen* [1991] did not lie within the 95% confidence limits determined by the technique developed in this thesis.

The second data set examined using the technique developed here was obtained from Unocal and consisted of dipmeter data from wells drilled in offshore Santa Maria Basin near Point Pedernales, southern California. This data set contained one almost vertical well, two nearly horizontal wells, and one moderately dipping well. The dipmeter data from the moderately dipping well contained no identifiable breakouts so the inversion relied upon the vertical and horizontal well logs. Due to the limits quantity of borehole breakout data and the lack of coverage of the borehole azimuth and borehole deviation space, the inversion generated results inconsistent with other regional stress indicators. However, even the S_H direction calculated by assuming that the borehole breakouts identified in the vertical well were caused by a stress state with one vertical principal stress direction was not consistent with the other stress state indicators from the region. This suggests that more

borehole breakout data are needed to sufficiently constrain the stress tensor there.

The last data set was obtained from Unocal and consisted of dipmeter well logs from 21 wells in three groups spanning a 38 km region in offshore Cook Inlet Basin, Alaska. The wells in Cook Inlet, Alaska produce oil from narrow NNE-trending anticlines. The large amount of data from the Cook Inlet field allowed an analysis of the stress state in physically distinct volumes of space. In the first analysis of borehole breakouts, these were grouped according to the bed that the breakouts occurred in. The most interesting results here identified two stress states in distinct beds that showed two markers identifying a WNW–ESE directed S_1 orientation in a nearly degenerate thrust faulting stress state. This orientation is perpendicular to NNE-trending structures in the oil field. Below this stress state was a normal faulting stress state with the S_2 (as S_H) azimuth trending ENE–WSW. Breakouts occurring in a single bed below the normal faulting stress state region were best fit by a nearly degenerate thrust faulting stress state with S_1 trending NNW–SSE parallel to the relative plate motion between the North America plate and the Pacific plate. The clockwise rotation of the stress tensor as a function of depth suggests that the stress field changes from a shallow stress state responsible for the local NNE-trending structures to a deeper one controlled by the North American and Pacific plates collision zone. The observed normal faulting stress state between the two thrust faulting stress states is anomalous and may represent some sort of transition from the shallow to the deep stress state. This behavior was only seen in examining small subsets of borehole breakouts identified in single beds. The quantity of data was not sufficient to allow this analysis on other beds. An analysis of the stress state as determined by breakouts separated into 500 m TVD depth intervals showed no substantial rotation of the S_1 azimuth as a function of depth. However, the most vertically oriented principal stress direction was consistently about 30° off from vertical. This suggests that while the stress state may not change greatly as a function of depth, the assumption of a vertical principal stress direction is not valid and inversions using borehole breakouts should take this into account whenever possible. However, inversion results using limited numbers of breakouts have produced stress states inconsistent with other stress indicators; use of a large number of borehole breakouts covering a large area of the borehole azimuth and deviation space is required to guarantee reliable results. The stress inversions of borehole breakouts grouped by oil field exhibited NNW–SSE oriented S_1 directions in a nearly degenerate thrust faulting stress state. The NNW–SSE orientation of S_1 is consistent with the NNW–SSE orientation of the relative plate between the North American and Pacific plates.

The overall objective of this thesis was to explore a new technique for constraining the complete stress tensor (directions of principal stresses, $S_1 \geq S_2 \geq S_3$, and stress ratio $\phi = (S_2 - S_3)/(S_1 - S_3)$) using borehole breakout data from deviated boreholes. If successful, this technique would provide more complete stress information than has usually been derived from breakouts, and would complement similar information usually derived from earthquake focal mechanisms at greater depths

[*Michael*, 1987]. Examination of three different data sets presented here (Siljan Deep Drilling Project [*Qian and Pedersen*, 1991], Point Pedernales, and Cook Inlet) reveals the limitations of the proposed technique as well as the conditions under which it can be expected to give an accurate assessment of the stress field. This technique works best with a large number of variably oriented boreholes containing high quality borehole breakouts. Some smaller data subsets that covered limited portions of the borehole azimuth and deviation space were shown to produce inconsistent stress state results. Other small data sets, such as the breakouts identified in selected marker horizons from the Baker platform in the Middle Ground Shoals field, yielded stress states consistent with stress states determined fro other small subsets of breakouts.

There are a large number of possible directions that further work could take using the technique developed here. Future work on the genetic algorithm and Powell optimizer technique could include deriving a method where the 95% confidence limits can be derived from the genetic algorithm inversion results instead of requiring an additional time consuming calculation. Additional sources of borehole information would allow for improvements in the stress tensor results. If borehole televiewer or FMS/FMI data were available, then borehole breakouts could be more accurately identified, leading to higher quality borehole breakout data sets for the inversion. By incorporating porepressure and leakoff tests the absolute magnitudes of the stresses could be obtained. In the same manner that the location of borehole breakouts on the borehole wall can be used to infer the farfield stress state, so too can naturally occurring or man-made hydrofractures be used. In particular, where both breakouts and hydrofractures are observed, then a larger quantity of data is available, potentially improving the stress state results. Higher quality and more detailed marker horizon data would allow for greater, more in depth studies of the stress in individual beds. If other, large borehole breakout data sets are gathered, additional refinements in understanding the stress state in small, localized regions, and depth variations in the three-dimensional stress tensor are possible. Large data sets also allow studies of the consistency of the orientations of the principal stress directions. Variations in the stress state as a function of scale length can be studied by comparing the stress state results using the technique developed here (scale lengths from 100's of meters to 10's of kilometers) to other techniques, such as the detailed study of borehole fractures to determine the stress state (scale lengths from meters to 10's of meters) [*Peška and Zoback*, 1995]. In conclusion, a large amount of stress state studies are possible using the technique developed in this thesis.

Appendix A Detailed Mathematical Derivations

A.1 Derivation of the Rotation Matrices

Rotation matrices are needed to take the representation of vectors and tensors from one reference frame to the other. The rotation matrix is derived by initially aligning a coordinate system with the **XYZ** axes and then applying two separate rotations to bring the coordinates into alignment with the **IJK** axes. The first rotation about the **Z** axis rotates the coordinate system clockwise by the angle δ. The resulting coordinate system will be referred as the $\xi\eta\zeta$ axes. The second step rotates the $\xi\eta\zeta$ axes about the ξ axis by a counterclockwise angle Ω, producing the **IJK** coordinate system. The two angles, δ and Ω, in geological terms, are the borehole trend and deviation, respectively.

Define **R** as the matrix which represents the transformation from **XYZ** to **IJK**. The elements of **R** can be obtained by writing the product of the separate rotations, each of which has a relatively simple matrix form. The initial rotation about **Z** can be described by a matrix **B**:

$$\mathbf{x}_{\xi\eta\zeta} = \mathbf{B}\mathbf{x}_{XYZ},$$

where $\mathbf{x}_{XYZ}$ represents a column vector in the **XYZ** coordinate system and $\mathbf{x}_{\xi\eta\zeta}$ represents a column vector in the $\xi\eta\zeta$ system. Similarly, the rotation about the ζ axis can be described by a matrix **A**,

$$\mathbf{x}_{IJK} = \mathbf{A}\mathbf{x}_{\xi\eta\zeta}.$$

Hence the matrix of the complete transformation

$$\mathbf{x}_{IJK} = \mathbf{R}\mathbf{x}_{XYZ}$$

is the product of the successive matrices,

$$\mathbf{R} = \mathbf{A}\mathbf{B}.$$

A matrix for the counterclockwise rotation about the **Z** axis by an angle α is given by

$$\mathbf{B} = \begin{pmatrix} \cos\alpha & \sin\alpha & 0 \\ -\sin\alpha & \cos\alpha & 0 \\ 0 & 0 & 1 \end{pmatrix}.$$

Since the rotation angle δ increases in a clockwise sense, the correct rotation matrix can be obtained if α is replaced with $-\delta$,

$$\mathbf{B} = \begin{pmatrix} \cos(-\delta) & \sin(-\delta) & 0 \\ -\sin(-\delta) & \cos(-\delta) & 0 \\ 0 & 0 & 1 \end{pmatrix} = \begin{pmatrix} \cos\delta & -\sin\delta & 0 \\ \sin\delta & \cos\delta & 0 \\ 0 & 0 & 1 \end{pmatrix}.$$

The second transformation is a counterclockwise rotation by an angle Ω about the ξ axis and is represented by

$$\mathbf{A} = \begin{pmatrix} 1 & 0 & 0 \\ 0 & \cos\Omega & \sin\Omega \\ 0 & -\sin\Omega & \cos\Omega \end{pmatrix}.$$

The product $\mathbf{R} = \mathbf{AB}$ is then

$$\mathbf{R} = \begin{pmatrix} \cos\delta & -\sin\delta & 0 \\ \sin\delta\cos\Omega & \cos\delta\cos\Omega & \sin\Omega \\ -\sin\delta\sin\Omega & -\cos\delta\sin\Omega & \cos\Omega \end{pmatrix}. \tag{A.1}$$

It can be shown that the inverse of a transformation $\mathbf{R}$ is given by the transpose, $\mathbf{R^T}$ [*Goldstein*, 1950]. The transformation from the **IJK** to the **XYZ** coordinate system is given by

$$\mathbf{R^T} = \begin{pmatrix} \cos\delta & \sin\delta\cos\Omega & -\sin\delta\sin\Omega \\ -\sin\delta & \cos\delta\cos\Omega & -\cos\delta\sin\Omega \\ 0 & \sin\Omega & \cos\Omega \end{pmatrix}. \tag{A.2}$$

To complete the final rotation given by the complete Euler angle description, the coordinate system is rotated about the **K** axis by the angle ψ to obtain

$$\begin{aligned} \mathbf{R_3} &= \begin{pmatrix} \cos\psi & \sin\psi & 0 \\ -\sin\psi & \cos\psi & 0 \\ 0 & 0 & 1 \end{pmatrix} \mathbf{R} \\ &= \begin{pmatrix} \cos\psi & \sin\psi & 0 \\ -\sin\psi & \cos\psi & 0 \\ 0 & 0 & 1 \end{pmatrix} \begin{pmatrix} \cos\delta & -\sin\delta & 0 \\ \sin\delta\cos\Omega & \cos\delta\cos\Omega & \sin\Omega \\ -\sin\delta\sin\Omega & -\cos\delta\sin\Omega & \cos\Omega \end{pmatrix} \\ &= \begin{pmatrix} \cos\delta\cos\psi + \sin\delta\cos\Omega\sin\psi & -\sin\delta\cos\psi + \cos\delta\cos\Omega\sin\psi & \sin\Omega\sin\psi \\ -\cos\delta\sin\psi + \sin\delta\cos\Omega\cos\psi & \sin\delta\sin\psi + \cos\delta\cos\Omega\cos\psi & \sin\Omega\cos\psi \\ -\sin\delta\sin\Omega & -\cos\delta\sin\Omega & \cos\Omega \end{pmatrix}. \end{aligned}$$

A.2 Checking the Rotation Matrices

Here the transformation matrix **R** is checked to see that it operates as it should. This will be done by constructing three perpendicular vectors in the geographic reference frame and seeing how each vector is represented in the borehole reference frame.

A.2.1 Construction and Rotation of the Downgoing Borehole Axis Vector

By the definition of the angles δ and Ω, the vector with unit length that points down along the borehole axis is

$$\mathbf{A}_{XYZ} = \begin{pmatrix} \sin\delta\sin\Omega \\ \cos\delta\sin\Omega \\ -\cos\Omega \end{pmatrix}.$$

Transform this vector into the **IJK** system. The result should be the vector with unit length in the $-\mathbf{K}$ direction.

$$\begin{aligned}
\mathbf{A}_{IJK} &= \mathbf{R}\mathbf{A}_{XYZ} \\
&= \begin{pmatrix} \cos\delta & -\sin\delta & 0 \\ \sin\delta\cos\Omega & \cos\delta\cos\Omega & \sin\Omega \\ -\sin\delta\sin\Omega & -\cos\delta\sin\Omega & \cos\Omega \end{pmatrix} \begin{pmatrix} \sin\delta\sin\Omega \\ \cos\delta\sin\Omega \\ -\cos\Omega \end{pmatrix} \\
&= \begin{pmatrix} \cos\delta\sin\delta\sin\Omega - \cos\delta\sin\delta\sin\Omega \\ \sin^2\delta\cos\Omega\sin\Omega + \cos^2\delta\cos\Omega\sin\Omega - \cos\Omega\sin\Omega \\ -\sin^2\delta\sin^2\Omega - \cos^2\delta\sin^2\Omega - \cos^2\Omega \end{pmatrix} \\
&= \begin{pmatrix} 0 \\ 0 \\ -1 \end{pmatrix}
\end{aligned}$$

A.2.2 Construction and Rotation of the I Axis

The representation of the **I** axis in the geographic reference frame is

$$\mathbf{I}_{XYZ} = \begin{pmatrix} \cos\delta \\ -\sin\delta \\ 0 \end{pmatrix}.$$

Following the same procedure as above, then

$$\mathbf{I}_{IJK} = \mathbf{R}\mathbf{I}_{XYZ}$$

$$
\begin{aligned}
&= \begin{pmatrix} \cos\delta & -\sin\delta & 0 \\ \sin\delta\cos\Omega & \cos\delta\cos\Omega & \sin\Omega \\ -\sin\delta\sin\Omega & -\cos\delta\sin\Omega & \cos\Omega \end{pmatrix} \begin{pmatrix} \cos\delta \\ -\sin\delta \\ 0 \end{pmatrix} \\
&= \begin{pmatrix} \cos^2\delta + \sin^2\delta \\ \cos\delta\sin\delta\cos\Omega - \cos\delta\sin\delta\cos\Omega \\ -\cos\delta\sin\delta\sin\Omega + \cos\delta\sin\delta\sin\Omega \end{pmatrix} \\
&= \begin{pmatrix} 1 \\ 0 \\ 0 \end{pmatrix}
\end{aligned}
$$

This agrees nicely with the representation of **I** in the borehole reference frame.

A.2.3 Construction and Rotation of the J Axis

The representation of **J** in the **XYZ** coordinate system is

$$
\mathbf{J}_{XYZ} = \begin{pmatrix} \sin\delta\cos\Omega \\ \cos\delta\cos\Omega \\ \sin\Omega \end{pmatrix}.
$$

Premultiply $\mathbf{J}_{XYZ}$ by the rotation matrix **R** to find **J**'s representation in its own coordinate system.

$$
\begin{aligned}
\mathbf{J}_{IJK} &= \mathbf{R}\mathbf{J}_{XYZ} \\
&= \begin{pmatrix} \cos\delta & -\sin\delta & 0 \\ \sin\delta\cos\Omega & \cos\delta\cos\Omega & \sin\Omega \\ -\sin\delta\sin\Omega & -\cos\delta\sin\Omega & \cos\Omega \end{pmatrix} \begin{pmatrix} \sin\delta\cos\Omega \\ \cos\delta\cos\Omega \\ \sin\Omega \end{pmatrix} \\
&= \begin{pmatrix} \cos\delta\sin\delta\cos\Omega - \cos\delta\sin\delta\cos\Omega \\ \sin^2\delta\cos^2\Omega + \cos^2\delta\cos^2\Omega + \sin^2\Omega \\ -\sin^2\delta\cos\Omega\sin\Omega - \cos^2\delta\cos\Omega\sin\Omega + \cos\Omega\sin\Omega \end{pmatrix} \\
&= \begin{pmatrix} 0 \\ 1 \\ 0 \end{pmatrix}
\end{aligned}
$$

The rotation matrices have been demonstrated to work. The next step is to rotate a stress tensor from one frame to the other, and after that to transform angles measured in the borehole frame to the geographic frame and back again.

A.3 Transformations of Stress Tensors between Frames

In this section the transformations for stress tensors between the borehole and geographic coordinate systems will be derived. The transformation from the geographic coordinate system (**XYZ**) to the borehole coordinate system (**IJK**) is needed to calculate the theoretical breakout position on the borehole wall. The reverse transformation, from the borehole coordinate system to the geographic coordinate system, will not be of any general use, but is presented here nonetheless. The reverse transformation would be useful if the **IJK** axes were to be aligned along the principal stress directions for an arbitrary stress tensor and the **XYZ** representation of the stress state was needed. However, since the **I** axis is defined to be horizontal (Figure 2.1), this introduces a constraint which makes it impossible to align the **IJK** axes with the principal stress directions for all stress tensors. Using the δ, Ω formalism to represent an arbitrary stress tensor is then useless, which reduces the importance of the reverse transformation.

The transformation of a tensor can be easily derived. First, consider a tensor **A** and think of it as an operator acting upon a vector **L** to produce a vector **M**:

$$\mathbf{M} = \mathbf{AL}.$$

If the coordinate system is transformed by a matrix **B** the components of the vector **M** in the new system will be given by

$$\mathbf{BM} = \mathbf{BAL}$$

which can also be written as

$$\mathbf{BM} = \mathbf{BAB}^{-1}\mathbf{BL}.$$

This equation can be interpreted as stating that the operator $\mathbf{BAB}^{-1}$ acting upon the vector **L**, expressed in the new system, produces the vector **L**, likewise expressed in the new coordinates. Therefore, $\mathbf{BAB}^{-1}$ may be considered to be the form taken by the operator **A** when transformed to a new set of axes.

A general three-dimensional tensor has nine components. However, the stress tensor is symmetric and this reduces the number of independent components to six. Let the stress tensor $\mathbf{S}_{XYZ}$ be written as follows in the geographic coordinate system

$$\mathbf{S}_{XYZ} = \begin{pmatrix} S_{ee} & S_{en} & S_{ue} \\ S_{en} & S_{nn} & S_{nu} \\ S_{ue} & S_{nu} & S_{uu} \end{pmatrix},$$

where e, n, and u refer to the east, north and up directions, respectively. The representation of this

tensor in the borehole coordinate system is obtained by applying the above transformation:

$$\begin{aligned}
\mathbf{S}_{IJK} &= \mathbf{R}\mathbf{S}_{XYZ}\mathbf{R}^{\mathbf{T}} \\
&= \begin{pmatrix} \cos\delta & -\sin\delta & 0 \\ \sin\delta\cos\Omega & \cos\delta\cos\Omega & \sin\Omega \\ -\sin\delta\sin\Omega & -\cos\delta\sin\Omega & \cos\Omega \end{pmatrix} \mathbf{S}_{XYZ} \begin{pmatrix} \cos\delta & \sin\delta\cos\Omega & -\sin\delta\sin\Omega \\ -\sin\delta & \cos\delta\cos\Omega & -\cos\delta\sin\Omega \\ 0 & \sin\Omega & \cos\Omega \end{pmatrix} \\
&= \begin{pmatrix} S_{ii} & S_{ij} & S_{ki} \\ S_{ij} & S_{jj} & S_{jk} \\ S_{ki} & S_{jk} & S_{kk} \end{pmatrix}.
\end{aligned}$$

The simplified individual components are

$$\begin{aligned}
S_{ii} &= S_{ee}\cos^2\delta - S_{en}\sin 2\delta + S_{nn}\sin^2\delta \\
S_{jj} &= (S_{nn}\cos^2\delta + S_{en}\sin 2\delta + S_{ee}\sin^2\delta)\cos^2\Omega + S_{uu}\sin^2\Omega + (S_{nu}\cos\delta + S_{ue}\sin\delta)\sin 2\Omega \\
S_{kk} &= (S_{nn}\cos^2\delta + S_{en}\sin 2\delta + S_{ee}\sin^2\delta)\sin^2\Omega + S_{uu}\cos^2\Omega - (S_{nu}\cos\delta + S_{ue}\sin\delta)\sin 2\Omega \\
S_{ij} &= [S_{en}\cos 2\delta + \frac{1}{2}(S_{ee} - S_{nn})\sin 2\delta]\cos\Omega + (S_{ue}\cos\delta - S_{nu}\sin\delta)\sin\Omega \\
S_{jk} &= (S_{nu}\cos\delta + S_{ue}\sin\delta)\cos 2\Omega + \frac{1}{2}(S_{uu} - S_{nn}\cos^2\delta - S_{ee}\sin^2\delta - S_{en}\sin 2\delta)\sin 2\Omega \\
S_{ki} &= (S_{ue}\cos\delta - S_{nu}\sin\delta)\cos\Omega - S_{en}\cos 2\delta\sin\Omega + \frac{1}{2}(S_{nn} - S_{ee})\sin\Omega\sin 2\delta
\end{aligned}$$

To find the reverse transformation, start with the following stress tensor in the borehole coordinate system:

$$\mathbf{S}_{IJK} = \begin{pmatrix} S_{ii} & S_{ij} & S_{ki} \\ S_{ij} & S_{jj} & S_{jk} \\ S_{ki} & S_{jk} & S_{kk} \end{pmatrix}.$$

To represent $\mathbf{S}_{IJK}$ in the geographic coordinate system apply the transformation

$$\mathbf{S}_{XYZ} = \mathbf{R}^{\mathbf{T}}\mathbf{S}_{IJK}\mathbf{R}.$$

The individual components of $\mathbf{S}_{XYZ}$ are

$$\begin{aligned}
S_{ee} &= S_{ii}\cos^2\delta + \sin 2\delta(S_{ij}\cos\Omega - S_{ki}\sin\Omega) + \sin^2\delta(S_{jj}\cos^2\Omega - S_{jk}\sin 2\Omega + S_{kk}\sin^2\Omega) \\
S_{nn} &= S_{ii}\sin^2\delta - \sin 2\delta(S_{ij}\cos\Omega - S_{ki}\sin\Omega) + \cos^2\delta(S_{jj}\cos^2\Omega - S_{jk}\sin 2\Omega + S_{kk}\sin^2\Omega) \\
S_{uu} &= S_{jj}\sin^2\Omega + S_{jk}\sin 2\Omega + S_{kk}\cos^2\Omega \\
S_{en} &= \cos 2\delta(S_{ij}\cos\Omega - S_{ki}\sin\Omega) + \frac{1}{2}\sin 2\delta(S_{jj}\cos^2\Omega + S_{kk}\sin^2\Omega - S_{jk}\sin 2\Omega - S_{ii}) \\
S_{nu} &= S_{jk}\cos\delta\cos 2\Omega - \sin\delta(S_{ki}\cos\Omega + S_{ij}\sin\Omega) + \frac{1}{2}\cos\delta\sin 2\Omega(S_{jj} - S_{kk})
\end{aligned}$$

$$S_{ue} = S_{jk}\sin\delta\cos 2\Omega + \cos\delta(S_{ki}\cos\Omega + S_{ij}\sin\Omega) + \frac{1}{2}\sin\delta\sin 2\Omega(S_{jj} - S_{kk})$$

A.4 Transforming Angles between the Borehole and Geographic Coordinate Systems

In the previous section the rotation matrices for converting the representation of vectors and tensors between the borehole and geographic coordinate systems were found. These matrices will be used to describe how the angles measured in one coordinate system translate to angles in the other coordinate system.

The following derivations transform geographic azimuths to angles measured counterclockwise from the **I** axis and back. I have chosen not to define an "azimuth" for the borehole coordinate system since north is not a natural direction in the **IJK** coordinate system.

Angles are transformed by first constructing a vector in the appropriate coordinate system that points in the direction of the angle. The rotation matrix $\mathbf{R}$, or the inverse rotation matrix $\mathbf{R^T}$, is then used to represent the vector in the other coordinate system. The vector is then projected onto either the **XY** or **IJ** plane. Finally, the angle between the projected vector and a coordinate system axis is calculated.

An ambiguity arises in projecting the vector to either the **XY** or **IJ** plane. Two natural directions exist in the system, the **Z** and **K** directions. In one case, some multiple of **Z** axis can be added to the vector to remove its out of the plane component. In the other case, a multiple of the **K** axis can be used. Both methods are equally valid, but the choice of the proper projection depends upon the use of the transformed angle.

Throughout this work the **Z** vector will be used to remove the out-of-the-plane component of transformed vectors, following the usage of *Mastin* [1988]. More importantly, use of the **K** vector fails for horizontal boreholes. For this reason, the first method will be used to present results and calculations. However, for completeness' sake, the borehole axis projections may prove useful and so will be calculated.

For example, the relative bearing is measured in the borehole coordinate system and the vector representing this angle would be constructed in the **IJK** coordinate system. This vector would then be transformed into the **XYZ** frame using $\mathbf{R^T}$. Finally, the **Z** component of the transformed vector would be removed, either by just setting it to zero which implicitly implies a projection along the **Z** axis, or subtracting a multiple of $\mathbf{K}_{XYZ}$.

A.4.1 Using Vertical Projections to Convert a Borehole Angle into a Geographic Azimuth

Define the angle as measured from the **I** axis towards the **J** axis as a. Then the vector representing this angle is

$$\mathbf{V}_{IJK} = \begin{pmatrix} \cos a \\ \sin a \\ 0 \end{pmatrix}.$$

Multiply $\mathbf{V}_{IJK}$ by $\mathbf{R^T}$ to find the vector as expressed in the geographic reference frame

$$\begin{aligned} \mathbf{V}_{XYZ} &= \begin{pmatrix} \cos\delta & \sin\delta\cos\Omega & -\sin\delta\sin\Omega \\ -\sin\delta & \cos\delta\cos\Omega & -\cos\delta\sin\Omega \\ 0 & \sin\Omega & \cos\Omega \end{pmatrix} \begin{pmatrix} \cos a \\ \sin a \\ 0 \end{pmatrix} \\ &= \begin{pmatrix} \cos\delta\cos a + \sin\delta\cos\Omega\sin a \\ -\sin\delta\cos a + \cos\delta\cos\Omega\sin a \\ \sin\Omega\sin a \end{pmatrix} \end{aligned}$$

A vector parallel to the **Z** axis will be used to project $\mathbf{V}_{XYZ}$ to the horizontal. However, the x and y components of $\mathbf{V}_{XYZ}$ will remain unchanged by the addition of a vector parallel to **Z**. The arctan then is used to find the azimuth, α, that $\mathbf{V}_{XYZ}$ makes with geographic north,

$$\alpha = \tan^{-1}\frac{(\mathbf{V}_{XYZ})_x}{(\mathbf{V}_{XYZ})_y} = \tan^{-1}\left(\frac{\cos\delta\cos a + \sin\delta\cos\Omega\sin a}{-\sin\delta\cos a + \cos\delta\cos\Omega\sin a}\right).$$

A.4.2 Using Vertical Projections to Convert a Geographic Azimuth into a Borehole Angle

The vector representing the geographic azimuth α is written as

$$\mathbf{V}_{XYZ} = \begin{pmatrix} \sin\alpha \\ \cos\alpha \\ 0 \end{pmatrix}.$$

The representation of $\mathbf{V}_{XYZ}$ in the **IJK** reference frame is found using the rotation matrix **R**:

$$\mathbf{V}_{IJK} = \begin{pmatrix} \cos\delta & -\sin\delta & 0 \\ \sin\delta\cos\Omega & \cos\delta\cos\Omega & \sin\Omega \\ -\sin\delta\sin\Omega & -\cos\delta\sin\Omega & \cos\Omega \end{pmatrix} \begin{pmatrix} \sin\alpha \\ \cos\alpha \\ 0 \end{pmatrix}$$

$$= \begin{pmatrix} \cos\delta\sin\alpha - \sin\delta\cos\alpha \\ \sin\delta\cos\Omega\sin\alpha + \cos\delta\cos\Omega\cos\alpha \\ -\sin\delta\sin\Omega\sin\alpha - \cos\delta\sin\Omega\cos\alpha \end{pmatrix}$$

The k component of $\mathbf{V}_{IJK}$ is brought to zero by subtracting a vector parallel to $\mathbf{Z}$ of suitable length. To do this it is first necessary to express the $\mathbf{Z}$ axis in the **IJK** frame.

$$\begin{aligned} \mathbf{Z}_{IJK} &= \begin{pmatrix} \cos\delta & -\sin\delta & 0 \\ \sin\delta\cos\Omega & \cos\delta\cos\Omega & \sin\Omega \\ -\sin\delta\sin\Omega & -\cos\delta\sin\Omega & \cos\Omega \end{pmatrix} \begin{pmatrix} 0 \\ 0 \\ 1 \end{pmatrix} \\ &= \begin{pmatrix} 0 \\ \sin\Omega \\ \cos\Omega \end{pmatrix} \end{aligned}$$

Let b be the multiple of $\mathbf{Z}_{IJK}$ such that

$$0 = (\mathbf{V}_{IJK})_k + b(\mathbf{Z}_{IJK})_k.$$

Then

$$\begin{aligned} 0 &= -\sin\delta\sin\Omega\sin\alpha - \cos\delta\sin\Omega\cos\alpha + b\cos\Omega, \\ b &= \tan\Omega\cos(\alpha - \delta). \end{aligned}$$

The projected vector is

$$\begin{aligned} \mathbf{F}_{IJK} &= \mathbf{V}_{IJK} + b\mathbf{Z}_{IJK} \\ &= \begin{pmatrix} \cos\delta\sin\alpha - \sin\delta\cos\alpha \\ \sin\delta\cos\Omega\sin\alpha + \cos\delta\cos\Omega\cos\alpha \\ -\sin\delta\sin\Omega\sin\alpha - \cos\delta\sin\Omega\cos\alpha \end{pmatrix} + \tan\Omega\cos(\alpha - \delta) \begin{pmatrix} 0 \\ \sin\Omega \\ \cos\Omega \end{pmatrix} \\ &= \begin{pmatrix} \sin(\alpha - \delta) \\ \sec\Omega\cos(\alpha - \delta) \\ 0 \end{pmatrix} \end{aligned}$$

The resulting angle is

$$a = \tan^{-1}\frac{(\mathbf{F}_{IJK})_y}{(\mathbf{F}_{IJK})_x} = \tan^{-1}\left(\frac{\sec\Omega\cos(\alpha - \delta)}{\sin(\alpha - \delta)}\right).$$

A.4.3 Using Borehole Projections to Convert a Borehole Angle into a Geographic Azimuth

Define a as the angle as measured from the **I** axis towards the **J** axis. Then the vector representing this angle is

$$\mathbf{V}_{IJK} = \begin{pmatrix} \cos a \\ \sin a \\ 0 \end{pmatrix}.$$

Multiply $\mathbf{V}_{IJK}$ with $\mathbf{R}^{\mathbf{T}}$ to find the vector as expressed in the geographic reference frame,

$$\begin{aligned} \mathbf{V}_{XYZ} &= \begin{pmatrix} \cos\delta & \sin\delta\cos\Omega & -\sin\delta\sin\Omega \\ -\sin\delta & \cos\delta\cos\Omega & -\cos\delta\sin\Omega \\ 0 & \sin\Omega & \cos\Omega \end{pmatrix} \begin{pmatrix} \cos a \\ \sin a \\ 0 \end{pmatrix} \\ &= \begin{pmatrix} \cos\delta\cos a + \sin\delta\cos\Omega\sin a \\ -\sin\delta\cos a + \cos\delta\cos\Omega\sin a \\ \sin\Omega\sin a \end{pmatrix} \end{aligned}$$

Remove the z component of $\mathbf{V}_{XYZ}$ by subtracting a vector parallel to **K** of suitable length. Find the representation of **K** in the geographic reference frame.

$$\begin{aligned} \mathbf{K}_{XYZ} &= \begin{pmatrix} \cos\delta & \sin\delta\cos\Omega & -\sin\delta\sin\Omega \\ -\sin\delta & \cos\delta\cos\Omega & -\cos\delta\sin\Omega \\ 0 & \sin\Omega & \cos\Omega \end{pmatrix} \begin{pmatrix} 0 \\ 0 \\ 1 \end{pmatrix} \\ &= \begin{pmatrix} -\sin\delta\sin\Omega \\ -\cos\delta\sin\Omega \\ \cos\Omega \end{pmatrix} \end{aligned}$$

Find b such that

$$0 = (\mathbf{V}_{XYZ})_z + b(\mathbf{K}_{XYZ})_z.$$

Then

$$\begin{aligned} 0 &= \sin\Omega\sin a + b\cos\Omega, \\ b &= -\sin a\tan\Omega. \end{aligned}$$

So the resulting vector which lies in the horizontal plane is

$$\mathbf{F}_{XYZ} = \mathbf{V}_{XYZ} + b\mathbf{K}_{XYZ}$$

$$= \begin{pmatrix} \cos\delta\cos a + \sin\delta\cos\Omega\sin a + \sin a\tan\Omega\sin\delta\sin\Omega \\ -\sin\delta\cos a + \cos\delta\cos\Omega\sin a + \sin a\tan\Omega\cos\delta\sin\Omega \\ 0 \end{pmatrix}$$

and the geographic azimuth, α, is the arc tangent of the x component of the above vector divided by its y component:

$$\alpha = \tan^{-1}\frac{(\mathbf{F}_{XYZ})_x}{(\mathbf{F}_{XYZ})_y} = \tan^{-1}\left(\frac{\cos\delta\cos a + \sin\delta\cos\Omega\sin a + \sin a\tan\Omega\sin\delta\sin\Omega}{-\sin\delta\cos a + \cos\delta\cos\Omega\sin a + \sin a\tan\Omega\cos\delta\sin\Omega}\right).$$

A.4.4 Using Borehole Projections to Convert a Geographic Azimuth into a Borehole Angle

The vector representing the geographic azimuth α is written as

$$\mathbf{V}_{XYZ} = \begin{pmatrix} \sin\alpha \\ \cos\alpha \\ 0 \end{pmatrix}.$$

This is rotated into the borehole reference frame with the rotation matrix $\mathbf{R}$:

$$\begin{aligned} \mathbf{V}_{IJK} &= \begin{pmatrix} \cos\delta & -\sin\delta & 0 \\ \sin\delta\cos\Omega & \cos\delta\cos\Omega & \sin\Omega \\ -\sin\delta\sin\Omega & -\cos\delta\sin\Omega & \cos\Omega \end{pmatrix}\begin{pmatrix} \sin\alpha \\ \cos\alpha \\ 0 \end{pmatrix} \\ &= \begin{pmatrix} \cos\delta\sin\alpha - \sin\delta\cos\alpha \\ \sin\delta\cos\Omega\sin\alpha + \cos\delta\cos\Omega\cos\alpha \\ -\sin\delta\sin\Omega\sin\alpha - \cos\delta\sin\Omega\cos\alpha \end{pmatrix} \\ &= \begin{pmatrix} \sin(\alpha-\delta) \\ \cos(\alpha-\delta)\cos\Omega \\ -\cos(\alpha-\delta)\sin\Omega \end{pmatrix} \end{aligned}$$

The vector addition of a suitable, parallel to $\mathbf{K}$ vector to $\mathbf{V}_{IJK}$ will result in a vector with a 0 k component. This addition will not affect the i and j component of $\mathbf{V}_{IJK}$, so the angle a can be quickly determined to be

$$a = \tan^{-1}\frac{(\mathbf{V}_{IJK})_j}{(\mathbf{V}_{IJK})_i} = \tan^{-1}\left(\frac{\cos(\alpha-\delta)\cos\Omega}{\sin(\alpha-\delta)}\right).$$

Appendix B Cook Inlet: Individual Discussion of Wells

This appendix presents discussion of the important notes, problems, or inconsistent breakout orientations from each Cook Inlet well. No stress state inversions were done using the breakouts identified from an individual well since the number of breakouts was small or occupied a limited area of the borehole orientation space as seen on lower hemisphere stereograph projection plots.

B.1 Gp11-13rd

Five different sections of digital dipmeter data, along with the directional survey and marker data, were received from Unocal. The maximum hole deviation in the digital dipmeter data is 19°. The five different sections of hole span the log depth ranges 2,398–2,773 m (file 30), 2,775–3,062 m (file 29), 2,982–3,062 m (file 28), 3,066–3,293 m (file 6), and 3,293–3,519 m (file 5). The file refers to the file number of the digital dipmeter Unocal sent. The depth range of the data from file 29 completely overlaps the depth range of the data in file 28. Since only one log is needed to cover the same depth interval and since file 29 covers a larger depth range than file 28, file 28 was not used.

This hole has relatively constant tool orientations throughout most of the hole according to the long stretches of almost constant pad 1 azimuth (Figure B.1). The caliper arm data is fairly well-behaved, with several sections of washed-out hole and 75 sections of in-gauge hole longer than 0.5 m totaling 186.9 m in length.

Out of the 1,1119 m of logged hole, 80.8 m of borehole breakouts were identified. All of the breakouts found are shown in Figure B.2. The two dipmeter runs (file 28 and file 29) that covered the same interval of hole from 2,982 to 3,062 m did not have any identified breakouts. Since all of the nonradial breakouts occur in the same 500 m interval from 2,500 to 3,000 m, no separate plots of the breakouts as a function of depth are shown.

Breakouts were found in the following markers: T3940SS (2 breakouts for 20.2 m), B3940SS (1 breakout for 0.4 m), TM40 (1 breakout for 4.4 m), T4142SS (1 breakout for 3.7 m), B4142SS (1 breakout for 0.2 m), B4344SS (1 breakout for 5.4 m), TM45 (2 breakouts for 7.8 m), TM46 (2 breakouts for 10.8 m), TMX (2 breakouts for 7.3 m), TM46 (1 breakout for 4.2 m), TMX (1 breakout for 1.8 m), T46XSSA47 (1 breakout for 1.5 m), B46XSSA47 (2 breakouts for 7.4 m), and TM48 (2 breakouts for 7.6 m). Breakouts may lie in more than one marker, which accounts for those markers that list breakouts shorter than the minimum breakout length of 3 m.

At shallower depths, the breakout pattern varies smoothly as a function of depth. At 2,422 m TVD, the breakouts are oriented N159.6°E and slowly rotate to N118.8°E at 2,809 m TVD. Eight meters lower is another breakout oriented N30.7°E, an 88.1° counterclockwise orientation change. From this point on, the breakouts continue to vary slowly to N1°W. The sharp transition occurs where the 8.5 m wide T46XSSA47 marker is bounded by TMX on top and by the B46XSSA47 marker on the bottom. While no information about the material properties or about the dips of the formations near this transition were received from Unocal, it is possible that material property or bedding dip differences between the two markers caused this large transition. The marker file does not indicate that any faults were crossed by this well. Only one breakout was identified in the T45XSS marker (Figure B.3).

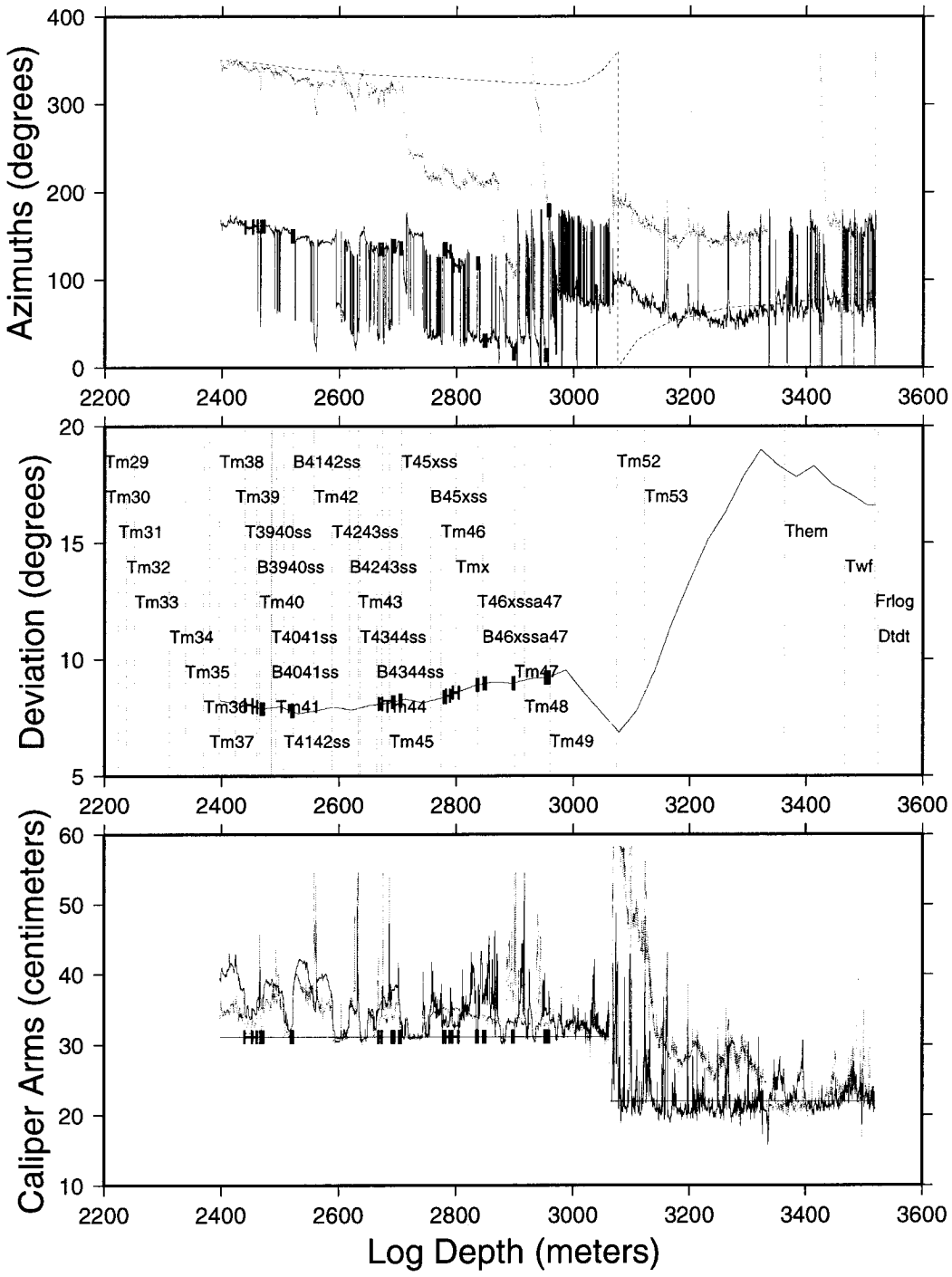

Figure B.1: Plots of the caliper-calibrated and declination-corrected digitized dipmeter and derived quantities data as a function of well depth from well Gp11-13rd. (top) Borehole elongation direction (solid line), pad 1 azimuth (dotted line), and borehole azimuth (dashed line). (middle) Borehole deviation (solid curve) and location of marker horizons (vertical lines with labels). (bottom) Bit size (straight solid line), caliper arm 1 (solid line), and caliper arm 2 (dotted line). Selected breakout regions are plotted as horizontal bars showing the depth extent of the breakouts.

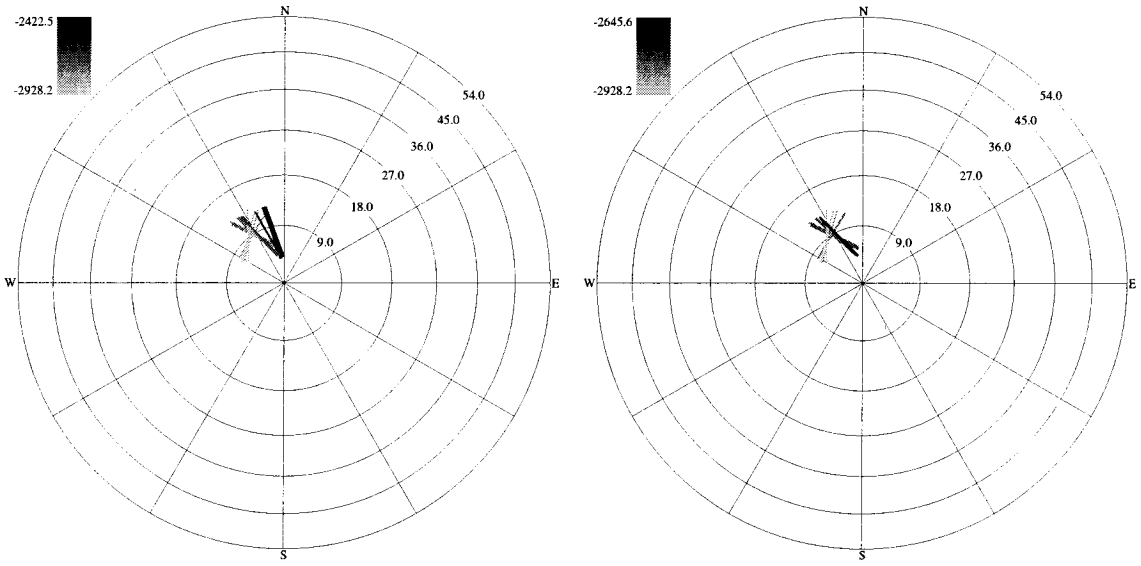

Figure B.2: Lower hemisphere stereographic projection plots of the selected breakouts from well Gp11-13rd. Line widths are proportional to the breakout length. (left) All selected breakouts. (right) All nonradial breakouts where the **IJK** breakout angle is not within 15° of the high side of the hole.

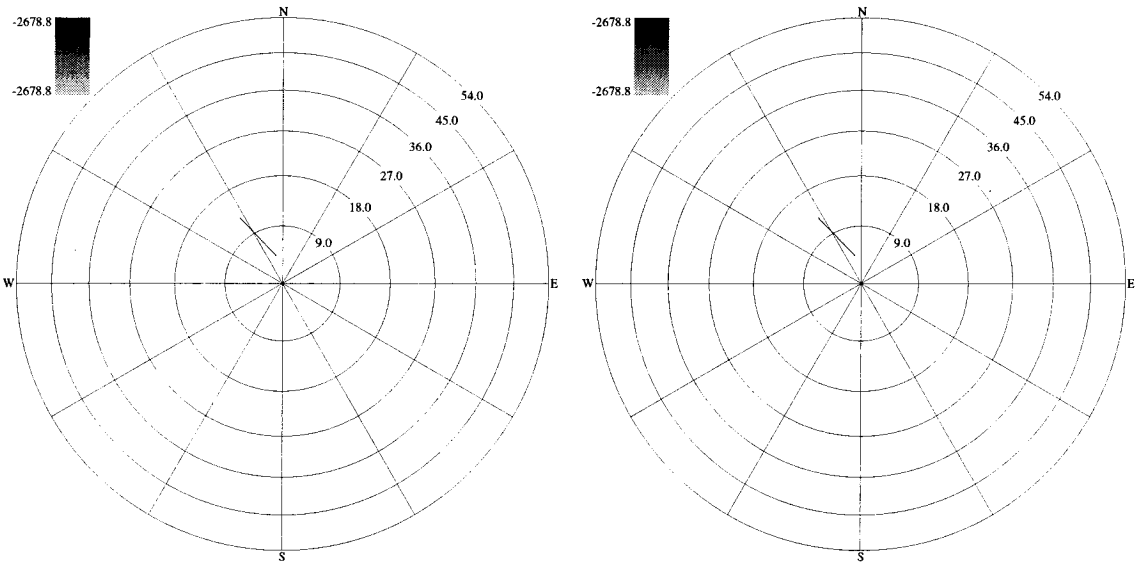

Figure B.3: Lower hemisphere stereographic projection plots of the selected breakouts from well Gp11-13rd in marker T45XSS. Line widths are proportional to the breakout length. (left) All selected breakouts in T45XSS. (right) All nonradial breakouts in T45XSS where the **IJK** breakout angle is not within 15° of the high side of the hole.

B.2 Gp13rd

Five different digitally logged sections of Gp13rd were received. The five different sections span the log depth ranges 2,437–2,546 m (file 11), 2,549–2,574 m (file 10), 2,565–2,771 m (file 8), 2,869–3,054 m (file 5), 2,965–3,137 m (file 3). The depth range of the data from file 8 almost completely overlaps the depth range of the data in file 10. Since only one well log is needed to cover the same depth interval and since file 8 covers a larger depth range than file 10, file 10 was not used in any breakout calculations. No breakouts were found in either file in the overlapping interval. File 3 and 5 also partially overlap each other. File 3 had two breakouts, the first at 2,990.1 m log depth which was not found in the other well log, and the second at depth 3,054.4 m was on the boundary of where file 5 ends. File 5 also has two breakouts which are just above the shallowest logged depth in file 3. Since there are no consistent breakouts found in both logs and one breakout is found in only one hole, file 5 was used since it has two breakouts that are not in conflict with the other file.

The maximum deviation throughout these sections is 17.4°, while the maximum deviation of the hole is 28.2°. The dipmeter tool had a tendency to rotate when it logged in-gauge sections of the hole (Figures B.4). In-gauge sections of the hole longer than 0.5 m accounted for 112.4 m of the dipmeter data, with an average length of 3.4 m.

The breakout selection scheme identified 28.8 m of breakouts averaging 5.8 m in length. All of the borehole breakouts are plotted in Figure B.5 and the nonradial breakouts separated into 500 m TVD intervals are plotted in Figure B.6. No breakouts were found in the T45XSS marker. The breakouts were observed in the T4243SS (2 breakouts for 8.7 m), the B4243SS (1 breakout for 0.7 m), and the T46XSSA47 (2 breakouts for 10.1 m) markers.

The breakouts are observed over a 487 m TVD interval from 2,308 m to 2,796 m. The breakout orientations range from ESE–WNW to NE–NW. However, as the borehole orientation moves from a WSW trend to a SE trend, the breakouts orientations decrease from N109.8°E to N48.1°E and than increase to N75.8°E. Since the breakouts from Gp13rd do not cover a large amount of borehole orientation space in the lower hemisphere stereograph projection plots, doing a numerical inversion of the data would not prove useful. It does not appear that any simple stress state would explain the breakout pattern due to the inconsistency of breakout rotations as a function of depth. However, the two deepest breakouts that are rotated clockwise with respect to the breakouts above them were found to be in the T46XSSA47 marker, the same marker where an 88.1° counterclockwise rotation was observed in Gp11-13rd's breakout orientations. The T46XSSA47 could have substantially different bedding dips or material properties to affect the stress state and hence the observed breakouts.

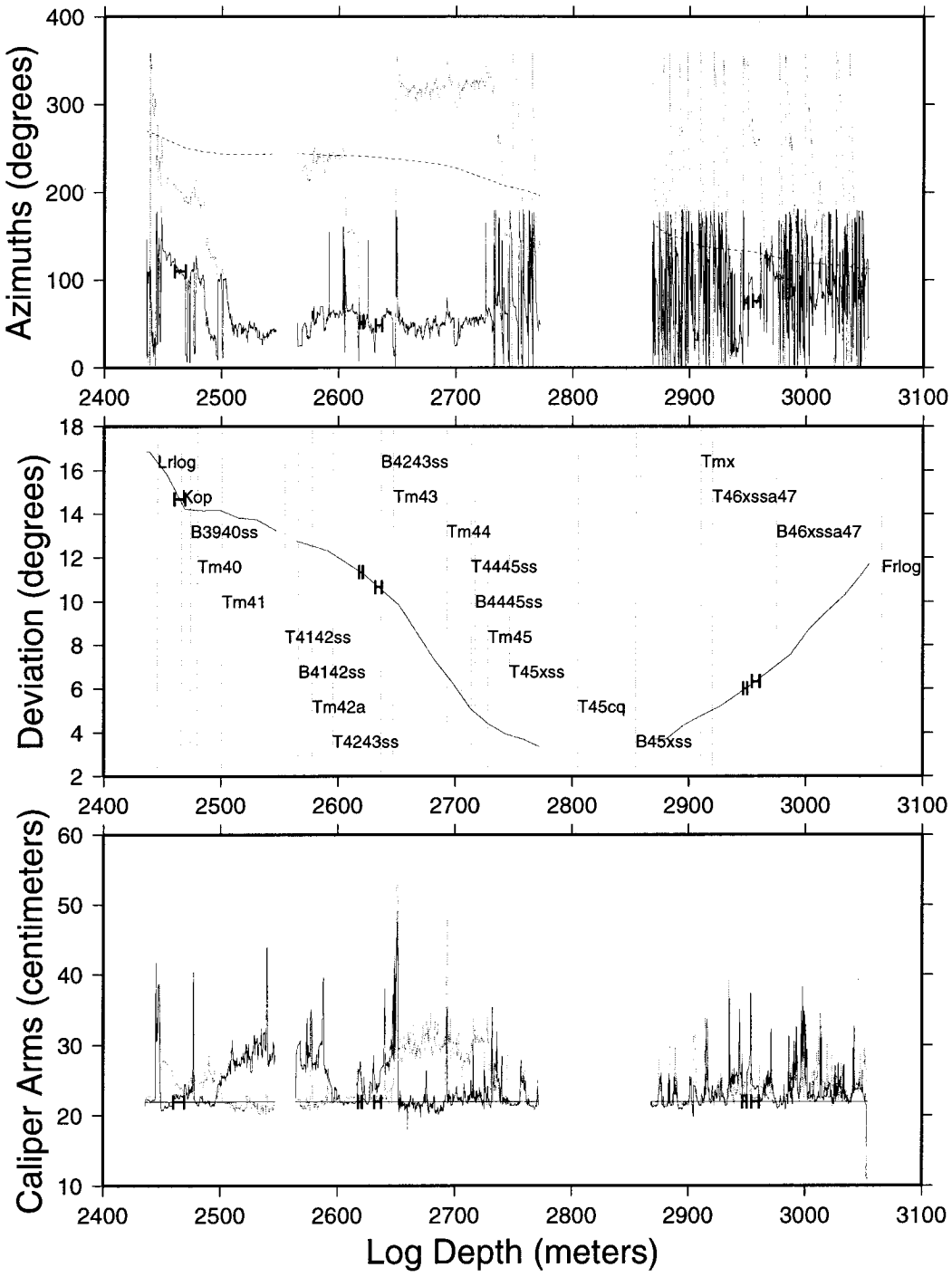

Figure B.4: Plots of the caliper-calibrated and declination-corrected digitized dipmeter and derived quantities data as a function of well depth from well Gp13rd. (top) Borehole elongation direction (solid line), pad 1 azimuth (dotted line), and borehole azimuth (dashed line). (middle) Borehole deviation (solid curve) and location of marker horizons (vertical lines with labels). (bottom) Bit size (straight solid line), caliper arm 1 (solid line), and caliper arm 2 (dotted line). Selected breakout regions are plotted as horizontal bars showing the depth extent of the breakouts.

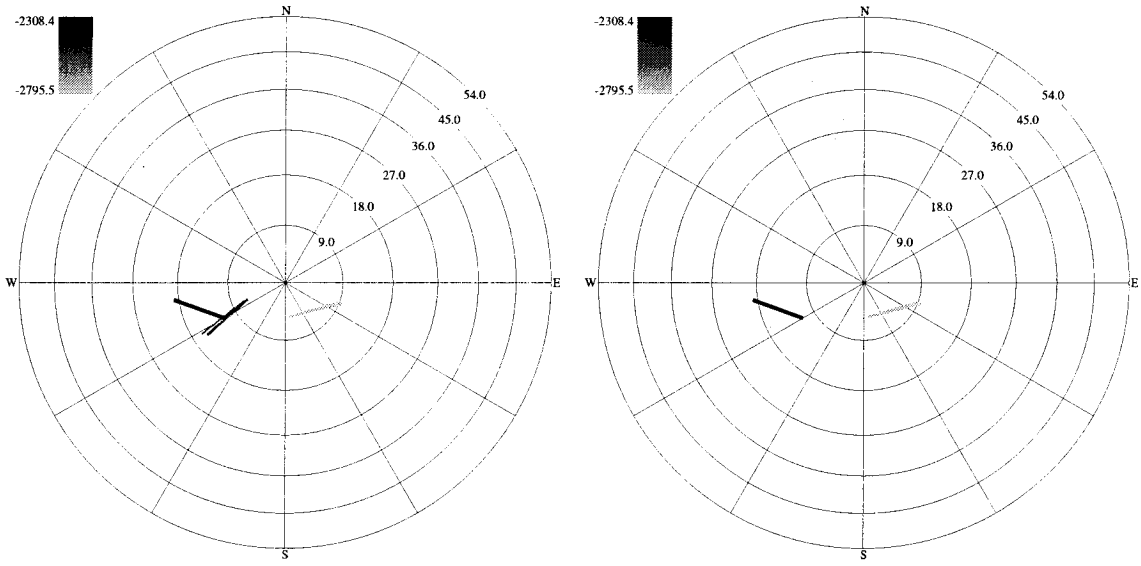

Figure B.5: Lower hemisphere stereographic projection plots of the selected breakouts from well Gp13rd. Line widths are proportional to the breakout length. (left) All selected breakouts. (right) All nonradial breakouts where the **IJK** breakout angle is not within 15° of the high side of the hole.

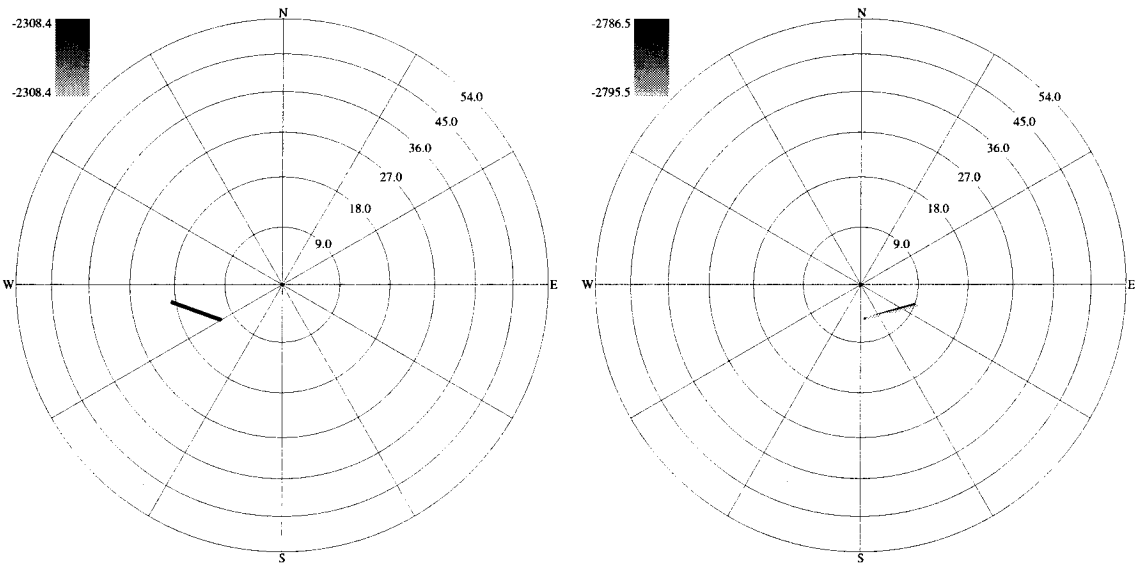

Figure B.6: Lower hemisphere stereographic projection plots of all nonradial breakouts from well Gp13rd between the true vertical depths of 2000–2500 m on the left and 2500–3000 m on the right.

B.3 Gp20rd

The digital dipmeter data for Granite Point 20rd came as three separate data files spanning the log depth ranges 2,127–2,438 m (file 8), 2,439–2,743 m (file 7), 2,744–3,179 m (file 6). The raw digital dipmeter data along with the calculated borehole elongation directions are shown in and combined in Figure B.7. Over half of the logged interval has one caliper arm in-gauge with the other caliper arm broken out. In only 110.1 m, or 10.5%, of the logged interval were both caliper arms in-gauge over a 0.5 m interval. No substantial tool rotation occurred in these intervals, probably due to the short (5.5 m average) length of the in-gauge sections.

The breakout selection scheme identified 12 breakouts having a combined length of 62.3 m. The deeper section of hole, below roughly 2,800 m log depth, is much more consistent and in-gauge than the upper section of hole. However, the shallower section had all but two of the identified breakouts. The shallower section is identified by one caliper arm consistently being in-gauge, while the other caliper arm is consistently at least 5 cm out of gauge. Only in those sections where the larger caliper arm showed enough caliper arm length consistently were breakouts identified.

Breakouts were identified in the following markers: TM26 (5 breakouts for 28.2 m), TM27 (1 breakout for 3.7 m), TM28 (1 breakout for 4.4 m), TM29 (2 breakouts for 6.5 m), TM35 (1 breakout for 3 m), TM43 (1 breakout for 4.1 m), TM44 (1 breakout for 3.7 m), and T4445SS (1 breakout for 0.7 m).

Granite Point 20rd breakouts have a consistent breakout orientation of roughly N65°E regardless of the borehole azimuth, which is varies from S82°W to S102°W, and the borehole deviation, which varies from 18° to 45° (Figure B.8). Since the breakout orientations are so constant, any stress state nodal points would not plot near the measured data on the lower hemisphere stereographic projection plot. Since all of the nonradial breakouts occur in the 2,000 to 2,500 m depth interval, the breakouts are not plotted separately in 500 m intervals. Also, no breakouts were found in the T45XSS marker.

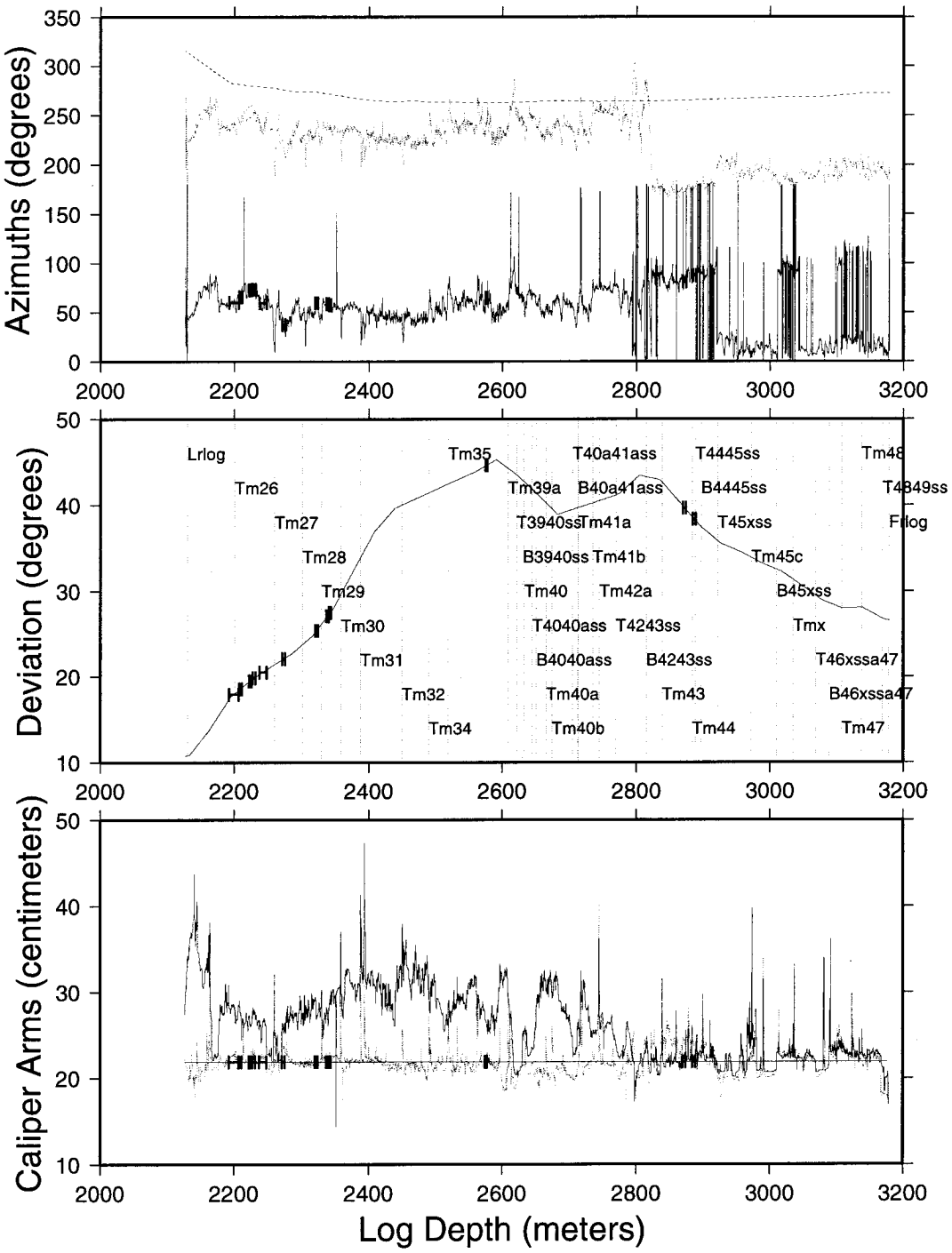

Figure B.7: Plots of the caliper-calibrated and declination-corrected digitized dipmeter and derived quantities data as a function of well depth from well Gp20rd. (top) Borehole elongation direction (solid line), pad 1 azimuth (dotted line), and borehole azimuth (dashed line). (middle) Borehole deviation (solid curve) and location of marker horizons (vertical lines with labels). (bottom) Bit size (straight solid line), caliper arm 1 (solid line), and caliper arm 2 (dotted line). Selected breakout regions are plotted as horizontal bars showing the depth extent of the breakouts.

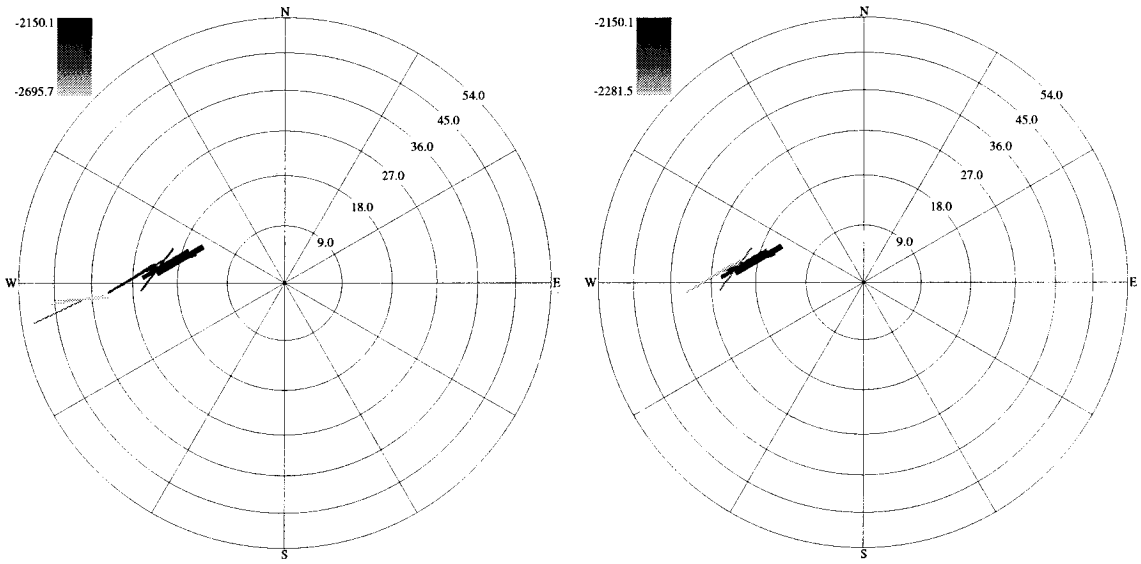

Figure B.8: Lower hemisphere stereographic projection plots of the selected breakouts from well Gp20rd. Line widths are proportional to the breakout length. (left) All selected breakouts. (right) All nonradial breakouts where the **IJK** breakout angle is not within 15° of the high side of the hole.

B.4 Gp32rd

Two digital dipmeter files, file 2 and file 3, were received for Granite Point 32rd. The top of both logged sections begin at 3,099 m log depth. File 3, which stops at 3,160 m log depth, is the shorter of the two sections; file 2 stops at 3,266 m. Both dipmeter runs have the same character caliper arm and pad 1 azimuth data (Figures B.9 and B.10). The dipmeter did not rotate throughout either logging run due to a sizeable difference between the two caliper arm diameters. No tool rotation occurred in the 8 different in-gauge sections of hole longer than 0.5 m, which amounted to 36.3 m (18%) of the dipmeter data.

The depth range 3,0989-3,160 m was logged with both dipmeter runs and over this depth interval, both dipmeter runs had 6 identified breakouts. The breakouts from each hole had similar depths, lengths, and most importantly, **IJK** breakout angle (the angle between the high side of the hole and the breakout as measured in the plane perpendicular to the borehole axis). Table B.1 lists the log depth, the breakout length, the **XYZ** breakout azimuth, and the **IJK** breakout angle. The largest difference between the measured **IJK** breakout angles for similarly measured breakouts is 4.9° for the second shallowest breakout. While the **IJK** breakout angles are very consistent between the two dipmeter runs, the total length of breakouts identified differs by 9.7 m, which is large given that the two dipmeters logged only 61 m of common hole. This difference could be due to the two separate logging runs where the tool drag from the first gauged out the bottom of the hole enough for the second run to identify more breakouts. Since the file 2 dipmeter log is longer, the remaining analysis of the breakout data was done using file 2.

Plotting the breakout azimuths on a lower hemisphere stereographic projection plot shows that all of the breakouts are aligned with the high and low sides of the borehole (Figure B.11). This observation combined with the observation of no pad 1 rotation in the top plot of Figure B.9 suggests that the dipmeter was tracking only the high and low side of the hole and that these breakouts are questionable. Most of the stress state analyses done later in this chapter use nonradial breakouts, and so the data from this borehole will be discarded. Even though the breakouts are questionable, it is an encouraging sign to have two dipmeter runs identify breakouts in same positions of the borehole.

None of the identified breakouts were found in the T45XSS marker. Breakouts were identified in the TM39AEST (2 breakouts for 13.7 m), T3940SS (2 breakouts for 8.5 m), B3940SS (1 breakout for 0.1 m), TM40 (2 breakouts for 8.0 m), T4040ASS (1 breakout for 3.4 m), B4040ASS (1 breakout for 11.2 m), TM40A (1 breakout for 33.5 m), B40A41ASS (1 breakout for 5.2 m), T40A41ASS (1 breakout for 3.0 m), TM41A (1 breakout for 3.0 m), and the T41A42ASS (3 breakouts for 16.4 m) markers.

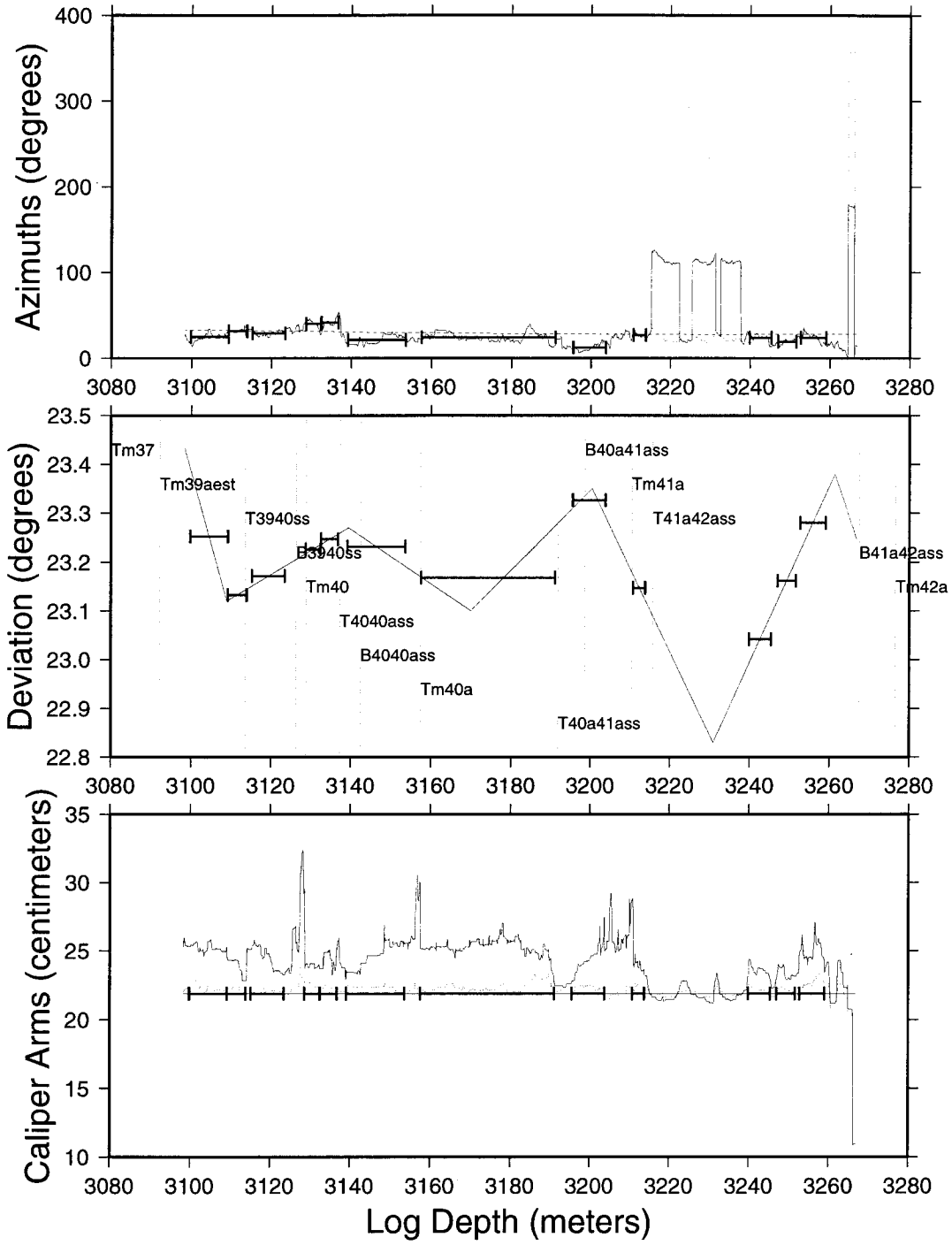

Figure B.9: Plots of the caliper-calibrated and declination-corrected digitized dipmeter and derived quantities data as a function of well depth from well Gp32rd file 2. (top) Borehole elongation direction (solid line), pad 1 azimuth (dotted line), and borehole azimuth (dashed line). (middle) Borehole deviation (solid curve) and location of marker horizons (vertical lines with labels). (bottom) Bit size (straight solid line), caliper arm 1 (solid line), and caliper arm 2 (dotted line). Selected breakout regions are plotted as horizontal bars showing the depth extent of the breakouts.

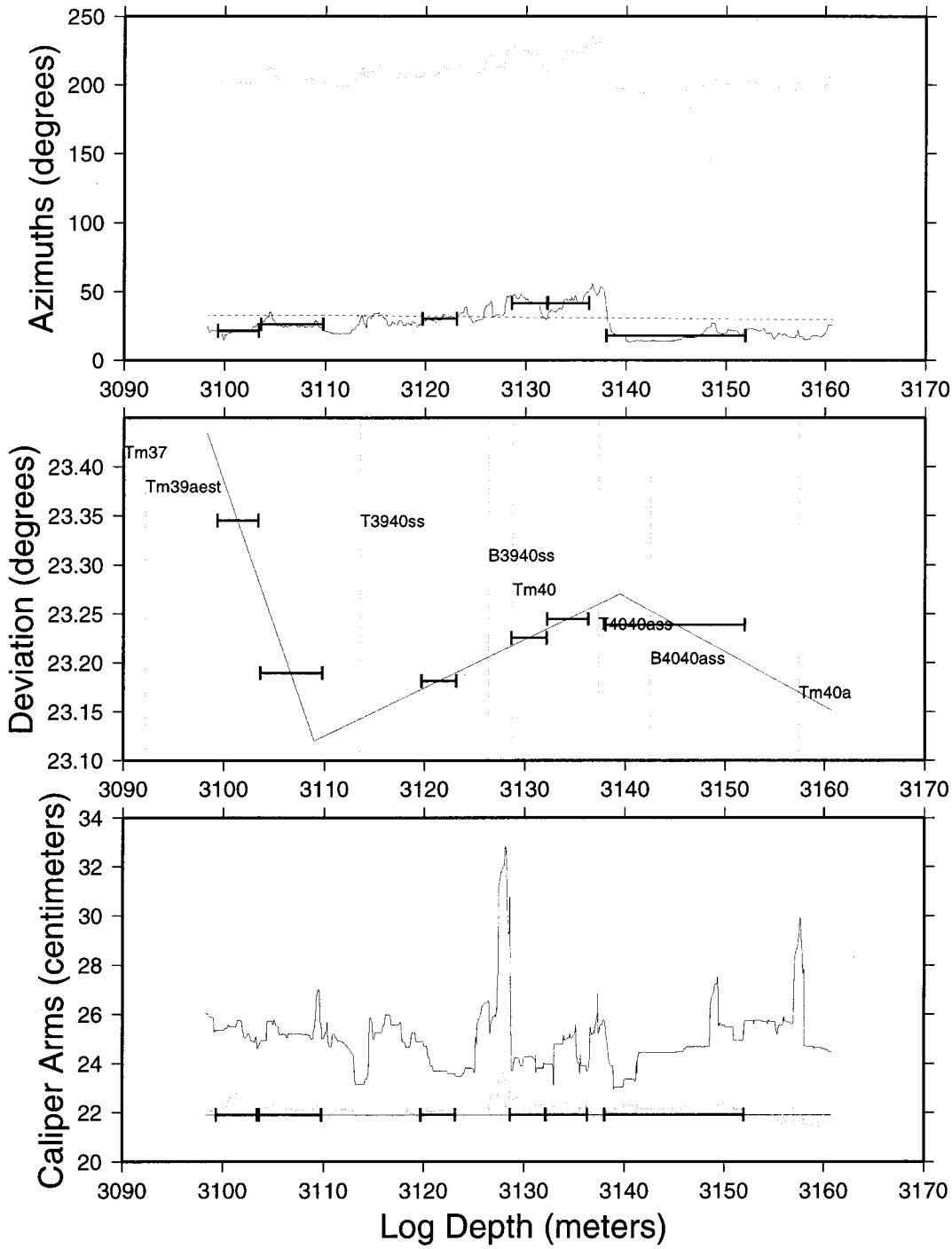

Figure B.10: Plots of the caliper-calibrated and declination-corrected digitized dipmeter and derived quantities data as a function of well depth from well Gp32rd file 3. (top) Borehole elongation direction (solid line), pad 1 azimuth (dotted line), and borehole azimuth (dashed line). (middle) Borehole deviation (solid curve) and location of marker horizons (vertical lines with labels). (bottom) Bit size (straight solid line), caliper arm 1 (solid line), and caliper arm 2 (dotted line). Selected breakout regions are plotted as horizontal bars showing the depth extent of the breakouts.

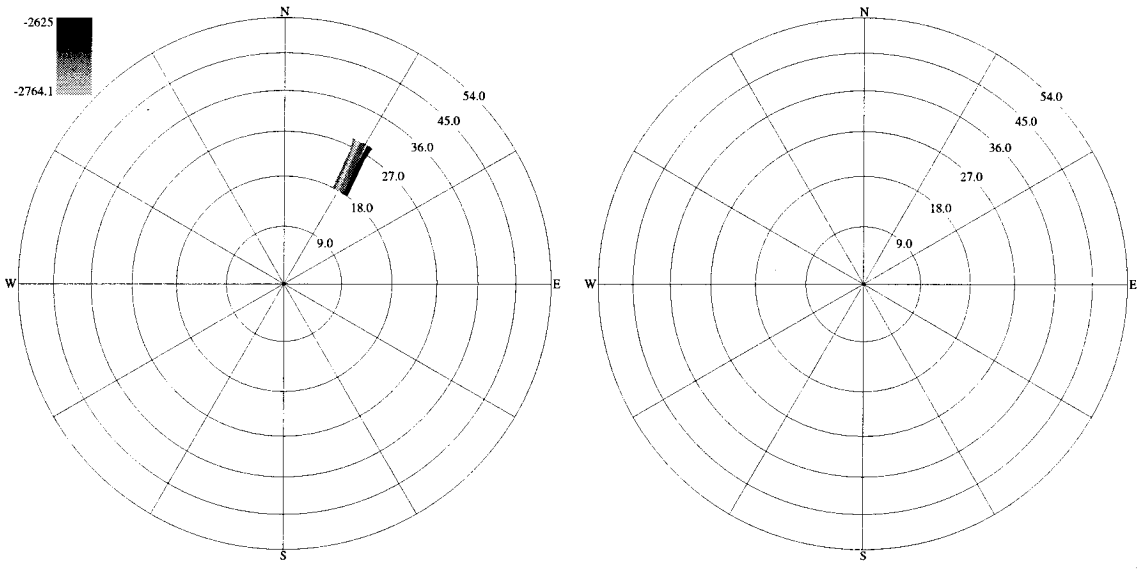

Figure B.11: Lower hemisphere stereographic projection plots of the selected breakouts from well Gp32rd. Line widths are proportional to the breakout length. (left) All selected breakouts. (right) All nonradial breakouts where the **IJK** breakout angle is not within 15° of the high side of the hole.

Table B.1: List of the breakouts identified in two separate dipmeter runs over the 3,099 to 3,160 m log foot depth interval in Gp32rd, with file 3 on the left and file 2 on the right. The identified **IJK** breakout angle results from the two log files agree within 5°.

Gp32rd file 3				Gp32rd file 2			
		XYZ	**IJK**			**XYZ**	**IJK**
Log depth, m	Length, m	Breakout Azimuth, °	Breakout Angle, °	Log depth, m	Length, m	Breakout Azimuth, °	Breakout Angle, °
3,101.3	4.0	21.4	100.5	3,104.5	9.4	25.1	97.1
3,106.7	6.2	26.2	96.0	3,111.6	4.6	31.5	91.1
3,121.4	3.5	30.2	91.6	3,119.3	8.2	28.8	93.0
3,130.4	3.5	41.6	80.4	3,130.6	3.9	39.8	82.1
3,134.2	4.1	41.4	80.4	3,134.6	4.3	41.3	80.4
3,145.0	14.0	17.8	101.5	3,146.4	14.6	21.3	98.2

B.5 Gp37

Two separate well log files covering almost exactly the same depth interval were received for Granite Point 37. The slightly longer dipmeter log, file 5, extends from 3,260 to 3,322 m and the shorter log file, file 6, extends from 3,262 to 3,322 m. The two well logs have almost identical caliper and pad 1 azimuth curves (Figures B.13 and B.13). The pad 1 azimuth curves are offset 180° from each other, but this has no effect on the resulting breakout angles due to symmetry. The maximum deviation in the entire well is 31.0°, while the maximum deviation in the 62.9 m interval is 19.9°. Two in-gauge sections of hole longer than 0.5 m were identified, totaling 11.0 m in length.

File 6 identified three breakouts, one more breakout than file 5 (Table B.2). The breakouts that were identified in file 5 were also identified in file 6's well log with almost exactly the same characteristics. The largest difference between the **IJK** breakout angles is 1.7° and the breakout lengths differ at most by 0.7 m. The midpoints of the breakouts are also very close, differing at most by 1.37 m. The one breakout that was found in file 6 that was not found in file 5 had a length of 3.24 m, which is just 0.24 m above the threshold breakout length. The other well log could have identified it, but the breakout length may have been too small. Since file 5 contains the least common denominator of breakouts, it was used in preference to file 6 for all analyses.

The two breakouts from file 5 are oriented roughly E–W (N95.0°E for the shallow breakout and N83.3°E for the deeper breakout). See Figure B.14 for the stereograph plot of the data. Since there is only one nonradial breakout, no separate plots are made of the nonradial breakouts separated into 500 m depth intervals. The marker file does not list any faults or oil pool boundaries being crossed by these well logs and none of the breakouts that were identified were found in the T45XSS marker. Both breakouts occurred in the T4243SS marker.

Table B.2: List of the breakouts identified in two separate dipmeter runs over the 3,262 to 3,322 m log foot depth interval in Gp37, with file 5 on the left and file 6 on the right. The identified **IJK** breakout angle results from the two log files agree within 5°.

Gp37 file 5				Gp37 file 6			
		XYZ	**IJK**			**XYZ**	**IJK**
Log depth, m	Length, m	Breakout Azimuth, °	Breakout Angle, °	Log depth, m	Length, m	Breakout Azimuth, °	Breakout Angle, °
3,266.0	5.3	95.0	99.6	3,266.7	4.7	95.2	99.4
				3,270.7	3.2	116.3	79.5
3,276.9	3.2	83.3	110.8	3,278.2	3.7	81.6	112.5

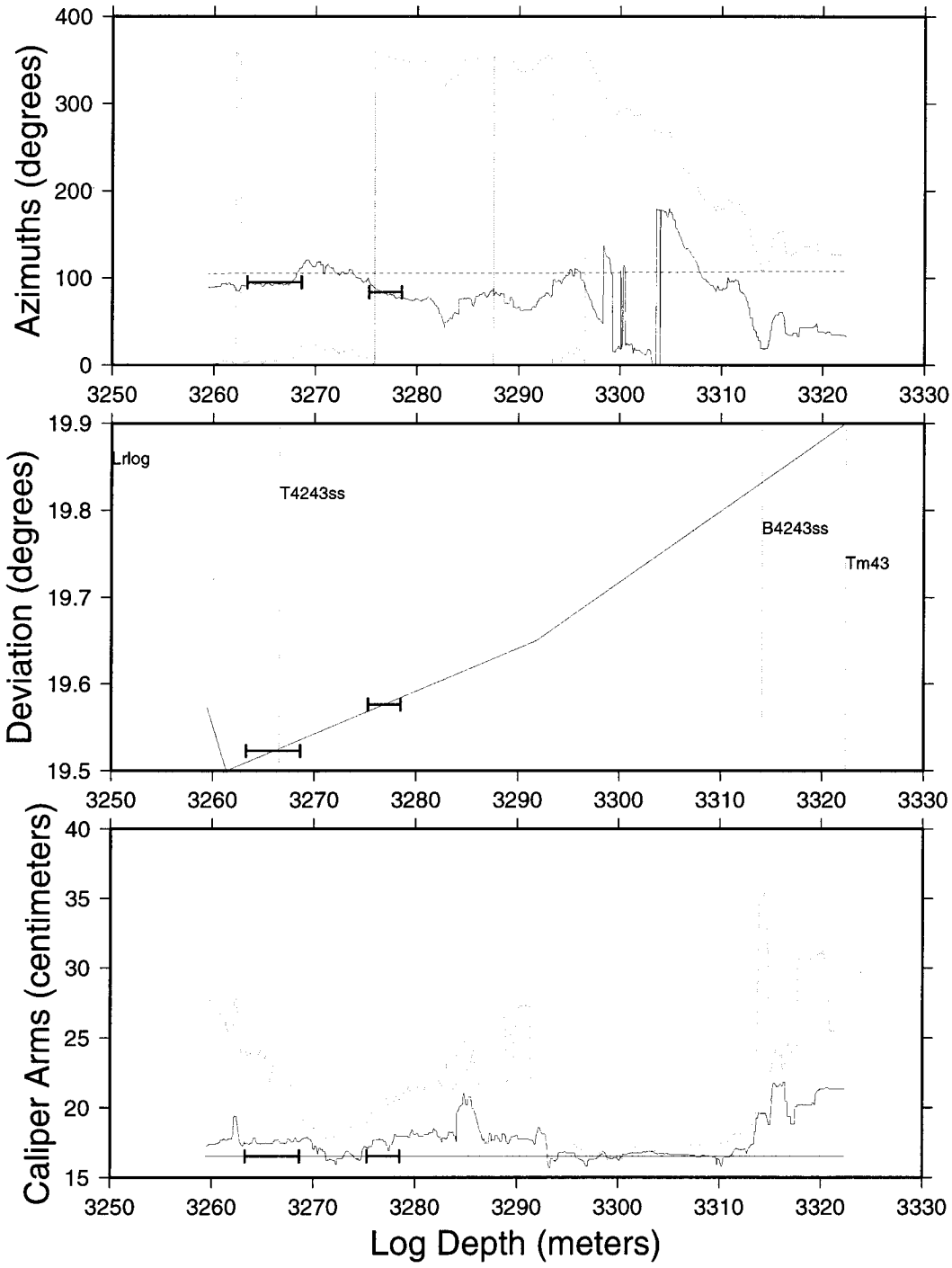

Figure B.12: Plots of the caliper-calibrated and declination-corrected digitized dipmeter and derived quantities data as a function of well depth from well Gp37 file 5. (top) Borehole elongation direction (solid line), pad 1 azimuth (dotted line), and borehole azimuth (dashed line). (middle) Borehole deviation (solid curve) and location of marker horizons (vertical lines with labels). (bottom) Bit size (straight solid line), caliper arm 1 (solid line), and caliper arm 2 (dotted line). Selected breakout regions are plotted as horizontal bars showing the depth extent of the breakouts.

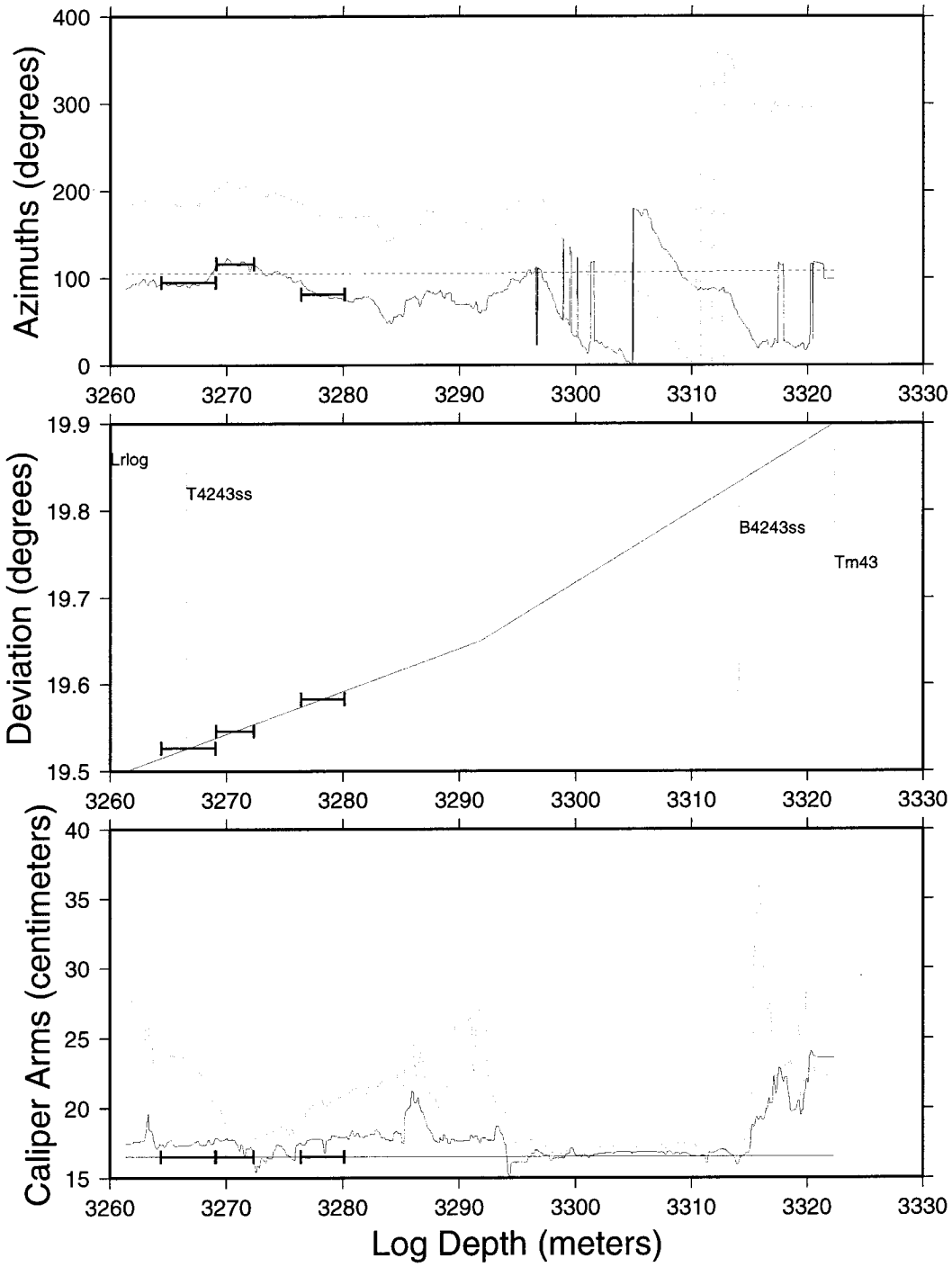

Figure B.13: Plots of the caliper-calibrated and declination-corrected digitized dipmeter and derived quantities data as a function of well depth from well Gp37 file 6. (top) Borehole elongation direction (solid line), pad 1 azimuth (dotted line), and borehole azimuth (dashed line). (middle) Borehole deviation (solid curve) and location of marker horizons (vertical lines with labels). (bottom) Bit size (straight solid line), caliper arm 1 (solid line), and caliper arm 2 (dotted line). Selected breakout regions are plotted as horizontal bars showing the depth extent of the breakouts.

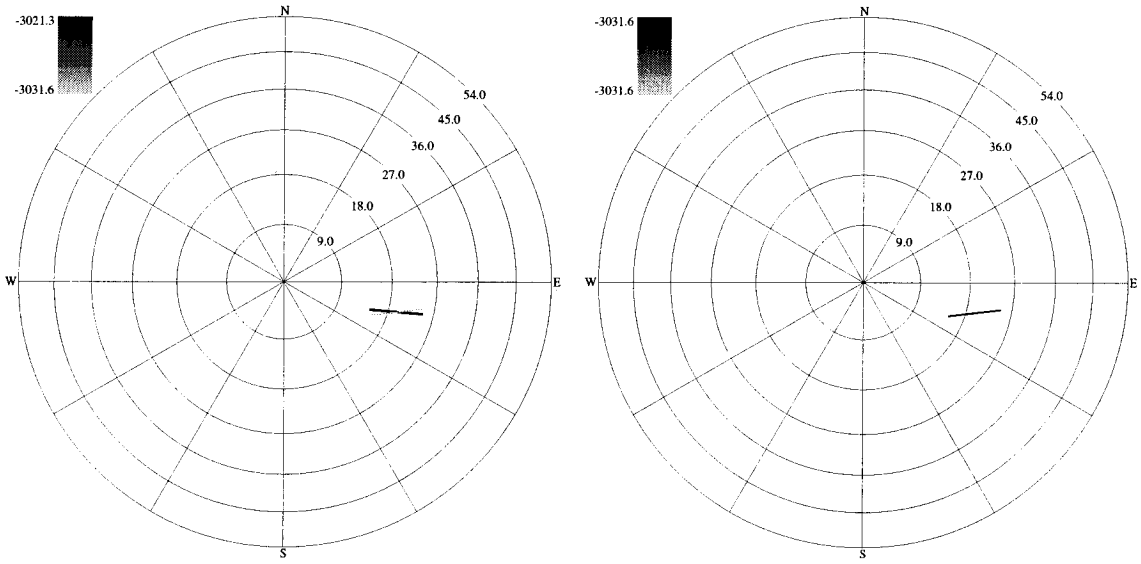

Figure B.14: Lower hemisphere stereographic projection plots of the selected breakouts from well Gp37. Line widths are proportional to the breakout length. (left) All selected breakouts. (right) All nonradial breakouts where the **IJK** breakout angle is not within 15° of the high side of the hole.

B.6 Gp42

The digital dipmeter data from Granite Point 42 came as three separate files, spanning the log depth ranges 3,148–3,311 m (file 13), 3,297–3,560 m (file 12), and 3,498–3,555 m (file 8). The maximum deviation of the hole in these intervals is 21.4°. Since file 12 completely overlaps the same section of hole logged by file 8, file 8's data was not used in subsequent calculations. The caliper logs has sections of continuous, roughly in-gauge sections of hole separated by broken-out and washed-out sections of hole (Figure B.15). The in-gauge sections have a large amount of tool rotation, as shown by the pad 1 azimuth data. There were 13 in-gauge sections of hole longer than 0.5 m, totaling 34.6 m in length, or 8.1% of the well log data.

Only three breakouts, all of them in file 12, were identified in this hole because so much of it was washed-out (Figure B.15). The three breakouts totaled 13.4 m in length, or 3.1% of the total length of dipmeter logs for this hole. The deepest identified breakout from file 12 occurs in the depth range recorded by file 8. However, the breakout was not identified in file 8, since the caliper arm data was much more inconsistent over same the interval where the breakout was identified in file 12. The three breakouts are oriented fairly consistently at an azimuth of 116.7N°E $\pm$ 6° (Figure B.16) and the two shallower breakouts occur at the top end of a section of hole where the tool was heavily rotating. No marker files for Granite Point 42 were received. Since only one nonradial breakout was identified, no separate plots of nonradial breakouts divided into 500 m intervals are shown.

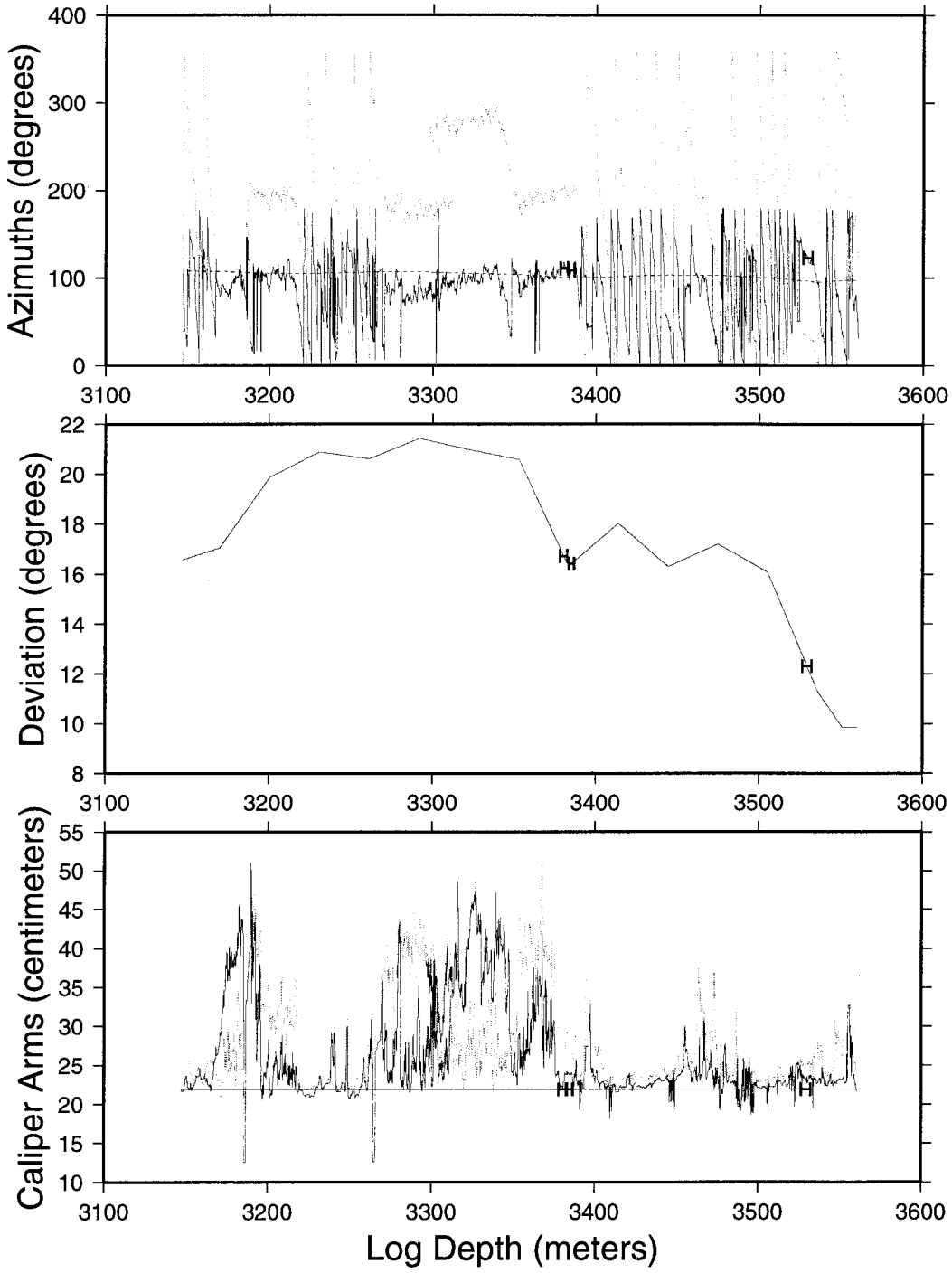

Figure B.15: Plots of the caliper-calibrated and declination-corrected digitized dipmeter and derived quantities data as a function of well depth from well Gp42. (top) Borehole elongation direction (solid line), pad 1 azimuth (dotted line), and borehole azimuth (dashed line). (middle) Borehole deviation (solid curve) and location of marker horizons (vertical lines with labels). (bottom) Bit size (straight solid line), caliper arm 1 (solid line), and caliper arm 2 (dotted line). Selected breakout regions are plotted as horizontal bars showing the depth extent of the breakouts.

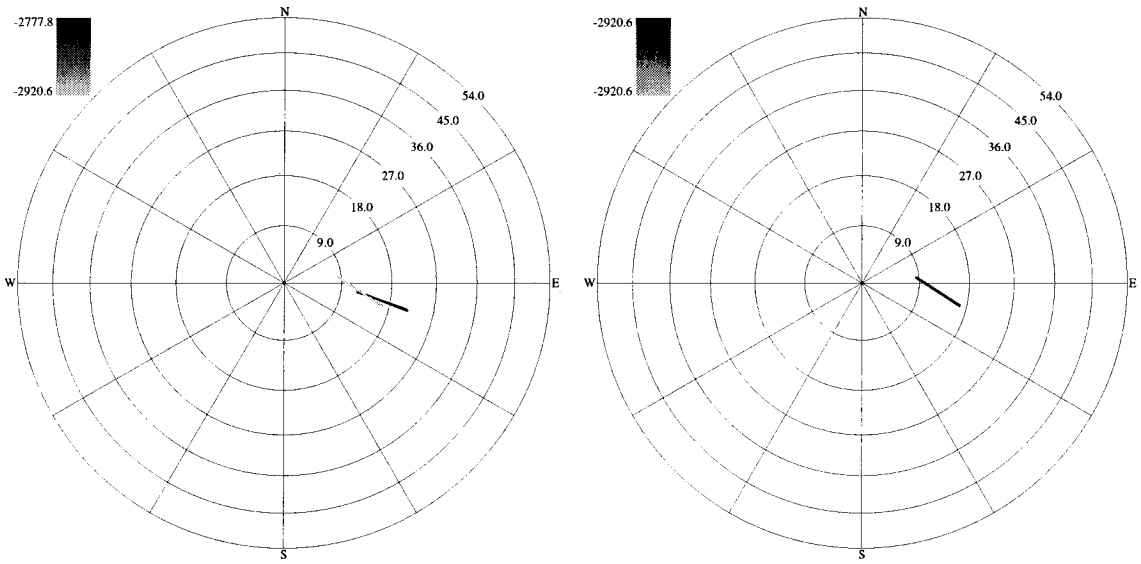

Figure B.16: Lower hemisphere stereographic projection plots of the selected breakouts from well Gp42. Line widths are proportional to the breakout length. (left) All selected breakouts. (right) All nonradial breakouts where the **IJK** breakout angle is not within 15° of the high side of the hole.

B.7 Gp50

The digital dipmeter data for Granite Point 50 came in two different files covering the depth ranges 2,487 to 2,590 m (file 9) and 2,598 to 3,062 m (file 8) log depth. The raw dipmeter data are shown in Figure B.17. The maximum deviation reached in these two sections was 20.0°. The tool has intermittent rotation throughout the 567 m of log. A total 77.7 m of in-gauge hole longer than 0.5 m was identified, which amounts to 13.7% of the log.

A total of 65.6 m of breakouts was identified from both dipmeter data sets (Figure B.18), which covers roughly 11.6% of the well log data. The breakouts from file 9 and file 8 have two quite different patterns. File 9's two breakouts are oriented roughly NE–SE to NNE–SSW. The borehole elongations from the deeper part of the hole (file 8) have a fairly consistent pattern except for the shallowest breakout. Excluding the shallowest breakout, which is in the T4243SS marker, the breakout orientations rotate from N120.8°E to N82.9°E as the borehole azimuth trends from N167.2°E to N138.5°E. This rotation occurs in the TM45, T45XSS, B45XSS, TM46, and TMX markers. This well crosses two faults at 3,382 and 3,648 m log depth, which is deeper than any available well log data.

Since all of the nonradial breakouts are between 2,500 and 3,000 m, no separate plots of nonradial breakouts separated into depth zones are shown. Instead, see Figure B.18. Breakouts were found in the following markers: TM41 (1 breakout for 5.2 m), B4142SS (1 breakout for 8.1 m), TM43 (1 breakout for 2.7 m), T4344SS (1 breakout for 0.8 m), TM45 (2 breakouts for 7.1 m), B45XSS (2 breakouts for 12.2 m), TM46 (3 breakouts for 15.4 m), and TMX (2 breakouts for 14.2 m).

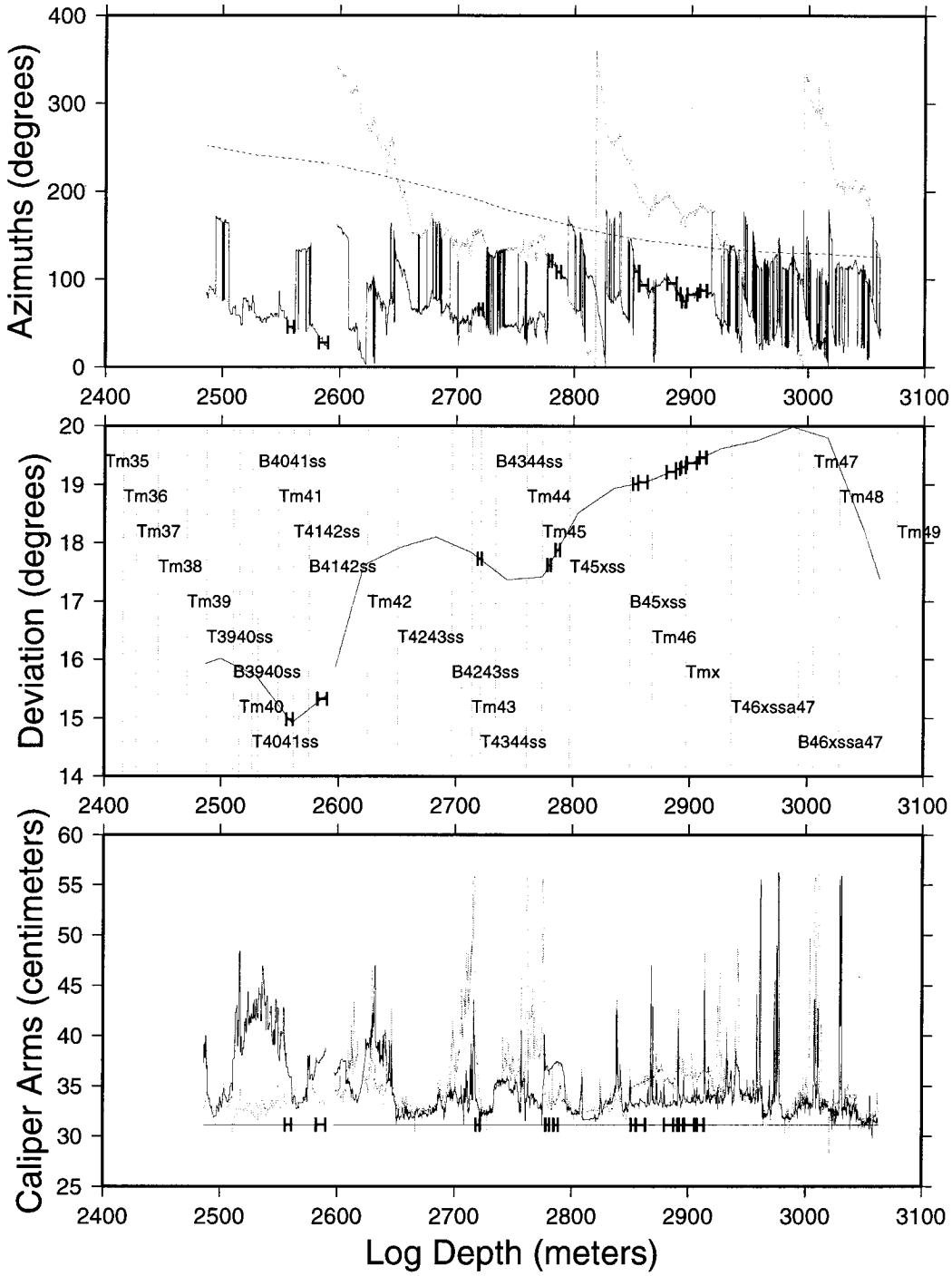

Figure B.17: Plots of the caliper-calibrated and declination-corrected digitized dipmeter and derived quantities data as a function of well depth from well Gp50. (top) Borehole elongation direction (solid line), pad 1 azimuth (dotted line), and borehole azimuth (dashed line). (middle) Borehole deviation (solid curve) and location of marker horizons (vertical lines with labels). (bottom) Bit size (straight solid line), caliper arm 1 (solid line), and caliper arm 2 (dotted line). Selected breakout regions are plotted as horizontal bars showing the depth extent of the breakouts.

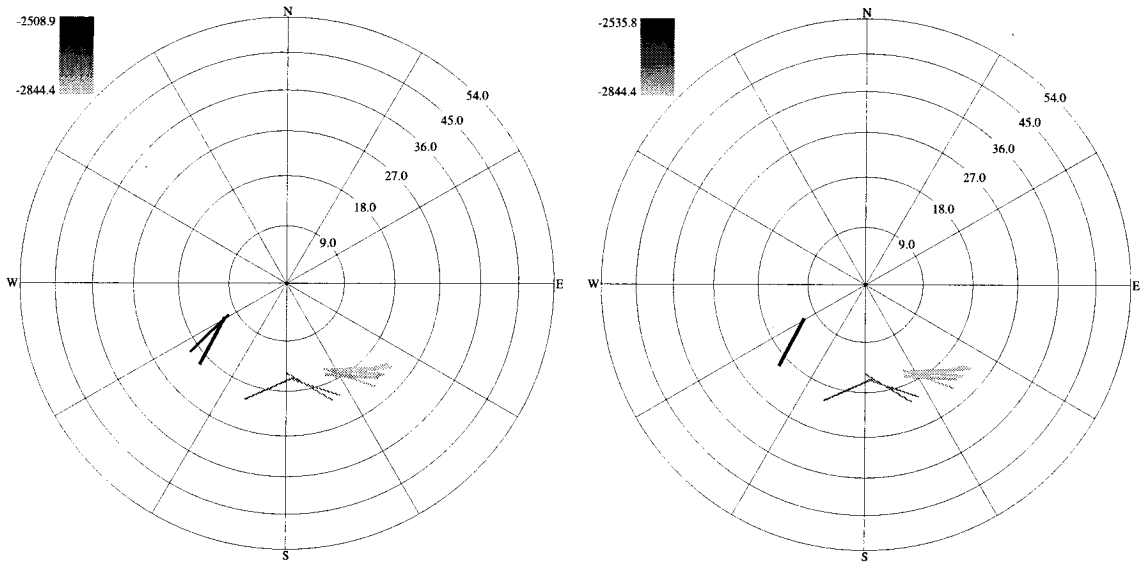

Figure B.18: Lower hemisphere stereographic projection plots of the selected breakouts from well Gp50. Line widths are proportional to the breakout length. (left) All selected breakouts. (right) All nonradial breakouts where the **IJK** breakout angle is not within 15° of the high side of the hole.

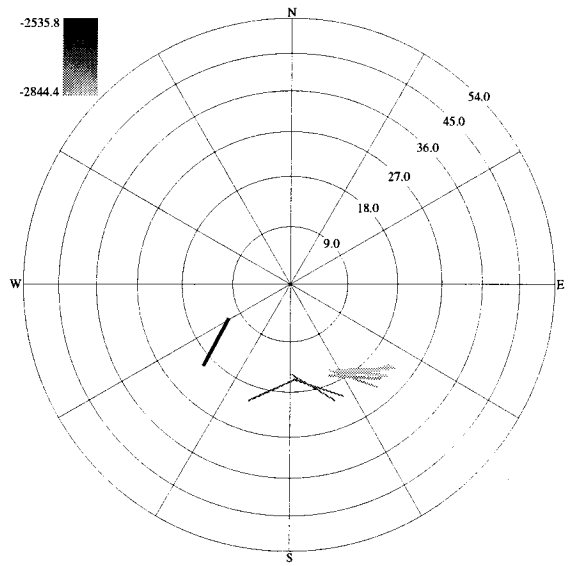

Figure B.19: Lower hemisphere stereographic projection plots of all nonradial breakouts from well Gp50 between the true vertical depths of 2500–3000 m.

B.8 Gp51

Two digital dipmeter logs were received for Gp51. The shallow dipmeter run (file 5) logged the log depth range 2,984 to 3,331 m and the deeper log (file 4) starts at 3,393 m log depth and continues to 3,523 m. The two dipmeter data sets are plotted together in Figure B.20. The maximum deviation of the data received was 36.1°, which is very close to the maximum deviation in the whole well of 37.9°. A total of 121.0 m of in-gauge sections of hole longer than 0.5 m were identified, which amounts to 25.3% of the available data.

A total of 12 breakouts adding up to 67.7 m in length of breakouts were identified in this hole, all of them occurring in the T45XSS marker. There are two distinct populations of breakout azimuths in the borehole (Figure B.21). The shallower breakouts, identified in file 5, range from 2,896 to 3,165 m TVD depth and are oriented from N70.0°E to N75.7°E. The deeper breakouts, identified in file 6, range from 3,260 to 3,323 m TVD depth and slowly rotate counterclockwise from N170.0°E to N145.4°E as the breakouts get deeper and the borehole deviation grows larger.

The transition from nearly radial breakouts in the shallow section to almost azimuth breakouts in the deeper section occurs in the T45XSS marker, which starts at 3,007.2 m log depth and ends at 3590.8 m log depth. The marker file does not list any faults that are crossed by this well. The character of the two well logs differ. The shallower well log has less variable pad 1 azimuth data and the caliper arms, except for a few large broken out sections, are much closer to each other than in the deeper well log. The deeper well log also has more breakouts, with the smaller caliper arm closer to the bit size (Figure B.20). However, it is not clear which set of breakouts should kept since all of the breakouts were selected using the same breakout selection criteria, the well does not cross any faults, and the well does not enter a different marker between the transition, and the differences between the two well logs are not large. For this reason, all of the breakouts from this well will be disregarded for the stress state inversion.

For completeness, the nonradial breakouts organized into 500 m TVD depth intervals are shown in Figure B.22.

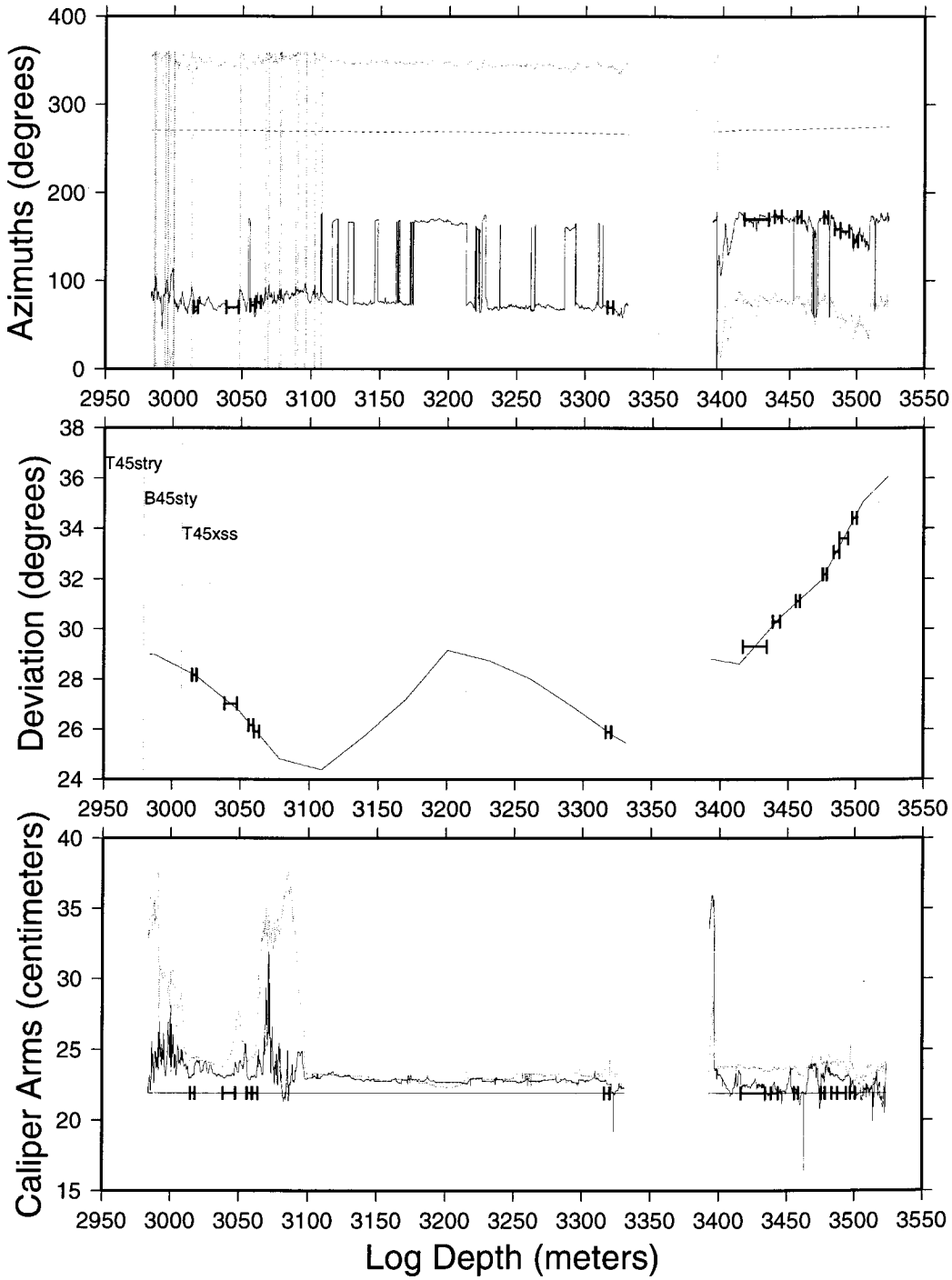

Figure B.20: Plots of the caliper-calibrated and declination-corrected digitized dipmeter and derived quantities data as a function of well depth from well Gp51. (top) Borehole elongation direction (solid line), pad 1 azimuth (dotted line), and borehole azimuth (dashed line). (middle) Borehole deviation (solid curve) and location of marker horizons (vertical lines with labels). (bottom) Bit size (straight solid line), caliper arm 1 (solid line), and caliper arm 2 (dotted line). Selected breakout regions are plotted as horizontal bars showing the depth extent of the breakouts.

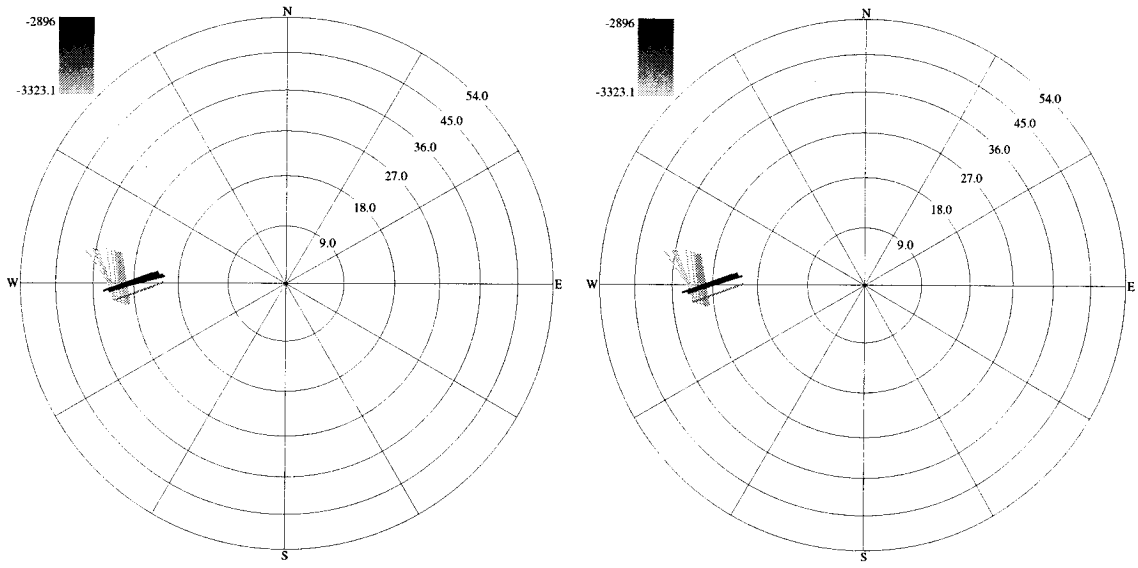

Figure B.21: Lower hemisphere stereographic projection plots of the selected breakouts from well Gp51. Line widths are proportional to the breakout length. (left) All selected breakouts. (right) All nonradial breakouts where the **IJK** breakout angle is not within 15° of the high side of the hole.

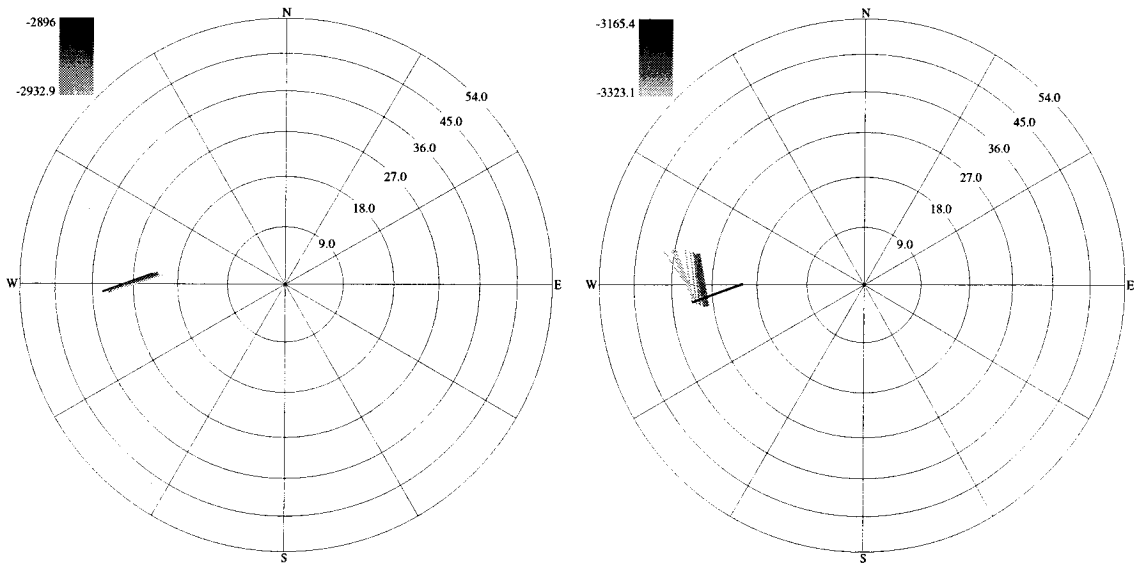

Figure B.22: Lower hemisphere stereographic projection plots of all nonradial breakouts from well Gp51 between the true vertical depths of 2500–3000 m on the left and 3000–3500 m on the right.

B.9 Mgs8rd

A single paper dipmeter log for Middle Ground Shoals 8 redrill was received. The paper log extends from 610 to 2,804 m log depth. The paper log was not digitized and breakout selection was done by eye. The identified breakouts were entered into the computer and were then passed through the breakout selection scheme to ensure that the breakouts met the breakout selection criteria.

Mgs8rd was logged by a low-angle dipmeter and reached deviations up to 28.8°. Deviations of the well at the locations of breakouts ranged from 2.1° to 16.7°. The deviations measured by the dipmeter agree with those from the directional survey, with an average difference of 0.6° and a maximum difference of 1.6°. However, the borehole azimuth measured by the directional survey and calculated from the dipmeter differed on average by 21.0°, with a maximum difference of 37.0°.

The borehole breakout selection criteria identified 30 breakouts covering 221.0 m, or 10.1%, of the hole (Figures B.23 and B.24). The breakouts were found between 726.1 and 2638.9 m TVD. Borehole elongations that are at least 15° away from the borehole azimuth are shown in Figure B.24. Figures B.27 and B.28 shows the nonradial breakouts separated into 500 m true vertical depth intervals. Borehole elongations were observed in the 28SS (1 breakout for 7.3 m), B28SS (1 breakout for 4.0 m), 30 (3 breakouts for 15.2 m), 31SS (1 breakout for 4.3 m), B31SS (6 breakouts for 38.1 m), B34SS (1 breakout for 15.2 m), 36SS (2 breakouts for 8.5 m), 38 (1 breakout for 6.1 m), B39SS (1 breakout for 5.5 m), 39ASS (1 breakout for 8.2 m), B39ASS (1 breakout for 6.1 m), B40SS (6 breakouts for 57.9 m, Figure B.25), A49SSEQ (1 breakout for 3.0 m), B (1 breakout for 3.7 m), D (1 breakout for 7.3 m, (Figure B.26), and E (3 breakouts for 19.2 m) markers.

The borehole breakout **IJK** angles from Mgs8rd are highly variable over a short depth interval. The largest angular difference between two consecutive breakouts was 84° which occurred over a 82 m depth range between the B39ASS and B40SS markers. **IJK** breakout angle differences larger than 15° between successive breakouts occur 9 times between breakouts in different markers and 4 times in the same marker, which suggests that the marker alone is not controlling the breakout orientations. Selecting the nonradial breakouts from the complete set of breakouts does not reduce the variability in the breakouts; there appears to be two separate intermingled populations of breakouts, one oriented NE–SW and the other oriented NW–SE (Figure B.24).

The borehole elongation pattern has several possible explanations. The first explanation is that the pattern is composed of two populations of borehole elongations, with the radial elongations caused by a different process, possibly tool drag, than the nonradial elongations. However, the nonradial borehole elongations do not have a clear pattern (Figure B.24). A second explanation is that orientations sampled by this borehole are close to a nodal point of the type shown in Figure 1.4. The pattern could easily be generated by a thrust stress field with a vertical principal stress. However, breakouts are not expected near nodal points of the theoretical breakout pattern. Examination of

other, more detailed data, such as formation microscanner or televiewer logs, would help to resolve which explanation is more accurate.

The breakouts observed in the B40SS marker show a clear preferred pattern of breakouts azimuthally oriented around a point deviating 5° from the vertical and trending due south (Figure B.25). This would suggest a normal stress state.

It appears that depending upon the subset of breakouts chosen from this well different stress state solutions are available. Thus, integrating this data with other wells is a viable way of making sense of this particular breakout data set.

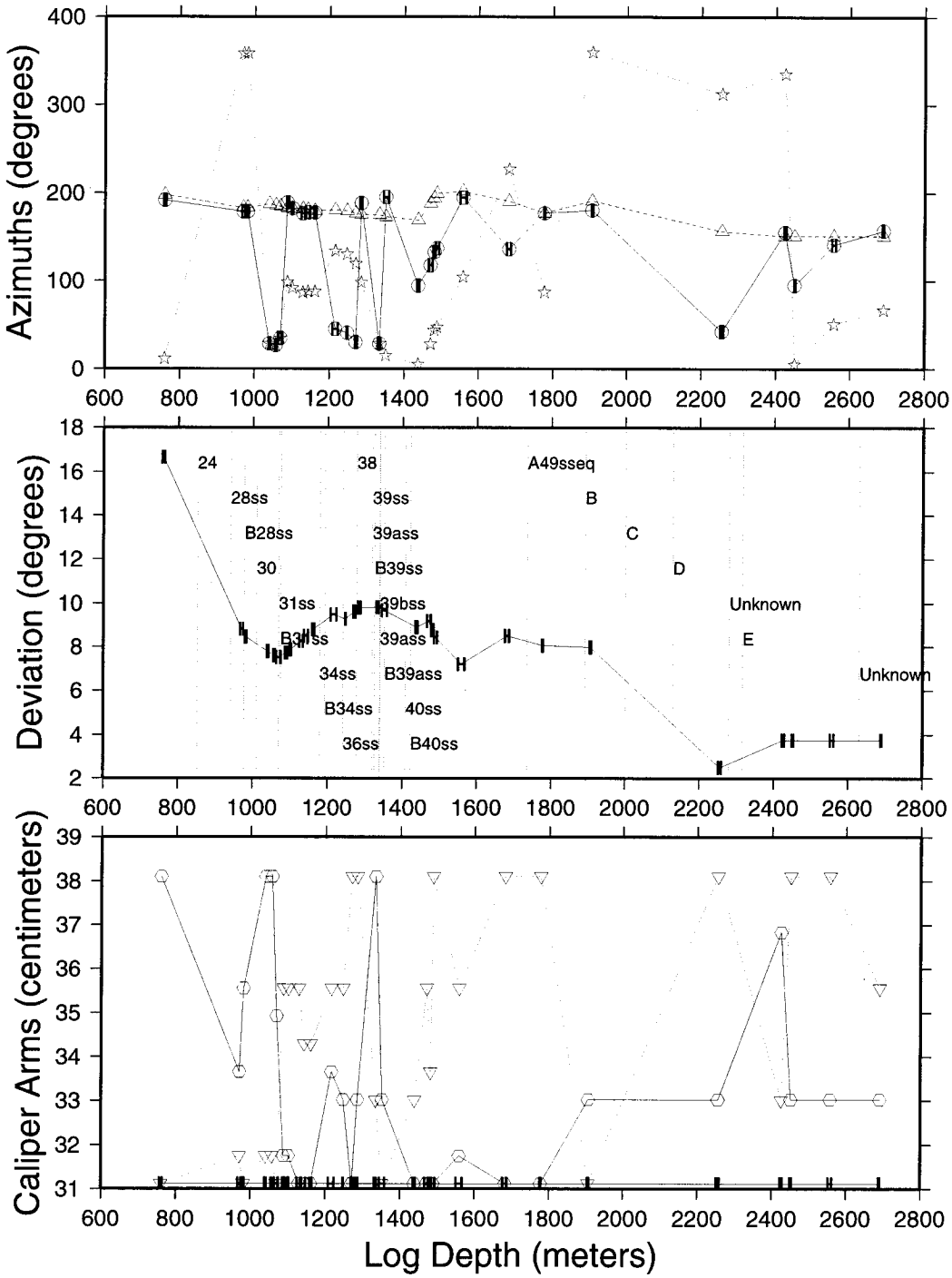

Figure B.23: Plots of the caliper-calibrated and declination-corrected selected breakout data as a function of well depth from well Mgs8rd. (top) Borehole azimuth (dashed line with triangles), pad azimuth (dotted line with stars), and breakout azimuth (solid line with circles). (middle) Borehole deviation (solid line) and location of marker horizons (vertical lines with labels). (bottom) Caliper arm 1 (solid line with hexagons), caliper arm 2 (dotted line with inverted triangles), and bit size (relatively constant solid line).

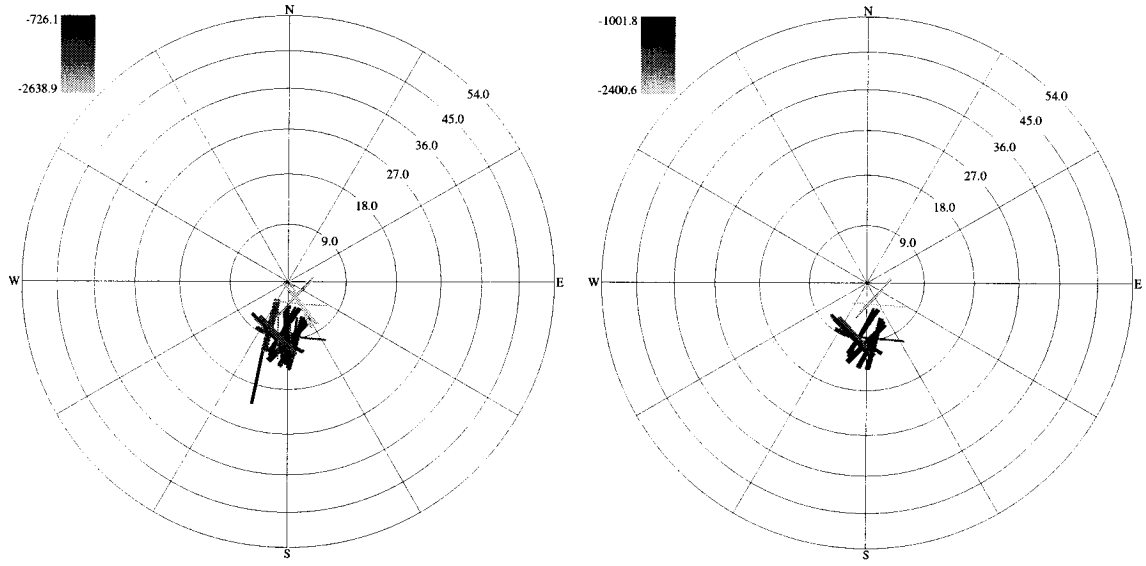

Figure B.24: Lower hemisphere stereographic projection plots of the selected breakouts from well Mgs8rd. Line widths are proportional to the breakout length. (left) All selected breakouts. (right) All nonradial breakouts where the **IJK** breakout angle is not within 15° of the high side of the hole.

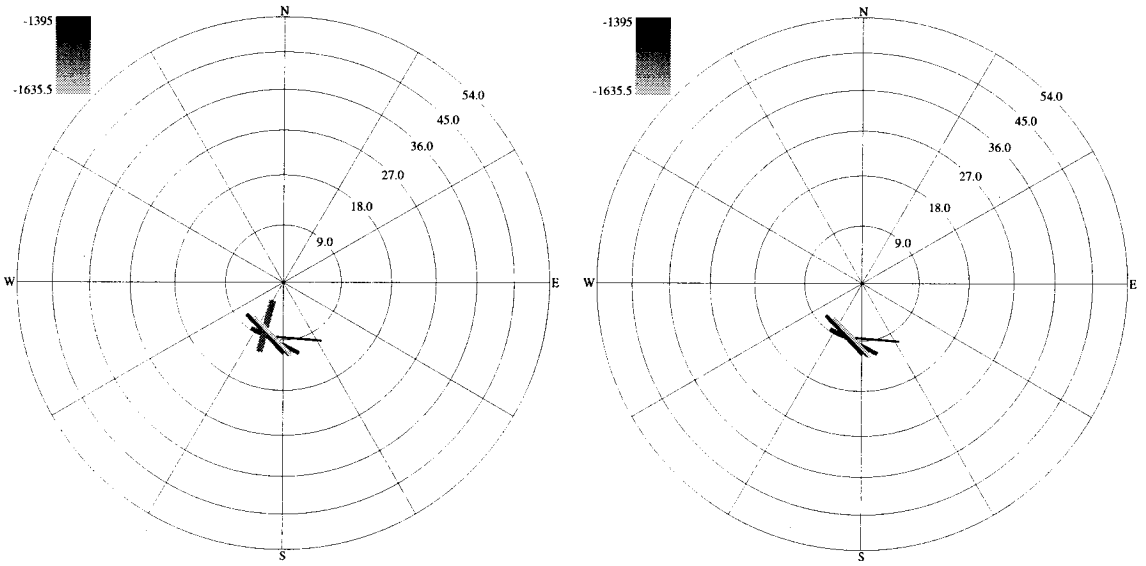

Figure B.25: Lower hemisphere stereographic projection plots of the selected breakouts from well Mgs8rd in marker B40SS. Line widths are proportional to the breakout length. (left) All selected breakouts in B40SS. (right) All nonradial breakouts in B40SS where the **IJK** breakout angle is not within 15° of the high side of the hole.

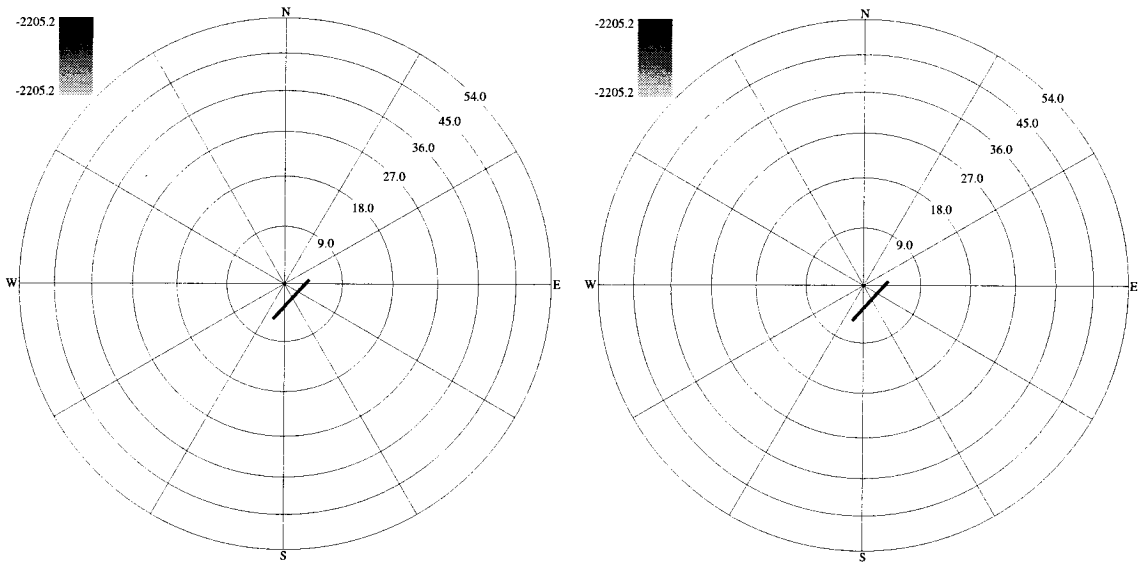

Figure B.26: Lower hemisphere stereographic projection plots of the selected breakouts from well Mgs8rd in marker D. Line widths are proportional to the breakout length. (left) All selected breakouts in D. (right) All nonradial breakouts in D where the **IJK** breakout angle is not within 15° of the high side of the hole.

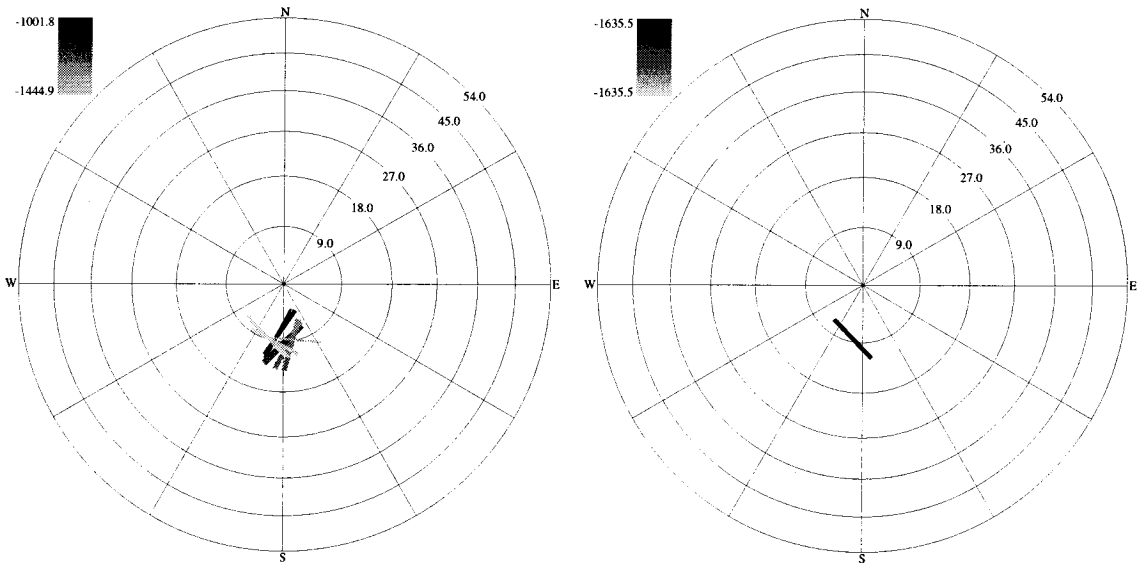

Figure B.27: Lower hemisphere stereographic projection plots of all nonradial breakouts from well Mgs8rd between the true vertical depths of 1000–1500 m on the left and 1500–2000 m on the right.

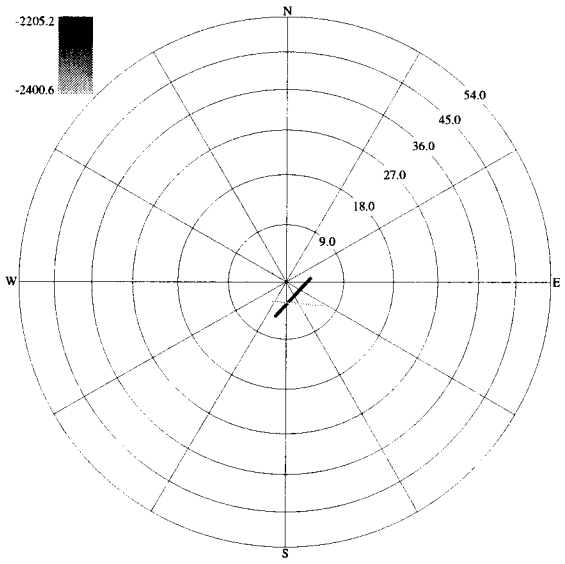

Figure B.28: Lower hemisphere stereographic projection plots of all nonradial breakouts from well Mgs8rd between the true vertical depths of 2000–2500 m.

B.10 Mgs12

A single high-angle dipmeter paper log spanning the log depth range 2,225–3,048 m for Middle Ground Shoals 12 was received from Unocal. The breakouts were identified by hand and then entered into the computer for further processing. The deviations from the directional survey and dipmeter logs differed on average by 1.8° and at most by 3.4°. Borehole deviations ranged from 13.5° to 17.0° where borehole elongations were found. The deviations at the depths of the breakouts are relatively low for a high-angle unit, but the well log started at 2,225 m and the well is highly deviated at shallower depths. The difference between the directional survey's borehole azimuth and the dipmeter's borehole azimuth varies from 13.3° to 33.0°. The magnetic declination in the area is 26°, so the large difference in borehole azimuths is puzzling.

Eighteen separate breakouts were identified, totaling 121.3 m in length, or 14.7% of the dipmeter log, between 1,933.8 and 2,701 m TVD (Figure B.30). Figure B.33 shows the nonradial breakouts separated into 500 m true vertical depth intervals. Borehole elongations were observed in the B (2 breakouts for 9.1 m), C (3 breakouts for 18.9 m), D (3 breakouts for 14.3 m, Figure B.31), E (3 breakouts for 19.5 m), F (1 breakout for 7.0 m), G1 (1 breakout for 3.0 m), G3 (2 breakouts for 16.5 m), G4 (1 breakout for 7.3 m) and TWF (4 breakouts for 25.6 m) markers. The breakouts in G3 and G4 are plotted together in Figure B.32.

The breakout pattern for Mgs12 is much more consistent than Mgs8rd. The breakouts generally trend radially, but there are many breakouts that are not within 15° of the high or low side of the hole (Figure B.30). This pattern could be caused by a thrust stress state environment with a nonvertical principal stress direction since the breakouts are not oriented to the center of the plot.

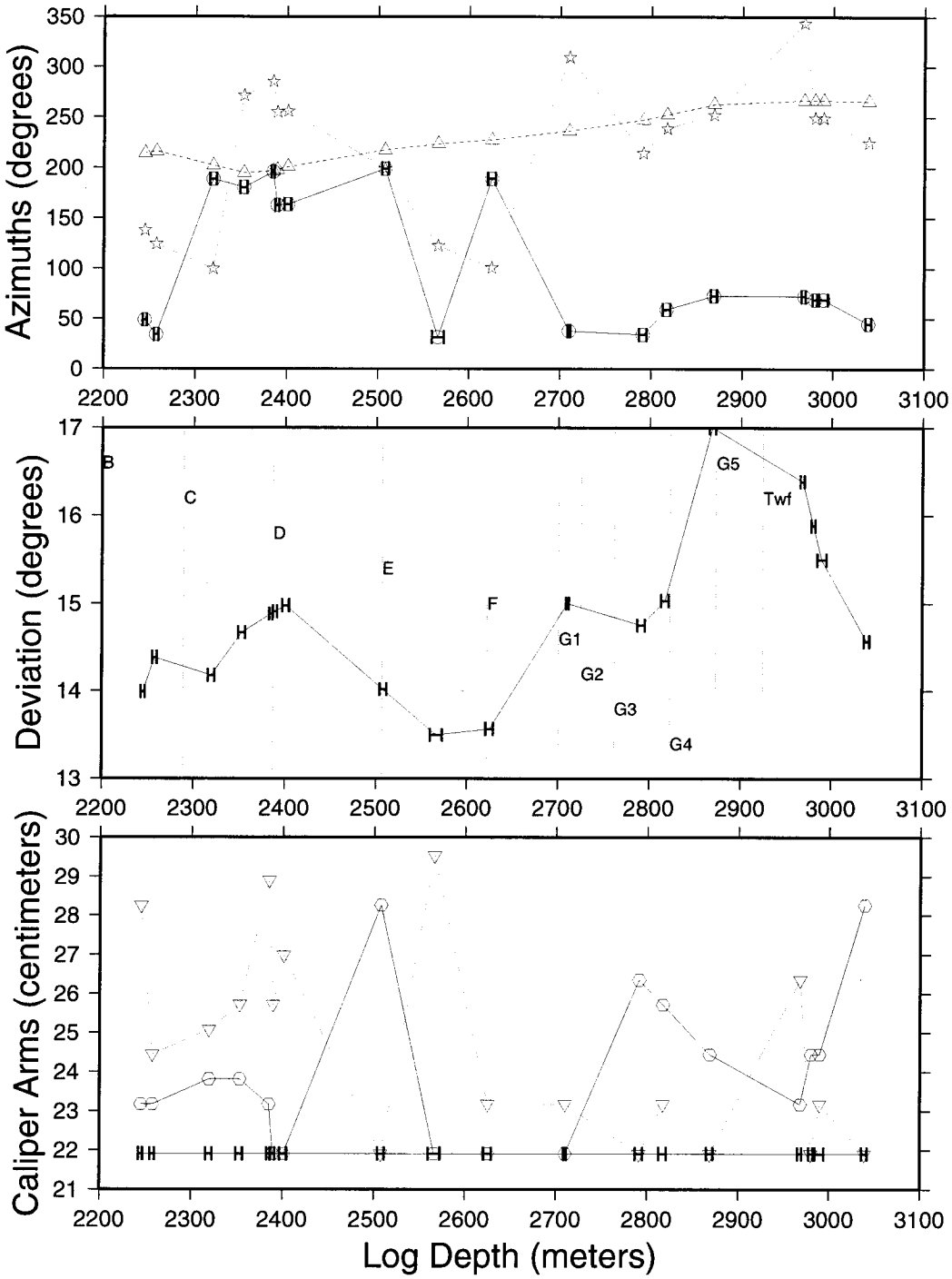

Figure B.29: Plots of the caliper-calibrated and declination-corrected selected breakout data as a function of well depth from well Mgs12. (top) Borehole azimuth (dashed line with triangles), pad azimuth (dotted line with stars), and breakout azimuth (solid line with circles). (middle) Borehole deviation (solid line) and location of marker horizons (vertical lines with labels). (bottom) Caliper arm 1 (solid line with hexagons), caliper arm 2 (dotted line with inverted triangles), and bit size (relatively constant solid line).

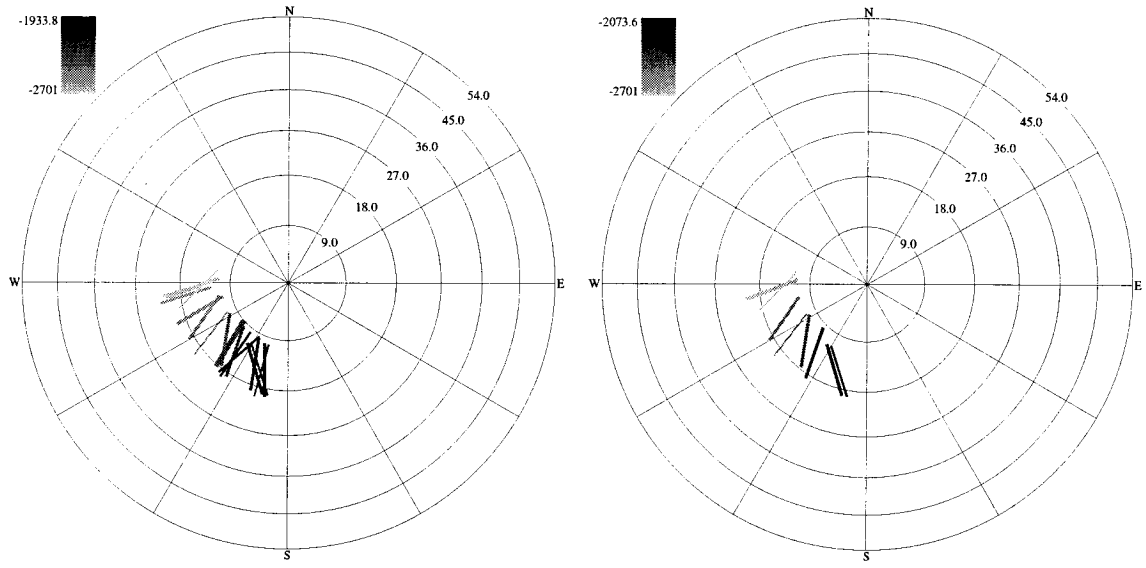

Figure B.30: Lower hemisphere stereographic projection plots of the selected breakouts from well Mgs12. Line widths are proportional to the breakout length. (left) All selected breakouts. (right) All nonradial breakouts where the **IJK** breakout angle is not within 15° of the high side of the hole.

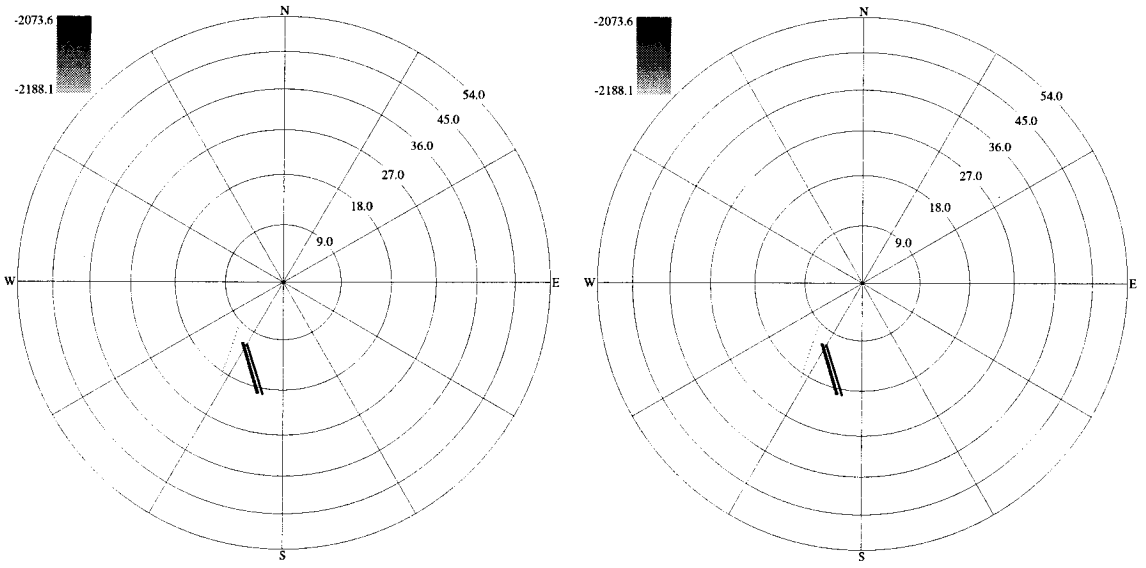

Figure B.31: Lower hemisphere stereographic projection plots of the selected breakouts from well Mgs12 in marker D. Line widths are proportional to the breakout length. (left) All selected breakouts in D. (right) All nonradial breakouts in D where the **IJK** breakout angle is not within 15° of the high side of the hole.

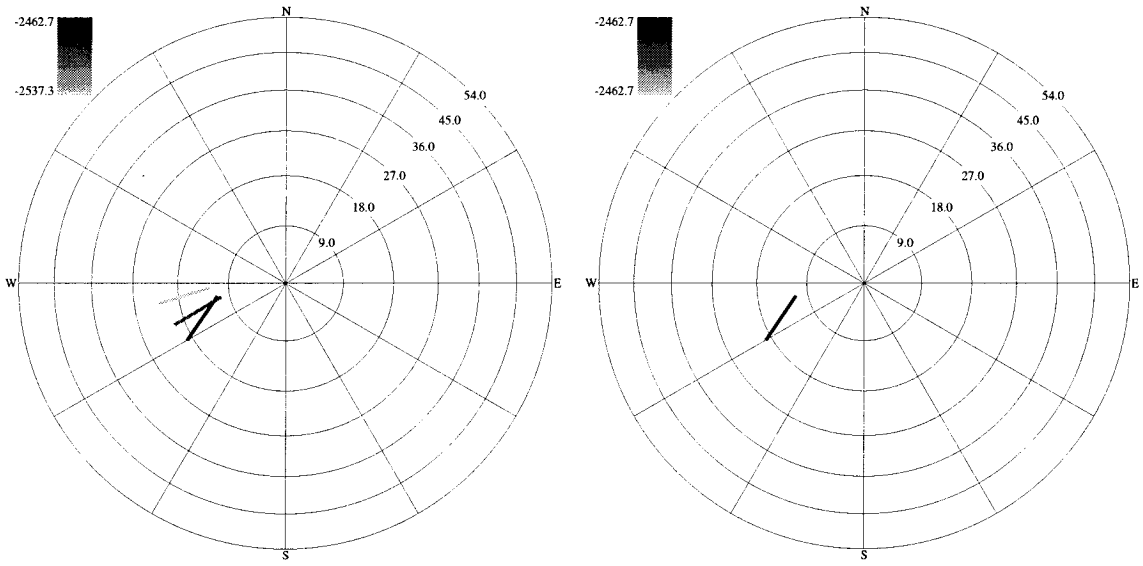

Figure B.32: Lower hemisphere stereographic projection plots of the selected breakouts from well Mgs12 in markers G3 and G4. Line widths are proportional to the breakout length. (left) All selected breakouts in G3 and G4. (right) All nonradial breakouts in G3 and G4 where the **IJK** breakout angle is not within 15° of the high side of the hole.

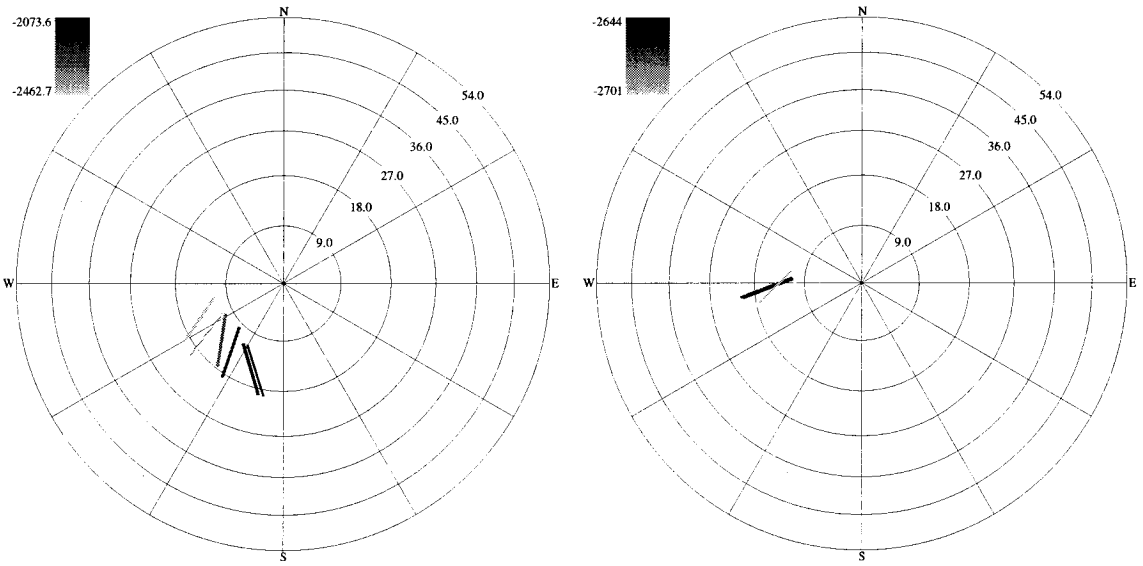

Figure B.33: Lower hemisphere stereographic projection plots of all nonradial breakouts from well Mgs12 between the true vertical depths of 2000–2500 m on the left and 2500–3000 m on the right.

B.11 Mgs13

Two paper low-angle dipmeter logs spanning the log depth range 610–3,258 m for Middle Ground Shoals 13 were received from Unocal. The dipmeter data was not digitized and the borehole breakouts were selected by eye, at which point the properties of the breakouts were entered into the computer for automatic processing and another round of breakout selection to make sure that the breakouts met the breakout selection criteria.

Deviations at the locations of borehole elongation range from 4.8° to 18.6°. The average difference between the dipmeter's and the directional survey's deviation was 1.5°, with a maximum difference of 5.0°. The difference between the directional survey's borehole azimuth and the dipmeter's calculated borehole azimuth range from 12.1° to 44.6°.

Only 3.7% (97.2 m) of the logged depth interval had identifiable breakouts. These are shown in Figure B.35. The same nonradial breakouts separated into 500 m intervals are shown in Figures B.38–B.39. Nonradial borehole elongations are shown in Figure B.35. Borehole elongations were found in the B40SS oil pool (4 breakouts for 19.8 m, Figure B.36) and in the G3 and G4 pools (2 breakouts for 8.5 m, Figure B.37). Other markers that had breakouts include: 40SS (1 breakout for 6.7 m) C (3 breakouts for 30.5 m), G1 (1 breakout for 4.9 m), and B (4 breakouts for 16.5 m).

This well has a low percentage of breakouts because a large amount of the dipmeter data has caliper arm data much larger or much smaller than the bit size. Elsewhere the tool was clearly rotating in in-gauge sections of the hole and otherwise appeared to be reasonably well-behaved.

There are two distinct populations of breakouts, one set of five shallow breakouts oriented between NNE–SSW to ENE–WSW and the deeper remaining breakouts oriented E–W (Figure B.35). Both sets of breakouts are very consistently oriented. If this hole is analyzed in isolation the overall E–W trend in the deeper sections of the hole suggests that the direction of S_H at this depth is approximately N–S. The borehole elongations observed in the B40SS oil pool have a radial, NNE breakout direction (Figure B.36), while the breakouts in the deeper G3 and G4 pools have a E–W trending borehole elongations (Figure B.37).

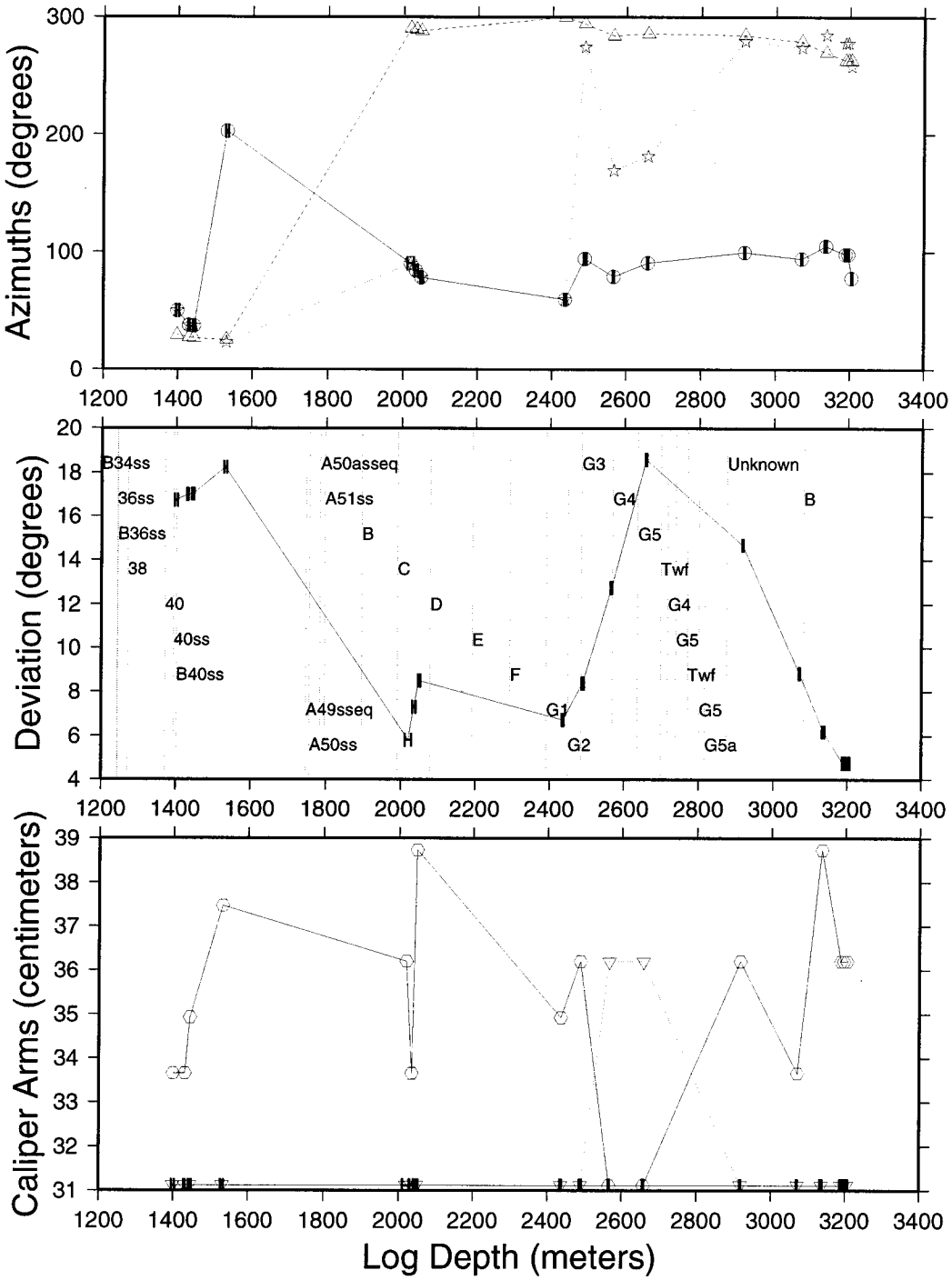

Figure B.34: Plots of the caliper-calibrated and declination-corrected selected breakout data as a function of well depth from well Mgs13. (top) Borehole azimuth (dashed line with triangles), pad azimuth (dotted line with stars), and breakout azimuth (solid line with circles). (middle) Borehole deviation (solid line) and location of marker horizons (vertical lines with labels). (bottom) Caliper arm 1 (solid line with hexagons), caliper arm 2 (dotted line with inverted triangles), and bit size (relatively constant solid line).

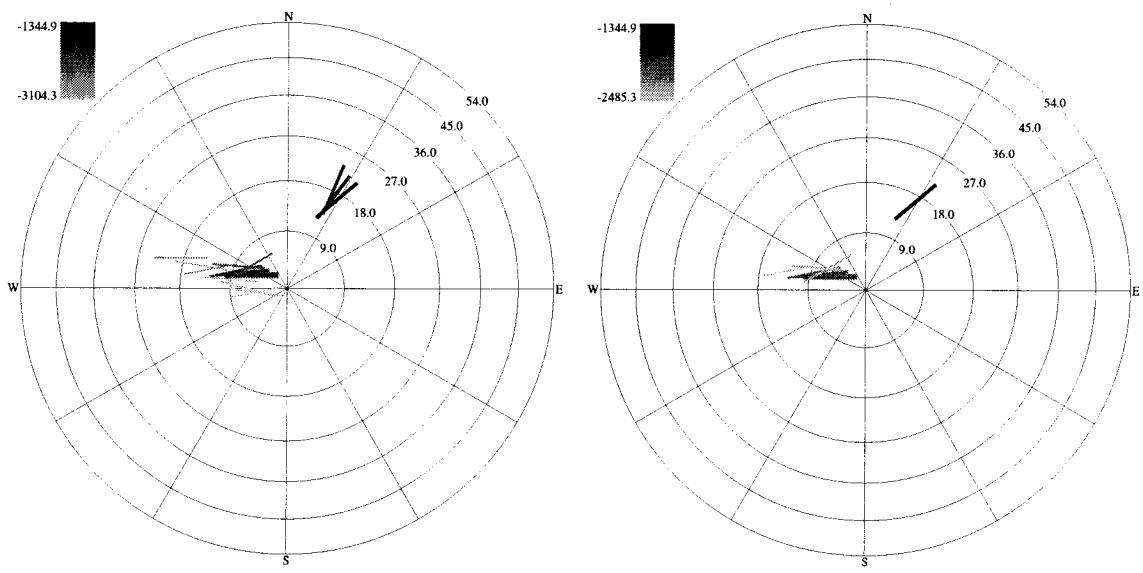

Figure B.35: Lower hemisphere stereographic projection plots of the selected breakouts from well Mgs13. Line widths are proportional to the breakout length. (left) All selected breakouts. (right) All nonradial breakouts where the **IJK** breakout angle is not within 15° of the high side of the hole.

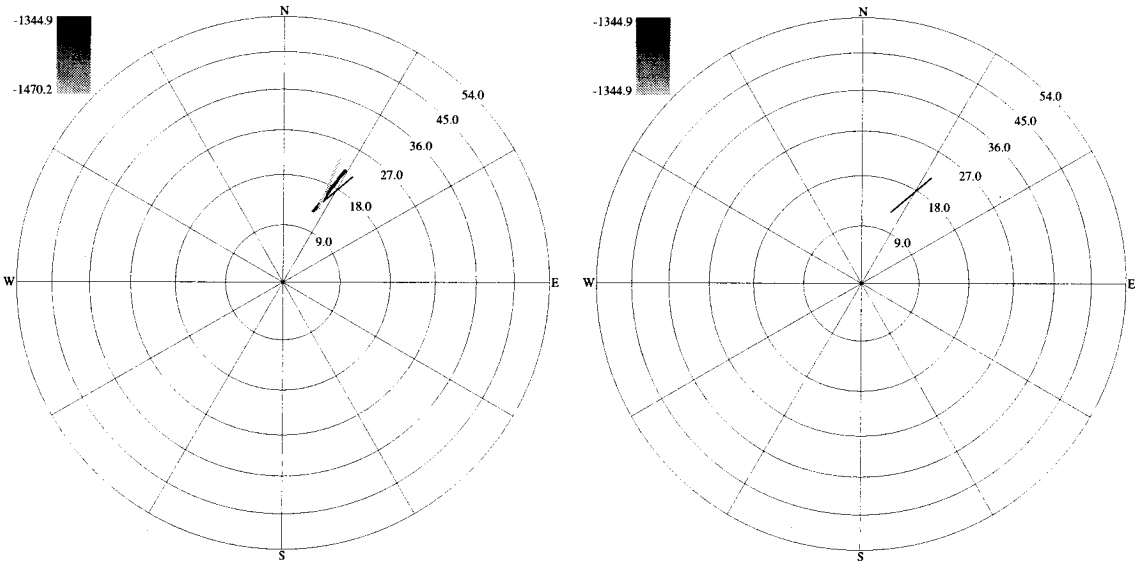

Figure B.36: Lower hemisphere stereographic projection plots of the selected breakouts from well Mgs13 in marker B40SS. Line widths are proportional to the breakout length. (left) All selected breakouts in B40SS. (right) All nonradial breakouts in B40SS where the **IJK** breakout angle is not within 15° of the high side of the hole.

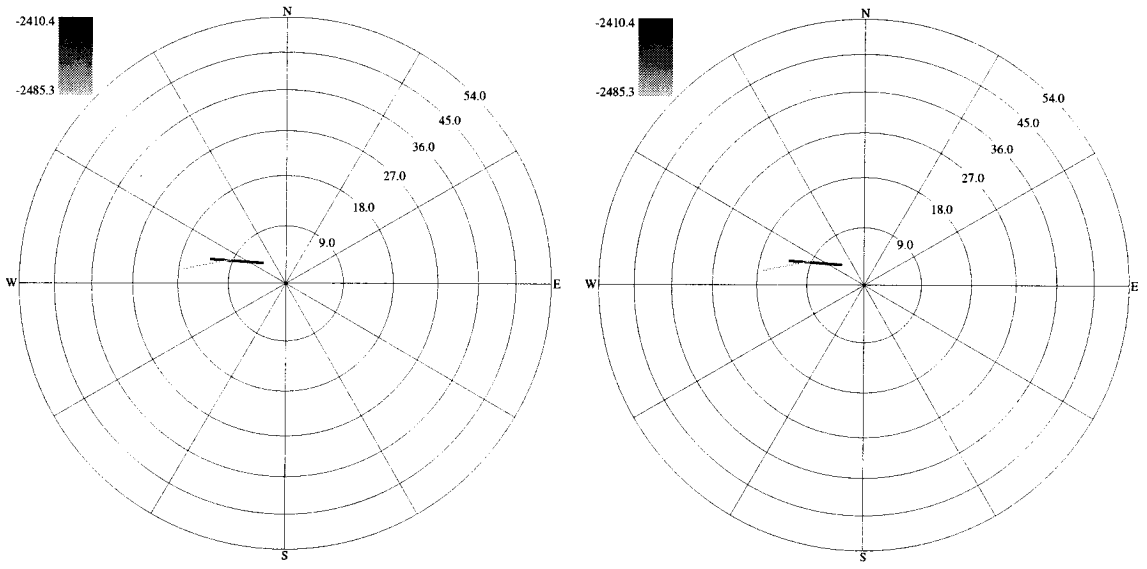

Figure B.37: Lower hemisphere stereographic projection plots of the selected breakouts from well Mgs13 in markers G3 and G4. Line widths are proportional to the breakout length. (left) All selected breakouts in G3 and G4. (right) All nonradial breakouts in G3 and G4 where the **IJK** breakout angle is not within 15° of the high side of the hole.

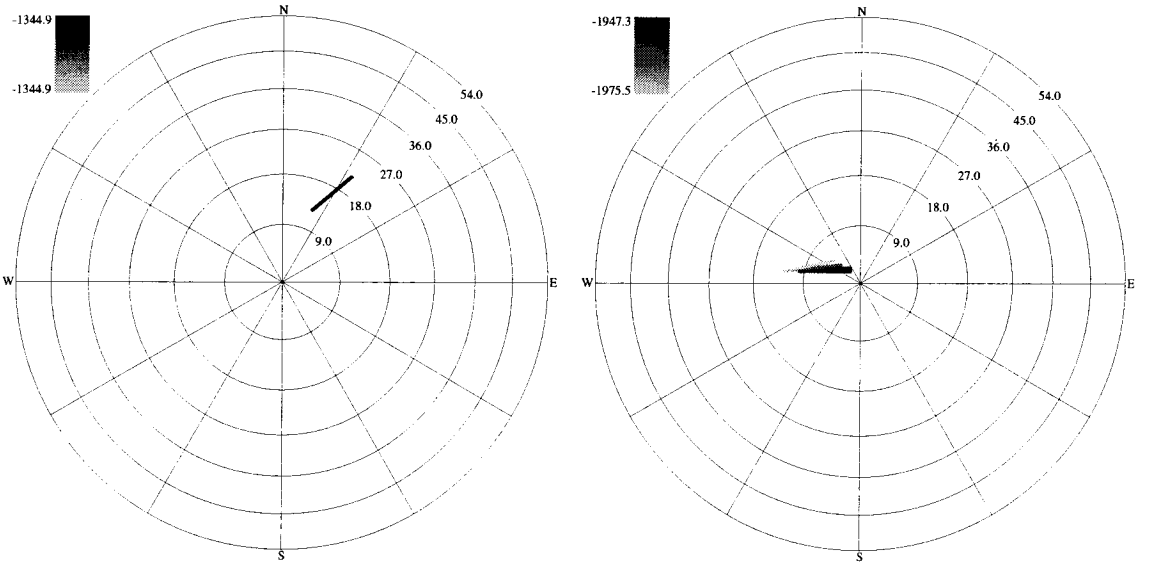

Figure B.38: Lower hemisphere stereographic projection plots of all nonradial breakouts from well Mgs13 between the true vertical depths of 1000–1500 m on the left and 1500–2000 m on the right.

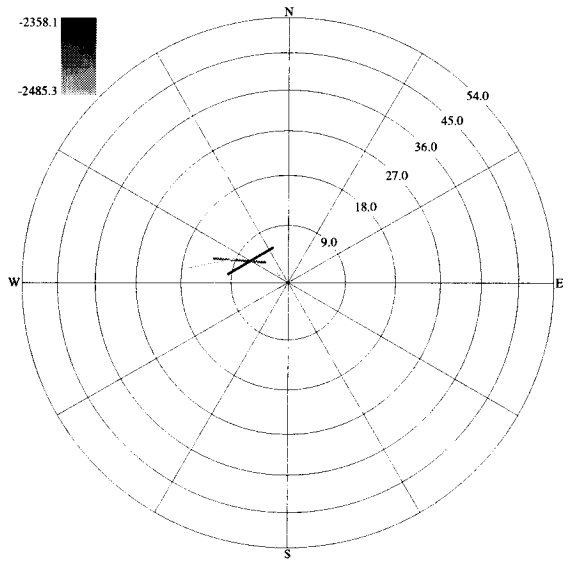

Figure B.39: Lower hemisphere stereographic projection plots of all nonradial breakouts from well Mgs13 between the true vertical depths of 2000–2500 m.

B.12 Mgs14

A single paper low-angle dipmeter log covering the log depth range 2,743–3,258 m for Middle Ground Shoals 14 was received from Unocal. The breakouts from this log were selected by eye. The properties of each breakout were entered into the computer to have the computer select only those breakouts that met the breakout selection criteria. The deviations between the directional survey and the dipmeter differ at most by 2.5°, with an average difference of 1.5°. The deviations of this hole reach 46°, but the well log starts at a depth of 2,743 m, below which the maximum borehole deviation is 29.0°. The borehole azimuth calculated from the dipmeter differs on average from the directional survey's borehole azimuth by 26.1°. The maximum difference between the two azimuths is 32.7°.

The breakout selection scheme identified 41.8 m of breakouts in the 515 m of well log, representing roughly 8.1% of the length of the hole. These are shown in Figures B.41 and B.41 along with those breakouts that have **IJK** breakout angles that differ from the high side or low side of the hole by 15°. Figure B.43 shows the breakouts separated into 500 m true vertical depth intervals. Of the oil pools examined for breakouts, only the G3 and G4 oil pools had any appreciable borehole elongations (Figure B.42).

The average breakout length was 10.4 m, which is why there are only 4 data points on the stereonet plots for this hole. However, the breakout directions are quite inconsistent and there are too few breakouts to analyze subsets of them. The breakouts occur over a relatively small 186 m true vertical depth interval. No faults were listed in the marker file to account for this pattern. A visual estimate of the stress implications of this breakout pattern would have a normal faulting stress state with the largest principal stress direction oriented roughly N0°E at a deviation of 25°. There are no faults listed in the marker file that this well crosses that could account for this variability.

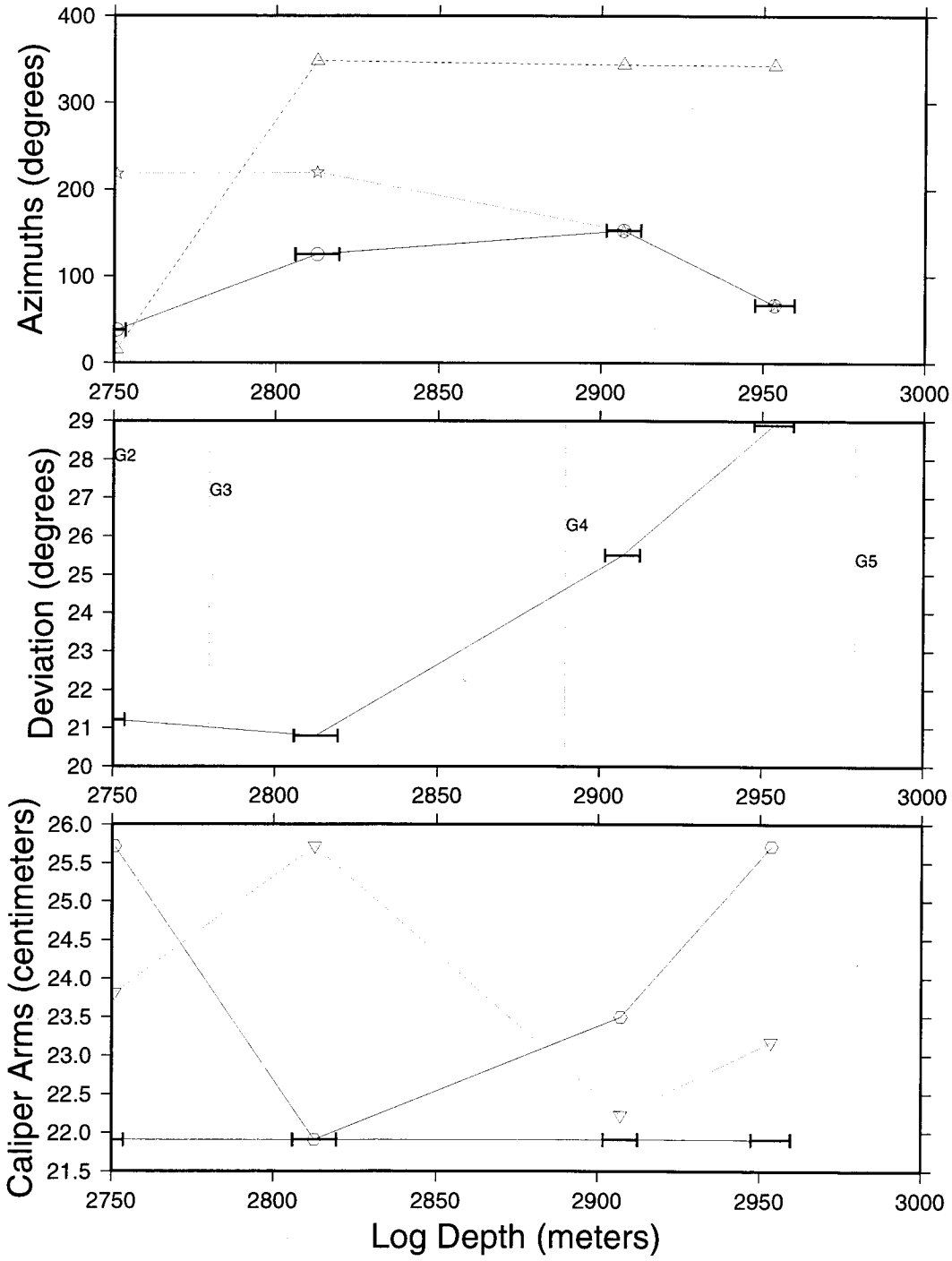

Figure B.40: Plots of the caliper-calibrated and declination-corrected selected breakout data as a function of well depth from well Mgs14. (top) Borehole azimuth (dashed line with triangles), pad azimuth (dotted line with stars), and breakout azimuth (solid line with circles). (middle) Borehole deviation (solid line) and location of marker horizons (vertical lines with labels). (bottom) Caliper arm 1 (solid line with hexagons), caliper arm 2 (dotted line with inverted triangles), and bit size (relatively constant solid line).

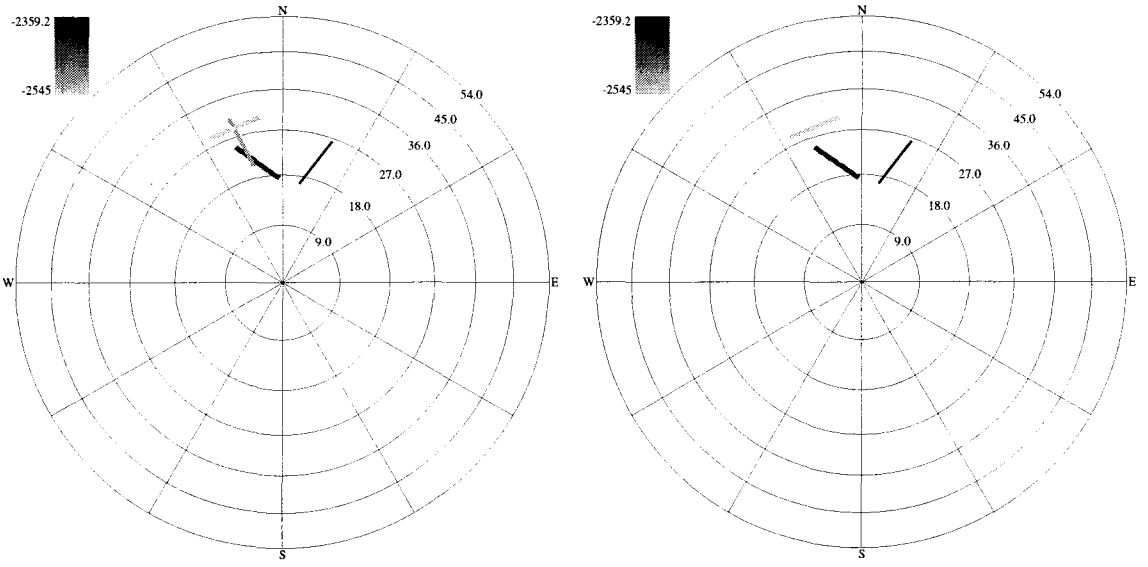

Figure B.41: Lower hemisphere stereographic projection plots of the selected breakouts from well Mgs14. Line widths are proportional to the breakout length. (left) All selected breakouts. (right) All nonradial breakouts where the **IJK** breakout angle is not within 15° of the high side of the hole.

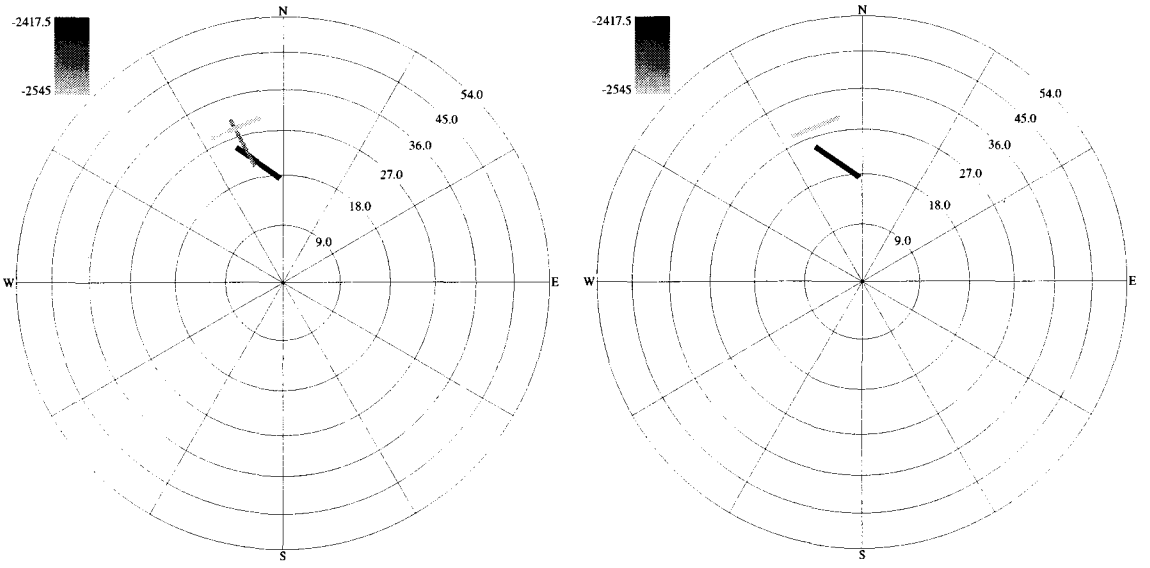

Figure B.42: Lower hemisphere stereographic projection plots of the selected breakouts from well Mgs14 in markers G3 and G4. Line widths are proportional to the breakout length. (left) All selected breakouts in G3 and G4. (right) All nonradial breakouts in G3 and G4 where the **IJK** breakout angle is not within 15° of the high side of the hole.

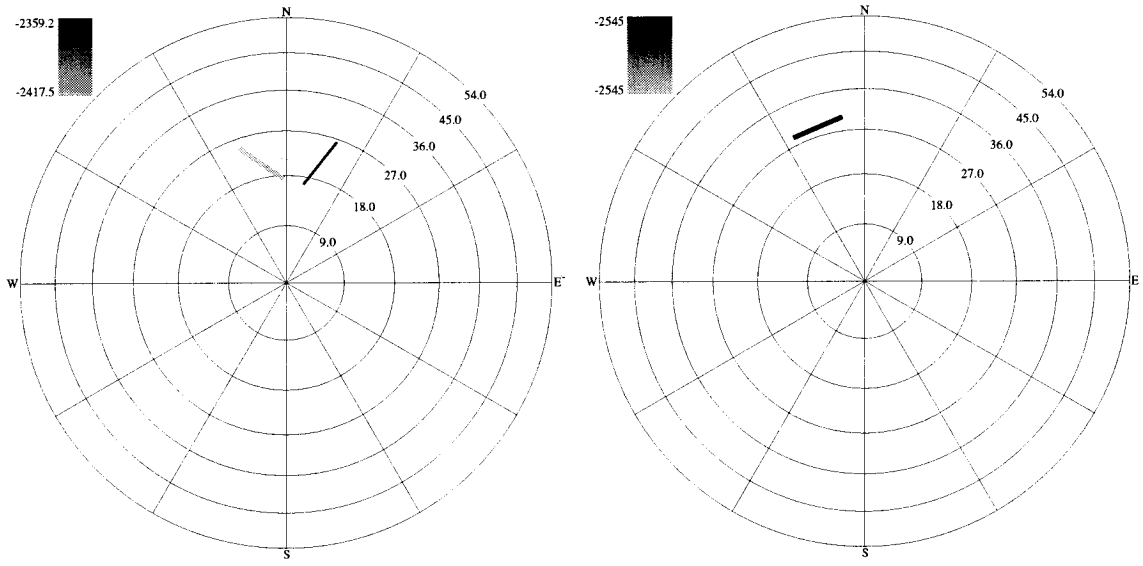

Figure B.43: Lower hemisphere stereographic projection plots of all nonradial breakouts from well Mgs14 between the true vertical depths of 2000–2500 m on the left and 2500–3000 m on the right.

B.13 Mgs15

Unocal provided a single paper high-angle dipmeter log covering the log depth range 1,067–2,835 m for Middle Ground Shoals 15 was received from Unocal. The paper log was examined by eye for breakouts and the selected breakouts were entered into the computer for automated processing and again passed through the breakout selection scheme to make sure that the breakouts had satisfied all of the criteria. The average difference between the dipmeter and directional survey deviation is 0.6°, with a maximum difference of 2.7°. The difference between the dipmeter and directional survey borehole azimuth ranged from 2.4° to 45.8°.

About 7.0% of the dipmeter log (123.7 m) had borehole elongations. The average breakout length was 6.2 m. All of the breakouts and the nonradial breakouts are shown in Figure B.45 while the same breakouts plotted in 500 m intervals are shown in Figure B.49. Breakouts were found in all of the markers that were specifically chosen for examination: B40SS (6 breakouts for 36.0 m, Figure B.46), D (2 breakouts for 22.3 m, Figure B.47), and G3 and G4 (1 breakout for 3.0 m, Figure B.48). The other markers that had breakouts were 38 (1 breakout for 6.1 m), A51SS (5 breakouts for 27.4 m), B (2 breakouts for 5.5 m), C (3 breakouts for 8.8 m), and G2 (1 breakout for 6.1 m).

This data set appears to be one of the two breakout data sets that clearly has radial and nonradial components where the nonradial component has a well defined breakout pattern, the other being Mgs29. The nonradial breakouts appear to rotate about a breakout nodal point located at an azimuth of S60°E deviating roughly 27°. Unfortunately, part of the breakout pattern for this nodal point includes breakouts that are radially oriented and will not be included in the nonradial stress inversions performed.

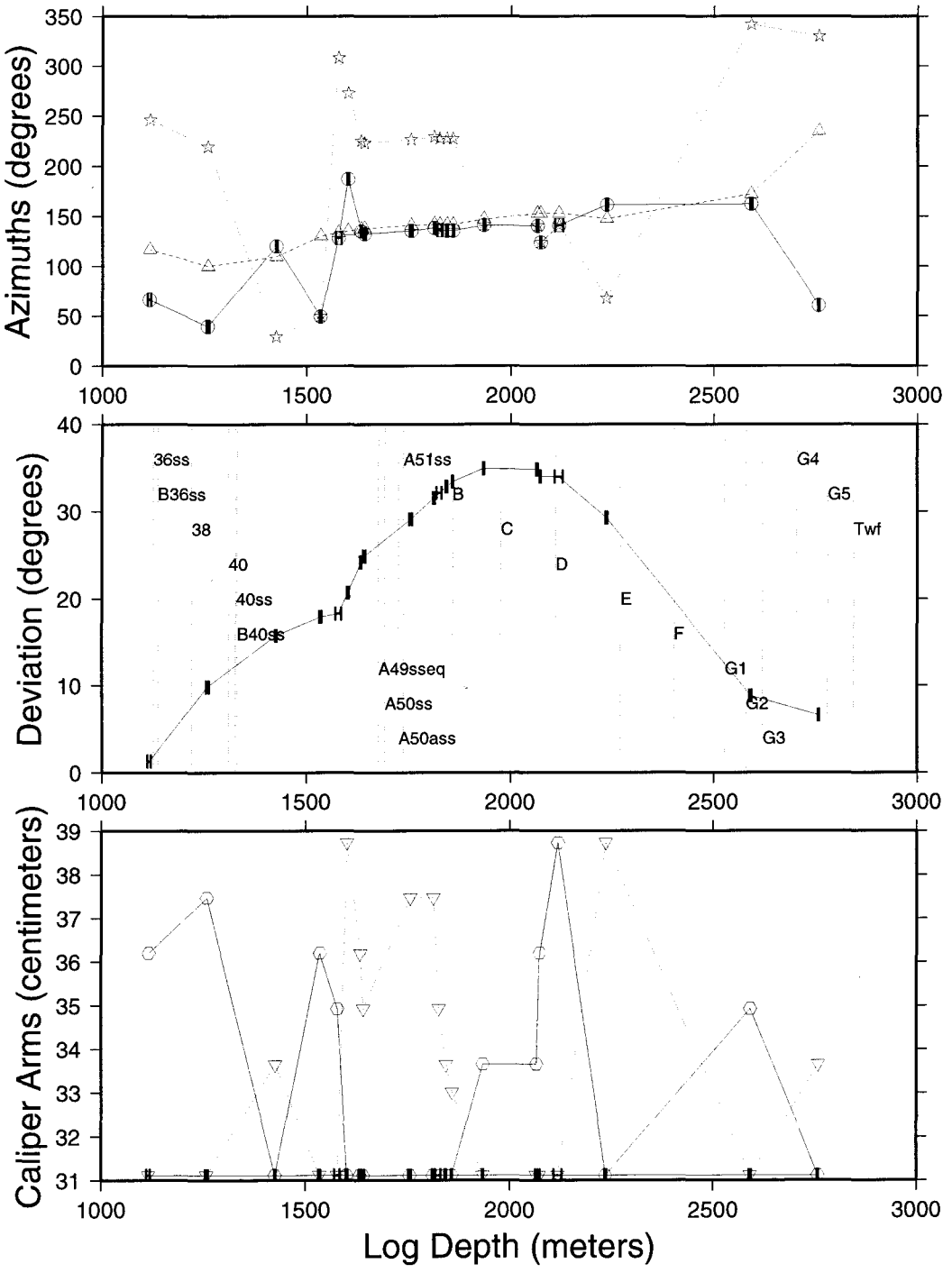

Figure B.44: Plots of the caliper-calibrated and declination-corrected selected breakout data as a function of well depth from well Mgs15. (top) Borehole azimuth (dashed line with triangles), pad azimuth (dotted line with stars), and breakout azimuth (solid line with circles). (middle) Borehole deviation (solid line) and location of marker horizons (vertical lines with labels). (bottom) Caliper arm 1 (solid line with hexagons), caliper arm 2 (dotted line with inverted triangles), and bit size (relatively constant solid line).

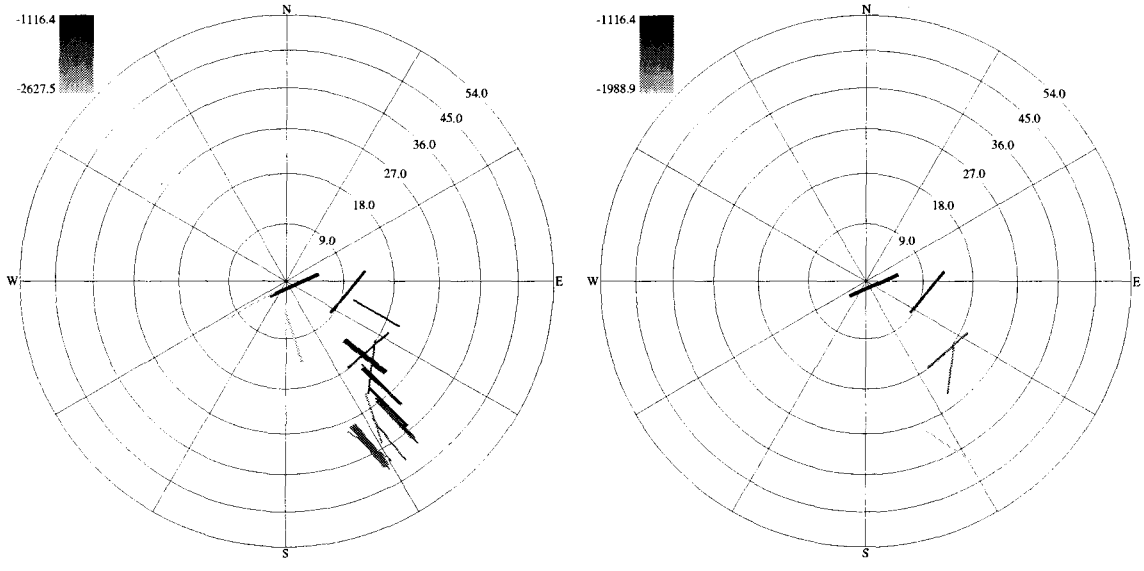

Figure B.45: Lower hemisphere stereographic projection plots of the selected breakouts from well Mgs15. Line widths are proportional to the breakout length. (left) All selected breakouts. (right) All nonradial breakouts where the **IJK** breakout angle is not within 15° of the high side of the hole.

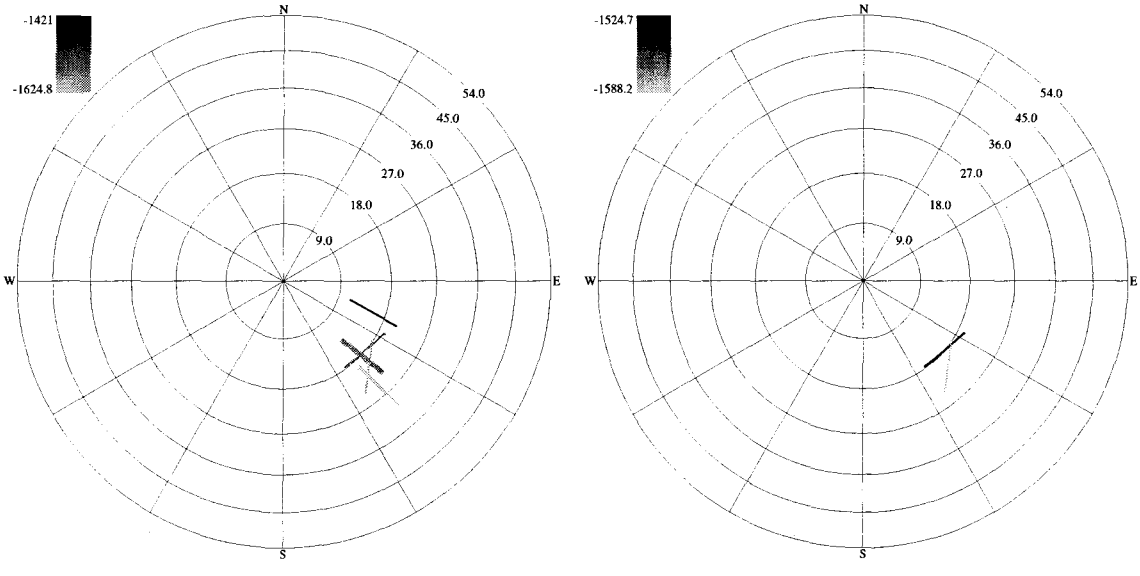

Figure B.46: Lower hemisphere stereographic projection plots of the selected breakouts from well Mgs15 in marker B40SS. Line widths are proportional to the breakout length. (left) All selected breakouts in B40SS. (right) All nonradial breakouts in B40SS where the **IJK** breakout angle is not within 15° of the high side of the hole.

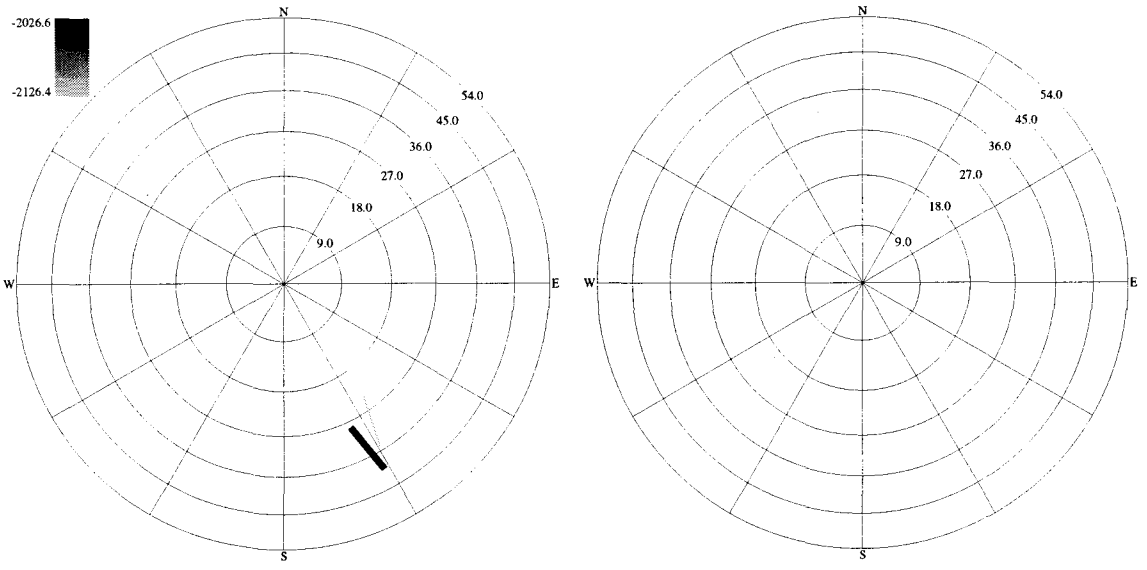

Figure B.47: Lower hemisphere stereographic projection plots of the selected breakouts from well Mgs15 in marker D. Line widths are proportional to the breakout length. (left) All selected breakouts in D. (right) All nonradial breakouts in D where the **IJK** breakout angle is not within 15° of the high side of the hole.

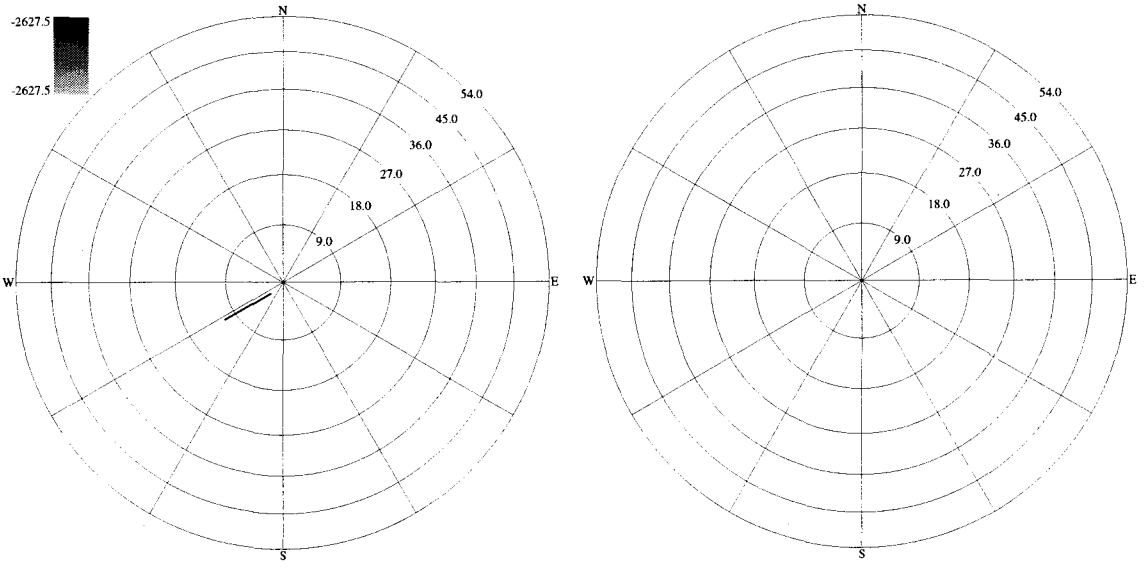

Figure B.48: Lower hemisphere stereographic projection plots of the selected breakouts from well Mgs15 in markers G3 and G4. Line widths are proportional to the breakout length. (left) All selected breakouts in G3 and G4. (right) All nonradial breakouts in G3 and G4 where the **IJK** breakout angle is not within 15° of the high side of the hole.

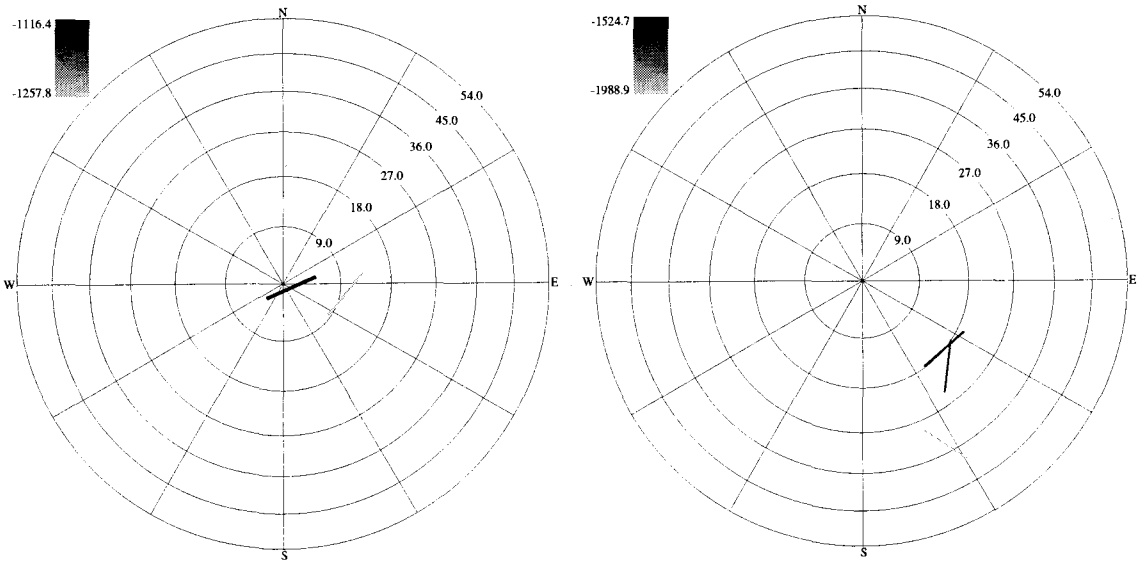

Figure B.49: Lower hemisphere stereographic projection plots of all nonradial breakouts from well Mgs15 between the true vertical depths of 1000–1500 m on the left and 1500–2000 m on the right.

B.14 Mgs16

A single low-angle dipmeter paper log was received from Unocal for Middle Ground Shoals 16. This well log covered the well log depths 1,219 to 2,926 m. The paper well log was examined by eye for possible breakouts and the properties of these possible breakouts was entered into the computer, where they were checked by a programmed version of the breakout selection scheme. The measured deviations between the dipmeter and directional survey differ on average by 1.1°, with a maximum difference of 2.3°. However, the borehole azimuth from the directional survey differs as much as 27.8° from the calculated azimuths from the dipmeter (the average difference is 18.0°).

Out of the 1,707 m of logged hole, 256.0 m of breakouts were identified in 23 separate breakouts. A plot of the breakout data as a function of depth appears in Figure B.50. Lower hemisphere stereographic projection plots of the breakouts and the nonradial breakout subset of all of the breakouts is plotted in Figure B.51. Figures B.55–B.56 show the breakouts separated into 500 m true vertical depth intervals. Breakouts were identified in the three markers that are being specifically examined for the Middle Ground Shoals field: B40SS (9 breakouts for 67.1 m, Figure B.52), D (1 breakout for 30.5 m, Figure B.53), and G3 with G4 (3 breakouts for 25.0 m, Figure B.54). Breakouts were also identified in the following markers: 38 (1 breakout for 13.4 m), A50SS (1 breakout for 5.2 m), A51SS (1 breakout for 6.4 m), C (1 breakout for 4.3 m), E (1 breakout for 63.4 m), and F (4 breakouts for 32.3 m).

This log has well-behaved in-gauge sections with tool rotation, some washed-out sections, key seats, and numerous sections that appeared to be well-behaved breakouts. Often these broken-out sections were quite consistent for long distances, and could have been picked less conservatively (and for greater distances down hole) than were picked here. Because this hole is not highly deviated, the breakout directions (particularly in the deepest section of the hole) are probably close to what one would expect to find in a vertical hole. Thus, these data can be taken as some indication of the direction of S_H.

This hole has two distinct populations of breakouts. The shallow set extends to 2,515.7 m TVD and is oriented for the most part between NE–SW and NNE–SSW. The deeper breakouts of the shallow set are rotated more clockwise than the shallower breakouts and may represent part of a radial breakout pattern not centered on the center of the plot. The deeper set of three breakouts starts at 2,735.7 m and is oriented just west of north. The marker file does not list any faults that this well crossed. Between 2,515.7 m and 2,735.7 m, the transition between the two sets of breakouts occurs partly in the F marker, covers all of the G2 marker, and ends in the G3 marker.

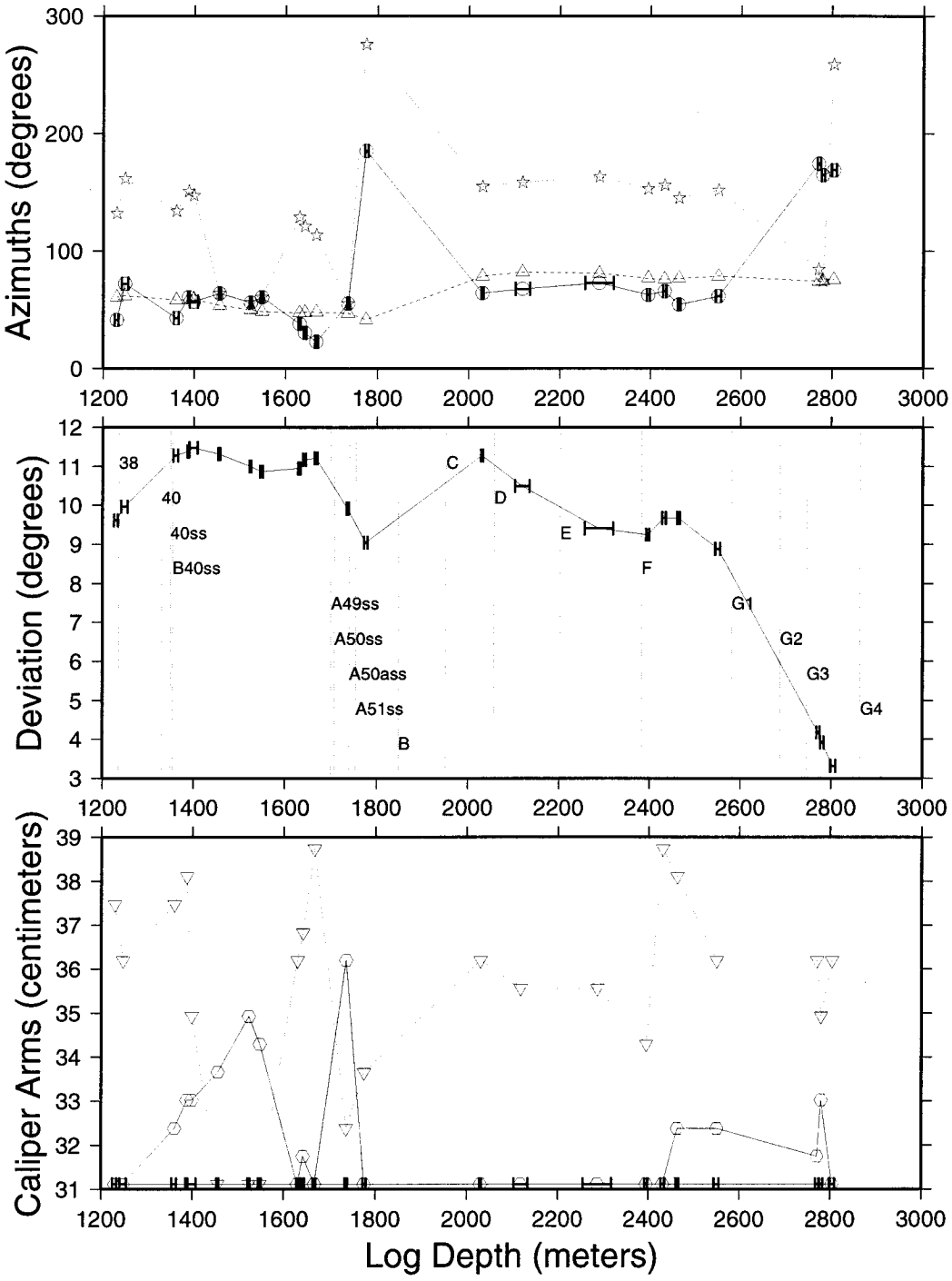

Figure B.50: Plots of the caliper-calibrated and declination-corrected selected breakout data as a function of well depth from well Mgs16. (top) Borehole azimuth (dashed line with triangles), pad azimuth (dotted line with stars), and breakout azimuth (solid line with circles). (middle) Borehole deviation (solid line) and location of marker horizons (vertical lines with labels). (bottom) Caliper arm 1 (solid line with hexagons), caliper arm 2 (dotted line with inverted triangles), and bit size (relatively constant solid line).

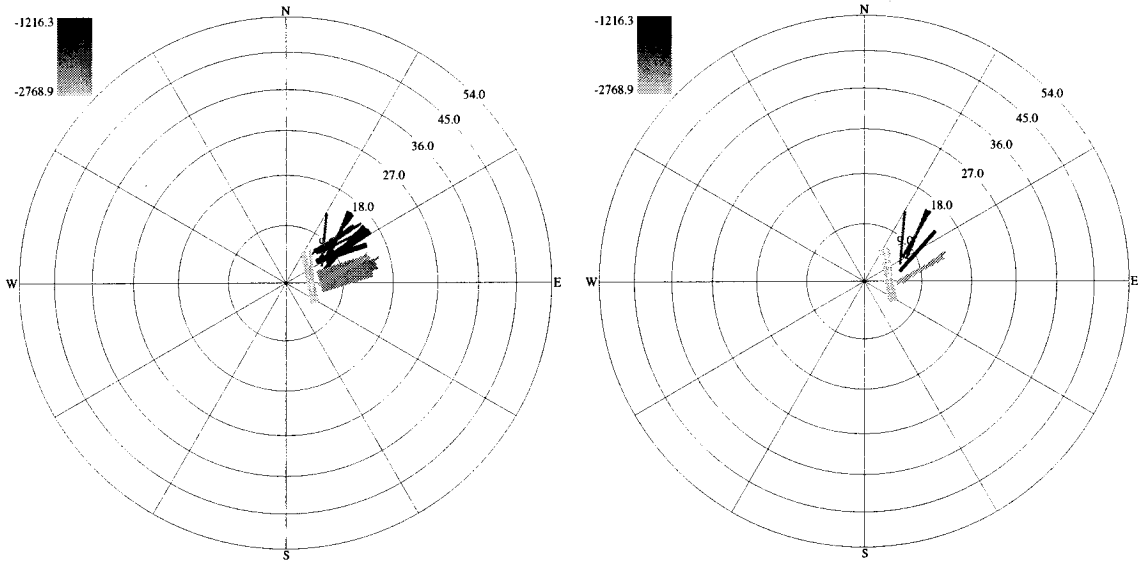

Figure B.51: Lower hemisphere stereographic projection plots of the selected breakouts from well Mgs16. Line widths are proportional to the breakout length. (left) All selected breakouts. (right) All nonradial breakouts where the **IJK** breakout angle is not within 15° of the high side of the hole.

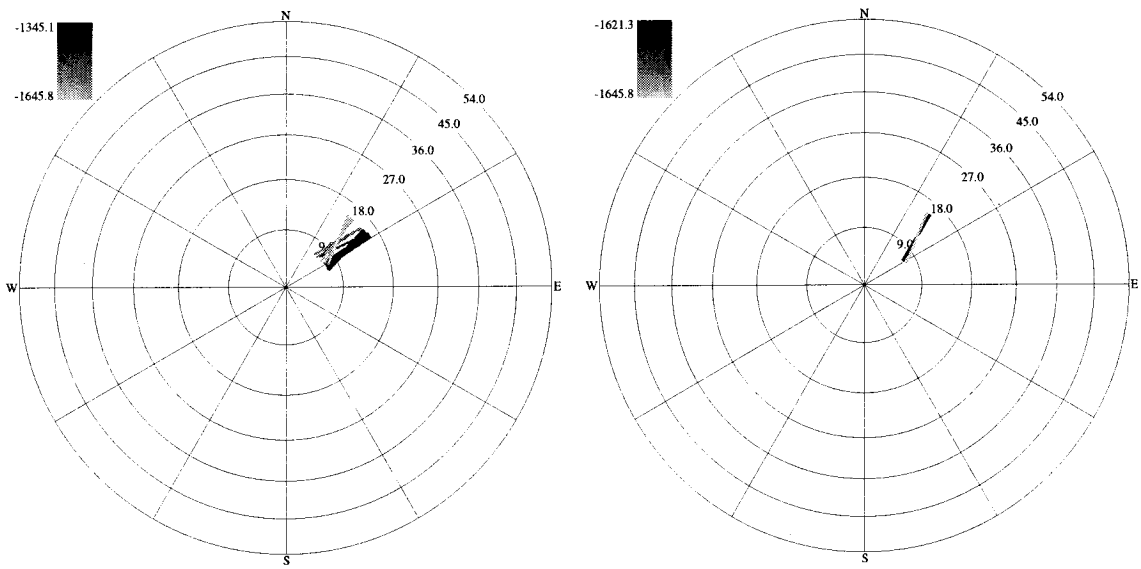

Figure B.52: Lower hemisphere stereographic projection plots of the selected breakouts from well Mgs16 in marker B40SS. Line widths are proportional to the breakout length. (left) All selected breakouts in B40SS. (right) All nonradial breakouts in B40SS where the **IJK** breakout angle is not within 15° of the high side of the hole.

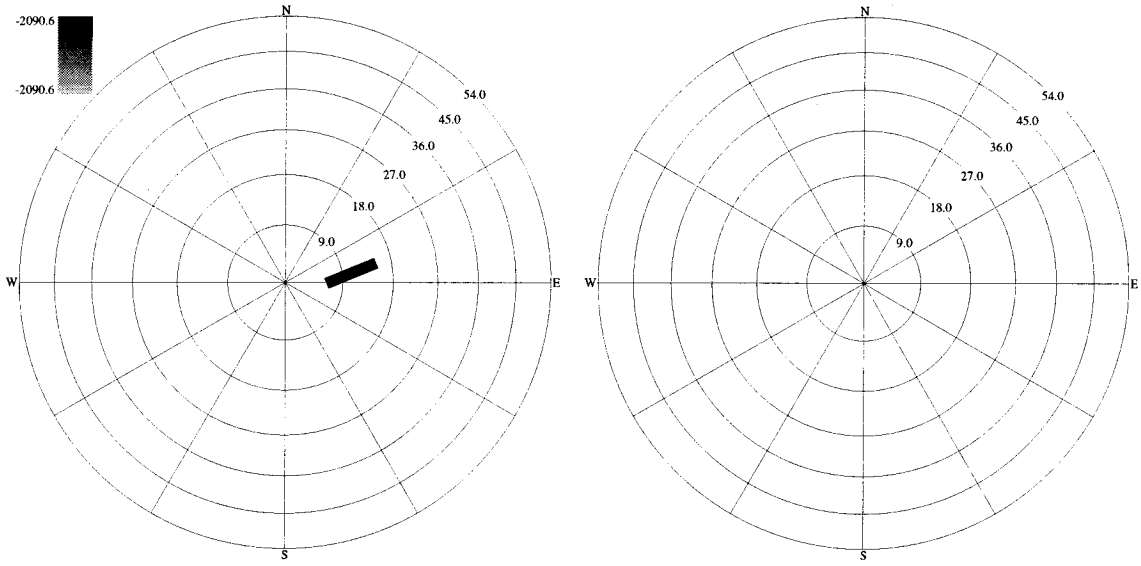

Figure B.53: Lower hemisphere stereographic projection plots of the selected breakouts from well Mgs16 in marker D. Line widths are proportional to the breakout length. (left) All selected breakouts in D. (right) All nonradial breakouts in D where the **IJK** breakout angle is not within 15° of the high side of the hole.

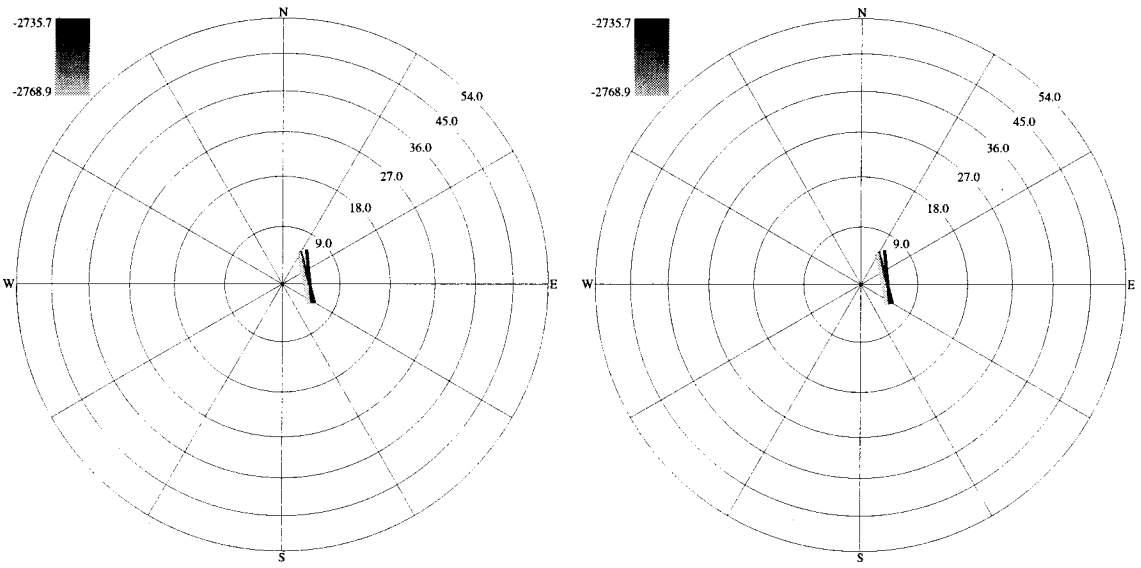

Figure B.54: Lower hemisphere stereographic projection plots of the selected breakouts from well Mgs16 in markers G3 and G4. Line widths are proportional to the breakout length. (left) All selected breakouts in G3 and G4. (right) All nonradial breakouts in G3 and G4 where the **IJK** breakout angle is not within 15° of the high side of the hole.

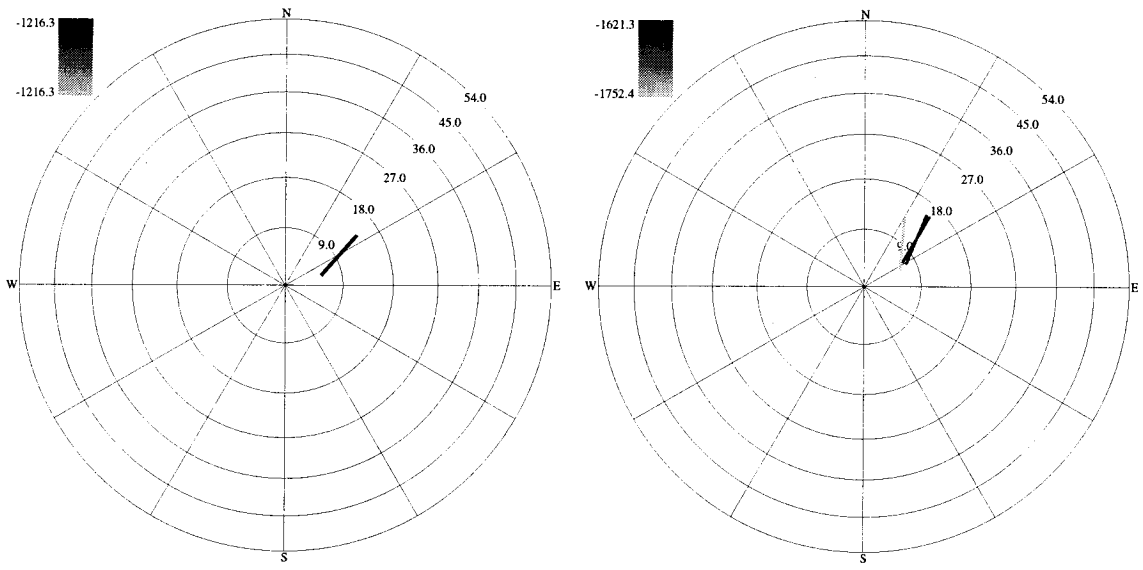

Figure B.55: Lower hemisphere stereographic projection plots of all nonradial breakouts from well Mgs16 between the true vertical depths of 1000–1500 m on the left and 1500–2000 m on the right.

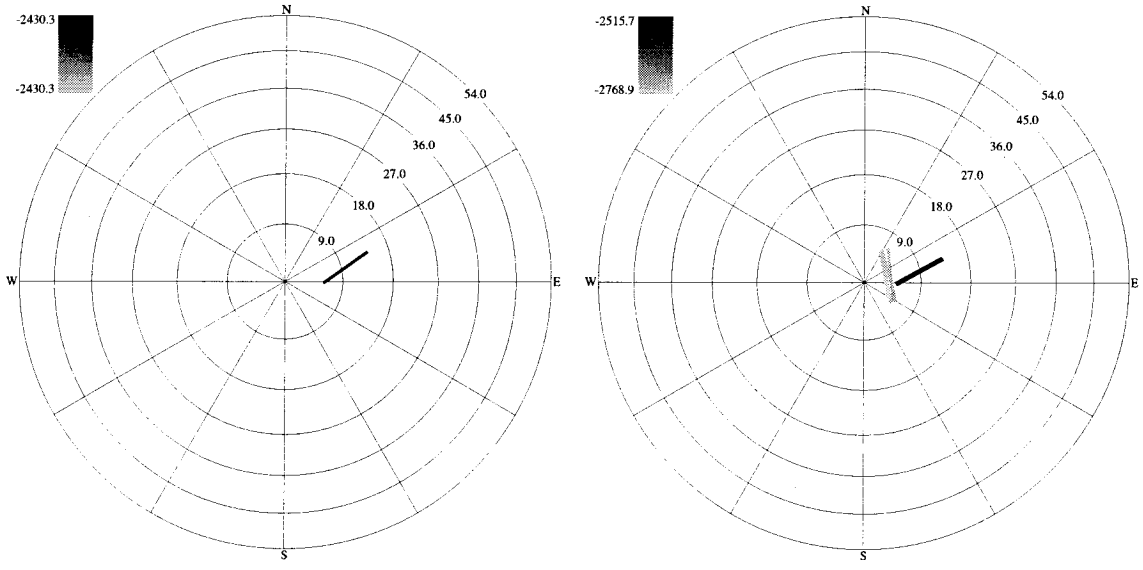

Figure B.56: Lower hemisphere stereographic projection plots of all nonradial breakouts from well Mgs16 between the true vertical depths of 2000–2500 m on the left and 2500–3000 m on the right.

B.15 Mgs28

Unocal provided digital dipmeter, directional survey logs and marker files for Middle Ground Shoals 28 (Figure B.57). This well had deviations up to 71°, which made it very promising for providing stress state information. Unfortunately, the caliper arms were much smaller than the bit size, which reflects the fact that the hole has a large channel dug in the bottom of the hole where the dipmeter tool lay while logging the hole (Rod Paulson, personal communication). Since the deviations are so high this is not too surprising. Because of the noncircular shape of the hole and the mismatched caliper arm and bit size data, no computer selected breakouts were identified.

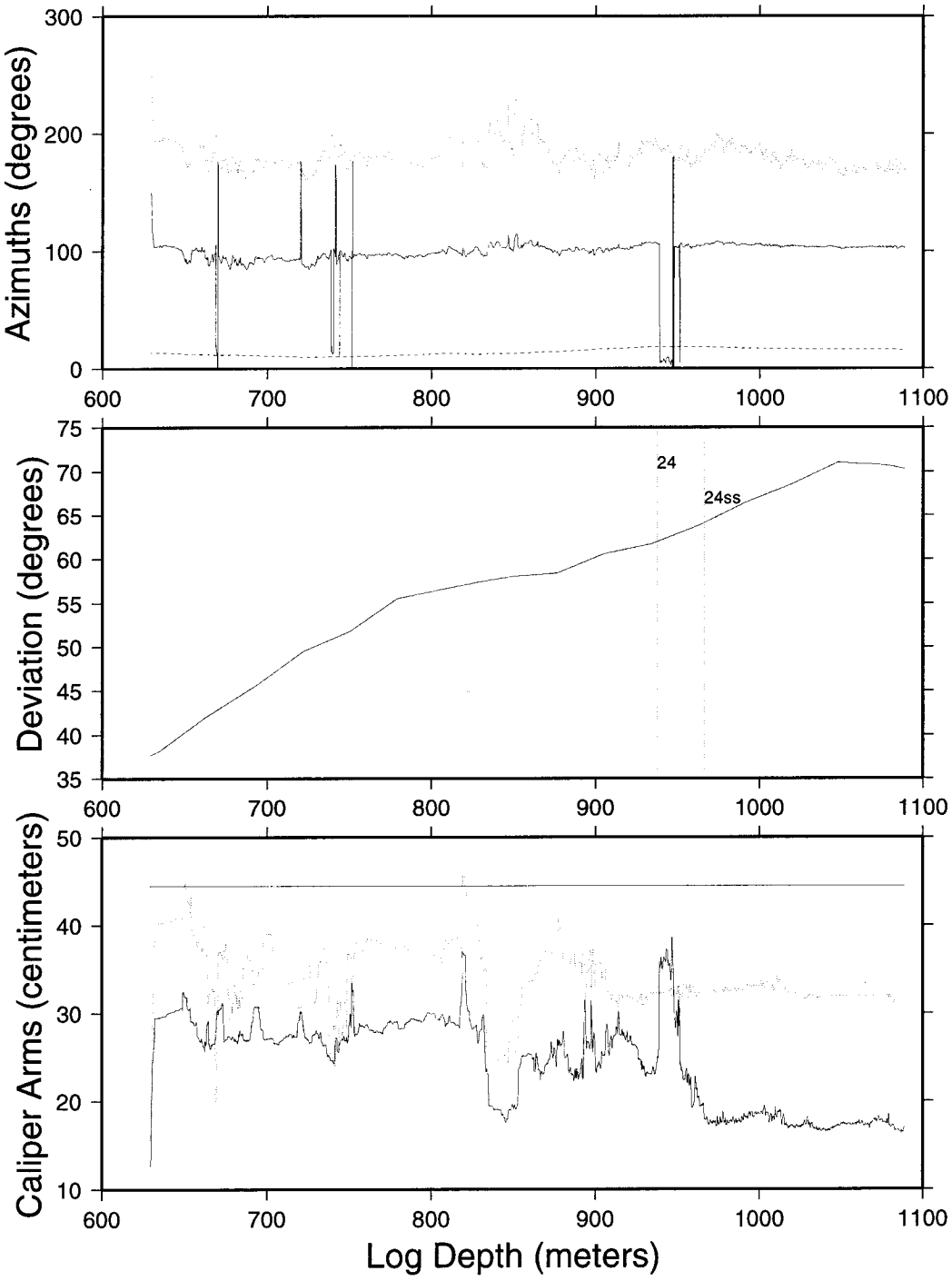

Figure B.57: Plots of the caliper-calibrated and declination-corrected digitized dipmeter and derived quantities data as a function of well depth from well Mgs28. (top) Borehole elongation direction (solid line), pad 1 azimuth (dotted line), and borehole azimuth (dashed line). (middle) Borehole deviation (solid curve) and location of marker horizons (vertical lines with labels). (bottom) Bit size (straight solid line), caliper arm 1 (solid line), and caliper arm 2 (dotted line). Selected breakout regions are plotted as horizontal bars showing the depth extent of the breakouts.

B.16 Mgs29

Mgs29 is the second Middle Ground Shoals well that digital data from both the directional survey and dipmeter tools was received from Unocal (Figure B.58). The type of dipmeter used to log this hole is unknown. The dipmeter logged the well depth interval from 1,795 to 2,746 m. The deviations agree within 1.4° between the directional survey data and the dipmeter data. Excluding the top part of the well log where the borehole deviation is very close to 0 and the borehole azimuth has no meaning, the minimum and maximum difference between the borehole and dipmeter borehole azimuths are 22.7° and 38.4°, respectively. The directional survey borehole azimuths are used for the breakout calculations for this hole.

In the 951 m of logged hole, 32 separate breakouts were identified totaling 244.9 m in length (Figure B.59). The same breakouts broken out into 500 m TVD intervals are shown in Figures B.61–B.62 and the nonradial breakouts are plotted in Figure B.59. Borehole elongations were found in the C (3 breakouts for 14.5 m), D (8 breakouts for 46.1 m, Figure B.60), E (6 breakouts for 54.9 m), and F (16 breakouts for 129.4 m) markers.

Except for a few breakouts near the bottom of the log, this well has a very consistent breakout pattern of an arc that follows the borehole's trend through orientation space. The shallow breakouts are almost radial, while the deeper ones seem to follow the change in the borehole's orientation. However, this is probably a coincidence between the borehole's path and the stress state that causes this pattern of breakouts. The maximum rate of change of the borehole's path is 1°/10 m, which is too small to affect the location of breakouts on the borehole wall.

This well is similar to Mgs15 where one radial breakout pattern overlies a nonradial data with a clearly defined pattern (Figure B.59). Examination of the nonradial breakouts from Mgs29 in isolation from breakout data sets seem to show a similar thrust faulting stress state with a nodal point somewhere east of south at a relatively high deviation. This is also similar to Mgs15's results. The location of the nodal point is less clear here since the breakouts do not change their orientation very quickly as a function of borehole orientation, suggesting that the nodal point is close, but not very close to the breakout data.

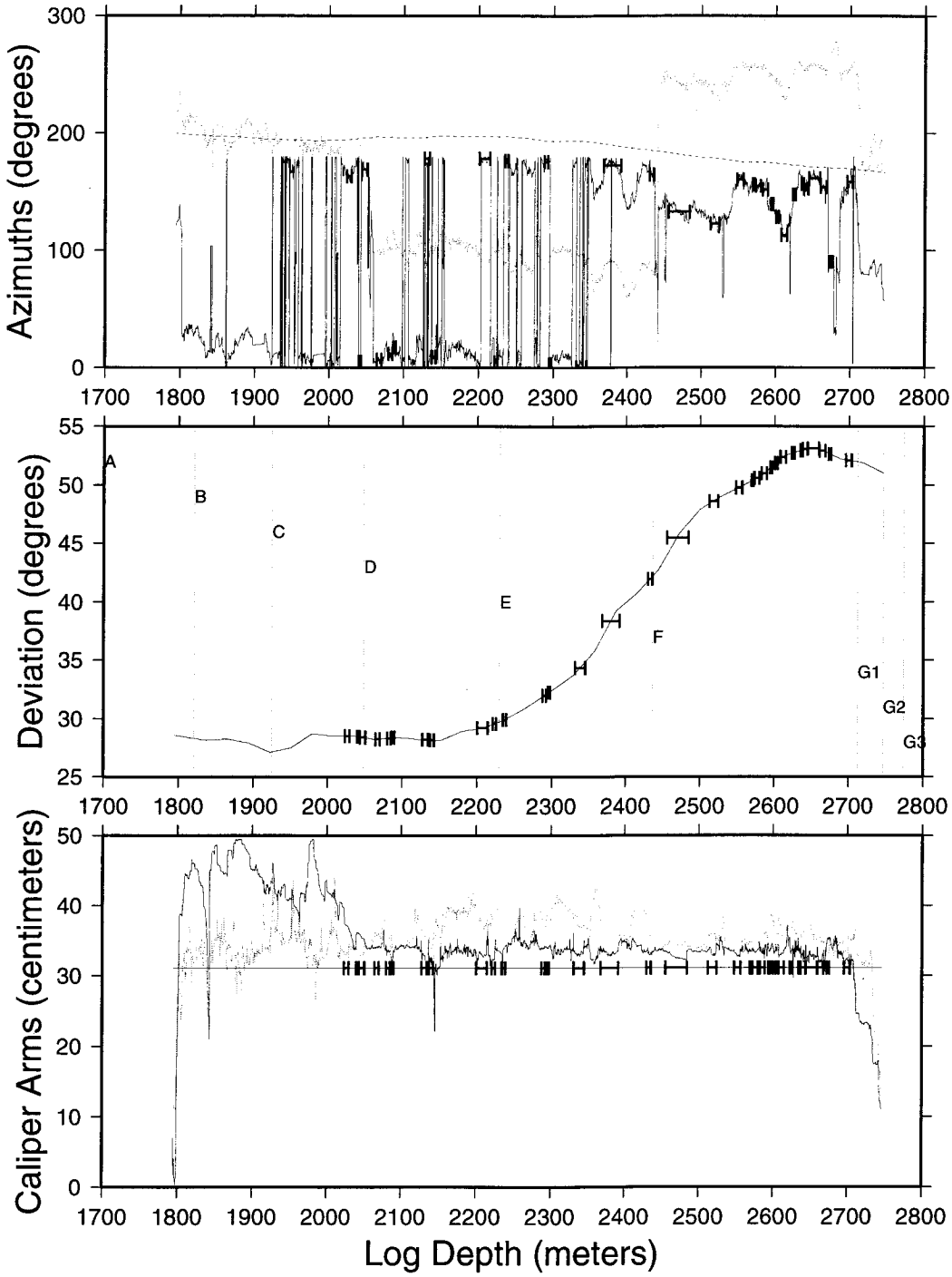

Figure B.58: Plots of the caliper-calibrated and declination-corrected digitized dipmeter and derived quantities data as a function of well depth from well Mgs29. (top) Borehole elongation direction (solid line), pad 1 azimuth (dotted line), and borehole azimuth (dashed line). (middle) Borehole deviation (solid curve) and location of marker horizons (vertical lines with labels). (bottom) Bit size (straight solid line), caliper arm 1 (solid line), and caliper arm 2 (dotted line). Selected breakout regions are plotted as horizontal bars showing the depth extent of the breakouts.

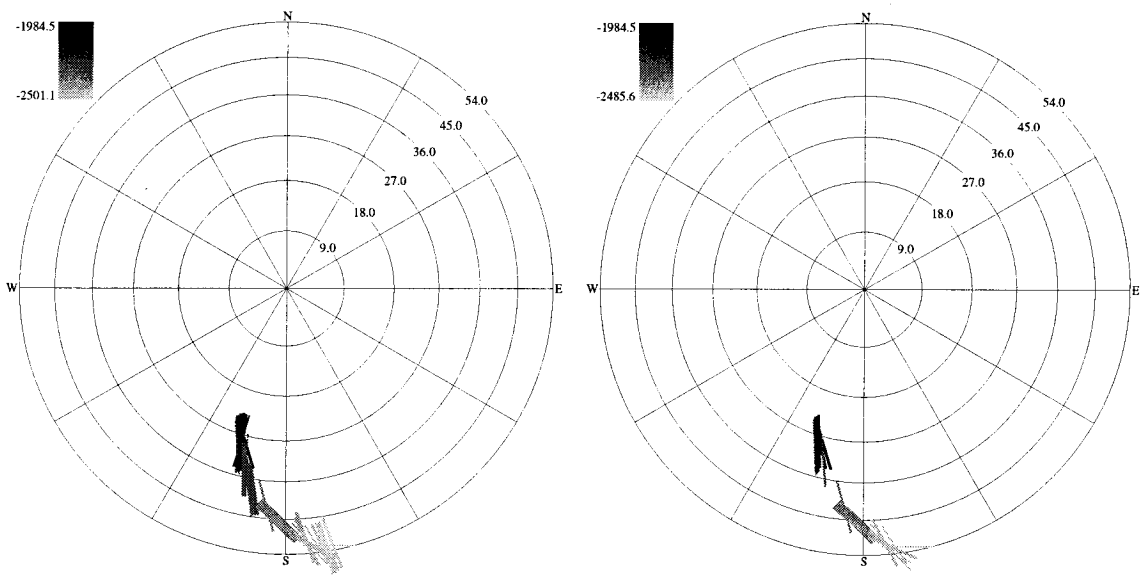

Figure B.59: Lower hemisphere stereographic projection plots of the selected breakouts from well Mgs29. Line widths are proportional to the breakout length. (left) All selected breakouts. (right) All nonradial breakouts where the **IJK** breakout angle is not within 15° of the high side of the hole.

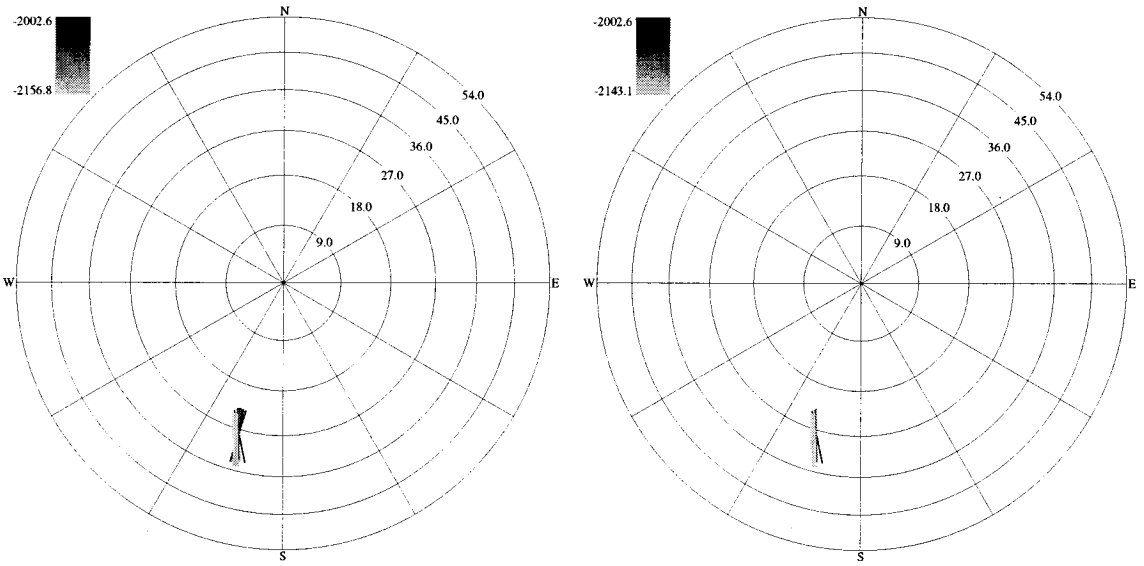

Figure B.60: Lower hemisphere stereographic projection plots of the selected breakouts from well Mgs29 in marker D. Line widths are proportional to the breakout length. (left) All selected breakouts in D. (right) All nonradial breakouts in D where the **IJK** breakout angle is not within 15° of the high side of the hole.

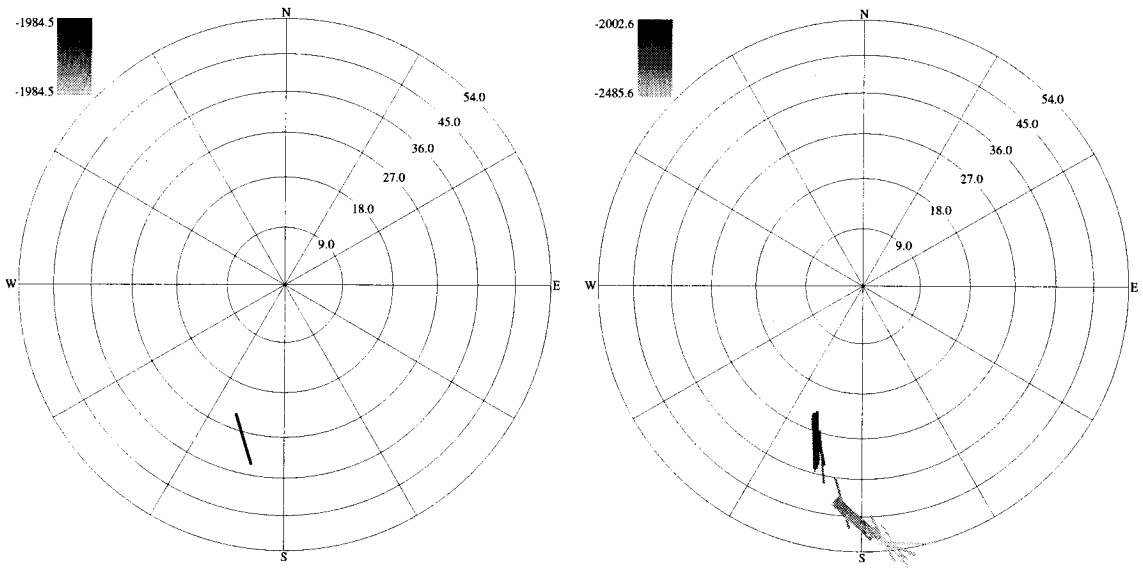

Figure B.61: Lower hemisphere stereographic projection plots of all nonradial breakouts from well Mgs29 between the true vertical depths of 1500–2000 m on the left and 2000–2500 m on the right.

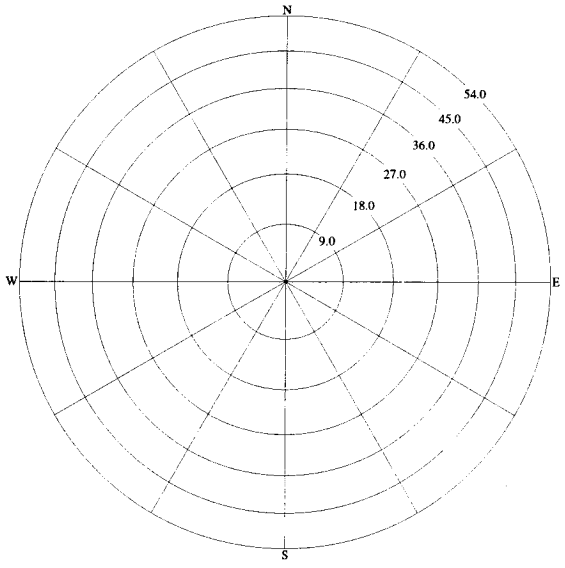

Figure B.62: Lower hemisphere stereographic projection plots of all nonradial breakouts from well Mgs29 between the true vertical depths of 2500–3000 m.

B.17 Mgs30

Unocal provided digital dipmeter and directional survey files for Middle Ground Shoals Mgs30 (Figure B.63). It is unclear whether a low-angle or high-angle dipmeter was used to log this hole, but it could have been a low-angle unit, since the deviations do not reach 36°. The borehole deviations range from 7.0° up to 30.1°. The maximum difference between the dipmeter and directional survey, in terms of borehole deviation, is 2.6°. The borehole azimuth as measured by the dipmeter differs on average by 18.3° from the borehole azimuth as measured by the directional survey, with the maximum difference being 23.5°.

Figure B.64 shows all the breakouts identified in this hole and the nonradial subset of these breakouts plotted separately. The marker file for this hole only listed two markers, F and G1, both of which had horizon tops deeper than the deepest identified breakout.

There are two populations of breakouts, a shallow set of three E–W to ESE–WNW breakouts and a deeper set of breakouts which have a large variation in breakout azimuth. There is a large change in the bit size between the shallow and deeper portions of the hole at 1,780 m log depth (Figure B.63). The shallow portion was drilled with a larger bit size (44.45 cm or 17.5 inches) and the deeper portion was drilled with a smaller bit size (31.12 cm or 12.25 inches). The change in bit size does not distinguish the change in the two populations of breakouts, since the shallowest breakout from the deeper set of breakouts was identified in the section of the hole drilled with the larger bit.

The three breakouts in the shallow set have azimuths between N89.3°E and N112.8°E. The deeper set of breakouts may be consistent with a nodal point located at a slightly higher deviation than the lowest deviation breakouts. If this were the case, then the breakouts would constrain a thrust faulting stress state (Figure 1.4) and the nodal point would match the nodal points found in the Mgs15 and Mgs29 wells. The resulting stress state would have NNW–SSE trending maximum horizontal principal stress direction. This interpretation also matches the interpretation from Mgs14 (Figure B.41) which shows breakouts at roughly the same position on the lower hemisphere stereographic projection plots. The possibility of this data suggesting this result will be examined later in conjunction with all of the data in Cook Inlet.

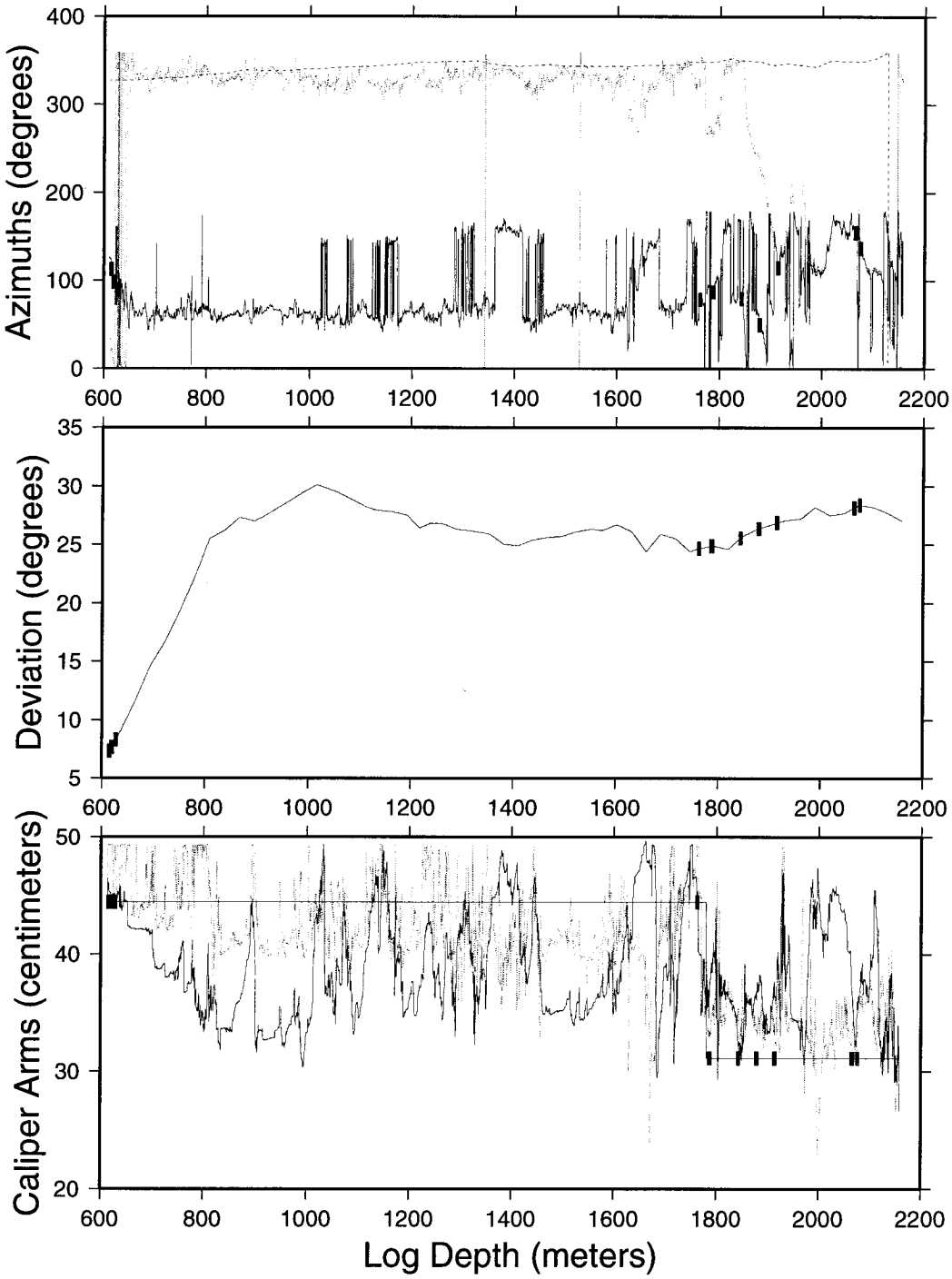

Figure B.63: Plots of the caliper-calibrated and declination-corrected digitized dipmeter and derived quantities data as a function of well depth from well Mgs30. (top) Borehole elongation direction (solid line), pad 1 azimuth (dotted line), and borehole azimuth (dashed line). (middle) Borehole deviation (solid curve) and location of marker horizons (vertical lines with labels). (bottom) Bit size (straight solid line), caliper arm 1 (solid line), and caliper arm 2 (dotted line). Selected breakout regions are plotted as horizontal bars showing the depth extent of the breakouts.

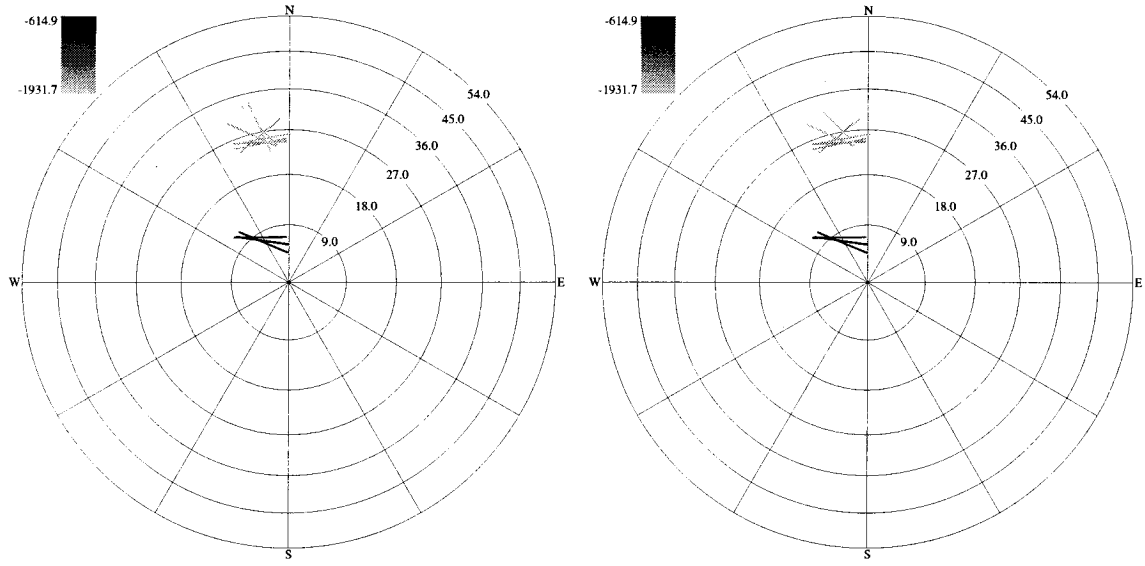

Figure B.64: Lower hemisphere stereographic projection plots of the selected breakouts from well Mgs30. Line widths are proportional to the breakout length. (left) All selected breakouts. (right) All nonradial breakouts where the **IJK** breakout angle is not within 15° of the high side of the hole.

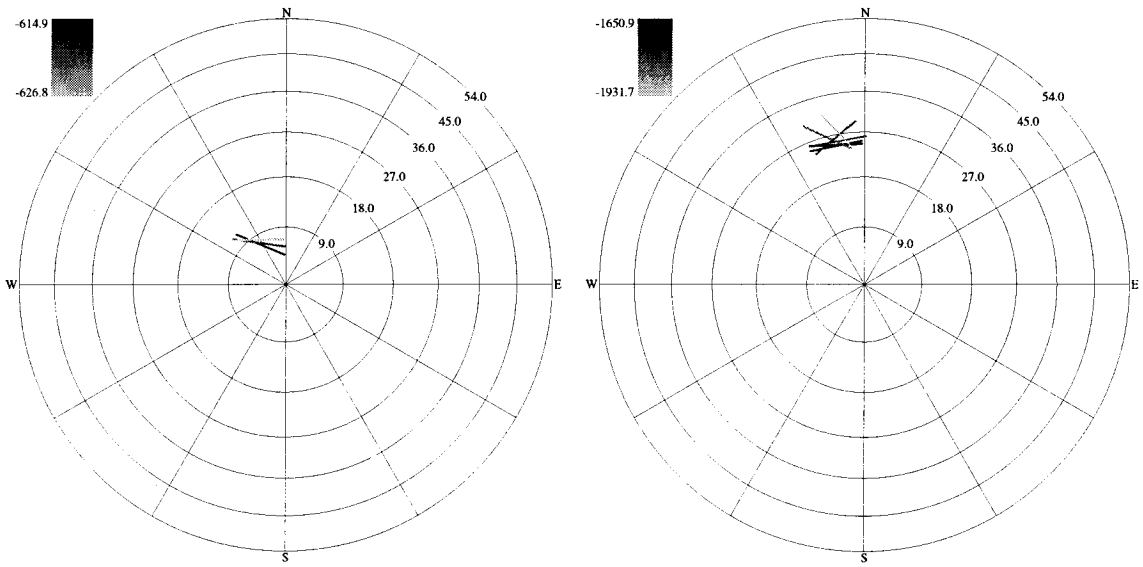

Figure B.65: Lower hemisphere stereographic projection plots of all nonradial breakouts from well Mgs30 between the true vertical depths of 500–1000 m on the left and 1500–2000 m on the right.

B.18 Smgs5

One paper well log for Smgs5 that logged the depth range 967.9 m to 3110.7 m log depth was received from Unocal. The paper well log was digitized by hand and breakouts were selected according to the breakout selection criteria for the Cook Inlet data. The digitized data and the selected breakouts are shown in Figure B.66. The largest deviation from this dipmeter log was 39.0°. The caliper arm data has a lot of variation over the entire depth range including a large amount of key seats. Thirty in-gauge sections of hole longer than 0.5 m were found, totaling 119.4 m in length.

Over the whole well log, 52 breakouts with a total length of 288.0 m were identified. The lower hemisphere stereographic projection plot of the breakouts shows a general trend of N–S directed shallow breakouts that rotate to NE–SW at the deep end of the hole (Figure B.67). The trend has a large amount of variability to it. There are thirteen breakouts that have **IJK** breakout angles that differ by at least 15° from the next shallower **IJK** breakout angle. Nine of these occur when the adjacent breakouts occur in different markers and the rest occur in the same marker. The largest **IJK** angle difference of 85.7° occurs between two breakouts separated by 41.2 m in the T22 marker. The high variability in the breakout angles will produce a poorer inversion fit, but none of the identified breakouts will be removed from the data set since I do not have that much information on the markers this well passes through.

The nonradial breakouts selected into 500 m TVD depth intervals are plotted in Figures B.69–B.71. Three breakouts were identified in the TE1 marker, the marker chosen for examination of breakout azimuths in a single marker for the Dillon platform breakouts (Figure B.68). Other breakouts were found in the following markers: T2 (2 breakouts for 12.4 m), T3 (2 breakouts for 8.0 m), T11 (3 breakouts for 18.2 m), T12 (2 breakouts for 8.4 m), T13 (2 breakout for 4.6 m), T14 (1 breakout for 3.9 m), T17 (2 breakouts for 10.3 m), T18 (2 breakouts for 8.1 m), T19 (1 breakout for 5.1 m), T20 (2 breakouts for 8.3 m), T21 (3 breakouts for 22.6 m), T22 (2 breakouts for 5.2 m), T23 (3 breakout for 20.7 m), T26 (1 breakout for 3.5 m), TA2 (5 breakouts for 18.7 m), BC2 (1 breakout for 2.9 m), TC3 (3 breakouts for 10.7 m), BD2 (1 breakout for 0.3 m), T40 (1 breakout for 2.8 m), and TE1 (3 breakouts for 16.6 m). Not all of the breakouts are listed here, since some of them lie in unidentified markers.

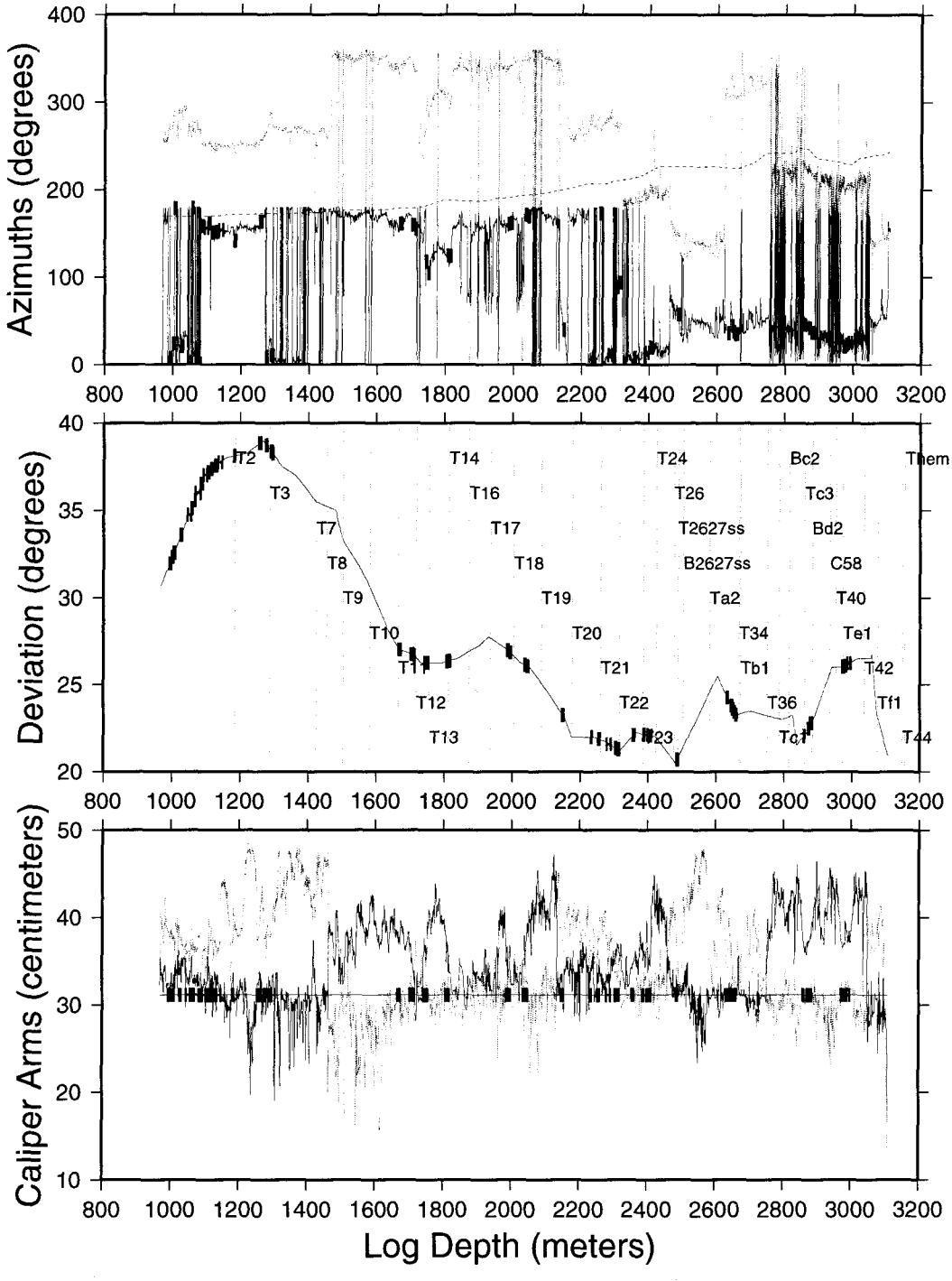

Figure B.66: Plots of the caliper-calibrated and declination-corrected digitized dipmeter and derived quantities data as a function of well depth from well Smgs5. (top) Borehole elongation direction (solid line), pad 1 azimuth (dotted line), and borehole azimuth (dashed line). (middle) Borehole deviation (solid curve) and location of marker horizons (vertical lines with labels). (bottom) Bit size (straight solid line), caliper arm 1 (solid line), and caliper arm 2 (dotted line). Selected breakout regions are plotted as horizontal bars showing the depth extent of the breakouts.

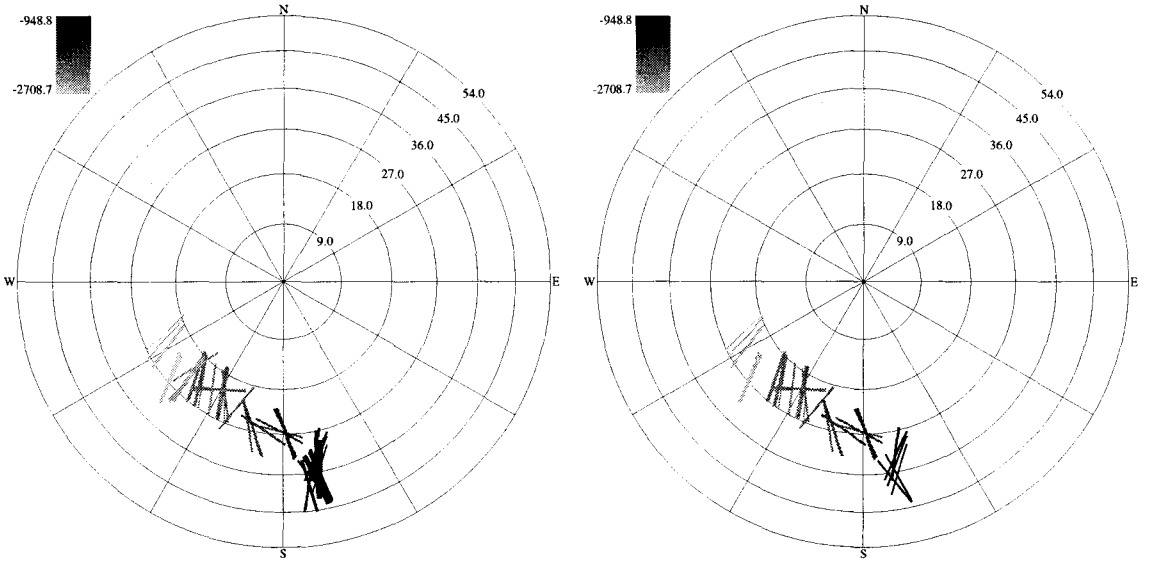

Figure B.67: Lower hemisphere stereographic projection plots of the selected breakouts from well Smgs5. Line widths are proportional to the breakout length. (left) All selected breakouts. (right) All nonradial breakouts where the **IJK** breakout angle is not within 15° of the high side of the hole.

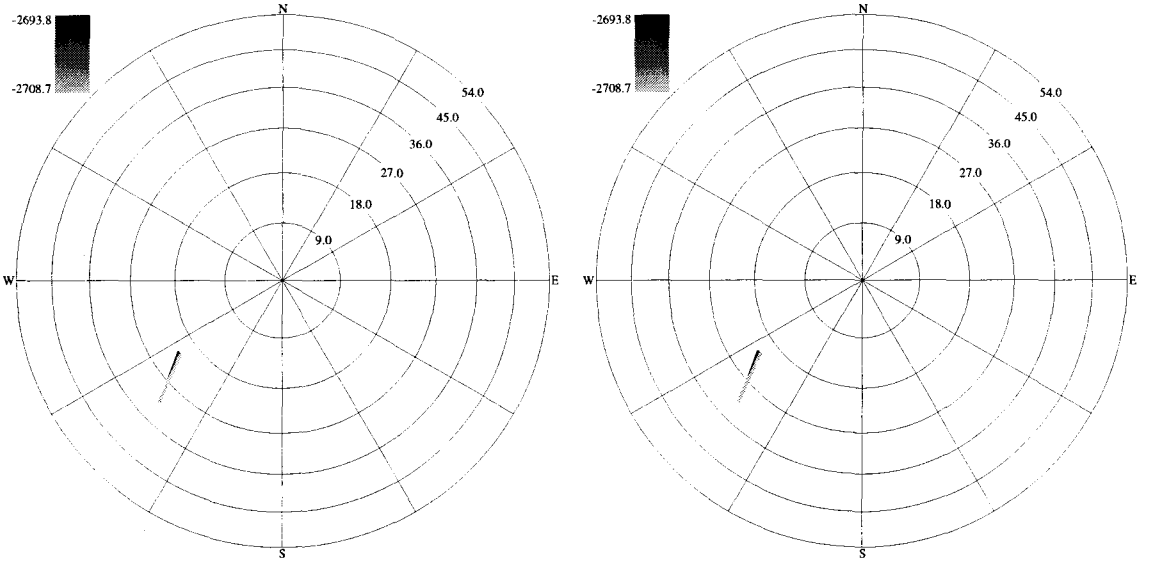

Figure B.68: Lower hemisphere stereographic projection plots of the selected breakouts from well Smgs5 in marker TE1. Line widths are proportional to the breakout length. (left) All selected breakouts in TE1. (right) All nonradial breakouts in TE1 where the **IJK** breakout angle is not within 15° of the high side of the hole.

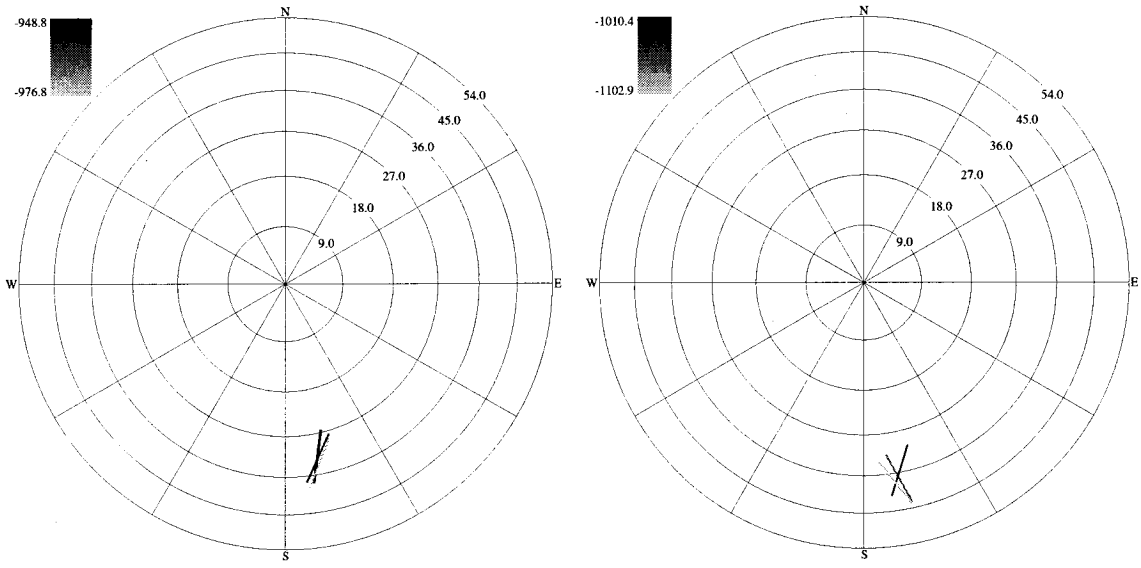

Figure B.69: Lower hemisphere stereographic projection plots of all nonradial breakouts from well Smgs5 between the true vertical depths of 500–1000 m on the left and 1000–1500 m on the right.

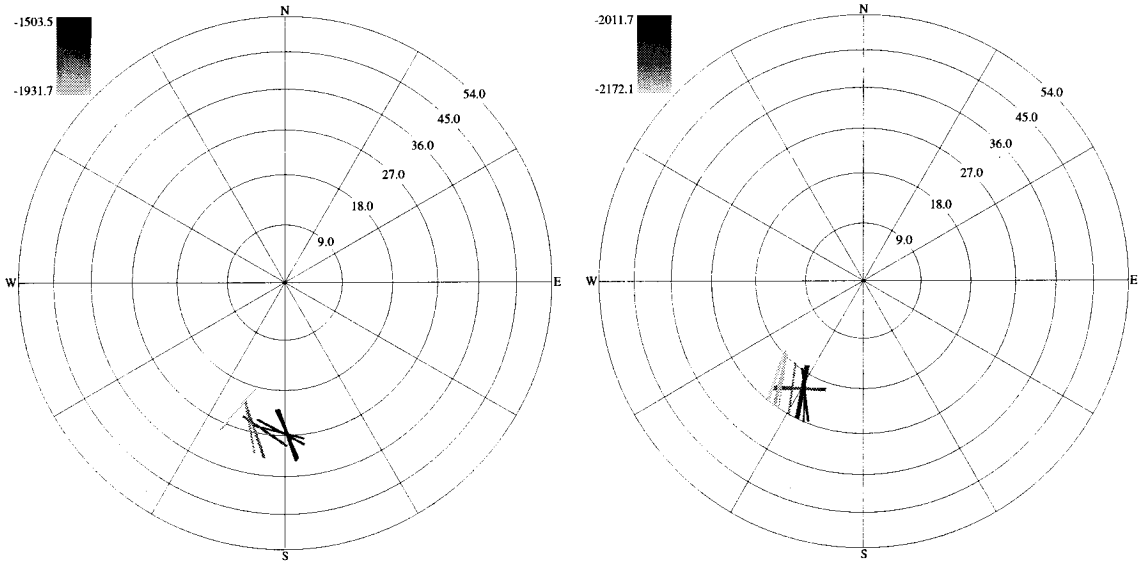

Figure B.70: Lower hemisphere stereographic projection plots of all nonradial breakouts from well Smgs5 between the true vertical depths of 1500–2000 m on the left and 2000–2500 m on the right.

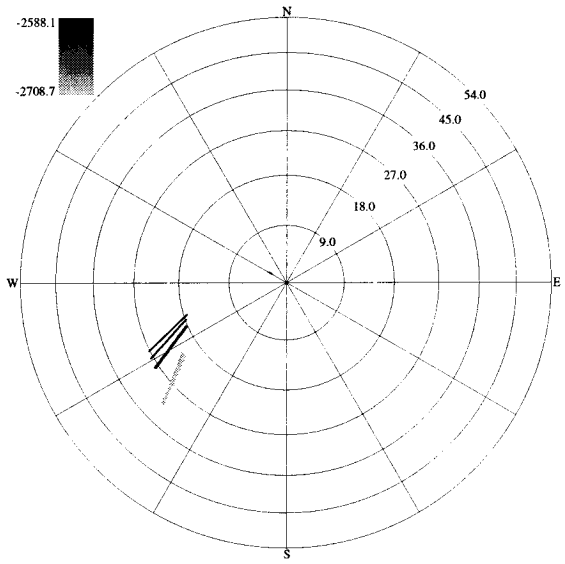

Figure B.71: Lower hemisphere stereographic projection plots of all nonradial breakouts from well Smgs5 between the true vertical depths of 2500–3000 m.

B.19 Smgs6

Unocal provided one paper dipmeter log for South Middle Ground Shoals 6. A well log digitizing company was hired by Unocal to digitize the paper log and they digitized the caliper arm, deviation, relative bearing and pad 1 azimuth data. The digitized caliper arm data was offset from the real caliper arm measurements on the paper log. From examining several caliper arm measurements between the digitized data and the paper log it appeared that the digitized data was 3.302 cm (1.3 inches) larger than the paper log values. An additive offset of -3.302 cm was applied to the digitized caliper arm data before any further processing. The final processed digital data is plotted in (Figure B.72). The digitized data spanned the log depth range from 834.1 m to 3,203.8 m. The highest measured deviations in the dipmeter data was 5°. A low-angle dipmeter tool was used to log this hole. There are 432.9 m of in-gauge hole at least 0.5 m long. However, the pad 1 azimuth shows a large amount of tool rotation in this hole.

The breakout selection criteria identified 65 breakouts which have a combined length of 360.6 m. No breakouts were found in the TE1 marker which was selected for the Dillon platform wells as a particular marker to study breakouts in. Nine breakouts spanning 42.1 m were identified in the C58 marker and the remaining breakouts were not located in any marker since the marker file did not cover the complete depth range spanned by the well log. The data are plotted on a lower hemisphere stereographic projection plot in Figure B.73 along with breakouts that have an **IJK** breakout angle more than 15° away from the high or low side of the hole. The borehole breakout orientations have a large degree of variability. There are sections of the hole where the breakout orientations are more consistent, but even some of these have a large angular distribution of orientation.

It appears that a combination of two effects caused the breakout orientation variability. The first is that dipmeter rotated only six times completely around over the 2,370 m section of hole (top of Figure B.72). The second factor is that the borehole breakout selection scheme was not strict enough for this well. The combination of the two factors caused breakouts to be identified at almost every azimuth. Even the breakouts observed in some of the 500 m TVD intervals show a similar amount of breakout azimuth variation (Figures B.75–B.76).

To examine if the breakout selection scheme criteria were not strict enough for this well, the data set was examined using two different methods. The first method made the breakout selection criteria tighter by halving the maximum allowed **IJK** breakout angle variation over the length of the breakout to 1.25°. The second test was to take the original set of breakouts and examine the paper log where the computer selected breakouts were identified and remove those breakouts by eye that did not meet the criteria that were used to pick the Middle Ground Shoals breakouts by eye. Both tests did not lead to an improvement in the breakout azimuth variability by discarding those breakouts that may have been spurious in the data set.

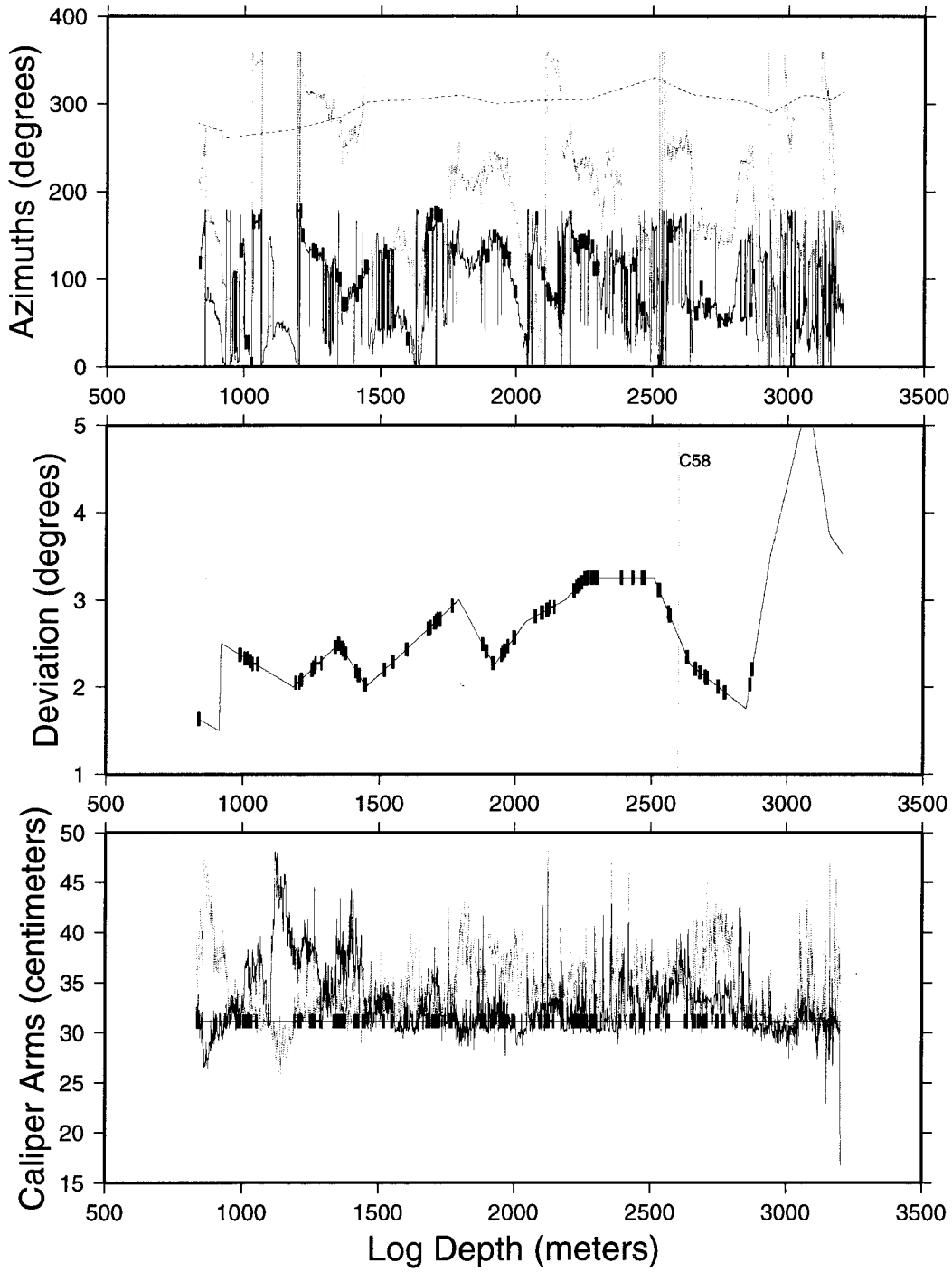

Figure B.72: Plots of the caliper-calibrated and declination-corrected digitized dipmeter and derived quantities data as a function of well depth from well Smgs6. (top) Borehole elongation direction (solid line), pad 1 azimuth (dotted line), and borehole azimuth (dashed line). (middle) Borehole deviation (solid curve) and location of marker horizons (vertical lines with labels). (bottom) Bit size (straight solid line), caliper arm 1 (solid line), and caliper arm 2 (dotted line). Selected breakout regions are plotted as horizontal bars showing the depth extent of the breakouts.

Through examining the data, it does not appear that there are any differentiating factors which would help discern a particular breakout direction as being the "correct" breakout direction. The only possible explanation for this pattern from a stress state interpretation is that the local stress state near the borehole is near a degenerate thrust or normal stress state (when $\phi \sim 1$ or $\phi \sim 0$). It was shown in Figure 1.2 that the theoretical breakout pattern for a well drilled parallel to one of the principal stress directions for a degenerate stress state will have widely varying breakout azimuths for small changes of the borehole azimuth and deviation.

The marker file for this well lists only a single horizon named C58 at 2,597.8 m log depth, so no interpretations of the breakouts are possible using this information. It has been shown that the compressive stress direction perpendicular to the anticline's fold axis varies with position due to the flexural strain in the fold [*Bruno and Winterstein*, 1992]. It is expected for a vertical well drilled into the crest of an anticline that the shallower breakouts would demonstrate a stress direction more aligned with the anticline's fold axis as compared to the deeper breakouts. If there is bedding plane slip between the beds the well crosses, then a pattern would emerge where the breakouts in the deeper sections of beds would show maximum horizontal stress directions more perpendicular to the fold axis and shallower breakouts would show maximum horizontal principal stress directions aligned with the anticline's fold axis. The breakout pattern would flip between two endpoint azimuths and this is not observed. It appears, then, that these breakouts are simply poorly identified borehole elongations and the data from this well will not be included in any stress state inversions.

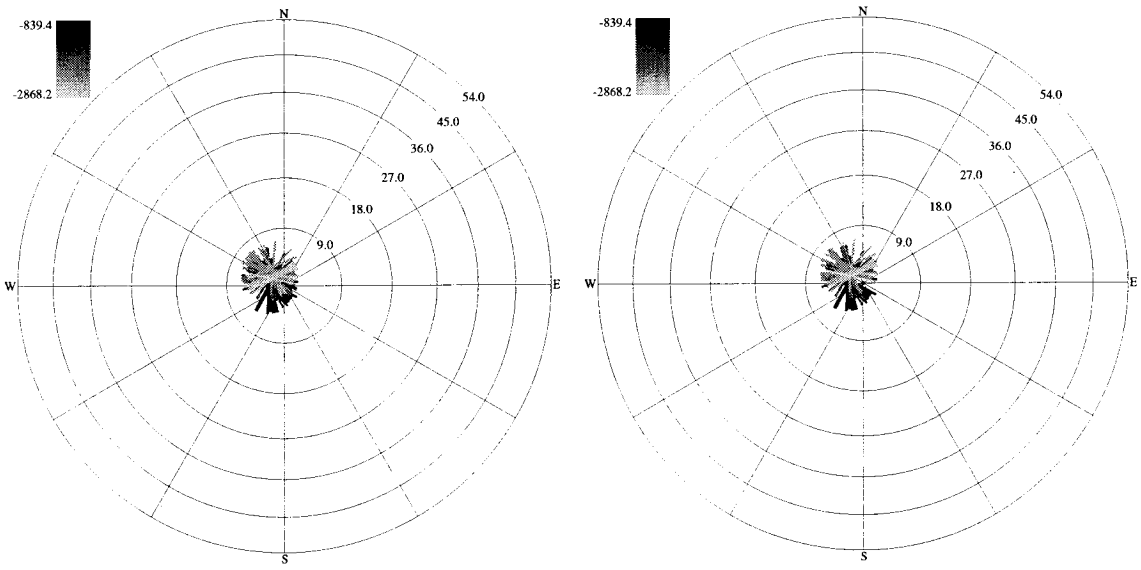

Figure B.73: Lower hemisphere stereographic projection plots of the selected breakouts from well Smgs6. Line widths are proportional to the breakout length. (left) All selected breakouts. (right) All nonradial breakouts where the **IJK** breakout angle is not within 15° of the high side of the hole.

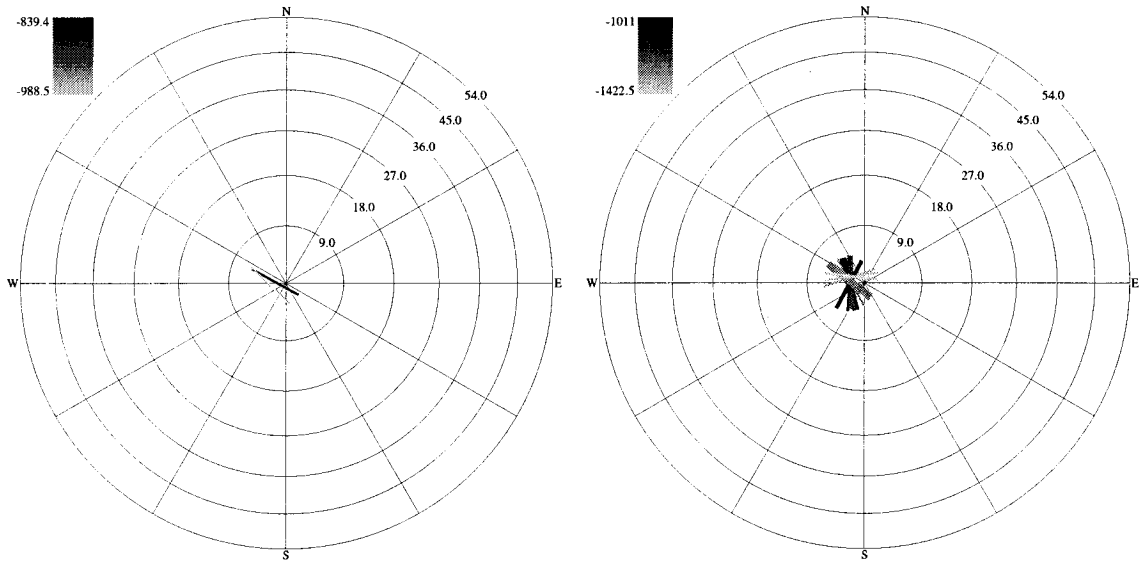

Figure B.74: Lower hemisphere stereographic projection plots of all nonradial breakouts from well Smgs6 between the true vertical depths of 500–1000 m on the left and 1000–1500 m on the right.

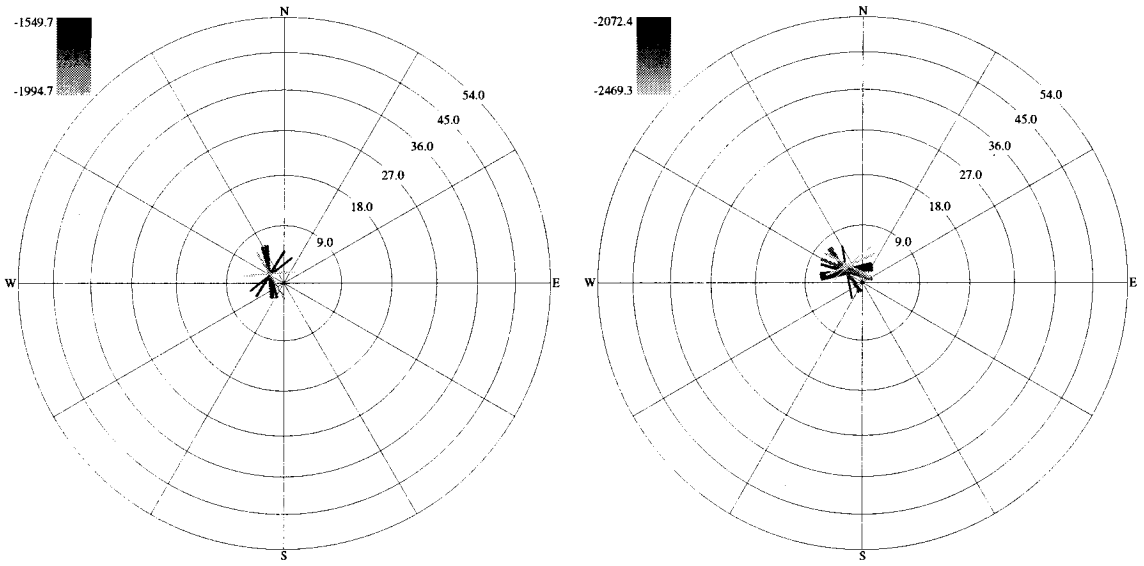

Figure B.75: Lower hemisphere stereographic projection plots of all nonradial breakouts from well Smgs6 between the true vertical depths of 1500–2000 m on the left and 2000–2500 m on the right.

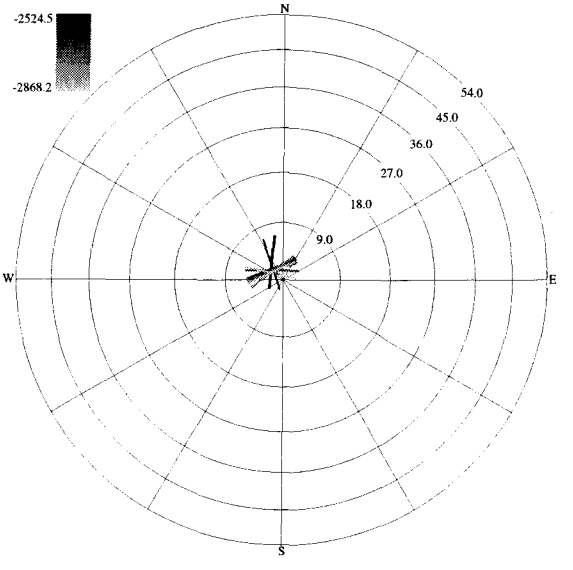

Figure B.76: Lower hemisphere stereographic projection plots of all nonradial breakouts from well Smgs6 between the true vertical depths of 2500–3000 m.

B.20 Smgs8

The paper well log for South Middle Ground Shoals 8 spans the log depth range 2625–3211 m. The well log was digitized by hand into the computer for computer selected breakouts (Figure B.78). The maximum deviation of the hole in this well log was 19.5°. In-gauge sections of the hole longer than 0.5 m accounted for 278.1 m, or 47.5%, of the length of logged hole.

Only a single breakout 4.5 m long was identified at 2,444.4 m TVD in the TC1 marker. It has roughly an azimuth orientation to it (Figure B.77). Identifying only one breakout is not too surprising, given that much of the caliper arm data was less than the bit size (Figure B.78).

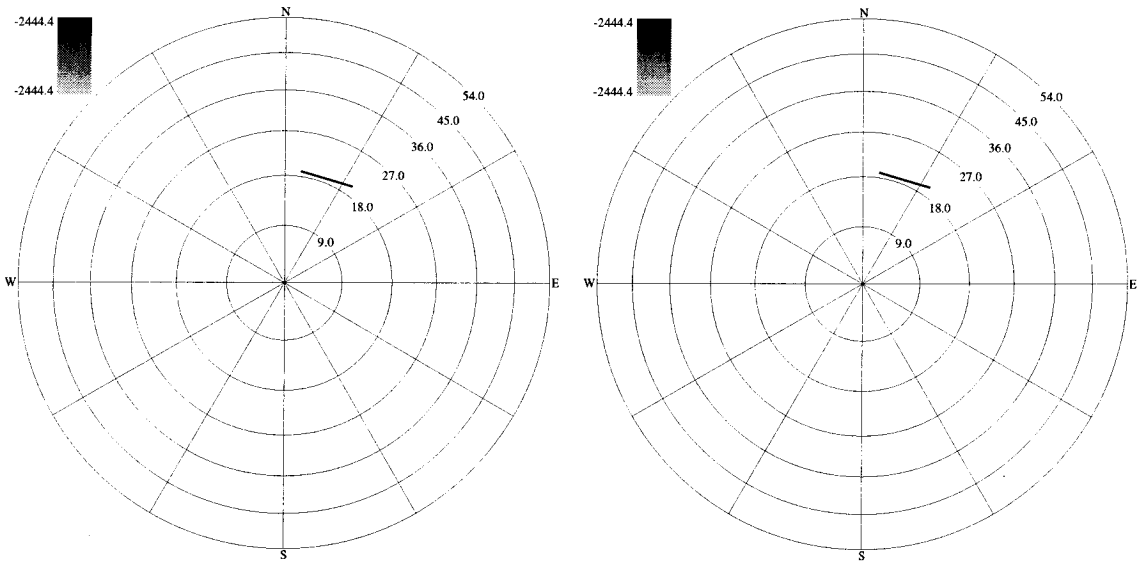

Figure B.77: Lower hemisphere stereographic projection plots of the selected breakouts from well Smgs8. Line widths are proportional to the breakout length. (left) All selected breakouts. (right) All nonradial breakouts where the **IJK** breakout angle is not within 15° of the high side of the hole.

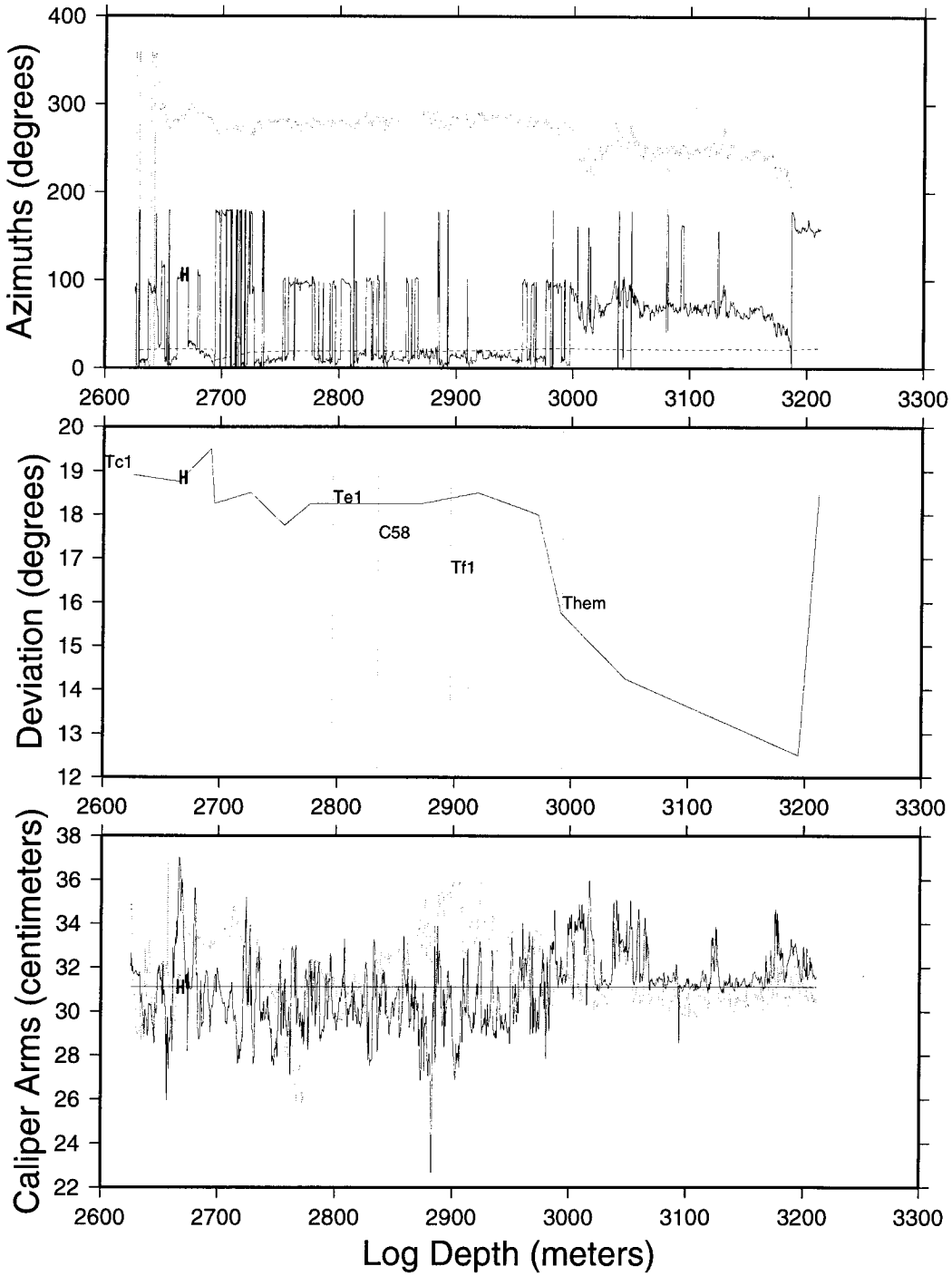

Figure B.78: Plots of the caliper-calibrated and declination-corrected digitized dipmeter and derived quantities data as a function of well depth from well Smgs8. (top) Borehole elongation direction (solid line), pad 1 azimuth (dotted line), and borehole azimuth (dashed line). (middle) Borehole deviation (solid curve) and location of marker horizons (vertical lines with labels). (bottom) Bit size (straight solid line), caliper arm 1 (solid line), and caliper arm 2 (dotted line). Selected breakout regions are plotted as horizontal bars showing the depth extent of the breakouts.

B.21 Smgs15

The dipmeter data for South Middle Ground Shoals 15 consists of a single paper well log which was digitized into the computer (Figure B.79). The dipmeter log extends from 3,225.7 to 3,931.8 m. The maximum observed borehole deviation in this section of hole is 43°. In-gauge sections of the hole longer than 0.5 m accounted for 132.1 m of the length of the hole.

Eleven breakouts totaling 56.5 m in length were identified in this section of hole. All but two of the eleven breakouts are within 15° of the high or low side of the hole (Figure B.80). Four of the identified breakouts occurred in the TE1 marker and all four are within 1.5° of the high side of the hole (Figure B.81). The remaining breakouts occurs in the TC3 (1 breakout for 3.5 m), and THEM (6 breakouts for 33.0 m) markers.

Since there are only two nonradial breakouts they are not plotted separately in 500 m TVD intervals.

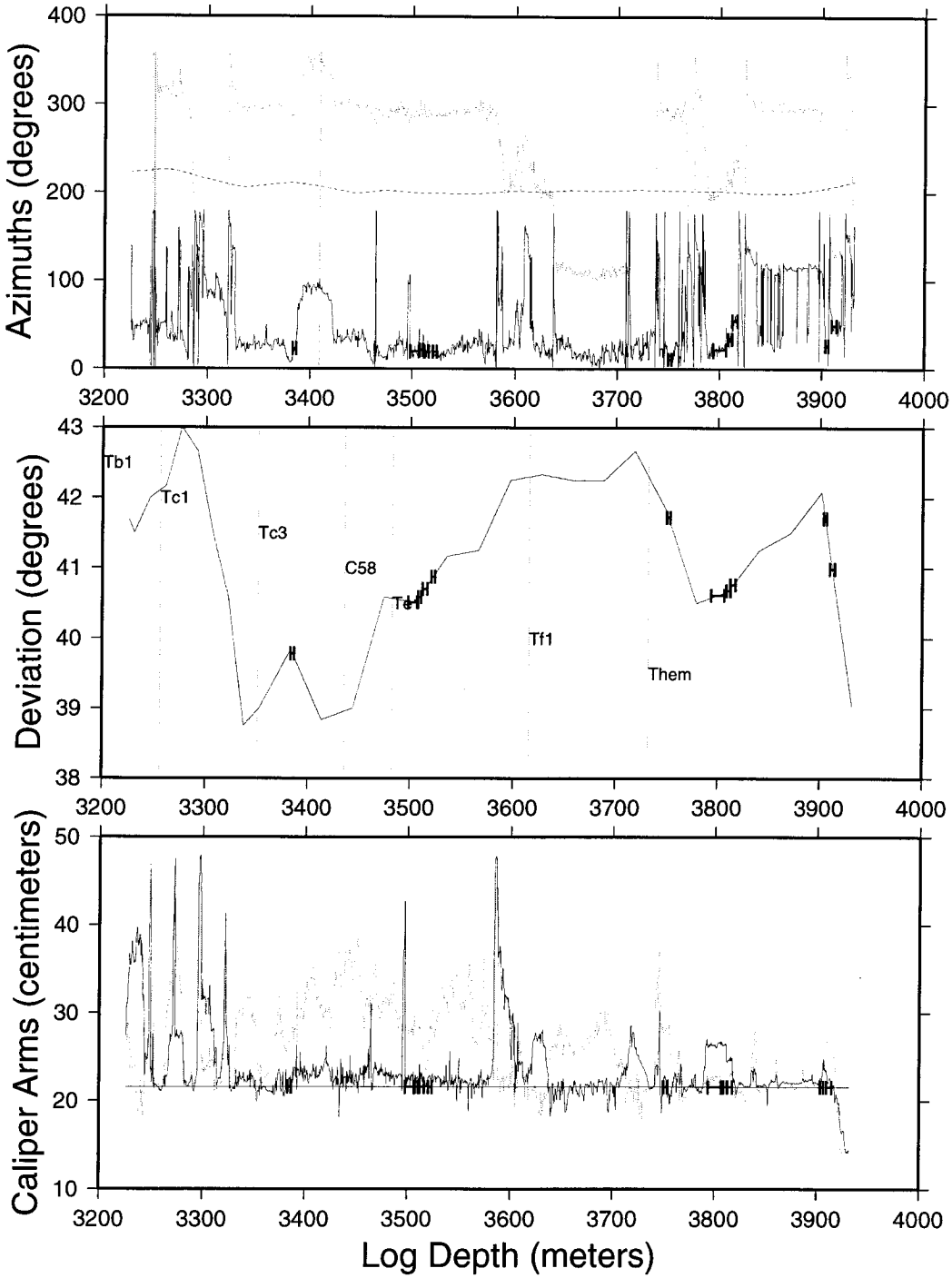

Figure B.79: Plots of the caliper-calibrated and declination-corrected digitized dipmeter and derived quantities data as a function of well depth from well Smgs15. (top) Borehole elongation direction (solid line), pad 1 azimuth (dotted line), and borehole azimuth (dashed line). (middle) Borehole deviation (solid curve) and location of marker horizons (vertical lines with labels). (bottom) Bit size (straight solid line), caliper arm 1 (solid line), and caliper arm 2 (dotted line). Selected breakout regions are plotted as horizontal bars showing the depth extent of the breakouts.

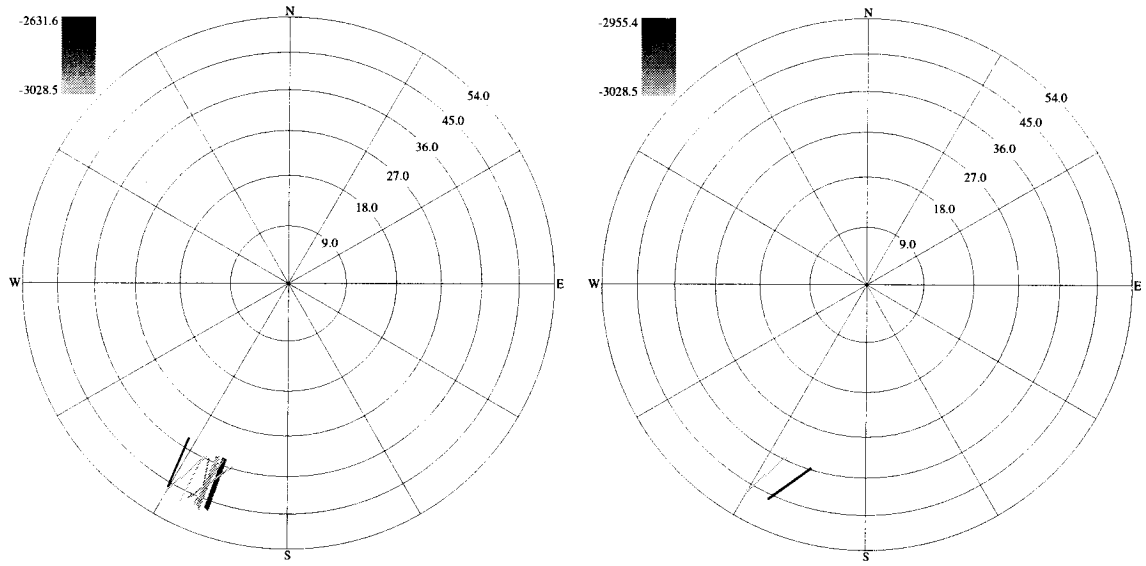

Figure B.80: Lower hemisphere stereographic projection plots of the selected breakouts from well Smgs15. Line widths are proportional to the breakout length. (left) All selected breakouts. (right) All nonradial breakouts where the **IJK** breakout angle is not within 15° of the high side of the hole.

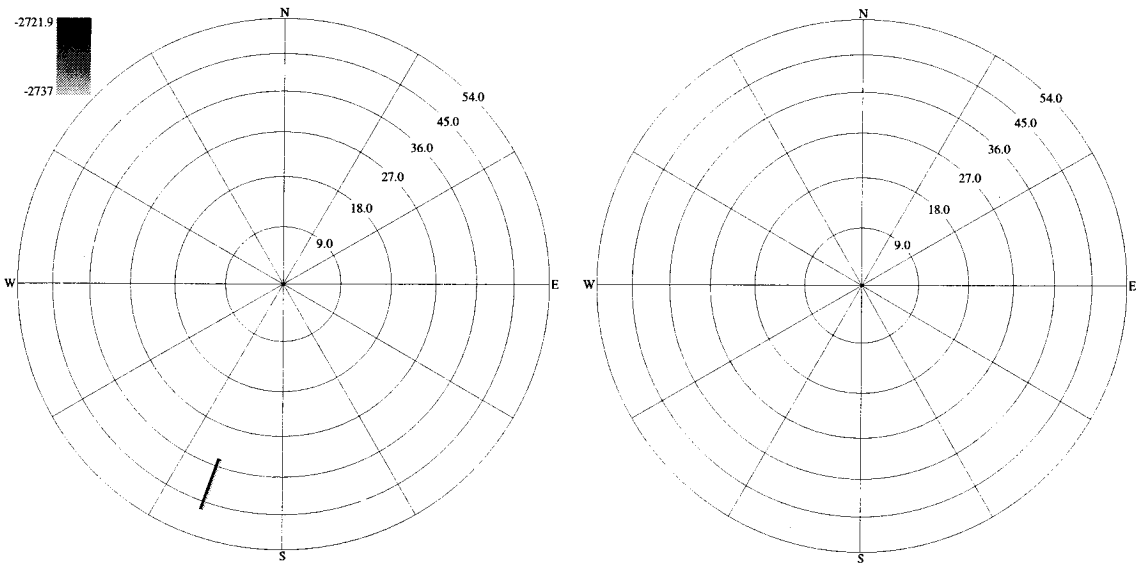

Figure B.81: Lower hemisphere stereographic projection plots of the selected breakouts from well Smgs15 in marker TE1. Line widths are proportional to the breakout length. (left) All selected breakouts in TE1. (right) All nonradial breakouts in TE1 where the **IJK** breakout angle is not within 15° of the high side of the hole.

Bibliography

Aadnoy, B. S., Inversion technique to determine the in-situ stress field from fracturing data, *J. Pet. Sci. Eng.*, *4*, 127–141, 1990a.

Aadnoy, B. S., In-situ stress direction from borehole fracture traces, *J. Pet. Sci. Eng.*, *4*, 143–153, 1990b.

Addis, T., D. Boulter, L. Roca-Ramisa, and D. Plumb, The quest for borehole stability in the Cusiana Field, Columbia, *Oilfield Review*, *5*(2), 33–43, 1993.

Angelier, J., Tectonic analysis of fault slip data sets, *J. Geophys. Res.*, *89*(B7), 5835–5848, 1984.

Bell, J. S., and D. I. Gough, Northeast-southwest compressive stress in Alberta: Evidence from oil wells, *Earth Planet. Sci. Lett.*, *45*(2), 475–482, 1979.

Bell, J. S., and D. I. Gough, The use of borehole breakouts in the study of crustal stress, in *Hydraulic Fracturing Stress Measurements*, edited by M. D. Zoback and B. C. Haimson, pp. 201–209, Nat. Acad. Press, Washington, D. C., 1983.

Bevington, P. R., *Data Reduction and Error Analysis for the Physical Sciences*, McGraw-Hill, New York, 1969.

Boss, R. F., R. B. Lennon, and B. W. Wilson, Middle Ground Shoal Oil Field, Alaska, in *North American Oil and Gas Fields*, no. 24 in AAPG Memoir, pp. 1–22, 1976.

Brent, R. P., *Algorithms for Minimization Without Derivatives*, Prentice-Hall, Englewood Cliffs, N. J., 1973.

Bruno, M. S., and D. F. Winterstein, Some influences of stratigraphy and structure on reservoir stress orientation, SPE 24746, Presented at *61st Annl Tech. Conf. of SPE,* Washington, DC, 1992.

Bunds, M. P., R. L. Bruhn, and W. T. Parry, Comparing nature and experiment at the top of the seismogenic zone: The Castle Mountain Fault, Alaska, http://www.mines.utah.edu/~wmgg/DeptPeople/Students/GradStudentBios/Bunds/BUNDS_POSTER/bunds.html.

Caldentey, C., and X. Lana, Implications of principal stress axes and eigenvalue ratios on critical orientation of fractures: Application to two tectonic regions in Alaska, *Pure And Applied Geophysics*, *133*(1), 87–102, 1990.

Clark, D. H., N. T. Hall, D. H. Hamilton, and R. G. Heck, Structural analysis of late Neogene deformation in the Central Offshore Santa Maria Basin, California, *J. Geophys. Res.*, *96*(B4), 6435–6457, 1991.

Crouch, J. K., S. B. Bachman, and J. T. Shay, Post Miocene compressional tectonics along the Central California Margin, in *Tectonics and Sedimentation Along the California Margin: Pacific Section S.E.P.M.*, edited by J. K. Crouch and S. B. Bachman, vol. 38, pp. 37–54, Soc. of Econ. Paleontol. and Mineral., Tulsa, Okla., 1984.

Daneshy, A. A., A study of inclined hydraulic fractures, *J. Soc. Pet. Eng.*, *13*, 61–68, 1973.

Davis, L., ed., *Genetic Algorithms and Simulated Annealing*, Morgan Kaufmann, San Francisco, Calif., 1987.

DeMets, C., R. G. Gordon, D. F. Argus, and S. Stein, Current plate motions, *Geophys. J. Int.*, *101*, 425–478, 1990.

Detterman, R. L., T. Hudson, G. Plafker, R. G. Tysdal, and J. M. Hoare, Reconnaissance geologic map along Bruin Bay and Lake Clark faults in Kenai and Tyonek Quadrangles, Alaska, *U.S. Geol. Surv. Open File Map*, *76-477*, 1976.

Estabrook, C. H., and K. H. Jacob, Stress indicators in Alaska, in *Neotectonics of North America, Decade Map*, edited by D. B. Slemmons, E. R. Engdahl, M. D. Zoback, and D. D. Blackwell, vol. 1, chap. 21, pp. 387–399, Geological Society of America, Boulder, Colorado, 1991.

Fairhurst, C., Methods of determining in situ rock stresses at great depths, *Tech. Rep. TRI-68*, Mo. River Div. Corps of Eng., Omaha, Neb., 1968.

Feigl, K. L., et al., Space geodetic measurement of crustal deformation in Central and Southern California, *J. Geophys. Res*, *98*(B12), 21,677–21,712, 1993.

Gephart, J. W., and D. W. Forsyth, An improved method for determining the regional stress tensor using earthquake focal mechanism data: Application to the San Fernando Earthquake sequence, *J. Geophys. Res.*, *89*(B11), 9305–9320, 1984.

Goldberg, D. E., *Genetic Algorithms in Search, Optimization, and Machine Learning*, Addison-Wesley, Reading, Mass., 1989.

Goldstein, H., *Classical Mechanics*, 2nd ed., Addison-Wesley, Reading, Mass., 1950.

Gough, D. I., and J. S. Bell, Stress orientation from oil-well fractures in Alberta and Texas, *Can. J. Earth Sci.*, *18*(3), 638–645, 1981.

Gough, D. I., and J. S. Bell, Stress orientations from borehole wall fractures with examples from Colorado, east Texas, and northern Canada, *Can. J. Earth Sci*, *19*, 1358–1370, 1982.

Haimson, B. C., and C. Fairhurst, In-situ stress determination at great depth by means of hydraulic fracturing, *Proc. U.S. Symp. Rock Mech.*, *11th*, 559–584, 1970.

Hiramatsu, Y., and Y. Oka, Stress around a shaft or level excavated in ground with a three-dimensional stress state, *Mem. Fac. Eng., Kyoto Univ.*, *24*, 56–76, 1962.

Hobbs, B. E., W. D. Means, and P. F. Williams, *An Outline of Structural Geology*, John Wiley, New York, 1976.

Holland, J. H., *Adaptation in Natural and Artificial Systems*, Univ. of Mich. Press, Ann Arbor, 1975.

Huang, W., Seismic strain rates and the state of tectonic stress in the southern california region, Ph.D. thesis, California Institute of Technology, 1995.

Hubbert, M. K., and D. G. Willis, Mechanics of hydraulic fracturing, *J. Pet. Technol.*, *9*(6), 153–168, 1957.

Jaeger, J. C., and N. G. W. Cook, *Fundamentals of Rock Mechanics*, 3rd ed., Chapman and Hall, New York, 1979.

Jolly, A. D., R. A. Page, and J. A. Power, Seismicity and stress in the vicinity of Mount Spurr volcano, south central Alaska, *J. Geophys. Res.*, *99*(B8), 15305–15318, 1994.

Kirsch, G., Die Theorie der Elastizität und die Defurfnisse der Fertigkeirslehre, *VDI Z.*, *42*, 797, 1898.

Laughbaum, G. H., C. A. Lyon, R. E. Barker, H. C. Hixson, J. H. McKeever, V. L. Vigoren, D. E. Atchison, and D. Adams, *Oil and gas fields in the Cook Inlet basin, Alaska*, Alaska Geological Society, Anchorage, Alaska, 1970.

Little, T. A., and C. W. Naeser, Tertiary tectonics of the Border Ranges fault system, Chugach Mountains, Alaska: Deformation and uplift in a forearc setting, *J. Geophys. Res*, *94*(B4), 4333–4359, 1989.

Lu, Z., M. Wyss, and H. Pulpan, Details of stress directions in the Alaska subduction zone from fault plane solutions, *J. Geophys. Res.*, *102*(B3), 5385–5402, 1997.

Magoon, L. B., Petroleum resources in Alaska, in *The Geology of Alaska*, edited by G. Plafker and H. C. Berg, vol. G-1 of *The Geology of North America*, chap. 30, pp. 311–366, Geological Society of America, 1994.

Mardia, K. V., *Statistics of Directional Data*, Academic, San Diego, Calif., 1972.

Mastin, L., Effect of borehole deviation on breakout orientations, *J. Geophys. Res.*, *93*(B8), 9187–9195, 1988.

Mastin, L. G., The development of borehole breakouts in sandstone, Master's thesis, Stanford Univ., Stanford, Calif., 1984.

McCrory, P. A., D. S. Wilson, J. C. Ingle, and R. G. Stanley, Neogene geohistory analysis of Santa Maria Basin, California, and its relationship to transfer of central California to the Pacific plate, *U.S. Geol. Surv. Bull., 1995-J*, 1995.

McCulloch, D. S., Regional geology and hydrocarbon potential of offshore central California, in *Geology and Resource Potential of the Continental Margin of Western North America and Adjacent Ocean Basins: Beaufort Sea to Baja California*, edited by D. W. Scholl, A. Grantz, and J. G. Vedder, vol. 6 of *Earth Sci. Ser.*, chap. 16, pp. 353–401, Circum-Pac. Counc. for Energy and Miner. Resour., Houston, Tex., 1987.

Michael, A. J., Determination of stress from slip data: Faults and folds, *J. Geophys. Res.*, *89*(B13), 11517–11526, 1984.

Michael, A. J., Use of focal mechanisms to determine stress: A control study, *J. Geophys. Res.*, *92*(B1), 357–368, 1987.

Michael, A. J., and B. R. Julian, Measuring the difference between two fault plane solutions, *unpublished manuscript*, 1994, Derivation of and C code calculating the rotation vector used to rotate one fault plane solution to another.

Miller, T. P., and D. H. Richter, Quaternary volcanism in the Alaska Peninsula and Wrangell Mountains, Alaska, in *The Geology of Alaska*, edited by G. Plafker and H. C. Berg, vol. G-1 of *The Geology of North America*, chap. 24, pp. 759–779, Geological Society of America, 1994.

Moos, D., and M. D. Zoback, Utilization of observations of well bore failure to constrain the orientation and magnitude of crustal stresses: Application to continental, Deep Sea Drilling Project and Ocean Drilling Project boreholes, *J. Geophys. Res.*, *95*(B6), 9305–9325, 1990.

Mount, V. S., and J. Suppe, Present-day stress orientations adjacent to active strike-slip faults: California and Sumatra, *J. Geophys. Res.*, *97*(B8), 1995–2013, 1992.

Nakamura, K., G. Plafker, K. H. Jacob, and J. N. Davies, A Tectonic stress trajectory map of Alaska using information from volcanoes and faults, *Bulletin of the Earthquake Research Institute*, (55), 89–100, 1980.

Nokleberg, W. J., G. Plafker, and F. H. Wilson, Geology of south-central Alaska, in *The Geology of Alaska*, edited by G. Plafker and H. C. Berg, vol. G-1 of *The Geology of North America*, chap. 10, pp. 311–366, Geological Society of America, 1994.

Page, R. A., N. N. Biswas, J. C. Lahr, and H. Pulpan, Seismicity of continental Alaska, in *Neotectonics of North America, Decade Map*, edited by D. B. Slemmons, E. R. Engdahl, M. D. Zoback, and D. D. Blackwell, vol. 1, chap. 4, pp. 47–68, Geological Society of America, Boulder, Colorado, 1991.

Parker, R. L., and M. K. McNutt, Statistics for the one-norm misfit measure, *J. Geophys. Res.*, *85*(B8), 4429–4430, 1980.

Peška, P., and M. D. Zoback, Compressive and tensile failure of inclined well bores and determination of in-situ stress and rock strength, *J. Geophys. Res.*, *100*(B7), 12,791–12,811, 1995.

Plafker, G., J. C. Moore, and G. R. Winkler, Geology of the southern Alaska margin, in *The Geology of Alaska*, edited by G. Plafker and H. C. Berg, vol. G-1 of *The Geology of North America*, chap. 12, pp. 389–449, Geological Society of America, 1994.

Plumb, R. A., and S. H. Hickman, Stress-induced borehole elongation: A comparison between the four-arm dipmeter and the borehole televiewer in the Auburn Geothermal well, *J. Geophys. Res.*, *90*(B7), 5513–5522, 1985.

Press, W. H., S. A. Teukolsky, W. T. Vetterling, and B. P. Flannery, *Numerical Recipes in C*, 2nd ed., Cambridge University Press, 1992.

Qian, W., and L. B. Pedersen, Inversion of borehole breakout orientation data, *J. Geophys. Res.*, *96*(B12), 20,093–20,107, 1991, (Correction, *J. Geophys. Res.*, *99*(B1), 707–710, 1994).

Ratchkovsky, N. A., J. Pujol, and N. N. Biswas, Relocation of shallow earthquakes in southern Alaska using Joint Hypocenter Determination method, *Journal of Seismology*, 1997, submitted.

Richardson, R. M., Hydraulic fracture in arbitrarily oriented boreholes: An analytic approach, in *Hydraulic Fracturing Stress Measurements*, edited by M. D. Zoback and B. C. Haimson, pp. 167–175, Nat. Acad. Press, 1983.

Schmoll, H. R., L. A. Yehle, C. A. Gardner, and J. K. Odum, *Guide to Surficial Geology and Glacial Stratigraphy in the Upper Cook Inlet Basin*, Alaska Geological Society, Anchorage, Alaska, 1984.

Shamir, G., and M. D. Zoback, Stress orientation profile to 3.5 km depth near the San Andreas fault at Cajon Pass, *J. Geophys. Res.*, *97*(B4), 5059–5080, 1992.

Sorlien, C. C., Structure and Neogene evolution of the Southern offshore Santa Maria Basin and Western Santa Barbara Channel, California, Ph.D. thesis, Univ. of Cailf., Santa Barbara, 1994.

Stock, J. M., J. H. Healy, S. H. Hickman, and M. D. Zoback, Hydraulic fracturing stress measurements at Yucca Mountain, Nevada, and relationship to the regional stress field, *J. Geophys. Res.*, *90*(B10), 8691–8706, 1985.

Timoshenko, S., and J. Goodier, *Theory of Elasticity*, McGraw-Hill, New York, 1970.

Vardoulakis, I., J. Sulem, and A. Guenot, Borehole instabilities as bifurcation phenomena, *Int. J. Rock. Mech. Min. Sci. & Geomech. Abstr.*, *25*(3), 159–170, 1988.

Varga, R. J., and R. G. Hickman, Fracture study of core from the Unocal #A-1 well, Pt. Pedernales Field, California, *Tech. Rep. ER-BE 92-17M*, unpublished Unocal Science & Technology Division Technical Memorandum, 1992.

Vernik, L., and M. D. Zoback, Estimation of maximum horizontal principal stress magnitude from stress-induced well bore breakouts in the Cajon Pass Scientific Research Borehole, *J. Geophys. Res.*, *97*(B4), 5109–5119, 1992.

Wahrhaftig, C., S. Bartsch-Winkler, and G. D. Stricker, Coal in Alaska, in *The Geology of Alaska*, edited by G. Plafker and H. C. Berg, vol. G-1 of *The Geology of North America*, chap. 31, pp. 937–978, Geological Society of America, 1994.

Youngdahl, C. K., and E. Sternberg, Three-dimensional stress concentration around a cylindrical hole in a semi-infinite elastic body, *J. Appl. Mech.*, *33*, 855–865, 1966.

Zajac, B., and J. M. Stock, Using borehole breakouts to constrain the complete stress tensor (abstract), *EoS Trans. AGU*, *73*(43), 559, 1992.

Zajac, B. J., and J. M. Stock, Using borehole breakouts to constrain the complete stress tensor: Results from the Sijan Deep Drilling Project and offshore Santa Maria Basin, California, *J. Geophys. Res.*, *102*(B5), 10,083–10,100, 1997.

Zemanek, J., E. E. Glenn, L. J. Norton, and R. L. Caldwell, Formation evaluation by inspection with the borehole televiewer, *Geophysics*, *35*(2), 254–269, 1970.

Zheng, Z., J. Kemeny, and N. G. W. Cook, Analysis of borehole breakouts, *J. Geophys. Res.*, *94*(B6), 7171–7182, 1989.

Zoback, M. D., and J. H. Healy, In situ stress measurements to 3.5 km depth in the Cajon Pass Scientific Research Borehole: Implications for the mechanics of crustal faulting, *J. Geophys. Res.*, *97*(B4), 5039–5057, 1992.

Zoback, M. D., and M. L. Zoback, Tectonic stress field of North America and relative plate motions, in *Neotectonics of North America, Decade Map*, edited by D. B. Slemmons, E. R. Engdahl, M. D. Zoback, and D. D. Blackwell, vol. 1, chap. 19, pp. 339–366, Geological Society of America, Boulder, Colorado, 1991.

Zoback, M. D., D. Moos, and L. Mastin, Well bore breakouts and in situ stress, *J. Geophys. Res*, *90*(B7), 5523–5530, 1985.

Zoback, M. L., 1st-order and 2nd-order patterns of stress in the lithosphere: The World Stress Map Project, *J. Geophys. Res.*, *97*(B8), 1703–1728, 1992.

Zoback, M. L., and M. D. Zoback, State of stress in the conterminous United States, *J. Geophys. Res.*, *85*(B11), 6113–6156, 1980.

Zoback, M. L., et al., Global patterns of intraplate stress: A status report on the world stress map project of the International Lithosphere Program, *Nature*, *341*(6240), 291–298, 1989.